

A Dinuclear Dihydride Complex for Bimetallic Reductive Activation and Transformation of A Range of Inert Substrates



Dissertation
For the award of the degree
“Ph.D. Division of Mathematics and Natural Sciences”
of the Georg-August-Universität Göttingen
Within the doctoral program
Chemistry
of the Georg-August-Universität School of Science (GAUSS)
Submitted by
Peng-Cheng Duan
From Hubei, P. R. China
Göttingen 2017

Thesis Committee

Prof. Dr. Franc Meyer

Institute of Inorganic Chemistry, Georg-August University Göttingen

Prof. Dr. Sven Schneider

Institute of Inorganic Chemistry, Georg-August University Göttingen

Members of the Examination Board

Reviewer: Prof. Dr. Franc Meyer

Institute of Inorganic Chemistry, Georg-August University Göttingen

Second Reviewer: Prof. Dr. Sven Schneider

Institute of Inorganic Chemistry, Georg-August University Göttingen

Further members of the Examination Board

Prof. Dr. Dietmar Stalke

Institute of Inorganic Chemistry, Georg-August University Göttingen

Prof. Dr. Manuel Alcarazo

Institute of Organic and Biomolecular Chemistry, Georg-August University Göttingen

Prof. Inke Siewert

Institute of Inorganic Chemistry, Georg-August University Göttingen

Jun.-Prof. Dr. Selvan Demir

Institute of Inorganic Chemistry, Georg-August University Göttingen

Date of the oral examination: 10:00 Am, 13th.Dec.2017

Contents

Chapter 1 General Introduction	1
1.1 Nickel-based Enzyme System	1
1.2 β -Diketiminato and pyrazole chemistry background	2
1.3 Preliminary work	5
Chapter 2 Objective	7
Chapter 3 Pairwise H₂/D₂ Exchange Mechanism Study	9
3.1 Introduction	10
3.2 Synthesis of sodium dinuclear nickel(II) dihydride complex	13
3.3 Dissociation hydride-K ⁺ interaction in bimetallic dinickel(II) complex ..	28
3.4 Kinetics of H ₂ /D ₂ exchange	36
3.5 Summary	40
Chapter 4 Dioxygen binding to a bimetallic dinickel(II) dihydride complex and redox interconversion of the μ-1,2-peroxo and superoxo intermediates	42
4.1 Introduction	43
4.2 Synthesis of a μ -1,2-peroxo bridged dinickel(II) complex	48
4.3 Dissociation the peroxo-K ⁺ interaction in bimetallic dinickel(II) complex	57
4.4 Synthesis of an μ -1,2-superoxo bridged dinuclear nickel(II) complex.....	63
4.5 Cleavage the oxygen-oxygen bond.....	72
4.6 Summary	76
Chapter 5 Disulfur binding to the dinuclear nickel(II) dihydride and stepwise transformation to the sulfide-ligand-radical	77
5.1 Introduction	78
5.2. Synthesis of a μ -1,2-disulphide dinuclear nickel(II) complex	80
5.3 Synthesis of a hydrosulfide dinuclear nickel(II) complex	86
5.4 Synthesis of μ -1,1-sulfide nickel(II) complex.....	89
5.5 Synthesis of a μ -1,1-sulfide radical nickel(II) complex.....	96
5.6 Summary	104

Chapter 6 Deprotonation and Isomerization of Phenylhydrazine in the dinuclear nickel(II) complex	106
6.1 Introduction	107
6.2 Synthesis of phenylhydrazido bridged complex	108
6.3 Deprotonation of phenylhydrazido bridge complex.....	113
6.4 Dissociation the phenylhydrazido-K ⁺ interaction in bimetallic nickel(II) complex.....	119
6.5 Dehydrogenation and protonation of phenylhydrazine bridge complex.....	124
6.6 Summary	127
Chapter 7 Azobenzene Activation	128
7.1 Introduction	129
7.2 Two electron reduction the azobenzene	130
7.2 One electron reduction of azobenzene	133
7.4 Summary	141
Chapter 8 N₂ to NH₃ Conversion in the dinuclear nickel(II) cofactor	142
8.1 Introduction	143
8.2 Synthesis [N ₂] ⁻ monoanionic radical	148
8.3 Hydrogen atom transfer to dinitrogen monoanionic radical	163
8.4 Cleavage of N-N double bonds	170
8.5 Protonation of hydrazido bridge complex.....	174
8.6 Synthesis the diazenido complex.....	178
8.7 Synthesis of terminal ammonia nickel complex.....	182
8.8 X-ray emission spectroscopy	185
8.9 Summary	190
Chapter 9 CO activation	192
9.1 Introduction	193
9.2 Synthesis carbon monoxide radical	194
9.3 Summary	201

Chapter 10 Metal-ligand Cooperation in C-H and H₂ Activation and Interconversion between Mono- and Dihydride Dinickel(II) Complexes and Reactivity.....	202
10.1 Introduction.....	203
10.2 Synthesis of nickel bromide precursor	204
10.3 Synthesis of bimetallic dinickel(II) monohydride complex	206
10.4 Synthesis of bimetallic dinickel(II) dihydride complex	210
10.5 Reactivity towards water	215
10.6 Reactivity towards lutidinium triflate	219
10.7 Summary.....	222
Chapter 11 Experimental Section	223
11.1 Material and Methods	223
11.2 Experiment.....	228
11.2.1 Synthesis of Ligand Precursors and Ligands	228
11.2.2 Complexes Syntheses	232
Chapter 12 DFT Calculations	266
Chapter 13 Crystallography	302
Chapter 14 Appendix.....	313
ESI-MS, NMR, IR, UV-Vis Spectra, SQUID and X-ray structures	313
Reference	347
List of Abbreviations	362
Formula Overview	364
Scientific Contribution.....	369
Acknowledgement.....	371
Curriculum Vitae.....	373

Chapter 1 General Introduction

1.1 Nickel-based Enzyme System

Seven out of the eight known nickel enzymes play important roles in the usage and/or production of gases (H_2 , O_2 , CO_2/CO , CH_4 and NH_3) (**Figure 1**) in the global biological C, N and O cycles. [1] For examples, Hydrogenase generates/utlized hydrogen gas; Ni-SOD generates oxygen; CODH interconverts CO and CO_2 ; ACS utilizes CO; MCR generates methane; urease produces ammonia (**Table 1**). [1] It has been found that the nickel sites in enzymes exhibit extreme plasticity in nickel coordination and redox chemistry.

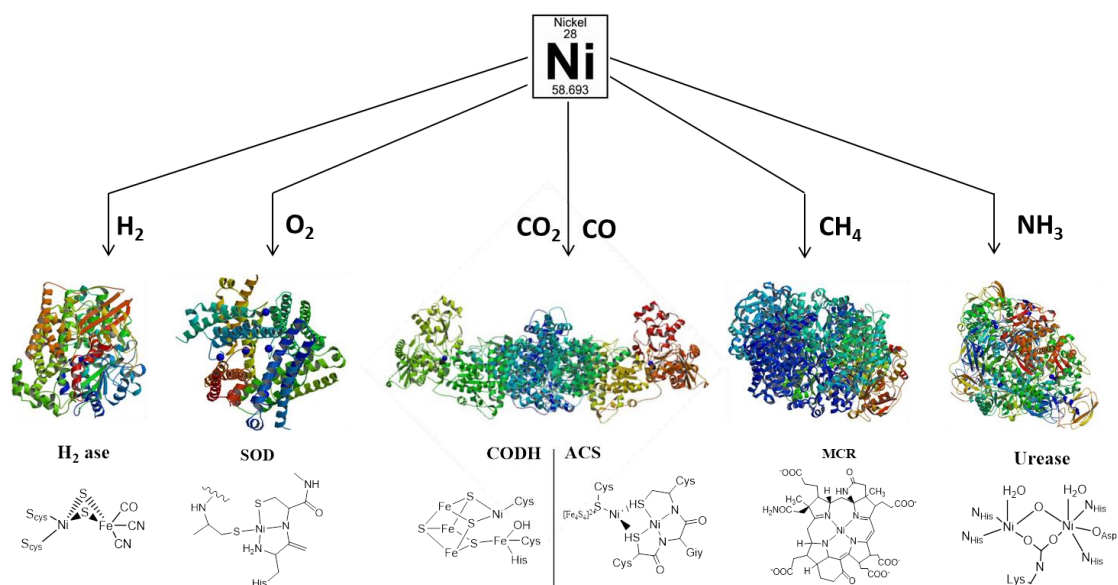


Figure 1: Selected nickel-containing enzyme systems involved in the regulation of global gas cycles and energy conversion processes.

Table 1: Nickel-containing enzymes.

Enzyme	Reaction
Hydrogenase	$2H^+ + 2e^- \rightleftharpoons H_2$ ($\Delta E^0 = -414$ mV)
Ni-SOD	$2H^+ + 2O_2 \rightarrow H_2O_2 + O_2$
CODH	$2H^+ + 2e^- + CO_2 \rightleftharpoons CO + H_2O$ ($\Delta E^0 = -558$ mV)
ACS	$CH_3-CFeSP + CoASH + CO \rightarrow CH_3-CO-SCoA + CFeSP$

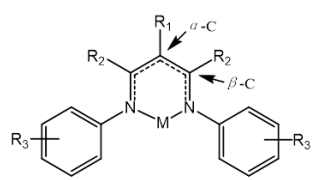
Urease	$\text{H}_2\text{N-CO-NH}_2 + 2\text{H}_2\text{O} \rightarrow 2\text{NH}_3 + \text{H}_2\text{CO}_3$
Glx I	Methylglyoxal \rightarrow Lactate + H_2O
ARD	1,2-Dihydroxy-3-oxo-5-(methylthio)pent-1-ene + O_2 \rightarrow HCOOH + Methylthiopropionate + CO
MCR	$\text{CH}_3\text{-COM} + \text{CoBSH} \rightarrow \text{CH}_4 + \text{CoM-SS-CoB}$

Although limited in number, Ni-containing enzymes exhibit a rich diversity of metalcenter structures and participate in a variety of important reactions. Several of the Ni-dependent enzymes require auxiliary proteins that participate in Ni delivery for metalcenter assembly or organometallic cofactor synthesis. Clearly, many exciting avenues of investigation exist for those interested in Ni! Therefore, understanding bio-related Ni chemistry is very useful.

1.2 β -Diketiminato and pyrazole chemistry background

The β -diketiminato unit (often called “nacnac” because of its addition of two nitrogen atoms to the common acac ligand) has gained great attention as a supporting ligand because the properties and reactions of the metal complexes are highly dependent since its introduction in 1968. [2] Backbone (β -C) or the N-aryl substituents influence the β -diketiminato sterics. The common substituents at the backbone are methyl, ^tBu or CF_3 . The N-aryl substituents of β -diketiminato ligands often contain Dipp, Tipp, Dep and Mes and so on (**Figure 2**). [3] N-Aryl β -diketiminato ligands have been most widely used, and they support a variety of metals in many oxidation states. Complexes of N-aryl β -diketiminato ligands have shown great reactivity and selectivity for a variety of methodologies, [4] including polymerization and functionalization of alkenes and cross-coupling reactions. In addition, late transition metal β -diketiminato complexes, such as Fe, Co and Ni, have been used to build low coordinate metal centers, mimicking the active sites of metalloproteinase. [5] Some late transition metal β -diketiminato complexes undergo monomer-dimer equilibrium that are highly sensitive toward the nature

of the aryl substituents in the β -diketiminato ligand. As the dinuclear active species, some bis(β -diketiminato) ligands (**Figure 3, I, II and III**) were designed in recent years. [6]



Dipp	2,6-diisopropylphenyl
Tipp	2,4,6-triisopropylphenyl
Dep	2,6-diethylphenyl
Mes	2,4,6-trimethylphenyl
An	1-anthracenyl
ArF	3,5-bis(trifluoromethyl)phenyl
Tbt	2,4,6-tris[bis(trimethylsilyl)]phenyl

Figure 2: Substituent patterns and abbreviations in β -diketiminato ligands.

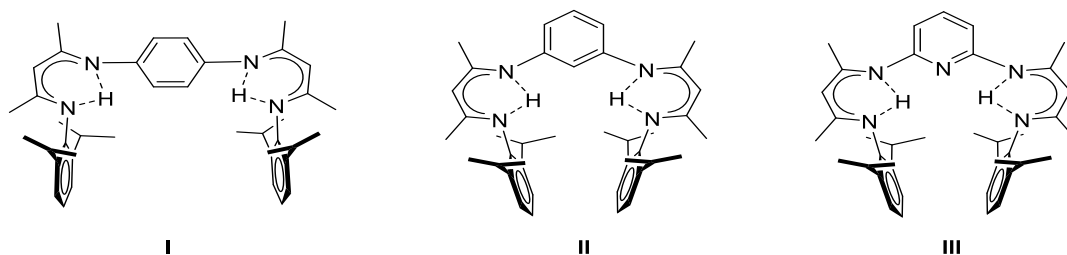


Figure 3: Some new bis(β -diketiminato) ligands reported in literatures.[6]

Pyrazolate ligands have rich coordination chemistry that includes *exo*-bidentate bridging (μ - $\eta^1:\eta^1$), terminal monodentate (η^1), *endo*-bidentate (η^2) and side-on, pentadentate (η^3) coordination modes (**Figure 4**). [7] In Meyer group, pyrazole-based ligands with a variety of chelating side arms represent valuable bridging scaffolds for pre-organizing two metal centers in a fashion which allows for metal-metal cooperativity during substrate transformations. [8] The metal...metal distance can be controlled by varying the length of the chelating side arms, short lengths favoring large inter-metallic distances and vice versa. [8] Several pyrazolate-bridged binuclear first-row transition metal complexes have recently appeared in literature. [8,9]

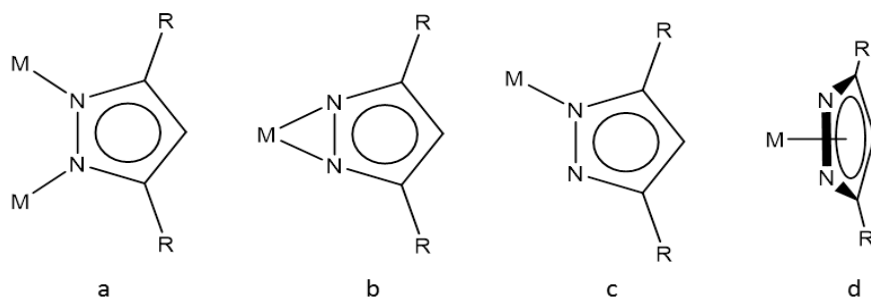


Figure 4: Typical coordination modes of pyrazolate ligands (R=H, alkyl, or aryl) towards metal ions (M, M'). a) exo-bidentate; b) endobidentate; c) monodentate; d) pentadentate.

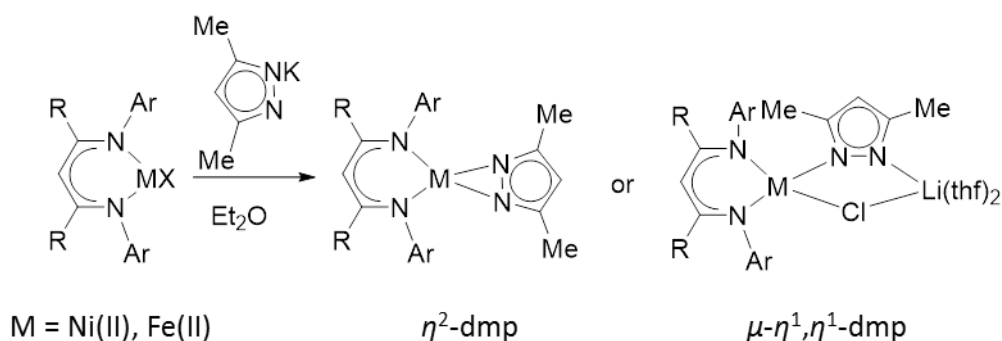
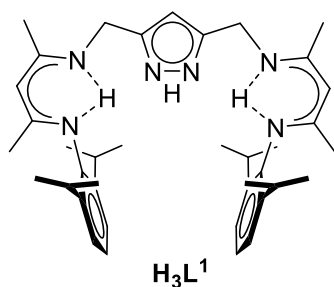


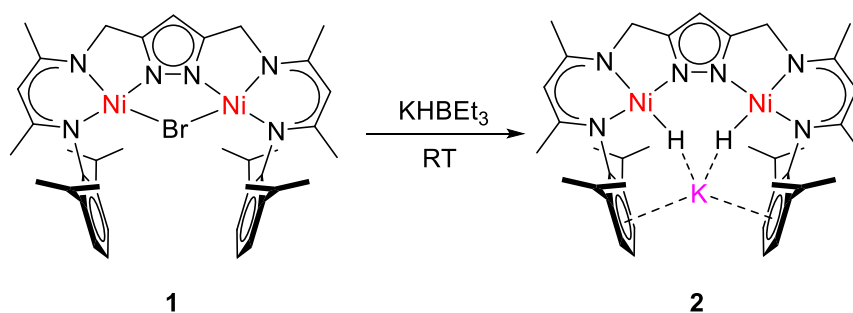
Figure 5: β -Diketiminato combine with pyrazole complexes in literature. ^[10]

The first bulky β -diketiminato combine with pyrazole complexes were reported in 2006 by *Holland* (**Figure 5**). ^[10] In this work, both η^1 and η^2 coordination to iron(II) and nickel(II) can be observed in the pyrazolate by the diketiminato ancillary ligand used. Account of the pyrazolate and β -diketiminato work, a new dinucleating scaffold **H₃L¹** (L¹ = $[\{\text{NC}(\text{Me})\text{C}(\text{H})\text{C}(\text{Me})\text{NC}_6\text{H}_3(\text{iPr})_2(\text{CH}_2)\}_2(\text{C}_3\text{N}_2\text{H})\}^{3-}$) (**Scheme 1**) that features a central pyrazolate bridging two-diketiminato compartments was introduced by *Manz*. ^[11]



Scheme 1: The scaffold was developed and employed as H_3L^1 by Manz.^[11]

1.3 Preliminary work



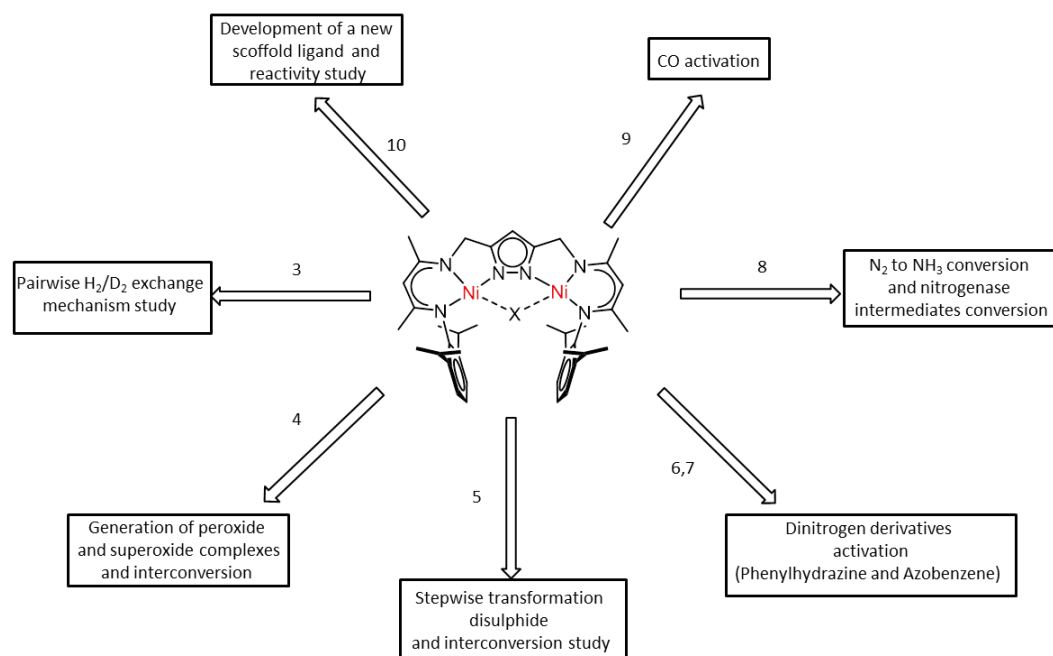
Scheme 2: Synthetic procedure for **2**.

Manz was able to synthesize a new dinucleating ligand scaffold comprising two nacnac compartments spanned by a central pyrazolate-bridge (H_3L^1). The bimetallic dinickel(II) dihydride complex **2** has been synthesized already from **1** with 2.5 equivalents KHBET_3 and characterized intensively.^[11] Complex **2** was determined by x-ray diffraction and showed pairwise H_2/D_2 exchange without H/D scrambling. Furthermore, it has been exploited for the reaction of $\mathbf{2}^-$ or $[\mathbf{2-D}]^-$ with phenylacetylene. Treating $[\mathbf{2-D}]^-$ with phenylacetylene leads to D_2 formation and two-fold reduction of the substrate, giving a product complex with unusual styrene-1,2-diyl bridging unit in the bimetallic pocket.^[11] Large parts of the project have recently published in Journal of the American Chemical Society (JACS), together with results from the present work. Parts of chapter 3 of the present monograph have been adapted from this publication with permission from ACS and from *Manz* doctoral thesis.^[11]

For the pairwise H₂/D₂ exchange, however, it is unknown whether the K⁺ cation plays an important role in the process or not. Extensive experiments have now been performed in order to understand the H₂/D₂ exchange mechanism. In addition, *Manz* produced complexes [L¹Ni₂(N_xH_y)]^{z-} that contain bridging units N₂H₃(1-), N₂H₂(2-), N₂H(1-) and NH₂(1-) relevant to intermediates of the nitrogenase mechanism, which are derived from N₂H₄ with **1**. [11a] A new way to these nitrogenase intermediates from the dinitrogen molecule will be discussed in this doctoral thesis.

Chapter 2 Objective

Molecules like H_2 , N_2 , O_2 , CO , CO_2 , NO and N_2O and so on are small but fascinating, universal and easily available. These molecules are involved in elementary reactions relevant to the efficient and reversible storage of energy. [12] The activation of these small molecules has a significant impact in biology, medicine, industry catalysis and environment protection. Mastering the chemistry of those molecules represents a prime challenge in the 21st century.



Scheme 3: Goals of the work, using the dinuclear dinickel complexes; the numbers above the arrows corresponding to the chapters.

The bimetallic dinuclear nickel(II) dihydride complex showed pairwise H_2/D_2 exchange without H/D scrambling property. [11] However, still some questions have left unanswered. This represented a starting point for this work. As depicted in **Scheme 3**, the results of this project are described in chapter 3.

In addition, reactivity towards phenylacetylene from **2** was further exploited by *Manz*. [11] Treating $[2-D]^-$ with phenylacetylene leads to D_2 formation and

two-fold reduction of the substrate, giving a product with unusual styrene-1,2-diyl bridging unit in the bimetallic pocket. Inspired by the H₂/D₂ exchange mechanism studies and phenylacetylene activation, reductive activation of O₂ was our first goal (chapter 4).

Owing to their importance, respective peroxo as well as persulfido complex have attracted much attention, resulting in a vast number of complexes for structural reactivity studies. In chapter 5, the dinuclear disulfido complex and its reactivity will be elaborately discussed.

Studies on the reactivity of the dinuclear nickel(II) dihydride complex towards dinitrogen (N₂) are explained in chapter 8. When providing an extra proton, **2** showed reactivity to the inert N₂ molecule and allows to isolate the exclusive [N₂]⁻ monoanionic radical complex which is characterized by x-ray diffraction and various spectroscopies. Moreover, N₂ to NH₃ conversion was studied in this doctoral thesis. Other nitrogenase intermediates (N₂H₄, N₂H₃, N₂H₂ and NH₂) were isolated in the system. These works are presented in chapter 8. The reactivity of [N₂]⁻ monoanionic radical complex towards carbon monoxide, as the isoelectronic species of N₂, has been also investigated and is described in chapter 9.

At last (chapter 10), a new scaffold ligand with bulky phenyl groups in the substituents was synthesized. The new system is similar to **H₃L¹**, thus allowed us to compare between the two related dinuclear nickel(II) hydride complexes and their reactivity.

Chapter 3 Pairwise H₂/D₂ Exchange Mechanism Study

Abstract: A new dinuclear nickel(II) dihydride complex Na[L¹Ni₂^{II}(H)₂] (**3**) was formed from nickel bromide precursor (**1**) with NaHBET₃ in THF solution. The dinuclear nickel(II) dihydride species shows pairwise H₂/D₂ exchange, just as with the complex K[L¹Ni₂^{II}(H)₂] (**2**). A mechanistic picture was provided by DFT calculations which suggested facile recombination of the two hydrides within the bimetallic cleft, with a moderate enthalpy barrier of ~62 kJ/mol, to produce H₂ and an antiferromagnetically coupled [L¹Ni₂]⁻ species. Interaction with the Lewis acid cation (Na⁺ or K⁺) significantly stabilizes the dihydride core. Treatment of **2** with dibenzo(18-crown-6) (DB18C6) led to the separated ion pair [L¹Ni₂^{II}(H)₂][K(DB18C6)] (**4**). The new [L¹Ni₂^{II}(H)₂][K(DB18C6)] (**4**) species could easily remove H₂ in the solid state, which was confirmed by SQUID and headspace GC experiments. Kinetic data for the M[L¹(Ni-H)₂] → H₂ transition derived from 2D ¹H EXSY spectra confirmed first-order dependence of H₂ release on **2** or **3** concentration and a strong effect of the alkali metal cation M⁺. Complex [L¹Ni₂^{II}(H)₂]⁻ having two adjacent terminal hydrides thus represents a masked version of a highly reactive dinuclear nickel(I) core.

3.1 Introduction

Hydride complexes of transition metals play an important role in organometallic chemistry especially related to homogeneous catalysis. [13] It often function as key intermediates for transferring proton (H⁺), hydrogen atom (H[•]), or hydride (H⁻) between molecules. Hydride complexes are also implicated in biological inorganic chemistry, where hydrides are known or thought to be present in key intermediates in H₂ utilization by hydrogenases^[14] and in N₂ reduction by iron-molybdenum nitrogenases. [15]

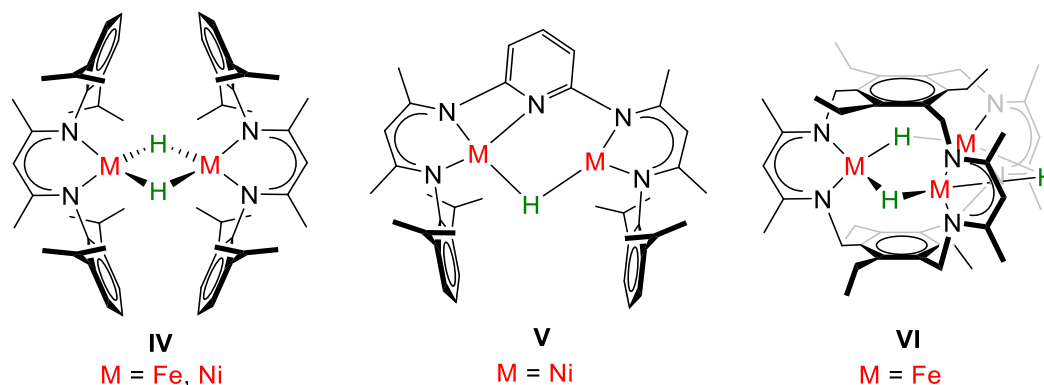


Figure 6: Selected examples of iron(II) and nickel(I/II) hydride complexes supported by β -diketiminato ligands.^[17-22]

The nitrogenase background provides a strong impetus for synthetic efforts targeting the use of transition metal hydrides as masked low-valent complexes capable of reductively activating small molecules. [16] β -Diketiminato ligands have proven extremely valuable in this content, and a particularly rich chemistry has evolved from the iron and nickel type **IV** complexes with $M(\mu\text{-H})_2M$ core mainly developed by the groups of *Holland* and *Limberg*, respectively (**Figure 6**; including variants thereof with other aryl and backbone substituents). [5c, 17] These bimetallic hydrides were shown to readily eliminate H₂ when treated with external donors or upon heating, leading to a variety of iron(I) and nickel(I) complexes.^[18, 19] Several other metal hydride complexes bearing polydentate or polyhapto ligands have been prepared using the super hydride route.^[20]

Bis(β -diketiminato)pyridine-ligated dinuclear nickel(II) hydride complex (PYP)-Ni(μ -H)Ni (**Figure 6, V**) has an unique Ni-H \rightarrow Ni core, which can be generated from (PYP)-Ni(μ -Br)NiBr with KHBET₃.^[20b] Diiron dihydride complex (PYP)-Fe₂(μ -H₂) was obtained from the reaction of (PYP)-Fe₂(μ -Br₂) and KHBET₃ at room temperature using the same ligand system.^[20d]

A cyclophane type scaffold containing three β -diketiminato binding pockets, developed recently by *Murray* and coworkers, gave access to tris(μ -hydride) trimetallic clusters such as the tri-iron(II) complex **VI (Figure 6)**.^[21] The latter showed CO-induced reductive elimination of H₂ to produce a low-valent Fe^I₂Fe^{II} species that reversibly regenerates the tri-hydride complex under H₂ atmosphere.^[22]

Infrared spectroscopy could be a very useful characterization tool for identifying metal-hydride complexes. Not many iron^[23] and cobalt^[24] complexes with a terminal hydride ligand have been reported. Nickel complexes with a terminal hydride ligand typically show a Ni-H stretching band at 1690–2000 cm⁻¹, although sometimes the intensity of the band could be too weak for a definitive identification.^[25]

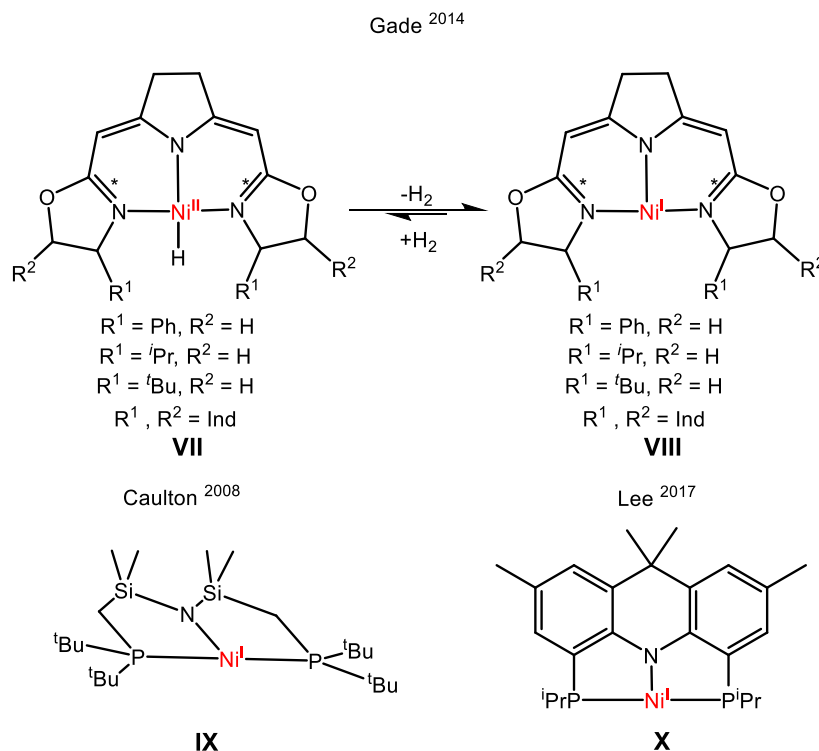
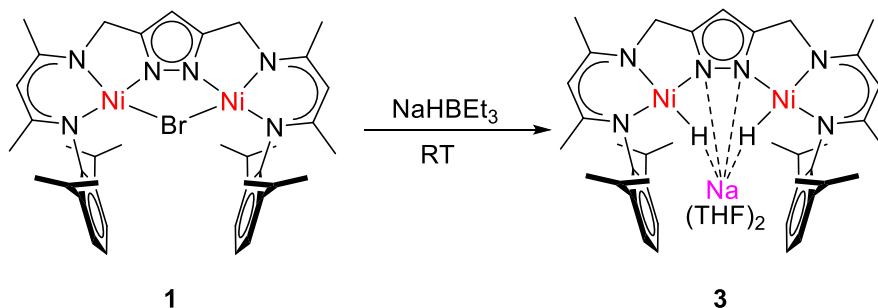


Figure 7: “T”-shaped Ni^I center complexes.^[26-28]

A “T”-shaped nickel(I) species were generated from H₂ elimination in corresponding nickel hydride complexes reported by the *Gade* group in 2014. ^[26] In solution, this Ni(II) hydride complex (**Figure 7, VII**) was found to be in equilibrium with the planar T-shaped, three-coordinate Ni(I) species (**Figure 7, VIII**). Except for this “T”-shaped Ni^I species, other analogous Ni^I species (**Figure 7, IX** and **X**) were reported by the *Caulton*^[27] and *Lee*^[28] groups, respectively. The coordination of σ -donors is not seen because of the σ -antibonding character of the SOMO $d_{x^2-y^2}$ of a d^9 center Ni^I metalloradical. The latter (**Figure 7, X**) shows reactivity towards unsaturated molecules (C₂H₄ and CO₂). Finally, hemolytic cleavage of challenging σ -bonds in substrates, such as H₂N-NH₂ and H₃C-CN highlights the power of utilizing the Ni^I metalloradical. ^[28]

3.2 Synthesis of sodium dinuclear nickel(II) dihydride complex



Scheme 4: Synthetic route for **3**.

In order to study the influence of the K⁺ cation coordination at the hydride unit in **2**, the K⁺ ion was successively replaced by Na⁺ ion, as the small ion radius of Na⁺ (0.97 Å) vs K⁺ (1.33 Å) [29] could be expected to lead to significant geometric changes. Treatment of **1** with 2.5 equivalents of NaHBEt₃ in THF gave a red solution in 20 mins and gas evolution was observed. The crude bimetallic compound **3** was obtained in 76% yield (**Scheme 4**). **3** was characterized by x-ray diffraction, FT-IR, 1D and 2D NMR spectroscopies and elemental analysis (C, H and N).

Suitable crystals for x-ray diffraction were grown from pentane diffusion into a solution of **3** in THF or by layering hexane on a solution of **3** in THF at RT. Its structure is similar to the previously reported potassium analogue **2**. [11] In **2**, the K⁺ ion is hosted between the two aryl rings of the DIPP substituents *via* cation- π interactions and locates within the plane defined by the pyrazolate-bridged dinuclear nickel dihydride core, presumably supported by attractive K⁺...hydride interactions. The distance between K⁺ and the centroid of the DIPP aryl rings is 2.84 Å, which lies in the typical range for cation- π bonding of K⁺ to aromatic systems. However, the smaller Na⁺ ion is situated above the pyrazolate-bridged dinickel dihydride core and outside of the DIPP cleft, with

close contacts to the two hydrides, the two pyrazolate-N atoms, and coordinated by two additional THF ligands. The molecular structure is shown in **Figure 8** and selected bond lengths (Å) and angles (°) are listed in **Table 2**.

3 crystallizes in the triclinic space group *P*-1. As shown in **Figure 8**, each nickel center is held within a N, N-chelate of a β -diketiminato arm and hydride ligand. Moreover, the two nickel centers are coordinated in square-planar fashion, with the sum angle of 360.26° and 359.90°, respectively. The distance of the two nickel ions of 4.105(5) Å is similar to **2** (4.158(7)/4.164(7) Å), suggesting that the alkali metal cation does not exert any major influence on the dinickel dihydride core.

The ¹H NMR spectrum showed a single set of resonance for the pyrazolate ligand and the two hydride ligands, indicating *C*_{2v} symmetry in solution. There must be rapid motion that enables the sodium to change its position in solution. The hydride resonance is at -23.54 ppm in **3** (**Figure 9**), slightly low field shifted compared with **2** (-24.16 ppm) (**Figure 10**). The alkali metal cation in **2** and **3** obviously have only a minor effect on the electronic shielding of the hydrides.

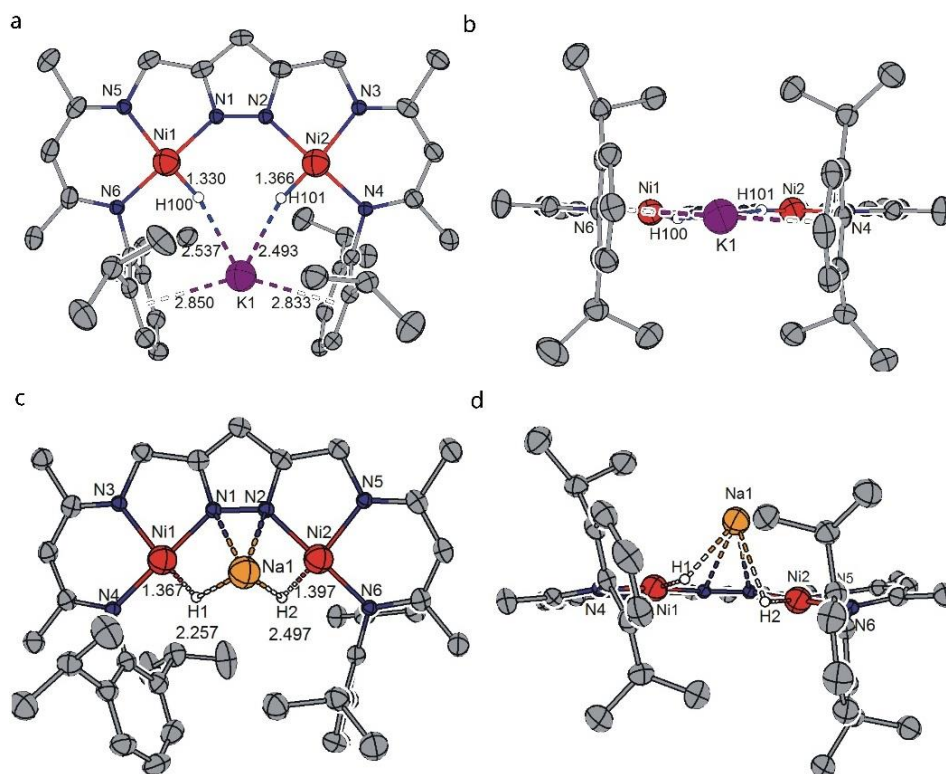


Figure 8: Molecular structures (50% probability thermal ellipsoids) of **2**^[11] (top; only one of two independent molecules shown) and **3** (bottom). Most hydrogen atoms except the Ni-bound hydride omitted for clarity.

Table 2: Selected bond lengths (Å) and bond angles (°) for **3**.

Atoms	Bond lengths	Atoms	Bond angles
Ni1-N4	1.869(2)	O1-Na1-Ni2	136.14(6)
Ni1-N1	1.872(2)	O2-Na1-Ni2	91.50(5)
Ni1-N3	1.905(2)	N2-Na1-Ni2	40.28(4)
Ni1-H1	1.37(2)	N1-Na1-Ni2	66.25(4)
Ni2-N6	1.866(2)	O1-Na1-Ni1	94.97(5)
Ni2-N2	1.882(2)	O2-Na1-Ni1	179.40(6)
Ni2-N5	1.921(2)	N2-Na1-Ni1	65.25(4)
Ni2-H2	1.40(2)	N1-Na1-Ni1	37.78(4)
Na1-H1	2.26(2)	Ni2-Na1-Ni1	88.98(2)
Na1-H2	2.50(2)	Ni2-Na1-H1	81.3(5)
Na1-O1	2.313(2)	Ni1-Na1-H1	25.3(5)
Na1-O2	2.336(2)	Ni2-Na1-H2	29.4(6)
Na1...Ni2	2.847(8)	Ni1-Na1-H2	73.2(5)
Na1...Ni1	3.008(8)	N4-Ni1-N1	176.93(7)

Ni1...Ni2	4.105(5)	N4-Ni1-N3	95.78(7)
		N1-Ni1-N3	84.39(7)
		N4-Ni1-Na1	119.59(5)
		N1-Ni1-Na1	62.28(5)
		N3-Ni1-Na1	127.82(5)
		N4-Ni1-H1	89.9(9)
		N1-Ni1-H1	90.2(9)
		N3-Ni1-H1	172.7(9)
		Na1-Ni1-H1	44.9(9)
		N6-Ni2-N2	178.19(7)
		N6-Ni2-N5	96.30(7)
		N2-Ni2-N5	83.93(7)
		N6-Ni2-Na1	116.50(5)
		N2-Ni2-Na1	61.83(5)
		N5-Ni2-Na1	112.97(5)
		N6-Ni2-H2	89.4(10)
		N2-Ni2-H2	90.2(10)
		N5-Ni2-H2	173.4(10)

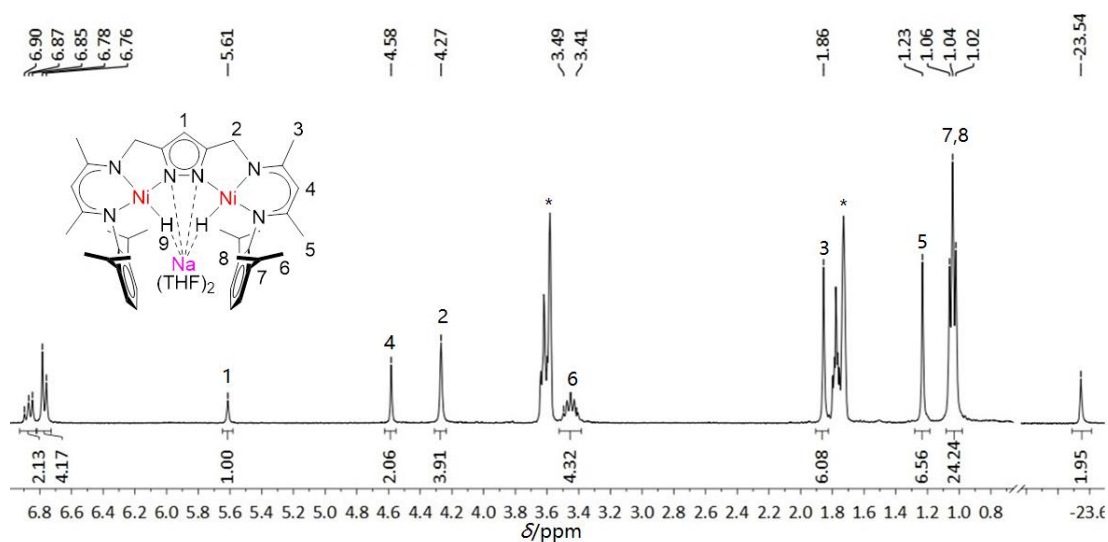


Figure 9: ¹H NMR spectrum (300 MHz) of **3** in THF-d₈. Residual solvents are marked with an asterisk (*).

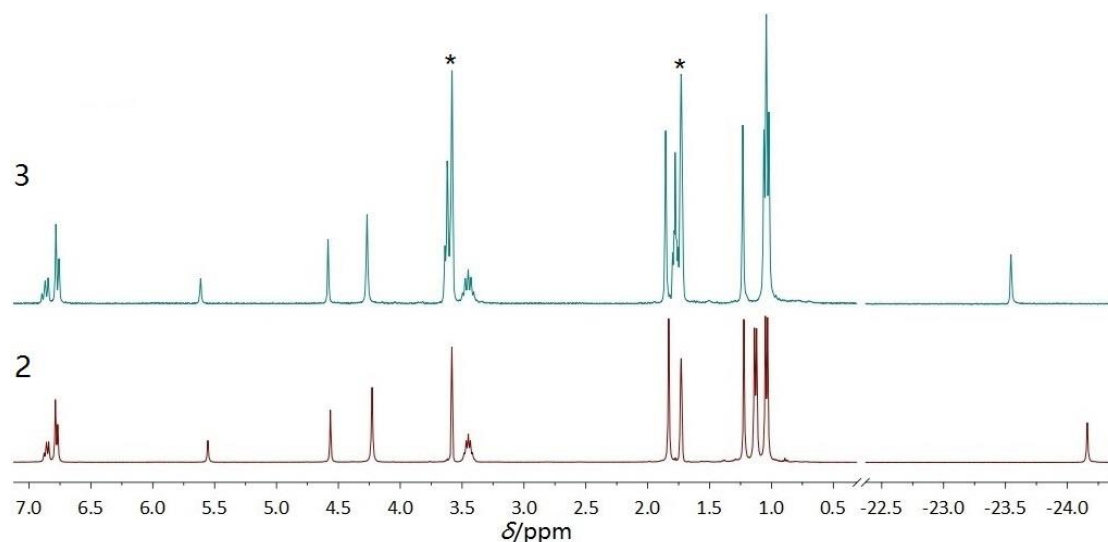
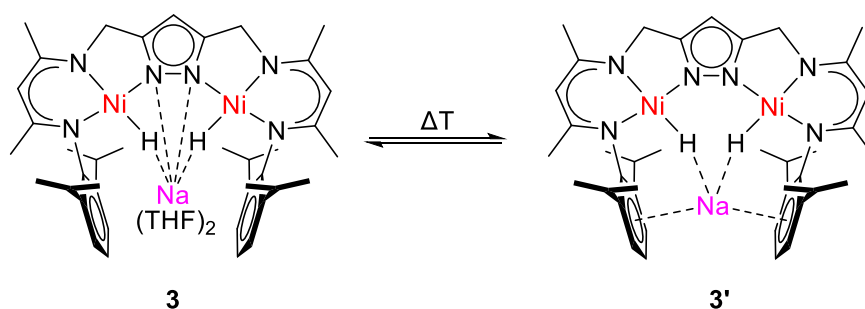


Figure 10: ¹H NMR spectra (400 MHz) of **2** and **3** (300 MHz) or in THF-d₈. Residual solvents are marked with an asterisk (*).

VT ¹H NMR experiments were conducted to understand the Na⁺ cation motion in solution. With the temperatures changing (**Figure 11**), the CH₃ group of the isopropyl substituents separate into two different doublets below 243 K, The “S” shape for the Ni-H peak at different temperature is possibly caused by the combined effects of the sodium cation motion and its dissociation equilibrium fashion. (**Figure 12**) Possible configurations of **3** are shown in **Scheme 5**.



Scheme 5: Possibility configurations of **3** at different temperatures in THF.

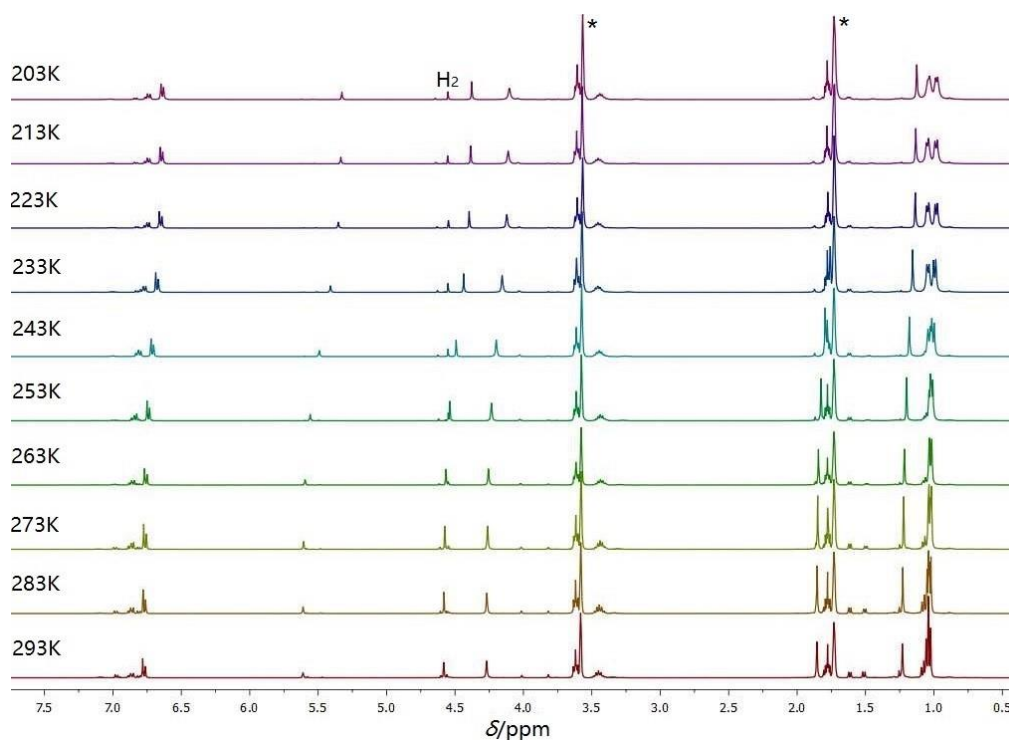


Figure 11: VT ¹H NMR spectra (0–7.5 ppm) (400 MHz) of **3** under H₂ atmosphere. Residual solvents are marked with an asterisk (*).

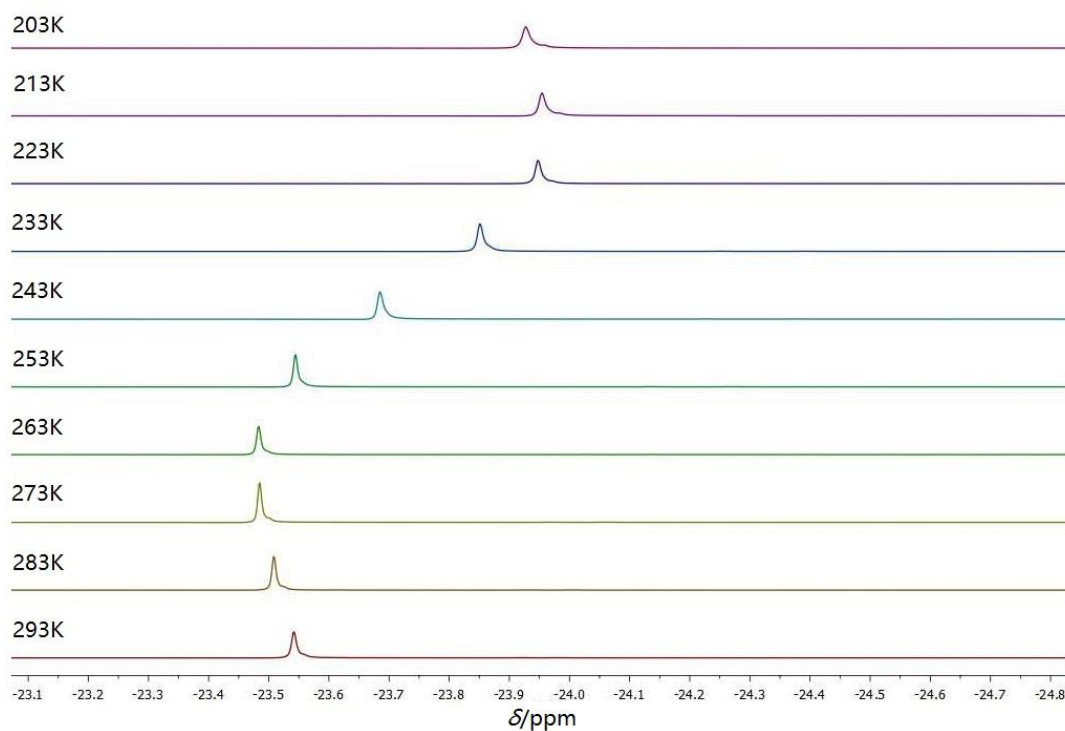
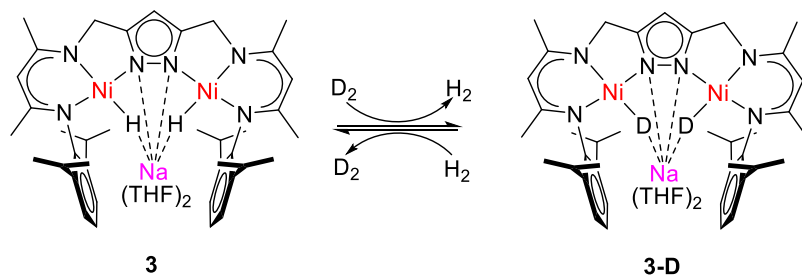


Figure 12: VT ¹H NMR spectra (400 MHz) of the Ni-H region of **3** in THF-d₈. The "S"-shape suggests a temperature depending binding of a Na⁺ or a structure rearrangement of **3**.



Scheme 6: One-step exchange of **3** with D₂.

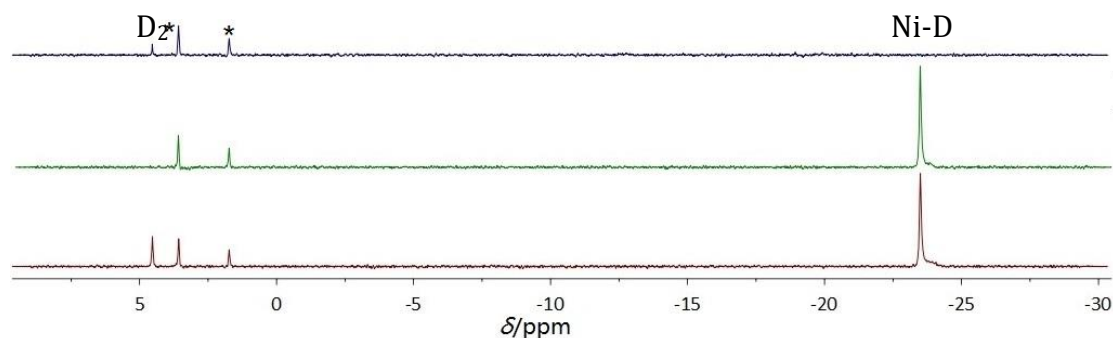


Figure 13: ²H NMR spectra (77 MHz) of H/D exchange of **3-D** in THF. After loading of dried D₂, Ni-D has formed and excess free D₂ exists in the solvent (Bottom). Pump-freeze-thaw procedure removes excess D₂ (Middle). After loading of the dried H₂, the Ni-D signal has vanished and new free D₂ forms immediately (Top). Residual solvent signals are marked with an asterisk (*).

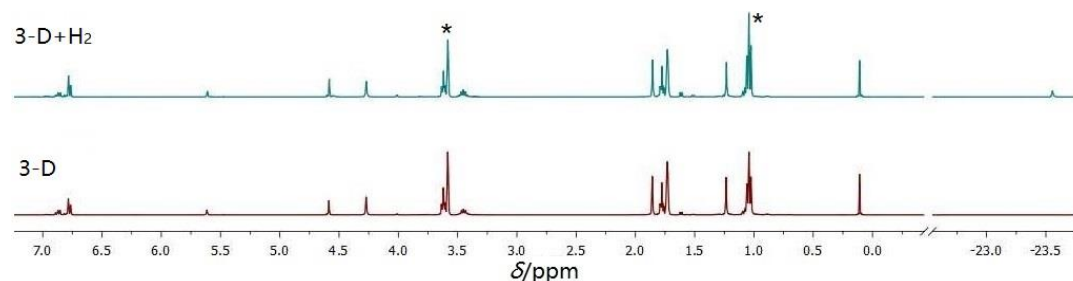


Figure 14: ¹H NMR spectra (400 MHz) of H/D exchange of **3-D** in THF-d₈. After loading of dried D₂, no Ni-H signal is observed (Bottom). After loading of dried H₂, **3** is formed (Top). Residual solvent signals are marked with an asterisk (*).

Upon addition of D₂ (1 atm) to a degassed solution of **3** in THF-d₈, the nickel bound hydrogen atoms are rapidly exchanged to give the deuterated **3-D** (**Scheme 6**). The reaction is reversed upon addition of H₂ to solutions of the deuterated complex in THF. This is proven by ²H NMR, which showed a resonance of 4.52 ppm for free D₂ (**Figure 13** and **Figure 14**).

As shown in **Figure 15**, the two bimetallic dihydride complexes show a Ni-H stretching band at 1961 cm⁻¹ (for **2**) and 1846 cm⁻¹ (for **3**), which are corresponding to other Ni-H stretching at 1690-2000 cm⁻¹.^[30] The Ni-H absorption band shifted to 1367 cm⁻¹ upon deuteration (for **2**) [$\nu(\text{Ni-H})/\nu(\text{Ni-D}) \approx 1.43$, calcd: 1.414] and 1337 cm⁻¹ (for **3**) [$\nu(\text{Ni-H})/\nu(\text{Ni-D}) \approx 1.38$, calcd: 1.414]. In line with the NMR data, the observed trend for the Ni-H stretches suggests that the Ni-H bond strength is affected in opposing directions by the alkali metal cation being located along the Ni-H vector, or perpendicular to it above the Ni-H bond.

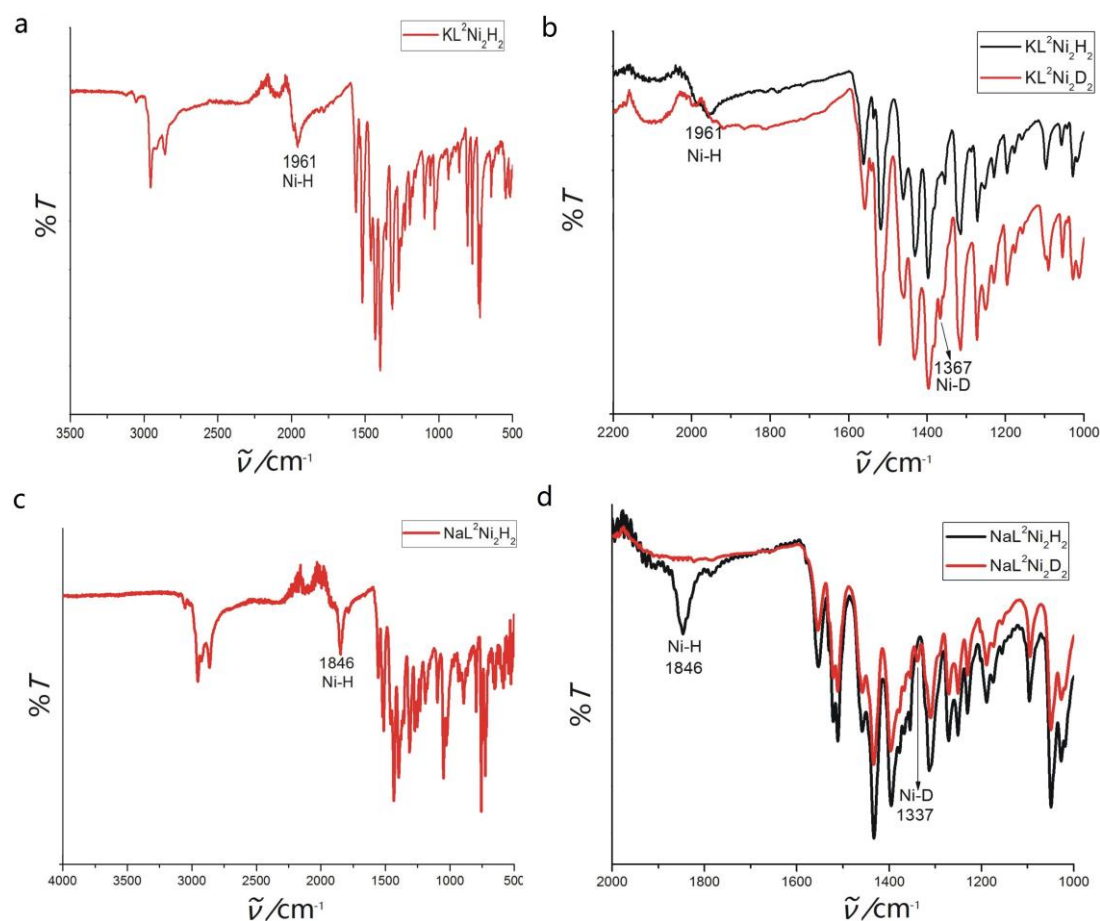


Figure 15: (a) FT-IR spectrum of fresh crystalline material of **2**; (b) Overlay of FT-IR spectra of **2** and **2-D** in the range 2200–1000 cm⁻¹; (c) FT-IR spectrum of fresh crystalline material of **3**; (d) Overlay of FT-IR spectra of **3** and **3-D** in the range 1900–1000 cm⁻¹.

To directly monitor the exchange processes and to confirm the pairwise exchange of both hydrides of a single molecule of **2**⁻ and **3**⁻, the following NMR experiment was designed: a solution of **2** was treated with a small amount of HD, not sufficient for full conversion to K[L¹Ni₂(H)(D)] (**2**-HD) but adjusted to provide roughly equal peak intensities for the two isotopologues. The reaction mixture then contained **2**, **2**-HD, H₂, and HD, all of which are detectable in the ¹H and ²H NMR (**Figure 16**) spectrum. The hydride resonances of **2** and **2**-HD differ slightly (-24.16 vs -24.18 ppm at rt; -24.03 vs -24.05 at 273 K) (**Figure 17**) because of a secondary isotope effect between the two hydrides. Importantly, the two-dimensional ¹H EXSY spectrum of the mixture (**Figure 18**) revealed correlations only between **2** and H₂ as well as between **2**-HD and HD, clearly evidencing a pairwise exchange of H₂ and HD, respectively, without any scrambling. All possible exchange processes in this scenario are shown in the upper part of **Figure 18**. To provide mechanistic insight for the H₂/D₂ exchange process and to explain the effect of the alkali metal ions on the stability of (and H₂ release from) the dihydride complex, ¹H-¹H EXSY of **2** with H₂ experiments were performed.

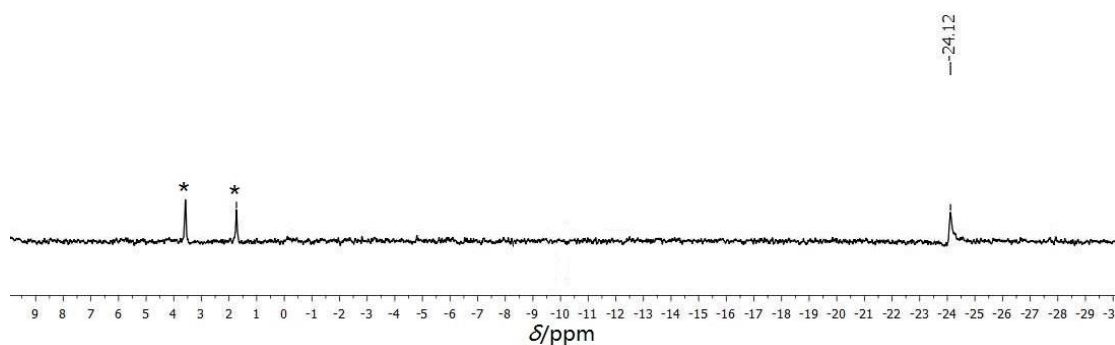


Figure 16: ²H NMR spectrum (77 MHz) of **2**-HD under Ar atmosphere in THF at 298 K. Residual solvents are marked with an asterisk (*).

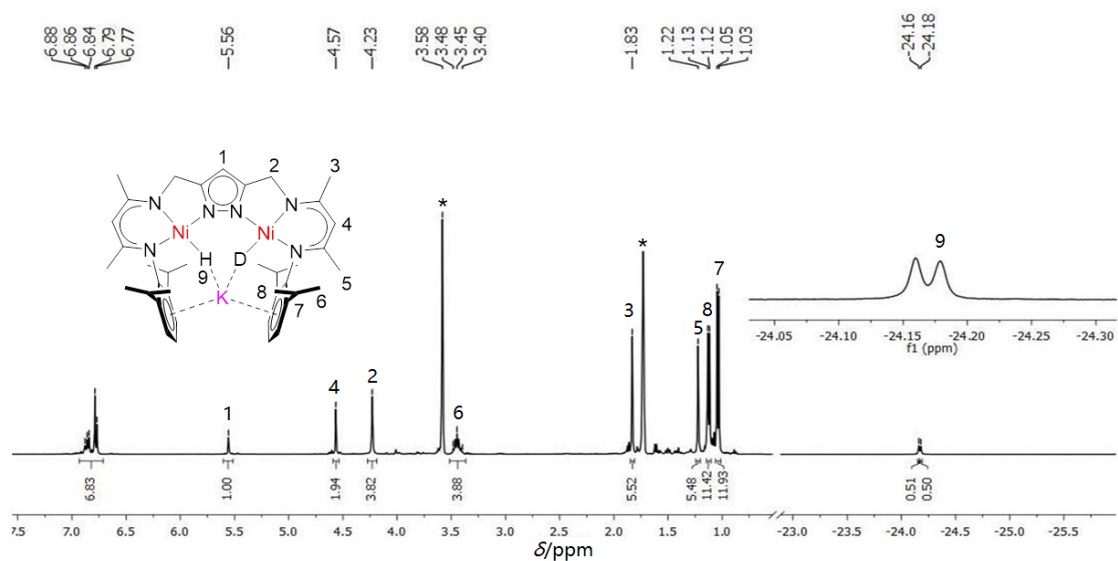


Figure 17: ¹H NMR spectrum (400 MHz) of a 1:2 mixture of **2** and **2-HD** under Ar atmosphere in THF-d₈ at 298 K. The two isotopologous complexes cannot be distinguished by ¹H NMR except for their hydride resonances (-24.16 vs -24.18 ppm, RT). Residual solvents are marked with an asterisk (*).

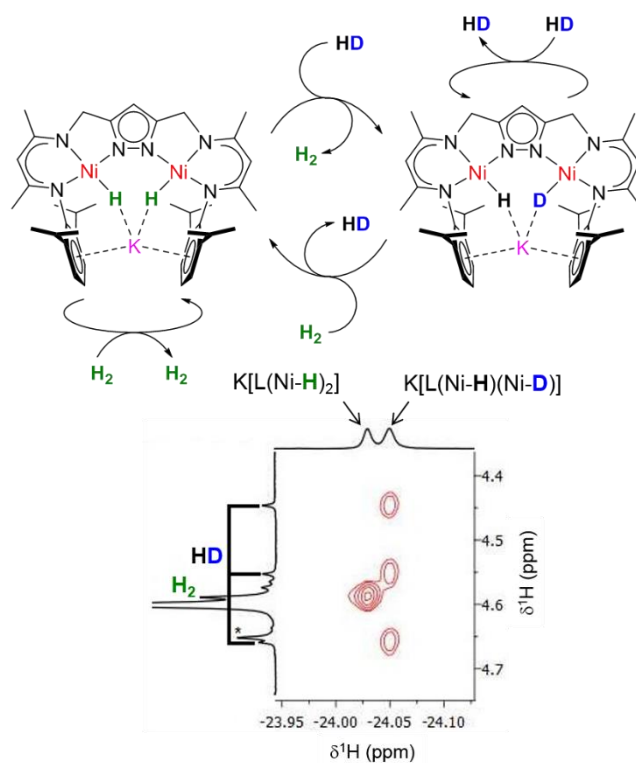


Figure 18: ¹H-¹H EXSY spectrum (400 MHz, 0.5 s mixing, 273 K) of a mixture of K·2, K·2-HD, H₂ and HD in THF-d₈ (bottom) and the possible exchange processes (top).

DFT Calculations. In collaboration with the group of Ricardo Mata, possible pathways for H₂/D₂ exchange were probed through DFT calculations. A scheme of pairwise mechanisms considered is displayed in **Figure 19**. For ease of discussion, we consider **2**⁻ without K⁺ cation as the reactant, D₂ as the entering molecule and **2-D**⁻+H₂ as the products. The K⁺ or Na⁺ cation were removed in this first set of calculations to allow for more flexibility in the exchange paths.

The first question is finding the preferred binding mode of D₂ to the complex. Although the η²-H₂ coordination is often discussed (**G** in **Figure 19**), we found no stable minimum for this structure. All attempts for a side-on coordination to the Ni centres resulted in an end-on weak coordination to the metal (r(H-Ni)≈2.6 Å, **A** in **Figure 19**). We carried out an extensive search of minima, placing the entering molecule close to the Ni centres in different orientations. The other minimum found was one whereby the entering D₂ occupies the position of the K⁺ (**C** in **Figure 19**). The latter is 11 kJ/mol less stable than the other minimum.

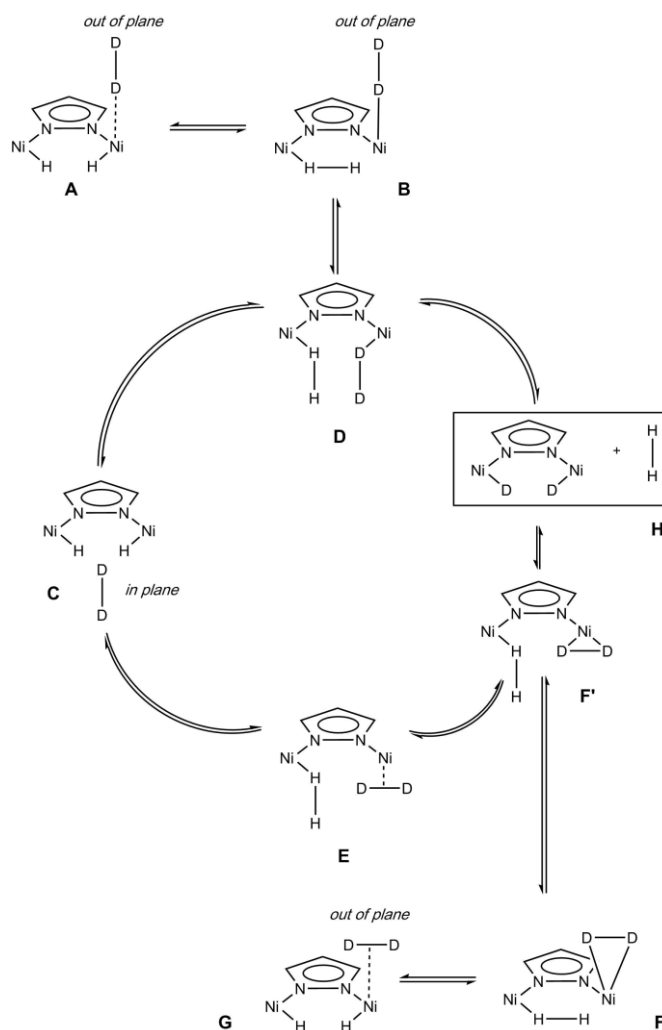


Figure 19: Concerted reaction pathways for H₂/D₂ exchange considered in this study.

As shown in **Figure 19**, all concerted pathways for insertion of D₂ starting from the aforementioned minima were particularly high in energy. The lowest connected path for insertion was through an early H₂ recombination in the pocket. Due to the high energies involved, we only obtained one half of the reaction path, which provided a lower bound for the electronic energy barrier of 136 kJ/mol. This would be too high in energy, so we excluded the possibility of a concerted mechanism. Another reason for exclusion is that a symmetric pathway would necessarily go through a double *end-on* H₂/D₂ coordination to Ni (**D** in **Figure 19**), which would be too unstable.

An alternative to the substitution mechanism would be a non-concerted pathway, with H₂ leaving the pocket and D₂ coordinating afterwards at the empty Ni^I sites. This would also be consistent with the non-scrambling exchange of H₂/D₂. Two sets of constrained optimizations were performed, fixing the distance between the two hydrides in **2** and **2**⁻. The results are shown in **Figure 20**.

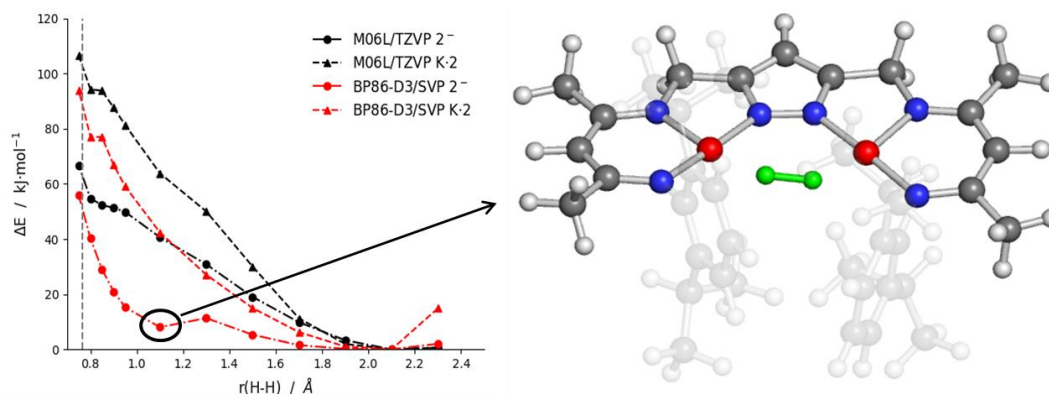


Figure 20: Potential energy surface plots for the recombination of the coordinated H atoms in **2**⁻ and **2**. Relaxed scans were computed along the H-H distance at the BP86-D3/def2-SVP level. The dotted vertical line represents the bond distance in the H₂ molecule at the same level of theory (0.767 Å). The reference point is provided by the most stable geometry; in both cases a distance of 2.1 Å is maintained.

In **Figure 20** are shown the results at the level of theory used for the optimizations (BP86-D3/SVP), and also energies for the meta-GGA M06L functional with a larger basis, but using the same geometries. For each point in the curve the singlet, the triplet and the broken symmetry state (with the two lone electrons at the Ni centers) were computed. Up to 0.95 Å the pure singlet state is the most stable. With shorter H-H distances, the broken symmetry state is found to be lowest, with the triplet still lying higher above in energy. The energy order of the states was further confirmed with the B3LYP and PBE0 functional at $r(\text{H-H})=0.8$ Å, providing the same qualitative picture. All results reported (including the optimized structures) correspond to the lowest electronic state found at each point.

Both BP86 and M06L agree in that H₂ recombination is favored when the K⁺ cation is not present. We start by discussing the latter curves. Estimation to the barrier for removal of the H₂ is provided at distances slightly above the optimal H-H bond value. In the case of **2**⁻, both methods agree in a barrier of about 60 kJ/mol. Carrying out a linear interpolation of the M06-L/TZVP energy curve, the barrier can be approximated by the energy value at the H₂ equilibrium bond distance, a value of 62.5 kJ/mol. The disagreement between the two functionals is foremost in the shape of the curve. In the case of BP86, we found a shallow minimum, which we were able to fully optimize and characterize at $r(\text{H-H})=1.16 \text{ \AA}$. This feature is not visible in the M06L curve. The electronic structure of this minimum is similar to the hydride complex, still keeping the Ni-H bonds. Due to the flatness of the potential in this region it was not possible to converge the transition state to the lower neighboring minimum. The impact of the zero-point vibrational energy correction on the energies cited above should be very small since the Ni-H harmonic vibrational frequency is roughly half of the H-H stretch frequency in the hydrogen molecule.

In **2**, the estimated activation barrier for removal of H₂ would lie between 80-105 kJ/mol (102.2 kJ/mol in the case of M06-L/TZVP). Along the relaxed surface scan the K⁺ remained relatively fixed in its position, approximately in plane with the leaving H₂ and thereby raising the energy. It is likely that the reported values correspond to an upper estimate. The cation could potentially change its position along the faces of the ligand rings, lowering the barrier.

The electronic structure calculations carried out quite clearly go against any concerted mechanism for substrate substitution. In a first step, the hydrides should recombine to H₂, leaving the pocket and two Ni^I centers with one vacant coordination each. The barrier for H₂ formation is quite low in the absence of K⁺

(about 60 kJ/mol), but could also be lowered if there is an exchange with the solvent or the cation is displaced.

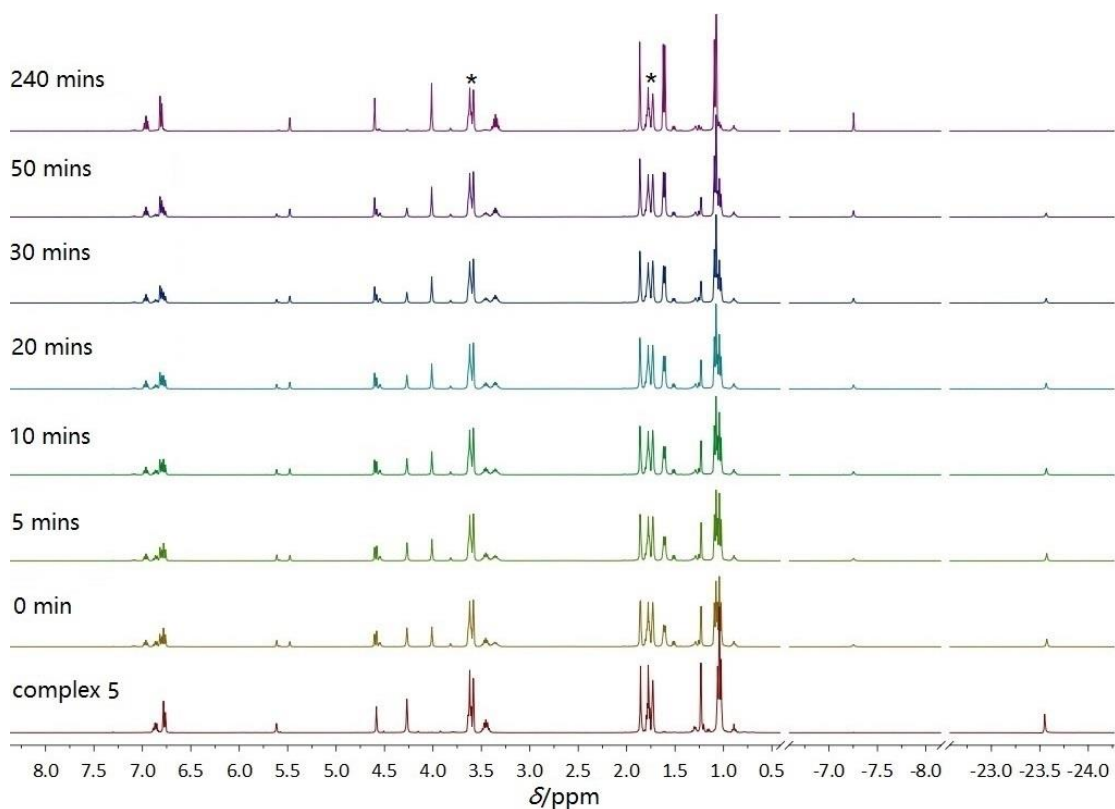
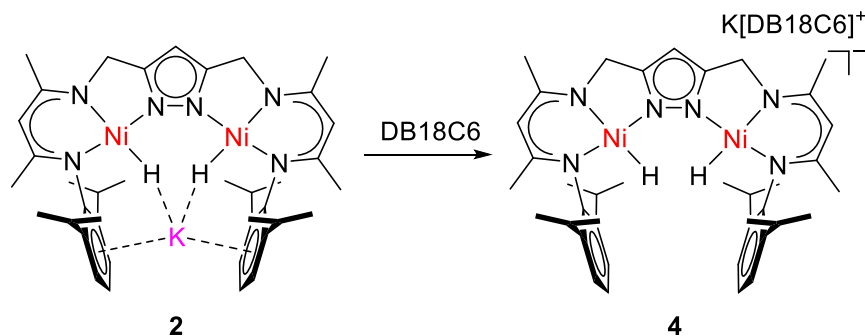


Figure 21: ¹H NMR spectrum (400 MHz) of **3** in THF-d₈ with 1 equivalent H₂O at different reacting times. Residual solvents are marked with an asterisk (*).

In *Manz* work, **2** reacts with one equivalent of H₂O to generate an intermediate hydride-hydroxide species, K[L¹(Ni-H)(Ni-OH)].^[11a] The hydride and hydroxide resonance are formed at -26.00 ppm and -2.07 ppm in the ¹H NMR spectrum, respectively. The new intermediate species showed a weak O-H stretching vibration at 3622 cm⁻¹ in the IR spectrum.^[11a] Whereas, no similar intermediate was observed by NMR spectroscopy in the reaction of **3** with water (**Figure 21**). The difference suggests that the alkali metals (K⁺ and Na⁺) play an important role in the intermediate formation process.

3.3 Dissociation hydride-K⁺ interaction in bimetallic dinickel(II) complex



Scheme 7: Synthetic route for **4**.

In complexes **2** and **3**, the alkali metal (K⁺ or Na⁺) is closely associated with the two hydride ligands. In addition, it exhibits different reactivity towards water. To further assess the effect of the alkali metal cation (K⁺ or Na⁺) and to prepare a new dinuclear dinickel dihydride complex with a vacant cleft, **2** was treated with (18-crown-6), [2,2,2]cryptand or DB18C6 to separate the K⁺ cation from the [L¹Ni₂(H)₂]⁻ anion (**Scheme 7**). No obvious color change was associated with these reactions, but the ionic products become poorly soluble in THF; these differences in solubility suggest that the alkali metal cations remain closely associated with the [L¹Ni₂(H)₂]⁻ anion and that contact ion pairs are present in THF solutions of **2** and **3**. Unfortunately, all crystallizing attempts for x-ray diffraction using [18-crown-6] or [2,2,2]cryptand failed. However, single crystals for x-ray diffraction using DB18C6 were obtained by layering hexane/Et₂O on a solution of **4** in THF at -30°C.

In **2** and **3**, the hydride ligands were located in the density difference map and their positions were allowed to refine freely. In **4**, a fixed isotropic displacement parameter of 0.08 Å² was applied to the hydride ligands. **4** crystallizes in the monoclinic space group C_{2/c}. The asymmetric unit contains two crystallograph-

ically independent molecules with crystallographically imposed C_2 symmetry (the idealized point group of the anion is C_{2v}); one of the two molecules is shown in **Figure 22**, selected bond lengths (Å) and angles (°) are listed in **Table 3**.

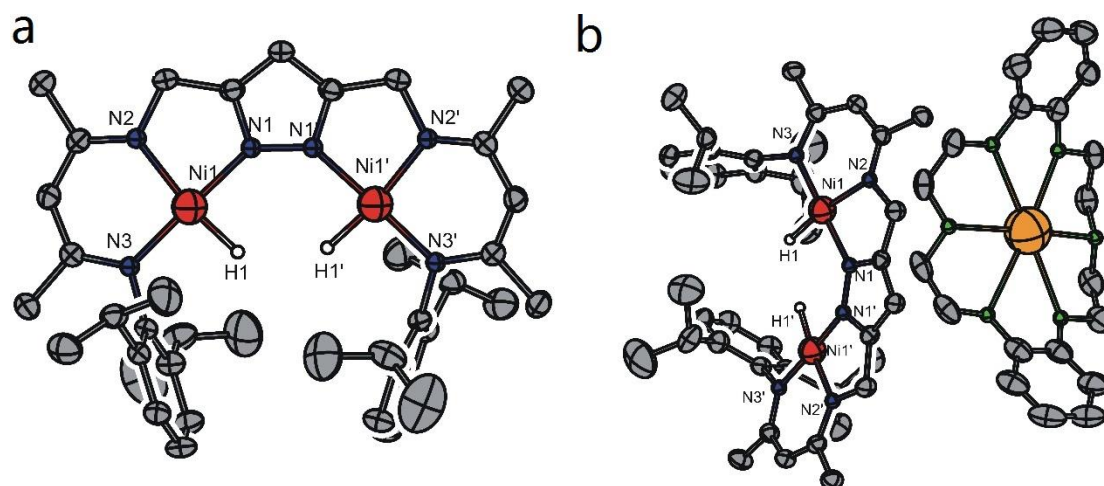


Figure 22: Molecular structure (50% probability thermal ellipsoids) of the anion of **4** (a, only one of two independent molecules shown) and **4** (b). Most hydrogen atoms omitted for clarity, except for the nickel-bound hydrides. Symmetry transformations used to generate equivalent atoms: (') $-x, y, 3/2-z$.

Table 3: Selected bond lengths (Å) and angles (°) for **4**.

Atoms	Bond lengths	Atoms	Bond Angles
Ni1-N3	1.873(2)	N3-Ni1-N1	177.25(8)
Ni1-N1	1.886(2)	N3-Ni1-N2	96.97(7)
Ni1-N2	1.920(2)	N1-Ni1-N2	83.99(7)
Ni2-N13	1.862(2)	N13-Ni2-N11	177.22(8)
Ni2-N11	1.879(2)	N13-Ni2-N12	96.76(9)
Ni2-N12	1.916(2)	N11-Ni2-N12	83.86(9)
Ni1...Ni1'	4.115(7)		
Ni1-H1	1.46(3)		

As shown in **Figure 22**, The core structure of the “naked” $[L^1Ni_2(H)_2]^-$ complex anion shows no significant differences compared to the neutral **2** and **3**. In **4**, the two nickel centers are coordinated in square-planar fashion, with the sum of angles being 359.95° . Each nickel center is held within an N, N-chelate of a β -diketiminato arm and bears a hydride ligand. Two Ni...Ni distances in the two

crystallographically independent molecules are 4.115 Å and 4.064 Å, respectively. The nickel-hydride ligands distances of 1.464 Å and 1.444 Å are longer than **2** and **3**. Selected metrical parameters of the three dinuclear nickel(II) dihydride complexes are listed in **Table 4**. In fact, Ni-H bonds in the range 1.32(2)–1.40(2) Å determined for **2** and **3** are shorter than most terminal Ni-H bonds reported in literature. However, all these data have to be considered with caution because of inherent ambiguities of H atom position derived from x-ray crystallography. In the absence of neutron diffraction data, NMR and IR signatures (*vide infra*) can be considered more reliable for assessing differences among the Ni-H moieties in the three compounds.

Solid structure is a diamagnetic reflecting the low-spin d⁸ configuration of the nickel(II) ions. However, VT NMR spectrum of **4** in THF-d₈ shows a 1/T (curie) behavior from the broad peaks indicating a paramagnetic species (**Figure A6**). It indicates that **4** is highly sensitive and decayed when crystals were dried under reduced pressure or kept at rt for some times. These findings will be discussed in more detail below.

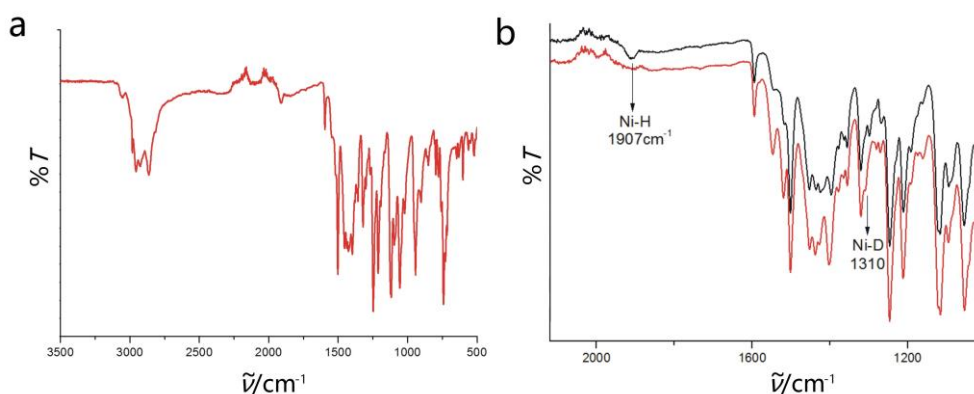


Figure 23: (a) FT-IR spectrum of fresh crystalline material of **4**; (b) Overlay of FT-IR spectra of **4** and **4-D** in the range 2200–1100 cm⁻¹;

As shown in **Figure 23**, after the K⁺ cation was dissociated by DB18C6, the Ni-H stretching band at 1913 cm⁻¹ is similar to **2** and **3**. The Ni-H absorption band shifted to 1310 cm⁻¹ upon deuteration (for KL¹Ni₂(μ-H)₂) [$\nu(\text{Ni-H})/\nu(\text{Ni-D}) \approx$

1.413, *calcd*: 1.414]. The metrical parameters of the three nickel(II) dihydride compounds are shown in **Table 4**.

Table 4: Metrical parameters for **2**, **3** and **4**.

Complex	2	3	4
Ni...Ni	4.158/4.164	4.105	4.115/4.064
Ni-N	1.878(2)-1.911(2)	1.866(2)-1.921(2)	1.862(2)-1.921(2)
Ni-H	1.32(2) - 1.38(3)	1.37(2)/1.40(2)	1.44(3)/1.46(3)
K-Cg	3.098(2) -3.239(2)	-	-
M-H	2.45(3) - 2.53(3)	2.26(2)/2.50(3)	-
Na-N	-	2.567(2)/2.705(2)	-
Ni...M	3.781(5) - 3.831(5)	2.847(8)/ 3.008(8)	-
N-Ni-N (<i>opposite</i>)	176.55(7) - 178.66(7)	176.93(7)/ 178.19(7)	177.22(8)/ 177.25(8)
N-Ni-H (<i>opposite</i>)	172.5(12) - 174.7(10)	172.7(9)/ 173.4(10)	171.0(13)/ 172.4(13)
ν (cm ⁻¹) (H ₂ /D ₂) ^a	1961/1367	1843/1337	1907/1353

a, Frequency of the Ni-H vibration determined by IR spectroscopy on solid samples of **2**, **3** and **4**.

H₂ loss from the “naked” dinuclear nickel(II) dihydride. Since the DFT calculation indicates that **4** easily release the H₂ from the Ni-H, we carried out temperature dependent magnetometric measurements for **2** and **4**, respectively, and monitoring the headspace of crystal of **4** by GC-MS experiment. The GC-MS experiment indeed shows the gradual formation of H₂.

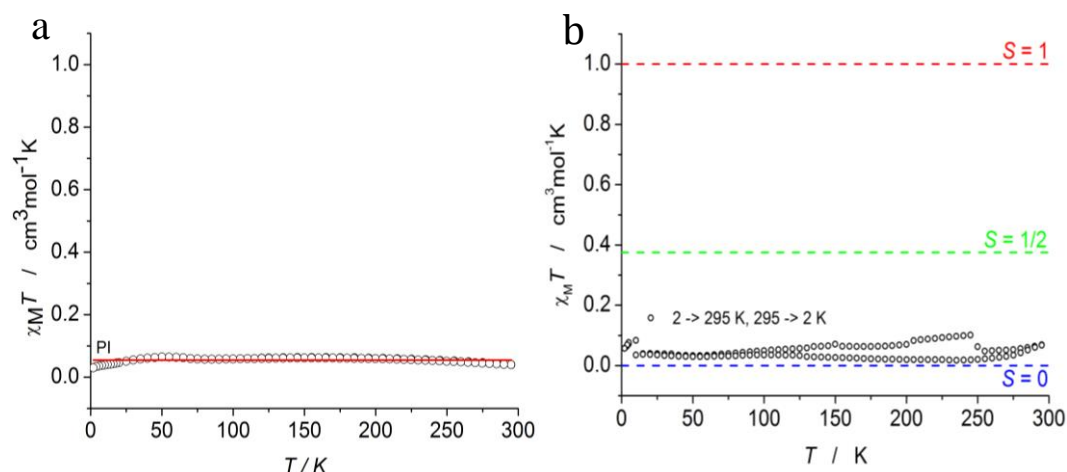


Figure 24: (a) $\chi_m T$ vs. T measurement in the temperature range of 2–295 K at 0.5 T for solid samples of **2**. The solid red lines represent the best global fit with $PI = 5.4\%$ ($S = 1$) and $TIP = 60.10 \times 10^{-6} \text{ cm}^3 \cdot \text{mol}^{-1}$; (b) $\chi_m T$ vs. T measurement in the temperature range of 2–295 K at 0.5 T for solid samples of **4** using crystalline material in a NMR tube with mother liquor.

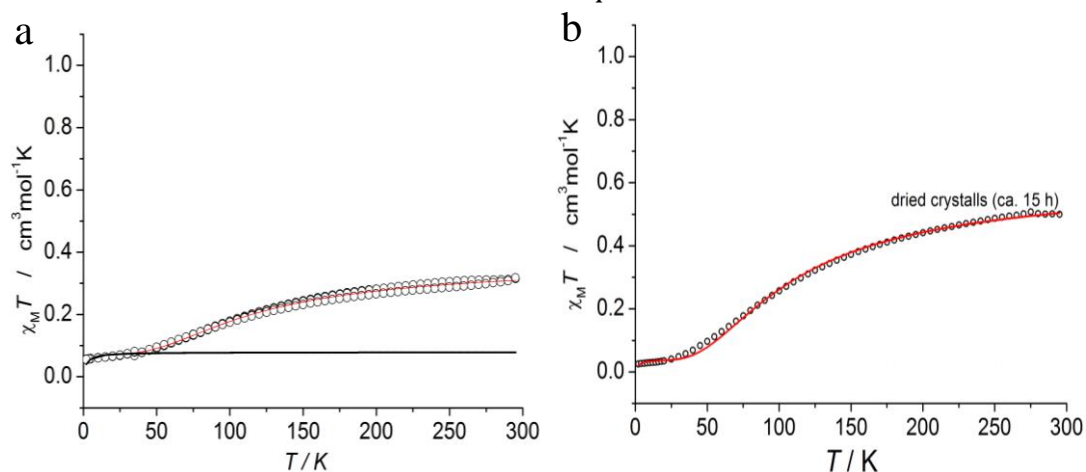
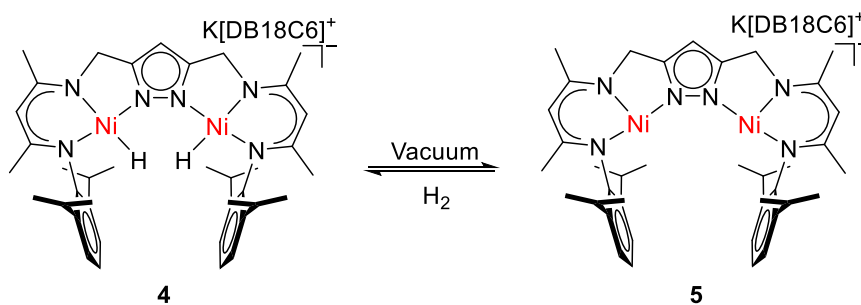


Figure 25: (a) $\chi_m T$ vs. T measurement in the temperature range of 2–295 K at 0.5 T for solid samples of **4** of crystalline material and dried in glove box for 1 hour. (b) $\chi_m T$ vs. T measurement in the temperature range of 2–295 K at 0.5 T for solid samples of complex **4** using crystalline material dried under vacuum for 15 hours.

Magnetic susceptibility data for crystalline material of **2** collected in the temperature range from 2–295 K, showed essentially diamagnetic behavior up to room temperature (**Figure 24a**). The solid red lines represent the best fit with $PI = 5.4\%$ ($S = 1$) and $TIP = 60.10 \times 10^{-6} \text{ cm}^3 \cdot \text{mol}^{-1}$. **4** was collected on freshly crystalline material that was sealed with a small amount of mother liquor in an

NMR tube to prevent the loss of the solvents and/or molecular hydrogen. The magnetic susceptibility of this sample showed diamagnetism (**Figure 24b**). When crystals of **4** were dried in a glovebox atmosphere for 1 h (mother liquor evaporated without applying vacuum), however, a paramagnetic contribution arises that amounts to 0.32 cm³·mol⁻¹·K (corresponding to 1.6 μB) at 295 K. SQUID data for a sample of crystalline **4** that has been thoroughly dried under vacuum for 15 h (resulting in a powder sample) shows a magnetic moment of 0.5 cm³·mol⁻¹·K (corresponding to 2.0 μB) at 295 K, not too far from the value expected for two $S = 1/2$ ions (2.45 μB for $g = 2.0$). The decrease of μB upon lowering the temperature (shown as $\chi_M T$ vs T plot in **Figure 25b**) indicates significant antiferromagnetic coupling. These experiments provide experimental evidence for the idea that the dinickel(II) dihydride core **4**⁻, in the absence of any alkali metal ion within the dihydride cleft, is prone to facile loss of H₂ and can be viewed as a masked dinickel(I) species. The presence of K⁺ (or Na⁺) obviously stabilizes the dinickel(II) dihydride complex and prevents H₂ loss, in line with the DFT results.



Scheme 8: Interconversion between square planar Ni^{II} and "T"-shaped Ni^I metalloradical species.

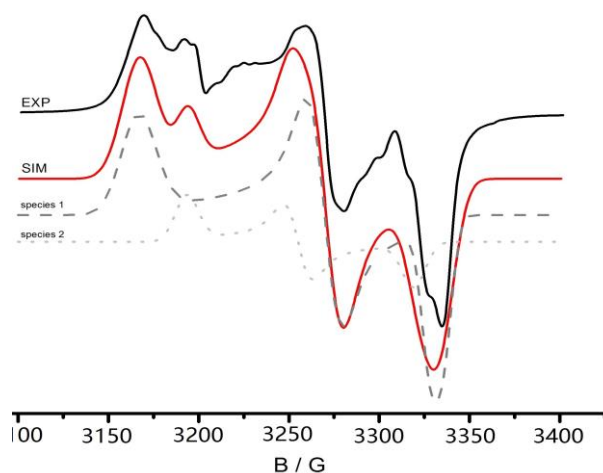


Figure 26: X-band EPR spectra (black line) in THF at 146 K of **5**. Frequency = 9.413 GHz, power = 10 mV. Simulations (red trace) provide (species 1, 84%) $g_1 = 2.128$, $g_2 = 2.061$, $g_3 = 2.0225$; (species 2, 16%) $g_1 = 2.11$, $g_2 = 2.07$, $g_3 = 2.03$; (species 2)

Reductive elimination of H₂ from **2**⁻ or **4**⁻ can be expected to yield a {L¹Ni¹} species. Related to the “T”-shaped Ni^I species [26-28], we presumed that the square planar geometry in *d*⁸ low spin Ni^{II} changes to the “T”-shaped of *d*_{x²-y² based radical in *d*⁹ Ni^I system. Consistent with the SQUID and GC experiments, the electron paramagnetic resonance (EPR) spectrum (**Figure 26**) of **5** (84%) shows three *g* values at frozen THF at 145 K or room temperature with ligand hyperfine structure resolved. It indicates that **5** is a double “T”-shaped Ni(I) species. The rhombic spectrum has principal *g* values of 2.128, 2.061 and 2.0225 and $g_{av} = 2.071$. And a second (16%) unidentified species with *g* values of 2.11, 2.07 and 2.03 was observed in the EPR spectrum. In addition, the x-band EPR spectroscopic data for a known “T”-shaped Ni^I species is *g* = 1.99, 2.22 and 2.33.[28] A structure optimization of **5** at the B3LYP/def2-SVP level was carried out setting out from the structure of **5** without the terminal two hydride ligands (**Figure 27**).}

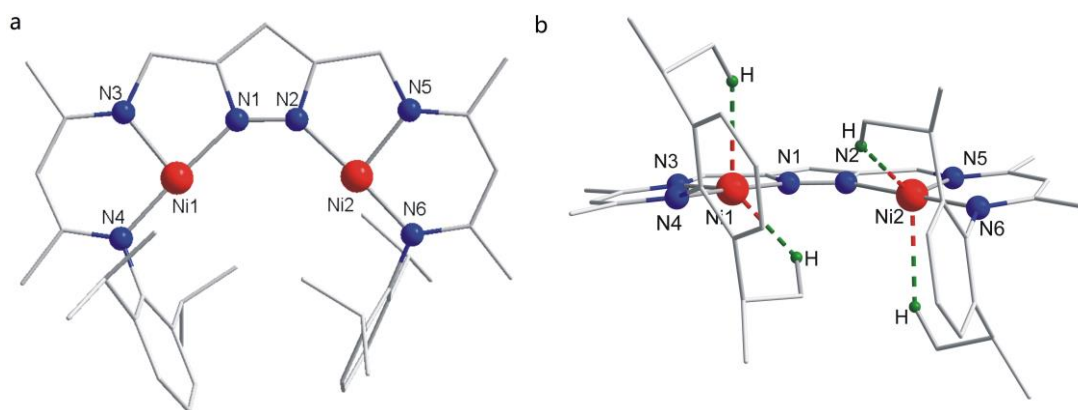


Figure 27: Structure of **5** as optimized at the B3LYP/Def2-SVP level. Most hydrogen atoms are omitted for clarity. Selected bond lengths (Å): Ni1-Ni2 4.107, Ni1-N1 1.893, Ni1-N3 1.914, Ni1-N4 1.859, Ni2-N2 1.893, Ni2-N5 1.914, Ni2-N6 1.859, Ni1-H 2.538, Ni1-H 2.292.

Keep a sample of **4** in a closed flask under vacuum for a week and dissolving the complex in THF under Ar atmosphere. Suitable crystals for x-ray diffraction were obtained by layering hexane/Et₂O on a solution of **5** in THF at RT. Complex **5** has better solubility than **4**. As shown in **Figure 28**, owing the low resolution as well as disorder, the data of **5** only allowed us to depict a model of its structure. The distances of Ni-N3 and Ni-N5 of 1.951 Å and 1.948 Å are longer than **4** with 1.92 Å. In the crystal structure, it clearly indicates that the two Ni^I atoms adopt “T”-shaped configuration.

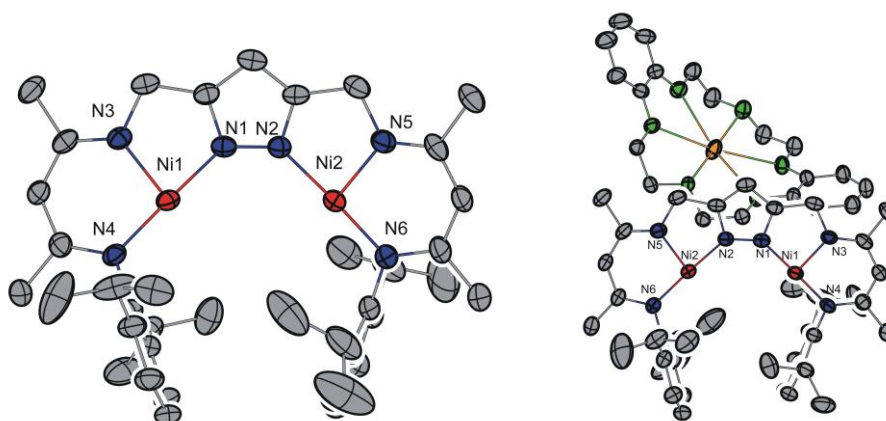


Figure 28: Molecular structure (30% probability thermal ellipsoids) of the anion of **5** (a) and **5** (b). All hydrogen atoms omitted for clarity.

3.4 Kinetics of H₂/D₂ exchange

NOESY is useful for determining which signals arise from protons that are close to each other in space even if they are not bonded. A NOESY spectrum yields through space correlation via spin-lattice relaxation. NOESY also detects chemical and conformation exchange. It called EXSY when used for this purpose.

When **2** was kept under H₂ atmosphere or **2-D** under D₂ in THF-d₈ or THF solution, ¹H-¹H/²D-²D NOESY spectra indicated that the coupling resonance between the Ni-H and H₂ or Ni-D and D₂ (**Figure 29** and **Figure 31**).

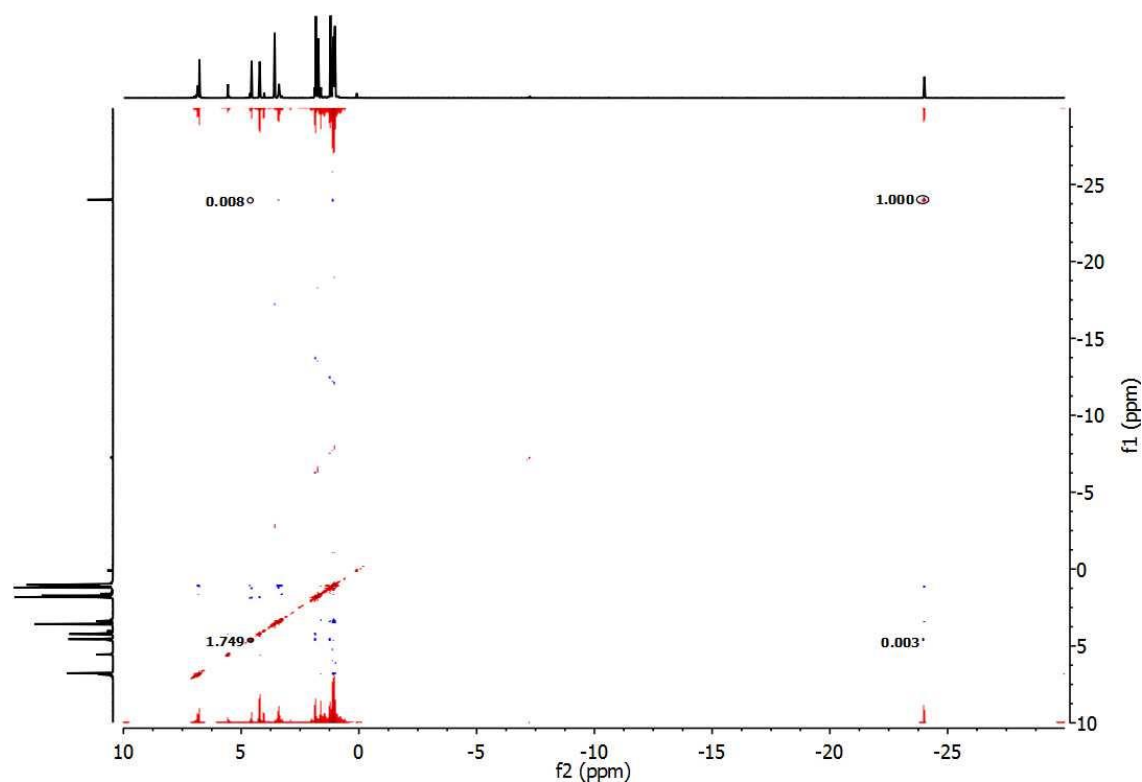
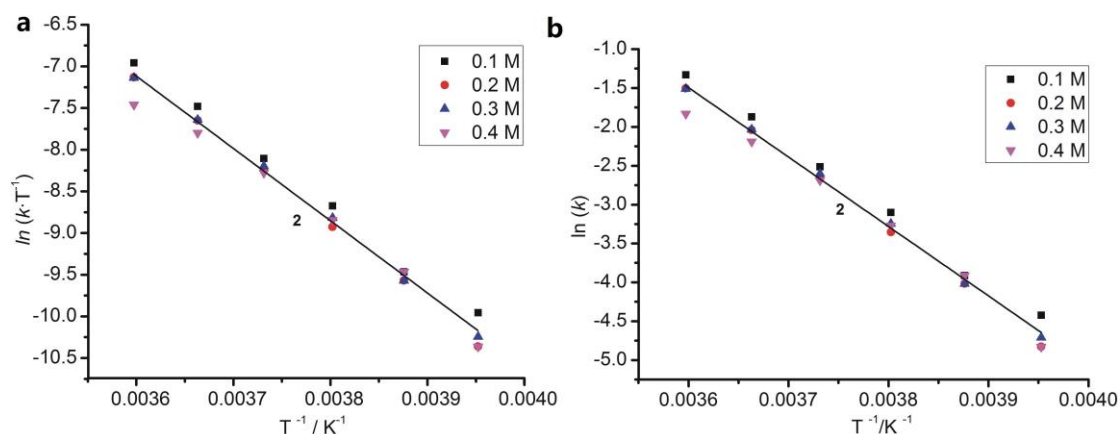


Figure 29: ¹H-¹H EXSY spectrum (400 MHz, 0.5 s mixing) of **2** (0.4 M) under H₂ atmosphere in THF-d₈ at 253 K. Cross peaks between the H₂ and hydride signals increase with increasing temperature and are therefore due to the exchange.

Table 5: Rate constants k (s⁻¹) for the (Ni-H)₂→H₂ exchange in **2** (0.1, 0.2, 0.3 and 0.4 M) as function of temperatures.

T/K	k/s^{-1}			
	0.1 M	0.2 M	0.3 M	0.4 M
278	0.264	0.222	0.221	0.16
273	0.154	0.13	0.131	0.112
268	0.081	0.07	0.074	0.068
263	0.045	0.035	0.039	0.038
258	0.02	0.018	0.018	0.02
253	0.012	0.008	0.009	0.008

**Figure 30:** Eyring plots (a) and Arrhenius plots (b) for the (Ni-H)₂ → H₂ exchange in **2** (0.1, 0.2, 0.3 and 0.4 M). Straight lines were separately fitted for the temperature regimes (average) at 283–308 K.

¹H-¹H EXSY spectra of mixtures containing **2** and H₂, recorded in the temperature range from 253 to 278 K (in steps of 5 K), showed exchange between H₂ and the Ni-bound hydrides. Rate constants for the exchange (**Table 5**), extracted from the EXSY spectra, were used to construct Eyring plots and Arrhenius plots (**Figure 30**) from which activation parameters could be derived. While a full EXSYCALC analysis was hampered by partial peak overlap that introduced large errors, it was possible to use two EXSY peaks to obtain pseudo-first order rate constants for the transition $[L^1(\text{Ni-H})_2]^- \rightarrow \text{H}_2$ in the initial build up regime ($k_{\text{ex}}\tau_{\text{mix}} < 0.2$), which is in the temperature range from 253 to 278 K (spectra

recorded in steps of 5 K). Samples with different concentrations of **2** yielded essentially the same pseudo-first-order rate constants (**Figure 30a**), in agreement with the reaction being first order in $[L^1(\text{Ni-H})_2]^-$. Arrhenius plotting (**Figure 30b**) gives an apparent activation energy $E_a = (74.1 \pm 0.4) \text{ kJ mol}^{-1}$ for **2**, attributed to the rate determining loss of H₂ from the dinickel(II) dihydride core (Eyring analysis gives $\Delta H^\ddagger = (72.1 \pm 1.5) \text{ kJ mol}^{-1}$). A similar hydride exchange between **2-D** and D₂ was observed in ²H-²H EXSY spectrum (**Figure 31**) but not quantitatively analyzed due to the much lower sensitivity of ²H.

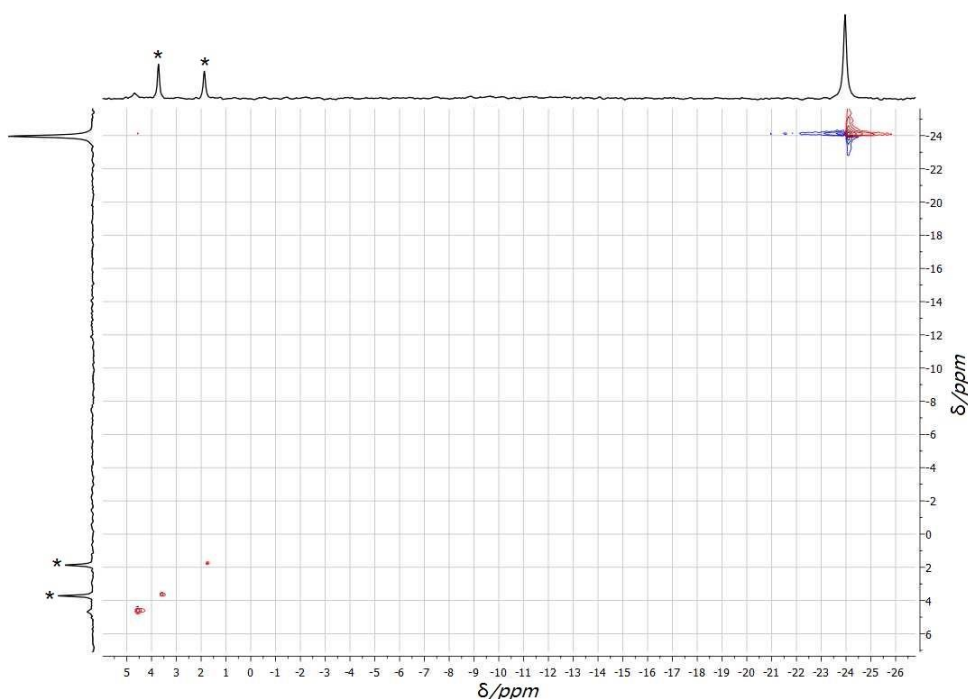
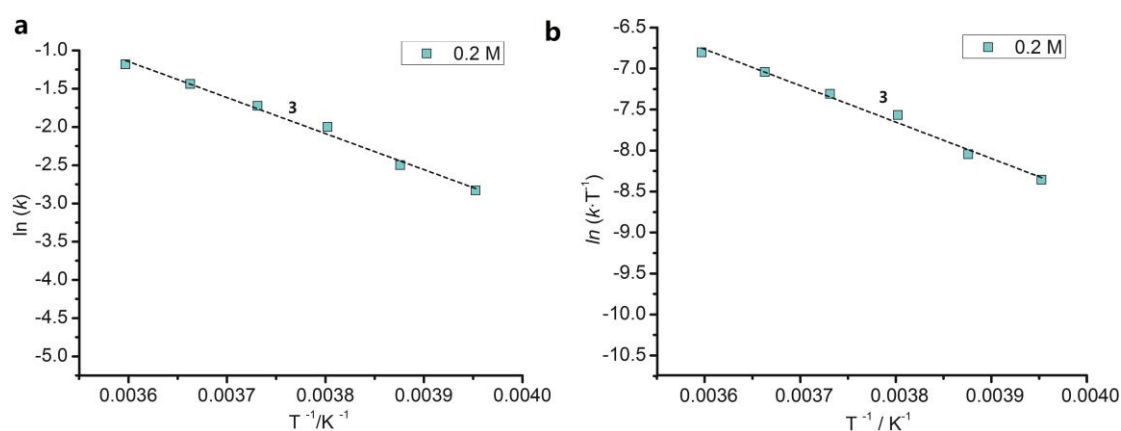


Figure 31: ²H-²H EXSY spectrum (77 MHz, 0.1 s mixing) of **2-D** under D₂ atmosphere in THF at 298 K (diagonal peak is not properly phased). A weak exchange peaks appears in the upper left corner between the D₂ (4.5 ppm) and hydride (-24 ppm) signals. Residual solvents are marked with an asterisk (*).

¹H-¹H EXSY spectra of mixtures containing **3** and H₂, recorded in the temperature range from 253 to 298 K (every 5 K recorded), showed exchange between H₂ and the Ni-bound hydrides (**Table 6**).

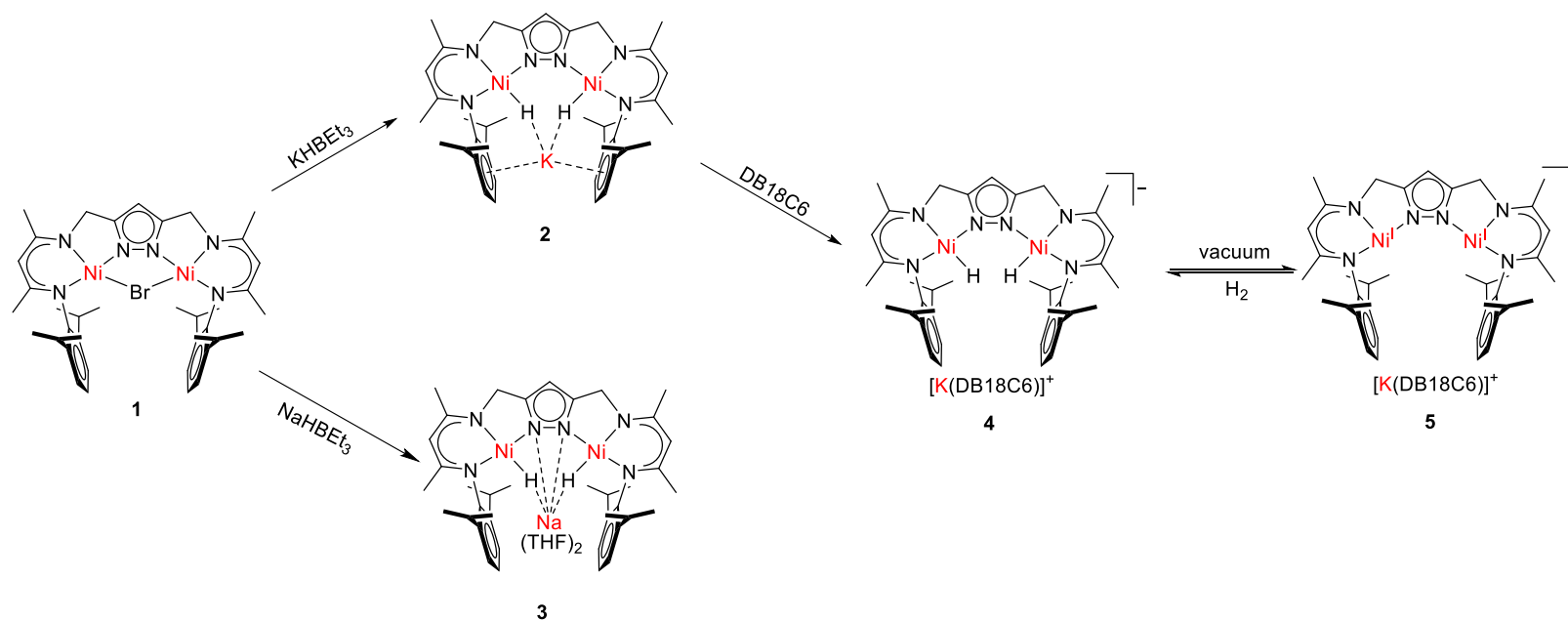
Table 6: Rate constants k (s⁻¹) for the (Ni-H)₂→H₂ exchange in **3** as function of temperatures.

T/K	k/s^{-1}
278	0.617
273	0.465
268	0.368
263	0.271
258	0.167
253	0.079

**Figure 32:** Arrhenius plots (a) and Eyring plots (b) for the (Ni-H)₂→H₂ exchange in **3**. Straight lines were separately fitted for the 253-278 K.

From the analysis of the ¹H-¹H NOESY spectra of **3** under H₂ atmosphere, first-order rate constants k were obtained for each temperature (278 K to 253 K) and used to derive the activation parameters $\Delta H^\ddagger = (39 \pm 3)$ kJ·mol⁻¹ from an Eyring plot (**Figure 32a**, **Table 6**). Arrhenius plotting (**Figure 32b**) gives an apparent activation energy $E_a = (39.2 \pm 0.6)$ kJ mol⁻¹.

3.5 Summary



Scheme 9: Synthetic routes for the dinuclear nickel(II) hydride **2**, **3**, **4** and double "T"-shaped **5**.

In summary, a new bimetallic dinuclear nickel(II) hydride **3** was synthesized from **1** with NaHBet₃. The reversible H/D exchanges of $\mathbf{M}[\mathbf{L}^1\mathbf{Ni}_2(\mu\text{-H})_2]$ (M= K and Na) with D₂ are associated to one step substitution of both Ni-H hydrogen atoms with the interacting substrate (D₂). Based on density functional theory (DFT) calculations which confirm the experimental results, a mechanistic picture of the exchange process was established. During all experiments no signs of an incipient HD formation was detected, which is in accordance with the non-scrambling exchange process. Meanwhile, a new double “T”-shaped Ni^I species (**5**) was obtained from complex **4** of solid state loss H₂ and characterized by x-ray diffraction. Therefore, the $[\mathbf{L}^1\mathbf{Ni}^{\text{II}}_2(\text{H})_2]^-$ complex (**2**⁻) can be viewed as a masked form of a reactive, antiferromagnetically coupled $[\mathbf{L}^1\mathbf{Ni}^{\text{I}}_2]^-$ species. The three bimetallic dinickel dihydride complexes increasingly recognized as a mean of avoiding unstable low-valent metal species or thermodynamically unfavorable one-electron reduced intermediates during the reductive activation of small molecules. The present bimetallic system based on the pyrazolate-bridged bis(nacnac) ligand appears particularly well suited for exploiting this concept. Next stage is studying the activation and transformation of a range of rather inert substrates using the new dinickel dihydride complex.

Chapter 4 Dioxygen binding to a bimetallic dinickel(II) dihydride complex and redox interconversion of the μ -1,2-peroxo and superoxo intermediates

Abstract Ni-O₂ intermediates have gained significant attention in the last few years with the identification of some new structure types. Lewis acid Ni^{II} complexes have been proven to react with dioxygen to give a very unstable organoperoxo complex, as proposed for the quercetin 2,4-dioxygenase enzymatic system. We herein report a new μ -1,2-peroxo dinickel(II) motif (**6**) which was obtained from a reaction of **2** with dioxygen. Excess dioxygen reaction with peroxo complex (**6**) generated a new μ -1,2-superoxo dinickel(II) compound (**9**). The thermal stable peroxo and superoxo bimetallic dinickel(II) complexes exhibit a μ -1,2-bonding geometry and have been investigated by UV/vis-, rRaman-, IR-, EPR spectroscopies, ESI mass spectrometry, SQUID measurement and DFT calculation. Eventually, interconversion of the μ -1,2-peroxo (**6**) and the μ -1,2-superoxo (**9**) *via* an excess of dioxygen or elemental potassium, respectively, has been accomplished.

4.1 Introduction

In principle, superoxo and peroxy nickel intermediates are not formed directly from the reaction of Ni^{II} complexes with O₂, but require prior reduction to Ni^I.^[31] Even though, Ni^{II} species which show reactivity towards O₂ are known in literature, the nature of the initial and final products are still very ambiguous.^[32] Recently, two outstanding examples have published from Ni^{II} species with oxygen directly and the final product was identified.^[33,34]

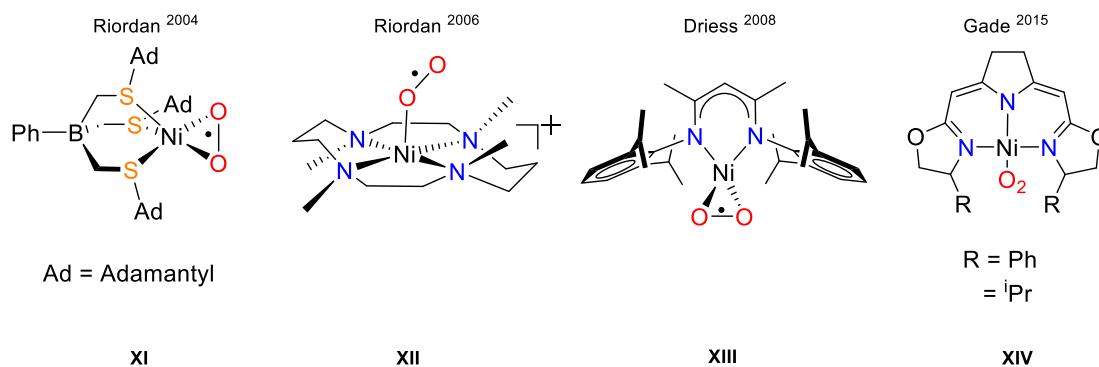


Figure 33: The reported superoxo ligand binding to the nickel metal.^[35-38]

Few superoxo nickel compounds were synthesized from dioxygen and Ni^I precursors (**Figure 33**). Ni–O₂ adducts (**Figure 33, XI and XII**) reported by *Riordan* group, resulted from one-electron reduction of O₂ by the respective Ni^I precursors at low temperature. These superoxo nickel complexes only exist at low temperature; they could only be characterized by DFT calculations and spectroscopies.^[35] The β -diketiminato superoxo nickel adduct (**Figure 33, XIII**) has been easily isolated by *Yao* and *Driess et.al.* in 2008, and its characterized by x-ray crystallography for the first time, and so far, the only crystallographically. The O–O bond length of 1.347(2) Å suggests that superoxo character and O–O stretching in IR spectrum is 971 cm⁻¹.^[36] In 2005, *Rettenmeier* and *Gade et.al.* obtained a new superoxo species (**Figure 33, XIV**) by exposing a chiral pincer ligand nickel(I) precursor to dioxygen. Unfortunately, this compound is only stable at low tem-

perature again. [37] Except for these superoxo compounds derived from oxygen and Ni^I precursor, some nickel superoxo complexes also can be obtained from a Ni^{II} precursor targeted with H₂O₂. [38]

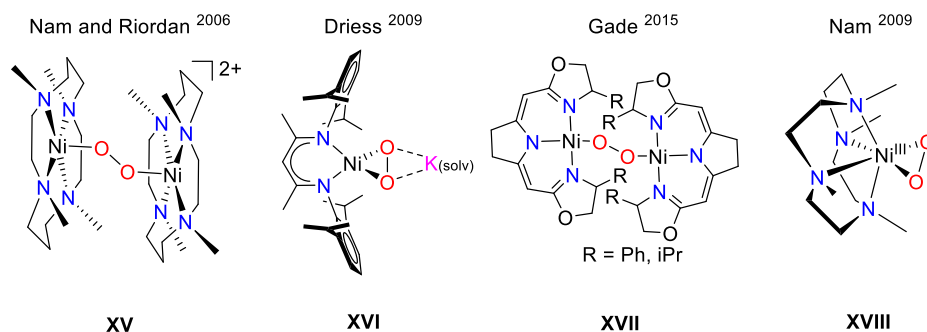


Figure 34: The reported peroxo ligand binding to the nickel. [39-42]

Furthermore, there are some other nickel peroxo complexes reported (**Figure 34**). The β -diketiminato superoxo nickel adduct (**Figure 34, XVI**) can be further converted into a peroxo ligand O₂²⁻ by one electron reduction from elementary potassium at RT in THF solution by Yao and Driess *et al.* in 2009. [39] The O–O distance of 1.468(2) Å is typically for metal peroxo compounds (1.4–1.5 Å). [40] The crystal structure showed uncommon [Ni(μ - η^2 : η^2 -O₂)K] core in which the K⁺ atom was weakly coordinated to the peroxo ligand (average K–O distance of 2.7 Å). In addition, Riordan *et al.* (**Figure 34, XV**) [41] and Gade *et al.* (**Figure 34, XVII**) [37] observed an interesting pattern in these superoxo and peroxo nickel(II) interconversion. The nickel(I) fragment reacts with oxygen most likely *via* a superoxo intermediate to give the only peroxo-bridged nickel complex characterized to date. In addition, a high valent Ni^{III} peroxo species (**Figure 34, XVIII**) was observed by Nam *et al.* in 2009 using [Ni^{II}(12-TMC)(O₂)] (12-TMC = 1,4,8,11-tetramethyl-1,4,8,11-tetraazacyclotetradecane) with five equivalents of H₂O₂ in the presence of trimethylamine in CH₃CN at 0°C, which was characterized by x-ray crystallography. [42]

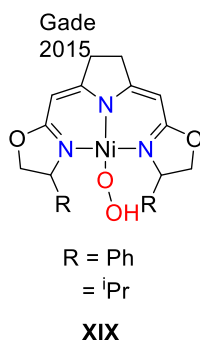


Figure 35: The reported peroxo ligand binding to the nickel. [47]

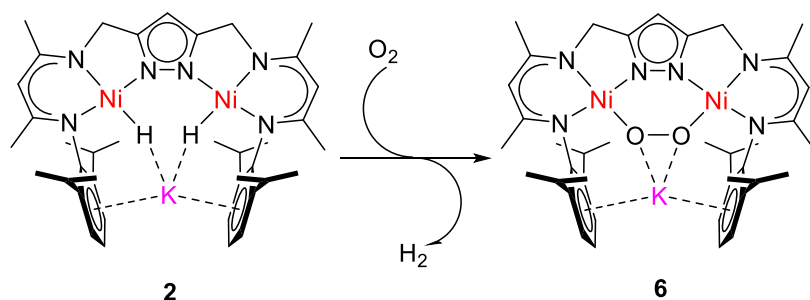
Transition-metal hydroperoxo (Cu and Fe) complexes play an important role in the enzymatic activation and the transport of dioxygen^[43] as well as reactive intermediates in catalytic oxygenations. [44] Although great efforts have been made to synthesize such metal complexes, only a limited of them have been structurally and spectroscopically characterized. [45] For over a decade, nickel hydroperoxo species have been considered to be a deactivated form of [NiFe] hydrogenase generated by oxygen. [46] Until now, only one example about nickel(II) hydroperoxo was reported by *Gade* in 2015 (**Figure 35, XIX**). [47] Selected spectroscopic features of these superoxo, peroxo and hydroperoxo with nickel metal are listed in **Table 7**.

Table 7: Selected spectroscopic features of synthetic mononuclear superoxo, peroxo and hydroperoxo species.

	S	Ni-O (Å) [a]	r(O-O) [Å] [a]	v(Ni-O) [cm ⁻¹] (Δ[¹⁸ O]) [cm ⁻¹] [c]	v(O-O) [cm ⁻¹] (Δ[¹⁸ O]) [cm ⁻¹] [c]	λ _{max} [nm] (ε [M ⁻¹ cm ⁻¹]) [d]	g values [e]	Ref
<i>Superoxonickel</i>								
[Ni ^{II} (O ₂)(PhTtAd)]	1/2	1.85 ^b	-	-	-	310(5900), 386(2900), 450(2500), 845(350)	2.24, 2.19, 2.01	35a
[Ni ^{II} (O ₂)(14-tmc)]	1/2	1.98	-	437(-21)	1131(-64)	345(5900), 328(sh), 339(800),	2.29, 2.21, 2.09	35b
[Ni ^{II} (O ₂)(13-tmc)]	1/2	1.91	-	-	1130(-60)	845(130), 684(60)	2.25, 2.21, 2.06	38b
[Ni ^{II} (O ₂)(Nacnac)]	1/2	1.817(2) 1.840(2)	1.347(2)	-	971(-52)	360(1500), 845(170), 980(430)	2.14, 2.12, 2.07	36
<i>Peroxonickel</i>								
[Ni ^{II} (O ₂)(^t BuNC) ₂]	0	1.902(7) 1.808(8)	1.45(1)	-	898 (-50)	380(316), 600(38)	-	48
[(Nacnac)Ni ^{II} (O ₂)K(solvent)]	0	1.820(2) 1.820(2)	1.468(2)	-	829 (-47)	-	-	39

$[\text{Ni}^{\text{III}}(\text{O}_2)(12\text{-tmc})]^+$	1/2	1.884(3) 1.894(3)	1.386(4)	-	1002 (-57)	350(300), 400(280) 650(100), 900(80)	2.2, 2.17, 2.06	42
$[\text{Ni}^{\text{III}}(\text{O}_2)(13\text{-tmc})]^+$	1/2	1.897(3) 1.898(3)	1383(4)	-	1008 (-58)	400(150), 700(80) 900(50)	2.19, 2.07	38b
<i>Hydroperoxonickel</i>								
$[\text{Ni}^{\text{II}}(\text{OOH})(\text{iso-pmbox})]$	0	1.846(2)	1.492(2)	-	-	-	-	47
[a] Unless otherwise stated, bond lengths are determined by x-ray diffraction. [b] Bond length determined by XAS. [c] Frequency of the Ni-O and O-O vibrations and the corresponding shifts upon labeling with ^{18}O determined by Raman or IR spectroscopy. [d] Uv-vis absorption features determined in solution. [e] <i>g</i> values determined by EPR spectroscopy.								

4.2 Synthesis of a μ -1,2-peroxo bridged dinickel(II) complex



Scheme 10: Synthetic route for **6**

As mentioned in chapter 3, the $[\text{L}^1\text{Ni}^{\text{II}}_2(\text{H}_2)]^-$ complex can be viewed as a masked form a reactive, antiferromagnetically coupled $[\text{L}^1\text{Ni}^{\text{II}}_2]^-$ species. In this concept, it has been exploited for the reactivity of $[\text{L}^1\text{Ni}^{\text{II}}_2(\text{H}_2)]^-$ toward dioxygen.

Treatment of a THF solution of **2** with one equivalent dioxygen (prior dried over concentrated H_2SO_4) (**Scheme 10**) results in a rapid color change from orange to dark red and formation of a new species identified by ^1H NMR spectroscopy (**Figure 36**). A new resonance corresponding with H_2 is also observed in *in situ* NMR spectra of reaction mixtures, implying H_2 upon reaction of **2** with dioxygen. When **2-D** was treated with dioxygen and the reaction monitored by ^2H NMR spectroscopy, the formation of D_2 was clearly detected (**Figure 37**).

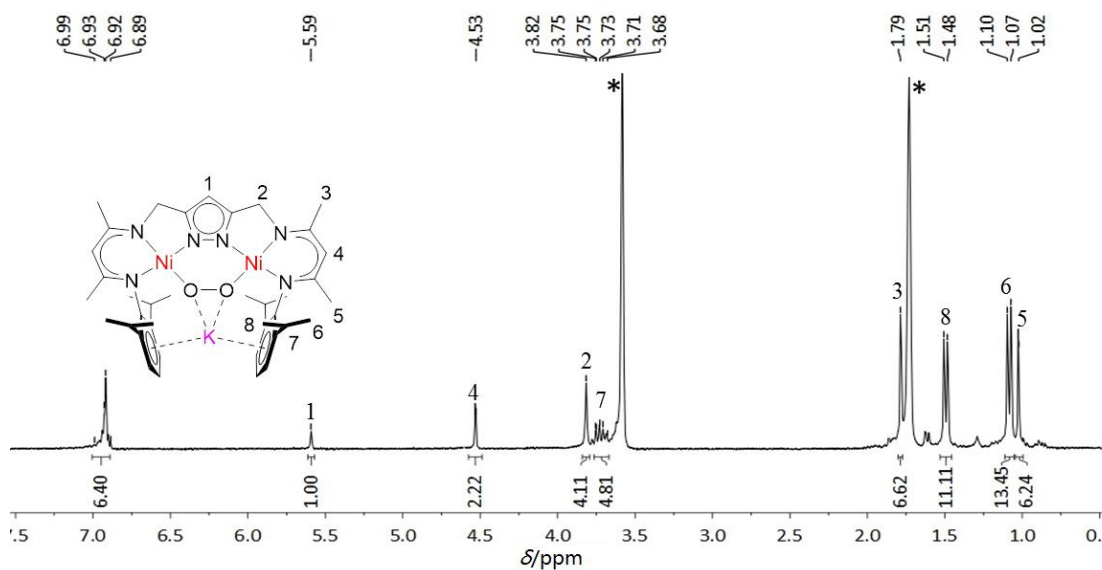


Figure 36: ^1H NMR spectrum (400 MHz) of **6** in THF-d_8 . Residual solvents are marked with an asterisk (*).

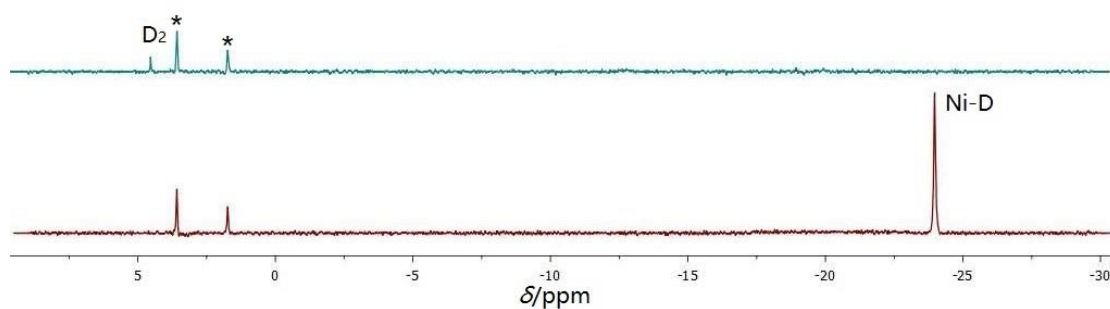


Figure 37: ^2H NMR (77 MHz) spectrum of excess O_2 introduced into **2-D**. Residual solvents are marked with an asterisk (*).

This formation of **6** is supported by x-ray diffraction and UV-Vis, FT-IR, Raman spectroscopies and ESI-MS spectrometry. Suitable crystals for x-ray diffraction were obtained by layering hexane on a solution of **6** in THF at -30°C . **6** crystallizes in the triclinic space group $P-1$. There are two crystallographically distinct molecules per asymmetric unit: one of the two molecules is **6**, the other one is hydroxide nickel complex (**11**). The molecular structure of **6** is shown in **Figure 38** and selected bond lengths (\AA) and angles ($^\circ$) are listed in **Table 8**. As shown in **Figure 38**, a six-membered $\{\text{N}_2\text{Ni}_2\text{O}_2\}$ twisted ring was formed by the nickel atoms, the nitrogen atoms from pyrazolate ligand and the oxygen atom from peroxo ligand. The two nickel(II) ions are hosted in the two $\{\text{N}_3\}$ -tridentate

binding sites of the trianionic ligand scaffold, bridged by the pyrazolate and a peroxo ligand. The distance of 3.880(1) Å between the two nickel(II) ions of **6** is shorter than **2**. The Ni–N(β -diketinato) distances are in the range of 1.904(2)–1.911(2) Å, which is longer than the distances of Ni–N(P_z) (1.835(2) and 1.854(2) Å), but similar to other mononuclear nickel peroxo complexes coordinating nacnac ligand (**Figure 34, XVI**). The Ni–O–O–Ni torsion angle around the O–O axis is 81.41(28)°. The K⁺ ion interacts with two aryl rings of the DIPP substitutes *via* cation- π (2.840(1) and 2.830(1) Å) and coordinates to both peroxo oxygen atom (O1 and O2) with 2.515(2) Å and 2.545(2) Å, respectively. The O–O separation of 1.482(2) Å is analogous to other metal peroxo complexes (1.4–1.5 Å).^[40]

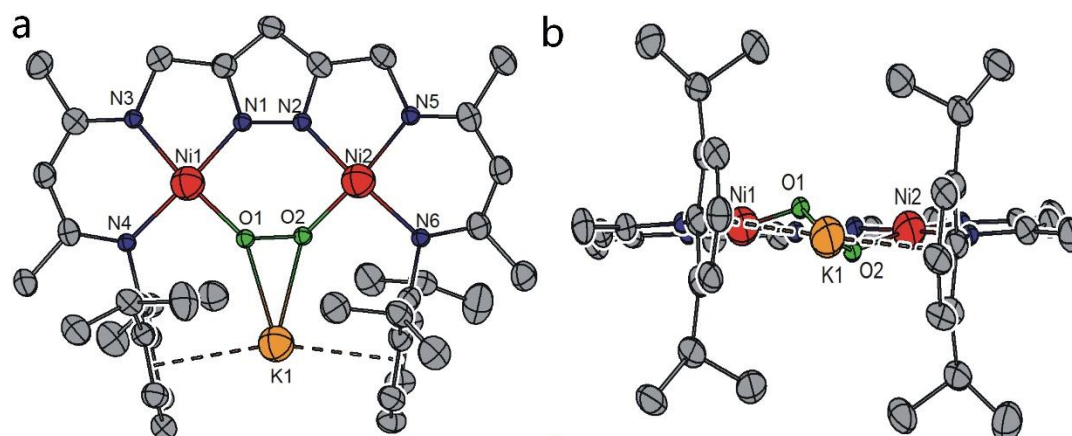


Figure 38: Molecular structure (50% probability thermal ellipsoids) of **6** (only one of two molecules shown). All hydrogen atoms omitted for clarity.

Table 8: Selected bond lengths (Å) and angle (°) for **6**.

Atoms	Bond lengths	Atoms	Bond angles
Ni1–N1	1.854(3)	N1–Ni1–O1	91.04(13)
Ni1–O1	1.861(3)	N1–Ni1–N3	82.48(14)
Ni1–N3	1.909(3)	O1–Ni1–N3	170.45(13)
Ni1–N4	1.922(3)	N1–Ni1–N4	175.98(14)
Ni2–N2	1.835(3)	O1–Ni1–N4	92.93(13)
Ni2–O2	1.861(3)	N3–Ni1–N4	93.67(13)
Ni2–N6	1.904(3)	N2–Ni2–O2	90.45(13)
Ni2–N5	1.911(3)	N2–Ni2–N6	176.13(14)
O1–O2	1.482(2)	O2–Ni2–N6	92.99(13)
K1–O1	2.545(2)	N2–Ni2–N5	82.89(14)

K1-O2	2.515(4)	O2-Ni2-N5	169.57(14)
Ni1...Ni2	3.880(8)	N6-Ni2-N5	93.45(14)
K-Cg (1)	2.840(1)	O2-O1-Ni1	118.2(2)
K-Cg (2)	2.830(1)	O1-O2-Ni2	118.0(2)
		Ni1-O1-O2-Ni2	81.41(28)

Cg(1) = centroid of the ring carbon atoms C10, C11, C12, C13, C15, C15 (left side);
Cg(2) = centroid of the ring carbon atoms C28, C29, C30, C31, C32, C33 (right side).

6 has been characterized by positive ion ESI-MS spectrometry in THF/MeCN mixture solution as well. The ESI-MS (+) of **6** exhibits a prominent signal at $m/z = 793.34$, (**Figure 40**), whose mass and isotope distribution pattern corresponds to $[\mathbf{6}+\text{H}]^+$ (*calcd* $m/z = 793.26$). Two peaks for labelling peroxy compounds were observed which shifted to $m/z = 819.24$ ($\mathbf{6}+\text{Na}$)⁺ and 835.19 ($\mathbf{6}+\text{K}$)⁺ when **6** was prepared with isotopically enriched ¹⁸O₂ (**Figure 40**).

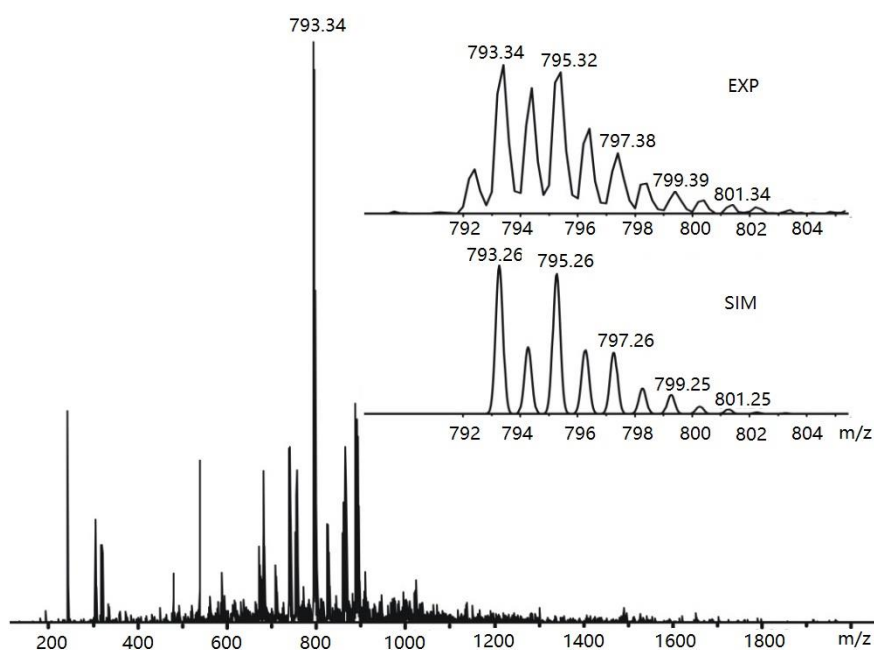


Figure 39: ESI-MS(+) of **6** in THF/CH₃CN. The inset shows the experimental (upper) and simulated (lower) isotopic distribution pattern for $[\mathbf{6}+\text{H}]^+$.

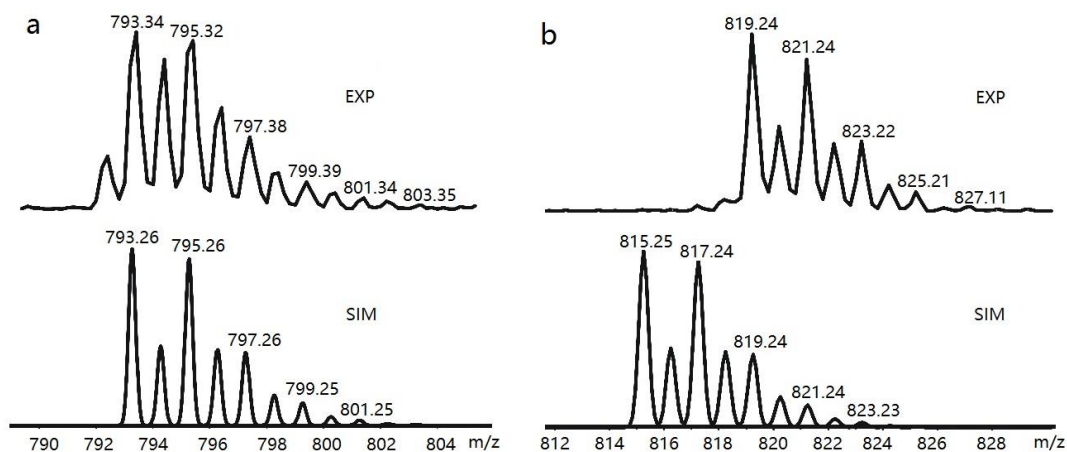


Figure 40: Experimental ($^{16}\text{O}_2$ and $^{18}\text{O}_2$) (upper) and simulated ($^{16}\text{O}_2$) (lower) isotopic distribution pattern for $[\mathbf{6}+\text{H}]^+$ (a) and $[\mathbf{6}+\text{Na}]^+$ (b).

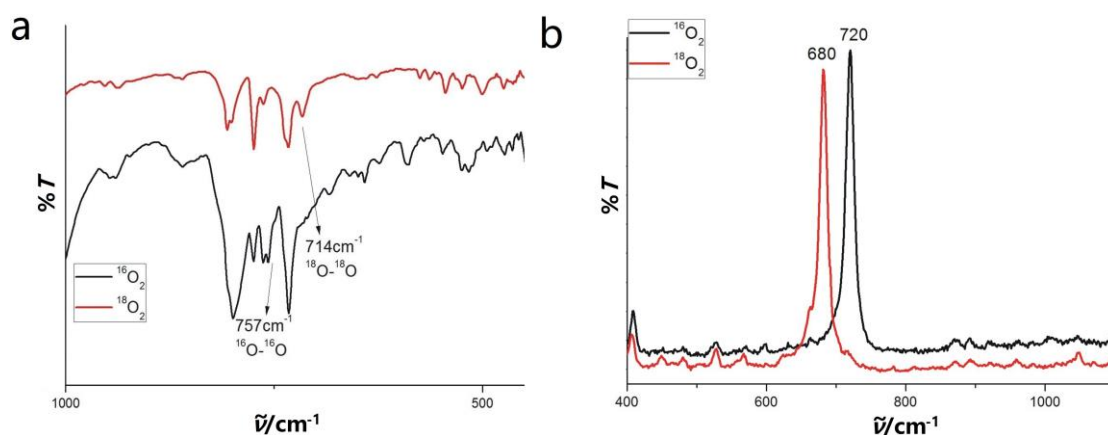


Figure 41: (a) Comparison of the IR spectra of crystalline material of **6** prepared using $^{16}\text{O}_2$ (black) and $^{18}\text{O}_2$ (red) in the range of 450 cm^{-1} to 1000 cm^{-1} ; (b) Comparison of the rRaman spectra of crystalline material of **6**: prepared using $^{16}\text{O}_2$ (black) and $^{18}\text{O}_2$ (red) in the range of 400 cm^{-1} to 1100 cm^{-1} .

Resonance Raman data of crystalline material of **6**- $^{16}\text{O}_2$ revealed a signal at 720 cm^{-1} , which shift to 680 cm^{-1} upon $^{18}\text{O}_2$ labelled ($\Delta^{16}\text{O}_2-^{18}\text{O}_2 = 40\text{ cm}^{-1}$, **Figure 41b**). However, comparison of IR spectra of **6** prepared using $^{16}\text{O}_2$ and $^{18}\text{O}_2$ between 450 and 1000 cm^{-1} , no obvious difference was observed. In view of the data from Raman and literature, I assigned the $^{16}\text{O}-^{16}\text{O}$ stretching vibration mode in **6** of 757 cm^{-1} ($\nu(^{18}\text{O}-^{18}\text{O}) = 714\text{ cm}^{-1}$) ($\Delta^{16}\text{O}_2-^{18}\text{O}_2 = 43\text{ cm}^{-1}$, **Figure 41a**).

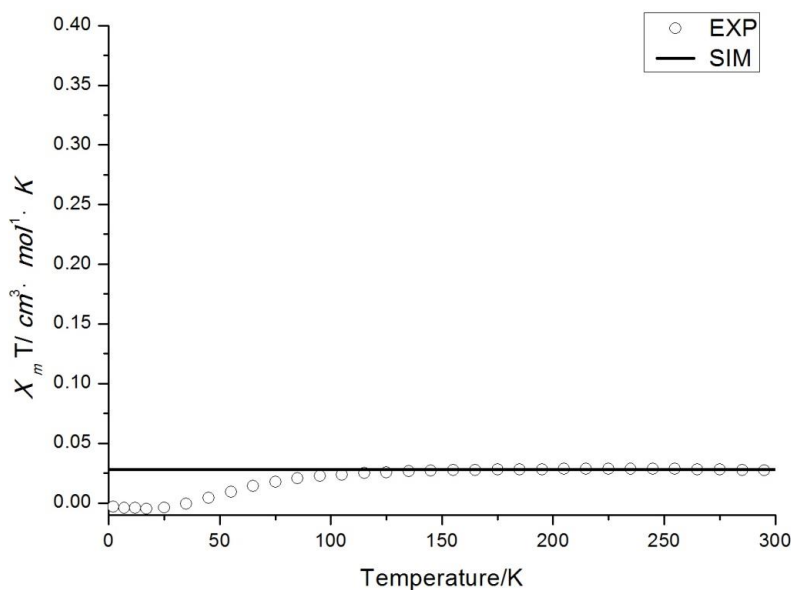
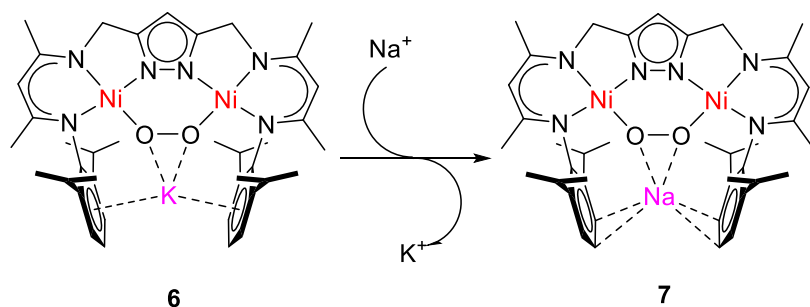


Figure 42: $\chi_m T$ vs. T measurement in the temperature range of 2–295 K at 0.5 T for solid samples of **6**. The solid red lines represent the best global fit with $PI = 2.8\%$ ($S = 1$) and $TIP = 430 \cdot 10^{-6} \text{ cm}^3 \cdot \text{mol}^{-1}$.

Magnetic susceptibility data for **6** collected in the temperature range from 2–295 K in crystalline material, show essentially diamagnetic behavior up to room temperature (**Figure 42**).

■ Reactivity of **6** towards Na^+ and PPh_3

Cation Exchange. No color change was observed in the reaction of **6** with excess NaBARF_4 in THF-d_8 for few days (**Scheme 11**). However, the ^1H NMR spectrum showed the resonance for isopropyl and CH_3 group in the DIPP substituents changed (**Figure 43**). It is assigned that a new species was formed. Nevertheless, suitable crystals for x-ray diffraction were obtained from hexane layer into $\text{THF} - 30^\circ\text{C}$ in two days. Owing the low resolution as well as disorder, the data of **7** only allowed us to depict a model of its structure similar to **6**. In the x-ray crystallography, the Na^+ cation is fixed by the two DIPP substituents.



Scheme 11: Cation exchange between the K^+ and Na^+ .

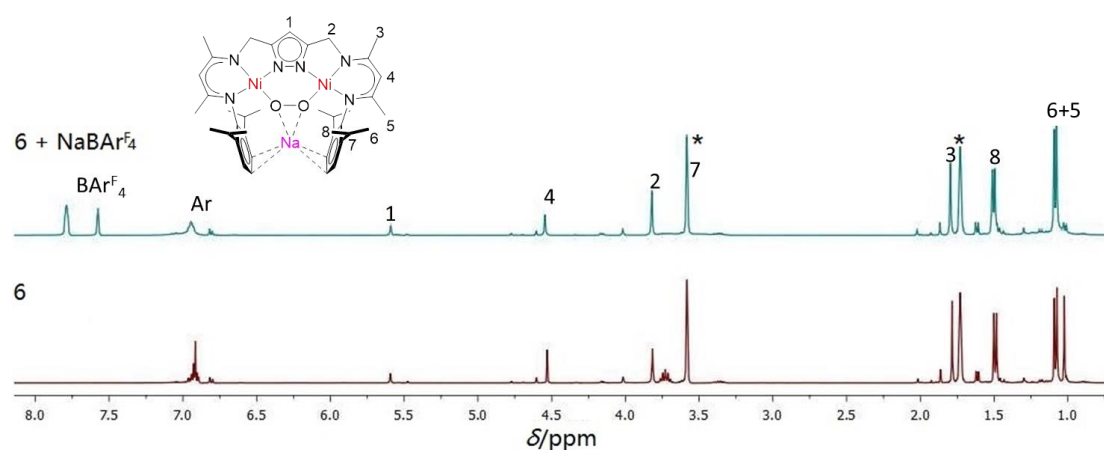
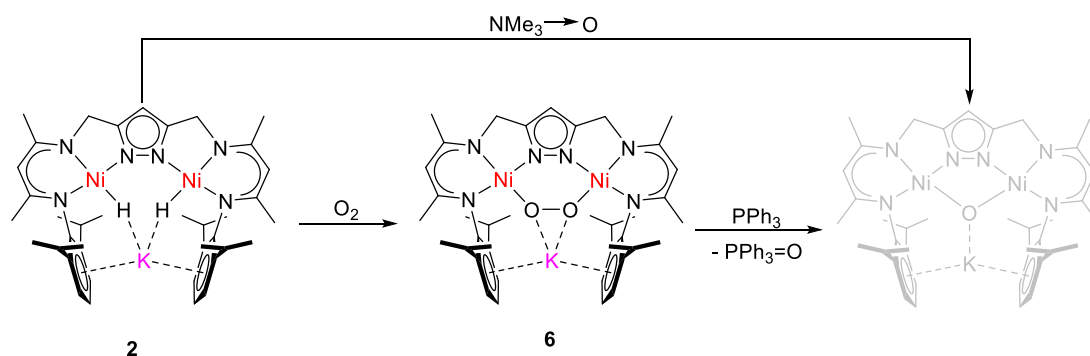


Figure 43: Comparison the ^1H NMR spectra of **6** and **7** in THF-d_8 . Residual solvents are marked with an asterisk (*).

Reaction with PPh_3 . As expected, **6** is a gentle oxygenation reagent as shown by its reaction with PPh_3 to afford $\text{PPh}_3=\text{O}$ and an unidentified dinickel species (**Scheme 12**).

Time depending ^1H (**Figure 44**) and ^{31}P NMR (**Figure 45**) spectra demonstrate the slow process of conversion from **6** to a new nickel species. After keeping the sample in THF-d_8 for two days, characteristic proton resonance of pyrazole of **6** decreased in the ^1H NMR spectrum (**Figure 44**). Eventually, **6** was completely consumed after few days. In the ^{31}P NMR, a new peak at 23.51 ppm for $\text{PPh}_3=\text{O}$ [49] was observed in one hour and gradually increase in the next two days (**Figure 45**). Same ^1H NMR spectrum of the unidentified nickel species was observed from **2** with $\text{NMe}_3 \rightarrow \text{O}$ also. Related to literature,^[36] I presumed that the unidentified new species is a dinickel μ -oxo complex. Recently, the unique

$\text{Ni}^{\text{II}}(\mu\text{-O})\text{Ni}^{\text{II}}$ core characterized by x-ray diffraction was reported by *Xue* and co-worker.^[50] This research project in our group is still going on.



Scheme 12: Generate new dinuclear nickel(II) species from **2** or **6**.

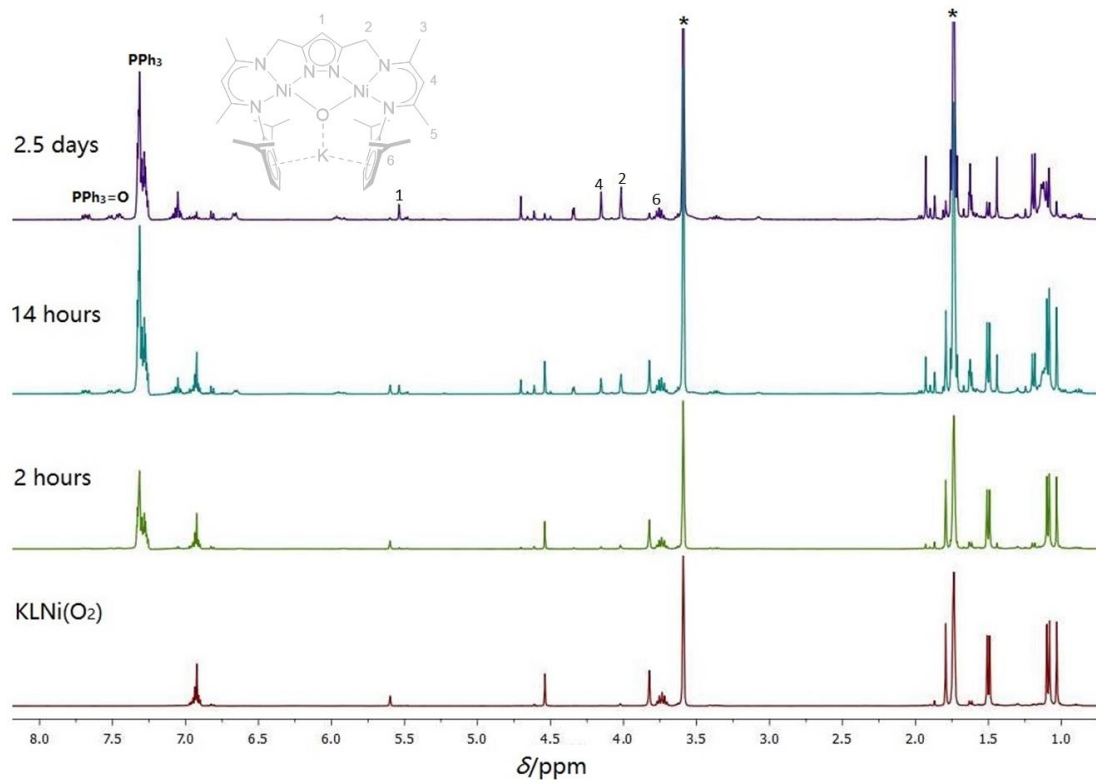


Figure 44: Slow transformation of **6** to $\text{KL}^1\text{Ni}_2(\mu\text{-O})$ in the presence of PPh_3 at room temperature in THF-d_8 demonstrated by stacked ^1H NMR spectra (400 MHz). Residual solvents are marked with an asterisk (*).

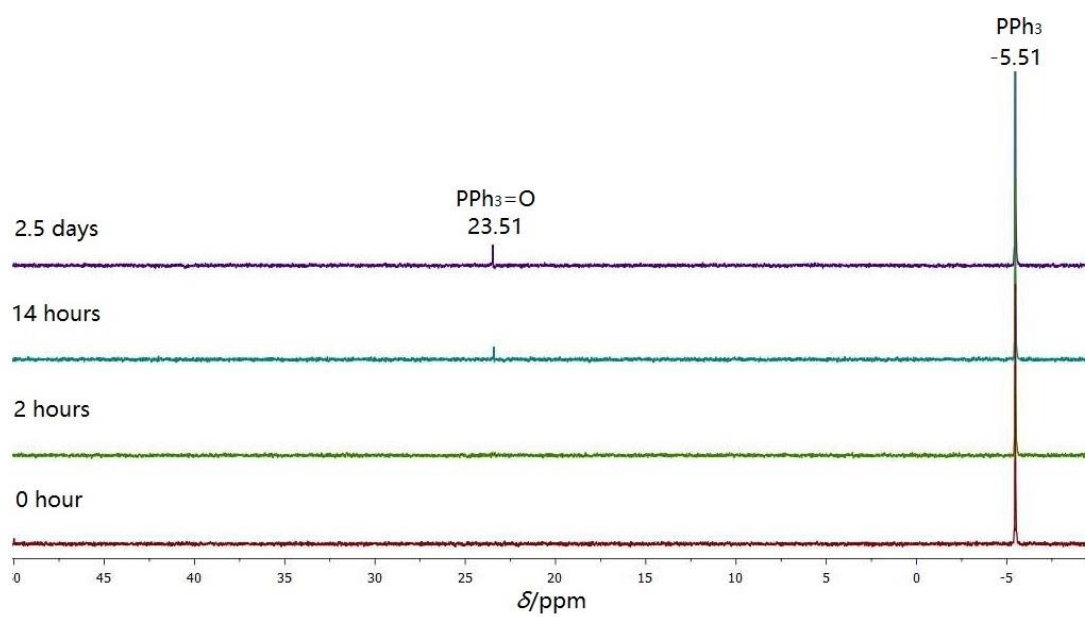
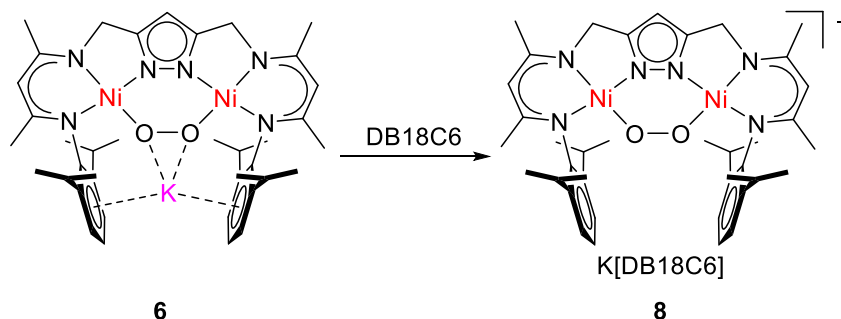


Figure 45: Time depending consuming of PPh_3 with **6** at the room temperature in THF-d_8 to new species process by stacked ^{31}P NMR spectra (160 MHz).

4.3 Dissociation the peroxy-K⁺ interaction in bimetallic dinickel(II) complex



Scheme 13: Synthetic route for **8**.

In the solid state of **6**, the K⁺ cation has interaction with the peroxy ligand. To further assess the electronic structure of peroxy without the effect of the alkali metal cations, **6** was treated with (18-crown-6), [2,2,2]cryptand or DB18C6 to separate the K⁺ cation from the [L¹Ni₂(O₂)]⁻ complex anion. No obvious color change was associated with these reactions, but the ionic products become poorly soluble in THF (**Scheme 13**); these differences in solubility suggest that the K⁺ cation remain closely associated with the [L¹Ni₂(O₂)]⁻ anion and that contact ion pairs are present in THF solutions of **8**. Unfortunately, all crystallizing attempts for x-ray diffraction using (18-crown-6) and [2,2,2]cryptand failed. Suitable crystals for x-ray diffraction using DB18C6 were obtained by layering mixture solvent Et₂O/Hexane on a solution of **8** in THF at -30°C.

It became obvious that, similar to the **6**, the product is composed of the ligand-nickel unit, binding a peroxy ligand entity. In **8**, the potassium is situated in the DB18C6 ligand and coordinated by two more THF ligands. The core structure of the “naked” complex anion is showed in **Figure 46** and selected bond lengths (Å) and angles (°) are listed in **Table 9**. The distance of Ni···Ni and peroxy ligand of 3.880(7) Å and 1.465(2) Å, respectively, are shorter than **6**. And the Ni-O-O-Ni

torsion angle around the O–O axis is defined as $89.92(1)^\circ$, which is close to a right angle (90°).

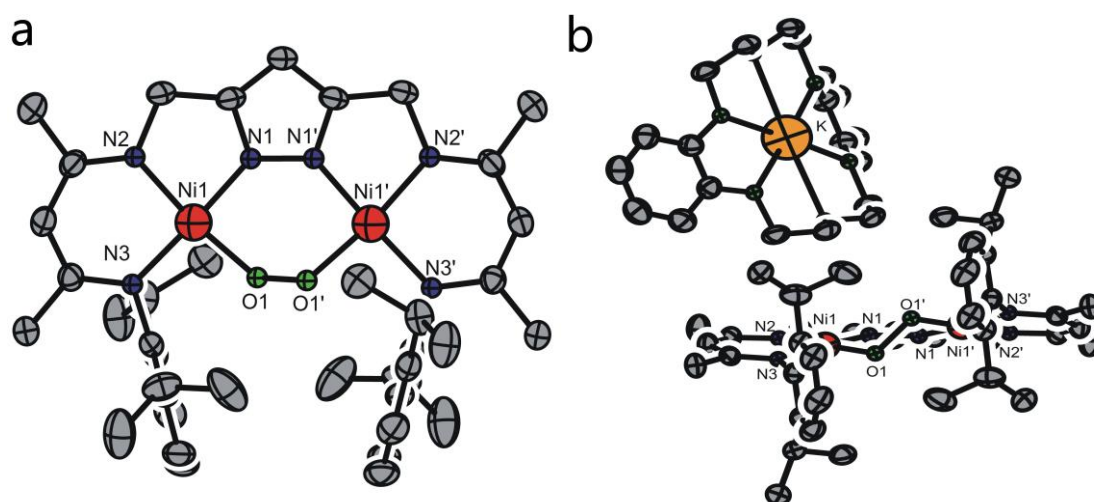


Figure 46: Molecular structure (50% probability thermal ellipsoids) of the anion of **8** (a) and **8** (b). Most hydrogen atoms omitted for clarity. Symmetry transformations used to generate equivalent atoms: (') $x, 3/2-y, 1-z$.

Table 9: Selected bond lengths (Å) and angles ($^\circ$) for **8**.

Atoms	Bond lengths	Atoms	Bond angles
Ni1-O1	1.834(2)	O1-Ni1-N1	91.08(8)
Ni1-N1	1.843(2)	O1-Ni1-N3	90.90(8)
Ni1-N3	1.894(2)	N1-Ni1-N3	175.89(9)
Ni1-N2	1.906(2)	O1-Ni1-N2	172.80(8)
O1-O1'	1.465(2)	N1-Ni1-N2	82.16(8)
Ni1...Ni1'	3.791(7)	N3-Ni1-N2	95.69(8)
		O1'-O1-Ni1	113.81(12)
		Ni1-O1-O1'-Ni1'	89.92(1)

8 is a diamagnetic compound and should lead to a rise of sharp signals in the ^1H and ^{13}C NMR spectra in the common chemical shift range at RT. However, at RT (**Figure 47**) or even at low temperature (**Figure A11**), the ligand system of **8** has broad peaks in the ^1H NMR spectrum. The resonance associated to the isopropyl CH function was overlaid by the solvent (THF- d_8), but was distinguished by means of a ^1H - ^1H COSY experiment. (**Figure A14**)

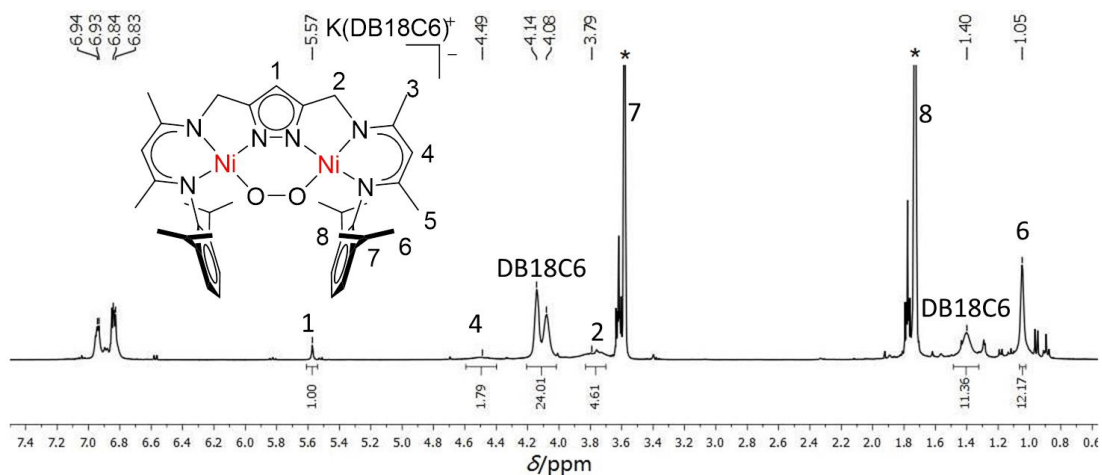


Figure 47: ^1H NMR spectrum of **8** in THF-d_8 (400 MHz) at RT. Residual solvents are marked with an asterisk (*).

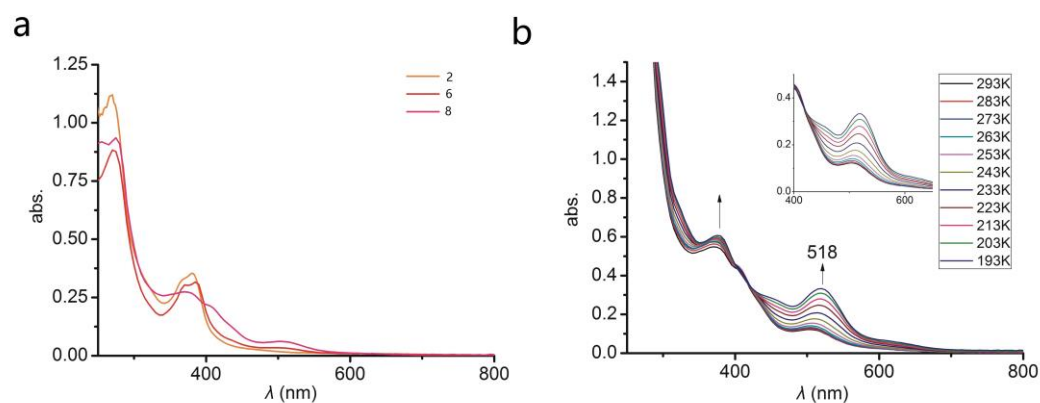


Figure 48: (a) UV-Vis spectra of **2**, **6** and **8**; (b) Variable temperatures (293 K-193 K) UV-Vis spectra in THF of **8**.

A new absorption band in the UV-Vis spectrum (**Figure 48a**) at 512 nm ($\epsilon \approx 240 \text{ M}^{-1}\cdot\text{cm}^{-1}$) in **6** and 518 nm ($\epsilon \approx 320 \text{ M}^{-1}\cdot\text{cm}^{-1}$) in **8** grew up after insert the dioxygen into **2** or **4**, which is attributed to the $\text{O}_2^{2-} \rightarrow \text{Ni(II)}$ charge transfer (CT) transitions. A similar band was reported in the complexes **XVI** and **XVIII** (**Figure 34**). The band at 380 nm ($\epsilon \approx 700 \text{ M}^{-1}\cdot\text{cm}^{-1}$) and a shoulder around 410 nm ($\epsilon \approx 530 \text{ M}^{-1}\cdot\text{cm}^{-1}$) in **8** were assigned to the ligand $\pi \rightarrow \pi^*$ transitions. With decreasing temperature (**Figure 48b**), the wavelength at 518 nm increased, which suggested the change in torsion angle (Ni-OO-Ni) and molecule orbital overlap of nickel and oxygen.

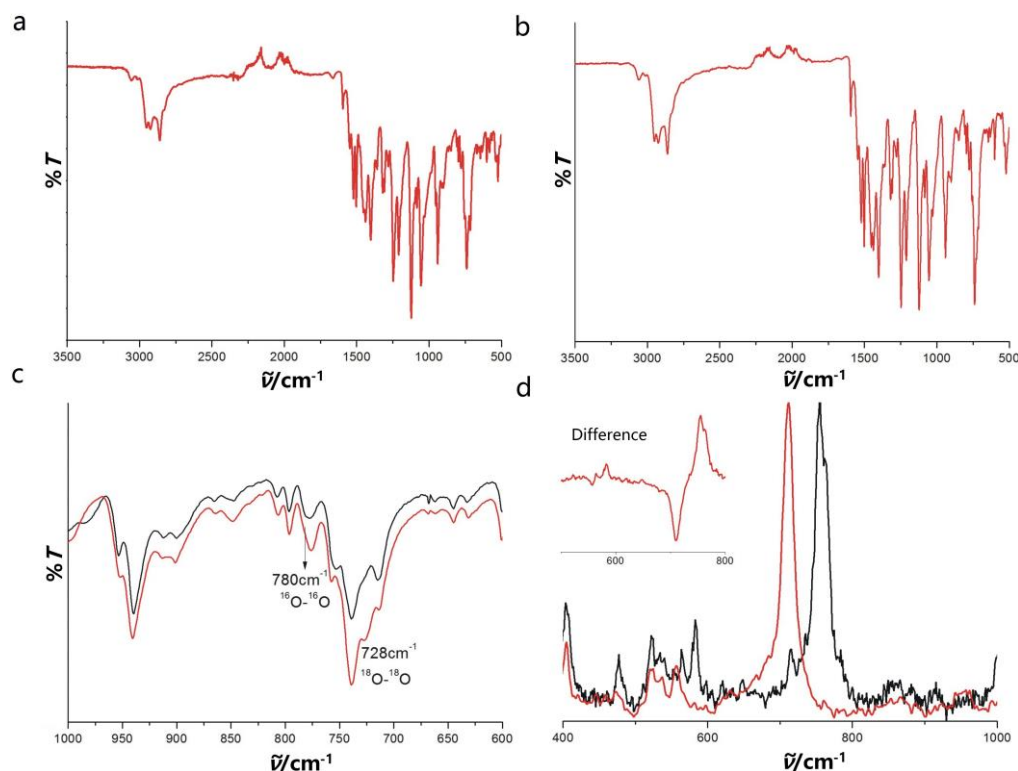


Figure 49: (a) IR spectrum of **8**- $^{16}\text{O}_2$; (b) IR spectrum of **8**- $^{18}\text{O}_2$; (c) Comparison of the IR spectra of **8**: Without (black) and after ^{18}O labelling (red) in the range of 1000 cm^{-1} to 600 cm^{-1} . (d) Comparison of the rRaman spectra of **8** (Normalized): Without (black) and after ^{18}O labelling (red) in the range of 400 cm^{-1} to 1000 cm^{-1} .

The resonance Raman vibration of O-O stretching was observed at 755 cm^{-1} ($\nu(^{18}\text{O}-^{18}\text{O}) = 715\text{ cm}^{-1}$) ($\Delta^{16}\text{O}_2-^{16}\text{O}_2 = 40\text{ cm}^{-1}$, **Figure 49d**), which is blue-shifted compared to **6** with O-O stretching vibration at 720 cm^{-1} . The O-O stretching vibration in **8** appears at 780 cm^{-1} in IR spectrum ($\nu(^{18}\text{O}-^{18}\text{O}) = 728\text{ cm}^{-1}$) ($\Delta^{16}\text{O}_2-^{18}\text{O}_2 = 52\text{ cm}^{-1}$, **Figure 49c**). The differences of **6** and **8** in IR and Raman spectra indicate that the peroxo ligand acts as a weaker electron acceptor without potassium ion interaction. The stronger σ donor interaction of the bridging peroxo removes more electron density from the antibonding $\text{O}_2^{2-}\pi^*$ orbital, resulting in a stronger O-O bond. Interestingly, the observed O-O stretching frequency of **6** and **8** are significantly lower than that other reported “side-on” Ni-peroxo compounds (**Table 7**).^[39, 42] Nevertheless, in comparison with the previously reported “end-on” bridging dinickel peroxo complexes **XV**^[41] and

XVII^[47], the O-O resonance Raman vibrational bands for **6** and **8** were found at similar wave-numbers.

The electronic structure of **8** is supported by the results of DFT studies (**Figure 50**; B3LYP hybrid functional, def2-tzvp and def2tzvp/j basis sets). The large Ni-O-O-Ni torsion angle and O-O distance in **6** and **8** are 81.41° and 89.91°, 1.482 Å and 1.468 Å, respectively. Whereas in the DFT calculation, the torsion angle of Ni-O-O-Ni is 83.7° and O-O bond distance is determined as 1.395 Å (**Table 10**). A possible explanation for these differences is because of the K⁺ cation position in the complex. The calculations of IR spectrum for O-O stretching frequency in DFT are much longer than the experimental data of **6** and **8** (**Table 11**). The reason of the difference is stay ambiguous.

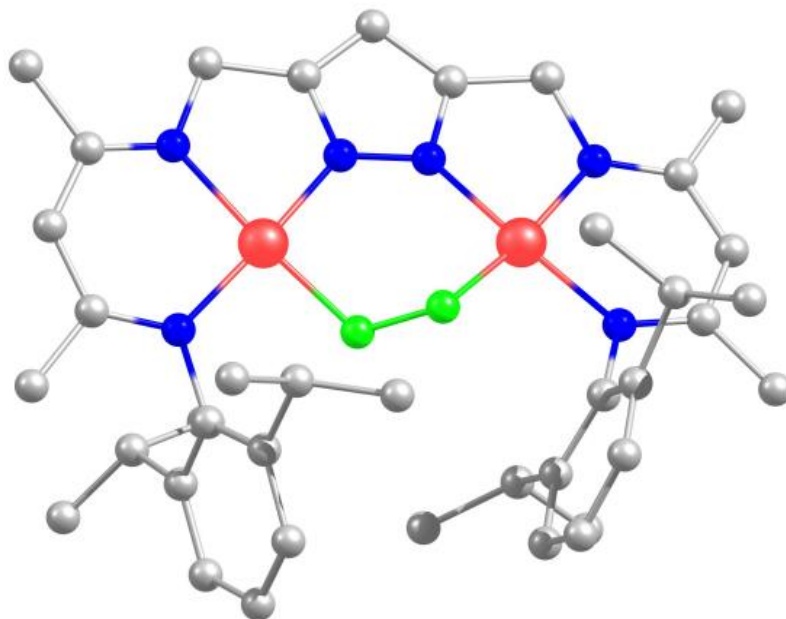


Figure 50: Calculated of molecular structure of the anion of **8**.

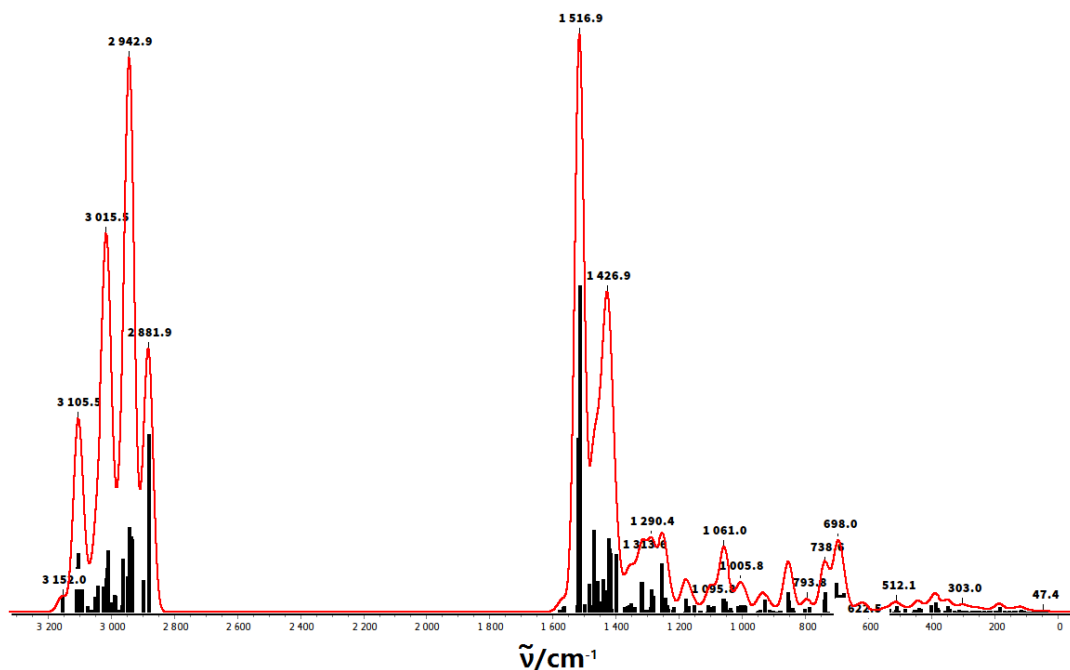


Figure 51: Calculated IR spectrum of the anion of **8**.

Table 10: Selected distances (Å) and angles (°) of the anion for **8**.

	$d(\text{O-O}) / \text{Å}$	$d(\text{Ni}\cdots\text{Ni}) / \text{Å}$	$\varphi(\text{Ni-O-O-Ni}) / ^\circ$
EXP (6)	1.482	3.880	81.41
EXP (8)	1.468	3.791	89.91
DFT	1.395	3.836	83.7

Table 11: $\nu(\text{O}\cdots\text{O})$ (IR) of the anion for **8**.

	$\nu(^{16}\text{O}-^{16}\text{O}) / \text{cm}^{-1}$	$\nu(^{18}\text{O}-^{18}\text{O}) / \text{cm}^{-1}$	$\Delta\nu / \text{cm}^{-1}$
EXP (6)	757	714	43
EXP (8)	780	728	52
DFT	857	810	48

4.4 Synthesis of an μ -1,2-superoxo bridged dinuclear nickel(II) complex

During the synthesis of **6**, a paramagnetic shift was observed in the ^1H NMR spectrum when **2** react with excess oxygen. To understand and identify the paramagnetic product, UV-Vis spectroscopy was employed to distinguish the new species.

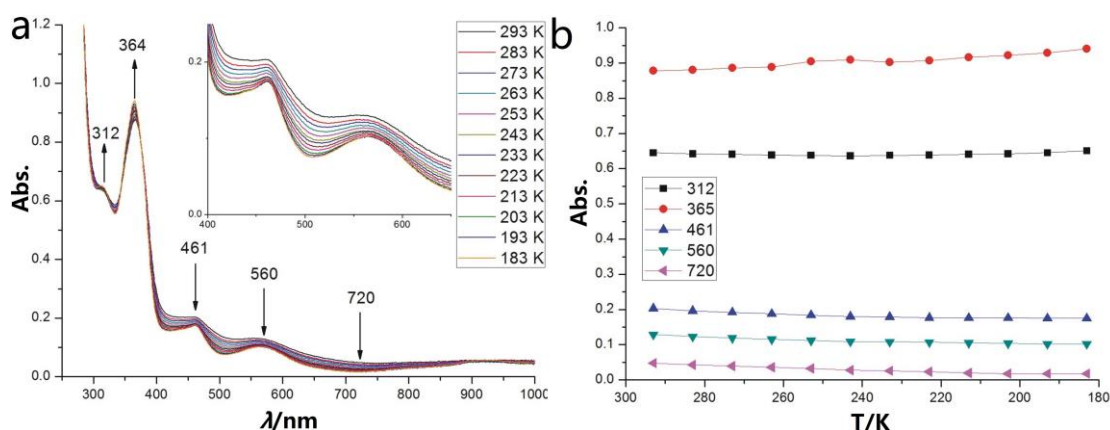
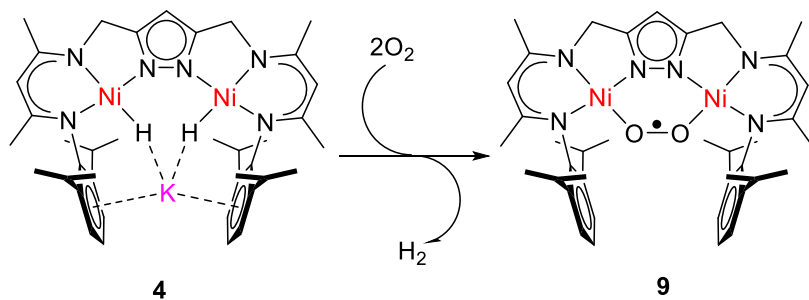


Figure 52: (a): VT UV-Vis spectra changes upon cooling from 293 K to 183 K in THF solution. (b) Plots of absorption at different temperatures.

The electronic spectra of **9** displays features at 312 ($\epsilon \approx 650 \text{ M}^{-1}\cdot\text{cm}^{-1}$) and 364 ($\epsilon \approx 880 \text{ M}^{-1}\cdot\text{cm}^{-1}$) nm, which are assigned ligand $\pi \rightarrow \pi^*$ transfer. However, three weak bands at 461 ($\epsilon \approx 200 \text{ M}^{-1}\cdot\text{cm}^{-1}$) and 560 ($\epsilon \approx 130 \text{ M}^{-1}\cdot\text{cm}^{-1}$) nm as well as 720 ($\epsilon \approx 20 \text{ M}^{-1}\cdot\text{cm}^{-1}$) nm are similar to that of complex **XIII** (Figure 33). The most likely explanation for the obtained UV-Vis spectrum is the formation of a superoxo dinickel complex while **2** reacts with excess dioxygen.



Scheme 14: Synthetic route for **9**.

Suitable crystals for x-ray diffraction were obtained by layering hexane on a solution of **9** in THF at -30°C . The molecular structure of **9** is shown in **Figure 53** and selected bond lengths (\AA) and angles ($^{\circ}$) are listed in **Table 12**. **9** crystallizes in the monoclinic space group $P2_1/c$. As shown in **Figure 53**, an almost planar six-membered $\{\text{N}_2\text{Ni}_2\text{O}_2\}$ ring was formed by the two-nickel atoms, the nitrogen atoms from pyrazolate ligand and the oxygen atom from superoxo ligand. The two nickel(II) ions are hosted in the two $\{\text{N}_3\}$ -tridentate binding sites of the tri-anionic ligand scaffold, bridged by the pyrazolate and a peroxo ligand. The two nickel(II) ions distance of $3.810(5) \text{ \AA}$ in **9** is similar to **8** of $3.791(5) \text{ \AA}$, which are all shorter than **6** of $3.880(8) \text{ \AA}$. The Ni-O-O-Ni torsion angle around the O-O axis is defined as $22.71(32)^{\circ}$. The remarkable short O-O bond length of $1.326(2) \text{ \AA}$, demonstrates superoxo character. In contrast, peroxo ligands have O-O ligands bond lengths longer than 1.40 \AA .

The superoxo character of **9** was confirmed by spectroscopies measurements and DFT calculation. Resonance Raman data of crystalline material of complex $\mathbf{9}\text{-}^{16}\text{O}_2$ revealed a signal at 1007 cm^{-1} , which shift to 951 cm^{-1} upon $^{18}\text{O}_2$ labelled. ($\Delta^{16}\text{O}_2\text{-}^{18}\text{O}_2 = 56 \text{ cm}^{-1}$, **Figure 54b**). The superoxo nature of **9** is also consistent with the $^{16}\text{O}\text{-}^{16}\text{O}$ stretching vibration mode of 982 cm^{-1} ($\nu(^{18}\text{O}\text{-}^{18}\text{O})=934 \text{ cm}^{-1}$).

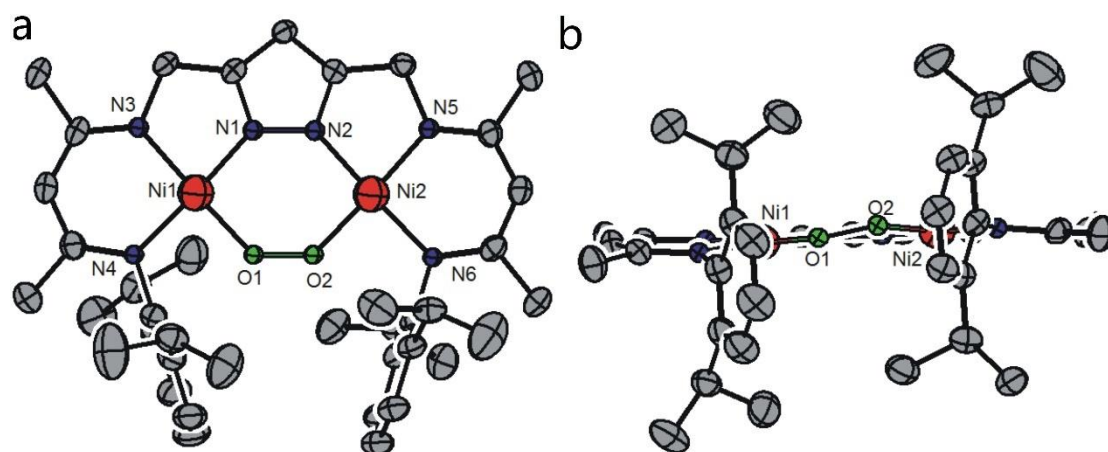


Figure 53: Molecular structure (50% probability thermal ellipsoids) of **9**. All hydrogen atoms omitted for clarity.

Table 12: Selected bond lengths (Å) and angles (°) for **9**.

Atoms	Bond lengths	Atoms	Bond angles
Ni1-N1	1.832(2)	N1-Ni1-O1	94.65(7)
Ni1-O1	1.834(2)	N1-Ni1-N3	83.43(7)
Ni1-N3	1.881(2)	O1-Ni1-N3	175.16(8)
Ni1-N4	1.901(2)	N1-Ni1-N4	175.88(8)
Ni2-O2	1.828(2)	O1-Ni1-N4	87.95(8)
Ni2-N2	1.837(2)	N3-Ni1-N4	94.22(7)
Ni2-N5	1.884(2)	O2-Ni2-N2	94.99(7)
Ni2-N6	1.907(2)	O2-Ni2-N5	175.87(8)
O1-O2	1.326(2)	N2-Ni2-N5	82.92(7)
Ni1...Ni2	3.810(5)	O2-Ni2-N6	87.36(7)
		N2-Ni2-N6	177.57(7)
		N5-Ni2-N6	94.78(7)
		O2-O1-Ni1	132.78(14)
		O1-O2-Ni2	131.01(14)
		Ni1-O1-O2-Ni2	22.71(32)

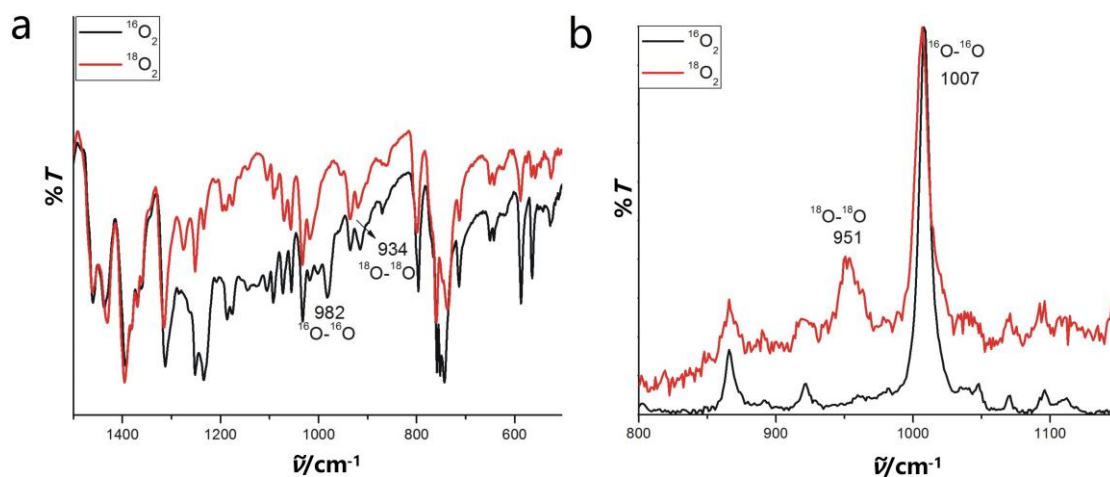


Figure 54: (a) Comparison of the IR spectra of crystalline material of **9** prepared using $^{16}\text{O}_2$ (black) and $^{18}\text{O}_2$ (red) in the range of 500 cm^{-1} to 1500 cm^{-1} ; (b) Comparison of the Raman spectra of crystalline material of **9**: prepared using $^{16}\text{O}_2$ (black) and $^{18}\text{O}_2$ (red) in the range of 800 cm^{-1} to 1150 cm^{-1} .

9 has been characterized by positive ion ESI-MS spectrometry in THF/ CH_3CN solution as well. The ESI-MS (+) of **9** shows three dominating peaks for the ions, deriving from **9** together with different cation (**Figure 55**) ($m/z = 792.4$ for $[\mathbf{9}+\text{K}]^+$, 776.4 for $[\mathbf{9}+\text{Na}]^+$ and 754.3 for $[\mathbf{9}+\text{H}]^+$). When isotopically labelled **9** is prepared, the mass peak corresponding to **9** shifted to $m/z = 796.4$ (**Figure 56b**).

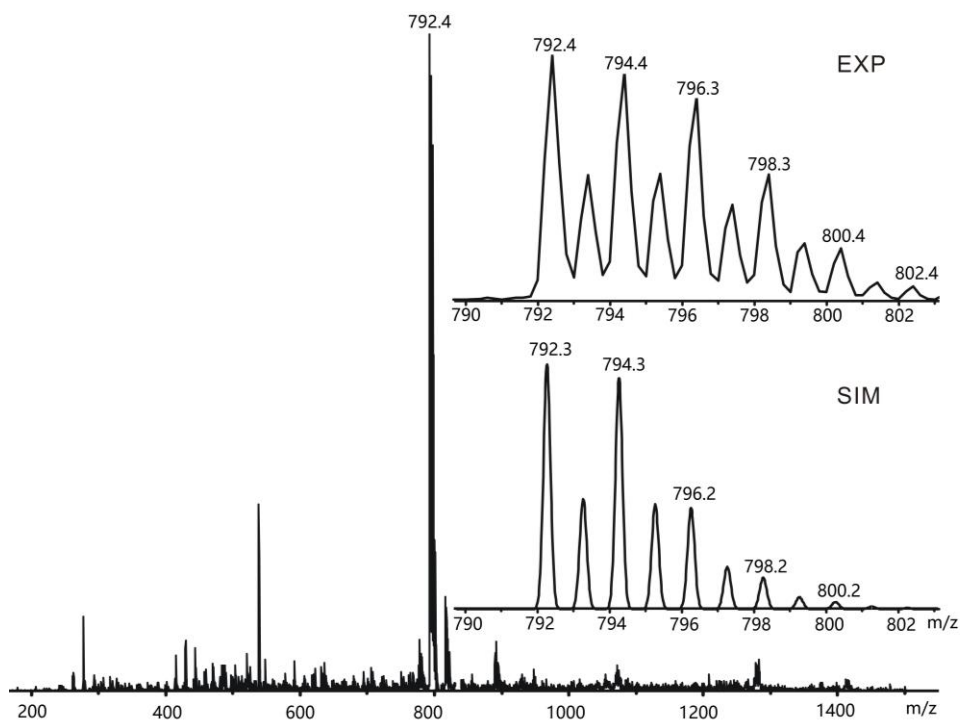


Figure 55: ESI-MS (positive) of **9** in THF/CH₃CN. The inset shows the experimental (upper) and simulated (lower) isotopic distribution pattern for [9+K]⁺.

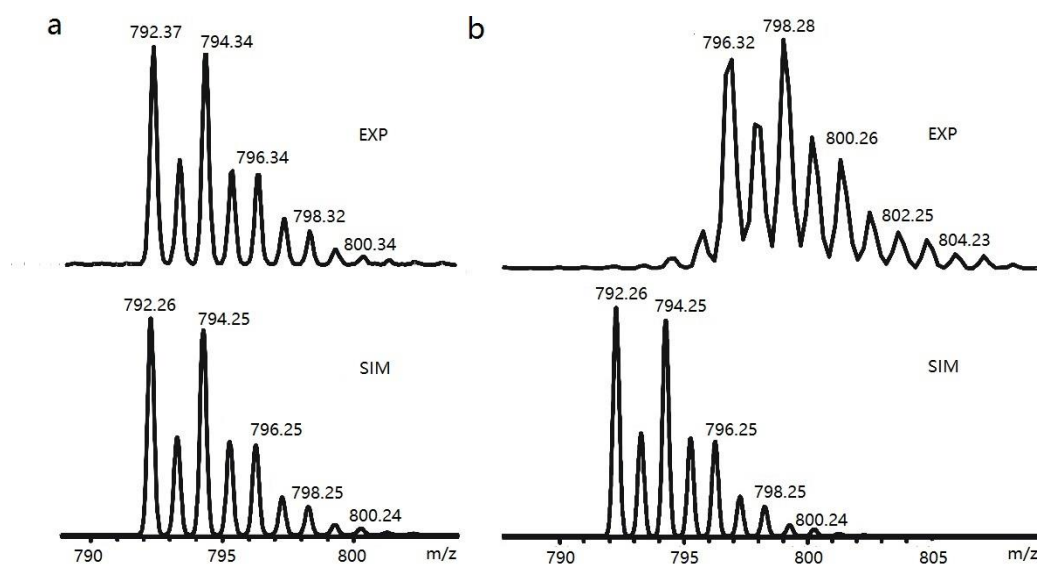


Figure 56: Experimental (¹⁶O₂ and ¹⁸O₂) (upper) and simulated (¹⁶O₂) (lower) isotopic distribution pattern for and [9+Na]⁺ (**a** and **b**).

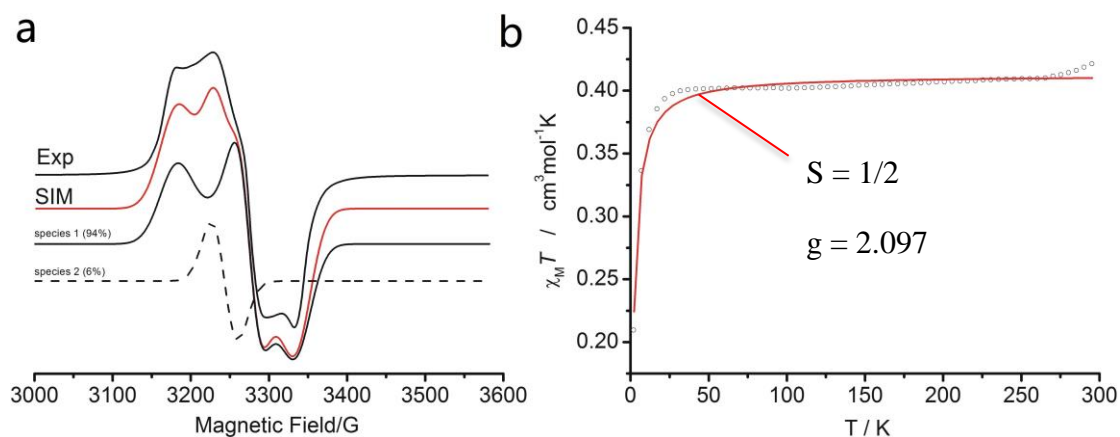


Figure 57: (a) X-band EPR spectra (black line) of **9** in THF at 145 K. Frequency = 9.41 GHz, power = 15 mW. Simulations (red trace) provide $g_{av} = 2.07$; (b) $\chi_M T$ vs. T measurement in the temperature range of 2–295 K at 0.5 T for solid samples of superoxo. The solid red lines represent the best global fit for data sets with $S = 1/2$ and $g = 2.10$. The decrease of $\chi_M T$ below 20 K is due to the combined effect of field saturation and weak intermolecular interaction according to a Weiss temperature of about $\theta = -1.7$ K.

The X-band EPR measurement in a frozen THF at 154 K of **9** in crystalline material reveals a paramagnetic ground state with spin of $S = 1/2$ (**Figure 57a**). The rhombic spectrum has principal g values of 2.02, 2.06 and 2.12, and the average $g = 2.07$. Meanwhile, the second species (6% amount) of paramagnetic substance was observed in the EPR spectrum and g value is at 2.07, which is similar to the KO_2 g value at 160 K in literature. ^[51] This first species average g value is in agreement with the effective magnetic moment observed for a solid sample in the temperature range 5–300 K ($0.41 \text{ cm}^3 \cdot \text{mol}^{-1} \cdot \text{K}$, corresponding to $\mu_{eff} = 1.81 \mu_B$ with $g_{av} = 2.100$. **Figure 57b**). The anisotropic g values of the first species are quite closely to complex **VIII** with $g = [2.138, 2.116 \text{ and } 2.067]$. Therefore, we assume that the unpaired electron is mostly located on the superoxo ligand.

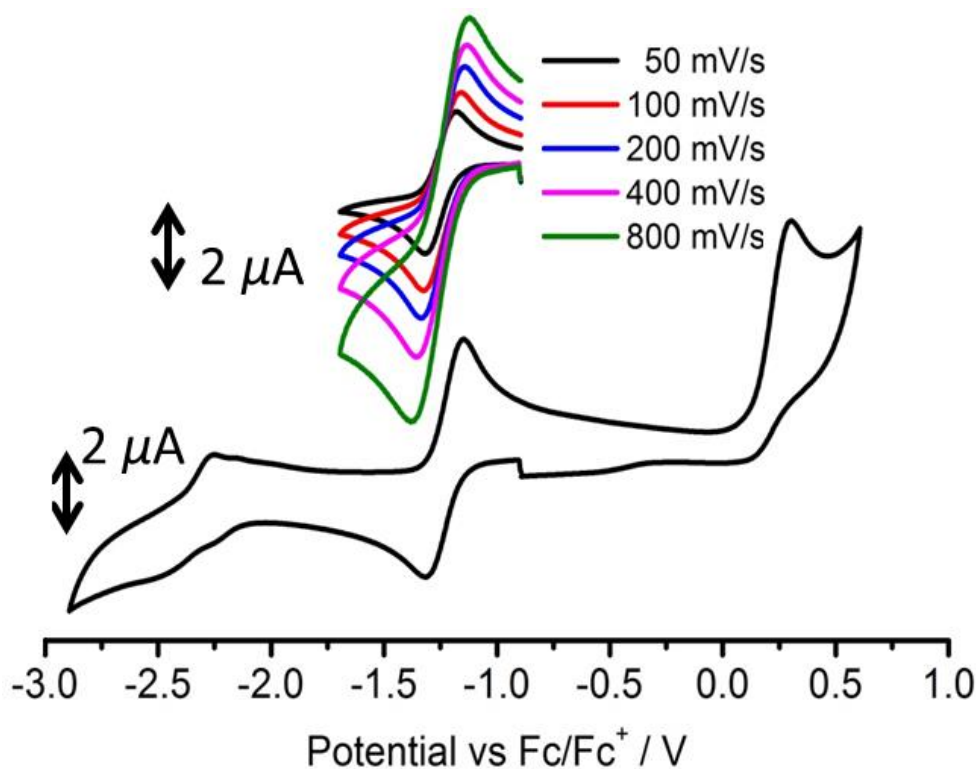


Figure 58: Cyclic voltammogram of **9** in THF 0.1 M Bu_4NPF_6 as an electrolyte at a scan rate of 50, 100, 200, 400 and 800 $\text{mV}\cdot\text{s}^{-1}$ vs. Fc/Fc^+ .

Cyclic voltammetry (CV) of **9** in a 0.1 M solution of NBu_4PF_6 in THF at RT showed a reversible redox wave of scan of $100 \text{ mV}/\text{s}^{-1}$ at $E_{1/2} = -1.22 \text{ V}$ (vs Fc/Fc^+), as well as an irreversible oxidation at higher potential (around +280 mV) (**Figure 58**). It indicates that **9** may be reduced by one electron to the peroxo dinickel complex. The similar behavior was observed in complex **XIII**.^[39] Reaction of **9** with elemental potassium results in a rapid color change from brown to red at room temperature. The final product **6** was identified by ^1H NMR spectrum after the work-up.

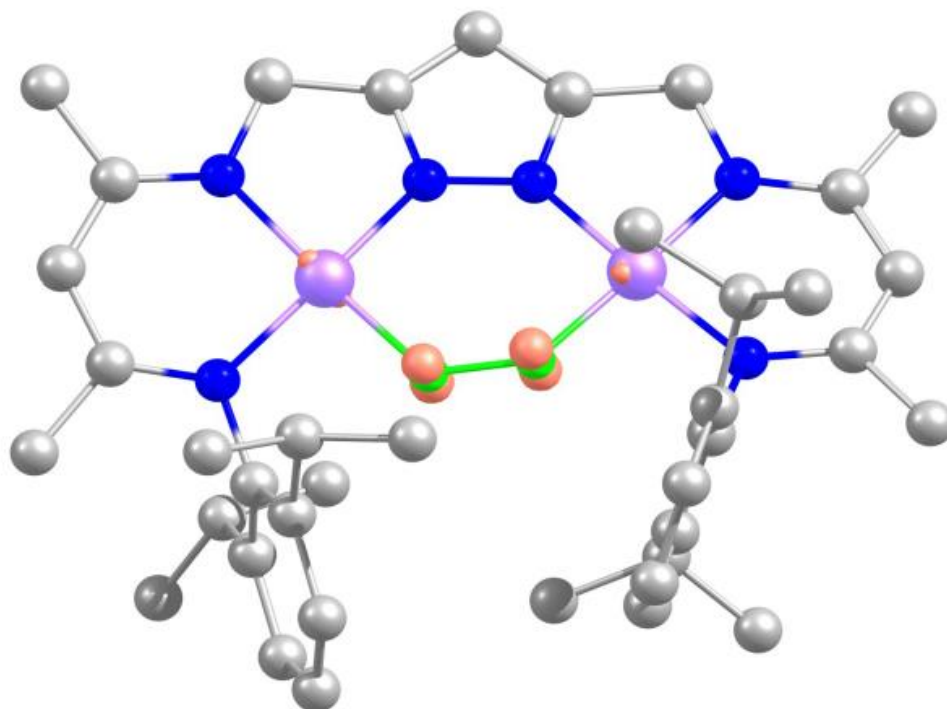


Figure 59: Spin density plot of **9**. Mulliken Spin Population: Ni1 = 0.080426, Ni2 = 0.079847, O1 = 0.398559, O2 = 0.399162.* Contour value: 0.08.

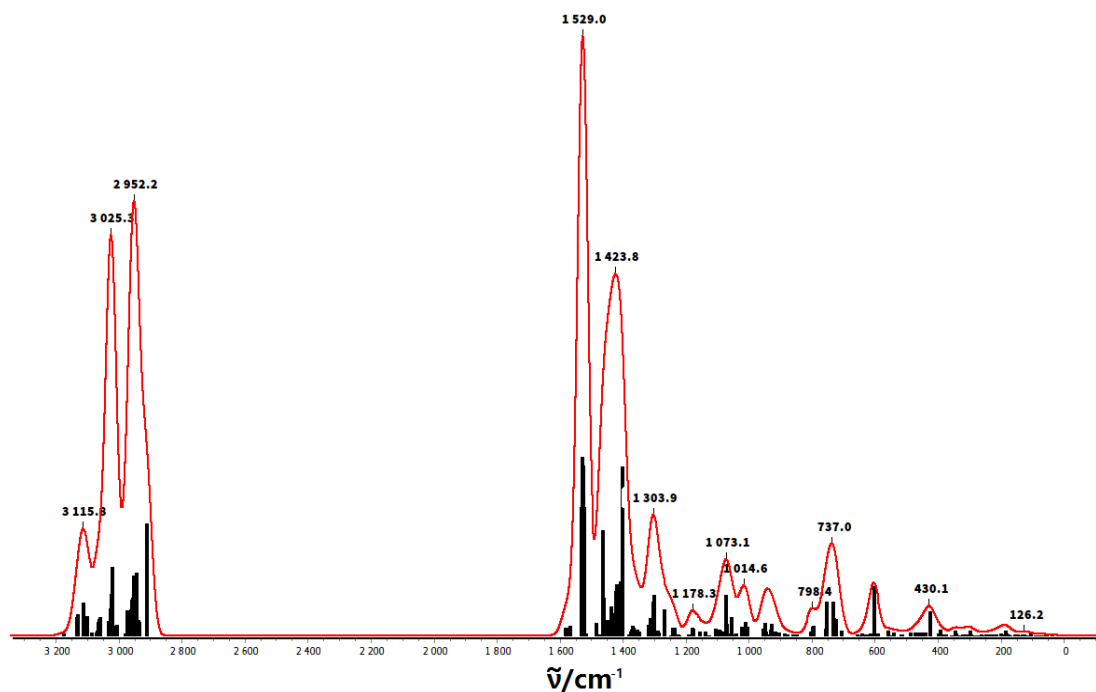


Figure 60: Calculated IR spectrum of **9**.

Table 13: Selected distance (\AA) and angles ($^\circ$) for **9**.

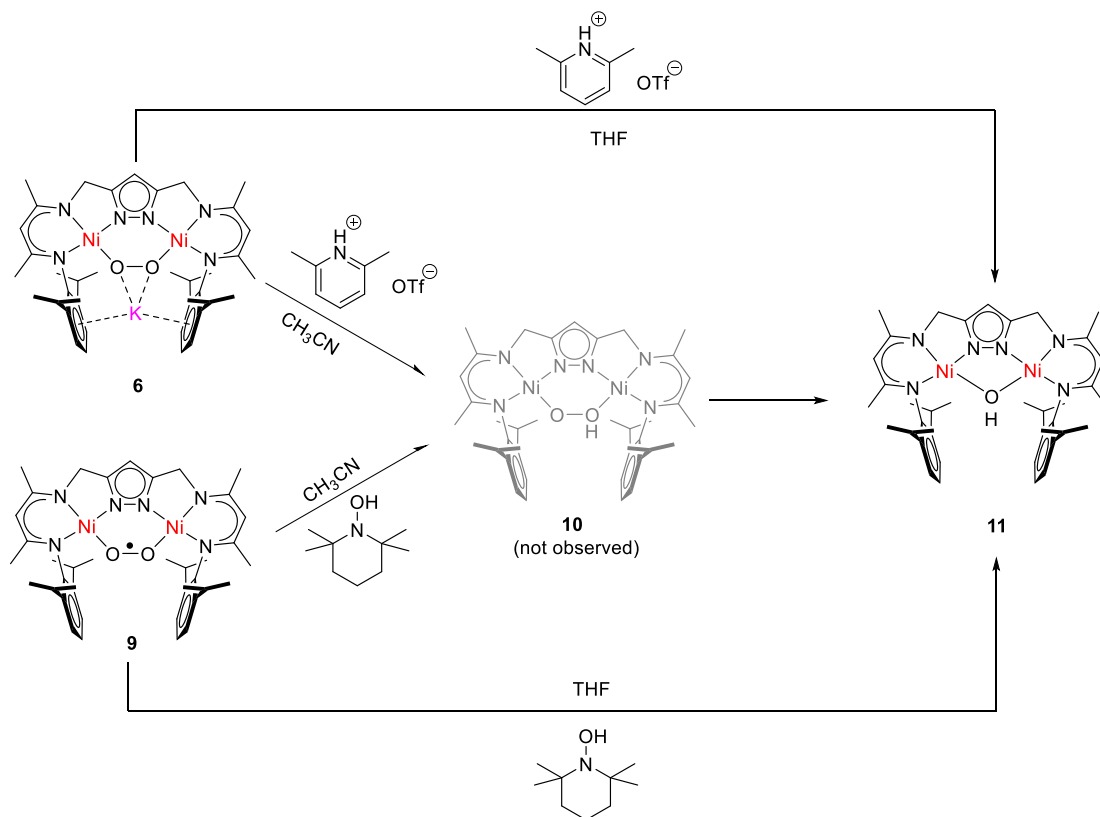
	$d(\text{O-O})/\text{\AA}$	$d(\text{Ni}\cdots\text{Ni})/\text{\AA}$	$\varphi(\text{Ni-O-O-Ni})/^\circ$
Exp	1.326	3.810	22.7
DFT*	1.357	3.838	34.3

Table 14: $\nu(\text{O}\cdots\text{O})$ (IR) for **9**.

	$\nu(^{16}\text{O}-^{16}\text{O})/\text{cm}^{-1}$	$\nu(^{18}\text{O}-^{18}\text{O})/\text{cm}^{-1}$	$\Delta\nu/\text{cm}^{-1}$
Exp	982	934	48
DFT*	950	895	54

The electronic nature of **9** as suggested by its geometric structure and magnetic properties was also confirmed by DFT calculations (**Figure 59**). The energy-minimized DFT calculated structure of **9** is in good agreement with that obtained by x-ray diffraction. The calculations revealed that the HOMO of **9** is the π^* orbital located on the superoxo ligand. The unpaired electron can be estimated at the Ni center (15%), and in the superoxo ligand (around 80%). As shown in **Table 13**, the bond lengths of the superoxo ligand and the distance between the two nickel atoms are 1.357 \AA and 3.838 \AA , respectively. They are longer than the experimentally determined values of 1.326 and 3.810 \AA . For the $^{16}\text{O}-^{16}\text{O}$ dioxygen stretching-vibration a value of 950 cm^{-1} was calculated compared to experimental data (982 cm^{-1}) as it is red shifted. (**Table 14** and **Figure 60**)

4.5 Cleavage the oxygen-oxygen bond



Scheme 15: Cleavage the O-O bond from **6** and **9** in THF.

It has been proven that the hydroperoxo metal complex (especially in copper) can be obtained from hydrogen atom abstraction from superoxo metal species or protonation from peroxo metal species. [52] The copper-hydroperoxo species spur us to synthesized hydroperoxo nickel complex from **6** and **9**. And, until now, only one hydroperoxo nickel example in structural characterization was reported by *Gade* in 2015. [47]

Reaction of **6** with [H-Lut]OTf or treatment of **9** with TEMPO-H in THF at RT or even at -78°C result in color change in 20 mins (**Scheme 15**). Dark green crystals were obtained from hexane layered into THF at -30°C in two days. In the solid state, the green compound is dinuclear nickel(II) hydroxide complex (**11**). Monitoring the hydrogen atom transfer (HAT) or protonation reaction by UV-Vis spectra, no intermediate was observed in these procedures. However, treatment of

the **6** with [H-Lut]OTf in CH₃CN at 243 K (**Figure 61**), the band at 512 assigned to the O₂²⁻→Ni charge transfer shifted to 460 nm, and a new band at 325 nm come out. Resonance Raman spectra of the hydroperoxo compound that were recorded using a 457 nm laser displayed only a weak band in the CH₃CN solution, and neither the assignment of the Ni-O nor of the O-O vibrational modes was possible by labeling experiments using ¹⁸O₂.

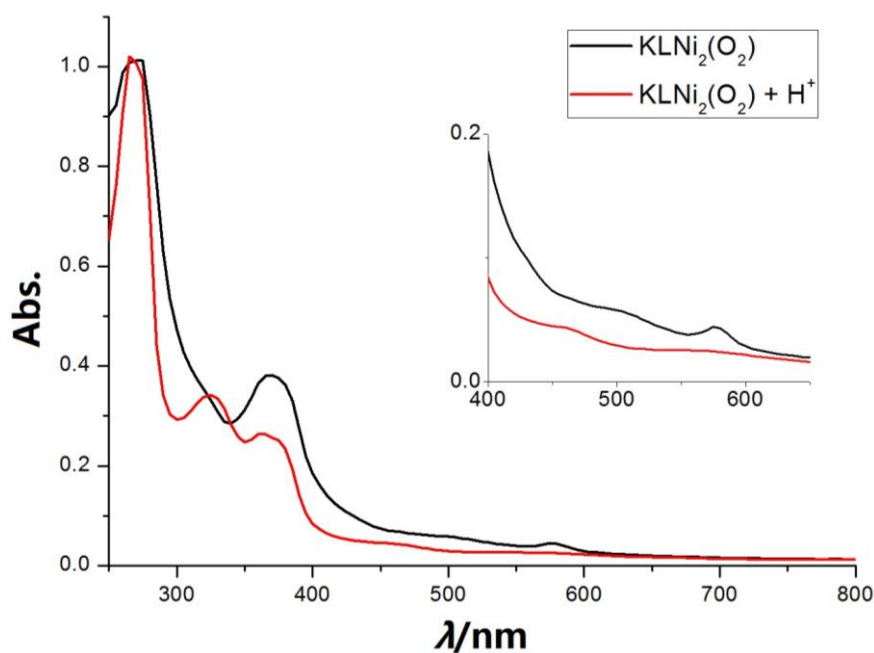


Figure 61: Monitoring the **6** with [H-Lut]OTf in CH₃CN at 243 K.

Complex **11** crystallizes in the *C2/c* space group. The distance of two nickel of 3.47 Å is shorter than **6** and **9** (**Figure 62**). In the ¹H NMR spectrum, the proton of the hydroxide occurs at -7.25 ppm in THF-d₈ (**Figure 63**).

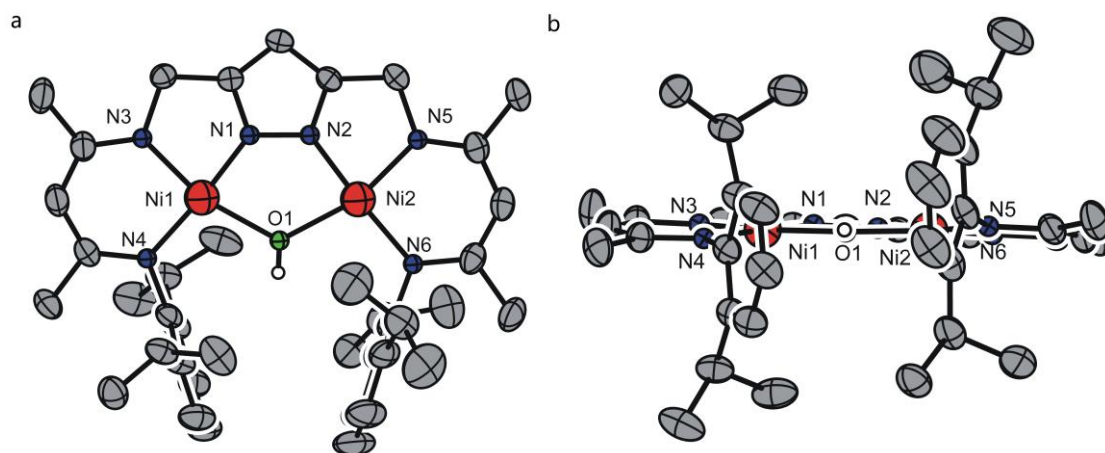


Figure 62: Molecular structure (30% probability thermal ellipsoids) of **11**. Most hydrogen atoms omitted for clarity, except for the OH unit.

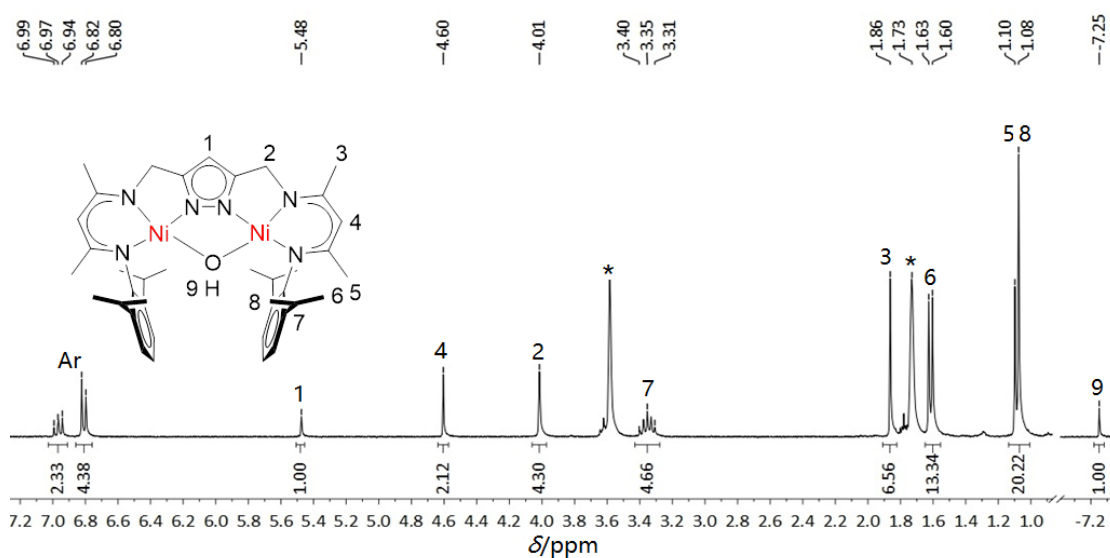


Figure 63: ^1H NMR spectrum of the **11** in THF-d_8 . Residual solvents are marked (*).

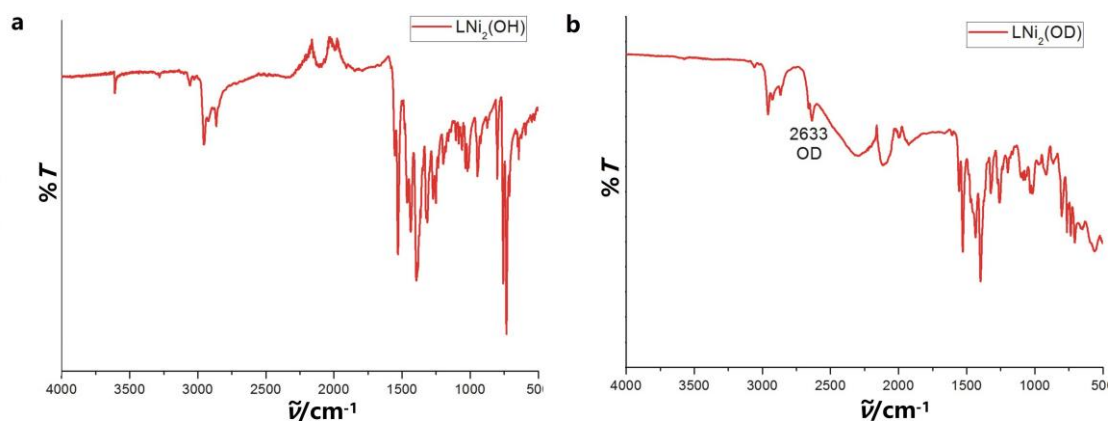
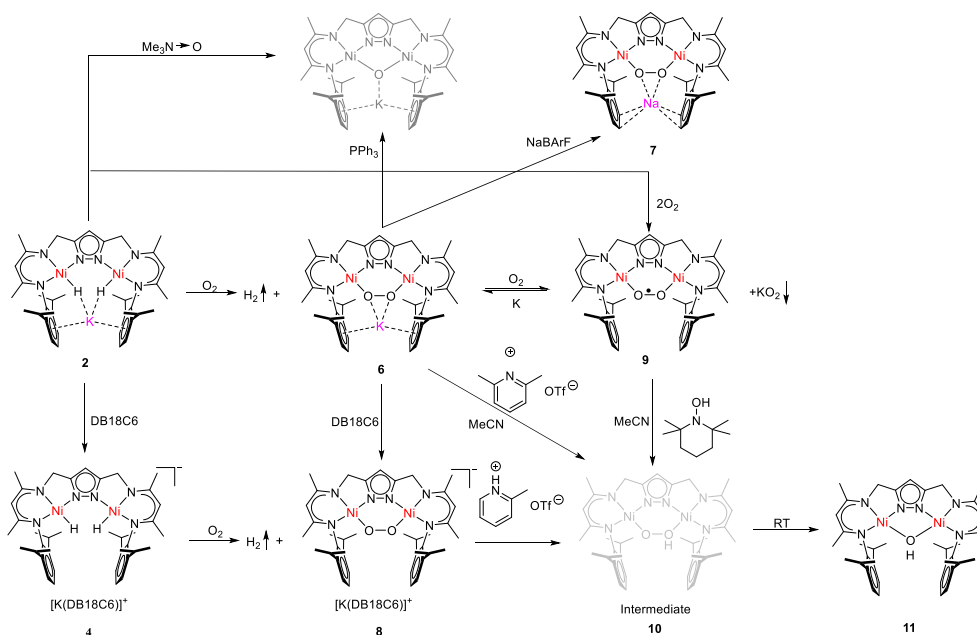


Figure 64: IR spectra of **11** (a) and **11-OD** (b) after exchange with D_2O .

Exchange with D₂O was proven by means of ¹H NMR and IR spectroscopy. After the addition of five equivalents of D₂O to a water free sample of **11** in THF-D₈, the associated signal (3622 cm⁻¹) has vanished immediately. Upon exchange with D₂O the signal of hydroxide vanishes, while a new sharp band emerges at 2633 cm⁻¹ ($\nu(\text{O-H})/\nu(\text{O-D}) \approx 1.38$) which is attributed to the O-D stretching vibration (**Figure 64b**)

4.6 Summary



Scheme 16: Transformation between the complex **6**, **7**, **8**, **9** and **11**.

From last chapter, we can conclude that $[L^1Ni^{II}_2(H)_2]^-$ complex in **2** can be viewed as a masked form of a reactive, antiferromagnetically coupled $[L^1Ni_2]^-$. Thus, definitive elucidation of the peroxo binding mode in $[L^1Ni_2(\mu-\eta^1,\eta^1-O_2)]$ was successfully prepared from **2** with dioxygen, revealing an “end-on” peroxo species **6** with a *cis*-geometry. In addition, **6** can further react with dioxygen resulting in a superoxo complex **9**. The two thermal stable peroxo and superoxo dinickel(II) complexes exhibit a μ -1,2- bonding geometry and have been investigated by UV-vis-, resonance Raman-, infrared-, EPR spectroscopies, SQUID measurements and DFT calculation. From the **6/9** redox potential in combination with chemical reduction and oxidation agents with K/O_2 , interconversion of the μ -1,2-peroxo and superoxo intermediates had been done successfully. Meanwhile, a “naked” peroxo complex **9** was obtained from **6** with DB18C6 in THF solution. Ongoing works focus on continuing to develop the peroxo and superoxo reactivity.

Chapter 5 Disulfur binding to the dinuclear nickel(II) dihydride and stepwise transformation to the sul- fide-ligand-radical

Abstract: A new μ -1,2- motif bimetallic dinuclear nickel(II) disulphide was isolated after reacting the $\text{K}[\text{L}^1\text{Ni}_2(\text{H}_2)]$ (**2**) with elemental sulfur with concomitant release of H_2 and characterized by x-ray diffraction. $\text{K}[\text{L}^1\text{Ni}_2(\mu\text{-}\eta^1, \eta^1\text{-S}_2)]$ (**12**) shows reactivity towards H_2O , PPh_3 and O_2 and result in the corresponding hydrosulfide (SH^-) (**13**), μ -sulfide (S^{2-}) (**14**), and μ -sulfide radical (S^\cdot) (**16**) complexes in appropriate condition. The thiol (SMe^-) (**15**) nickel(II) complex was gained from μ -sulfide (S^{2-}) nickel complex (**16**) with MeI. In addition, interconversions between S_2^{2-} , S^{2-} and S^\cdot have been done successfully from chemical reduction or oxidation agents.

5.1 Introduction

Coordination chemistry of the transition metals bearing the ligands SH^- , S^{2-} , S_2^{2-} , or S_2^{3-} found widespread interesting during the last two decade because they could serve as models for biological system. Understanding the nature of the metal-sulfur linkages at active sites can offer insight on ways to improve catalysis and provide a better understanding of cluster formation and cluster interconversion reactions in general. Therefore, many multinuclear and binuclear complexes coordinating sulfur have been described, in which the metal atoms are bridged by unsubstituted sulfur atoms. [53] Nickel sulfides, in particular, are key components of natural hydrogenases. [54]

In these sulfur motifs, to the best of our knowledge, only one μ -1,2 disulfide nickel complex (**Figure 65, XXI**) was reported in literature with crystal structure, and some other examples of “end-on” motif (**Figure 65, XX**) are in spectroscopies characteristic so far. [55,56]

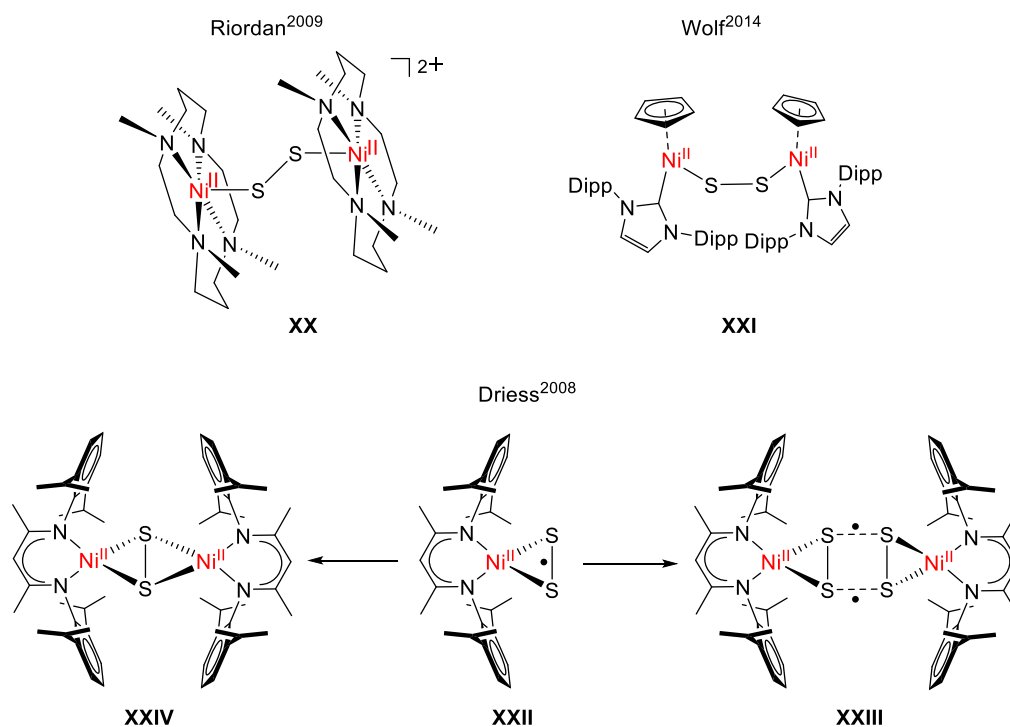


Figure 65: Selected examples of nickel(II) S_2^{2-} or S_2^- complexes.

It is less known about the complexes containing the paramagnetic supersulfide S_2^- ligand, despite the fact the species can be key intermediates in metal-mediated X-X bond activation.^[57] Interesting nickel supersulfide S_2^- complex (**Figure 65, XXII**) supported by β -diketiminato ligand has been reported by *Driess et.al.* in 2008 and exhibit sulfur-ligand-centered radical character.^[53e] The compound featuring a four-member, rectangular-shaped S_4 ring in the solid state (**Figure 65, XXIII**). Sulfur transfer from **XXII** to PPh_3 furnishes $PPh_3=S$ and the corresponding disulfide nickel complex (**Figure 65, XXIV**) in quantitative yield.

Some terminal sulfide (S^{2-}) complexes are known with transition metals^[58] with different ligand systems. Nickel and iron linear sulfide complexes were reported by the group of *Holland*^[59] and *Limberg*^[60], respectively (**Figure 66**). The existence of the $[Ni=S]$ intermediate has been proven by *Jones*, and the sulfide-bridge-radical intermediate could react with substances containing nitrones.^[61] *Driess* and co-workers reported that the $[Ni=S]$ intermediate rapidly dimerizes to formed the disulfide bridged complex (**Figure 65, XXIII**)^[53e]. However, the only structural characterized $[Ni=S]$ intermediate was introduced by *Hayton* and coworker in 2015 (**Figure 66, XXVI**).^[62] The short Ni-S distance of 2.064(6) Å–2.084(1) Å are reflecting a partial multiple-bond character between the nickel and sulfur. The new nickel sulfide radical compound reacts with N_2O ,^[62] CS_2 ,^[63] CO ^[64] and NO ^[64], which led to the formation of novel nickel sulfide species complexes.

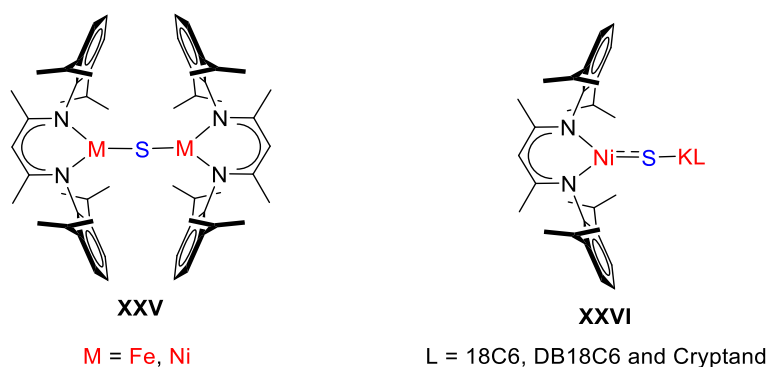
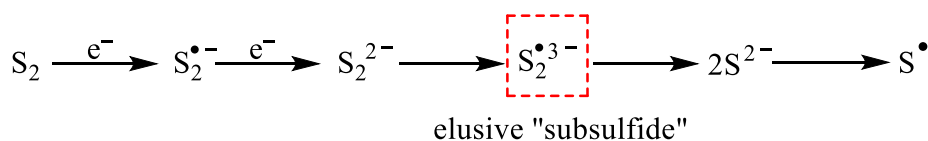


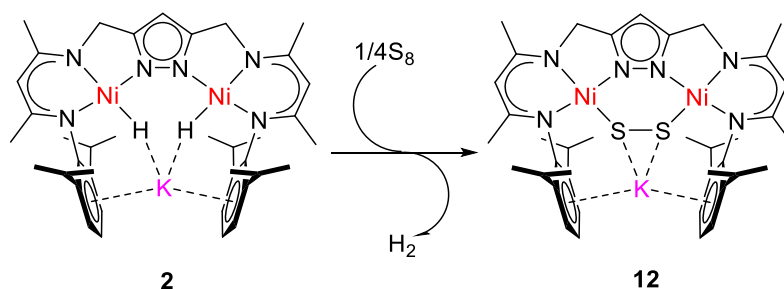
Figure 66: Selected examples of $Ni^{II} S^{2-}$ (**XXV**) or S^- (**XXVI**) complexes.^[59,60]

Reduction or oxidation of the disulfide motif from S_2 to S_2^{2-} , S^{2-} and S^- requires two, four or one electrons (**Scheme 17**). In literature, mostly they only talked about the sulfur substance from S_8 to S_2^{2-} , S_2^{2-} to S^{2-} or S^{2-} to S^- directly. [53-64] Therefore, how to reduce the S_2 to S^- step by step is an interesting work. Hence, we designed a new system, which can be used to study the "step-by-step" transformation with dinickel metals.



Scheme 17: Stepwise transformation of the dichalcogen S_2 substance.

5.2. Synthesis of a μ -1,2-disulphide dinuclear nickel(II) complex



Scheme 18: Synthetic route for **12**.

The structural novelty of the nickel oxygen site provide ample inspiration for synthetic sulfur model studies, particularly those aimed at understanding the reactivity of sulfur ligated.

Treatment of a THF solution of **2** with stoichiometry elemental sulfur results in a rapid color change from orange to blood red (**Scheme 18**) and formation of a new species identified by 1H NMR spectroscopy (**Figure 67**). A new resonance corresponding with H_2 is observed in 1H NMR spectra of reaction mixtures, implying H_2 evolution upon reaction of **2** with sulfur. When **2-D** was treated with

elemental sulfur and the reaction monitored by ^2H NMR spectroscopy, the formation of D_2 was clearly detected. The new species is diamagnetic and gives rise to sharp signals in the ^1H and ^{13}C NMR spectra in the typical chemical shift range at RT for L^{3-} ligands (**Figure 67**). The ^1H NMR spectrum of this compound revealed a symmetric species as expected in solution state. The resonance associated to the isopropyl CH function was overlaid by residual solvent (THF- d_8), but was distinguished by means of a ^1H - ^1H COSY experiment (**Figure A21**).

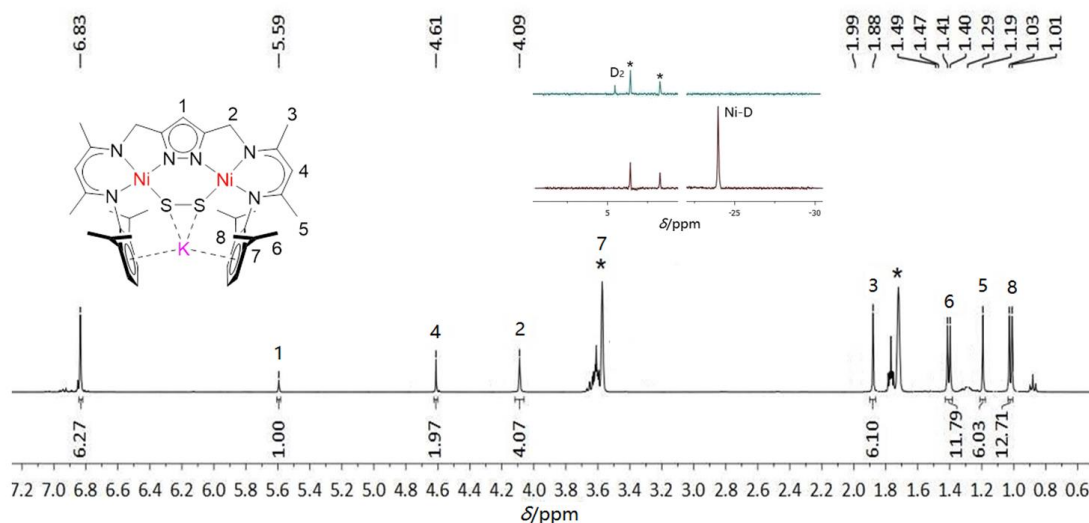


Figure 67: ^1H NMR (400 MHz) spectrum of **12** in THF- d_8 at room temperature. Residual solvents are marked with an asterisk (*). The inset shows ^2H NMR spectrum (77 MHz, 298K) of **2** with elemental sulfur.

Red plate-like crystals suitable for x-ray diffraction were obtained by layering hexane on a solution of **12** in THF at -30°C in 80% yield. As expected, the new species is similar to **6**. As far as we are aware, **12** is the first μ -1,2-disulphide bimetallic nuclear nickel complex with K^+ cation. **12** crystallized in the monoclinic space group $P2_1/n$ with four molecules in the unit cell. The molecular structure of **12** is shown in **Figure 68** and selected bond lengths (\AA) and bond angles ($^\circ$) are listed in **Table 15**. The nickel centers are coordinated in a slightly distorted square-planar fashion with the sum angles being 360.14° and 361.02° , respectively. Each nickel center is hosted within the nitrogen atom from the pyrazolate

ligand system and the disulfide ligand. The Ni...Ni distance of 4.290(2) Å is longer than the previously discussed **2** and **6**, which is related to the large *van der Waals radius* of sulfur as for hydrogen and oxygen. The S-S distance of 2.036(3) Å is similar to **XXI** (**Figure 65**) (2.045(1) Å)^[56], which implies a less activated S-S bond (compared with S₈) in the disulphide bridge, possibly due to a reduced back-donation from the nickel centers compared to those disulphide nickel complexes. The Ni-S distances of 2.167(2) Å and 2.160(2) Å in **12** are close to the Ni-S distance in **XXI**.^[56] The K⁺ is sandwiched between the two aryl groups of the DIPP in **12**, which is similar to **2** and **6** also. The aryl(center)-alkali metal distances amount 3.357(2) Å and 3.259(2) Å, which implies *cation-π* interaction. The potassium cation is also tightly coordinated to both disulfide atoms (S1, S2), with K1-S1 and K1-S2 separation of 3.103(2) Å and 3.157(2) Å, respectively. The Ni1-S1-S2-Ni2 torsion angle 81.20(2)° is similar to the angle observed in **6** with 81.41(3)°.

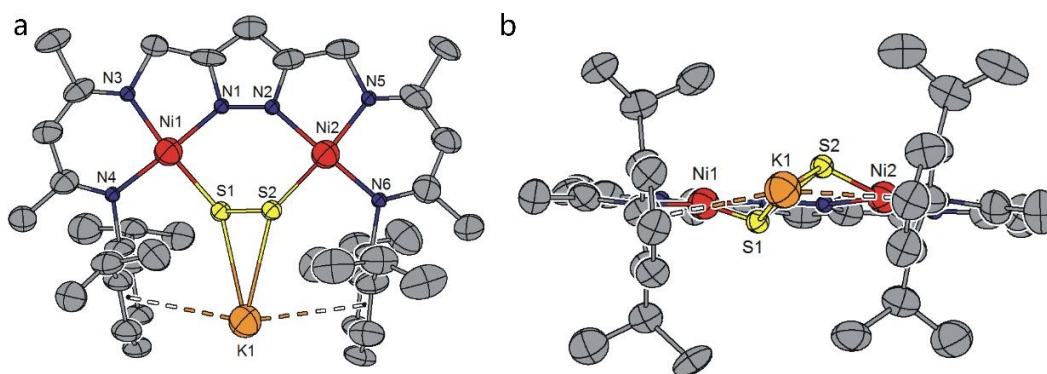


Figure 68: Molecular structure (50% probability thermal ellipsoids) of **12**. All hydrogen atoms omitted for clarity.

Table 15: Selected bond lengths (Å) and bond angles (°) for **12**.

Atoms	Bond lengths	Atoms	Bond angles
Ni1-N3	1.915(5)	N3-Ni1-N4	92.4(2)
Ni1-N4	1.925(5)	N3-Ni1-N1	84.9(2)
Ni1-N1	1.928(6)	N4-Ni1-N1	177.1(2)
Ni2-N5	1.904(5)	N3-Ni1-S1	170.03(2)
Ni2-N6	1.914(6)	N4-Ni1-S1	92.41(2)
Ni2-N2	1.931(6)	N1-Ni1-S1	90.41(2)

Ni1-S1	2.167(2)	N5-Ni2-N6	93.8(2)
Ni2-S2	2.160(2)	N5-Ni2-N2	84.4(2)
S1-S2	2.036(3)	N6-Ni2-N2	174.1(2)
K1-S1	3.103(3)	N5-Ni2-S2	167.80(2)
K1-S2	3.157(3)	N6-Ni2-S2	92.51(2)
Ni1...Ni2	4.290(2)	N2-Ni2-S2	90.38(2)
K1-Cg(1)	3.357(3)	Ni1-S1-S2	108.48(1)
K1-Cg(2)	3.259(3)	Ni2-S2-S1	106.89(1)
		S1-K1-S2	37.95(7)
		Ni1-S1-S2-Ni2	81.20(2)

Cg(1) = centroid of the ring carbon atoms C10, C11, C12, C13, C15, C15 (left side);
Cg(2) = centroid of the ring carbon atoms C28, C29, C30, C31, C32, C33 (right side).

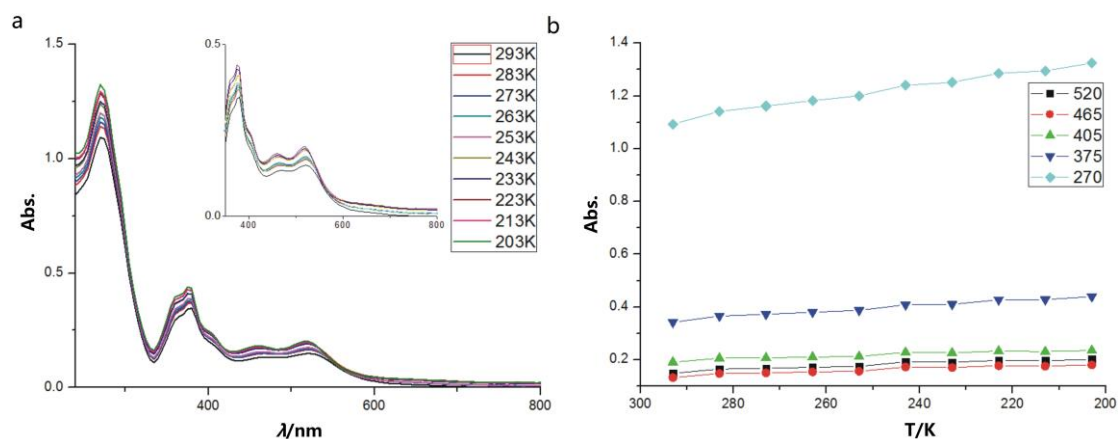


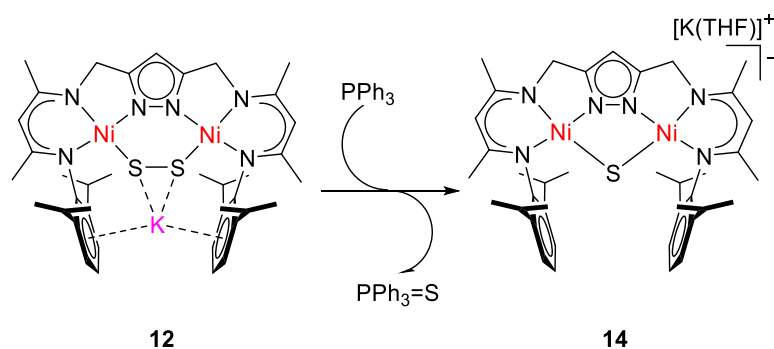
Figure 69: (a) UV-Vis spectra of the **12** at different temperatures (293 K–203 K) in THF; (b) Plots of the absorption bands at different temperatures.

Further analysis data have done by UV-Vis, IR and Raman spectroscopy for **12**. The UV-Vis spectrum of **12** displays an intense band at $\lambda_{\max} = 465$ nm ($\epsilon \approx 130$ M⁻¹·cm⁻¹) and a similar intense band at ~ 520 nm ($\epsilon \approx 149$ M⁻¹·cm⁻¹) was observed (**Figure 69a**). It is tentatively assigned to the disulfide $\pi^*_{\sigma} \rightarrow \text{Ni}^{\text{II}}$ and $\pi^*_{\nu} \rightarrow \text{Ni}^{\text{II}}$ $d_{x^2-y^2}$ charge-transfer (CT) transitions, respectively, from comparison with the absorption spectra of analogous $\text{Cu}_2(\mu\text{-}\eta^1, \eta^1\text{-S}_2)$ [65].

■ **Reactivity.** Exposure of **12** to air affords a gradual color change from blood red to brown in two hours. ¹H NMR spectroscopy indicates that the brown complex is a hydrosulfide-bridged complex. The result will be discussed in chapter

5.3.

Meanwhile, sulfur transfer from **12** to PPh_3 furnishes $\text{Ph}_3\text{P}=\text{S}$ and the corresponding dinuclear nickel sulfide **14** in quantitative yield (**Scheme 19**). Time dependent ^1H and ^{31}P NMR spectra demonstrate the slow conversion from **12** to **14**. During two days, the characteristic proton resonances for pyrazole of **12** gradually decrease (**Figure 70**). In the ^{31}P NMR, a new peak for $\text{S}=\text{PPh}_3$ at 42.16 ppm was observed in one hour and gradually increased in the next two days (**Figure 71**). Eventually, **12** was completely consumed after three days. The x-ray structure of **14** will be discussed in chapter 5.4.



Scheme 19: Reaction of **12** with PPh_3 in THF-d_8 .

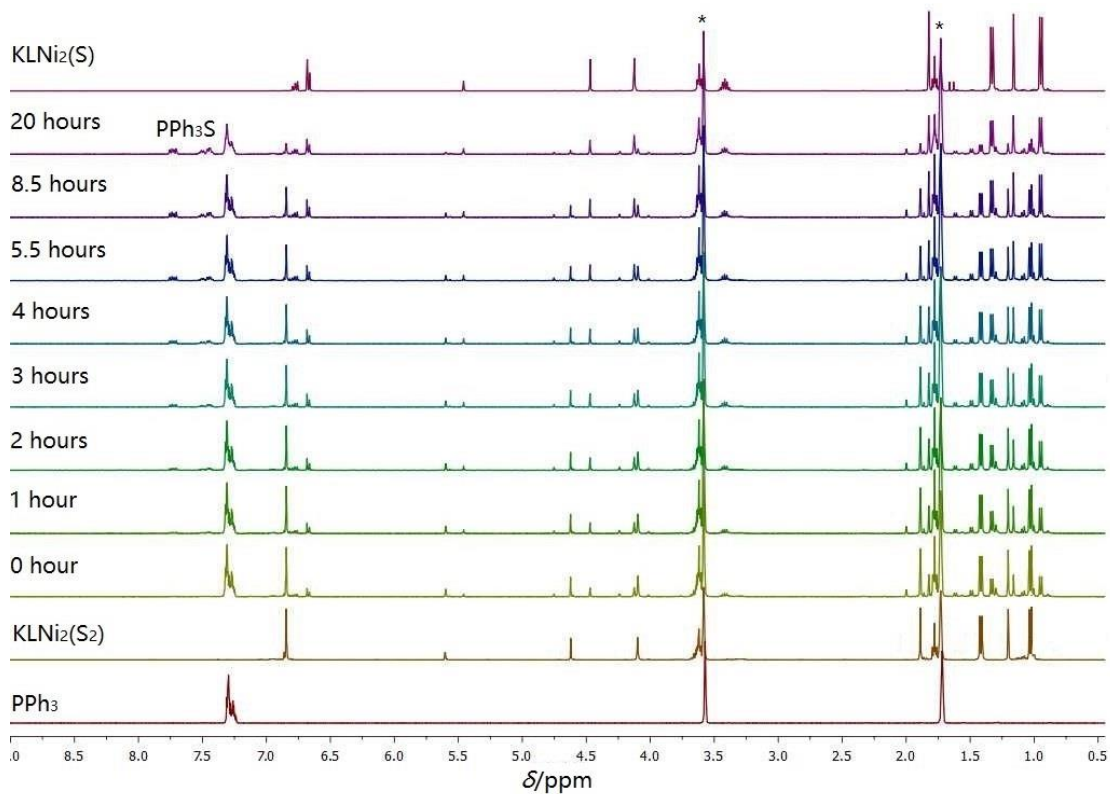


Figure 70: ^1H NMR illustrates slow conversion of **12** to **14** in the presence of PPh_3 at RT in THF-d_8 demonstrated. Residual solvents are marked with an asterisk (*).

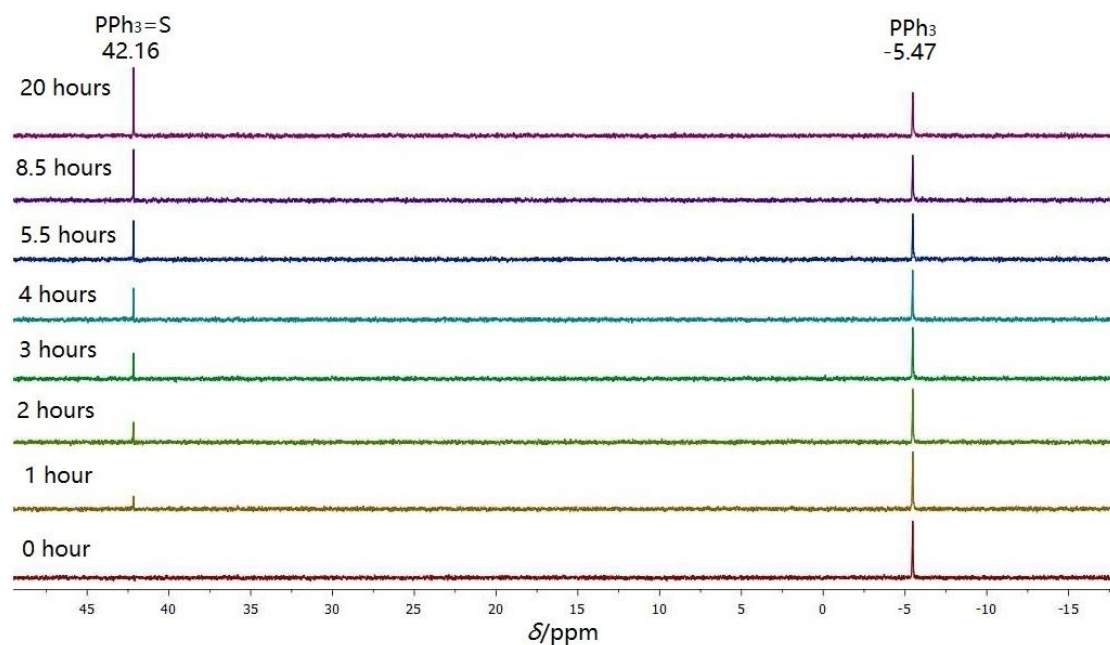


Figure 71: ^{31}P NMR illustrates slow conversion of PPh_3 to $\text{PPh}_3=\text{S}$ at RT in THF-d_8 of **12** to **14**.

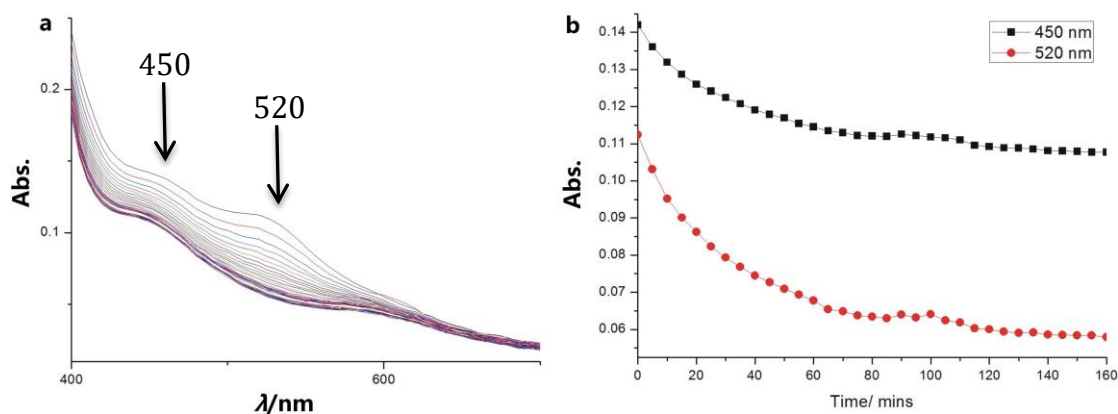
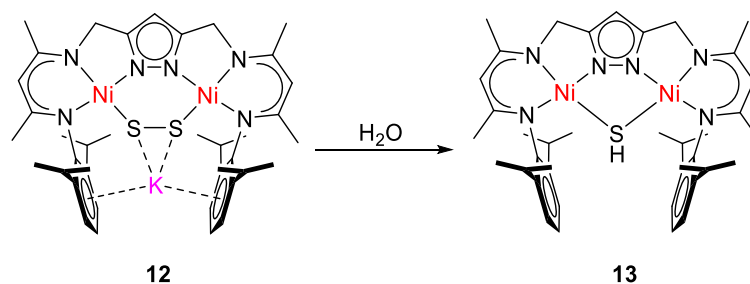


Figure 72: (a) Monitoring the band at 450 and 520 nm in UV-vis spectroscopy from **12** with PPh₃; (b) changing the absorbance of **12** with PPh₃ at 450 and 520 nm upon the time consuming.

Monitoring the reactivity of **12** with PPh₃ in UV-Vis spectroscopy, the absorption bands at 450 and 520 nm which are belong to the disulfide $\pi^*_{\sigma} \rightarrow \text{Ni}^{\text{II}}$ and $\pi^*_v \rightarrow \text{Ni}^{\text{II}} d_{x^2-y^2}$ are decreasing with time consuming. After few hours, the bands are stable. (**Figure 72**),

5.3 Synthesis of a hydrosulfide dinuclear nickel(II) complex



Scheme 20: Synthetic route for **13**.

As we mentioned of the reactivity of **12**, the hydrosulfide bridged **13** was obtained from **12** to air. Besides this way, several other pathways were found for synthesizing of this complex. The procedures were described in the experimental section.

Dark green crystals suitable for x-ray diffraction were obtained by layering hexane on a solution of **13** in THF at RT in 73% yield. **13** crystallized in the monoclinic space group $P2_1/c$ with four molecules in the unit cell. Both nickel centers are coordinated in a slightly distorted square-planar fashion. The molecular structure of **13** is shown in **Figure 73** and selected bond lengths (Å) and bond angles (°) are listed in **Table 16**. The Ni...Ni distance of 3.707 Å is shorter than **11**. The Ni1-S1-Ni2 angle $111.7(4)^\circ$ is similar to **11** also. The Ni-SH bond lengths of 2.274(5) Å and 2.265(5) Å are significantly shorter than other reported Ni^{II}-SH complexes. [66] The SH protons could be unambiguously located in a fourier-difference map and defined by ¹H NMR spectrum.

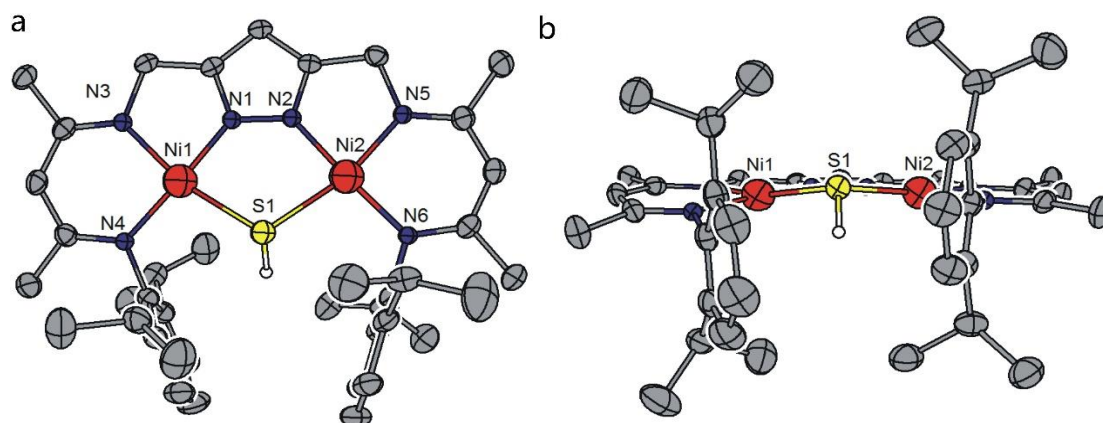


Figure 73: Molecular structure (50% probability thermal ellipsoids) of **13**. Most hydrogen atoms omitted for clarity except for SH unit.

Table 16: Selected bond lengths (Å) and bond angles (°) for **13**.

Atoms	Bond lengths	Atoms	Bond angles
Ni1-N1	1.826(2)	N1-Ni1-N4	173.91(7)
Ni1-N4	1.894(2)	N1-Ni1-N3	82.38(6)
Ni1-N3	1.896 (1)	N4-Ni1-N3	94.49(6)
Ni1-S1	2.274(5)	N1-Ni1-S1	84.25(5)
Ni2-N2	1.829(1)	N4-Ni1-S1	99.64(5)
Ni2-N6	1.899(1)	N3-Ni1-S1	163.72(5)
Ni2-N5	1.901(2)	N2-Ni2-N6	176.86(6)
Ni2-S1	2.265(5)	N2-Ni2-N5	81.94(6)
Ni1...Ni2	3.707(5)	N6-Ni2-N5	95.03(6)
		N2-Ni2-S1	84.52(5)

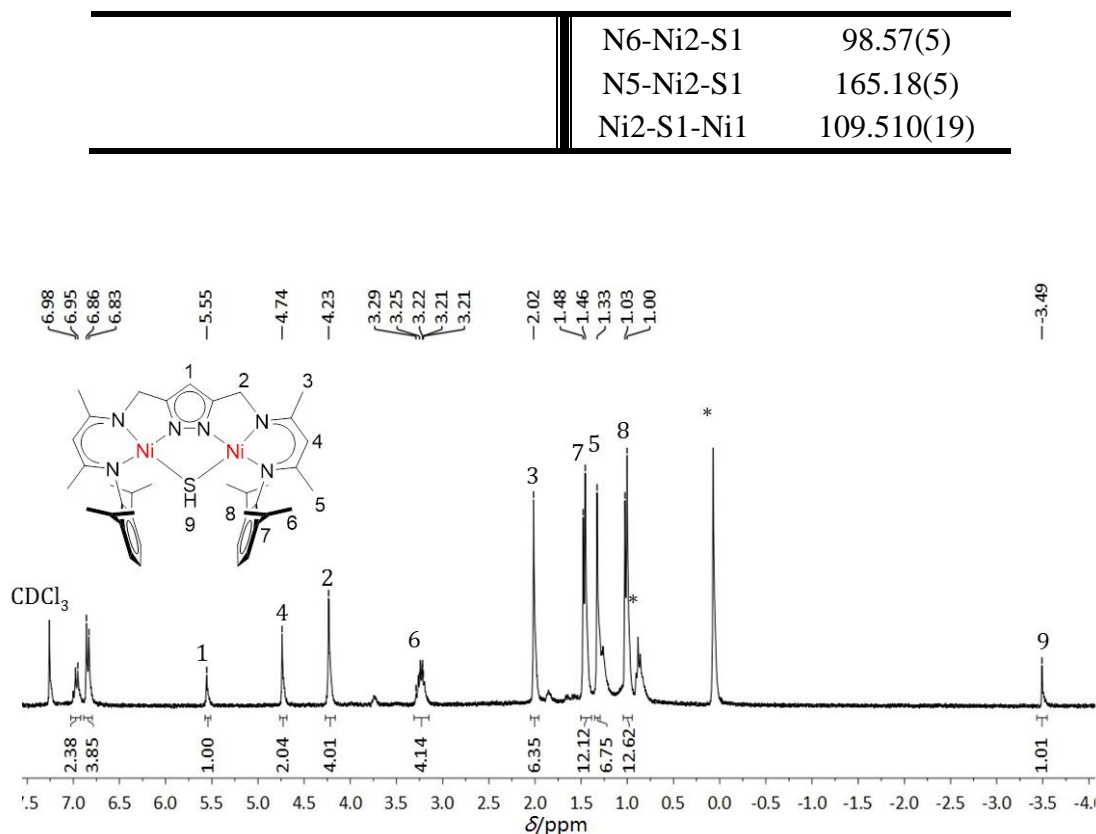
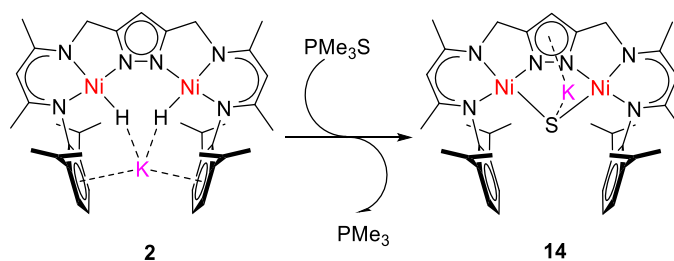


Figure 74: ^1H NMR spectrum (300 MHz) of **13** in CDCl_3 . Impurity is indicated(*).

13 is diamagnetic complex and gives rise to sharp signals in the ^1H and ^{13}C NMR spectra in the typical chemical shift range for the pyrazolate and β -diketiminato ligands (**Figure 74**). In the ^1H NMR spectrum, the bridged hydrosulfide protons resonate at $\delta = -3.49$ ppm. The positive ion ESI-MS of a freshly prepared THF solution of **13** shows a nickel-containing fragment at $m/z = 755.47$ ($(\mathbf{13}+\text{H})^+$). A weak vibration of the S-H was observed at 2557 cm^{-1} in the IR spectrum for **13**. The origin of the SH vibration could be verified by the FT-IR measurement of the deuterated **13**-SD, which was synthesized by H/D exchange using deuterium-methanol (MeOD). The S-D band lies at $\nu(\text{S-D}) 1817\text{ cm}^{-1}$ ($\nu(\text{S-H})/\nu(\text{S-D}) = 1.41$) (**Figure A26**), which is similar to literature.^[67]

5.4 Synthesis of μ -1,1-sulfide nickel(II) complex

Scheme 21: Synthetic routes for **14**.

In chapter 5.2, **14** was obtained from **12** by treating with PPh_3 . Here, a new synthetic procedure was introduced (**Scheme 21**). No obvious color change was observed from **2** with $\text{PPh}_3=\text{S}$ in THF solution. The experimental process was monitored by ^1H NMR spectroscopy. A weak and broad peak at 4.55 ppm was observed during the reaction of **2** with $\text{PMe}_3=\text{S}$ in the NMR tube, which is attributed to the H_2 release (**Figure 75**). The 1D and 2D NMR spectra of **14** were shown in **Figure 76** and appendix

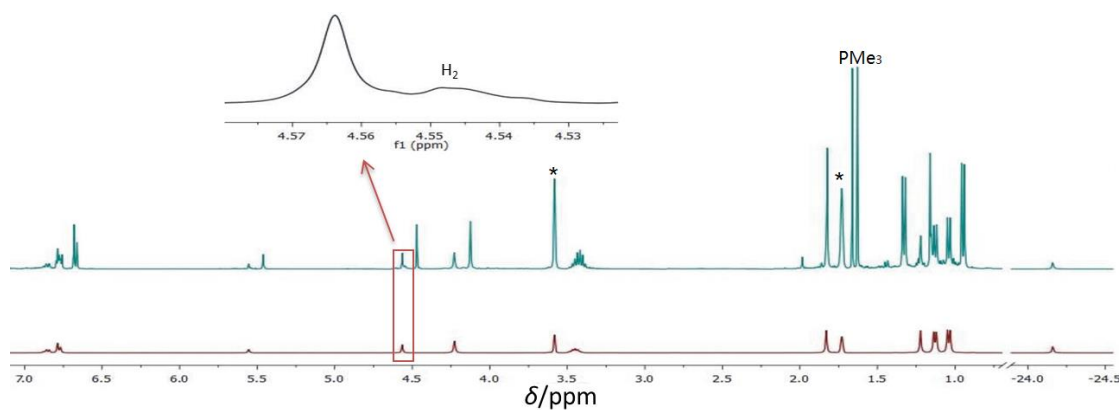


Figure 75: Monitoring the reaction of $\text{PMe}_3=\text{S}$ with **2** in THF-d_8 (400 MHz). Residual solvents are marked with an asterisk (*).

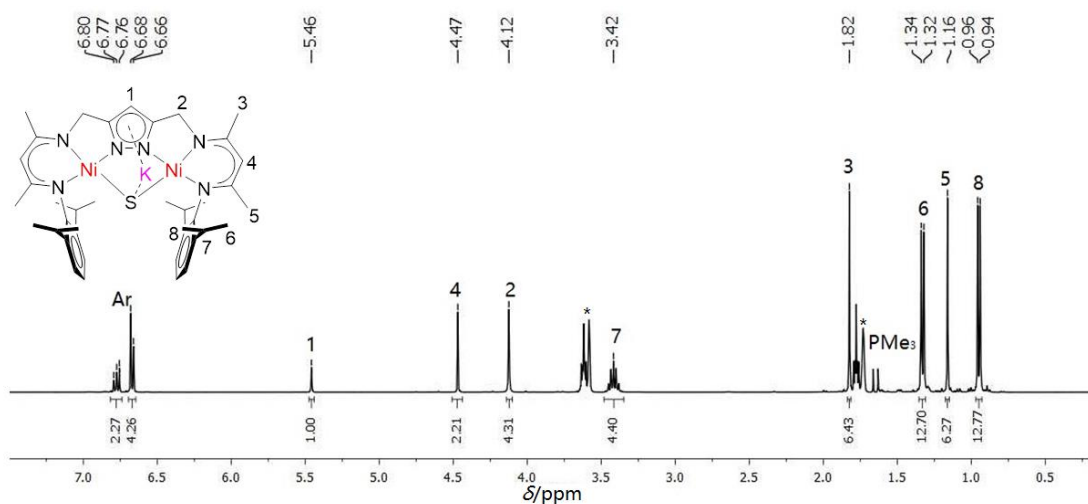


Figure 76: ^1H NMR spectrum (400 MHz) of **14** in THF-d_8 . Residual solvents are marked with an asterisk (*).

No obvious color change was observed in **2** with $\text{PMe}_3=\text{S}$ at RT. Nevertheless, orange crystals suitable for x-ray diffraction were obtained by layering hexane on a solution of **14** in THF in two days. **14** crystallized in the triclinic space group *P*-1 with two molecules in the unit cell. The molecular structure of **14** in ORTEP diagram is shown in **Figure 77** and selected bond lengths (\AA) and bond angles ($^\circ$) are listed in **Table 17**. A five-membered planar ring was formed by the nickel centers, nitrogen atom from pyrazolate and the μ -sulfide ligand. It became clear that the new μ -sulfide compound is similar to the hydrosulfide complex. The two nickel centers are coordinated by the S atom and the N atom in a square planar fashion (sum of bond angles 361.07° and 360.02° , respectively). The distance of two nickel centers with $3.652(5)$ \AA is slightly shorter than **13** with $3.707(5)$ \AA . The Ni-S distances in **14** of $2.224(7)$ \AA and $2.240(7)$ \AA are shorter than related **13** (2.274 \AA and 2.265 \AA). The Ni1-S-Ni2 angle $109.05(3)^\circ$ is also smaller than **13**. The alkali-metal, K^+ cation, is located outside the molecule anion and coordination with three THF molecules and pyrazole-N. The aryl-alkali metal distances amount $2.994(7)$ \AA , which implies that the *cation*- π interaction between the potassium and five-member ring.

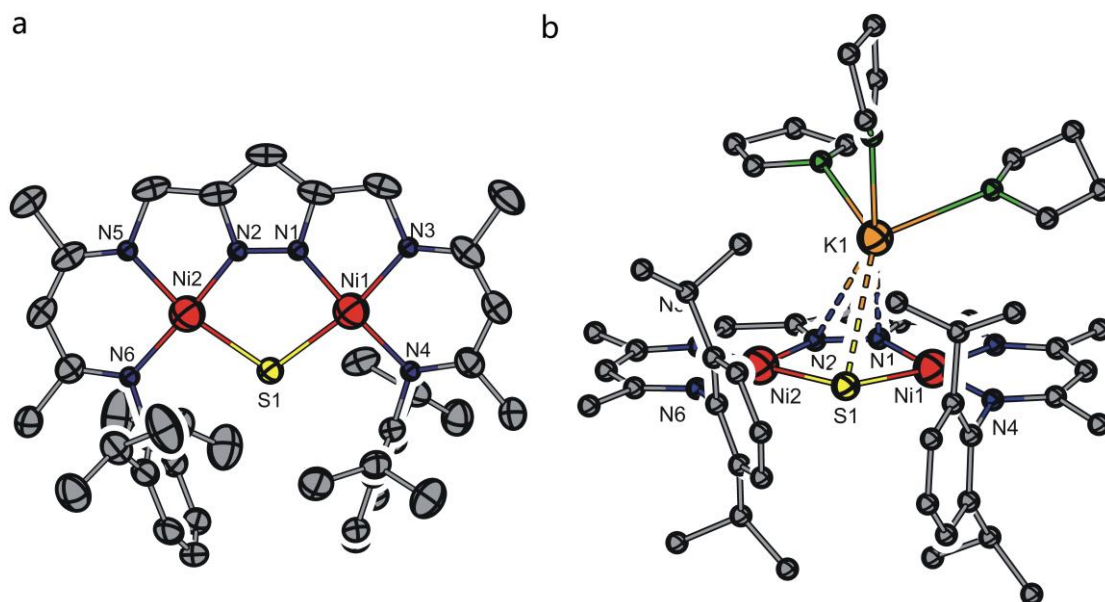


Figure 77: Molecular structure (30% probability thermal ellipsoids) of the anion of **14** (a) and **14** (b). All hydrogen atoms omitted for clarity.

Table 17: Selected bond lengths (Å) and bond angles (°) for **14**.

Atoms	Bond lengths	Atoms	Bond angles
Ni1-N1	1.816(2)	N1-Ni1-N4	176.47(9)
Ni1-N4	1.904(2)	N1-Ni1-N3	82.01(10)
Ni1-N3	1.925(2)	N4-Ni1-N3	94.51(9)
Ni1-S1	2.240(7)	N1-Ni1-S1	86.10(7)
Ni1-K1	3.198(7)	N4-Ni1-S1	97.40(6)
Ni2-N2	1.820(2)	N3-Ni1-S1	168.02(7)
Ni2-N6	1.914(2)	N1-Ni1-K1	72.26(7)
Ni2-N5	1.932(2)	N4-Ni1-K1	109.43(6)
Ni2-S1	2.244(7)	N3-Ni1-K1	105.21(7)
Ni2-K1	3.791(7)	S1-Ni1-K1	69.47(2)
K1-N1	3.160(2)	N2-Ni2-N6	176.17(9)
K1-N2	3.446(2)	N2-Ni2-N5	82.12(9)
K1-S1	3.197(1)	N6-Ni2-N5	94.41(9)
Ni1...Ni2	3.652(5)	N2-Ni2-S1	85.81(7)
		N6-Ni2-S1	97.73(6)
		N5-Ni2-S1	167.60(7)
		N2-Ni2-K1	65.09(6)
		Ni1-S1-Ni2	109.05(3).

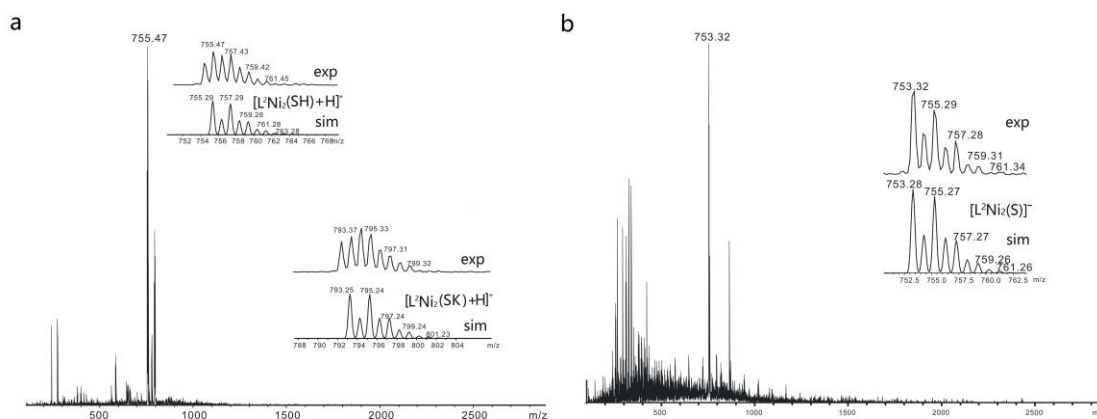


Figure 78: (a) positive ion ESI-MS of **14**; (Inset) experimental (upper) and simulated (middle and bottom) isotopic distribution pattern for the peaks pattern around $m/z = 755.47$ and 792.29 characteristic for the $[\mathbf{14}+\mathbf{H}]^+$ and $[\mathbf{14}]^+$; (b) ESI-MS (-) spectrum of **14**; (Inset) experimental (upper) and Simulated (bottom) isotopic distribution pattern for the peaks pattern around $m/z = 753.32$ characteristic for the $[\mathbf{14}-\mathbf{K}]^-$.

14 has been characterized by positive and negative ion ESI-MS in MeCN/THF mixture solvent (**Figure 78**). Positive ion ESI-MS (**Figure 78a**) spectrometry shows two dominate peaks characteristic for **14** and **13** compounds. Main peak corresponds to the $[\mathbf{13}+\mathbf{H}]^+$, and the signal of 793.37 is attributed to the $[\mathbf{14}+\mathbf{H}]^+$. In the negative ion ESI-MS (**Figure 78b**), the dominate peak belongs to the $[\mathbf{14}-\mathbf{K}]^-$ signal.

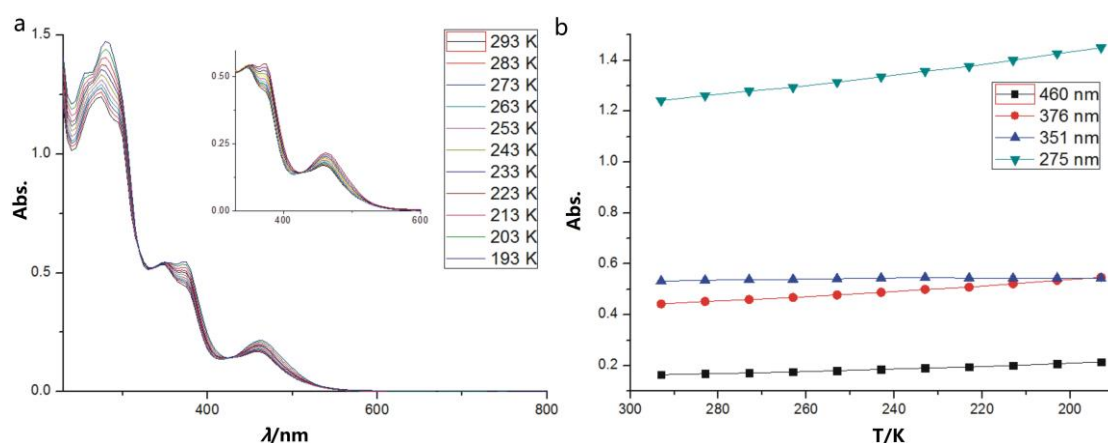


Figure 79: (a) UV-Vis spectra of **14** at different temperatures (293 K – 193 K) in THF; (b) Plots of the absorption bands at different temperatures.

The UV-Vis spectrum (**Figure 79a**) of **14** displays bands at 460, 376, 351 and 275 nm. The bands at 275 ($\epsilon \approx 11100 \text{ M}^{-1}\cdot\text{cm}^{-1}$) and 351 nm ($\epsilon \approx 4910 \text{ M}^{-1}\cdot\text{cm}^{-1}$)

are assigned to the ligand-metal charge-transfer transitions. The intense band at 460 nm ($\epsilon \approx 2000 \text{ M}^{-1}\cdot\text{cm}^{-1}$) is to the sulfide $\pi^*_{\sigma} \rightarrow \text{Ni}^{\text{II}}$ charge-transfer (CT) transitions corresponds to literature. [65]

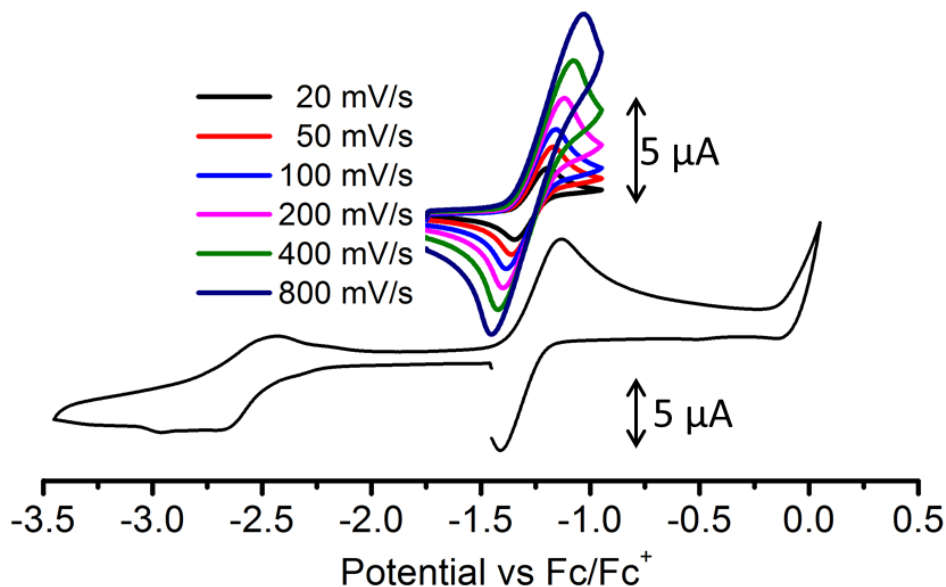
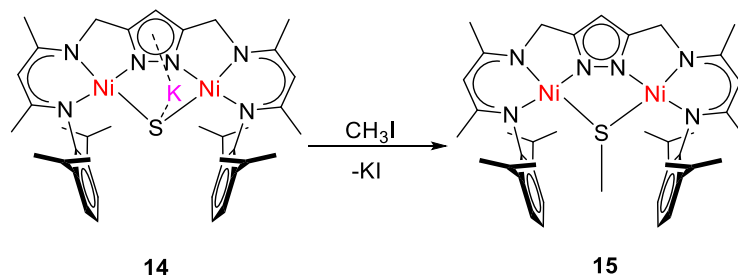


Figure 80: CV of **14** in THF at RT, with NBu_4PF_6 as supporting electrolyte (0.1 M) at different scan rates.

Cyclic voltammetry (CV) of **14** in a 0.1 M solution of NBu_4PF_6 in THF (**Figure 80**) at room temperature showed a reversible redox wave of scan of 100 mV at $E_{1/2} = -1.25 \text{ V}$ (vs Fc/Fc^+). It indicates that **14** may be oxidized by one electron to the sulfur radical dinickel complex. The chemical oxidation experiment will be discussed in the next section.

■ **Reactivity of 14.**



Scheme 22: Reactivity of **14** towards MeI.

As shown in **Scheme 22**, **14** exhibits reactivity towards CH_3I . Treatment of **14** with CH_3I at RT results in a rapid color change from red to green. Green crystals suitable for x-ray diffraction were obtained by layering hexane on a solution of **15** in THF at -30°C . **15** crystallized in the triclinic space group *P*-1 with two molecules in the unit cell. The molecular structure of **15** in ORTEP diagram is shown in **Figure 81** and selected bond lengths (Å) and bond angles ($^\circ$) are listed in **Table 18**. As expected, the sulfide was methylated from MeI in THF solution. The distance of C-S is 1.841(3) Å.

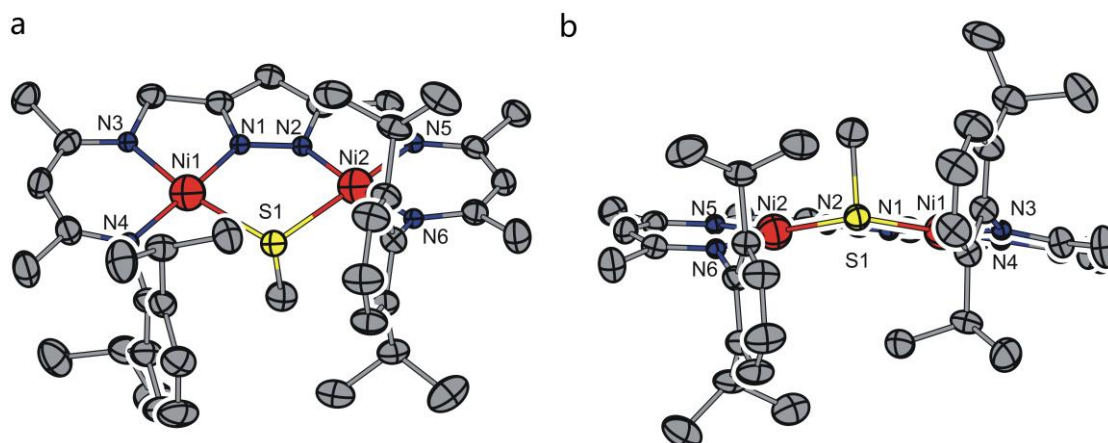
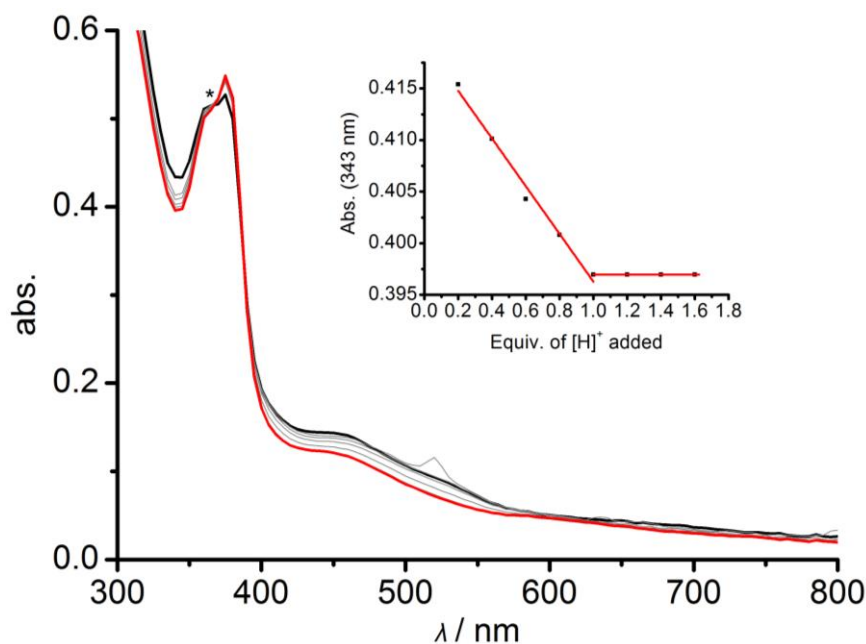


Figure 81: Molecular structure (30% probability thermal ellipsoids) of **15**. Most hydrogen atoms omitted for clarity.

Table 18: Selected bond lengths (Å) and bond angles (°) for **15**.

Atoms	Bond lengths	Atoms	Bond angles
Ni1-N1	1.821(2)	N1-Ni1-N3	81.84(9)
Ni1-N3	1.899(2)	N1-Ni1-N4	176.16(9)
Ni1-N4	1.899(2)	N3-Ni1-N4	94.95(9)
Ni1-S1	2.281(8)	N1-Ni1-S1	86.00(7)
Ni2-N2	1.818(2)	N3-Ni1-S1	167.70(7)
Ni2-N5	1.895(2)	N4-Ni1-S1	97.13(7)
Ni2-N6	1.890(2)	N2-Ni2-N5	81.88(10)
Ni2-S1	2.264(8)	N2-Ni2-N6	173.28(9)
C40-S1	1.841(3)	N5-Ni2-N6	95.59(9)
Ni1...Ni2	3.649(8)	N2-Ni2-S1	86.11(7)
		N5-Ni2-S1	162.93(7)
		N6-Ni2-S1	97.61(7)
		C40-S1-Ni1	97.80(1)
		C40-S1-Ni2	92.74(1)
		Ni1-S1-Ni2	106.81(3)

**Figure 82:** Stepwise protonation of **14** with [H-Lut]OTf at RT in THF, monitored by UV-vis absorption spectroscopy (1 cm path length). The asterisk marks the isosbestic point at 368 nm. Inset: decrease of the absorption at 343 nm depending on the number of equivalents of [H-Lut]OTf added.

As shown in **Figure 82**, when **14** reacts with [H-Lut]OTf, the characteristic charge transfer (CT) absorption band of **14** at 455 nm and 343 nm decrease, the band at 375 nm increase, with a clean isosbestic point (*) at 368 nm. Transformation was complete after 1 equivalent of acid was added, and **13** was stable in the presence of excess acid.

5.5 Synthesis of a μ -1,1-sulfide radical nickel(II) complex

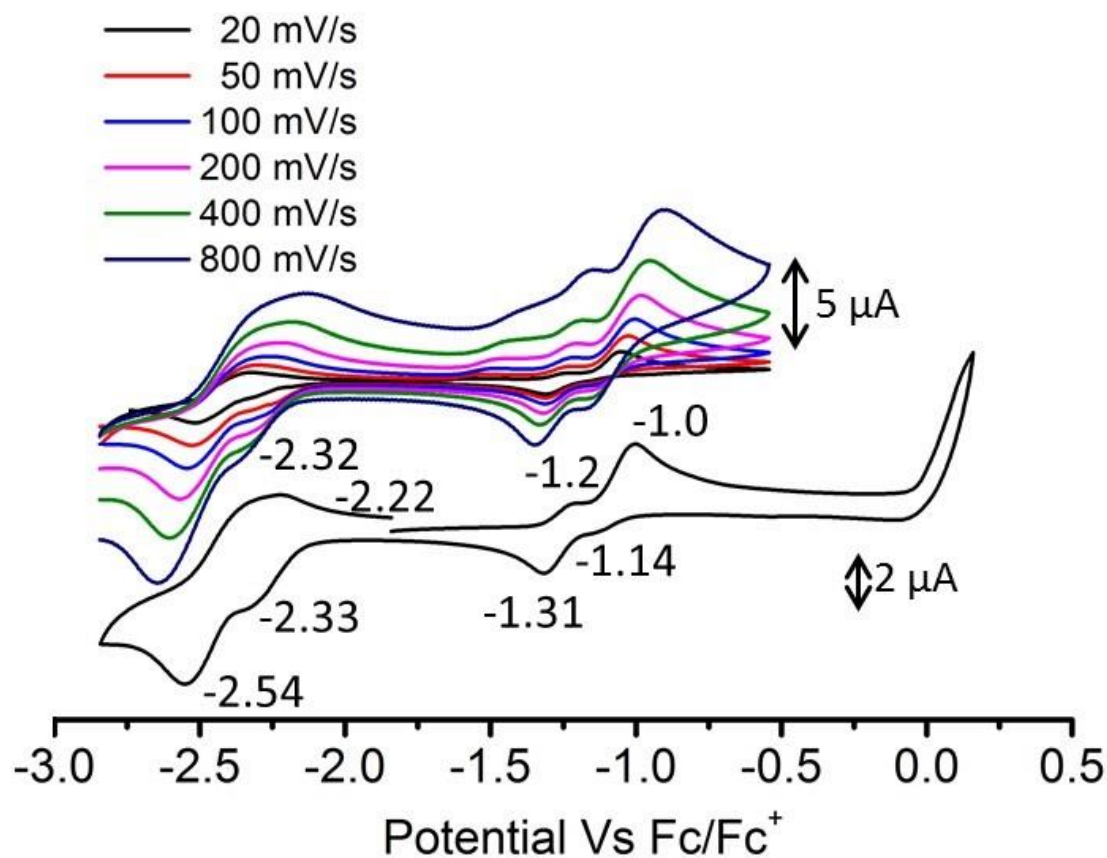
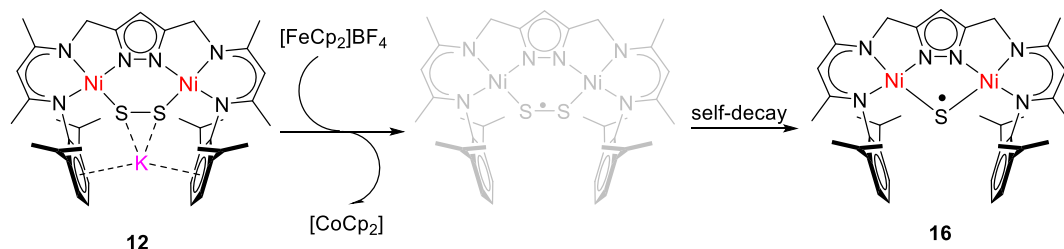


Figure 83: CV of **12** in THF at RT, with NBu_4PF_6 as supporting electrolyte (0.1 M) at different scan rates.

Cyclic voltammogram (**Figure 83**) of **12** in a 0.1 M solution of NBu_4PF_6 in THF at RT shows two quasi-reversible redox wave $E_{1/2}$ at -1.2 and -1.26 V implying that the disulphide nickel complex may be oxidized by one electron to supersulfide nickel species. In fact, the chemical oxidation of **12** dissolved in THF with $[\text{FeCp}_2]\text{BF}_4$ at -30°C leads to an immediate color change of the solutions from

wine-red to brown-black (**Scheme 23**). UV-Vis spectrum of the species in THF displays bands at 270 ($\epsilon \approx 2800 \text{ M}^{-1}\cdot\text{cm}^{-1}$), 319 ($\epsilon \approx 1280 \text{ M}^{-1}\cdot\text{cm}^{-1}$), 373 ($\epsilon \approx 820 \text{ M}^{-1}\cdot\text{cm}^{-1}$) and 457 nm ($\epsilon \approx 200 \text{ M}^{-1}\cdot\text{cm}^{-1}$) in **Figure 84a**. It confirms that a new species was obtained from the chemical oxidation.



Scheme 23: Synthetic route for **16**.

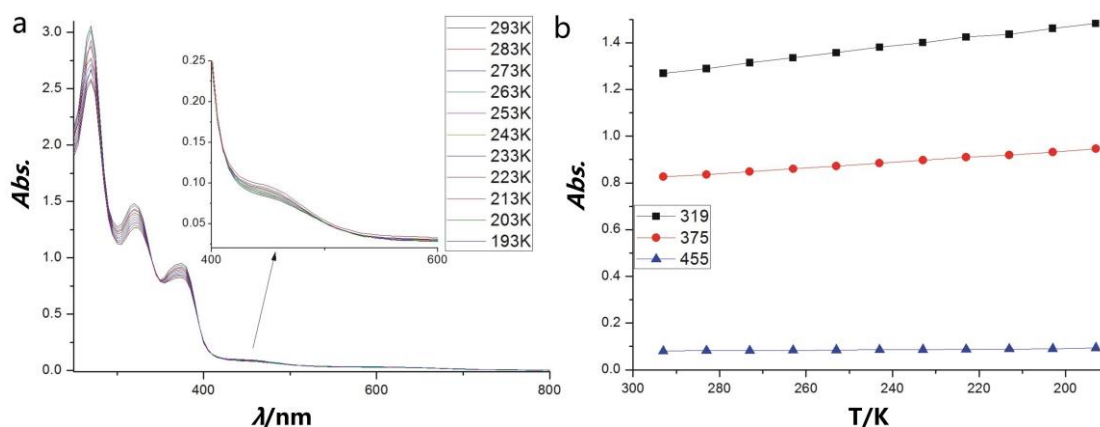


Figure 84: (a) UV-Vis spectra of **16** at different temperatures (293 K–193 K) in THF; (b) Plots of the absorption bands of **16** at different temperatures.

Green block shape crystals suitable for x-ray diffraction were obtained in 70% yield by layering hexane on a solution of **16** in THF at -30°C . **16** crystallized in the monoclinic space group $P2_1/c$ with four molecules in the unit cell. The molecular structure of **16** is shown in **Figure 85** and selected bond lengths (\AA) and bond angles ($^{\circ}$) are listed in **Table 19**.

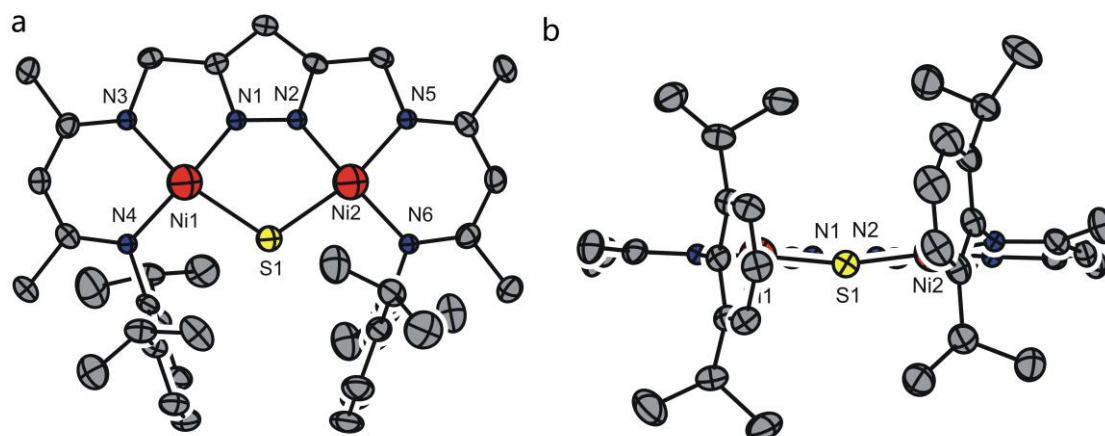


Figure 85: Molecular structure (50% probability thermal ellipsoids) of **16**. All hydrogen atoms omitted for clarity.

Table 19: Selected bond lengths (Å) and bond angles (°) for **16**.

Atoms	Bond lengths	Atoms	Bond angles
Ni1-N1	1.825(2)	N1-Ni1-N3	82.03(9)
Ni1-N3	1.896(2)	N1-Ni1-N4	177.01(9)
Ni1-N4	1.898(2)	N3-Ni1-N4	95.00(9)
Ni1-S1	2.278(7)	N1-Ni1-S1	85.33(7)
Ni2-N2	1.827(2)	N3-Ni1-S1	166.54(7)
Ni2-N5	1.893(2)	N4-Ni1-S1	97.66(7)
Ni2-N6	1.893(2)	N2-Ni2-N5	82.25(9)
Ni2-S1	2.289(7)	N2-Ni2-N6	174.11(10)
Ni1...Ni2	3.705(5)	N5-Ni2-N6	94.47(9)
		N2-Ni2-S1	85.15(7)
		N5-Ni2-S1	165.18(7)
		N6-Ni2-S1	98.72(7)
		Ni1-S1-Ni2	108.44(3)

Selected metrical parameters of the three sulfide complexes are listed in **Table 20**. **14** appears shorter Ni-S distance than **13** and **16**. In the solid state, no proton close to the sulfide bridge ligand was observed. The Ni-S bond lengths in **16**, however, are slightly longer than the additive covalent radii for nickel-sulfur single bonds (2.13 Å). [68] For comparison, $[\{L^{tBu}Ni\}(\mu-S)]$,^[62] $[\{(IPr)Ni\}_2(\mu-S)_2]$ (IPr=1,3-bis(2,6-diisopropylphenyl)imidazol-2-ylidene),^[53e] and $[\{PhB(CH_2StBu)_3\}Ni]_2(\mu-S)$ ^[58e] display comparable Ni-S bond lengths of

2.0651(7), 2.0972(6), 2.0714(4) and 2.084(6) Å, respectively, despite each possessing a bridging S²⁻ or S⁻ ligand. Overall, this suggests similar magnitudes of π -bonding in both classes of materials.

Table 20: Selected metrical parameters of **13**, **14** and **16**.

Complex	13	14	16
Ni...Ni (Å)	3.707	3.652	3.705
Ni-S (Å)	2.274	2.240	2.278
	2.264	2.244	2.289
Ni-N (Å)	1.826-1.900	1.816-1.932	1.825-1.898
Ni-S-Ni (°)	109.51	109.05	108.45

The ¹H and ¹³C NMR spectra of **16** show a paramagnetically shifted resonance. However, the x-band electron paramagnetic resonance (EPR) measurement of a frozen THF at 10 K revealed that Ni^{III} exists at low concentration of **16** (**Figure 86a**). And the x-band EPR spectrum of **16** in THF in 2 mM revealed no Ni^{III} exists in the solution anymore and the intensity of the spectra account for only *ca.* 20% of the expected spin concentration (numerical integration and comparison with a Cu^{II} standard) (**Figure 86b**). The difference of EPR spectra in different concentration remind the sulfur radical **16** may has two different valence transfer in the solution. One of them is the unpaired electron moves between the Ni-S systems (**Scheme 24a**). The other possibility for the low concentration is a dimerization transfer from the sulfur radical complex (**Scheme 24b**).

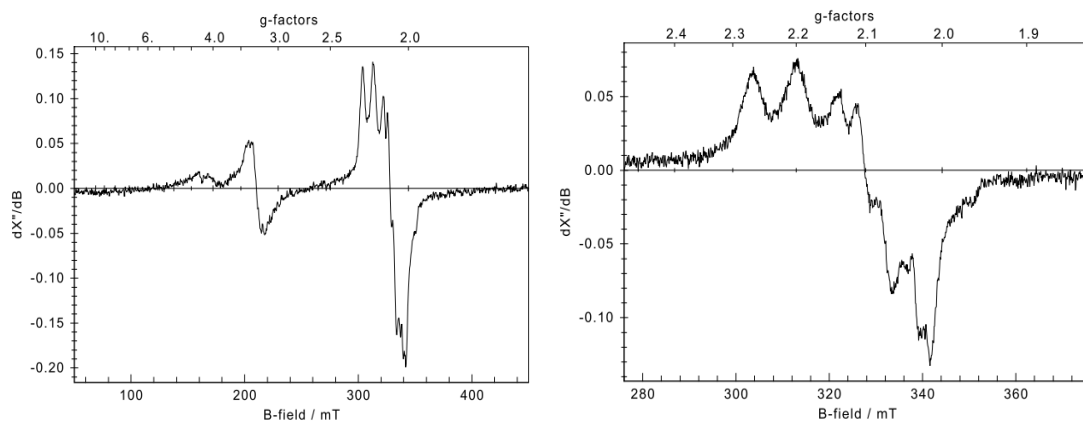
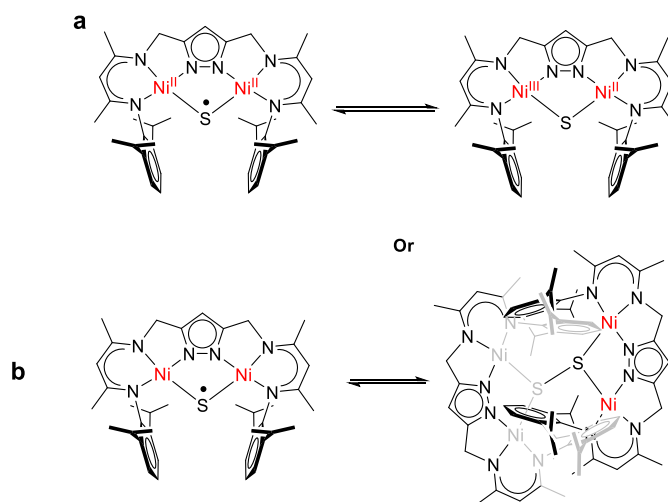


Figure 86: (a) X-band EPR spectra of **16** at low concentration in frozen THF solution at 30 K. (b) X-band EPR spectra of **16** at 2 mM in frozen THF solution at 30 K.



Scheme 24: Possible formulation of the Ni-S species in the solution.

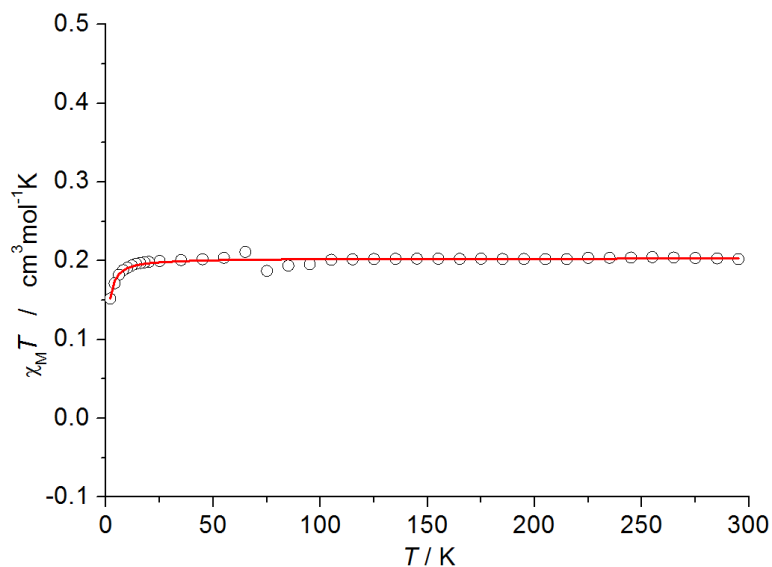


Figure 87: (a) $\chi_{\text{m}}T$ vs. T measurement in the temperature range of 2–295 K at 0.5 T for solid samples of **16**. The solid red line represents the best fit $g = 2.0$ (54%) with $DI = 46\%$ ($S = 0$) and $TIP = 507 \times 10^{-6} \text{ cm}^3 \cdot \text{mol}^{-1}$.

Magnetic susceptibility data for **16** collected in the temperature range from 2–295 K in crystalline material, shows essentially paramagnetic behavior of $S = 1/2$ spin system (54%) (**Figure 87**). The solid red line represents the best fit and relatively high amount of diamagnetic impurity with $DI = 46\%$ ($S = 0$) and $TIP = 507 \times 10^{-6} \text{ cm}^3 \cdot \text{mol}^{-1}$. An explanation for the essential amount of diamagnetic impurity could be fast decomposition of **16** at RT.

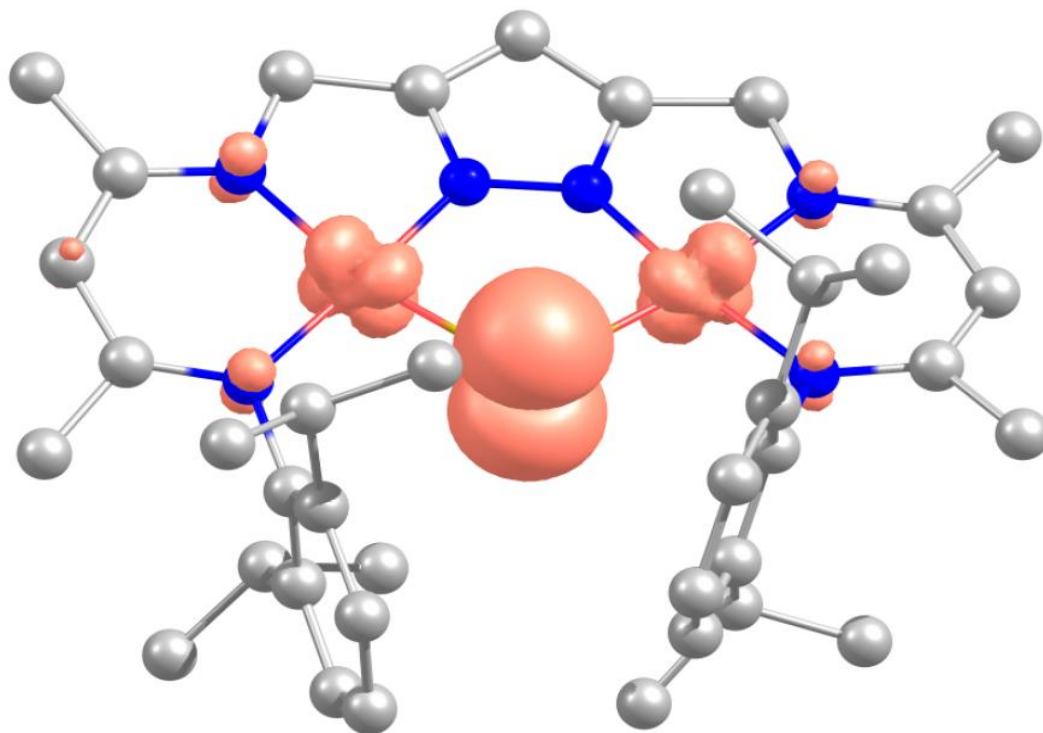


Figure 88: Spin density plot of **16**. Mulliken Spin Population: Ni1 = 0.151717, Ni2 = 0.133588, S3 = 0.619900.

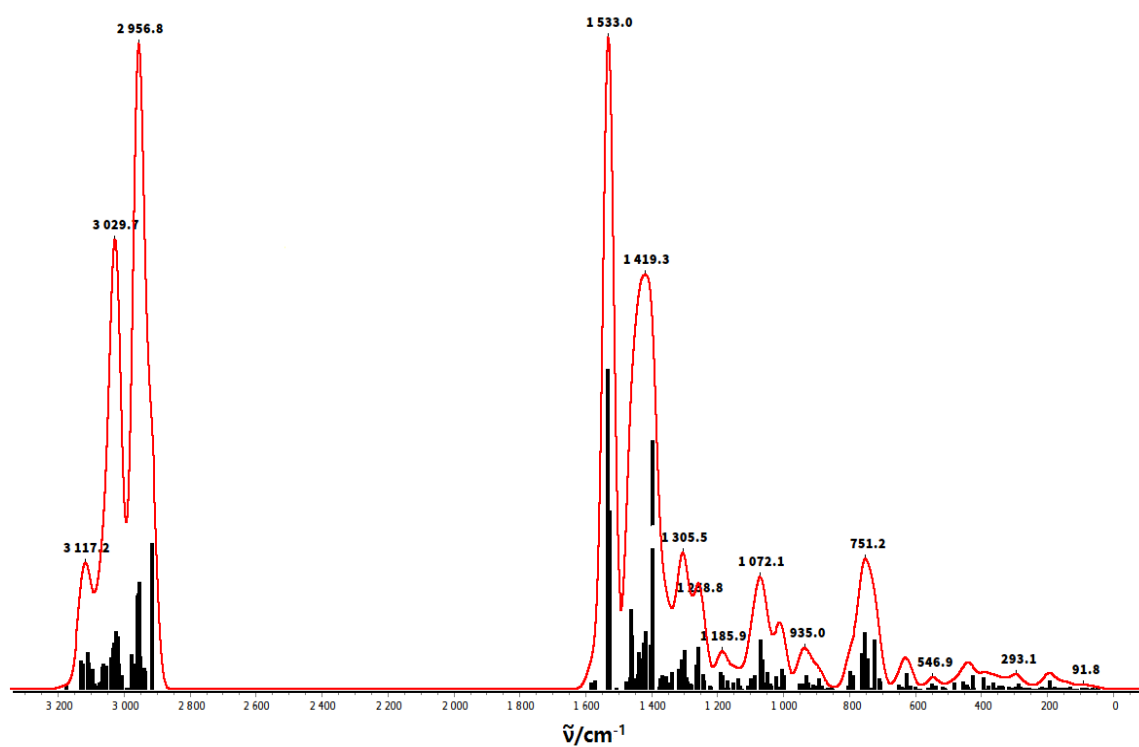


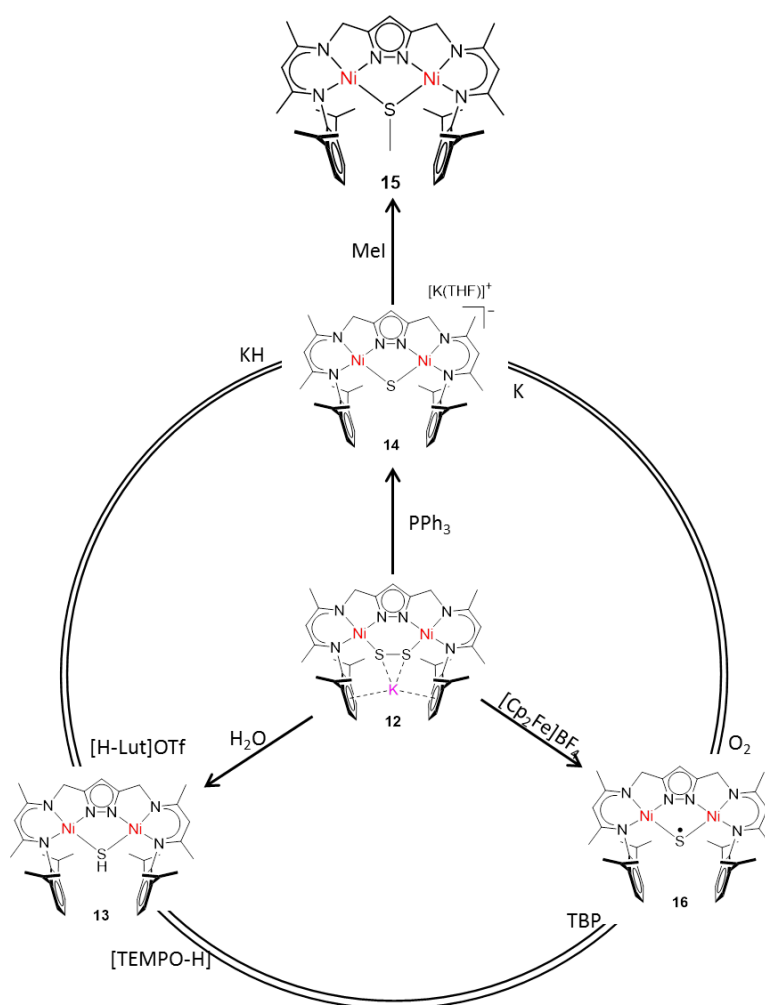
Figure 89: Calculated IR spectrum of **16**.

Table 21: Selected distance (\AA) and angles ($^\circ$) for **16**.

	$d(\text{Ni-S})/\text{\AA}$	$d(\text{Ni}\cdots\text{Ni})/\text{\AA}$	$\varphi(\text{Ni-S-Ni})/^\circ$
Exp	2.278/2.290	3.705	108.4
DFT*	2.189/2.199	3.600	110.2

The electronic nature of **16** as suggested by its geometric structure and magnetic properties was also confirmed by DFT calculations (**Figure 88**). The spin density can be estimated at the Ni center (28%), and at the sulfur ligand (around 62%). Therefore, the unpaired electron mostly located on sulfur atom. As shown in **Table 21**, the distances of Ni-S of 2.278/2.290 \AA are larger in the experimental data than the DFT calculations of 2.189/2.199 \AA . It can be assigned that the unpaired electron stays in the Ni-S-Ni system in the solid state.

5.6 Summary



Scheme 25: Activation and transformation of the substrates contains sulfur in the dinuclear nickel(II) complexes.

In this chapter, we could show that the reaction of elemental sulfur with **2** results in quite different reaction products depending on the exact reaction conditions (**Scheme 25**).

Firstly, elemental sulfur can react in similar way as dioxygen does with **2** and S_2^{2-} can be formed. This the first “*end-on*” heteronuclear dinuclear nickel(II) disulfide complex.

Secondly, treatment of **12** with PPh_3 , H_2O and $[Cp_2Fe]BF_4$ result into different

species with μ -sulfide, hydrosulfide and sulfur monoanionic radical.

Thirdly, interconversion between **13**, **14** and **16** have successfully done by chemical agents.

At last, the dinuclear nickel μ -sulfide complex reactivity toward CH_3I is verified.

In addition, further thermodynamics between **13**, **14** and **16** are ongoing.

Chapter 6 Deprotonation and Isomerization of Phenylhydrazine in the dinuclear nickel(II) complex

Abstract: A new dinuclear nickel(II) phenylhydrazido(1-) complex (**17**) was synthesized from dinickel bromide precursor (**1**) with phenylhydrazine in the presence of KC_8 . Treatment of **17** with KH or in the presence of dibenzo(18-crown-6) leads two hetero-bimetallic trinuclear complexes (**18** and **19**). For these two complexes, two geometrical isomers are present in solution, and mechanistic insight into the isomerization process was obtained by VT 1H NMR spectroscopy.

6.1 Introduction

In the last two decades, many chemists studied the reactivity of coordinated dinitrogen towards protons, other hydrogen sources and relevance to the mechanism of action nitrogenase. [69] A large number of transition metal complexes containing substituted or unsubstituted hydrazido, hydrazine or diazene ligands have been reported. [70] However, only few examples were reported with nickel as the desired metal. [71,72] As shown in **Figure 90 (XXVI-XXIX)**, there has been some effort to obtain synthetic phenylhydrazido mode for the nickel or iron phenylhydrazine in the β -diketiminato ligand by *Limberg*[72] and *Holland*[73] groups.

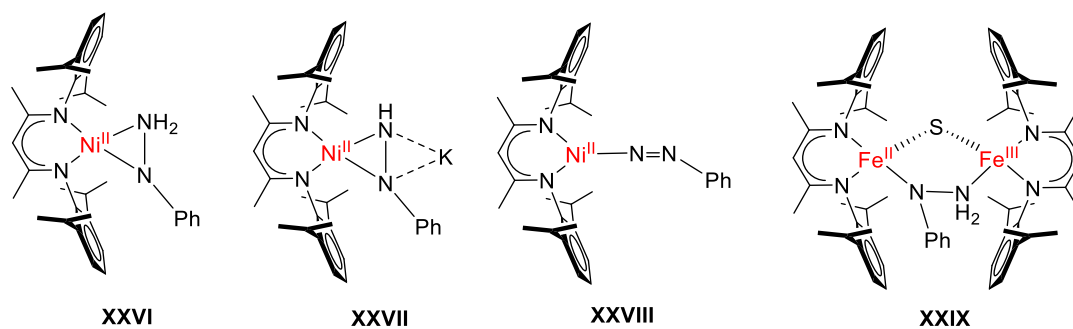
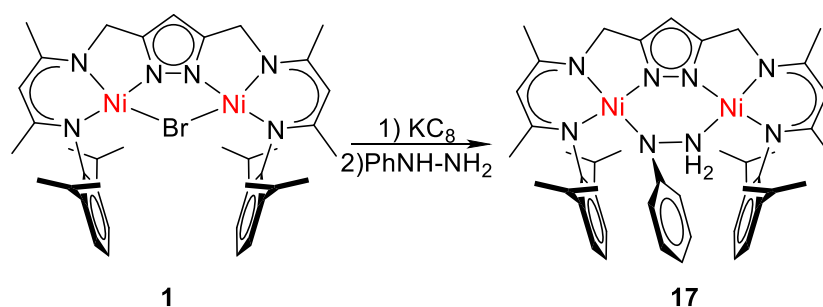


Figure 90: Selected examples of nickel(II) and iron(II/III) phenylhydrazine/phenylhydrazido/diazene complexes supported by β -diketiminato ligand. [72,73]

6.2 Synthesis of phenylhydrazido bridged complex



Scheme 26: Synthetic route for **17**.

Previously, treatment of **1** with hydrazine dissolved in THF solution led to appropriate products, so that phenylhydrazine was employed instead of the parent N_2H_4 .^[11a] However, this reaction only works in the presence of stoichiometry KC_8 or $tBuOK$ (**Scheme 26**). During the reaction of **1** with phenylhydrazine in the presence of KC_8 in THF solution, gas evolution (H_2) was found and a dark red solution was obtained immediately. However, same compound was obtained even though excess KC_8 was employed in the reaction. This complex was fully characterized by x-ray diffraction, 1D and 2D NMR, FT-IR spectroscopy, ESI-MS spectrometry and CV measurement as well as elemental analysis.

Dark red crystals suitable for x-ray diffraction were obtained by slow diffusion of pentane into a solution of **17** in THF at room temperature. **17** crystallizes in the triclinic space group $P-1$, the molecular structure of **17** is shown in **Figure 91** and selected bond lengths (\AA) and angles ($^\circ$) are listed in **Table 22**. **17** contains an anionic phenylhydrazido(1-) ligand binding in a $\mu-\eta^1:\eta^1$ -mode, and thus the two Ni ions are surrounded by four N donor atoms in a distorted square planar way. The Ni-N^{Ph}-N^{NH}-Ni torsion angle around the N-N axis is $78.66(3)^\circ$. The N-N bond length of the phenylhydrazido(1-) ligand amounts to $1.441(4) \text{\AA}$ and therefore lies within the range that is typical for η^1 -organohydrazido(1-) ligands citation. ^[74] The bond length of Ni-NH₂

(1.946(3) Å) is slightly longer than that of Ni-NPh bond length (1.914(3) Å). This is in contrast to the literature known complexes **XXVI**^[72] and $[\text{Ru}(\eta^2\text{-NH}_2\text{NPh})(\text{dmpe})_2]\text{BPh}_4$ ^[75], where the Ni-NPh and Ru-NPh bonds are significantly longer than the Ni-NH₂ and Ru-NH₂ bonds.

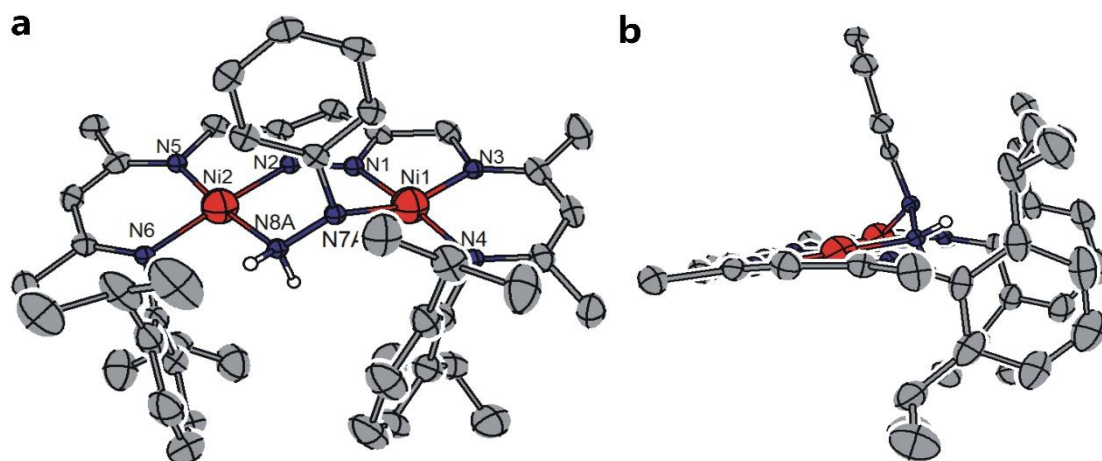


Figure 91: Molecular structure (50% probability thermal ellipsoids) of **17**. Most hydrogen atoms omitted for clarity, except for the NH₂ group.

Table 22: Selected bond lengths (Å) and angles (°) for **17**.

Atoms	Bond lengths	Atoms	Bond angles
Ni1-N1	1.852(3)	N1-Ni1-N3	83.62(11)
Ni1-N3	1.882(3)	N1-Ni1-N4	169.45(11)
Ni1-N4	1.897(3)	N3-Ni1-N4	95.08(11)
Ni1-N7A	1.914(3)	N1-Ni1-N7A	89.61(11)
Ni2-N2	1.862(3)	N3-Ni1-N7A	164.58(12)
Ni2-N5	1.881(3)	N4-Ni1-N7A	94.05(11)
Ni2-N6	1.903(3)	N2-Ni2-N5	83.40(11)
Ni2-N8A	1.946(3)	N2-Ni2-N6	174.99(11)
N7A-N8A	1.441(4)	N5-Ni2-N6	94.44(11)
Ni1-N7A	1.914(3)	N2-Ni2-N8A	90.14(11)
Ni2-N8A	1.946(3)	N5-Ni2-N8A	172.69(11)
Ni1...Ni2	3.918(2)	N6-Ni2-N8A	92.27(11)
		N8-N7-Ni1	116.02(2)
		N7-N8-Ni2	120.74(2)
		Ni1-N7A-N8A-Ni2	78.66(3)

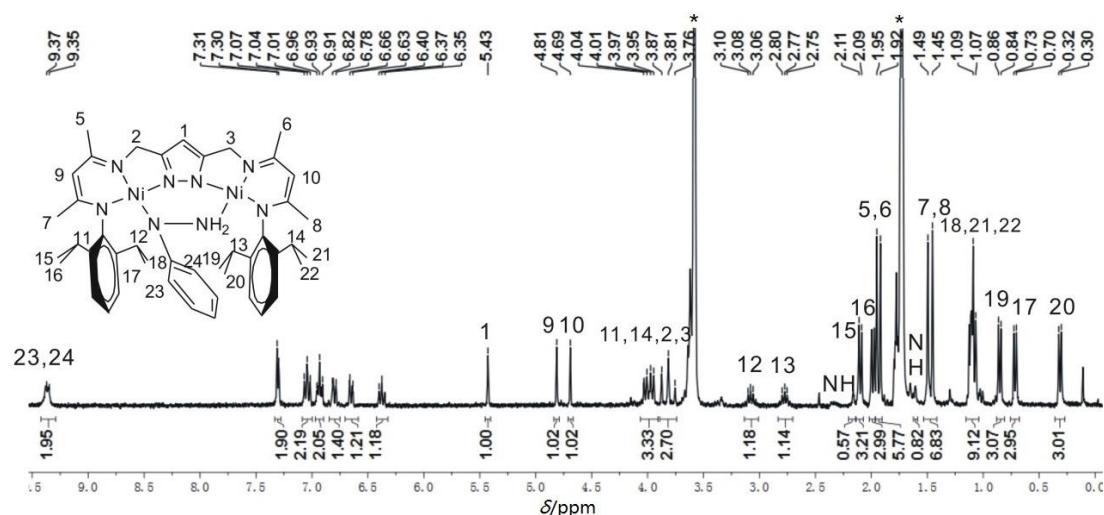


Figure 92: ^1H NMR (400 MHz) spectrum of **17** in THF-d_8 . Residual solvents are marked with an asterisk (*).

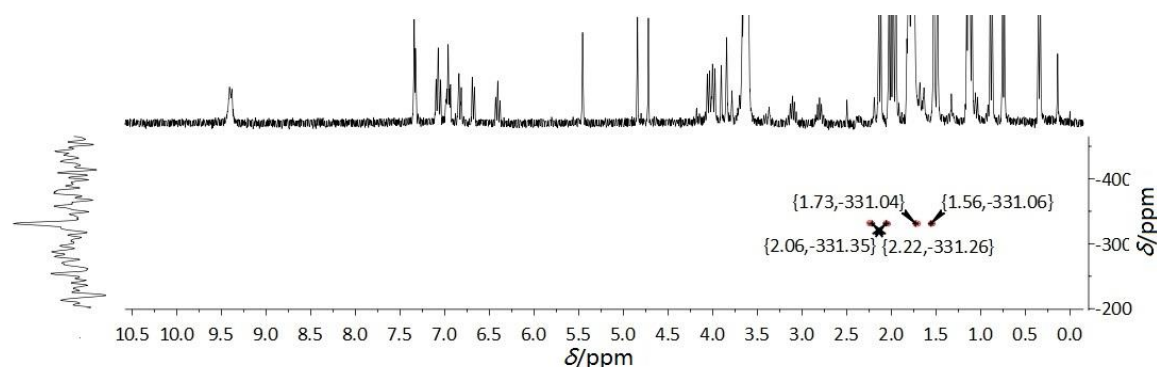


Figure 93: ^1H - ^{15}N HMBC (52 MHz) spectrum of **17** in THF-d_8 .

The resulting phenylhydrazido(1-) ligand undoubtedly is bound as the NH_2 - NPh -tautomer: The two protons were located in the fourier map and further support came from NMR experiments. For the NH protons of the NH_2 - NPh anionic unit, two doublet resonances with an integral of one were found at 1.60 ppm and 2.16 ppm in the ^1H NMR spectrum, respectively (**Figure 92**). The assignment of the NH was also confirmed using a 2D ^1H - ^{15}N HMBC experiment (**Figure 93**). Two ^{15}N correlations with these two protons ($^2J_{\text{NH}} = 67.74$ Hz) became evident, suggesting two NH protons, residing at the same N atom. In order to know the stereochemistry of the NH_2 group of the bridging phenylhydrazido, a ^1H - ^1H NOESY experiment was conducted. It reveals a weak NOE correlation of

one NH protons to the phenyl group of the bridging phenylhydrazido at room temperature (**Figure 94**).

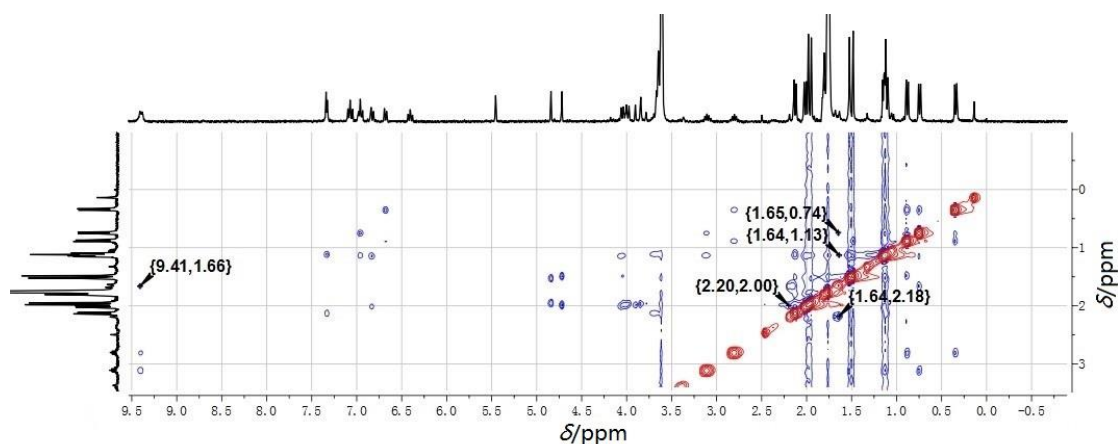


Figure 94: ^1H - ^1H NOESY (400 MHz) spectrum of **17**. The protons belonging to the NH_2NPh bridged show a NOE correlation to the CH proton of the phenyl groups. $^1J_{\text{NH}}$ correlation of **17** are marked.

Apart from the NH_2 resonance, the *ortho* protons from phenylhydrazido resonance is at 9.36 ppm, low field shifted compared with **XXVI** (5.06 ppm) (**Figure 90**).^[72] This may be because the phenyl ring from phenylhydrazido unit current effect to the ligand. To investigate the two protons, a variable temperature ^1H NMR was conducted from 183 K to 323 K (**Figure 95**). From 263 K to 243 K, no signals were observed for the *ortho* protons of phenyl group. On cooling to 233 K, the ^1H NMR spectrum appears two separate broad doublets at 8.80 and 9.84 ppm, respectively. The two peaks could result from a hindered rotation of the phenyl group at low temperatures. No coupling resonance was found in the ^1H - ^1H NOESY between the isopropyl group and the *ortho* protons of the phenyl group, which implies that the phenyl group only shown rotation activity without vibration of the ligand planar.

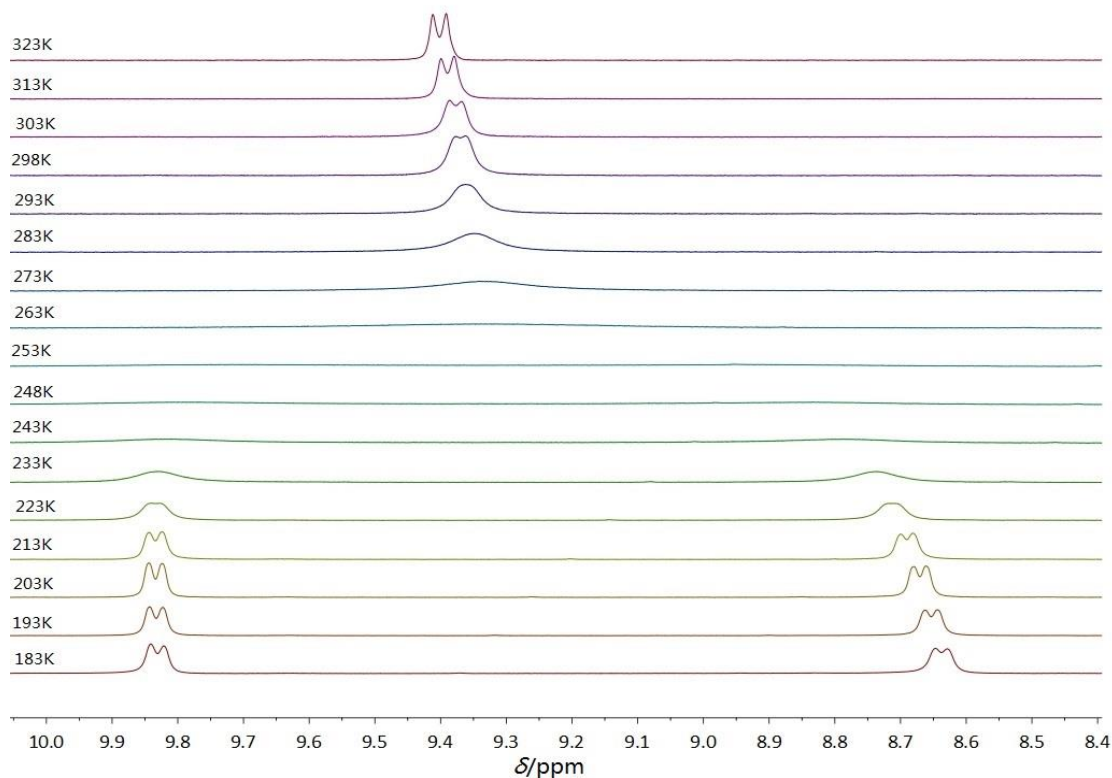


Figure 95: The field from 8.4 to 10.0 ppm in variable temperature (183 K – 323 K) ^1H NMR (400 MHz) spectra of **17** in THF-d_8 .

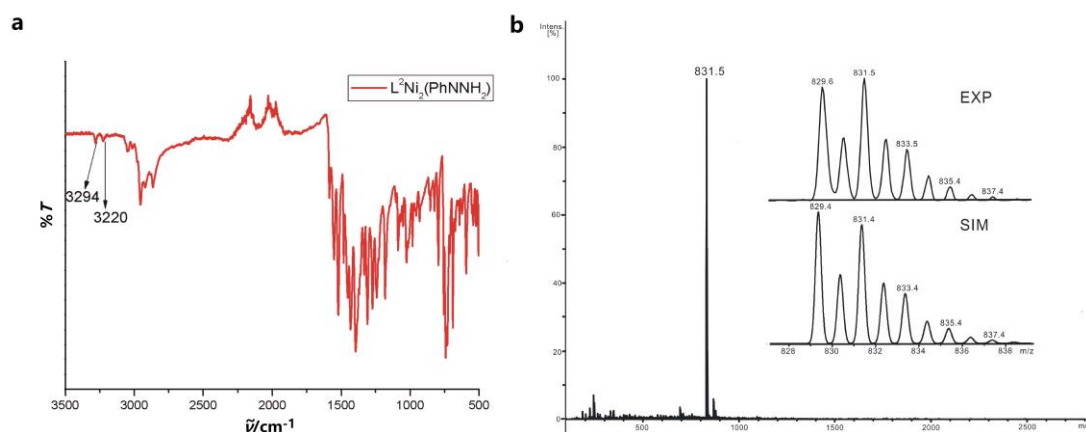
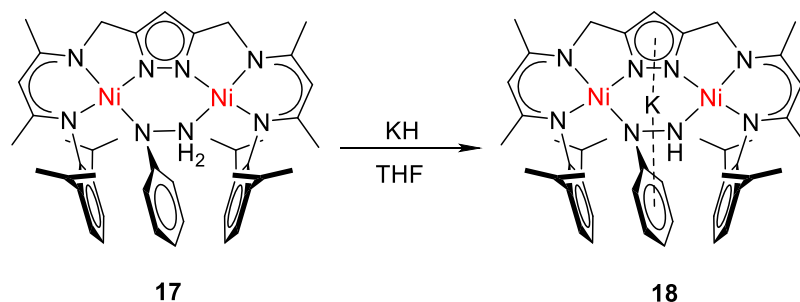


Figure 96: (a) FT-IR spectrum of **17** in crystalline material; (b): positive ion ESI-MS of **17** in THF; (Inset) experiment (upper) and simulated (lower) isotope distribution pattern for the peak pattern around $m/z = 829.6$ characteristic for the $[\mathbf{17}+\text{H}]^+$ ion.

IR spectroscopy (**Figure 96a**) of **17** clearly shows two bands belonging to the stretching vibration of an NH moiety at 3294 and 3220 cm^{-1} , thus further proving the presence of such a functionality. Additionally the positive ion ESI-MS

spectrum (**Figure 96b**) of **17** shows a major peak $m/z = 829.6$ consistent with the simulated isotope pattern of the molecular ion peak $[\mathbf{17}+\text{H}]^+$.

6.3 Deprotonation of phenylhydrazido bridge complex



Scheme 27: Synthetic route for **18**.

In order to examine whether it is possible to further activate the N–N bond of the phenylhydrazido(1–) ligand, **17** was treated with one equivalent KH, which led to a color change from red to green in two hours (**Scheme 27**). **18** was completely characterized by x-ray diffraction, 1D and 2D NMR, FT-IR spectroscopy and elemental analysis.

Black block crystals were obtained by layering hexane into THF solution at -30°C in two days, which was suitable for single-crystal x-ray diffraction and the yield of the compound was about 43%. **18** crystallizes in the triclinic space group $P-1$. The molecular structure of **18** was shown in **Figure 97** and selected bond lengths (\AA) and angles ($^{\circ}$) were listed in **Table 23**. In the case of **XXVI**, the phenylhydrazido(1–) was singly deprotonated by KC_8 , and the K^+ cation was fixed by 18-crown-6. Nevertheless, the new species is in a bad crystal quality so that no x-ray diffraction data is present for comparison with our data. To our best knowledge, **18** is the first Ni-K phenylhydrazido(2–) complex which has been structurally characterized.

The anion of **18** is obviously like **17**. In the solid structure of **18** (**Figure 97**),

the K^+ cation is coordinated by the pyrazole-N and three THF molecules, and locates between the pyrazole and phenyl rings. The distances between the K^+ cation and the phenyl group, pyrazole moieties are 2.973(2) Å and 3.129(2) Å, respectively. The distance of the two nickel atoms of 3.850(7) Å is slightly shorter than the parent phenylhydrazido **17**. In **18**, the distance of N–N in NNHPh unit with 1.404(3) Å is shorter than **17** with 1.441(2) Å. The dihedral angle of between the pyrazole and the phenylhydrazido ring is about 88.223(8)°. The Ni–N^{Ph}–N^{Ph}–Ni torsion angle around the N–N axis as defined is 73.55(1)°.

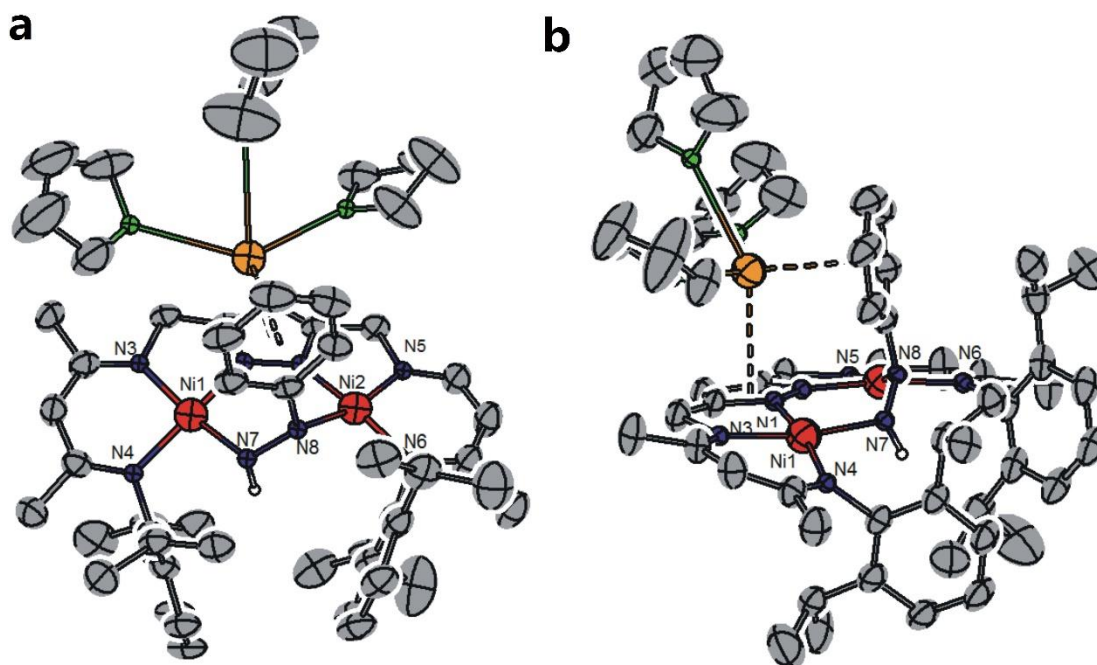
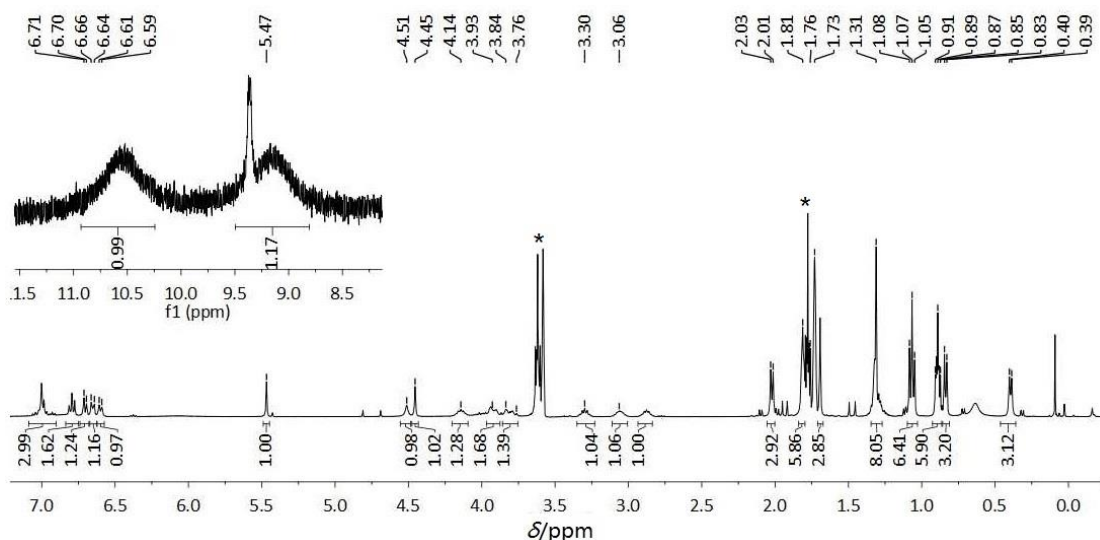


Figure 97: Molecular structure (50% probability thermal ellipsoids) of **18**. Most hydrogen atoms omitted for clarity, except for N7-H.

Table 23: Selected bond length (Å) and angles (°) for **18**.

Atoms	Bond lengths	Atoms	Bond angles
Ni1-N1	1.872(3)	N1-Ni1-N7	93.48(11)
Ni1-N7	1.907(3)	N1-Ni1-N4	170.42(11)
Ni1-N4	1.913(3)	N7-Ni1-N4	91.64(11)
Ni1-N3	1.932(3)	N1-Ni1-N3	82.44(12)
Ni2-N2	1.843(3)	N7-Ni1-N3	169.82(12)
Ni2-N8	1.903(3)	N4-Ni1-N3	93.77(12)
Ni2-N6	1.904(3)	N2-Ni2-N8	87.19(11)
Ni2-N5	1.908(3)	N2-Ni2-N6	173.28(12)
N7-N8	1.404 (3)	N8-Ni2-N6	95.09(11)
Ni1...Ni2	3.850(7)	N2-Ni2-N5	82.95(12)
K-Cg(1)	3.129(2)	N8-Ni2-N5	165.79(11)
K-Cg(2)	2.973(2)	N6-Ni2-N5	95.86(12)
		N8-N7-Ni1	118.09(1)
		N7-N8-Ni2	121.83(2)
		N8-N7-C40	113.38(1)
		Ni1-N7-N8-Ni2	73.55(1)
		Ni1-N1-K1A	110.11(1)
		Pz-K-Ar	101.00(3)

Cg(1) = centroid of the ring carbon atoms C1, C2, C3, N1, N2 (pyrazole ring);
 Cg(2) = centroid of the ring carbon atoms C40, C41, C42, C43, C44, C45 (phenyl ring).

**Figure 98:** ¹H NMR (400 MHz) spectrum of **18** in THF-d₈. Inset: excerpt range 8.5 – 11.5 ppm. Residual solvents are marked with an asterisk (*).

To further confirm the identity, an NMR spectroscopic analysis was performed. ^1H and ^{13}C $\{^1\text{H}\}$ NMR spectra (**Figure 98** and **Figure A33**) showed that the complex is diamagnetic and asymmetric. The resulting phenylhydrazido(2-) ligand undoubtedly is bound as the NH-NPh- tautomer: the proton was located in the fourier map and further support came from NMR experiments. The assignment of NH was also confirmed using a 2D ^1H - ^{15}N HMBC experiment. One ^{15}N correlation with this one proton became evident, suggesting NH proton (**Figure 99**). Additionally, IR spectroscopy (**Figure 100a**) of **18** clearly showed the presence of a NH function through a band belonging to its stretching vibration at 3244 cm^{-1} .

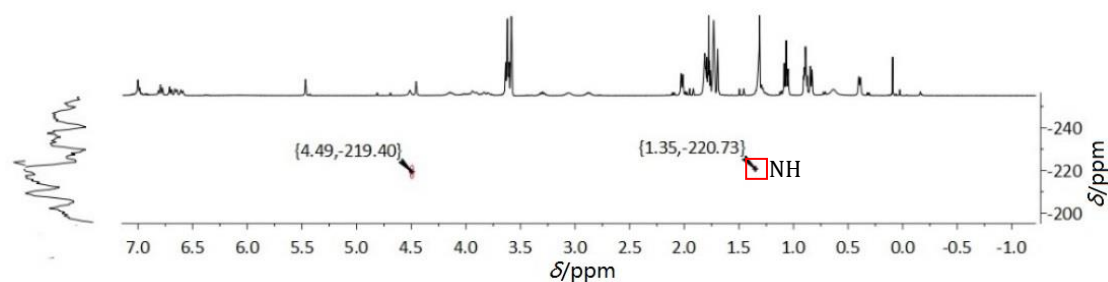


Figure 99: ^1H - ^{15}N NMR (52 MHz) spectrum of **18**.

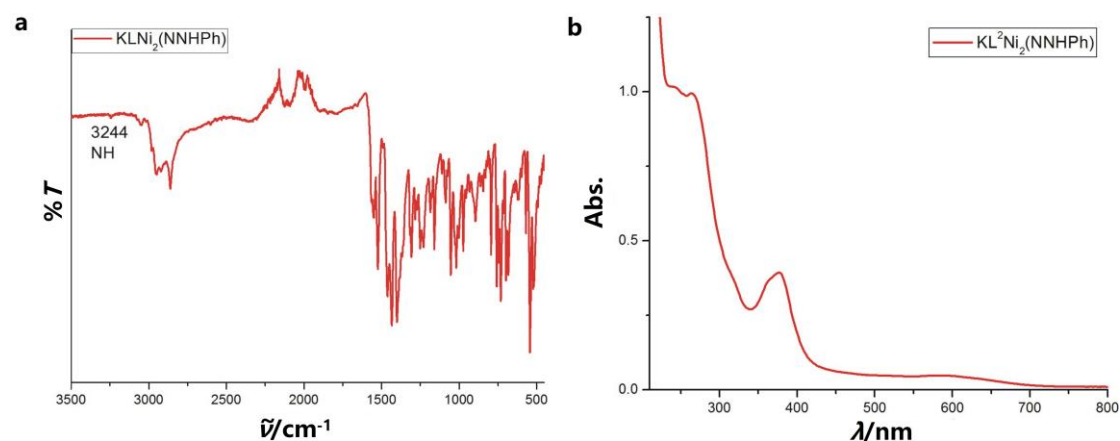


Figure 100: (a) ATR-IR spectrum of **18** in crystalline material. (b) UV-vis spectrum of **18** in THF.

Two separate broad peaks around 9.17 and 10.57 ppm as well as a sharp peak at 9.35 ppm were observed in the ^1H NMR spectrum (**Figure 98**) of **18** at RT. It attributed that the K^+ is dissociation equilibrium in solution at RT (**Scheme 28**).

In order to investigate the different configuration, VT NMR experiments were conducted (**Figure 101**). At higher temperature (above 273K), the two broad peaks disappeared and the sharp peak gains intensity. At temperatures between 273 K and 243 K, the sharp peak vanishes. When decreasing the temperature even more, four broad peaks (two new weak broad peaks) can be observed in the ^1H NMR spectra. It assumed that the K cation and the proton of NH group position influenced the ^1H NMR spectrum with temperatures changing (**Scheme 28**). A new experiment was conducted to prove the hypothesis. It will be discussed in the next section.

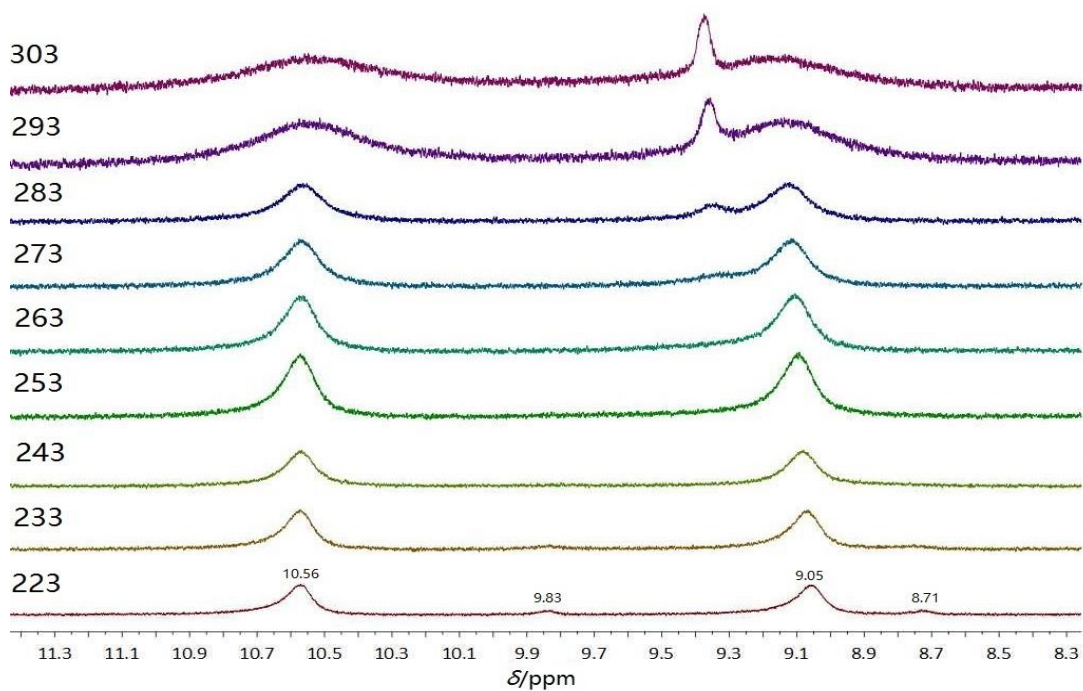
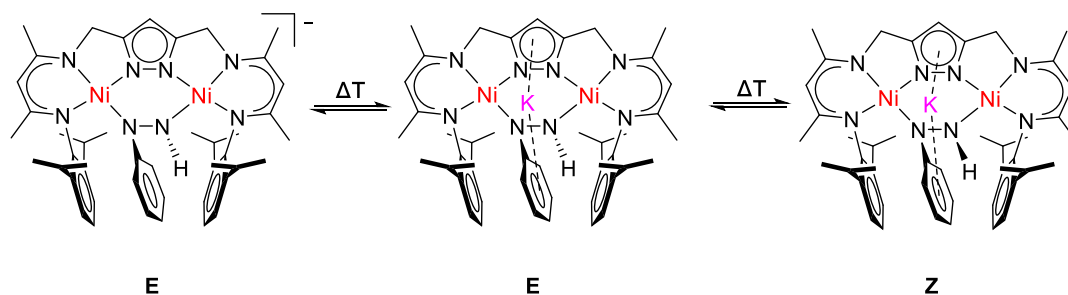
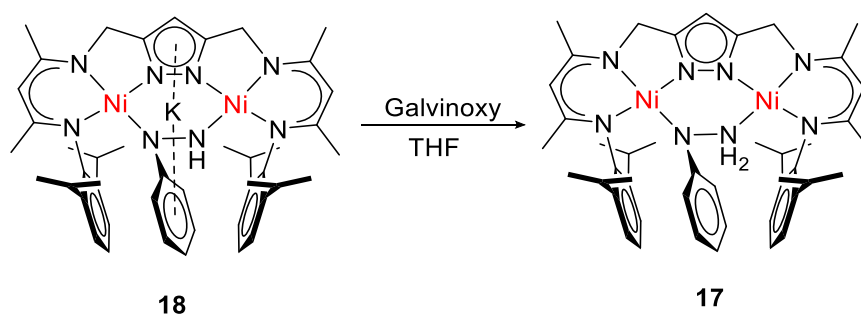


Figure 101: VT ^1H NMR spectrum of **18** in THF-d_8 .



Scheme 28: K^+ dissociation equilibrium and two possible configurations of **18** in solution state.



Scheme 29: Protonated of **18** with galvinoxyl in THF.

Since the bimetallic dinickel phenylhydrazido(2-) complex was synthesized, H-atom-transfer agents were employed to remove the final H atom in **18**. Unfortunately, all attempts to generate the phenylhydrazido radical complex failed. When the galvinoxyl free radical was used (**Scheme 29**), an EPR silent reaction mixture and some purple crystals were obtained in two days. The x-ray structure indicated that the purple compound is a potassium galvinoxyl complex (**Figure 102**).

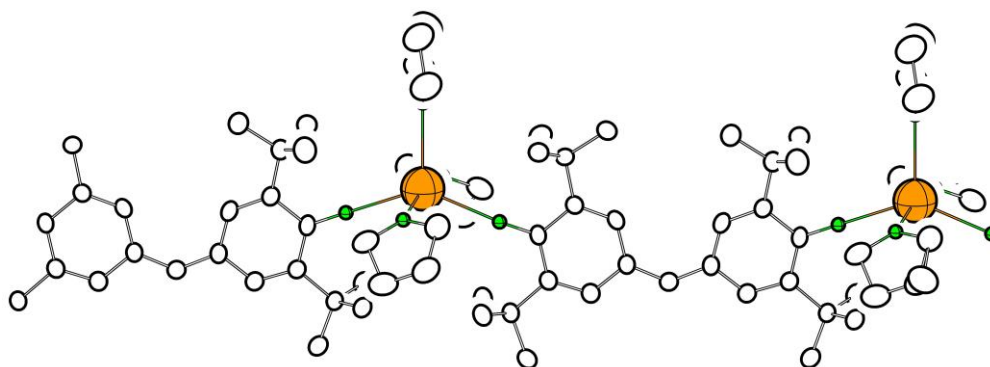
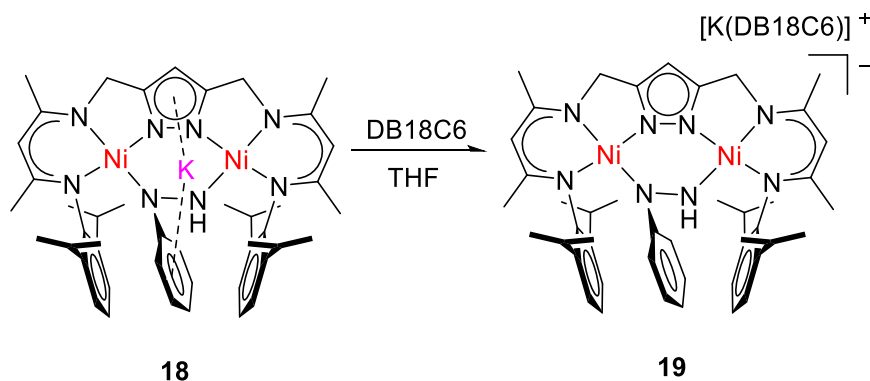


Figure 102: Molecular structure of byproduct using 50% thermal ellipsoids.

6.4 Dissociation the phenylhydrazido-K⁺ interaction in bimetallic nickel(II) complex



Scheme 30: Synthetic route for **19**.

From the ¹H NMR experiments (**Figure 101**) conducted for **18**, it is assumed that the K⁺ cation and the hydrogen atom in the NH group have an influence on the chemical shift of the hydrogen atom of the phenyl group upon the temperature change. To remove this influence and separate the K⁺ cation from the anion, DB18C6 was employed. Treatment of a THF solution of **18** with DB18C6 resulted in a color change from deep green to blackish green in 20 mins (**Scheme 30**). The color change suggested that a new species was generated. The new **19** was completely characterized by x-ray diffraction, 1D and 2D NMR, UV-vis and FT-IR spectroscopy as well as elemental analysis.

Black crystals suitable for x-ray diffraction were obtained by slow diffusion of pentane/Et₂O into a solution of **19** in THF at room temperature. **19** crystallizes in the *Pbca* space group. The molecular structure of **19** is shown in **Figure 103** and selected bond lengths (Å) and angles (°) are listed in **Table 25**.

It became obvious that, similar to the case of the **18**, the product is composed of the ligand–nickel unit, binding a (PhNNH)²⁻ entity. The K⁺ is coordinated to the six oxygen atoms of the crown ether and two Et₂O molecules. The distance of the N–N bond in PhNNH(2⁻) ligand is 1.401 Å, which is same of **18**. The distance

of the two nickel centers of 3.835(7) Å is slightly shorter than in **18** (3.850(7) Å). The dihedral angle between the ligand and the phenylhydrazido(2-) ring of 84.087(14)° is smaller than **18** of 86.478(80)°. Selected metrical parameters of the phenylhydrazido(1-/2-) complexes are listed in **Table 24**.

Table 24: Selected metrical parameters of **17**, **18** and **19**.

Complex	17	18	19
Space group	Triclinic	Triclinic	Orthorhombic
Ni...Ni (Å)	3.943	3.850	3.835
N-N distance (Å)	1.460	1.403	1.400
Ni-NPh	1.911	1.903	1.901
Ni-NH	1.962	1.907	1.898
NH stretching (cm ⁻¹)	3294 3220	3244	3244
N-N-C _(ph) (°)	112.12	113.38	112.24
Ni-N-N-Ni(°)	78.54	73.55	71.90
δ(NH) (ppm)	1.60/2.10	1.35	1.53

To further confirm the identity of the solution state of **19**, an NMR spectroscopic analysis was performed. As expected, the complex was diamagnetic, and the ¹H (**Figure 104**) and ¹³C {¹H} NMR (**Figure A37**) data revealed that the potassium anion is encapsulated by the crown ether in the solution. The difference between the ¹H NMR spectra of **19** and **18** lies in the NH shift, which is at 1.53 ppm and 1.35 ppm, respectively. The position of the NH proton was confirmed by ¹H-¹⁵N HMBC (**Figure 105**). Additionally, the field of NH proton in **19** in ¹H NMR spectrum is similar to the spectrum of **XXVII** (**Figure 90**).^[72]

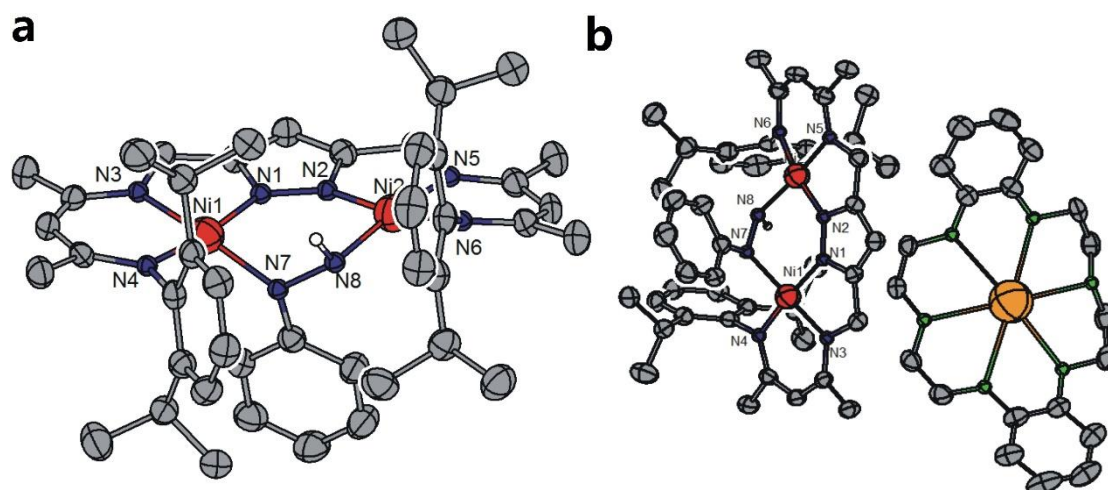


Figure 103: Molecular structure (50% probability thermal ellipsoids) of the anion of **19** (a) and **19** (b). Most hydrogen atoms omitted for clarity, except for N8-H.

Table 25: Selected bond lengths (Å) and angle (°) for **19**.

Atoms	Bond lengths	Atoms	Bond angles
Ni1-N1	1.853(3)	N1-Ni1-N7	87.76(13)
Ni1-N7	1.901(3)	N1-Ni1-N4	171.03(12)
Ni1-N4	1.916(3)	N7-Ni1-N4	95.83(13)
Ni1-N3	1.916(3)	N1-Ni1-N3	82.62(13)
Ni2-N2	1.858(3)	N7-Ni1-N3	162.59(13)
Ni2-N8	1.898(3)	N4-Ni1-N3	95.85(13)
Ni2-N6	1.913(3)	N2-Ni2-N8	94.15(13)
Ni2-N5	1.934(3)	N2-Ni2-N6	170.40(13)
N7-N8	1.401(6)	N8-Ni2-N6	90.89(13)
Ni1...Ni2	3.835(7)	N2-Ni2-N5	82.38(13)
		N8-Ni2-N5	168.80(14)
		N6-Ni2-N5	94.14(13)
		N8-N7-Ni1	121.6(2)
		N7-N8-Ni2	119.0(2)
		Ni1-N7-N8-Ni2	71.90(3)

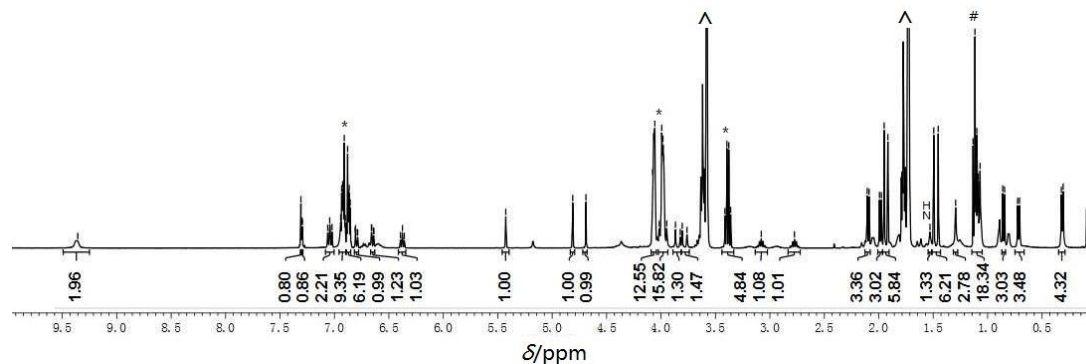


Figure 104: ^1H NMR (400 MHz) spectrum of **19** in THF-d_8 . Residual solvents are marked \wedge . * Dibenzo(18-crown-6); # Pentane.

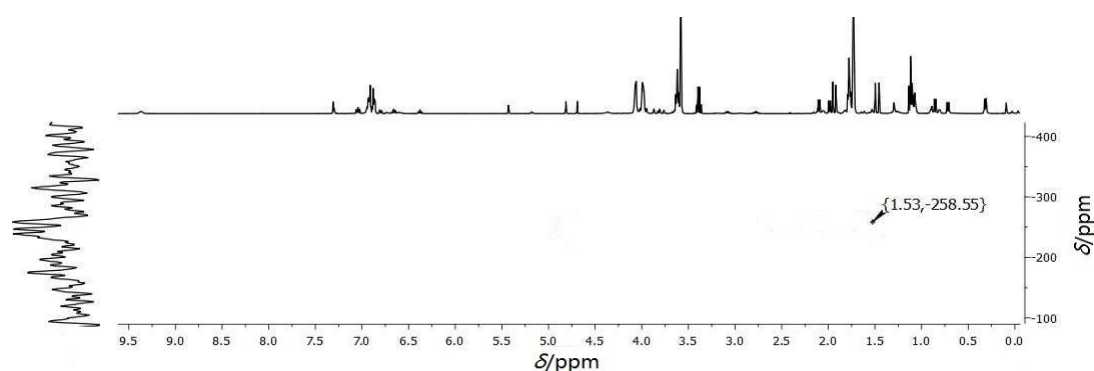


Figure 105: ^1H - ^{15}N HMBC (52 MHz) spectrum of **19** in THF-d_8 .

In the ^1H NMR spectrum of **19** at RT, a peak at 9.35 ppm for *ortho* protons of the phenyl group is observed, which is the same as **17**. With the temperature rising (above 293 K), **19** has same variation tendency for phenyl ring of phenylhydrazido(2-) as **17**. It indicates that the phenyl group of phenylhydrazido(2-) rotation free without K^+ position influence. When decreasing the temperature, the signal of the *ortho* protons of phenyl group in the phenylhydrazido(2-) split gave four doublets with an integration of 1:2:1:2. The four peaks are at 8.64, 8.93, 9.84 and 10.61 ppm in the ^1H NMR spectrum. Taking the ^1H NMR experiments of **17** and **18** into consideration, it is assumed that the two isomers of **19** exist at low temperature in the solution state. The two-possible configurations are shown in **Scheme 31**. The hydrogen atom in the NH group of phenylhydrazido(2-) is on the same/opposite side as the phenyl group of the phenylhydrazido(2-).

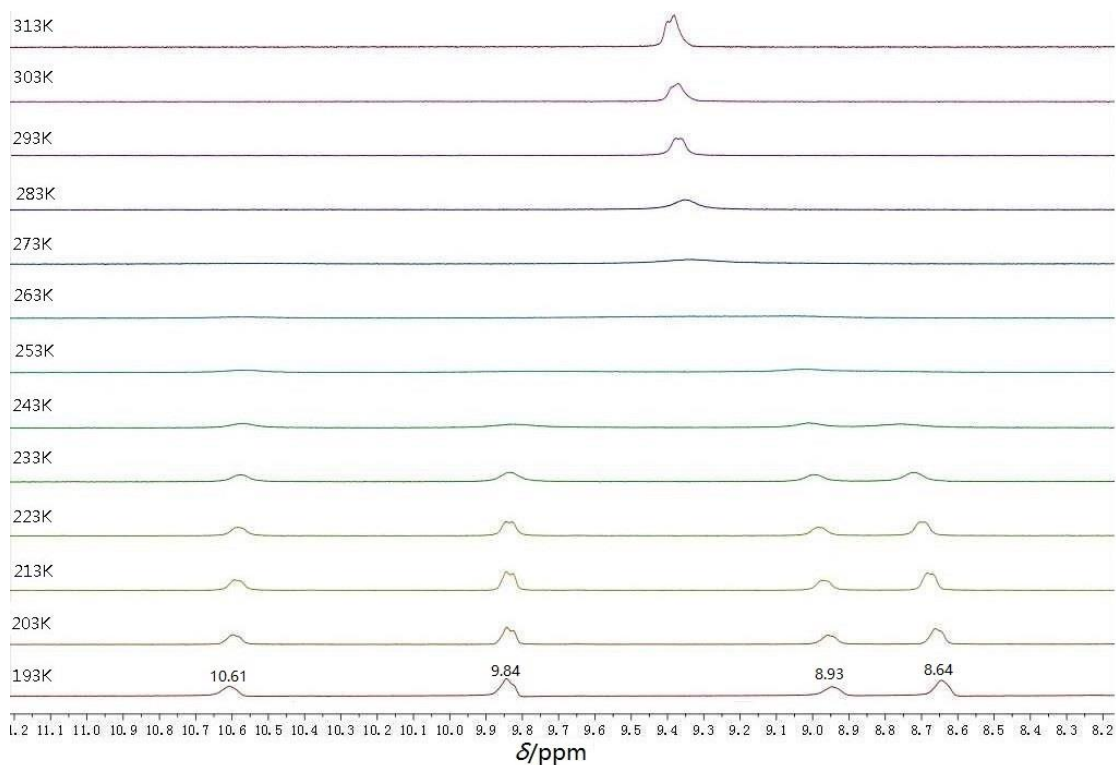
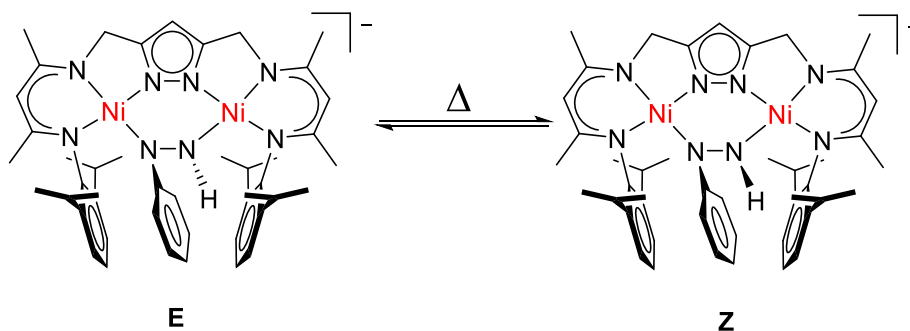


Figure 106: The field of ^1H NMR (400 MHz) spectra in THF-d_8 from 8.4 to 10.0 ppm in VT (193 K–313 K) of **19**.

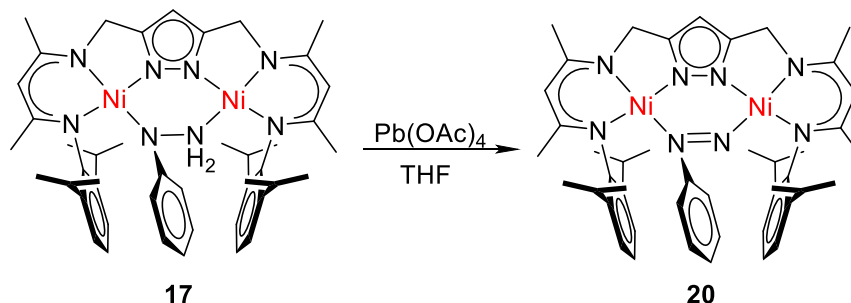


Scheme 31: Two possible configurations of **19** in solution.

The IR spectrum revealed band at 3244 cm^{-1} for the NH stretching vibration.

The band is the same for **18**, and similar to **XXVII** with 3309 cm^{-1} . [72]

6.5 Dehydrogenation and protonation of phenylhydrazine bridge complex



Scheme 32: Synthetic route for **20**.

The redox chemistry of **17** was further exploited since the deprotonation of the phenylhydrazido(1-) was successfully done. DIAD, TEMPO, TBP and galvinoxyl radical were used for the oxidize of phenylhydrazido(1-) ligand, however, the desired result was not achieved. Nevertheless, dehydrogenation of the phenylhydrazido(1-) in **17** was achieved with Pb(OAc)₄ under light exclusion giving **20**

IR spectrum (**Figure 107a**) of **20** shows no NH stretching. Additionally, the positive ion ESI-MS (**Figure 107b**) of **20** shows a major peak at $m/z = 827.6$ consistent with the simulated isotope pattern of $[\mathbf{20}+\text{H}]^+$. Attempt for recrystallized the suitable single crystals for x-ray diffraction could not be obtained yet.

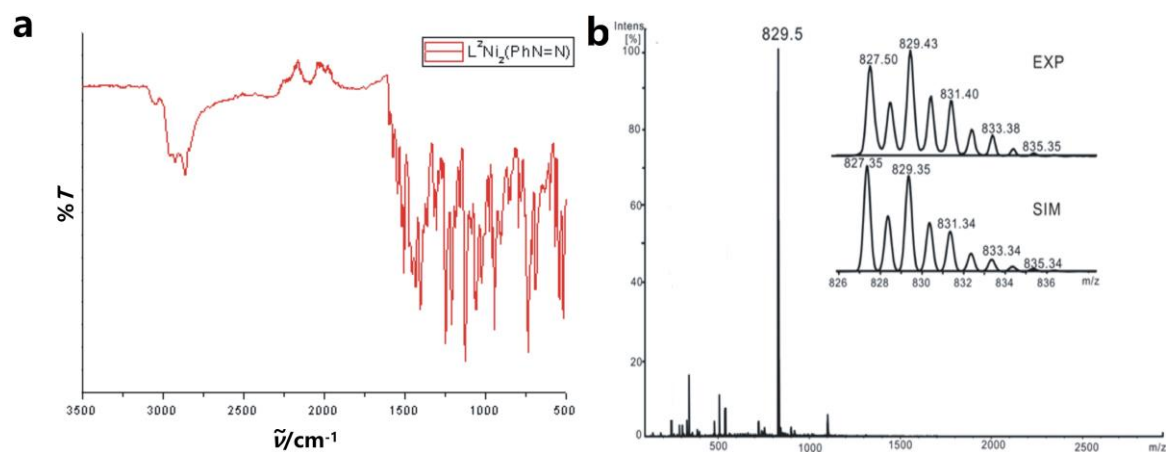
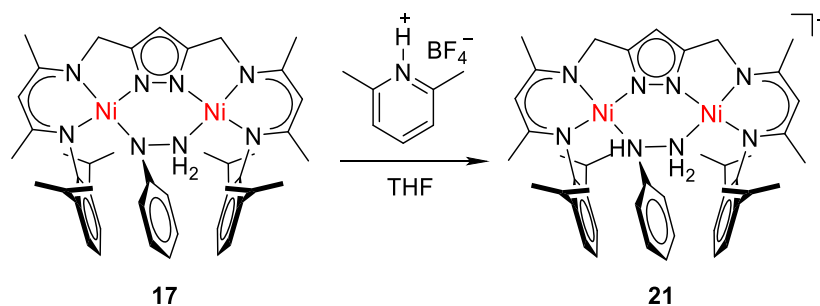


Figure 107: (a) FT-IR spectrum of **20** in crystalline material; (b) ESI-MS of **20** in THF; (Inset) experiment (upper) and simulated (lower) isotope distribution pattern for the peak pattern around $m/z = 827.50$ characteristic for the $[\mathbf{20}+\text{H}]^+$ ion.



Scheme 33: Synthetic route for **21**.

Addition of the proton source $[\text{H-Lut}]\text{X}$ ($\text{X} = \text{CF}_3\text{SO}_3, \text{BF}_4$) into the THF solution of **17** results in an immediate color change from red to green. A green precipitate is formed within 10 mins with CF_3SO_3 as the counter ion. When changing the counter ion from CF_3SO_3^- to BF_4^- , green precipitate was formed at -30°C in two hours. This newly precipitated species exhibit bad solubility in THF, toluene, pentane and hexane, among others.

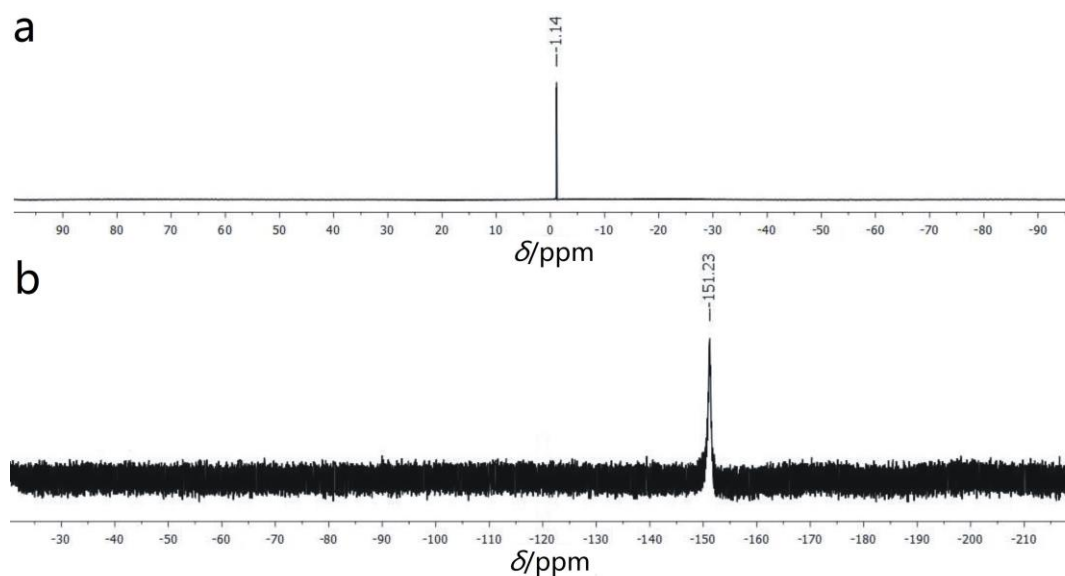
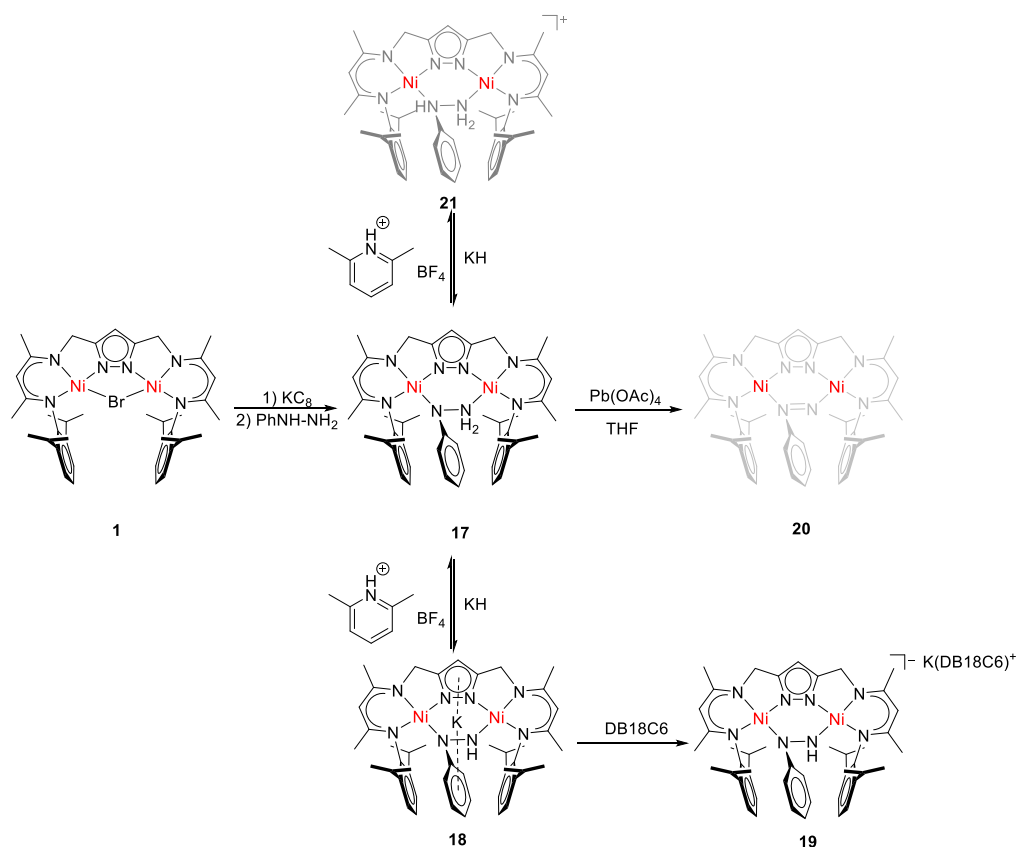


Figure 108: ^{11}B NMR and ^{19}F NMR spectrum of **21** in CD_3CN .

^{11}B and ^{19}F NMR spectra of the green crude precipitate revealed one signal at -1.14 and -151.23 ppm, respectively, which clearly showed the BF_4^- counter ion in **21** (Figure 108). In comparison to the IR spectrum of **17**, **21** shows three additional bands at 3354 , 3307 and 3285 cm^{-1} , which are assigned to the (NHNH_2Ph) bridge band vibrations. These vibrations for the N-H stretch are very similar to the mononuclear iron complex with a “side on” bound phenylhydrazine complex at 3346 , 3271 and 3230 cm^{-1} [76]. A new band at 1023 cm^{-1} indicated the BF_4 counter ion in the new complex. Additionally, the positive ion ESI-MS spectrum of **21** shows a major peak at $m/z = 829.6$ consistent with the simulated isotope pattern of $[\text{M}-\text{BF}_4]^+$. Until now, no suitable crystals for x-ray diffraction were obtained.

6.6 Summary



Scheme 34: General transformation between the **17**, **18**, **19**, **20** and **21**.

In summary, we present the oxidized, protonated and deprotonated phenylhydrazine species in this chapter. The nickel bromide precursor (**1**) reacts with phenylhydrazine in the presence of KC_8 yield a new phenylhydrazido(1⁻) bridge **17** by H_2 evolution. Deprotonation of **17** with KH at RT led to H_2 formation, and a new phenylhydrazido(2⁻) complex **18** is produced. In the phenylhydrazido(2⁻) complex **18**, the potassium cation is fixed by the pyrazolate and phenylhydrazido(2⁻) ligand system. When potassium chelating reagent DB18C6 used, the potassium can be removed away of the pyrazolate ligand system. On the other hand, the phenylhydrazido(1⁻) can be dehydrogenated by means of Pb(OAc)_4 , which result in a new μ -1,2-diazendo moiety.

Chapter 7 Azobenzene Activation

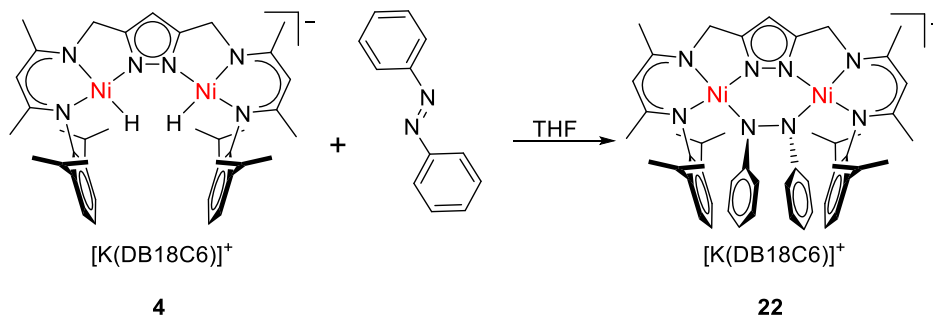
Abstract: In this work, we explore the N=N bond reduction reaction using the $[L^1Ni_2(H_2)]^-$ species with or without K^+ cation. Specifically, this “naked” dinuclear nickel(II) dihydride complex (**4**) reacts with azobenzene (PhN=NPh) to perform a two-electrons reduction, where two electrons come from H_2 reductive elimination and the N-N single bond formed. Whereas the alkali metal ions (K^+) significantly stabilized the dihydride complex against H_2 release, the azobenzene (PhN=NPh) demonstrate one-electron reduction from the dinuclear nickel(II) dihydride (**2**).

7.1 Introduction

Azobenzene, as the simplest example of an aryl azo compound, is linked by an N=N double bond, which is investigated cleavage by transition and f-block metal complexes in the last three decades. [77] The product from reduction of RN=NR is typically an imido complex with a coordinated NR group. Some synthetic 2Fe-2S clusters cleave azobenzene to form bridging imido groups in cubane-type products were reported also. [78] In past years, many early transition-metal, [79] lanthanide, [80] and main-group metal complexes [81] bearing reduced azobenzene ligands have been synthesized. However, the research efforts have been mainly focused on the N–N bond activation of azobenzene. Mechanistic studies on the reaction of a β -diketiminato subunits bridged Fe(μ -H)Fe complex with azobenzene, which leads to N=N bond cleavage, indicated that substrate binding triggers reductive H₂ release. [82, 83].

Treating [L^INi^{II}₂(H)₂][−] (**2**[−]) with phenylacetylene leads to H₂ formation and twofold reduction of the substrate, giving a product complex with unusual styrene-1,2-diyl bridging unit in the bimetallic pocket. [11] Alkali metal ions Na⁺ and K⁺ were found to be closely associated with the dinickel dihydride core in **2**[−] and also with the olefinic C=C bond in the case of acetylene. [11] In this mechanism, dihydride reductively eliminate H₂ to generate a coordinately unsaturated species in which the Ni^{II} have been reduced to Ni^I by a total of two electrons, and the resulting reduced species can thus be generated without any strong reducing agents. In this chapter, we focus on the one or two electron reduction of the N–N double bond and the cleavage of the N–N double bond of azobenzene.

7.2 Two electron reduction the azobenzene



Scheme 35: Synthetic routes for **22**.

Treatment of a THF solution of **4** with azobenzene results in an immediate the color change from orange to black (**Scheme 35**). No intensity gas was observed during the reaction. Beside this way, anther pathways were found for synthesizing of **22**. The procedures were described in the experimental section.

Crystals suitable for x-ray diffraction were obtained by layering a hexane/Et₂O mixture on a solution of **22** in THF at -30°C. **22** crystallized in the monoclinic space group *P*-1, and molecular structure was shown in **Figure 109**. To our the best knowledge, **22** is the first dinuclear nickel complex binding an azobenzene(2-) ligand in a μ -1,2 geometry. Taking the structure of **22** consideration, I presumed the two hydride ligands reductively eliminated H₂ to generate a coordinating unsaturated species [L¹Ni₂]⁻ in which the metals have been reduced by a total of two electrons and the resulting reduced the azobenzene substrate even though no gas was observed. The distance of N-N bond of 1.401 Å is longer than the N=N bond of free azobenzene with 1.25 Å, and is closer to the N-N bond of free hydrazine (1.45 Å).^[84] Surprisingly, the related **22** is not characterized by longer N-N bonds, but rather the N-C(Ph) bond diminishes to 1.408 Å (*cf.* 1.443 Å in *trans* azobenzene)^[79b]. The N-N-Ph bond angle (109.145° and 109.78°) is also changed on reduction; it is unlike that in the parent azobenzene (120°) but is remarkably close to the values expected for a tetrahedral atom.

The azobenzene molecule is no longer coplanar; the plane of the arene ring is twisted by 64.977° from the C-N-N plane. [85]

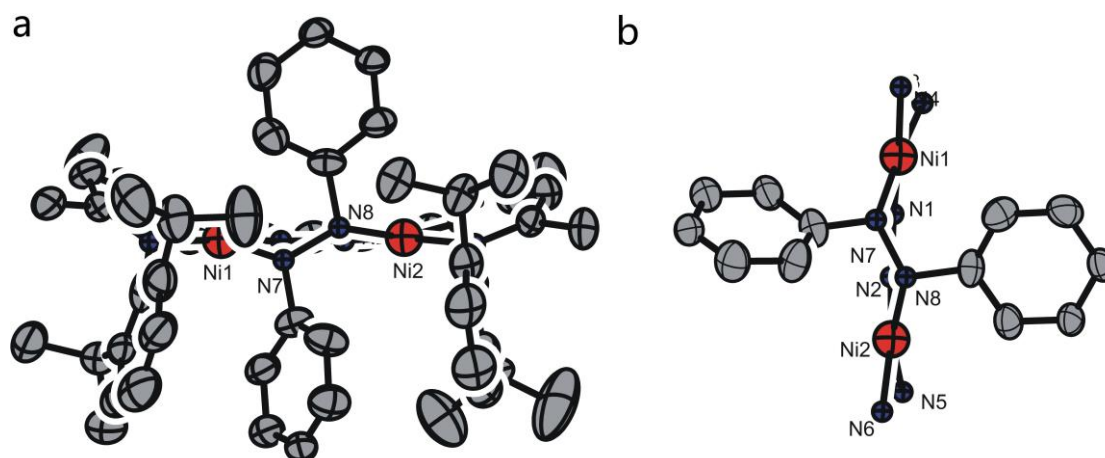


Figure 109: Molecular structure (50% probability thermal ellipsoids) of the anion of **22** (a) and **22** (b). All hydrogen atoms omitted for clarity.

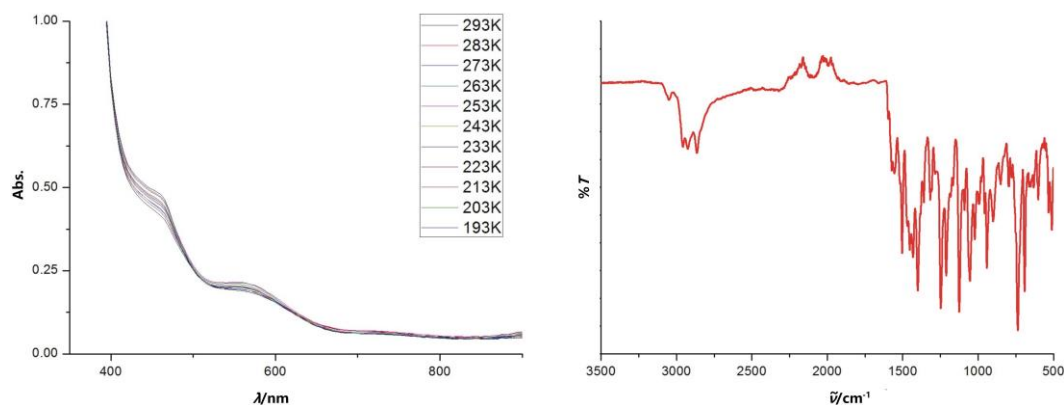


Figure 110: (a) VT UV-vis spectrum of **22** in THF from 400 nm to 900 nm. (b) FT-IR spectrum of **22** in crystalline material.

The UV-vis spectrum (**Figure 110a**) has a distinct absorption at 473 nm ($\epsilon = 470 \text{ M}^{-1}\cdot\text{cm}^{-1}$) and a small broad band at 585 nm ($\epsilon = 220 \text{ M}^{-1}\cdot\text{cm}^{-1}$) in THF solution. No N-N vibration can be distinguished from IR spectroscopy (**Figure 110b**). The ESI-MS(+) of THF/ CH_3CN (**Figure A41**) mixture solutions of **22** shows a dominate peak characteristic of the $[\text{K}(\text{DB18C6})]^+$, and a small peak at $m/z = 665.46$ is characteristic for the $[\text{L}^1\text{Ni}+2\text{H}]^+$.

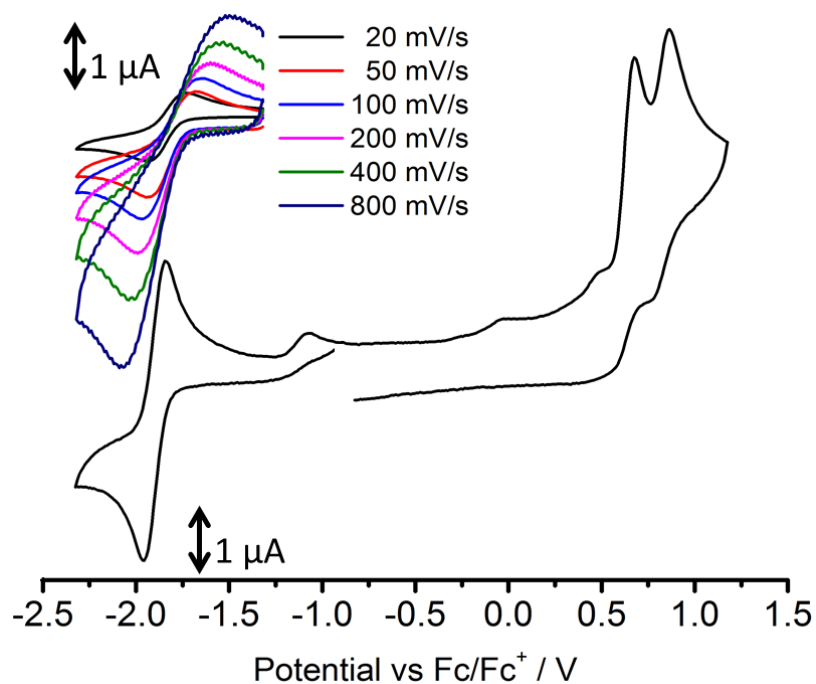
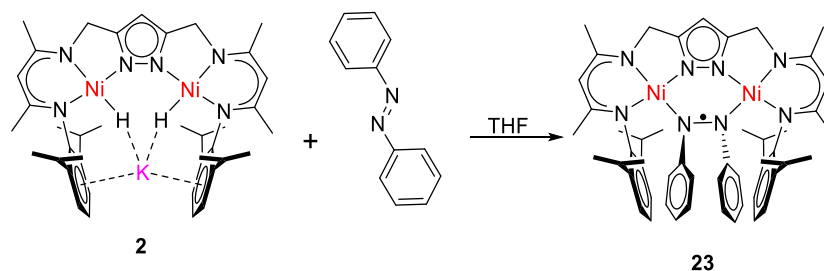


Figure 111: Cyclic voltammogram curves of **22** in THF/0.1 M NBu₄PF₆ as an electrolyte at scan rates 100, 500 and 1000 mV/s vs Fc/Fc⁺ in the -2.5–1.5 V potential range.

The cyclic voltammogram of **22** in THF at room temperature exhibits a reversible redox wave of 100 Mv/s⁻¹ at $E_{1/2} = -1.91$ V (vs Fc/Fc⁺) (**Figure 111**), as well as two irreversible oxidation at higher potential. It indicates that the azobenzene(2-) may be oxidized by one electron to the azobenzene radical complex.

7.2 One electron reduction of azobenzene

**Scheme 36:** Synthetic routes for **23**.

Without the alkali metal (K^+) interaction of the dihydride complex, the azobenzene was reduced by two electrons to an azobenzene(2^-) species. Related the previously work in chapter 3, the alkali metal ions (K^+) significantly is stabilized the dihydride complex against H_2 release. Keep this in mind, treatment of complex **2** with azobenzene in THF solution results in an immediate a color change from red to black. Suitable crystals for x-ray diffraction were obtained from hexane layer into THF at -30°C in two days with 10% yield (The yield increased to 70% when employing a new method that is discussed in experimental section). Surprisingly, **23** exhibits a monoanionic azobenzene(1^-) radical bridge compound. The N–N distance in azobenzene(1^-) of 1.353 (4) Å is in between that of the N=N double bond in azobenzene (1.25 Å) and the sp^3 - sp^3 N–N single bond typical of hydrazine (1.45 Å), ^[84a] thus showing that the azobenzene is reduced. **23** crystallizes in the triclinic space group $P-1$, and the molecular structures in ORTEP are shown in **Figure 112** and selected bond lengths (Å) and angles ($^\circ$) are listed in **Table 26**. To the best of our knowledge, this is the first nickel complex with a bridging azobenzene radical.

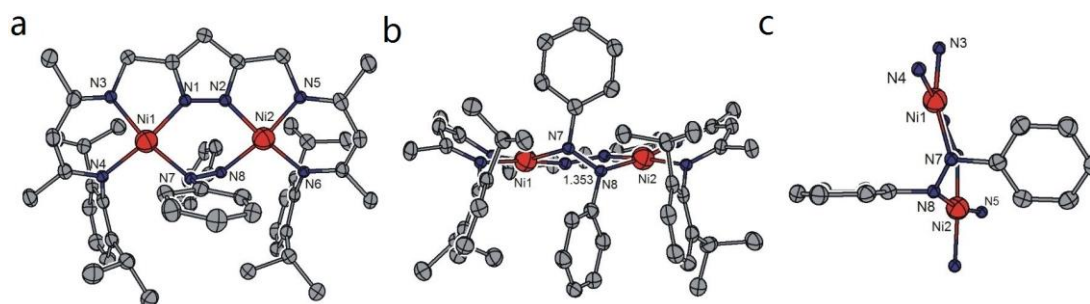
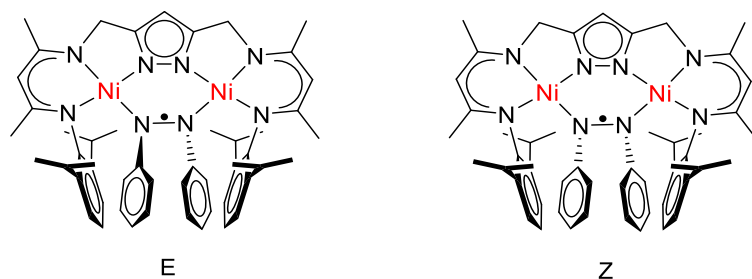


Figure 112: Molecular structure (50% probability thermal ellipsoids) of **23**. All hydrogen atoms omitted for clarity. (a) top view; (b) side view; (c) azobenzene ligand, N atoms from pyrazolate ligand and nickel central.

Table 26: Selected bond lengths (Å) and angles (°) for **23**.

Atoms	Bond lengths	Atoms	Bond angles
Ni1-N1	1.892(2)	N1-Ni1-N3	82.27(10)
Ni1-N3	1.899(2)	N1-Ni1-N4	171.37(10)
Ni1-N4	1.934(2)	N3-Ni1-N4	91.21(10)
Ni1-N7	1.959(2)	N1-Ni1-N7	86.47(10)
Ni2-N2	1.868(2)	N3-Ni1-N7	159.31(11)
Ni2-N5	1.889(2)	N4-Ni1-N7	101.41(10)
Ni2-N6	1.920(2)	N2-Ni2-N5	82.77(10)
Ni2-N8	1.921(2)	N2-Ni2-N6	173.42(10)
N7-N8	1.353(4)	N5-Ni2-N6	93.45(10)
Ni1-Ni2	3.993(7)	N2-Ni2-N8	86.04(10)
		N5-Ni2-N8	168.13(10)
		N6-Ni2-N8	98.05(10)
		N8-N7-Ni1	117.81(18)
		N7-N8-Ni2	120.51(19)
		Ni1-N7-N8-Ni2	121.10(19)
		C40-N7-Ni1	111.05(18)
		C46-N8-Ni2	121.10(19)
		C40-N7-N8-C46	163.62(25)



Scheme 37: Two possible conformations of the azobenzene radical.

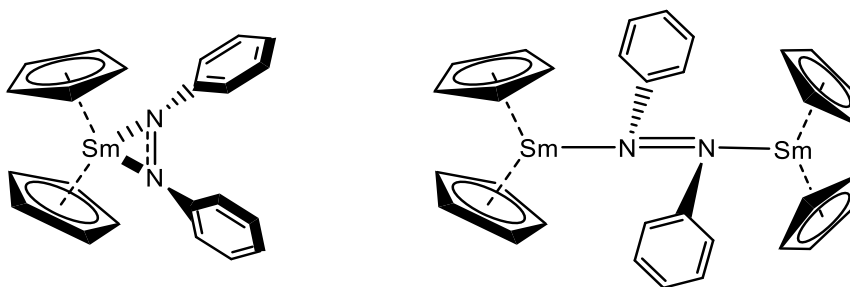


Figure 113: Selected examples of binding modes of azobenzene motifs. ^[80a, e]

As shown in **Scheme 37**, the azobenzene radical adopts an E-conformation, the two phenyl rings are located in on the opposite sides of the ligand. A similar conformation was reported with the Sm metal. ^[80a] However, here the azobenzene was not reduced by the metal but coordinated with a N=N double bond in the original state with the azobenzene (**Figure 113**) ^[80a]. The Ph–N=N–Ph dihedral angle of **23** is 66.123°, which is larger than that found in the azobenzene radical complexes. ^[80a] The torsion angle of C_(Ph)–N=N–C_(Ph) is 163.62°. A similar value of azobenzene radical was observed in the known complexes (C₅Me₅)₂Sm(PhNNPh)(THF) (1.32 and 1.39 Å), ^[80a]

[η^5 -2,5-(Me₃C)₂-3,4-Me₂C₄P]₂Tm(PhNNPh) (1.35 Å), ^[80e]

[η^5 -2,5-(Me₃Si)₂-3,4-Me₂C₄P]₂Sm(PhNNPh) (1.35 Å), ^[80e]

[(*i*-Pr₃Si)₂N]₂Sm(PhNNPh) (1.357 Å), ^[80i] and (nacnac)Mg(PhNNPh) (1.35 Å) ^[81f]

in which the azobenzene ligands are unambiguously described as radical mono anion. Each nickel center hosts in the two {N₃}-tridentate binding sites and ligated by an extra nitrogen atom from azobenzene ligand. Ni1 adopts a twisted tetracoordinated geometry with a sum angle of 361.37°. Additionally, the dis-

tance between the two nickel and the torsion angle of Ni-N-N-Ni is 3.993(7) Å and 86.91°, respectively.

The UV-Vis spectrum (**Figure 114**) of **23** has an obvious absorption at 465 nm ($\epsilon = 600 \text{ M}^{-1} \text{ cm}^{-1}$) and two broad feature at 579 ($\epsilon = 625 \text{ M}^{-1} \text{ cm}^{-1}$) and 731 ($\epsilon = 586 \text{ M}^{-1} \text{ cm}^{-1}$) nm in THF, which can be ascribed to the presence of the electron in the lowest antibonding orbital. [86] Similarly, the azobenzene radical compounds (nacnac)Mg(PhNNPh) [81f] and Na(PhNNPh) [86] have bands at 404, 628 nm and 433, 628 nm, respectively.

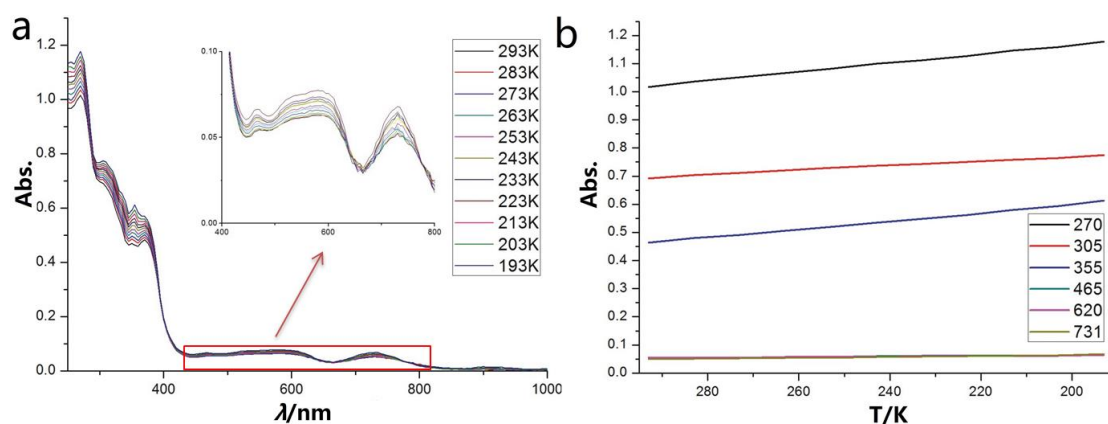


Figure 114: (a) VT UV-vis spectrum of **23** in THF from 293 K to 193 K. (b) plots of the absorption band at different temperatures.

The x-band EPR spectrum of **23** in THF at room temperature, shows a narrow and almost isotropic spectrum with $g_1 = g_2 = g_3 = 2.043$ (Gaussian line shapes) with no discernable hyperfine interactions to the central metal ion or the nitrogen atoms (**Figure 115a**). Thus, shape and position of the signal support **23** to be a typical organic radical, with the allocation of the unpaired electron in **23** on the azobenzene-bridged ligand. Whereas the Mg-nacnac compounds with an azobenzene radical, the unpaired electron located on the two nitrogen nuclei ($I = 1$). The ^{14}N coupling constant is $\sim 7.6 \text{ G}$. [81f]

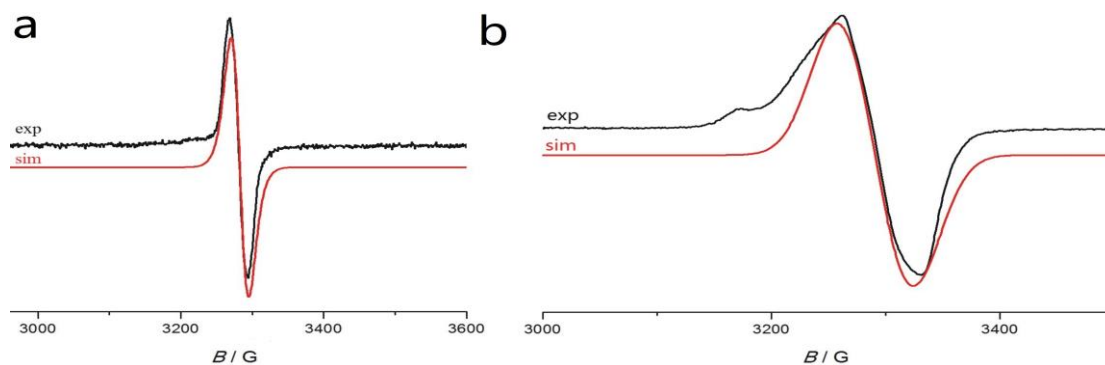


Figure 115: Experiment and simulated at room temperature EPR spectra of **23** in THF. (a) 298 K; (b) 153K.

23 can also be generated by a one reduction involving the monoanionic $[\text{N}_2]^-$ nickel complex **24** (chapter 8.2), which is generated and isolated by the reaction of **2** with N_2 in the presence of external $[\text{H}]^+$. Freshly generated **24** mixing with 1 equivalent azobenzene in THF, gave a color change from brown to black. The UV-Vis changes correspond with those seen for the azobenzene radical complex obtained from **1a** with azobenzene. Isolation of the solid product and redissolution into THF also gives the same EPR spectrum.

The electronic nature of **23** is suggested by its geometric structure (**Figure 116**). The energy-minimized DFT calculated structure of **23** is in good agreement with that obtained by x-ray diffraction. The unpaired electron is located on the azobenzene ligand with around 65%. The distance of dinitrogen atoms of the azobenzene ligand and the two nickel centers of 1.340 Å and 3.979 Å from DFT calculation are slightly shorter than the experimental data of 1.353 Å and 3.993 Å (**Table 27**). The calculated IR spectrum shows the dinitrogen stretch at 1234 cm^{-1} for the ^{14}N -azobenzanyl bridging ligand (**Table 28**).

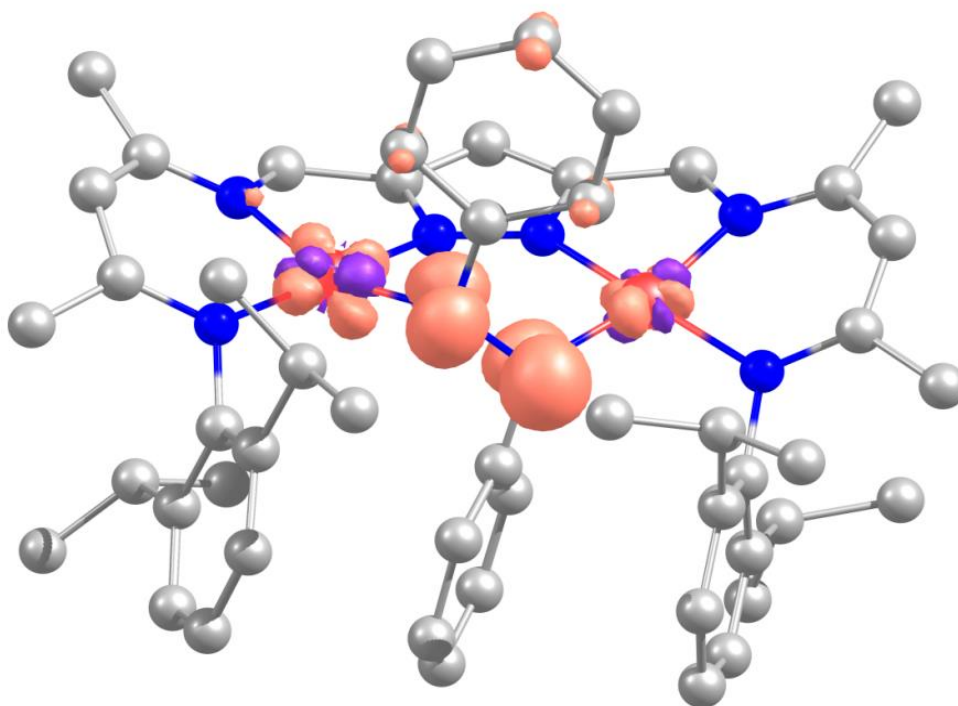


Figure 116: Spin density plot of **23**. Mulliken Spin Population: Ni1 = 0.094794, Ni2 = 0.05976, N9 = 0.249510, N10 = 0.372491.

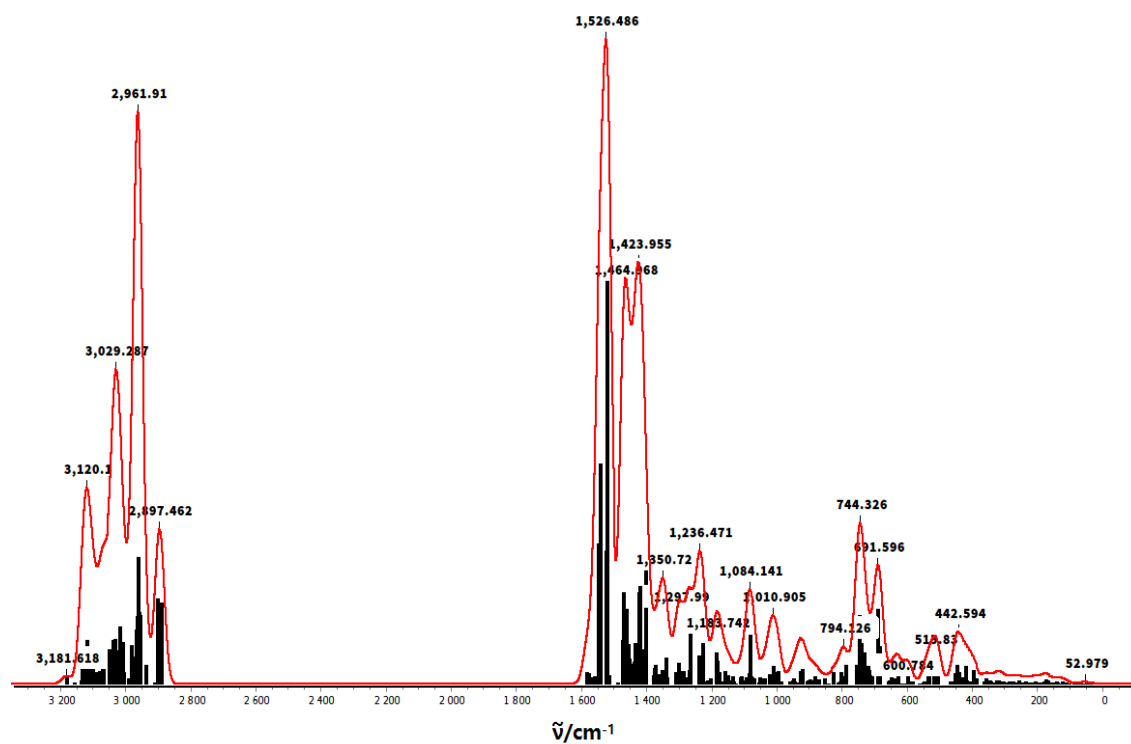


Figure 117: Calculated IR spectrum of **23**.

Table 27: Selected distances (\AA) and angles ($^\circ$) for **23**.

	$d(\text{N-N})/\text{\AA}$	$d(\text{Ni}\cdots\text{Ni})/\text{\AA}$	$\Phi(\text{Ni-N-N-Ni})/^\circ$
Exp	1.353	3.993	86.9
DFT	1.340	3.979	89.2

Table 28: $\nu(\text{N}\cdots\text{N})$ (IR) for **23**.

	$\nu(^{14}\text{N}-^{14}\text{N})/\text{cm}^{-1}$	$\nu(^{15}\text{N}-^{15}\text{N})/\text{cm}^{-1}$	$\Delta\nu/\text{cm}^{-1}$
Exp	-	-	-
DFT	1234	1215	21

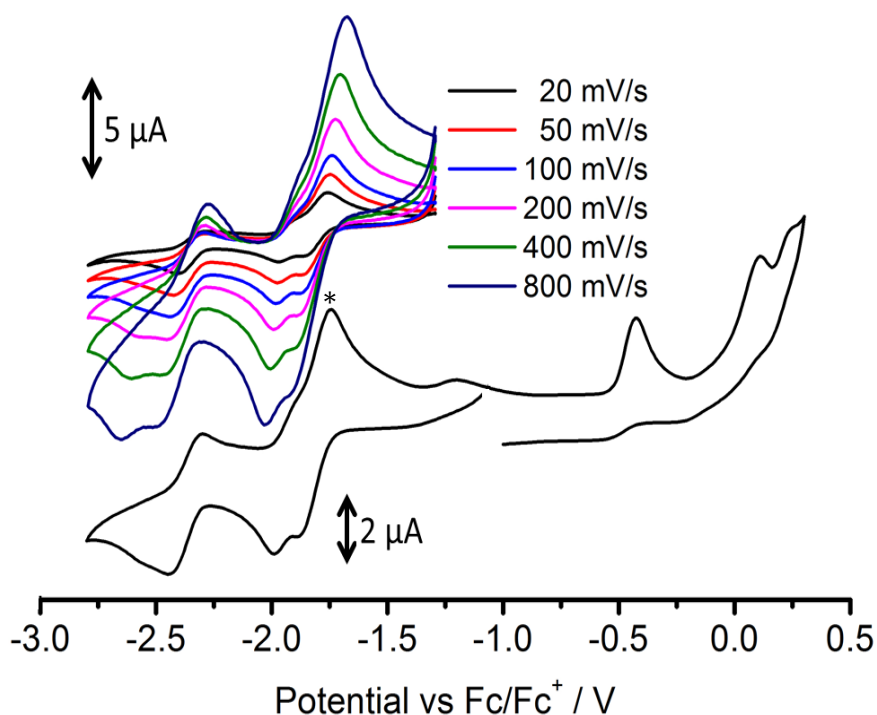
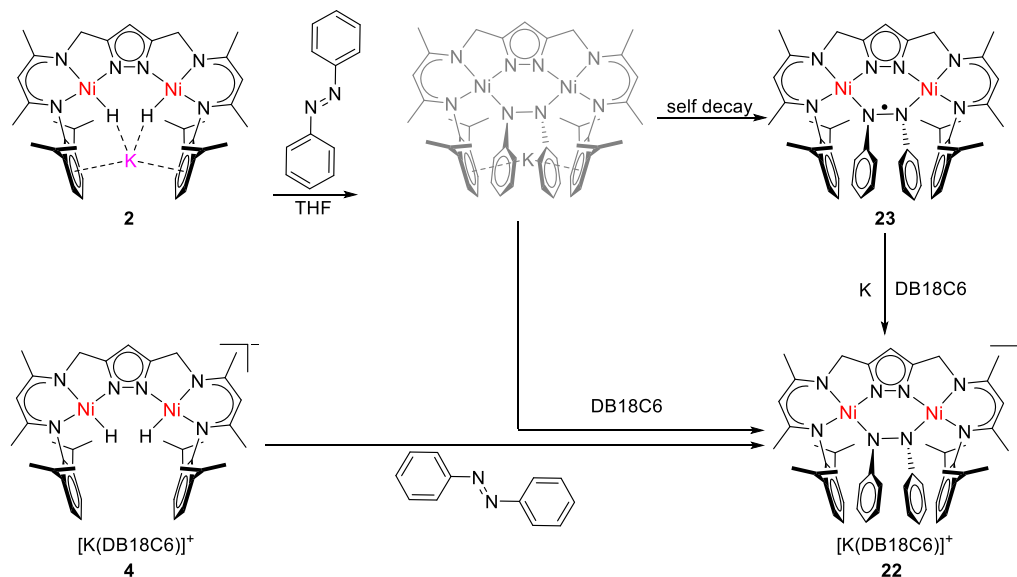


Figure 118: Cyclic voltammogram curves of **23** in THF/0.1 M NBu₄PF₆ as an electrolyte at scan rates 100, 500 and 1000 mV/s vs Fc/Fc⁺ in the -3.0–0.5 V potential range. Impurity is marked (*).

The cyclic voltammogram of **23** in THF at room temperature exhibits a quasi-reversible redox wave of 100 Mv/s⁻¹ at $E_{1/2} = -1.91$ V (vs Fc/Fc⁺) (**Figure 118**). It indicates that the azobenzene(1-) may be reduced by one electron to the azobenzene(2-) complex. Reaction of **23** with elemental potassium results in a rapid color change from purple to brown in the presence of DB18C6 at room temperature. The final product **22** was identified by ¹H NMR spectrum after the work-up.

7.4 Summary



Scheme 38: Activation of azobenzene and reduce the azobenzene monoanionic radical.

In summary, the two different $[L^1Ni_2]^-$ and $[L^1Ni_2(H_2)]^-$ cores (with or without K^+ cation stabilized) can be viewed as two different species for azobenzene activation. In case of the $[L^1Ni_2]^-$ core, the azobenzene has two electrons reduction and a N-N single bond formation. Whereas in the $[L^1Ni_2(H_2)]^-$ core, the azobenzene substance is only reduced once to generate a new azobenzene(1-) monoanionic radical complex. Meanwhile, the new azobenzene monoanionic radical is allowed reduced by elemental potassium. This paradigm may be useful for understanding the role of the K^+ cation in the dinickel dihydride system (**Scheme 38**). Ongoing works are focusing on cleaving the N-N double bond and protonating the N-N single bond.

Chapter 8 N₂ to NH₃ Conversion in the dinuclear nickel(II) cofactor

Abstract: Treatment of **2** with N₂ in the presence of stoichiometric H⁺ allowed isolation of [N₂]⁻ mono-radical bimetallic dinickel(II) complex and it was characterized by x-ray diffraction first time. The anionic [N₂]⁻ species can be functionalized by a hydrogen atom transfer to generate the N₂H⁻ bridging complex. Then the [N₂H]⁻ as an intermediate for the reduction of N₂ to NH₃ when supplied with reduction agent KH at room temperature. In addition, nitrogenous intermediates, including hydrazine (N₂H₄), Hydrazido (N₂H₃⁻ or N₂H₂²⁻) were isolated and characterized by x-ray diffraction, and interconversion has successfully done by chemical reagent.

8.1 Introduction

The conversion of dinitrogen to more valuable compounds is a challenge that has confirmed by chemists for over a century. In nature, the dinitrogen is reduced by nitrogenase enzymes, which contain large metalloproteins and promote a sequence of proton-coupled electron-transfer reactions to accomplish the reduction. ^[87] Industrially, the Haber-Bosch ammonia synthesis hydrogenates N₂ at high temperature (> 400°C) and high pressure (> 200 atm) over an iron-based catalyst surface. ^[88] The energy issues inspiring the transition metal complexes with N₂ as one of the ligands have allowed chemists to conduct fundamental studies into dinitrogen reduction.

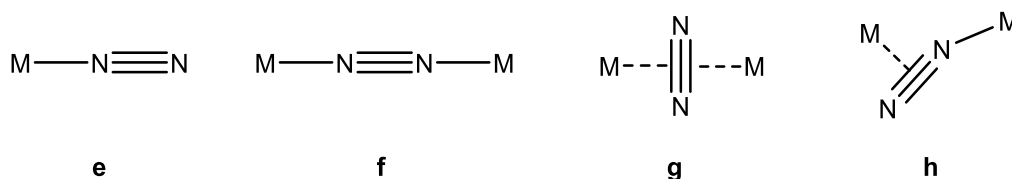


Figure 119: Most common binding motifs with dinitrogen complexes.

It is now well known that N₂ can coordinate to almost all transition metal, and a range of different binding modes have been observed (**Figure 119**). ^[89] When dinitrogen acting as a ligand, the commonly observed oxidation states are 0, 2⁻ and 4⁻, and a few examples for complexes with 3⁻ radical anion. ^[90] Until now, the mono anionic 1⁻ oxidation state of N₂ was only detected in the MO (M = Mg, Ca) surfaces at low temperatures. ^[91]

Though the transition metals with dinitrogen compound is well known. Surprisingly, over the past decades, only few isolable Ni(N₂) compounds were reported in literature. ^[18, 92] And Ni complexes are generally considered to bind N₂ without substantial bond weakening, ^[89] and previous efforts toward N₂ splitting in Ni metal were unsuccessful.

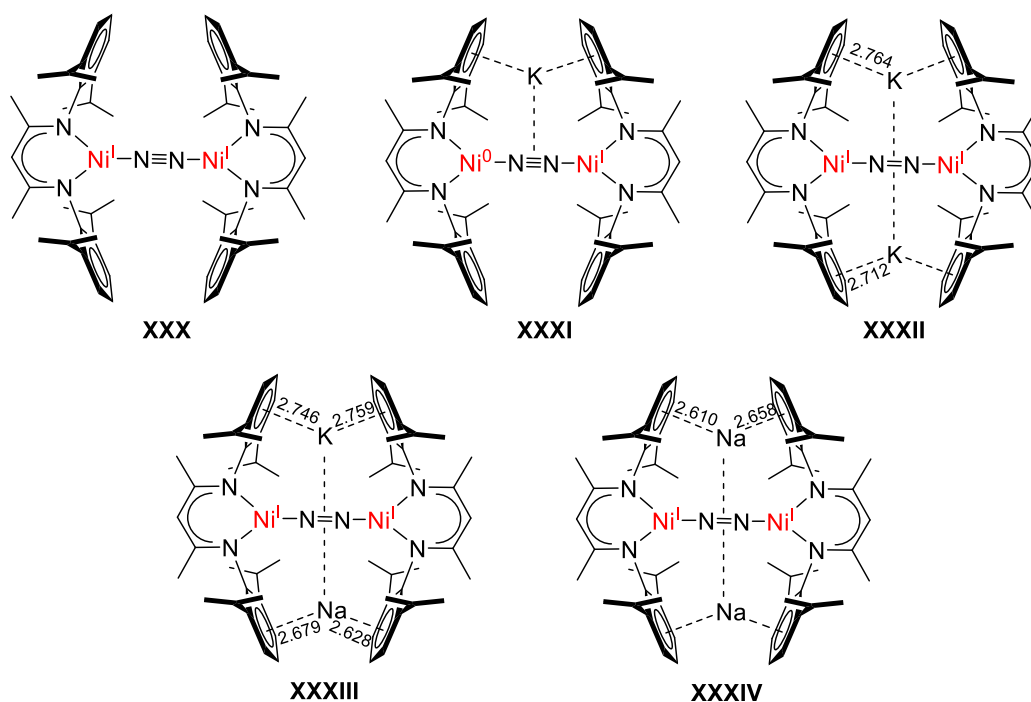
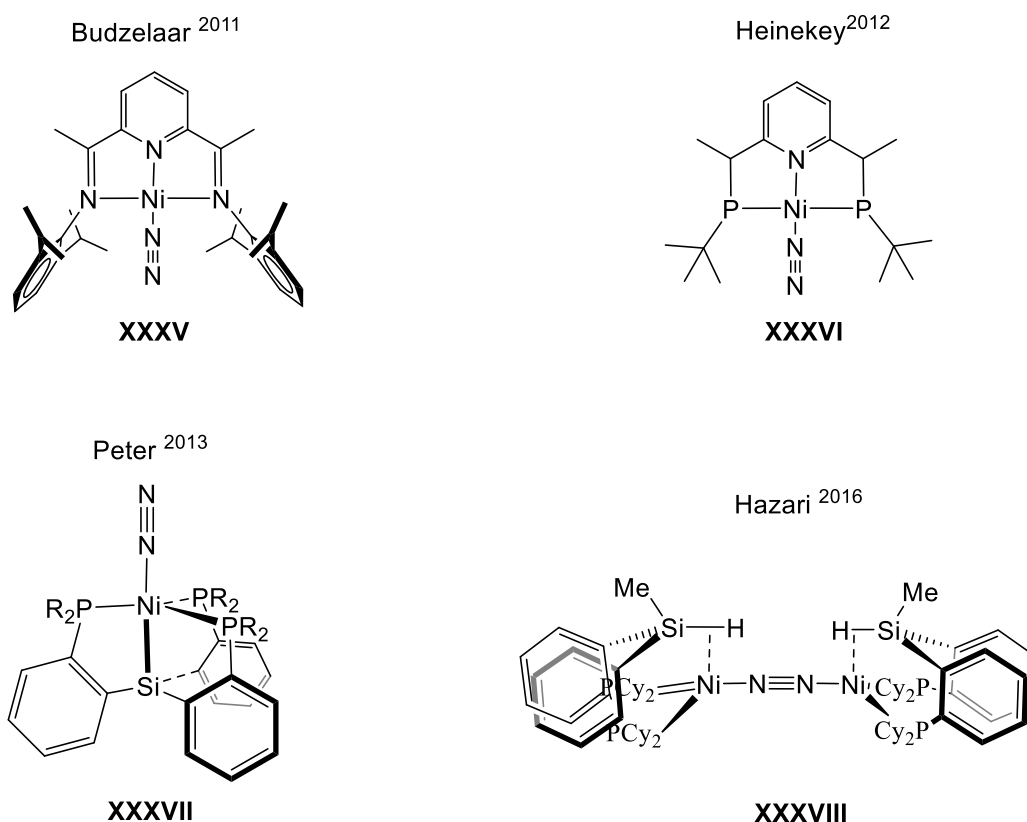


Figure 120: Dinitrogen compounds with nickel in the β -diketiminato ligand. [92b,c]

The impressive dinitrogen nickel complexes work from *Limberg et al.*, [92b,c] they are able to isolate a neutral complex and odd or evenly charged reduction products stemming from a precursor material (**Figure 120, XXX-XXXIV**). The remarkable example for **XXXI** from the series of the nickel dinitrogen complexes is an analogous regarding the linearity of the MN_2M bridge. However, a typical spectrum for **XXXI** was observed from EPR measurement, and without any $^{14}N_2$ coupling. It is attributed to the electron couples very strongly antiferromagnetically to one of the original unpaired Ni^I electrons, and the question arises as to whether it has been added to a d orbital ($\rightarrow Ni^0$) or to an N-based orbital. On the other hand, the stretching frequencies for the N-N bond in these compounds (**XXX-XXXIV**) decrease while the bond distance of dinitrogen enlarges. (**Table 29**). [92b,93] Some other $Ni-N_2$ adducts were reported since the remarkable nickel dinitrogen by *Limberg* and co-workers, but no any weakly activation were happened for these nickel dinitrogen compounds. Some “side-on” and “end-on” $Ni-N_2$ examples were shown in **Figure 121**. [92e-i]

Table 29: Reported stretching frequencies (cm⁻¹) and bond length (Å) for the N–N bond of free N₂ and activated forms.

	N ₂ ^[94]	XXX	XXXI	XXXII	XXXIII	XXXIV
ν_{IR}	–	2164	–	–	–	–
ν_{Raman}	2331	–	1825	1696	1689	1685
$d_{(\text{NN})}$	1.098	1.120	1.143	1.185	1.195	1.192

**Figure 121:** Selected examples for the Ni–N₂ adducts were reported since 2010. [92d-f,92k]

N₂ to NH₃ conversions have been reported in many transition metals already, [95,96] but not for the nickel center metal. The favorable thermodynamics associated with N₂ hydrogenation to ammonia demonstrates that the challenge with nitrogen fixation is principally kinetic in origin. The pathways typically associated with both proton-coupled electron transfer (PCET) or Hydrogen atom transfer (HAT) often avoid high-energy intermediates and therefore may

facilitate smooth N-H bond formation and ultimately release of free ammonia, offering a potential advantage over conventional dinitrogen reduction strategies. [97] It is important to note that the homogeneous ammonia synthesis catalysts reported by *Schrock* and *Nishibayashi* could operate by PCET or HAT, [98] as the combination of strong pyridinium acids and metallocene reductants can, in principle, lead to the in situ formation of pyridinyl radical species with exceedingly weak N-H bonds (BDFE N-H ~35 kcal/mol)

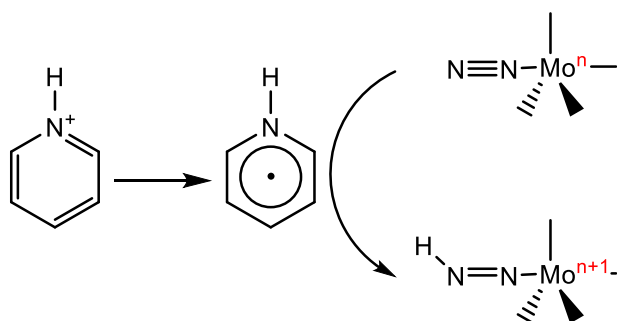


Figure 122: Delivery of a hydrogen atom equivalent to a bound dinitrogen fragment by a pyridinyl radical species.

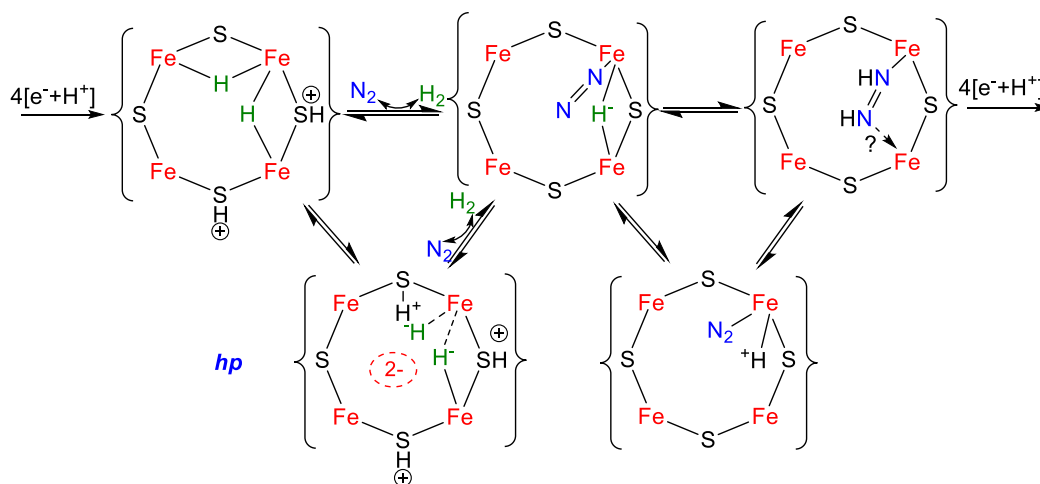
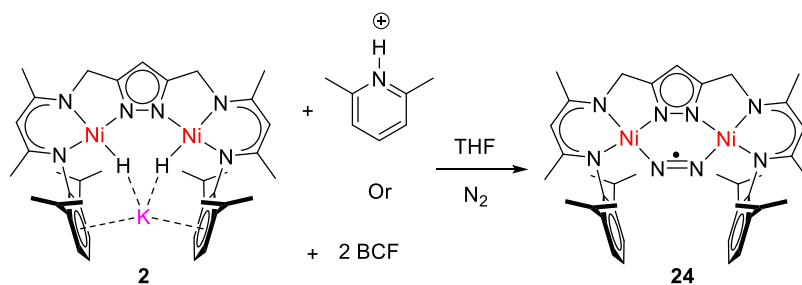


Figure 123: The bridging hydrides of E₄ (green) are positioned to share a Fe “vertex”, as suggested by hydride protonation (*hp*) mechanism of H₂ release upon N₂ binding.

Biology is offering blueprints for the use of metal hydride species in the reductive binding and activation of inert substrates. In this case, reducing equivalents

are stored as hydrides, preferably at multi-metallic sites, which upon reductive elimination of H₂ unmask the low-valent metal species. This strategy avoids strong reducing agents and may bypass highly unfavorable one-electron reduced substrate intermediates. The prominent metalloprotein exploiting this mechanism is the FeMo cofactor of nitrogenase, where binding of inert N₂ is preceded by charging of the Fe/S active site with four electrons and four protons, and is accompanied by the obligatory release of one molecule of H₂.^[99, 100] It has recently been shown that photolysis of the charged state, denoted E₄(4H) according to the Low-Thorneley kinetic scheme for the nitrogenase mechanism,^[100a] generates an intermediate E₄(H₂;2H) described as an H₂ complex of the doubly reduced Fe/S cluster.^[101] It has further been suggested that this H₂ complex may be a thermally populated intermediate on the trajectory of reductive elimination of H₂ from, and reaction of N₂ with, the E₄(4H) state (**Figure 123**).

Recently, *Manz* has prepared complexes including $\mu\text{-}\eta^1,\eta^1$ -ligands like N₂H₄, N₂H₃⁻, N₂H₂⁻, N₂H⁻ from **1** with N₂H₄, which are supposed to represent important intermediates in the process of N₂ fixation and activation. In his work, the compounds of N₂H_x (x = 1, 2, 3 or 4) species were characterized by x-ray or spectroscopies.^[11] In an effort to access and rationalize the dinitrogen fixation in the dinickel system, we sought to (i) do dinitrogen activation in the masked [L¹Ni¹]⁻ species; (ii) expand the interconversion between all the N_xH_y (x = 1 and 2, y = 0, 1, 2, 3 or 4) species.

8.2 Synthesis [N₂]⁻ monoanionic radical

Scheme 39: Synthetic route for **24**.

H₂ reductive elimination from metastable hydride complexes have been used previously as a route to dinitrogen complex, [102] there are three literature examples of N₂ binding directly from crystallographically verified hydride complexes. [92c,103] This H₂-N₂ exchange is interest in the context of catalytic N₂ reduction because the formation of N₂ complexes in this way avoids the use of harsh reducing agents. Solution of **2** in aromatic and hydrocarbon solvents show no signs of decomposition or new species by ¹H NMR when heated to 60°C for several days under Ar or N₂ atmosphere.

Inspired the work from FeMo-co hydride protonation (hp) and reductive elimination (re) mechanism study from *Hoffmann*, [100a] two new approaches were tried to do the dinitrogen activation (**Scheme 39**). (I) Treatment of **2** with absolutely dry [H-Lut][OTf] or [H-Lut][BF₄] under N₂ atmosphere results in a color change from orange to brown red immediately, and gas evolution was observed. The gas was verified and was quantified as 1.4 equivalents (vs 1 equivalent of **2**) by analyzing the gas phase of the reaction mixture using gas chromatography (**Table A1**, **Table A2** and **Figure A42**). After the reaction, colorless substance (KCF₃SO₃) was obtained from parent solution. Filter the parent solution and the volatile removed under vacuum. The crude product can dissolve in many solvents, such as pentane, hexane, diethyl ether, THF and toluene. Nevertheless, suitable crystals for x-ray diffraction were obtained from hexane lay-

ered into saturation solution of **24** in THF at -30°C . (II) afterward, a new method was observed to produce the dinitrogen complex. Treatment of **2** with 2 equivalents strong Lewis acidic BCF (tri(pentafluorophenyl)borane) gives a color change from orange to brown-red in 20 mins and evolution of gas bubbles was observed slowly. No precipitate was observed from the reaction mixture even after a prolonged period. Suitable crystals for x-ray diffraction were obtained from THF slow evaporation at room temperature in a week.

Treatment of **2** with stoichiometry BCF in solution of THF- d_8 , ^1H NMR spectrum indicates that still has unreacted **2**. The peak at -2.91 ppm in the ^{11}B NMR (**Figure 124**) and three peaks at -136.07 ppm (d, $^3J_{\text{FF}} = 23$ Hz, 6F), -168.1 ppm (t, $^3J_{\text{FF}} = 20$ Hz, 3F) and -171.0 ppm (m, 6F) in the ^{19}F NMR spectrum were observed (**Figure 125**), which are similar to the K[HBCF] complex spectrum in the ^{11}B and ^{19}F NMR. [104] A paramagnetic resonance was observed in the ^1H NMR spectrum (**Figure 126**) once two equivalents of BCF was added.

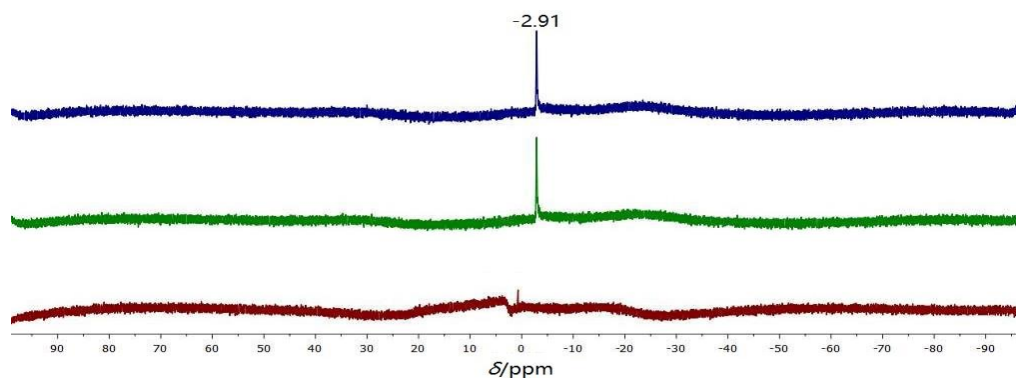


Figure 124: ^{11}B NMR spectrum of **2** with 1 equiv BCF in two days.

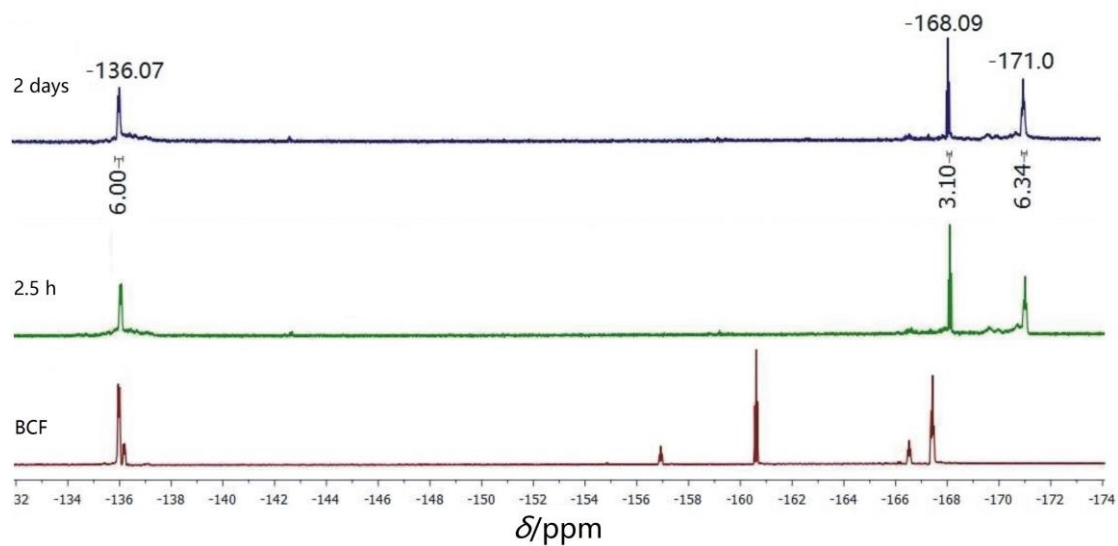


Figure 125: ¹⁹F NMR spectrum of **2** with stoichiometry BCF in two days

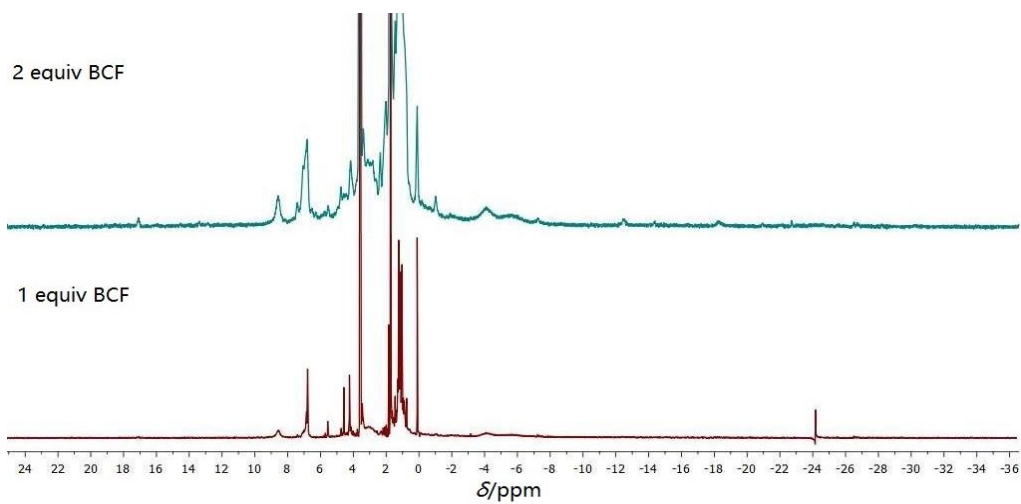


Figure 126: ¹H NMR spectrum of **2** with one equivalent BCF and two equivalent BCF.

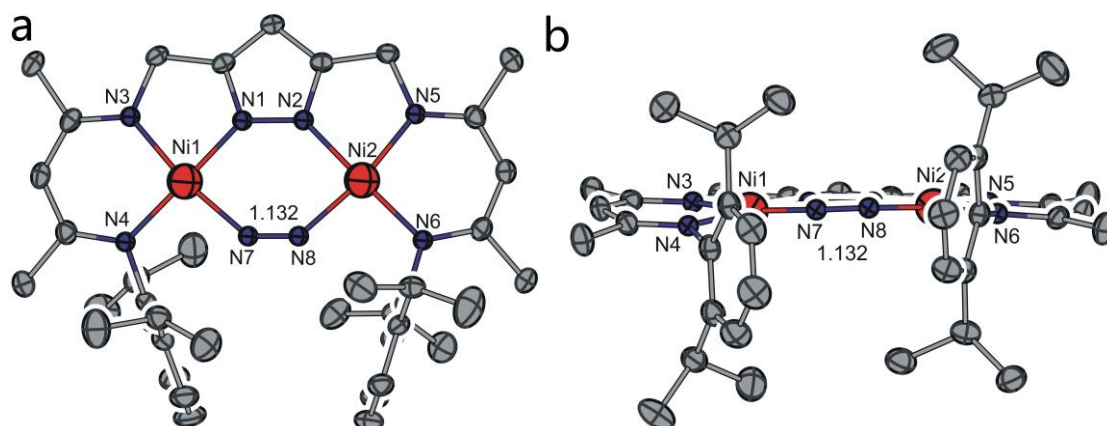


Figure 127: Molecular structure (50% probability thermal ellipsoids) of **24**. All hydrogen atoms omitted for clarity.

Table 30: Selected bond lengths (Å) and angles (°) for **24**.

Atoms	Bond lengths	Atoms	Bond angles
Ni1-N1	1.865(1)	N1-Ni1-N7	87.07(5)
Ni1-N7	1.884(1)	N1-Ni1-N3	83.80(5)
Ni1-N3	1.886(1)	N7-Ni1-N3	169.39(5)
Ni1-N4	1.898(1)	N1-Ni1-N4	175.35(5)
Ni2-N2	1.874(1)	N7-Ni1-N4	94.54(5)
Ni2-N8	1.883(1)	N3-Ni1-N4	94.98(5)
Ni2-N5	1.899(1)	N2-Ni2-N8	87.37(5)
Ni2-N6	1.907(1)	N2-Ni2-N5	83.13(5)
N7-N8	1.132(4)	N8-Ni2-N5	170.35(5)
Ni1-Ni2	3.962(5)	N2-Ni2-N6	178.25(5)
		N8-Ni2-N6	94.01(5)
		N5-Ni2-N6	95.51(5)
		N8-N7-Ni1	139.5(2)
		N7-N8-Ni2	138.5(2)
		Ni1-N7-N8-Ni2	2.82(6)

24 was characterized by x-ray diffraction, FT-IR-, Raman-, UV-Vis-, EPR-, XES-, spectroscopies, CV-, SQUID- measurements and DFT calculations as well as elemental analysis (C, H and N). **24** crystallizes in the monoclinic space group $P2_1/c$ with four molecules in the unit cell. The molecular structure of **24** in ORTEP diagram is shown in **Figure 127** and selected bond lengths (Å) and an-

gles (°) are listed in **Table 30**. An almost planar six-membered {N₂Ni₂N₂} ring was formed by the two nickel center atoms, pyrazolate–N and dinitrogen ligand. In **24**, two nickel(II) ion host in the two {N₃}-tridentate binding sites of the tri-anionic ligand scaffold, bridged by the pyrazolate and nitrogen atom from dinitrogen ligand (**Figure 127**). Both nickel centers are coordinated in an expected square-planar fashion, with the sum angles being 360.3° and 360.03°, respectively. This is in agreement with the low-spin *d*⁸ configuration. The distance of the two nickel ions and torsion angle of Ni–N–N–Ni are 3.962(5) Å and 2.82(6)°, respectively. The N–N bond distance of dinitrogen ligand of 1.132 is consistent with other reported Ni(N₂) complexes (**Table 35**),^[92] and is slightly longer than the free dinitrogen molecule of 1.10 Å.^[94] Compared with other transition metals dinitrogen compounds,^[89] the dinitrogen molecule is weakly activated. To our the best knowledge, complex **24** is the first [N₂][−] monoanionic radical complex characterized by x-ray diffraction.

From the solid state, **24** is not a neutral molecule if the dinitrogen is considered as a neutral molecule fashion. Then there is one proton missing in the solid structure. However, the ¹H NMR spectrum of **24** in THF-*d*₈ shows a paramagnetically shifted resonance (contained some decayed hydroxide nickel complex **11**). Then the question arises as the paramagnetically shifted resonances from the unpaired electron added to a *d* orbital (→Ni^I) or to an N-based orbital. It is noteworthy that to the Ni^I compound, reduction results in a large decrease in the vibrational energy (299 cm^{−1} for the dinickel (I/0) and 428 cm^{−1} for the dinickel (0) species), although N–N bond distance increase by < 0.1 Å for the two electron reduction^[105]. One electron reduction of [NiNNNi] core in **XXXI** by potassium has N–N bond length at 1.143 Å and rRaman frequencies at 1825 cm^{−1}.^[92b] In order to know whether the unpaired electron is located on the nickel center or on the dinitrogen ligand; firstly the IR and rRaman spectrum were employed. A sharp band separately observed at 1896 cm^{−1} in IR

spectra and at 1900 cm⁻¹ in rRaman, which are attributed to the ¹⁴N₂ stretching of dinitrogen ligand (**Figure 128**). The dinitrogen $\nu_{(N_2)}$ band for **24** appear at lower frequencies than the value for free dinitrogen molecule (2331 cm⁻¹)^[106] and **XXX** (2164 cm⁻¹)^[92b], **XXXV** (2156 cm⁻¹)^[92e], **XXXVII** (2223 cm⁻¹ and 2234 cm⁻¹)^[92f] and **XXXVIII** (2145 cm⁻¹)^[92i], but the value is similar to **XXXI** (1825)^[92b]. The ¹⁵N₂ stretching of **24** in IR and rRaman were observed at 1830 cm⁻¹ and 1836 cm⁻¹, respectively (¹⁴N-¹⁵N = 63 cm⁻¹) ($\nu(^{14}N_2)/\nu(^{15}N_2) = 1.034$; *calcu* $\nu(^{14}N_2)/\nu(^{15}N_2) = 1.035$) (**Figure 128**). Two bands (1900 and 1836 cm⁻¹) for N₂ stretching in labeling **24** were observed. We assumed that ¹⁵N₂ ligand exchanged with ¹⁴N₂ in solution.

In **XXXI**, DFT predicts a doublet ground state and a spin-density distribution corresponding to one spin-up electron at each nickel atom and one spin-down electron in an N-N π^* orbital between the Ni atoms. And EPR spectrum is typical for Ni^I species. Therefore, I believed that the unpaired electron has been added to a *d* orbital of nickel instead of N-based orbital.^[92b]

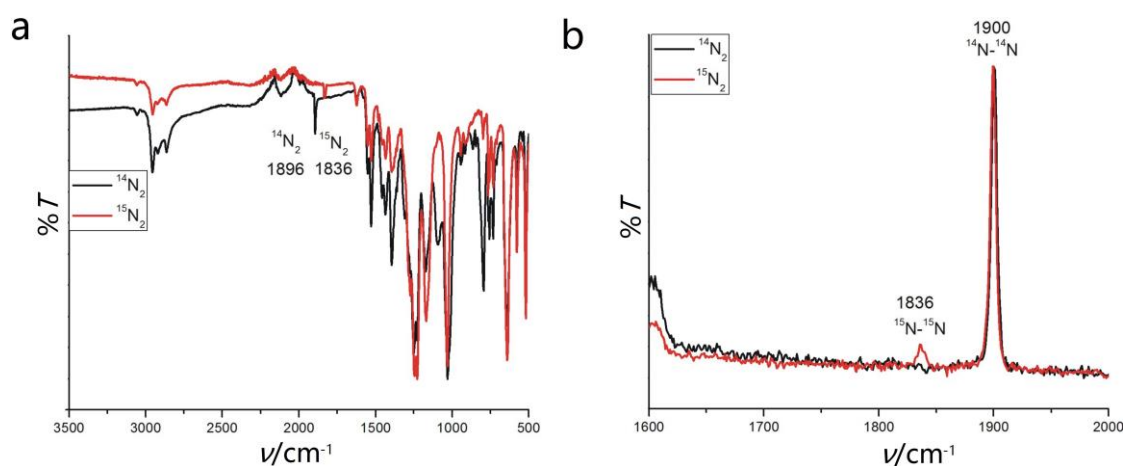


Figure 128: (a) IR spectra (3500–500 cm⁻¹) of **24** in crystalline material at room temperature; the ¹⁴N₂ spectrum is in black and ¹⁵N₂ spectrum is in red. (b) Resonance Raman spectra (1600–2000 cm⁻¹) of **24** in crystalline material at room temperature; the ¹⁴N₂ spectrum is in black and ¹⁵N₂ spectrum is in red.

24 was analyzed by UV-vis spectroscopy (**Figure 129**) which showed a new band at 320 nm ($\epsilon = 1600 \text{ M}^{-1}\cdot\text{cm}^{-1}$) and a shoulder around 500 nm ($\epsilon = 400 \text{ M}^{-1}\cdot\text{cm}^{-1}$). These two bands are assigned to N₂→Ni^{II} charge transfer (CT) transitions.

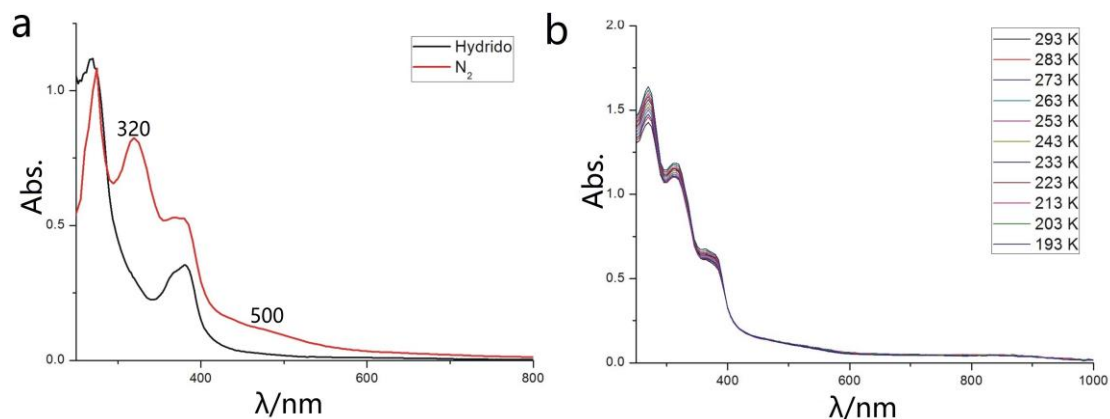


Figure 129: (a) UV-vis spectra in THF of **2** and **24**; (b) VT UV-vis spectra in THF from 293 K to 193 K of **24**.

In collaboration with Eckhard Bill and Van Gastel Maurice from Max-Planck Institute for Chemical Energy Conversion, X-band EPR, cw Q-band EPR and Davies ENDOR on THF solutions of **24** were performed to confirm the identity of **24** has $S=1/2$ in solution. X-band EPR measurements of **24** in solid state at 10 K shows wide splitting (**Figure 130a**), whereas in THF solution at 30 K demonstrates a different and much more narrow peak (**Figure 130b**). No clearly information were obtained for **24** in solid or solution X-band EPR spectra. The cw-Q-band EPR was conducted for **24**. Q-band EPR measurements of **24** in THF at 30 K exhibits two components in solution (**Figure 131a**). The spectrum can be simulated with two sub-spectra corresponding to the two components which the component **24**⁻¹ (green) with g values (2.13, 2.13 and 1.99) ($g_{\text{av}} = 2.08$) and the component **24**⁻² (blue) with g values (2.08, 2.08 and 2.06) ($g_{\text{av}} = 2.07$). The ratio of the two components is around 0.44:0.56.

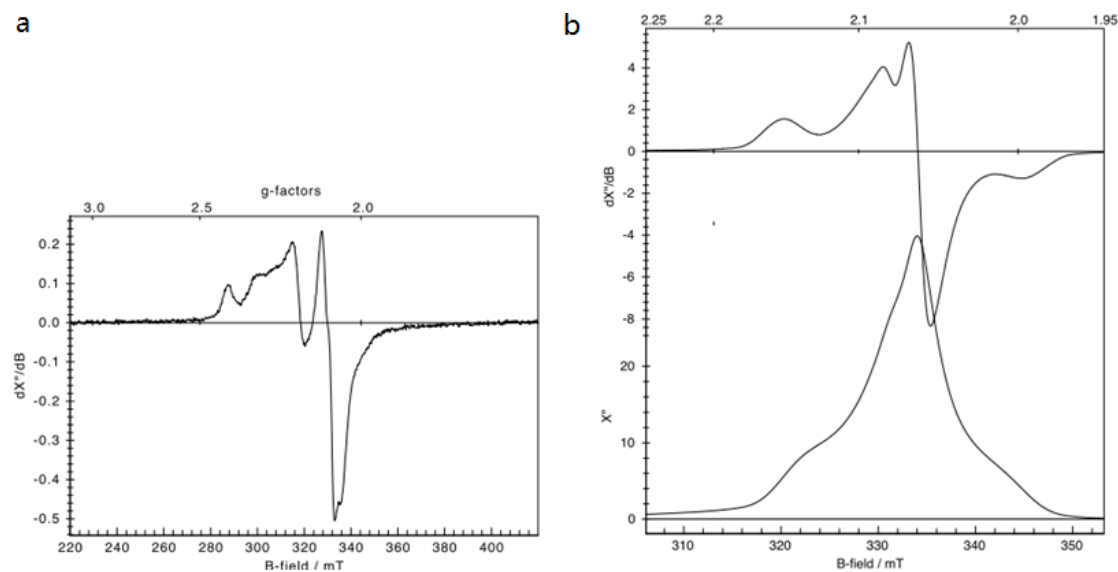


Figure 130: (a) X-band EPR spectra of **24** in solid material at 30K, Frequency = 9.6 GHz, power = 2 mW. (b) First derivative (upper) and theoretical absorption (lower) x-band EPR spectra of **24** in THF at 30 K. Frequency = 9.6 GHz, power = 0.05 mW.

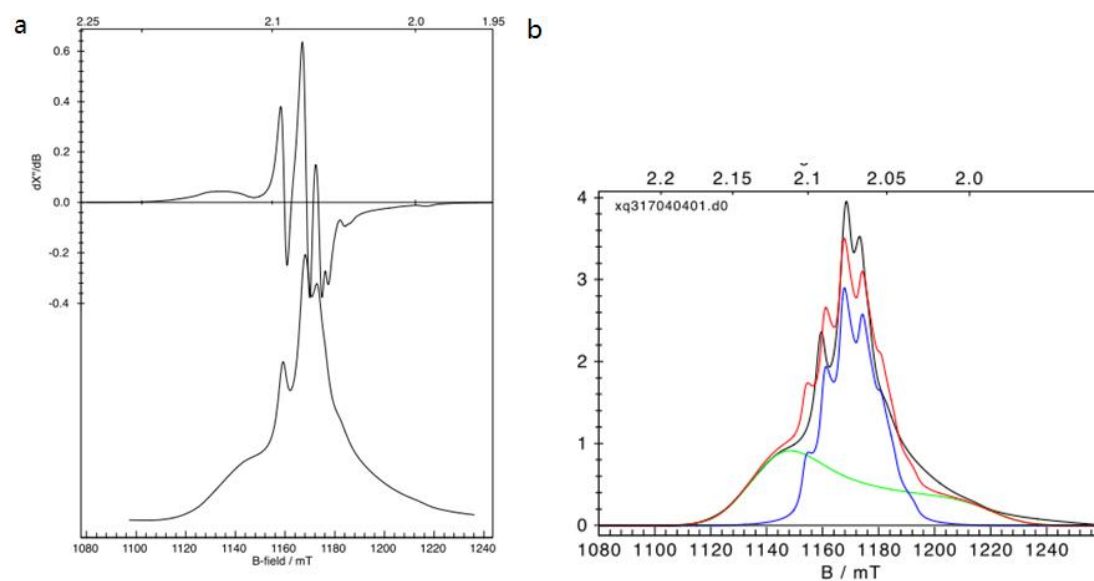


Figure 131: (a) First derivative (upper) and theoretical absorption (lower) cw-Q-band EPR spectra of **24** in THF at 30 K; (b) Simulated EPR spectra with two sub-spectra corresponding to **24**⁻¹ (green) and **24**⁻² (blue).

Table 31: the g values of the components and component ratio.

	24 ⁻¹ (green)	24 ⁻² (blue)
g_x	2.13	2.08
g_y	2.13	2.08
g_z	1.99	2.06
ratio (%)	43.6	56.4

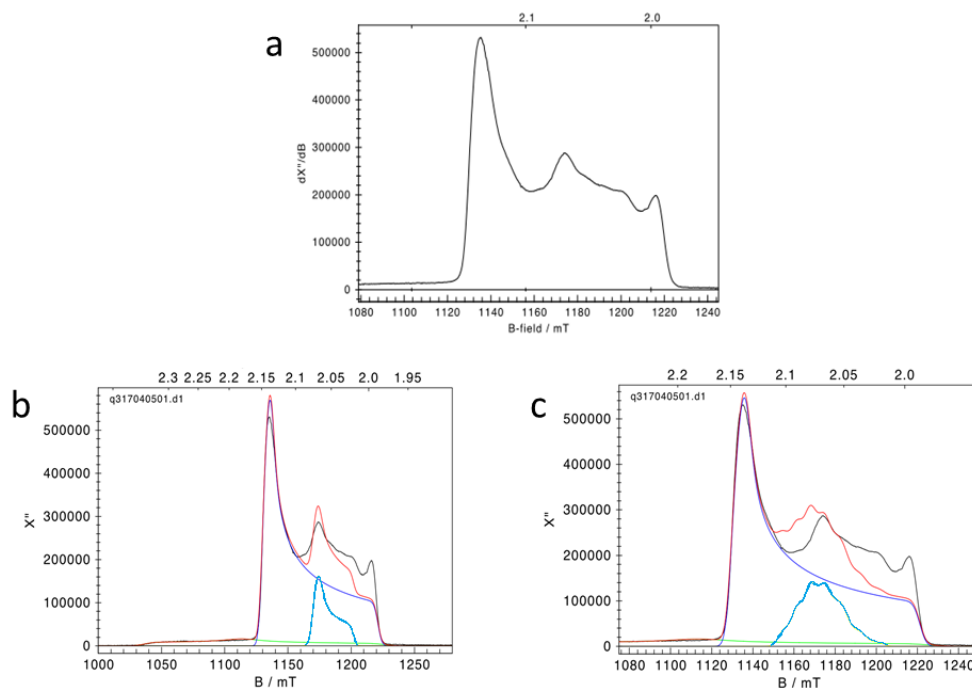
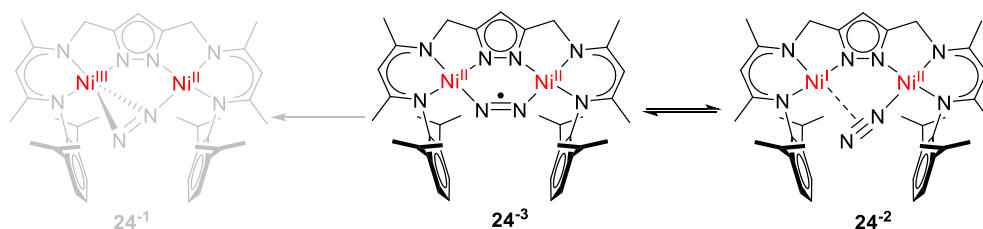


Figure 132: (a) Theoretical absorption pulse Q-band spectrum of **24** in THF at 10 K, Frequency = 34 GHz, power = 5 mV; (b) Simulated EPR spectrum, alternative fit with conditions for three component, the first two sub spectra (green and blue) suggest nickel-based spin; whereas the sub spectrum **24⁻³** (turquoise) is corresponds to the N₂ based. (c) Simulated EPR spectrum, alternative fit with conditions for **24⁻³** (turquoise) taken (hyperfine interaction with two ^{14}N).

Table 32: the *g* values of the components and components ratio.

	24- ¹ (green)	24- ² (blue)	24- ³ (turquoise)
<i>g_x</i>	2.34	2.14	2.08
<i>g_y</i>	2.18	2.15	2.07
<i>g_z</i>	1.98	1.99	2.05
ratio (%)	8.0	76.2	15.8

However, the hyperfine Q-band spectrum clearly showed that three components in solution of **24**. The sub-spectra of green part with *g* values are 2.34, 2.18 and 1.98 and blue part with *g* values are 2.14, 2.15 and 1.99, respectively (**Figure 132**). The wide-split *g* values of the first two sub spectra suggest nickel-based spin. Two simulations were done for the third component. The turquoise sub spectrum (**Figure 132b**) show that the ¹⁴N with *g* values of 2.08, 2.07 and 2.020 or hyperfine interaction (**Figure 132c**) in the two ¹⁴N with *g* values of 2.080, 2.07 and 2.05. I presumed that the three components are three configurations of **24** in solution (**Figure 133**).

**Figure 133:** Three possible configurations of **24** in solution.

EPR measurements show that **24** has three components in solution. The electronic nature of **24** suggested by its geometric structure was confirmed by DFT calculations (**Figure 134**). The energy-minimized DFT calculated structure of **24** is in good agreement with that obtained by X-ray diffraction. The unpaired electron can be estimated at the Ni center around 50 % and at the N₂ ligand around 45 %. Therefore, the unpaired electron are delocalized on the [NiNNNi] system. The distance of Ni...Ni and N₂ ligand of 1.151 Å and 3.964 Å from DFT

calculation are longer than the experimental data of 1.132 Å and 3.962 Å (**Table 33**). The N₂ stretching of 1927 cm⁻¹ for ¹⁴N₂ in calculated IR spectrum is lower than experimental data of 1896 cm⁻¹ (**Figure 135** and **Table 34**).

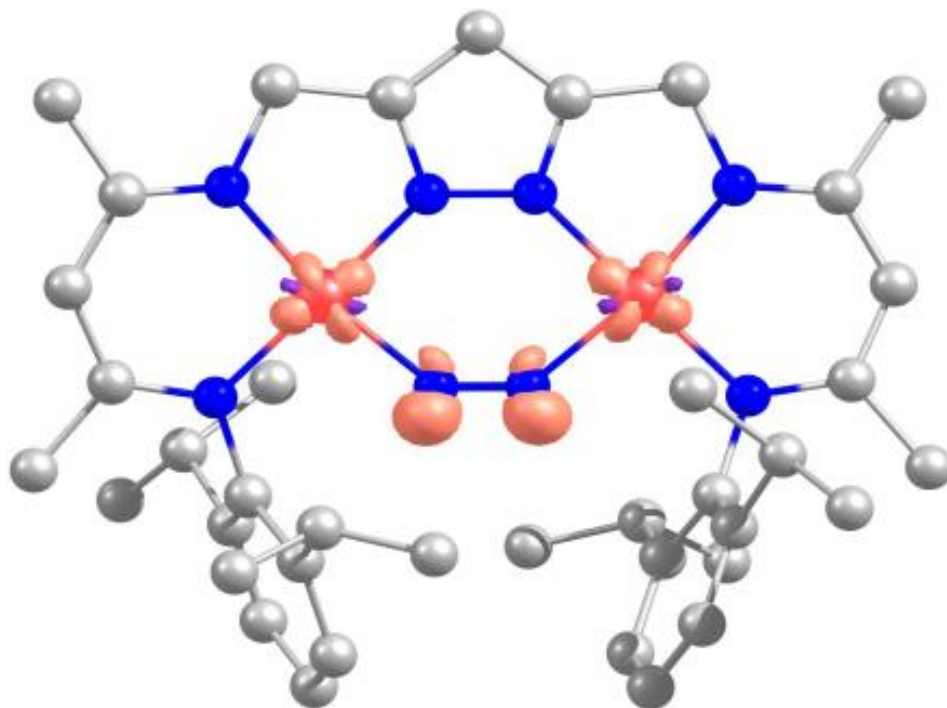


Figure 134: Spin density plot of **24**. Mulliken Spin Population: Ni1 = 0.251814, Ni2 = 0.251829, N1 = 0.218855, N2 = 0.222082.

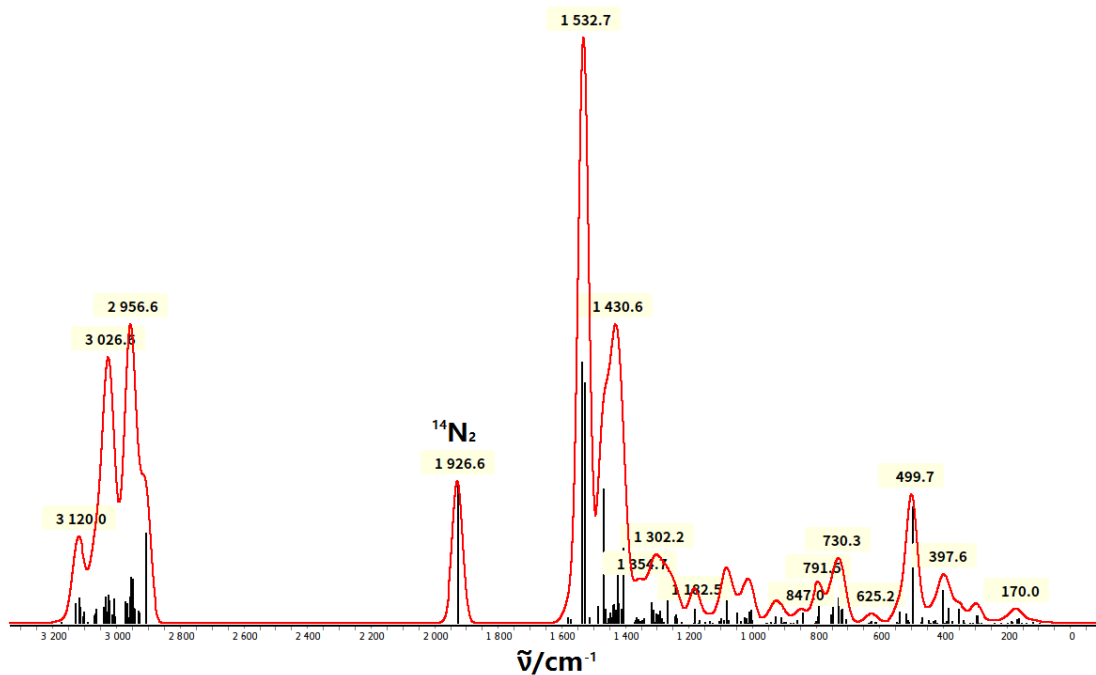


Figure 135: Calculated IR spectrum of **24**.

Table 33: Selected distances (Å) and angles (°) for **24**.

	$d(\text{N-N})/\text{Å}$	$d(\text{Ni}\cdots\text{Ni})/\text{Å}$	$\Phi(\text{Ni-N-N-Ni})/^\circ$
Exp	1.132	3.962	2.82
DFT	1.151	3.964	2.4

Table 34: $\nu(\text{N}\cdots\text{N})$ (IR) for **24**.

	$\nu(^{14}\text{N-}^{14}\text{N})/\text{cm}^{-1}$	$\nu(^{15}\text{N-}^{15}\text{N})/\text{cm}^{-1}$	$\Delta\nu/\text{cm}^{-1}$
Exp	1896	1836	60
DFT	1927	1863	64

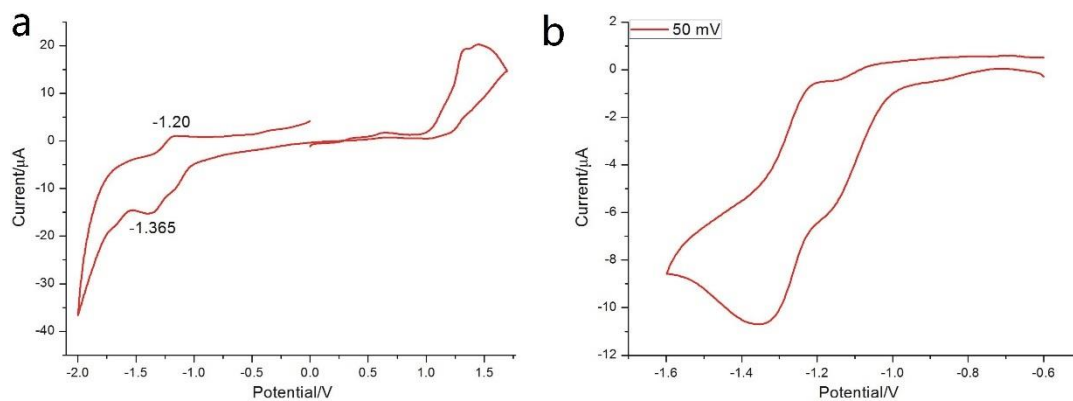


Figure 136: Cyclic voltammogram of **24** in THF/0.1 M Bu₄NPF₆ at a scan rate of 50 mV/s vs Fc/Fc⁺.

The electrochemical behavior of **24** was investigated by cyclic voltammetry in the presence of 0.1 M NBu₄PF₆ in THF solution at RT (**Figure 136**). The cyclic voltammetry shows a quasi-reversible redox wave of scan of 100 mV/s⁻¹ at $E_{1/2} = -1.28$ V (vs. Fc/Fc⁺), indicates that the dinitrogen radical is possible reduce to diazenido.

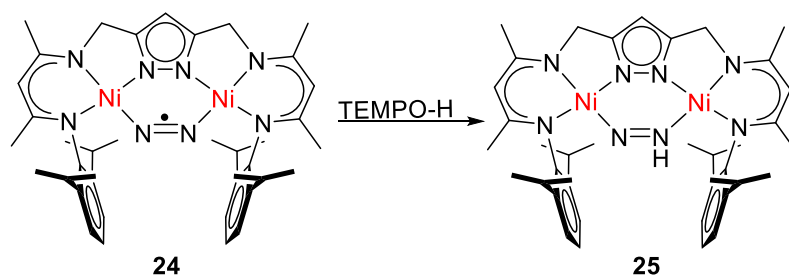
Table 35: Comparison with bond lengths and ν (N₂) stretching vibration frequencies of formally monovalent iron, cobalt and nickel di-nitrogen and compounds reported previously.

Complex	Coordination Nr.	M-N (Å)	N-N (Å)	ν_{NN} (cm ⁻¹)	Ref
Free N ₂	-	-	1.098	2331	106
[Fe(nacnac ^{Me}) ₂ (μ -N ₂)	3	1.745(3), 1.775(2)	1.186(7), 1.172(5)	1810 ^a	108
K ₂ [Fe(nacnac ^{Me}) ₂ (μ -N ₂)	3	1.741(5); 1.761(7)	1.215(6)	1625, 1437	108
[Fe(nacnac ^{Me})(^t Bupy)] ₂ (μ -N ₂)	4	1.816(2)	1.151(3)	1770 ^a	108
[Fe(nacnac ^{tBu}) ₂ (μ -N ₂)	3	1.770(5), 1.779(5)	1.182(5)	1778 ^b	5c
K ₂ [Fe(nacnac ^{tBu}) ₂ (μ -N ₂)	3	1.763(6), 1.765(6)	1.241(6)	1589 ^a /1123	5c
Na ₂ [Fe(nacnac ^{tBu}) ₂ (μ -N ₂)	3	1.749(3), 1.746(3)	1.238(4)	1583 ^a /1127	5c
[Co(nacnac ^{tBu}) ₂ (μ -N ₂)	3	1.840(8)	1.139(2)	1742	107
K ₂ [Co(nacnac ^{tBu}) ₂ (μ -N ₂)	3	1.750(1)	1.220(2)	1599	107
Na ₂ [Co(nacnac ^{tBu}) ₂ (μ -N ₂)	3	1.743(7), 1.735(6)	1.211(3)	1598	107
Mg[Co(nacnac ^{tBu}) ₂	-	-	-	1868	108
[Ni(nacnac ^{tBu}) ₂ (μ -N ₂)	3	1.836(3), 1.830(3)	1.120(4)	2164 ^b	92b
K[Ni(nacnac ^{tBu}) ₂ (μ -N ₂)	3	1.770(7)	1.143(8)	1825 ^a	92b
K ₂ [Ni(nacnac ^{tBu}) ₂ (μ -N ₂)	3	1.931(5)	1.185(8)	1696 ^a	92b
[SiP ⁱ Pr ₃] ₂ Ni(μ -N ₂)	5	1.905(2)	1.087(2)	2223 ^b	92f

[SiPPh ₃]Ni(μ -N ₂)	5	1.891(2)	1.083(2)	2234 ^b	92f
[DIMPY](Ni)(μ -N ₂)	4	1.099(1)	0.92	2156 ^b	92e
[Cu ₃ (nacnac ^{Me} Ph ₂)](μ -N ₂)	3,4	2.209(2), 2.028(2)	1.096(1)	1952 ^a	105
[(SiP ^{<i>ipr</i>} ₃)Fe(N ₂)]Na(THF) ₃	5	1.763(3)	1.147(4)	1891 ^b	76
[(SiP ^{<i>ipr</i>} ₃)Fe(N ₂)]Na(12-crown-4) ₂	5	1.795(3)	1.132(4)	1920 ^b	76
[(TPB)Fe-NN]Na	5	1.776(2)	1.149(3)	1877 ^b	76
[(TPB)Fe-NN]Na(12-crown-4)	5	1.776(2)	1.144(3)	1905 ^b	117
[{(AltraPhos)Fe} ₂ (μ -N ₂)]K(18-crown-6)	5	1.783(3)	1.135(4)	1925 ^b	109
L ¹ Ni ₂ (μ -N ₂)	4	1.884(3), 1.875(2)	1.132(4)	1893 ^b /1098 ^b 1900 ^a	this work

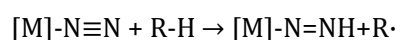
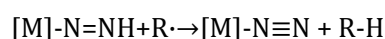
a rRaman spectra; b IR spectra

8.3 Hydrogen atom transfer to dinitrogen monoanionic radical

Scheme 40: Synthetic routes for **25**.

The first N-H bond-forming step in hypothetical dinitrogen reduction cycle generates a transition metal diazenido ligand, M-N=NH. While a number of substituted diazenides, M-N=N-E have been prepared with boryl^[110], silyl^[111], benzyl^[112] and alkyl^[113] substituents, the only structurally characterized “parent” (E=H) example by *Schrock*.^[114]

Attempt to chemically reduce $\mu\text{-}\eta^1\text{:}\eta^1\text{-N}_2$ to $\mu\text{-}\eta^1\text{:}\eta^1\text{-N}_2\text{H}$ with well-defined hydrogen-atom-transfer agents (*i.e.*, catechol, hydroquinone and 1,4 cyclohexadiene) did not yield the desired products. Only decay hydroxide **11** was obtained because the dinitrogen bridge compound is extremely sensitive to moisture. In order to prevent **11** formation from the reduce $\mu\text{-N}_2$ reaction, dried TEMPO-H (65.2 kcal mol⁻¹ in benzene)^[115] was employed for the HAT reaction, leading to the isolation of the targeted compounds. As a consequence, the bond dissociation free energies (BDFE) in N-H bond of **25** is more than BDFE of TEMPO-H (Eqs **1** and **2**).



25 from this reaction was identified from 1D and 2D NMR, IR-, Raman-, XES-spectroscopies and x-ray diffraction. The molecular structure of **25** in ORTEP

diagram is shown in **Figure 137** and selected bond lengths (Å) and angles (°) are listed in **Table 36. 25** crystallizes in the monoclinic space group $P2_1/c$ with two molecules in the unit cell. As shown in **Figure 137**, a six-membered {N₂Ni₂N₂} ring was formed by the two nickel atoms, the nitrogen atoms from pyrazolate ligand and other two nitrogen atoms from diazenido(1-) ligand. The distance of N-N of 1.275 Å for the N₂H⁻ is in the range of complexes with diazenido ligand (1.20 – 1.29 Å).^[116]

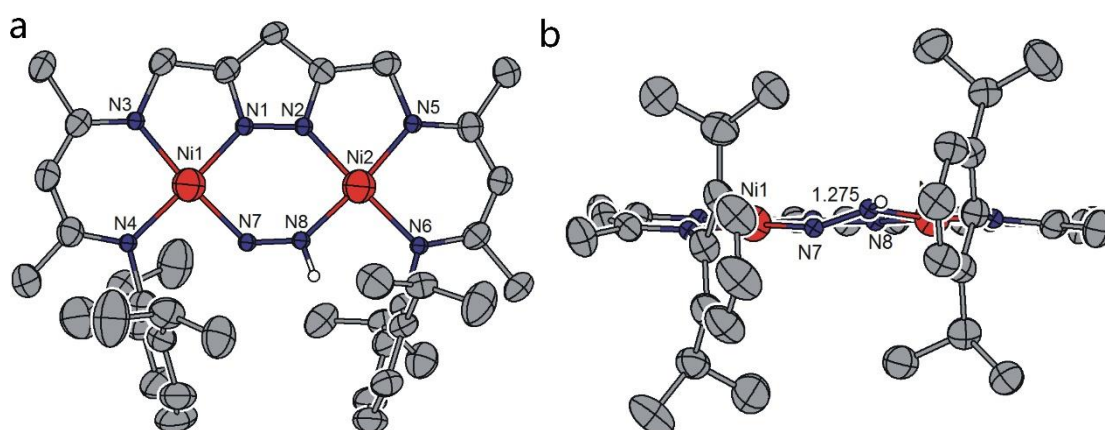


Figure 137: Molecular structure (30% probability thermal ellipsoids) of **25**. Most hydrogen atoms omitted for clarity, except for the N8-H.

Table 36: Selected bond lengths (Å) and angles (°) for **25**.

Atoms	Bond lengths	Atoms	Bond angles
Ni1-N1	1.844(3)	N1-Ni1-N7	91.05(16)
Ni1-N7	1.869(4)	N1-Ni1-N3	83.43(14)
Ni1-N3	1.898(3)	N7-Ni1-N3	174.48(17)
Ni1-N4	1.922(4)	N1-Ni1-N4	176.40(13)
Ni2-N2	1.857(3)	N7-Ni1-N4	91.75(17)
Ni2-N8	1.858(4)	N3-Ni1-N4	93.77(14)
Ni2-N5	1.902(3)	N2-Ni2-N8	90.82(16)
Ni2-N6	1.925(3)	N2-Ni2-N5	83.02(14)
N7-N8	1.275(6)	N8-Ni2-N5	172.66(14)
Ni1...Ni2	3.892(7)	N2-Ni2-N6	176.70(15)
		N8-Ni2-N6	91.99(16)
		N5-Ni2-N6	94.30(14)
		N8-N7-Ni1	131.0(3)
		N7-N8-Ni2	131.2(3)
		C2-N1-Ni1	119.5(3)

Ni1-N7-N8-Ni2	47.55(6)
---------------	----------

In HAT experiment, no obvious color change found during the reaction. The labeling diazenido bridging compound was prepared by this way under Ar atmosphere. In the resonances Raman spectrum, the N₂ unit in **25** has diazene character with the $\nu_{\text{NN}} = 1392 \text{ cm}^{-1}$ and is shifted further to 1323 cm^{-1} upon ¹⁵N₂ enrichment (**Figure 138**). In comparison to free diazene ($\nu_{\text{NN}} = 1529 \text{ cm}^{-1}$) [117], mononuclear complex with “*end-on*” coordinated N=NH ($\nu_{\text{NN}} = 1457 \text{ cm}^{-1}$) [114] or dinuclear complex with *end-on* coordinate NH=NH or N=N ($\nu_{\text{NN}} = 1365 \text{ cm}^{-1}$ or 1358 cm^{-1}) [118], the N=N stretching frequency for **25** is agreement with the range of these complexes. To our best knowledges, this is the first bimetallic complex with *end-on* N₂H⁻ ligand.

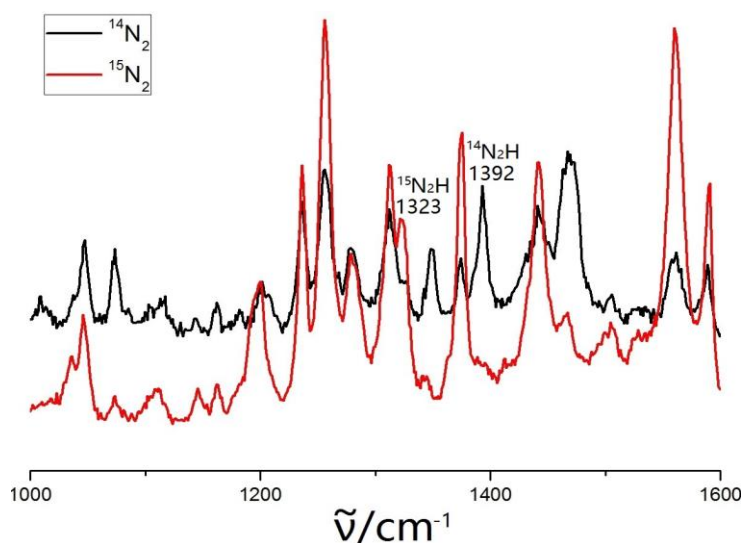
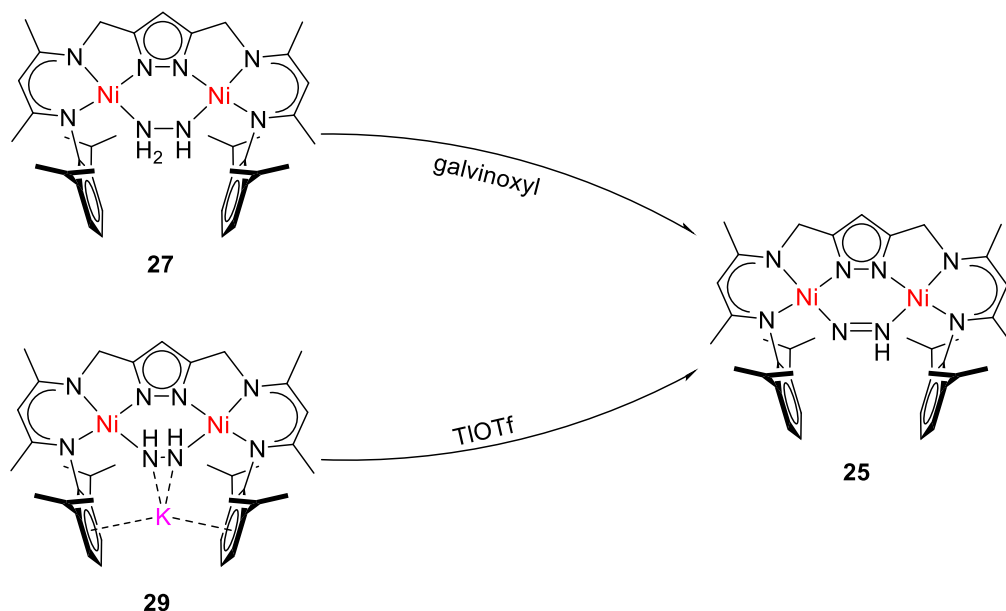


Figure 138: Comparison of the Raman spectra of **25**: Without (black) and after ¹⁵N labelling of the “NiNNNi” subunit (red) in the range of 1000 cm^{-1} to 1600 cm^{-1} .

In *Manz* work, the $\mu\text{-}\eta^1, \eta^1\text{-N}_2\text{H}$ bridging dinickel complex was obtained by oxidize the hydrazido complex (**27**) with 2,2,6,6-tetramethylpiperidin-1-yl)oxyl (TEMPO). The solid state of **25** was clearly characterized by x-ray diffraction. [11a] However, investigations on complex **25** by NMR showed that temperature above

0°C led to decomposition of **25** in solution. Whereas, treatment **27** with a milder oxidant (galvinoxyl free radical) results in a much clear reaction (**Scheme 41**). It could be shown that the clean **25** is stable in solution at RT.



Scheme 41: Synthetic route for **25** from **27** and **29**.

In the ¹H NMR spectrum, a shifted resonance that is attributed to the N=NH proton at 9.46 ppm was observed (**Figure 139**). VT ¹H NMR spectra (**Figure A44**) show that an asymmetric structure **25** even at high temperature (above 293 K). It indicates that the proton in the N=NH unit has fast dynamic rearrangement. The ¹⁵N shift of the NH was determined by means of ¹H-¹⁵N HMBC (52 MHz) to give a resonance at 3 ppm ($J_{\text{NH}} = 74$ Hz) (**Figure 140**). The IR spectrum shows a band at 3025 cm⁻¹ (**Figure 141a**), which was assigned to the NH stretching vibration of the bridging ligand. Compared to free diazene ($\nu = 3128$ cm⁻¹) [¹¹⁷], $\mu\text{-}\eta^1,\eta^1\text{-N}_2\text{H}$ ($\nu = 3242$ cm⁻¹) and $\mu\text{-}\eta^1,\eta^1\text{-N}_2\text{HAr}$ ($\nu = 3220$ cm⁻¹) [¹¹⁹] ligands, the NH vibration of the compound is significantly weak. The lower wavenumber may be attributed to the negative charge of the diazene ligand. The positive ion ESI-MS spectrometry of **25** shows a dominating peak characteristic of the [**25**+H]⁺ at 753.49, and the isotope patterns matched this simulated. (**Figure 141b**)

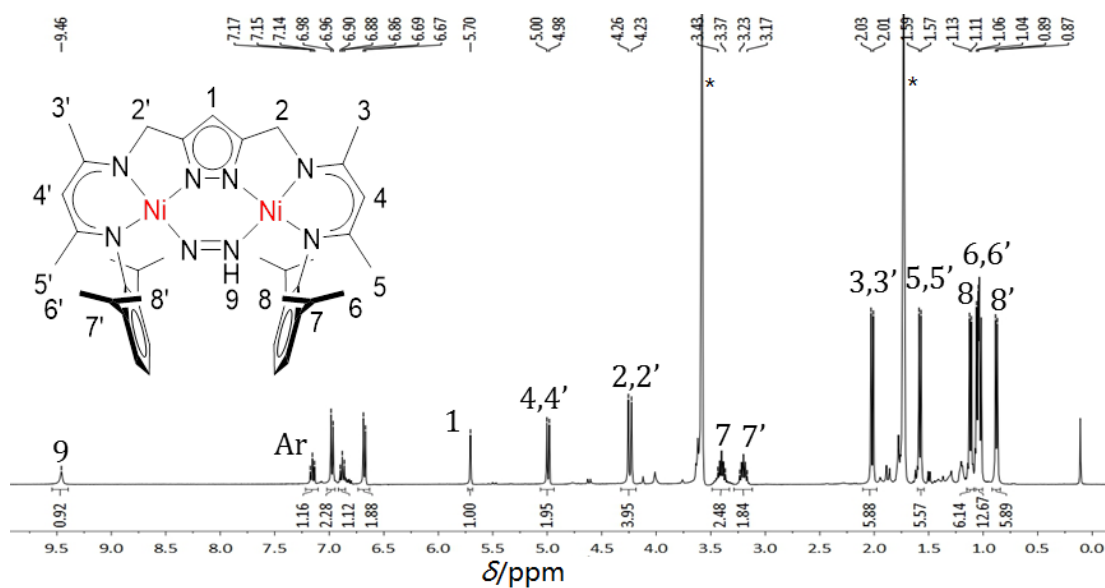


Figure 139: ¹H NMR spectrum (400 MHz) of **25** in THF-d₈. Residual solvents are marked (*).

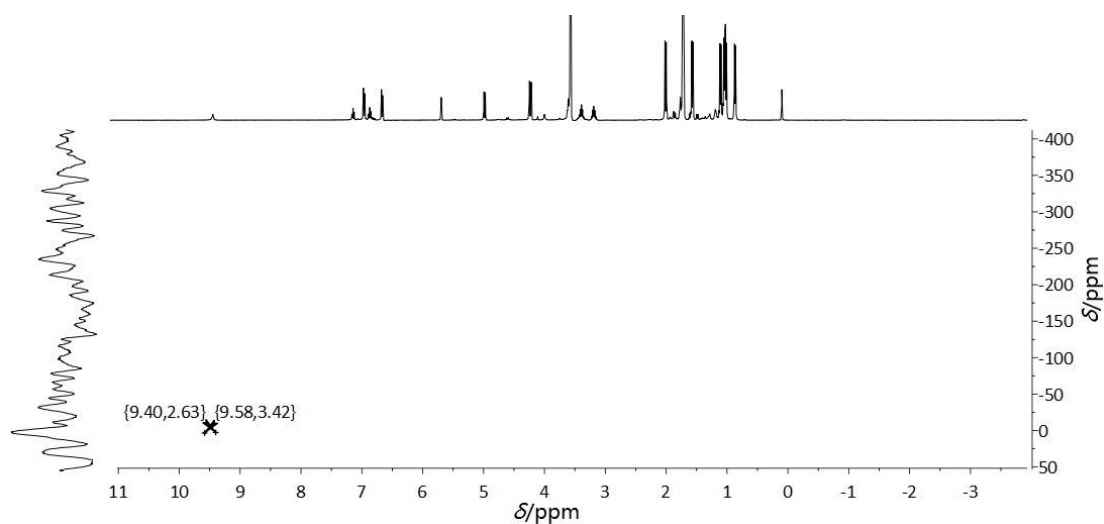


Figure 140: ¹H-¹⁵N HMBC (52 MHz) spectrum of **25** in THF-d₈. ¹J_{NH} correlations of **25** are marked.

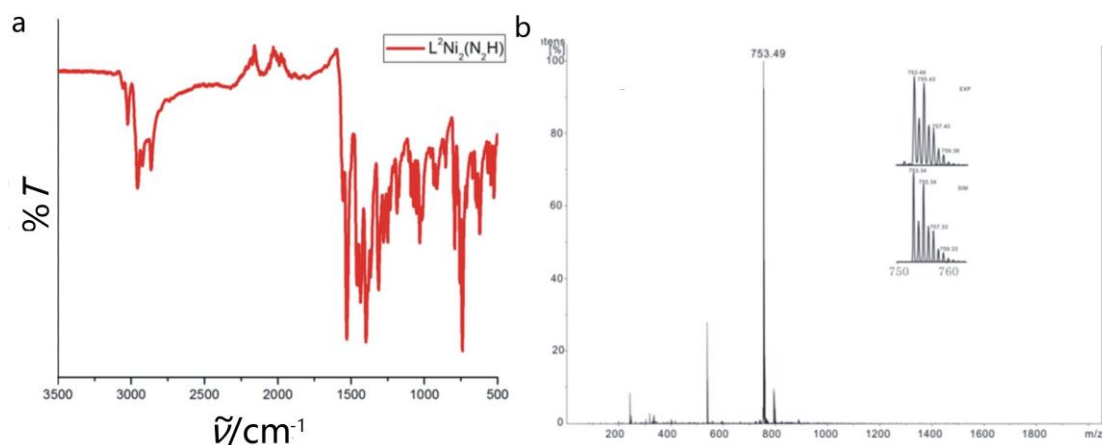


Figure 141: FT-IR spectrum of **25** in fresh crystalline material and ESI-MS in THF. The inset shows the experimental (top) and simulated (bottom) isotopic distribution pattern for [25+H]⁺.

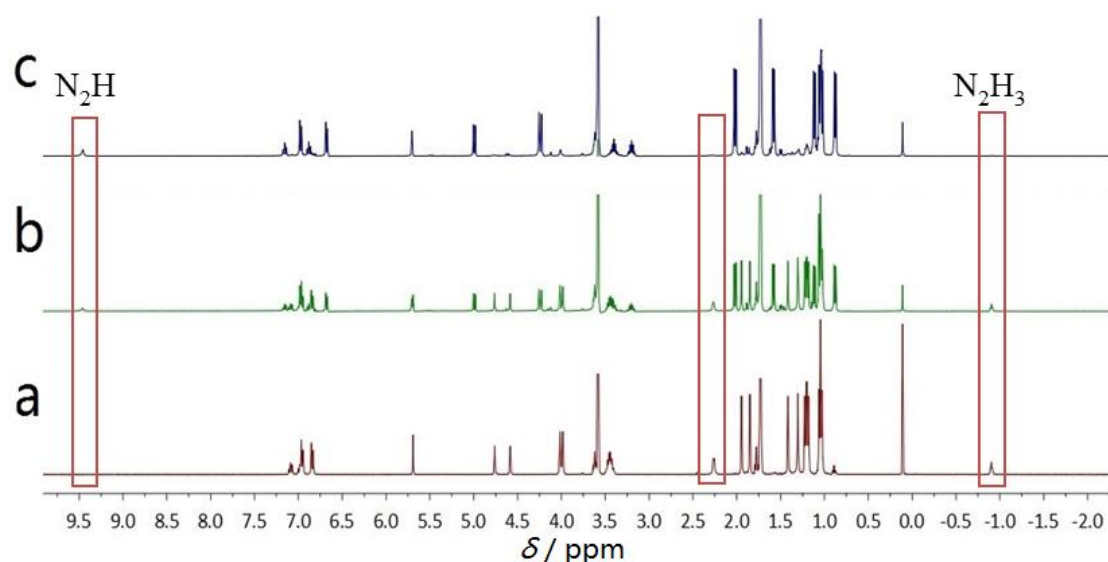


Figure 142: ¹H NMR spectra of the **25** with different amounts of galvinoxyl free radical. (a) **25**; (b) with 1 eq. galvinoxyl radical; (c) with 2 eq. galvinoxyl radical. NH peaks are marked.

Following the clean compound was obtained from **27** with galvinoxyl free radical, a series of experiments to identify intermediate compound (Ni-NH=NH-Ni) were conducted. ¹H NMR spectra show the presence of the diazenido and hydrazido in 1:1 ratio of 1 equivalent galvinoxyl free radical reacts with **27** in THF at room temperature. It indicates that the Ni-NH-Ni bridging is not formed during this process. Pure diazenido complex can be obtained if only 2 equivalents Gal-

vinoxyl free radical reaction with hydrazido bridging compound. However, a paramagnetic substance was obtained once 3 equivalents galvinoxyl radical was employed. X-band EPR measurements of the crystals in frozen THF at 153 K revealed a paramagnetic ground state with spin of $S = 1/2$ also (**Figure 143**). The rhombic spectrum of EPR measurements indicate an oxidation state of + I at the nickel ions. The EPR spectrum could be simulated reasonably well by adopting a set of rhombic g values (2.32, 2.12 and 2.05) ($g_{av} = 2.16$). The g values are consistent with the reported Ni^I species (LNi^I(CH₃Ph)^[120] (2.46, 2.17 and 2.14) and LNi^I(2,4-Lutidine)^[121] (2.44, 2.13 and 2.07), L = {ArNC(Me)}₂CH).

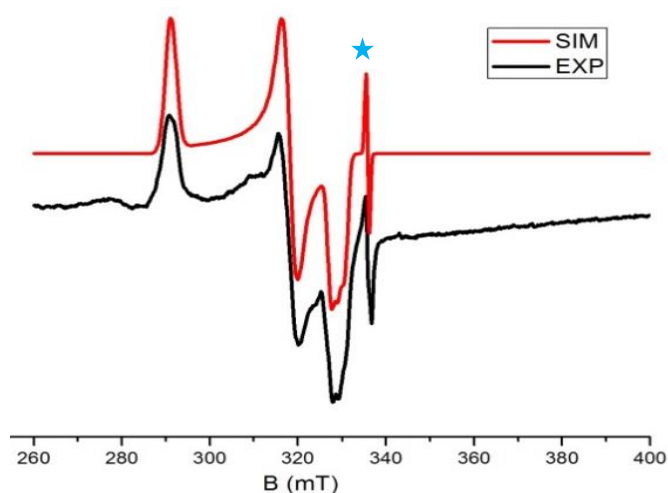


Figure 143: X-band EPR spectrum of **27** with 3 equivalents Galvinoxyl, in THF at 158 K (microwave frequency 9.450 GHz, power 8 mW, modulation 0.4 mT/100 kHz). The red line is a powder simulation with g as indicated. ★Organic radical.

The EPR spectrum shows the paucity of Ni^I species, obtained from **27** reaction with excess galvinoxyl radical. However, the x-ray diffraction unequivocally demonstrates that the bridge is N=NH unit. It indicates that the Ni^I species is in equilibrium with **25** in solution in presence of galvinoxyl radical.

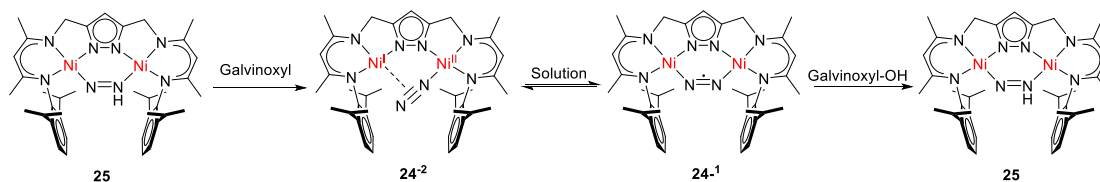
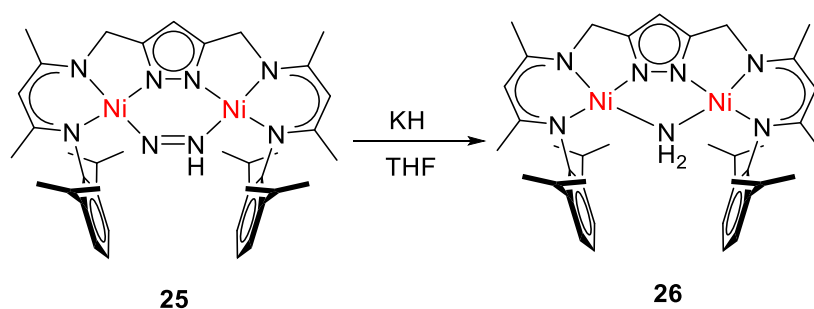


Figure 144: **25** and **24-1** are in equilibrium in the presence of galvinoxyl.

Besides of the HAT reaction and oxidize of hydrazido, complex **25** also can be obtained from **29** with TlOTf at room temperature. Treatment **29** with TlOTf in the young NMR tube, the color changed from green to brown immediately. The compound in this method was characterized by x-ray diffraction in low yield (~10%).

8.4 Cleavage of N-N double bonds



Scheme 42: Synthetic routes for **26**.

Attempts to chemically reduce μ -N₂ to μ -NH₂ at RT or elevated temperature with reductant (KH, NaH and NaBH₄) did not yield the desired product. However, after HAT reaction, a diazenido complex was obtained from dinitrogen radical compound. Dissolving **25** in presence of KH in THF in two hours, the color changed from red to yellow. After work-up of the reaction mixture, ¹H NMR and ¹H-¹⁵N HMBC spectra indicated that the new compound is amido compound. The two spectra were shown in the **Figure 145** and **Figure 146**.

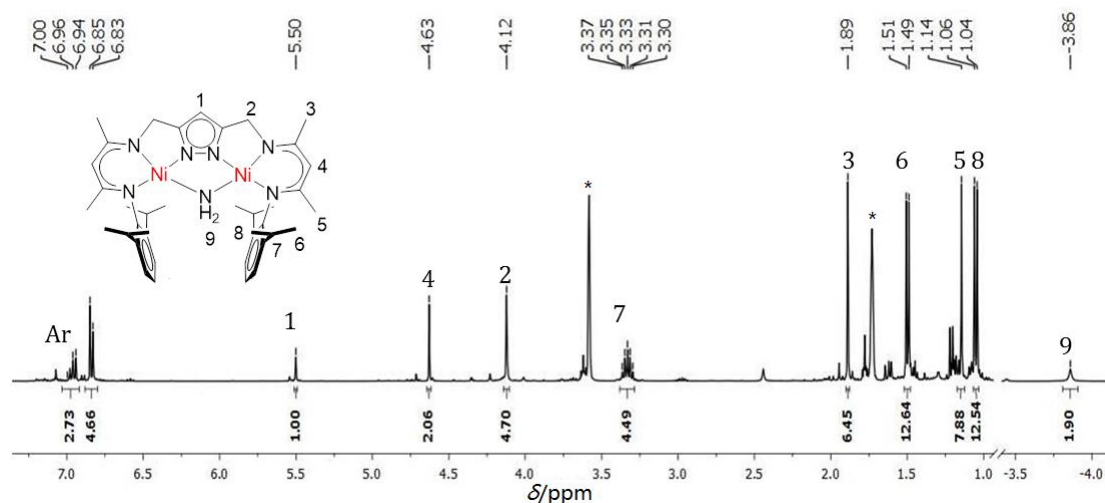


Figure 145: ¹H NMR (400 MHz) spectrum of **26**. Residual solvents are marked (*).

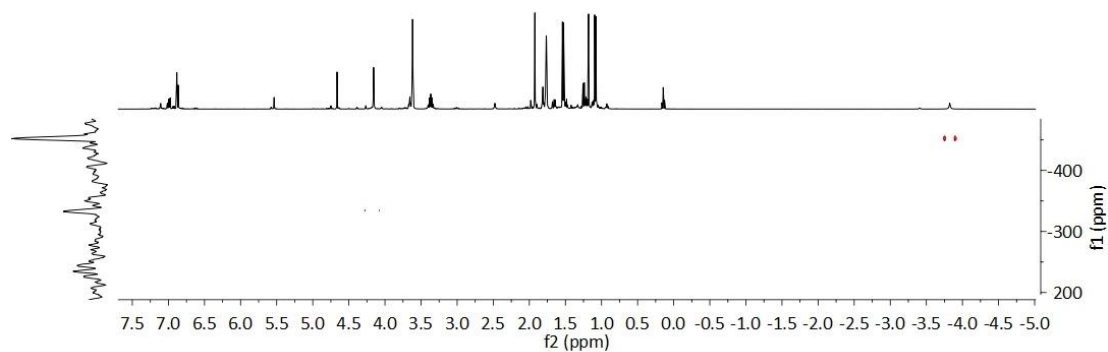
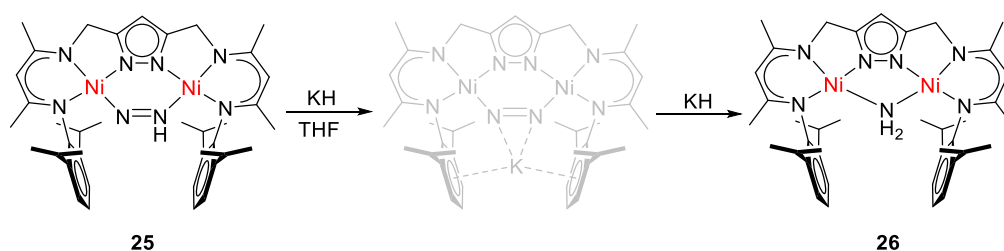


Figure 146: ¹H-¹⁵N HMBC (52 MHz) spectrum of **26**.



Scheme 43: Alternative proposed pathways for the formation of **26**.

One possible conceivable mechanism for the formation of **26** might proceed as follows. The diazenido (N=NH)¹⁻ **25** was first converted to an intermediate nickel diazenido (N=N)²⁻ species by deprotonation with KH. Then the bimetallic dinickel complex is unstable and captured the hydrogen atom from solvent or KH, which results amido bridge **26** (Scheme 43).

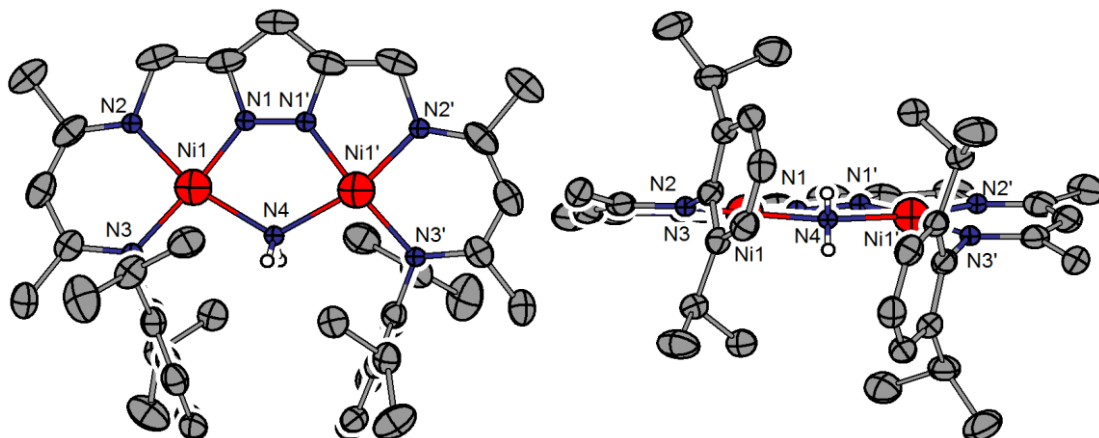


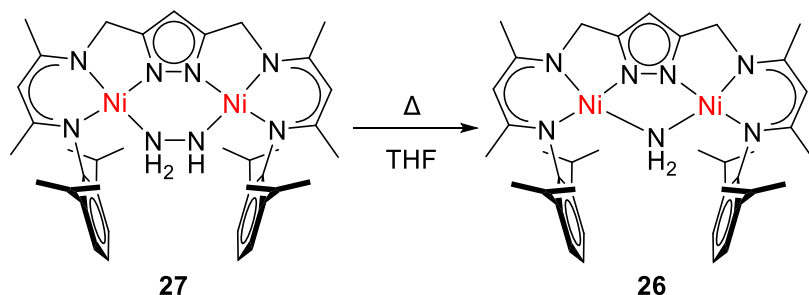
Figure 147: Molecular structure (50% probability thermal ellipsoids) of **26**. Most hydrogen atoms omitted for clarity, except for NH₂ group.

Table 37: Selected bond lengths (Å) and angles (°) for **26**.

Atoms	Bond lengths	Atoms	Bond lengths
Ni1-N1	1.803(3)	N1-Ni1-N3	173.22(10)
Ni1-N3	1.895(2)	N1-Ni1-N2	81.29(12)
Ni1-N2	1.906(2)	N3-Ni1-N2	95.03(11)
Ni1-N4	2.003(2)	N1-Ni1-N4	83.62(11)
N4-Ni1'	2.003(2)	N3-Ni1-N4	100.36(10)
		N2-Ni1-N4	164.44(11)

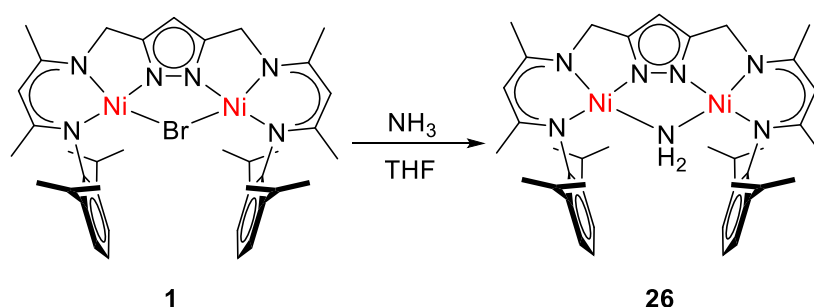
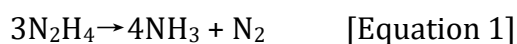
Symmetry transformation used to generate equivalent atoms: (') 1-x, y, 3/2-z.

Yellowish block crystals suitable for x-ray diffraction were obtained by layering hexane on a solution of **26** in THF at -30°C. The molecular structure of **26** is shown in **Figure 147** and selected bond lengths (Å) and angles (°) are listed in **Table 37**. **26** crystallizes in the monoclinic space group $P2_1$ with two molecules in the unit cell. As shown in **Figure 147**, a six-membered {N₂Ni₂N₂} ring was formed by the two nickel atoms, the nitrogen atoms from pyrazolate ligand and other two nitrogen atoms from hydrazine ligand. The two nickel atoms are planar tetracoordinated by three nitrogen atoms from pyrazolate ligand and another nitrogen atom from amido ligand.



Scheme 44: keep **26** under elevated temperature (70°C) for 15-17 weeks.

As presented in *Manz* work (**Scheme 44**) [11a], at elevated temperatures (60–70 °C), **27** was slowly transformed to the amido **26** in 15-17 weeks. Coordinated hydrazine is known to disproportionate and decompose to ammonia and dinitrogen [Equation 1], especially in the presence of transition metals. [122]



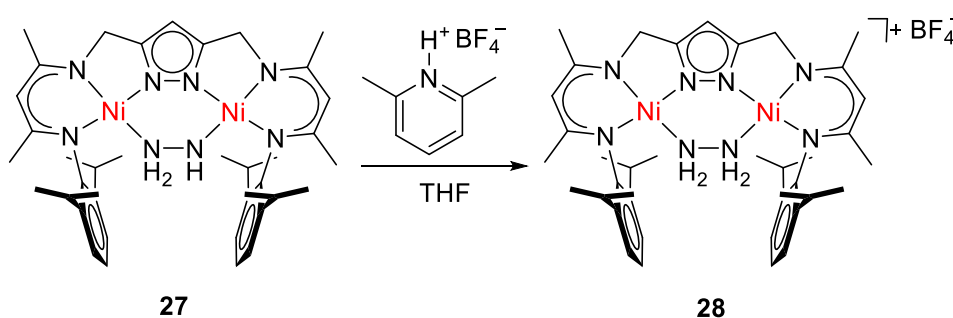
Scheme 45: Synthetic route for **26** from complex **1**

Beside the two methods for the amido complex from **25** and **27**, a new approach is introduced to synthesize from **1**. Treatment of a solution of **1** with NH₃ (0.5 M in THF) at –78°C for 2 hours and warm to RT stirred for 10 hours, the color changed from brown to red (**Scheme 45**). Suitable crystals for x-ray diffraction were obtained by layering hexane on a solution of **26** in THF at –30°C in two days. The products were identified by ¹H NMR also (**Figure 145** and **Figure 146**).

Indophenol Assay. To a frozen solution of **26** (10 mg, 3.9 μ mol) was added HCl in diethyl ether, which resulted in an immediate color change from red to brown. The mixture was warmed to room temperature and stirred overnight, after which

all volatiles were removed under reduced pressure. The pale-yellow residue was dissolved in a phosphate buffer (5 mL, 50 mM, pH 6.94), filtered through a fine-fritted glass funnel packed with celite, the residue was washed with deionized water (3 × 1 mL), and the filtrate was diluted to 10 mL with deionized water in a volumetric flask. Ammonia was quantified as 0.6 equivalents using the indophenol method as previously published. [123]

8.5 Protonation of hydrazido bridge complex



Scheme 46: Synthetic route for **28**.

It has been already proven that the hydrazido bridge complex can be protonated by [H-Lut]OTf at room temperature. [11a] However, information regarding the structure of the complex in the solid state was not reported. Good quality crystals for x-ray diffraction could be obtained during the course of this work by changing the counter anion from triflate to tetrafluoroborate ion. Treatment of **27** with one equivalent [H-Lut]BF₄ in THF results in a color change from red to green immediately (**Scheme 46**). **28** was able to characterize by 1D and 2D NMR, IR-, UV-vis-spectroscopies, X-ray diffraction, and elemental analysis.

Green block crystals for x-ray diffraction were grown by layering hexane on a solution of **28** in THF at -30°C in two days. The asymmetric unit contains two crystallographically independent molecules; one of the two molecules is shown in **Figure 148**. **28** crystallizes in the monoclinic space group $P2_1$ with two molecules in the unit cell. The molecular structure of **28** in ORTEP diagram is shown

in **Figure 148** and selected bond lengths (Å) and angles (°) are listed in **Table 38**. As shown in **Figure 148**, a six-member {N₂Ni₂N₂} ring was formed by the two nickel atoms, the nitrogen atoms from pyrazolate ligand and other two nitrogen atoms from hydrazine ligand. The two nickel atoms are planar tetracoordinated by three nitrogen atoms from pyrazolate ligand and another nitrogen atom from hydrazine ligand.

The distances of nickel centers and N-N bond are 3.973(5) Å and 1.470(3) Å, respectively, which are all longer than **27**. The distance of Ni-N(hydrazine) of 1.945 Å and 1.950 Å are also longer than **27**. Even though the hydrazine ligand has longer distance than hydrazido ligand, the torsion angle \angle Ni1-N7-N8-Ni2 = 89.10° is slightly smaller than **27**, which is attributed to the pyrazole with much more torsion resistance. Furthermore, hydrogen bonds were observed in the hydrazine ligand and solvent molecules and the distances of the hydrogen bonds are 1.952(6) Å and 2.013(6) Å.

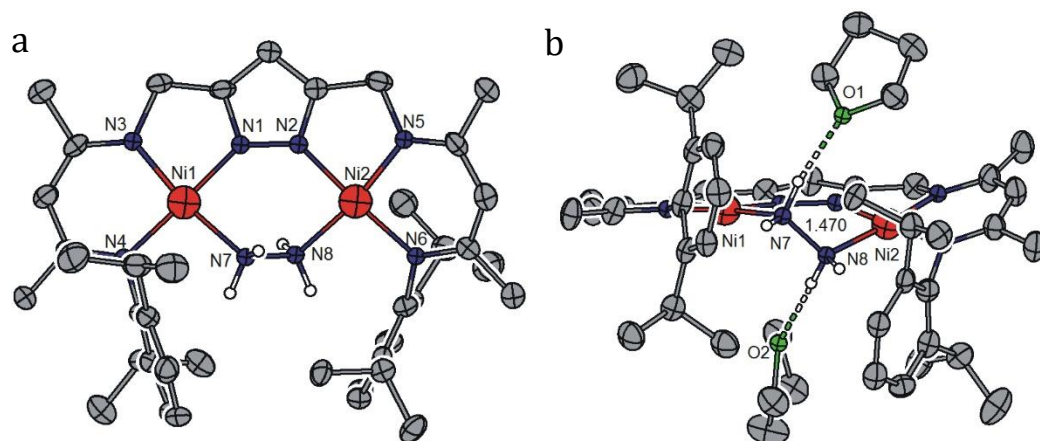


Figure 148: Molecular structure (50% probability thermal ellipsoids) of **28**. Most hydrogen atoms omitted for clarity, except for the N₂H₄ unit.

Table 38: Selected bond length (Å) and angles (°) for **28**.

Atoms	Bond lengths	Atoms	Bond angles
Ni1-N1	1.870(6)	N1-Ni1-N3	83.7(3)
Ni1-N3	1.878(6)	N1-Ni1-N4	175.5(3)
Ni1-N4	1.900(6)	N3-Ni1-N4	94.5(3)

Ni1-N7	1.945(6)	N1-Ni1-N7	88.0(2)
Ni2-N2	1.858(6)	N3-Ni1-N7	171.7(3)
Ni2-N5	1.875(6)	N4-Ni1-N7	93.9(2)
Ni2-N6	1.889(6)	N2-Ni2-N5	83.3(3)
Ni2-N8	1.950(6)	N2-Ni2-N6	177.1(2)
N7-N8	1.470(3)	N5-Ni2-N6	93.9(3)
Ni1...Ni2	3.973(1)	N2-Ni2-N8	87.1(2)
		N5-Ni2-N8	170.0(3)
		N6-Ni2-N8	95.6(2)
		N8-N7-Ni1	116.0(5)
		N7-N8-Ni2	113.6(5)
		Ni1-N7-N8-Ni2	89.1(3)

The ¹H NMR spectrum of **28** revealed a symmetric species as expected in solution. The resonance associated to the isopropyl CH function was overlaid by the residue solvent (THF-d₈), but was distinguished by means of a ¹H-¹H COSY experiment. A resonance at 3.74 ppm corresponds to a normalized integral of four, which is assigned to the neutral hydrazine ligand N₂H₄ (**Figure 149**). The found resonance concurs with other reported proton resonances of bridged $\mu\text{-}\eta^1,\eta^1\text{-N}_2\text{H}_4$ in dimeric iron and tungsten complexes. A side on $\eta^2\text{-N}_2\text{H}_4$ coordinated mononuclear Ni^{II} complex showed a ¹H NMR shift at 3.50 ppm. In ¹H-¹⁵N HMBC spectrum, the ¹J_{NH} correlation occurred at -348 ppm (¹J_{NH} = 71 Hz).^[124]

Investigation by IR spectroscopy revealed bands at 3204, 3247, 3260 and 3382 cm⁻¹, which lie in the typical range of NH stretching. In comparison, free hydrazine has N-H absorption at 3329 cm⁻¹ and 3398 cm⁻¹,^[125] and absorption at 3270–3114 cm⁻¹ has been observed for some other N₂H₄ bridged ligand.^[124] Moreover, IR clearly showed two bands at 1623 cm⁻¹ and 1648 cm⁻¹ that can be assigned to the NH₂ deformation vibrations. Further experiments showed that it is possible to perform reaction with complex **28** with KH in Young NMR tube as alternative route to **27**.

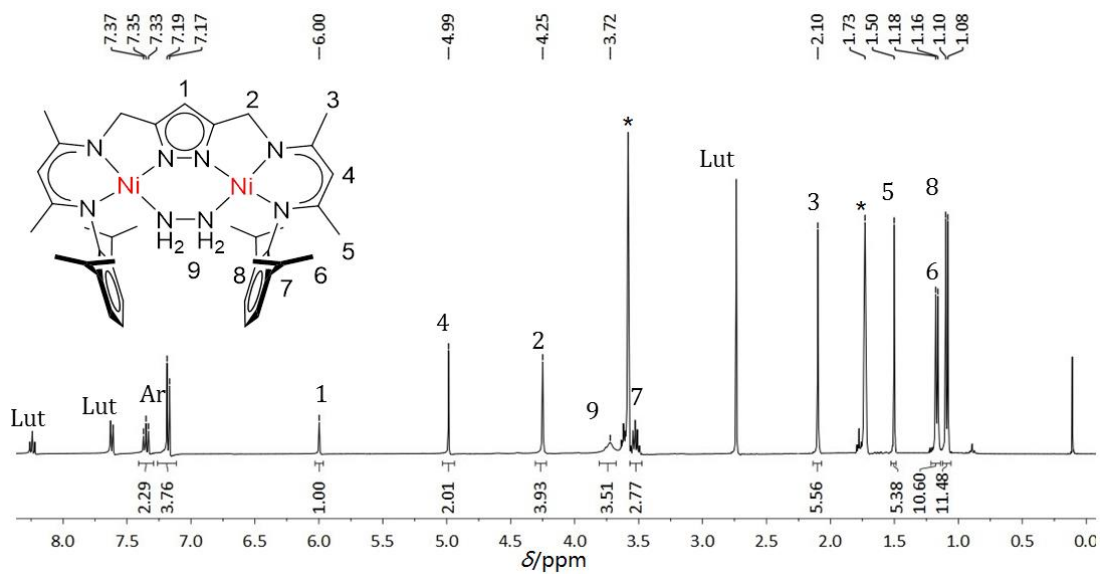


Figure 149: ¹H NMR (400 MHz) spectrum of **28** in THF-d₈ at RT. Residual solvents are marked (*).

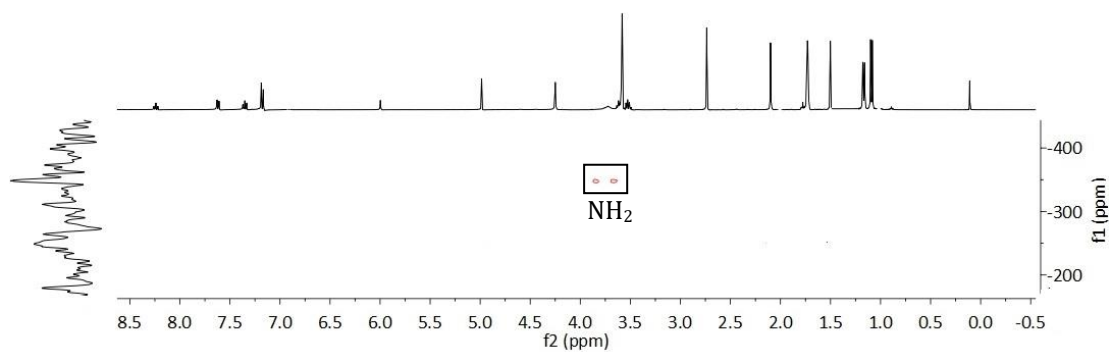
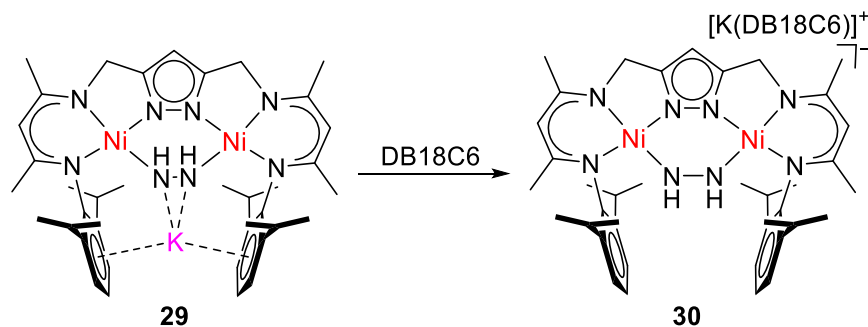


Figure 150: ¹H-¹⁵N HMBC (52 MHz) spectrum of **28** in THF-d₈ at room temperature.

8.6 Synthesis the diazenido complex



Scheme 47: Synthetic route for **30**.

The $\mu\text{-}\eta^1\text{:}\eta^1\text{-HN-NH}$ species (**29**), which is incorporation of the potassium clamped by the two DIPP groups, was characterized by x-ray and spectroscopies very well. [11a] No further reactivity was observed in this complex for redox chemistry. Inspirations of **4**, DB18C6 and cryptand then employed to rupture the metal- π interaction. Adding the DB18C6 into **29** results in the color changed gradually from deep green to brown in 30 mins.

No suitable crystals for x-ray diffraction were obtained because of the crystals are easily decomposed even in solution. But the ¹H NMR spectrum confirms that the K⁺ was dissociated by the DB18C6 (**Figure 151**). The singlet proton resonance of N₂H₂²⁻ in **29** is at 1.03 ppm, which is shifted to 1.63 ppm in **30** (**Figure 151**) in ¹H NMR. The ¹H-¹⁵N HMBC experiment illustrates the N₂H₂²⁻ ligand presence (**Figure 152**). The ¹J_{NH} correlation with ¹⁵N chemical shift at -239 ppm (¹J_{NH} = 14 Hz), which is similar to the N₂H₂²⁻ in **29**

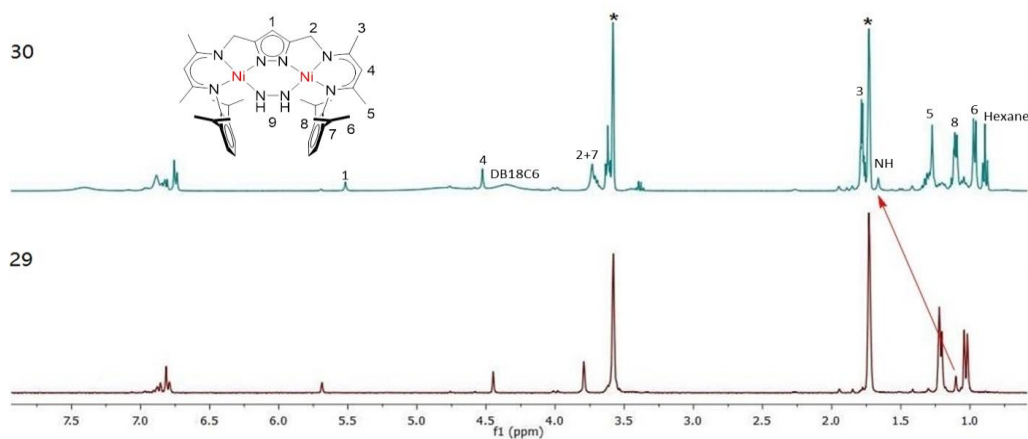


Figure 151: Comparison the ¹H NMR spectra (400 MHz) of **29** and **30** in THF-d₈. Residual solvents (THF-d₈) are marked (*).

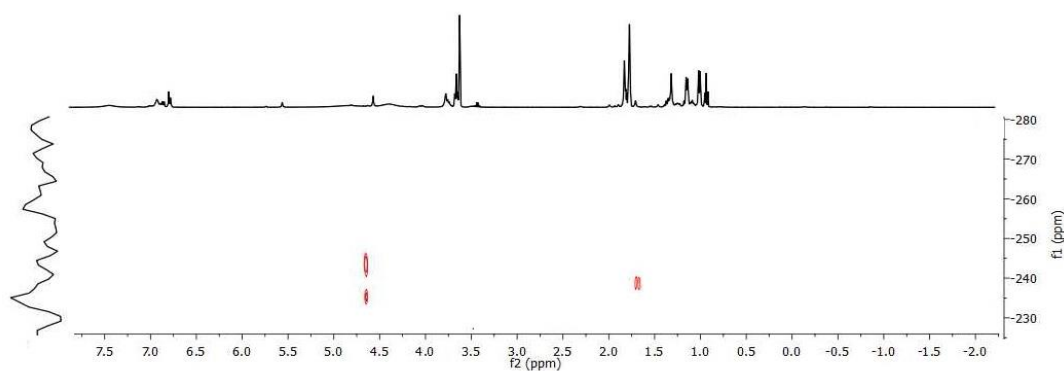


Figure 152: ¹H-¹⁵N HMBC spectrum (52 MHz) of **30**. The $\mu\text{-}\eta^1\text{-}\eta^1\text{-N}_2\text{H}_2$ ligand shows a strong $^1J_{\text{NH}}$ correlation.

The NH stretching vibration of **29** is at 3190 cm⁻¹ in the IR spectroscopic (**Figure 153a**). After dissociate the K⁺ cation from [L1Ni(N₂H₂)]⁻ by DB18C6 or [2,2,2]cryptand, the NH stretching vibration appears at 3263 and 3123 cm⁻¹ for **30** and **31** (**Figure 153b**).

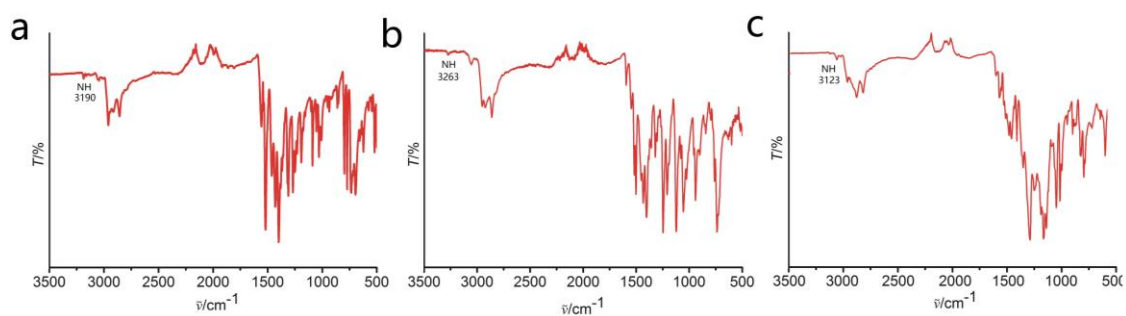


Figure 153: IR spectrum of **29** (a), **30** (b) and **31** (c).

However, black block crystals suitable for x-ray diffraction were obtained from THF or toluene slow evaporation at room temperature while the [2,2,2]cryptand instead of the DB18C6. The molecular structure of **31** is shown in **Figure 155** and selected bond lengths (Å) and angles (°) are listed in **Table 39**.

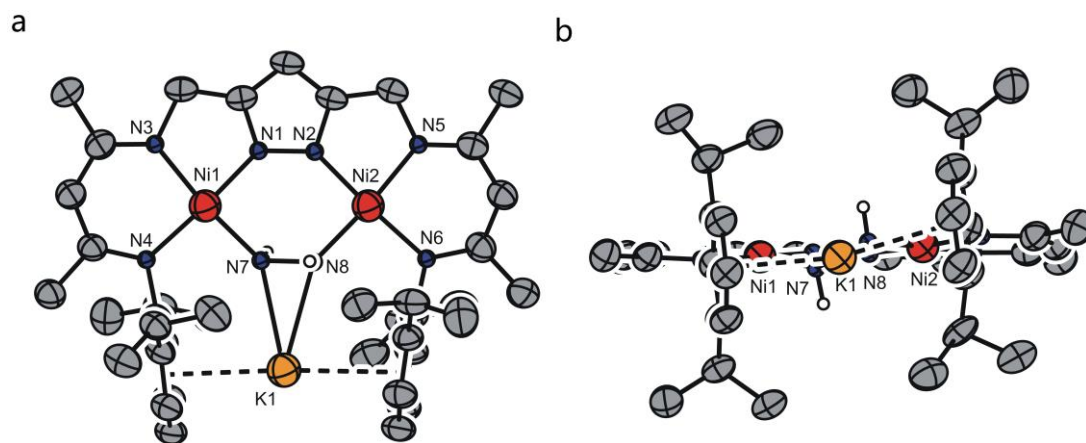


Figure 154: Molecular structure (50% probability thermal ellipsoids) of **29**. ^[11a] Most hydrogen atoms omitted for clarity, except for the N₂H₂ unit.

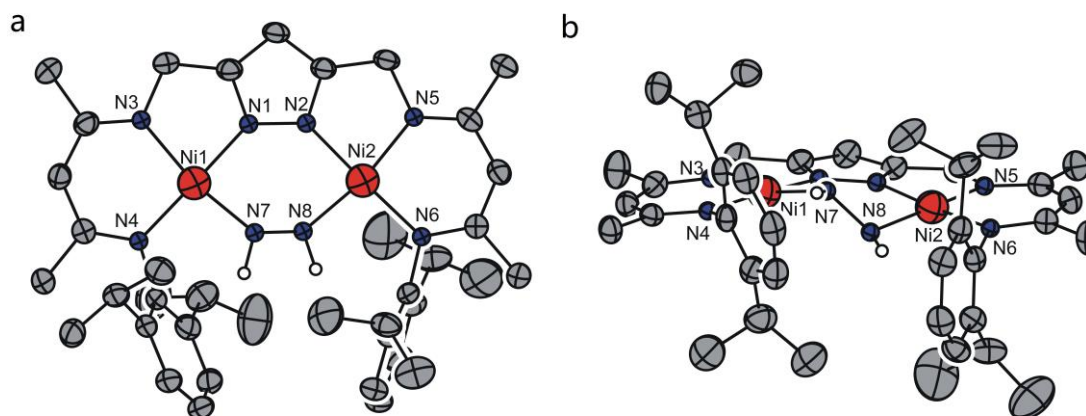


Figure 155: Molecular structure (50% probability thermal ellipsoids) of the anion of **31**. Most hydrogen atoms omitted for clarity, except for the N₂H₂ unit.

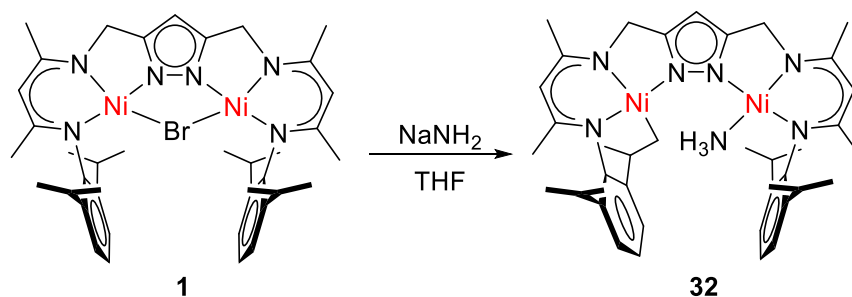
Table 39: selected bond length (Å) and angles (°) for **31**.

Atoms	Bond lengths	Atoms	Bond angles
Ni1-N1	1.884(2)	N1-Ni1-N7	85.73(12)
Ni1-N7	1.885(3)	N1-Ni1-N3	83.09(10)
Ni1-N3	1.928(2)	N7-Ni1-N3	165.60(13)

Ni1-N4	1.892(2)	N1-Ni1-N4	175.74(11)
Ni2-N2	1.884(2)	N7-Ni1-N4	96.29(12)
Ni2-N8	1.892(3)	N3-Ni1-N4	95.48(10)
Ni2-N5	1.931(2)	N2-Ni2-N8	87.12(12)
Ni2-N6	1.899(2)	N2-Ni2-N5	82.79(10)
N7-N8	1.431(5)	N8-Ni2-N5	167.93(13)
Ni1-Ni2	3.939(6)	N2-Ni2-N6	176.62(11)
		N8-Ni2-N6	95.48(12)
		N5-Ni2-N6	94.88(10)
		N8-N7-Ni1	116.1(2)
		N7-N8-Ni2	115.3(2)
		Ni1-N7-N8-Ni2	92.91(7)

31 crystallizes in the orthorhombic space group *Pbca* with eight molecules in the unit cell. As shown in **Figure 155**, a twist six-membered {N₂Ni₂N₂} ring was formed by the two central nickel atoms, pyrazolate-N and hydrazido(2-) ligand. Both metal centers are coordinated in an expected square-planar fashion, with the sum angles of 360.3° and 360.03°, respectively. This is in agreement with the low-spin d₈ configuration. The distance of the two nickel centers and the torsion angle of Ni-N-N-Ni are 3.939(5) Å and 92.91(6)°, respectively. No 1D and 2D NMR spectrum provided because **31** has bad solubility in THF and toluene. The NH stretching vibration of **31** is at 3123 cm⁻¹ in the IR spectroscopic (**Figure 153c**).

8.7 Synthesis of terminal ammonia nickel complex



Scheme 48: Synthetic route for **32**.

Using the LiNH₂ with **1** in THF solution resulted in a color change from brown to red in two days. Whereas, the ¹H NMR spectrum demonstrated two species (amido and ammonia bridging) existing. However, treatment of **1** with NaNH₂ in THF solution resulted in a color change from brown to orange in two day (**Scheme 48**). The crude product was detected by ¹H NMR and ¹³C NMR after filtration indicated that the new compound features a terminal ammonia ligand.

In the ¹H NMR spectrum, a signal set for the protons of the pyrazole ligands in the regular shifted resonances from 0–10 ppm was observed that was characteristic for an asymmetrical dinickel complex. Notable features in the ¹H NMR spectrum include a signal for terminal ammonia ligand. The N-H peak of NH₃ group was located at –3.28 ppm (**Figure 156**), and a diagnostic band was observed at 3023 cm⁻¹ by IR spectroscopy (**Figure A54**). The ¹H–¹⁵N HMBC is shown in **Figure 157**. ¹J_{NH} correlation for the NH₃ occurred at –400.1 ppm (¹J_{NH} = 57 Hz), which is close to the free NH₃ molecule (¹J_{NH} = 61.2 Hz).^[126] The 2D NMR spectra of **32** are shown in Appendix. The proton of NH of the series N_xH_y species in ¹H NMR spectra is shown in **Figure 158** and **Figure 159**.

The asymmetry of the compound is reflected by the ¹H NMR experiment, in particular by distinct resonances associated to the isopropyl and methylene group. The isopropyl group was separated to two multi-peaks at 3.21 ppm and 3.84 ppm.

However, the integration of the two isopropyl groups is two. It indicates that the intramolecular C–H amination was happened in the methylene group. Some small red crystals were obtained from hexane layered in to THF at -30°C . Unfortunately, the crystal of **32** is not suitable for x-ray diffraction.

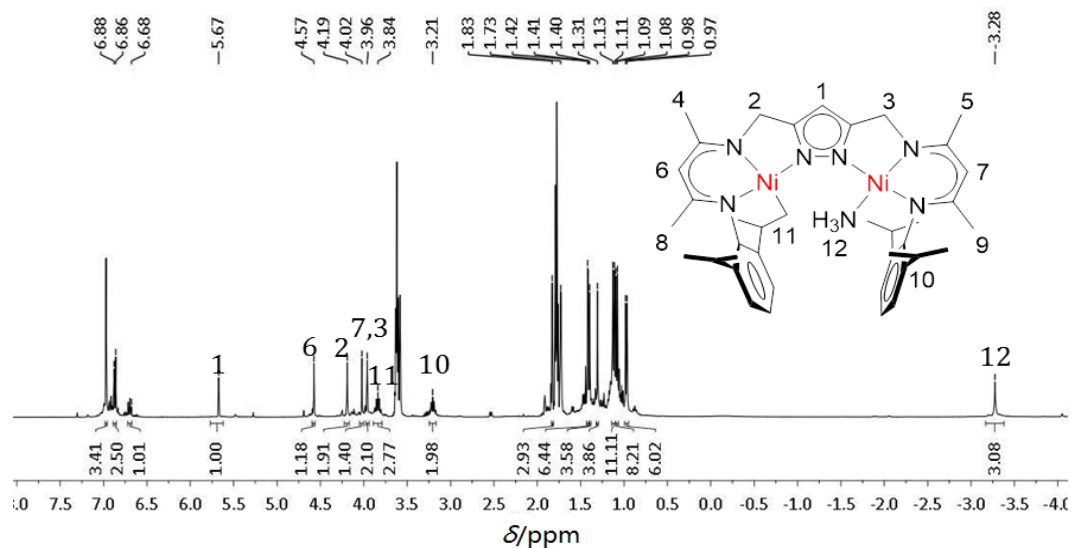


Figure 156: ^1H NMR (400 MHz) spectrum of **32** in THF-d_8 (400 MHz).

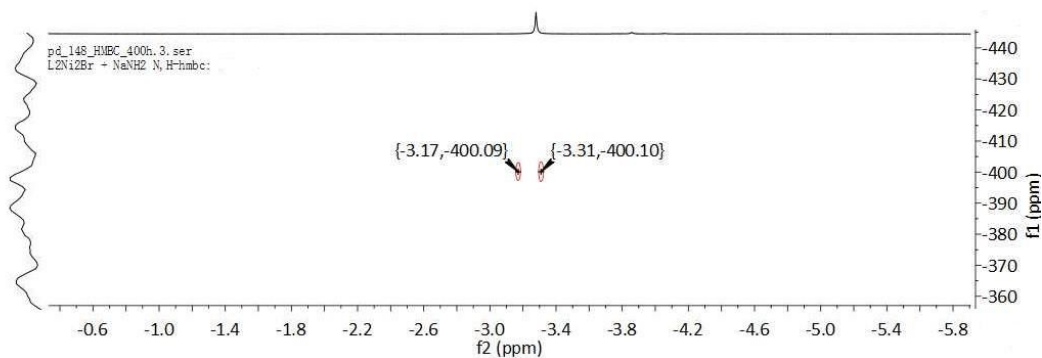


Figure 157: ^1H - ^{15}N HMBC (52 MHz) of **32**. A correlation of the ^1H - ^{15}N resonance is observed for the NH_3 bridging ligand.

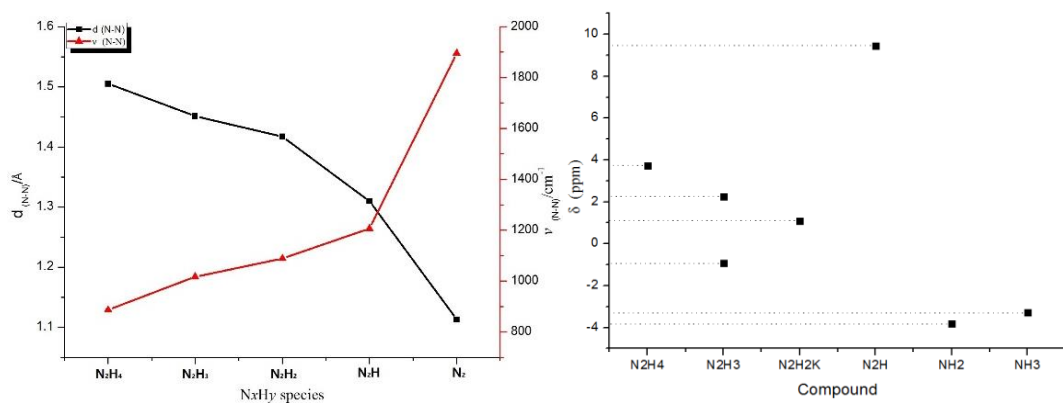


Figure 158: left: the spots of the $d_{(N-N)}$ and $\nu_{(N-N)}$ in the series complexes; Right: the plots of the NH resonance of these complexes.

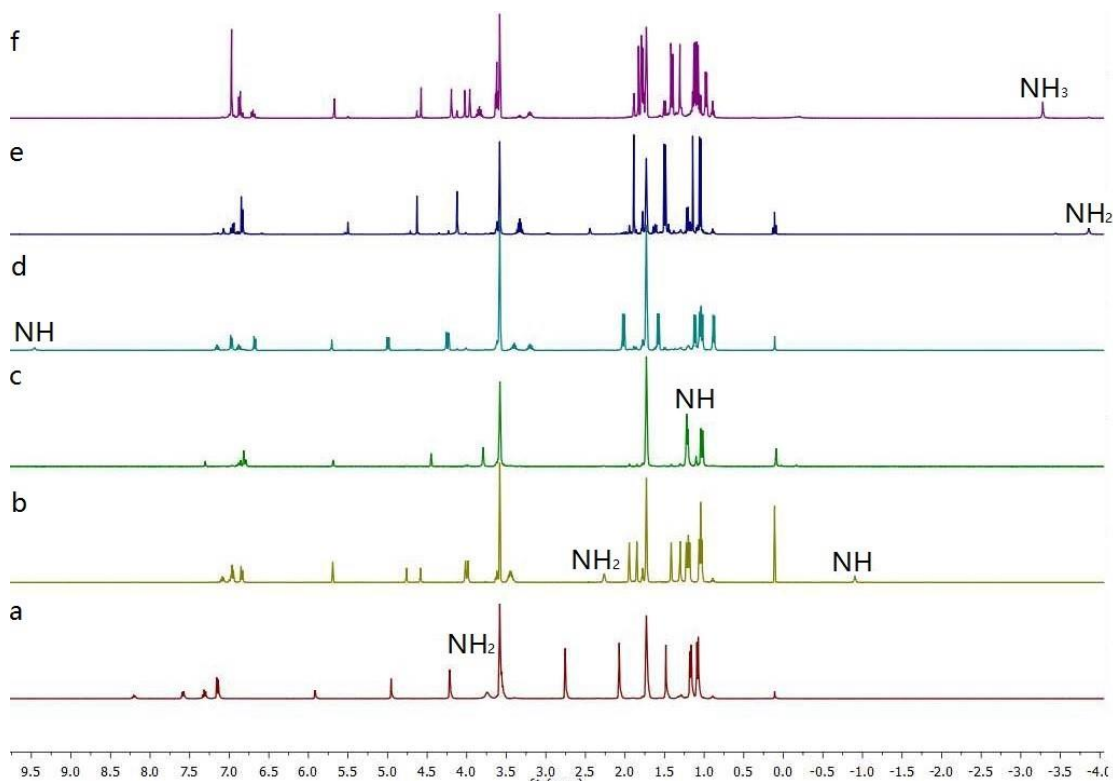


Figure 159: ¹H NMR spectra of the series of N_xH_y complexes; (a) **28**, (b) **27**; (c) **29**, (d) **25**, (e) **26** and (f) **32**.

8.8 X-ray emission spectroscopy

In collaboration with the group of Serena DeBeer, the complexes **24**, **25** and **27** were further characterized by K β X-ray emission spectroscopy (XES). Additionally, the spectrum for the nickel(II) precursor **1** was recorded, which allowed to distinguish between N₂H_x (x = 0, 1 and 2) and ligand-related features.

X-ray Emission Spectroscopy (XES) has found many application in transition metal chemistry as it provides useful information about ligand identity, metal–ligand bonding, and metal spin state.^[127] The experiment involves the detection of the emission of photons (electron decay) following the ionization of an Ni-1s electron. There are three features of an XES spectrum that contain the most relevant chemical information: the K β' and K $\beta_{1,3}$ lines resulting from an electric dipole allowed 3p to 1s transition,^[128] and the K $\beta_{2,5}$ and K β'' lines (or valence to core region, V2C) arising from a valence electron (ligand np or ns) to metal 1s transition.^[129] The K $\beta_{1,3}$ (main line, ~7030–7080 eV) region is dominated by 3p-3d exchange correlation with some contribution from 3p spin–orbit coupling, resulting in sensitivity toward spin state, but little sensitivity toward ligand identity.^[128]

X-ray emission measurement for **24** (N₂), **25** (N₂H) and **27** (N₂H₃) were recorded in HERFD-XAS. An analysis of the synchrotron data suggests that it is consistent with the expected electronic structure. DFT calculations are in agreement with the intensity variations observed in the VTC XES data.

Figure 160a shows the Ni K β mainline (3p → 1s transitions) for this series collected with Debeer's house experiment. While there is some difference in the spectra each of the Ni dimers reaches its maximum at 8265.1 eV compared with the maximum of Ni(acac)₂ at 8265.8 eV.

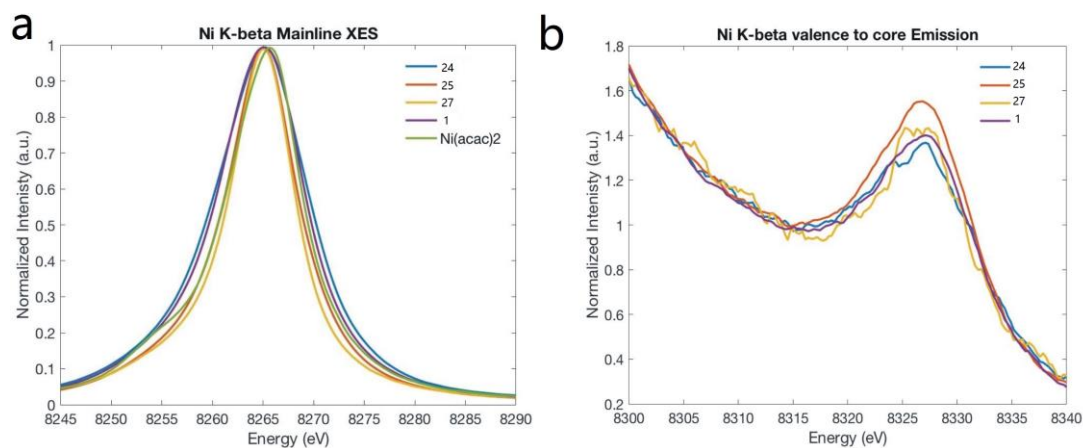


Figure 160: (a) K β main line emission and (b) valence to core XES spectra for **24**, **25** and **27** highlighting the paramagnetic of L¹Ni₂(μ -Br) as compared to the diamagnetic of the other compounds.

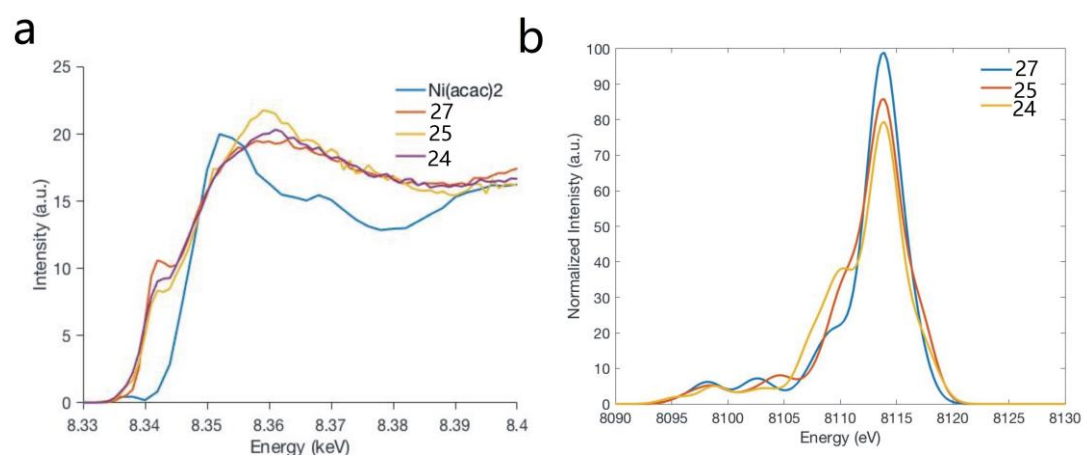


Figure 161: (a) XAS spectra of complexes **24**, **25** and **27** collected at CHESS synchrotron; (b) VTC XES spectra of complexes **24**, **25** and **27** calculated with density functional theory.

As shown in **Figure 161a**, the Ni(acac)₂ as measured is likely Ni(acac)₂(H₂O), whereas **24**, **25** and **27** are more rigorously square planer. This change in symmetry manifests itself in the edge of the XAS spectrum which is dominated by 1s \rightarrow 4p transitions. In the case of the octahedral Ni(acac)₂(H₂O)₂ complex all 1s \rightarrow 4p transitions will be nearly degenerate. However, in the case of **24**, **25** and **27** the 1s \rightarrow 4p_z transition is found at significantly lower energy than the 1s \rightarrow 4p_{x/y} due

to the absence of an axial ligand. This $1s \rightarrow 4p_z$ transition gives rise to the feature at ~ 8.342 keV in all of **24**, **25** and **27**, and the $1s \rightarrow 4p_{x/y}$ would be found at higher energy. DFT calculation results of **24**, **25** and **27** show in the **Figure 161b**.

Table 40: Parameters comparing optimized geometries and crystal structures for **24**, **25** and **27**

	24	24 (exp)	25	25 (exp)	27	27 (exp)
N-N	1.151	1.132	1.237	1.275	1.448	1.467
Ni-N	1.861	1.883	1.879	1.858	1.935	1.907
Ni-N	1.858	1.884	1.807	1.869	1.880	1.889

To gain more insights about **24**, **25** and **27**, we carried out a detailed analysis by mapping the electronic-structure in different transition.

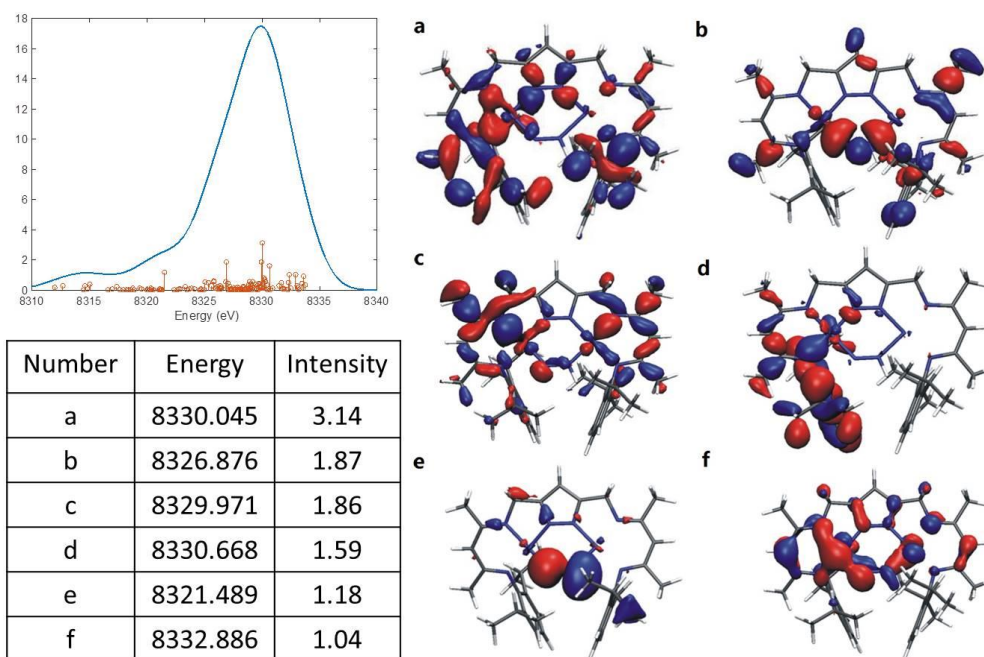


Figure 162: Calculated V2C spectrum of **24** with the molecular orbitals that strongly contribute to the observed transitions.

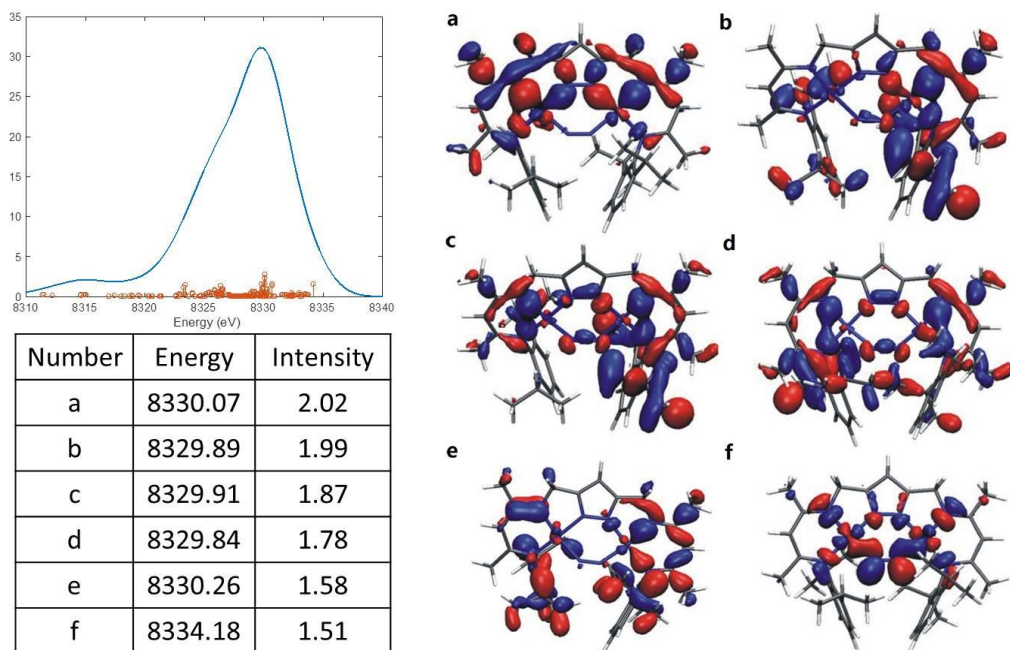


Figure 163: Calculated V2C spectrum of **25** with the molecular orbitals that strongly contribute to the observed transitions.

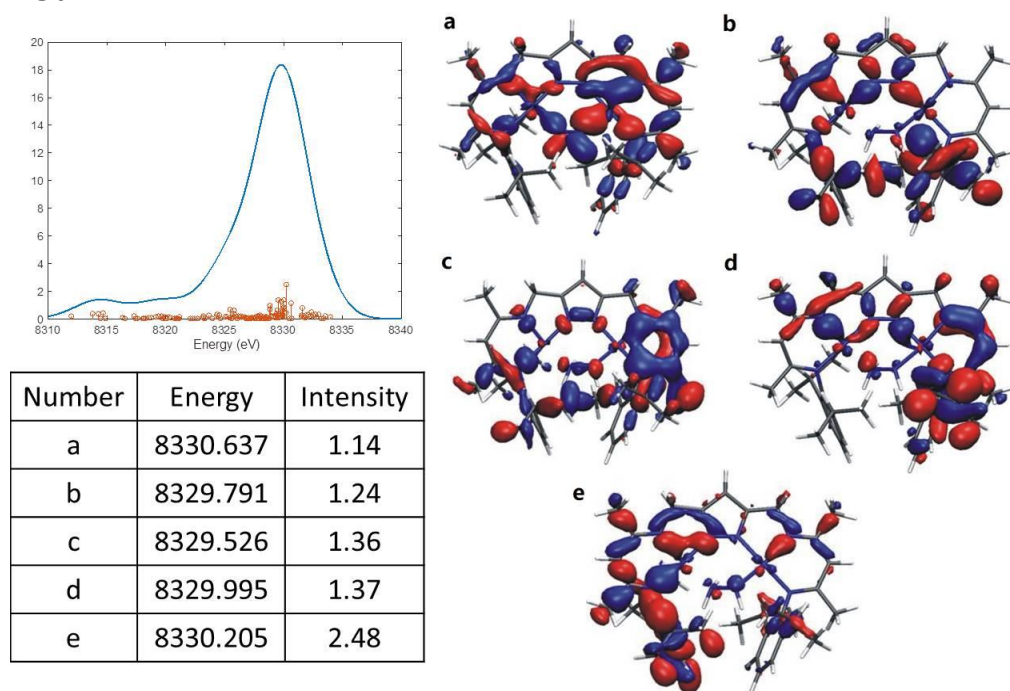


Figure 164: Calculated V2C spectrum of **27** with the molecular orbitals that strongly contribute to the observed transitions.

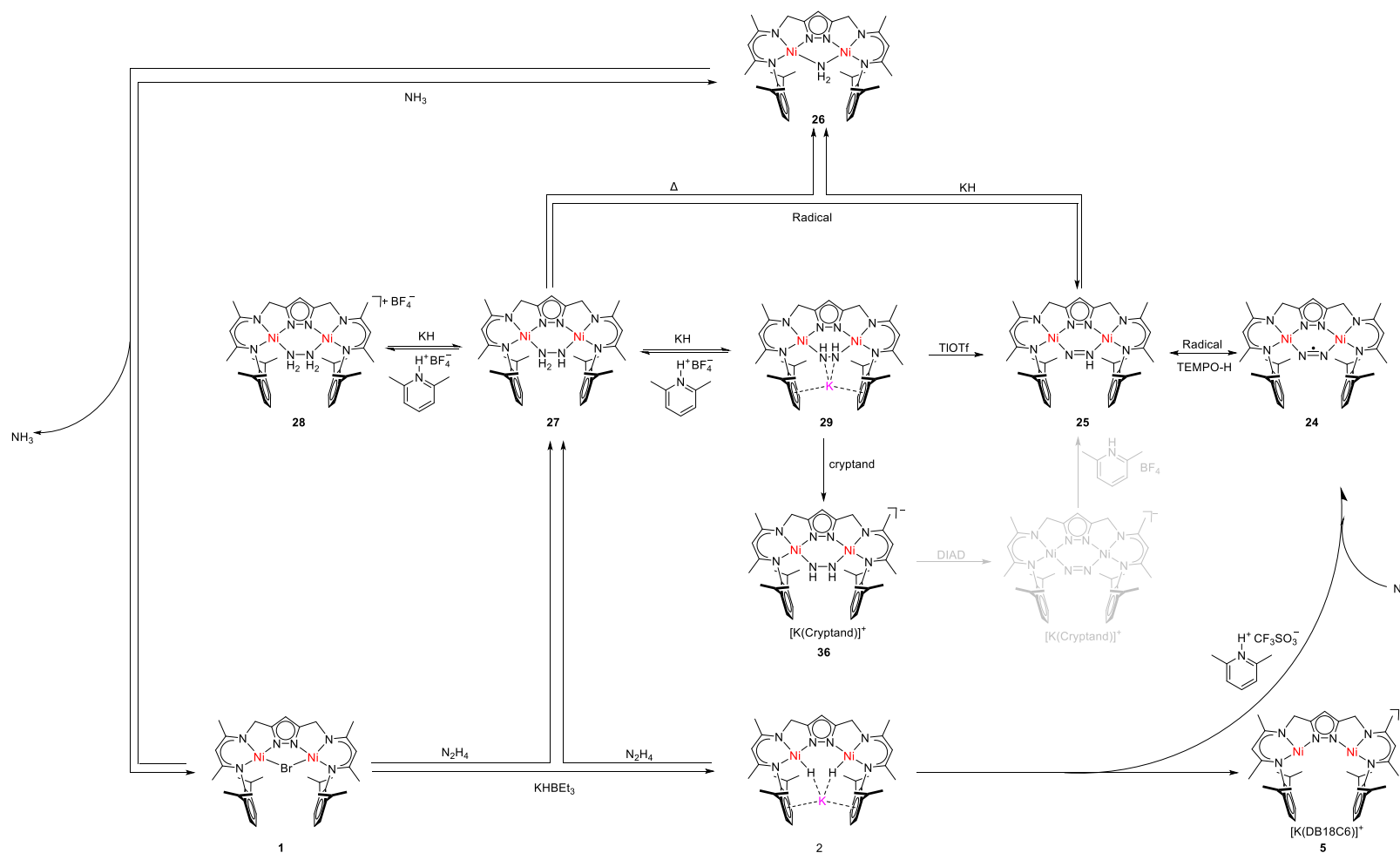
Table 41: Parameters from Fits to experiments XES of Main Line and V2C using 6 peaks to model the V2C for **24**, **25** and **27**.

	24	25	27
Peak 1 (eV)	8321.5	8329.84	8329.53
Peak 1 int.	1.18	1.78	1.36
Peak 2 (eV)	8326.9	8329.89	8329.79
Peak 2 int.	1.87	1.99	1.24
Peak 3 (eV)	8329.9	8329.91	8329.99
Peak 3 int.	1.86	1.87	1.37
Peak 4 (eV)	8330.0	8330.07	8330.21
Peak 4 int.	3.14	2.02	2.48
Peak 5 (eV)	8330.7	8330.26	8330.64
Peak 5 int.	1.59	1.58	1.14
Peak 6 (eV)	8332.9	8334.18	-
Peak 6 int.	1.04	1.51	-

In summary, the individual transitions are plotted as sticks below the envelopes. For two reasons it is difficult to analyze the spectrum in terms of orbital populations. Firstly, it is clear that the valence to core region is comprised of many individual transitions, so the spectrum cannot be attributed to a single orbital. Moreover, looking at some of the most intense transitions reveals that the underlying orbitals are very delocalized. Consequently it is difficult to ascribe intensity to particular orbital types i.e. N p-orbitals, but the XAS spectra and the K_β main-line spectra are consistent with low spin Ni(II).

8.9 Summary

In summary, the monoanionic [N₂]⁻ radical complex was isolated from the dinitrogen insert into [L¹Ni₂(H₂)]⁻ species and characterized by x-ray diffraction and spectroscopy. In particular, the N₂⁻ anion does effectively facilitate the delivery of H-atoms to N₂ generating the N₂H⁻ bridging. Eventually the N₂H⁻ nickel complex easily produce NH₃ through chemical reduction. In addition, the demonstration that the [L¹Ni₂]⁻ cleft can accommodate the nitrogenous intermediates including N₂H₄, N₂H₃⁻, N₂H₂²⁻ (“naked” or within K⁺ diazene species) and that interconversion by chemical reduction or protonation. All the complexes and interconversion are shown in **Scheme 49**. The XAS spectra and the K_β mainline spectra for **24**, **25** and **27** are consistent with low spin Ni^{II} for all the complexes.



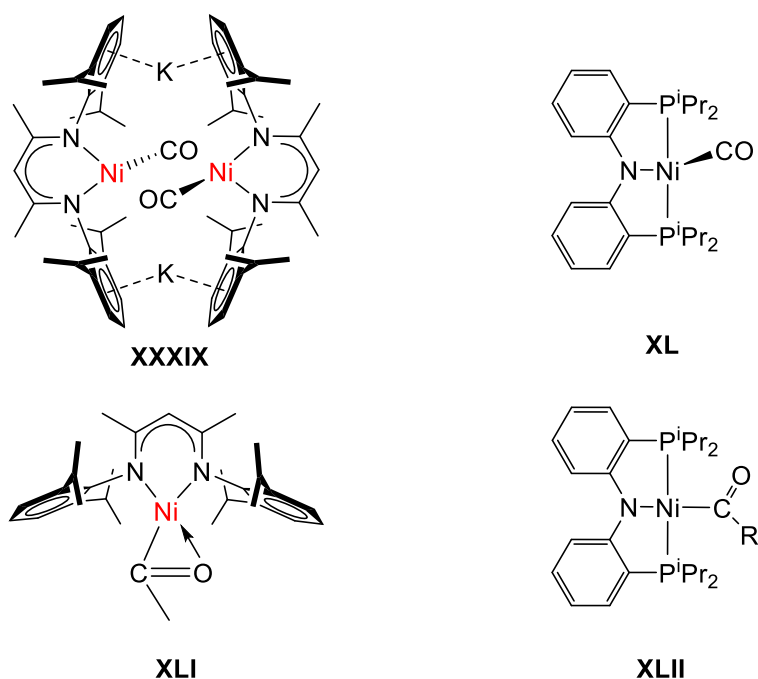
Scheme 49: Interconversion in a range of the N_xH_y. (The gray part is still ongoing)

Chapter 9 CO activation

Abstract: A new nickel carbonyl has been realized using the $[\text{N}_2]^-$ monoanionic radical dinuclear nickel(II) complex (**29**) with carbon monoxide at RT. Interestingly, the carbon monoxide has some $[\text{CO}]$ character and characterized by x-ray diffraction, IR-, EPR- spectroscopies and DFT calculation.

9.1 Introduction

Carbon monoxide is a key natural small molecule utilized in various organometallic reactions. In fact, nickel mono-carbonyl species are relatively uncommon and their reactivity is therefore still unexplored comprehensive. Ni^I-CO species have been proposed as potential active species in the so-called “paramagnetic mechanism”.^[130] However, the chemical validity has not been evaluated in terms of the reactivity of the monovalent nickel mono-carbonyl adducts. Several nickel carbonyl complexes and their reactivity were reported by the *Limberg*^[131,132] and *Lee*^[133], respectively (**Scheme 50: XXXIX - XLII**).

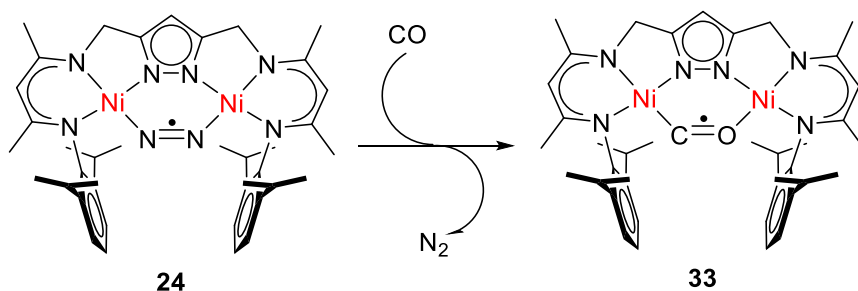


Scheme 50: Selected examples of Ni-CO complexes and acetyl-coenzyme synthase (ACS) catalysis .^[131-133]

Complex **XXXIX** was obtained from CO with mixed-valence nickel hydride complex in THF. The trigonal planar coordinated Ni centers hold by two potassium ions. The CO absorption is at far lower wave number (1772, 1754 cm⁻¹).^[131] Considering the low coordination number and oxidation state of the nickel central, the new type Ni-CO unit seemed ideal for the CODH/ACS catalysis. A new

$\text{C}(\text{O})\text{CH}_3$ species (**XLI**) was obtained from the MeI with **XXXIX** at RT. The $\text{C}(\text{O})\text{CH}_3$ resonance is at 243.8 ppm in the ^{13}C NMR spectrum, which is characteristic for η^2 -acetyl ligands. And the CO and isotopic $^{13}\text{C}\text{O}$ absorption is at 1584 cm^{-1} and 1545 cm^{-1} in the infrared spectroscopy spectrum, respectively. [132] In 2014, Lee reported three different oxidation state of nickel carbonyl species (**XL**), [133] formally +2, +1 and 0. The reactivity of these three nickel carbonyl species with MeI was examined to compare and contrast the C-C bond formation (**XLII**).

9.2 Synthesis carbon monoxide radical



Scheme 51: Synthetic route for **33**.

In order to establish a new nickel carbonyl species, an experiment was conducted from **2** with CO at 50°C directly. But ^1H NMR spectroscopy indicates that final product with more than three species. Unfortunately, the analysis data of the mixture are not allowed us to figure out exactly what they are. Since the $[\text{N}_2]^-$ monoanionic radical compound isolated with impressive yield, it is an opportunity to do the carbon monoxide activation from $[\text{N}_2]^-$ species.

Treatment of a solution of $[\text{N}_2]^-$ monoanionic radical complex in THF with CO (priority dried under concentrated H_2SO_4) at -78°C results a color change from brown-red to wine-red in 1 hour. Its UV-Vis spectrum (**Figure 165**) displays a similar band to **33**, attributing that the CO has similar electron structure of N_2 .

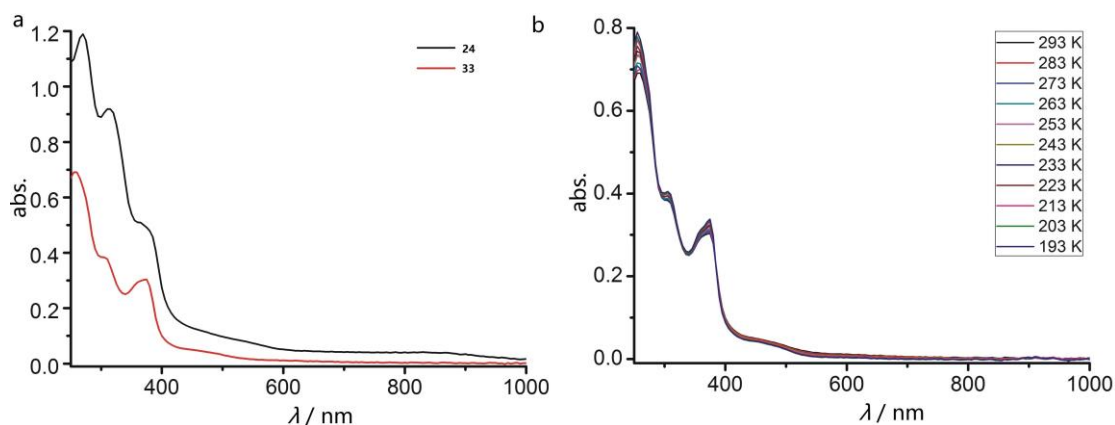


Figure 165: (a) UV-vis spectra of **24** and **33** in THF solution; (b) Variable temperatures UV-vis spectra of complex **33** in THF solution.

IR spectroscopy was employed since the UV-Vis spectroscopy identified the new species unclearly. In the IR spectrum, three bands at 1958, 1879 and 1735 cm^{-1} (**Figure 166a**) were observed for the crude product, which are different from $[\text{N}_2]^-$ species of 1896 cm^{-1} . But only one band at 1735 cm^{-1} (**Figure 166b**) for **33** was observed in crystalline material in IR spectrum. To confirmed its assignment of $\nu(\text{CO})$, the ^{13}C isotopologue CO was used to synthesize **33**. Two medium bands at 1912 and 1837 cm^{-1} ($\nu(^{12}\text{CO}) - \nu(^{13}\text{CO}) = 46/42 \text{ cm}^{-1}$) for crude products (**Figure 167a**) and 1691 cm^{-1} ($\nu(^{12}\text{CO}) - \nu(^{13}\text{CO}) = 44 \text{ cm}^{-1}$) (**Figure 167a**) band for microcrystalline material were observed. It indicates that the three bands are all belongs to different CO molecule. According the DFT calculated IR spectrum of **33**, the $[\text{CO}]^-$ (**Figure 168**) monoanionic radical stretching located at 1760 cm^{-1} , which is similar to the experimental data of 1735 cm^{-1} (**Table 42**). Therefore, I believed that at least two different species were generated in this reaction.

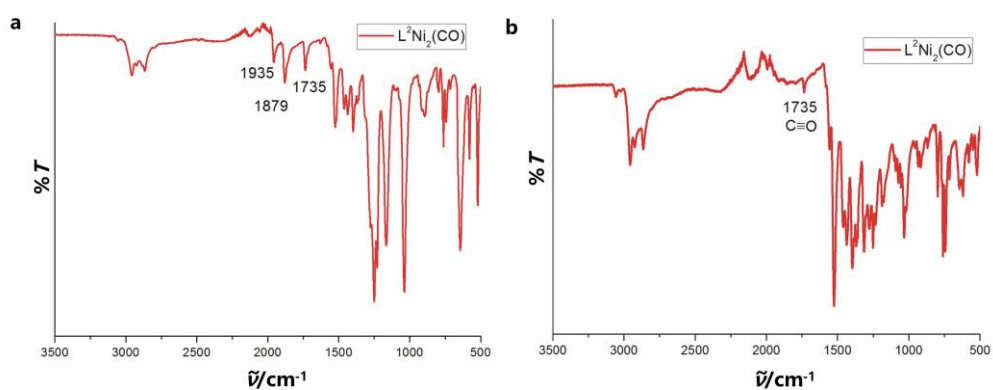


Figure 166: IR spectrum of **33** of ^{12}CO in crude and microcrystal materials.

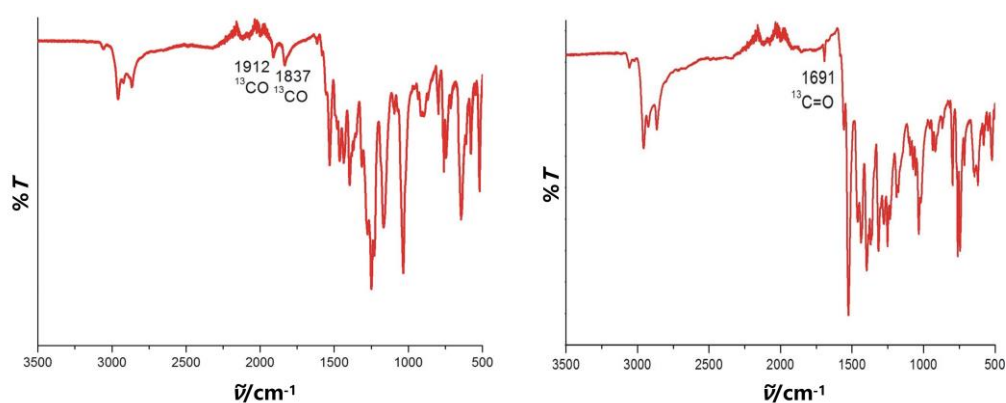


Figure 167: IR spectrum of **33** of ^{13}CO in crude and microcrystal materials.

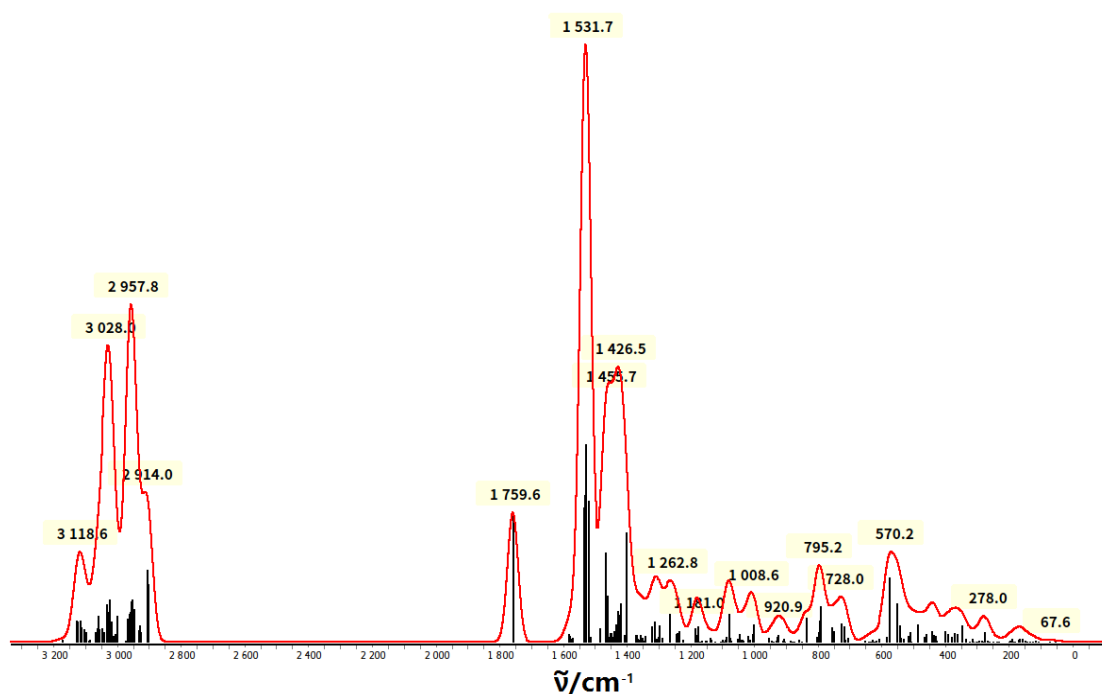


Figure 168: Calculated IR spectrum of **33**.

Table 42: $\nu(\text{C}\cdots\text{O})$ (IR) for **33**.

	$\nu(^{12}\text{C}-^{16}\text{O})/\text{cm}^{-1}$	$\nu(^{13}\text{C}-^{16}\text{O})/\text{cm}^{-1}$	$\Delta\nu/\text{cm}^{-1}$
Exp	1735	1693	42
DFT	1760	1720	40

Nevertheless, orange single crystals suitable for x-ray diffraction were obtained by layering hexane or pentane on a solution of **33** in THF -30°C . The molecular structure of **33** is shown in **Figure 169** and selected bond lengths (\AA) and angles ($^\circ$) are listed in **Table 43**. **33** crystallizes in the monoclinic space group $P2_1/c$ with four molecules in the unit cell. As shown in **Figure 169**, an almost planar six-membered $\{\text{N}_2\text{Ni}_2\text{CO}\}$ ring was formed by the nickel center, pyrazolate and carbon monoxide ligands. Both metal centers are coordinated in an expected square-planar fashion as was the case for the previously mentioned complexes containing nitrogen based bridging ligands. And the distance of the two nickel and torsion angle of Ni-C-O-Ni are $3.914(5) \text{\AA}$ and $9.077(6)^\circ$, respectively. The bond distance of carbon monoxide of $1.200(4) \text{\AA}$ is only slightly shorter than the doubly bridging CO 1.22\AA and longer than that in free CO molecule (1.128\AA) [134]. Its longer than the dinitrogen ligand bridged of **24**.

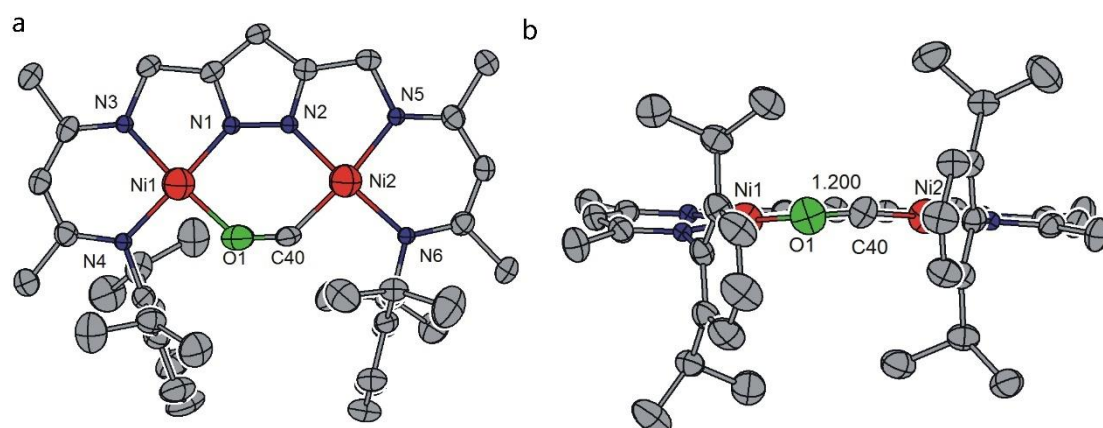


Figure 169: Molecular structure (50% probability thermal ellipsoids) of **33**. All hydrogen atoms omitted for clarity.

Table 43: Selected bond lengths (Å) and angles (°) for **33**.

Atoms	Bond lengths	Atoms	Bond angles
Ni1-N1	1.850(2)	N1-Ni1-N3	83.83(10)
Ni1-N3	1.881(2)	N1-Ni1-O1	89.96(10)
Ni1-O1	1.891(3)	N3-Ni1-O1	171.08(11)
Ni1-N4	1.900(2)	N1-Ni1-N4	175.97(10)
Ni2-C40	1.860(3)	N3-Ni1-N4	94.72(10)
Ni2-N2	1.866(2)	O1-Ni1-N4	91.89(10)
Ni2-N5	1.922(2)	C40-Ni2-N2	89.94(11)
Ni2-N6	1.923(2)	C40-Ni2-N5	172.06(11)
C40-O1	1.200(4)	N2-Ni2-N5	82.85(10)
Ni1...Ni2	3.914(5)	C40-Ni2-N6	93.14(11)
		N2-Ni2-N6	176.65(10)
		N5-Ni2-N6	94.15(10)
		C40-O1-Ni1	136.2(2)
		O1-C40-Ni2	136.2(2)
		Ni1-C-O-Ni2	9.077(6)

The two nickel atoms adopt d^8 square planar configuration, it indicates that the unpaired electron stay in the CO ligand rather than nickel. To our best knowledge, this is the first $[\text{CO}]^-$ monoanionic radical complex and characterized by x-ray diffraction. The X-band EPR measurement in a frozen THF at 154 K of **33** in crystalline material reveals a paramagnetic ground state with spin of $S = 1/2$. The elaborate discussion of EPR spectrum needs more professional understanding.

33 has been characterized by ESI-MS spectroscopy in a THF solution as well. The positive ion ESI-MS of **33** in THF solution shows three dominating peaks for the ions, deriving from $[\text{L}^1\text{Ni}_2]^+$ ($m/z = 723.52$), $[\text{L}^1\text{Ni}_2(\text{COH})+\text{H}]^+$ ($m/z = 751.46$) and $[\text{L}^1\text{Ni}_2(\text{COH})+\text{K}]^+$ ($m/z = 789.31$). When complex **33** prepared with isotopically labelled ^{13}CO , the mass peak corresponding to **33** shifted to m/z 752.38 $[\text{L}^1\text{Ni}_2(^{13}\text{COH})+\text{H}]^+$ (**Figure 170**). This shift is one mass unit upon substitution of ^{12}CO with ^{13}CO indicates that complex contains a CO unit.

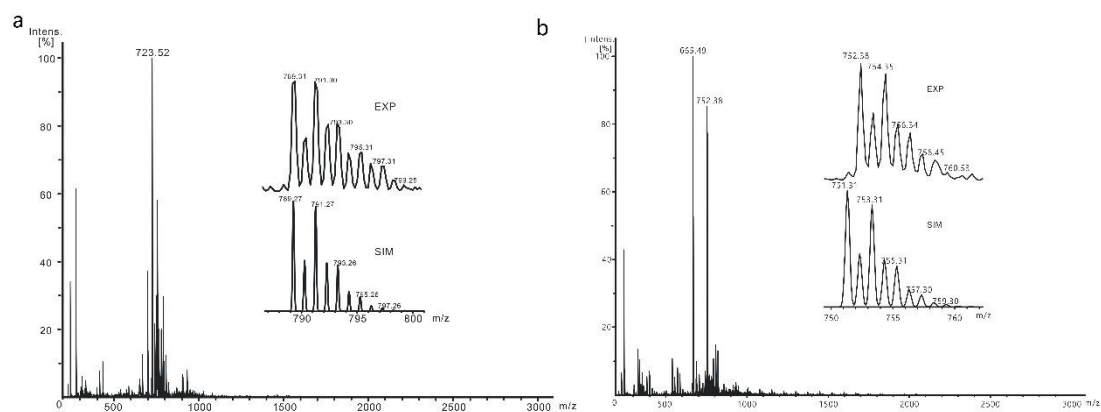


Figure 170: (a) ESI-MS ion spectrum of **33** and (b) **33**- ^{13}C O in THF; (Inset) Experiment (upper) and Simulated (lower) isotope distribution pattern for the peak pattern around $m/z = 789.31$ for the $[\text{L}^1\text{Ni}_2(^{12}\text{COH})+\text{K}]^+$ and around $m/z = 752.38$ characteristic for the $[\text{L}^1\text{Ni}_2(^{13}\text{COH})+\text{H}]^+$.

The electronic nature of **33** as suggested by its geometric structure was confirmed by DFT calculations (**Figure 171**). The energy – minimized DFT-calculated structure of **33** is in good agreement with that obtained by x-ray diffraction. According the DFT calculation, the bond length of CO unit of 1.184 Å is slightly shorter than the experiment data (**Table 44**). However, the distance of the two nickel(II) ions from DFT of 4.023 Å is longer than the experiment data. The HOMO of **33** from DFT calculation reveal that unpaired electron principally located on the Ni-C system. The spin density of Ni1 and Ni2 are 0.138 and 0.422, respectively. And the spin density of O and C are 0.010 and 0.338, respectively.

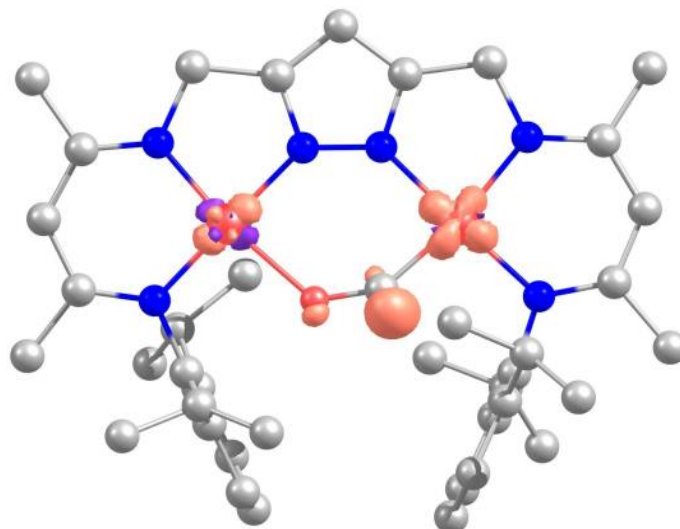
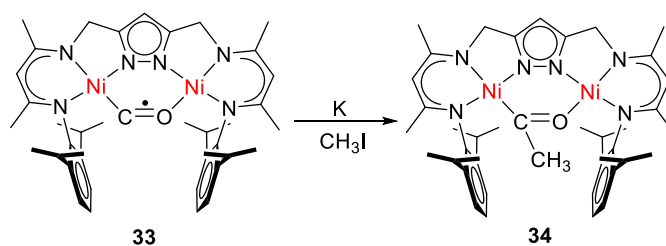


Figure 171: Spin density plot of **33**. Mulliken Spin Population: Ni1 = 0.137693, Ni2 = 0.421986, O = 0.009731, C = 0.337647.

Table 44: Selected distances (Å) and angles (°) for **33**.

	$d(\text{C-O}) / \text{Å}$	$d(\text{Ni} \cdots \text{Ni}) / \text{Å}$	$\varphi(\text{Ni-C-O-Ni}) / ^\circ$
Exp	1.200	3.914	9.1
DFT	1.184	4.023	9.1

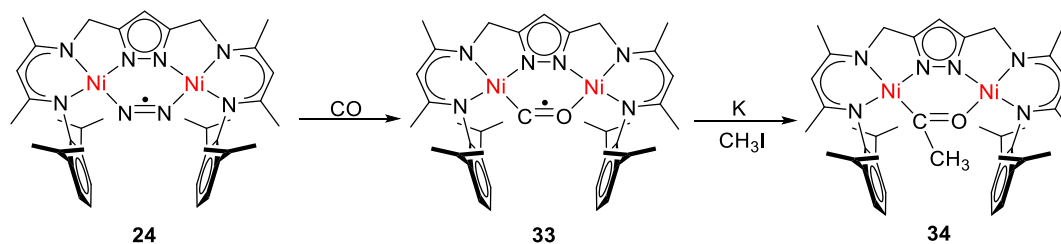
■ Reactivity



Scheme 52: Reactivity towards MeI.

Complex **33** does not show any reactivity toward iodomethane directly. However, in presence of K, complex **33** shows reactivity towards MeI. Treatment of **33** with MeI in the presence of K results in a color change from brown-red to orange (**Scheme 52**). The crude product has three bands at 1993, 1842 and 1626 cm^{-1} in IR spectrum (**Figure A56**). Unfortunately, all crystallizing attempts for x-ray diffraction failed.

9.3 Summary



Scheme 53: Activation of carbon monoxide and methylation of the $[\text{CO}]^-$ radical.

In summary, we have reported the synthesis and characterization by x-ray diffraction and IR, MS, EPR spectroscopies of the first monoanionic $[\text{CO}]^-$ radical complex. The reactivity of the remarkable $[\text{CO}]^-$ radical species with iodomethane was examined (**Scheme 53**). Ongoing works are focusing on methoxide and methylation of the $[\text{CO}]^-$ radical complex.

Chapter 10 Metal-ligand Cooperation in C-H and H₂ Activation and Interconversion between Mono- and Dihydride Dinickel(II) Complexes and Reactivity

Abstract: A new compartmental ligand scaffold H_3L^2 ($\text{L}^2 = \{\text{NC}(\text{Me})\text{C}(\text{H})\text{C}(\text{Me})\text{NC}_6\text{H}_3(\text{Ph})_2(\text{CH}_2)\}_2(\text{C}_3\text{N}_2\text{H})^{3-}$) was synthesized and gave a series of Ni-H complexes, which are isolated after reacting the precursor $[\text{L}^2\text{Ni}_2(\mu\text{-Br})]$ with MHBET_3 ($\text{M} = \text{K}$ and Na). Surprisingly, only monohydride dinickel complex (**40**) was obtained when the alkali metal is K^+ . And mono- and di-hydride mixture complexes were observed in the ^1H NMR spectroscopy and were characterized by x-ray diffraction once the alkali is Na^+ . Monohydride complex easily transfers to dihydride complex under H_2 atmosphere. Reactivity of these Ni-H species towards H_2O and Lewis acid were studied.

10.1 Introduction

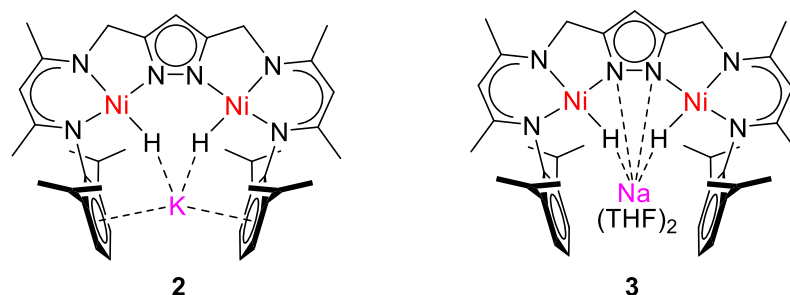


Figure 172: Dinickel dihydride complexes with different alkali metal (K^+ , Na^+). [11b]

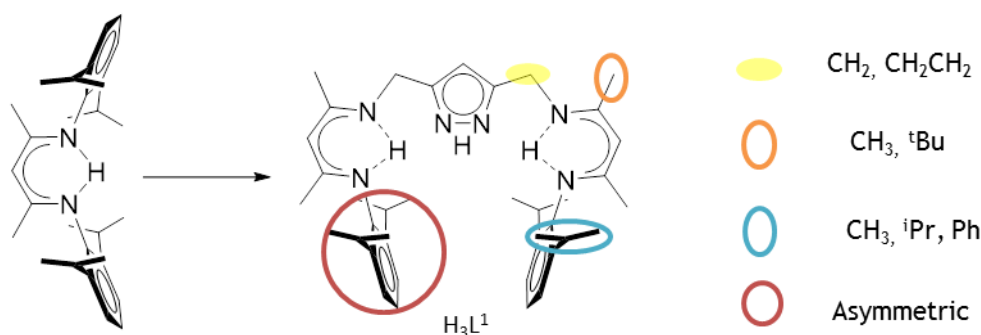
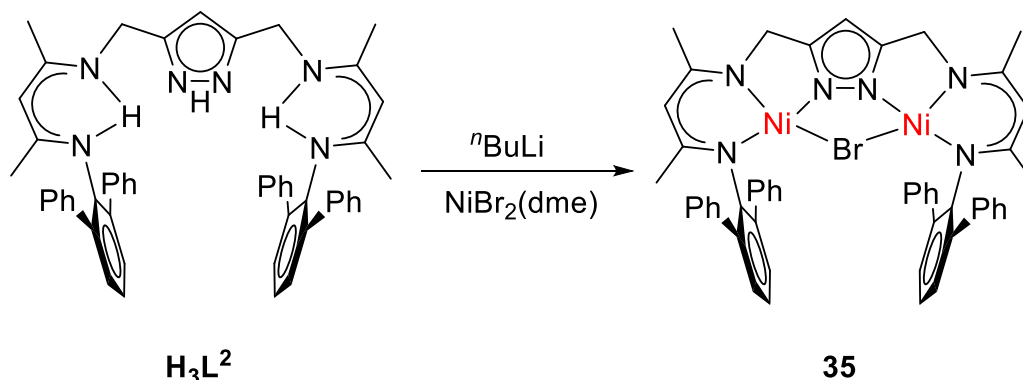


Figure 173: Ligand H_3L^1 was employed in previous work, and new ligands system proposed for next stage.

We had previously shown that a series of dinuclear nickel(II) dihydride complexes (**Figure 172**) $M[L^1Ni_2^{II}(H_2)]$ ($M = Na$ and K), which are characterized by x-ray diffraction and exhibit pairwise H_2/D_2 exchange property. [11] In order to extend nickel chemistry, we chose to follow a different strategy in the next work, (i) elongation of the linkages between the central pyrazole; (ii) change bulky group in the backbone of β -diketiminato; (iii) introduced different group in the substitutes; (iv) linkage two different groups in the N-aryl substitutes. (**Figure 173**) In this chapter, a new phenyl substituent instead of isopropyl substituent has successfully done.

10.2 Synthesis of nickel bromide precursor

Scheme 54: Synthetic route for **35**.

The multistep synthesis of the new ligand **H₃L²**, starting from recently reported pyrazole building blocks, is described in the experimental section. ^[11b] As **H₃L¹** ligand, nickel bromide precursor was synthesized by the reaction of the **H₃L²** ($\text{L}^2 = \{[\text{NC}(\text{Me})\text{C}(\text{H})\text{C}(\text{Me})\text{NC}_6\text{H}_3(\text{C}_6\text{H}_5)_2(\text{CH}_2)]_2(\text{C}_3\text{N}_2\text{H})^{3-}\}$) with $[\text{NiBr}_2(\text{dme})]$ ($\text{dme} = 1,2\text{-dimethoxyethane}$) in the presence $n\text{BuLi}$ in THF solution at 50 °C in 56 % yield. The yields of **35** dropped to 12% when the reaction was preformed at RT. Suitable crystals for x-ray diffraction were obtained from the CH_2Cl_2 slow evaporation.

The molecular structure of **35** is shown in **Figure 174** and selected bond lengths (Å) and angles (°) are listed in **Table 45**. Two nickel centers are in an almost square-planar coordination environment and the distance of 3.781(7) Å in the two nickel atoms is slightly shorter than in **1** of 3.807(5) Å ^[11a]. The Ni1-Br1-Ni2 angle of 105.82(2)° is close to the valence angles for a tetrahedral coordination geometry (109.47°).

At room temperature, ¹H NMR spectrum of **35** in CD_2Cl_2 displayed a series of ligand peaks without apparent coupling (**Figure 175**). The positive ion ESI-MS of **35** in THF shows a prominent peak characteristic of the $[\text{35}+\text{H}]^+$ at 937.2. And the isotope patterns matched this simulated (**Figure A57**).

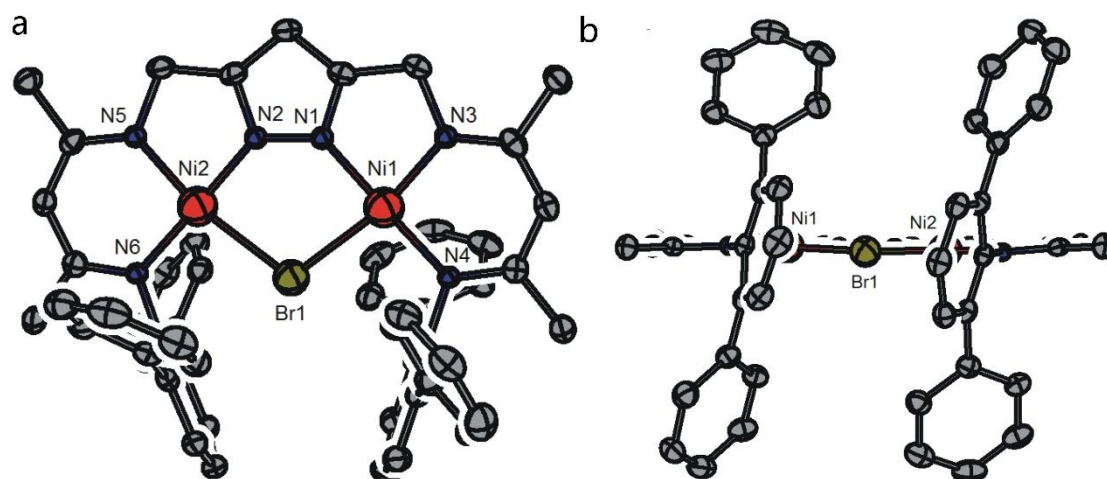


Figure 174: Molecular structure (50% probability thermal ellipsoids) of **35**. All hydrogen atoms have been omitted for clarity.

Table 45: Selected bond lengths (Å) and angles (°) for **35**.

Atoms	Bond lengths	Atoms	Bond angles
Ni1-N1	1.841(2)	N1-Ni1-N3	82.82(10)
Ni1-N3	1.879(2)	N1-Ni1-N4	178.75(10)
Ni1-N4	1.892(2)	N3-Ni1-N4	95.93(10)
Ni2-N2	1.836(2)	N1-Ni1-Br1	85.70(7)
Ni2-N5	1.877(2)	N3-Ni1-Br1	168.33(7)
Ni2-N6	1.885(2)	N4-Ni1-Br1	95.55(7)
Ni1-Br1	2.365(4)	N2-Ni2-N5	83.03(10)
Ni2-Br1	2.376(4)	N2-Ni2-N6	177.90(10)
Ni1...Ni2	3.781(7)	N5-Ni2-N6	95.36(10)
		N2-Ni2-Br1	85.83(7)
		N5-Ni2-Br1	168.84(7)
		N6-Ni2-Br1	95.76(7)
		Ni1-Br1-Ni2	105.821(15)

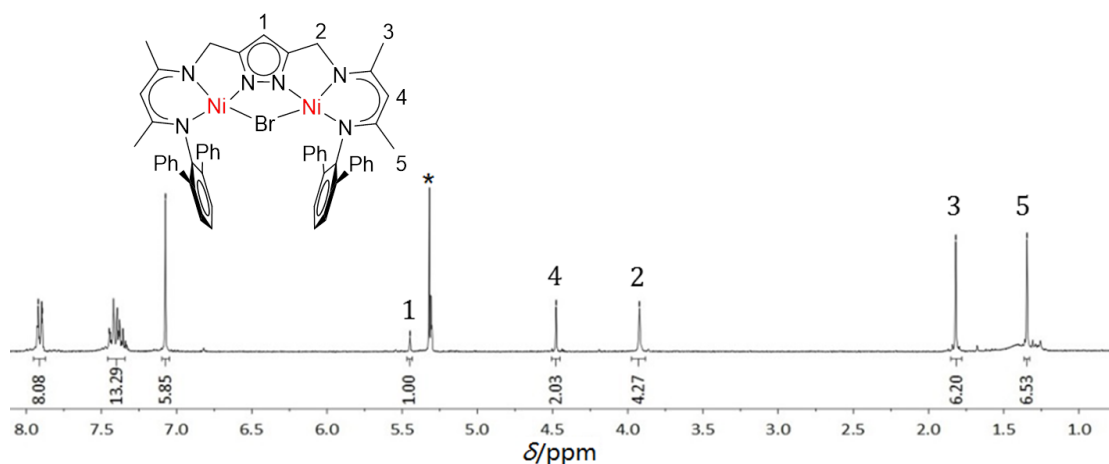
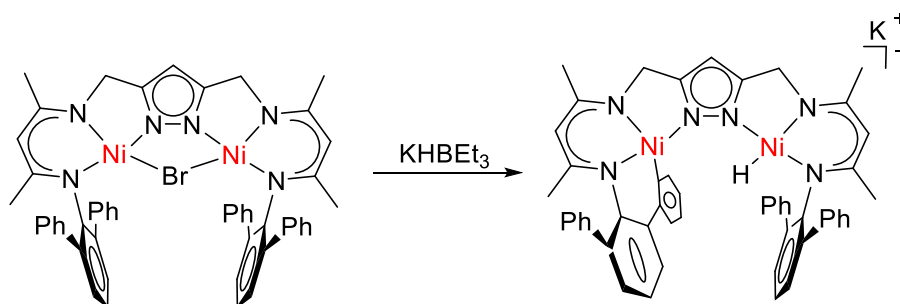


Figure 175: ^1H NMR (400 MHz) spectrum of **35** in CD_2Cl_2 . Residual solvents are marked with an asterisk (*).

10.3 Synthesis of bimetallic dinickel(II) monohydride complex



Scheme 55: Synthetic route for **36**.

35 represents a suitable precursor for the synthesis of the dinickel dihydride complex which is like the previous work from *Manz*.^[11a] Treatment of **35** with 2 equivalents KHBET_3 in THF solution results in a color change from green to red in 30 mins (**Scheme 55**). And the new species has a resonance at -26.12 with integration of one where is typically hydride ligand of diamagnetic nickel hydride resonate (from -6 to -26 ppm)^[25f] in the ^1H NMR spectrum (**Figure 176**). Except for the Ni-H resonance, the ^1H NMR spectrum indicates that the new species is an asymmetric complex, which the resonances shift signals at 4.43, 4.21, 4.06 and 4.00 ppm are corresponding to CH_2Pz groups and the integration of these four

peaks is 1:1:1:1. The $^1J_{\text{CH}}$ correlation of these peaks is 128.93 Hz.

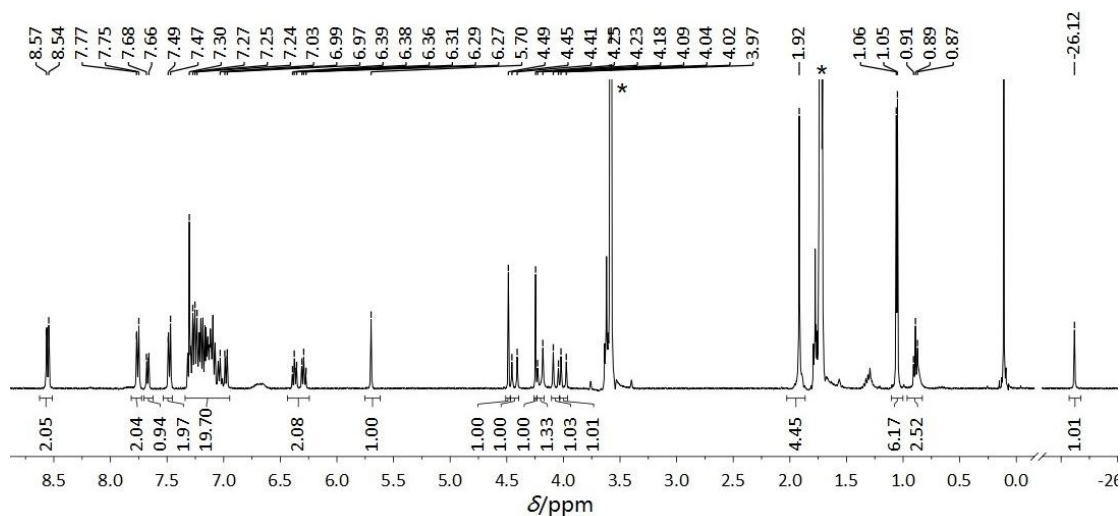


Figure 176: ^1H NMR (400 MHz) spectrum of **36** in THF-d_8 . Residual solvents are marked with an asterisk (*).

Suitable crystals for x-ray diffraction were obtained from pentane slow diffusion on a solution of **36** in THF at RT. The molecular structure of **36** is shown in **Figure 177** and selected bond lengths (\AA) and angles ($^\circ$) are listed in **Table 46**. The x-ray crystallography of **36** indeed confirms only one hydride ligand coordinate with Ni central, and the terminal hydride ligand stays in the Fourier map. One of the two nickel centers connected with hydride ligand is surrounded by its ligand in a distorted square-planar fashion. The Ni-H distance in **36** of 1.291(3) \AA is shorter than **2**, **3** and **4**. Whereas the second one is located in twist tetrahedrally coordination environment. The distance between the two nickel atoms of 4.266(7) \AA is much longer than the corresponding **35** (3.782 (7) \AA). Meanwhile, the nearby phenyl groups of side arm are subject to C-H oxidative addition to generate NiPh-(“NNN”). The structure of **36** is completed by one K^+ cation located by the intramolecular phenyl group from substitute, pyrazolate linked and the intermolecular phenyl group. A consequence of these K-arene/N contacts (2.78-3.28 \AA) involves a 1D chain formation. (**Figure 177c**).

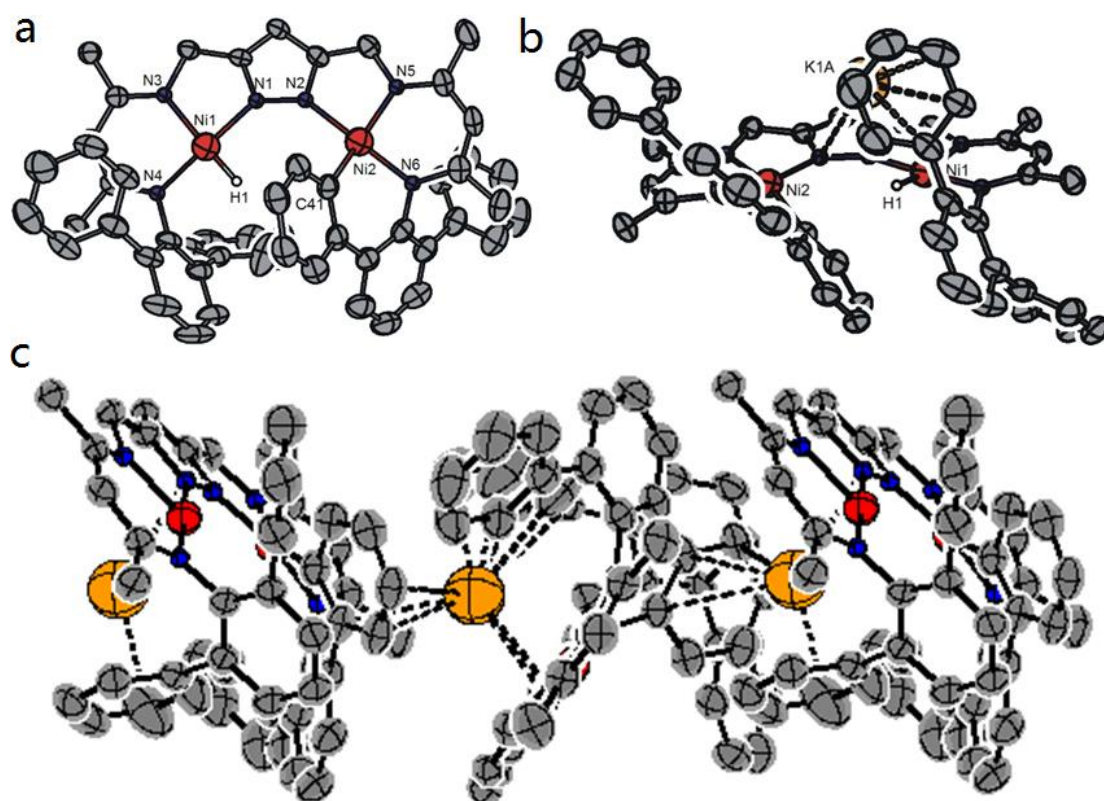
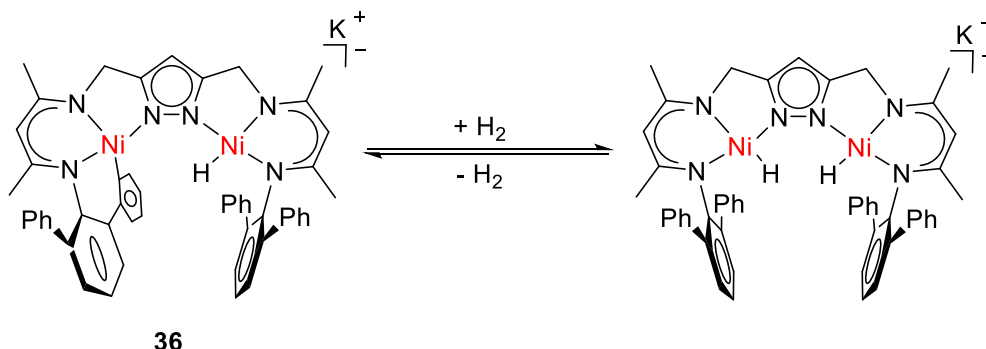


Figure 177: Molecular structure (50% probability thermal ellipsoids) of the anion of **36** (a, only one of two independent molecules shown), **36** (b) and 1D chain of **36** (c). Most hydrogen atoms omitted for clarity, except for the nickel-bound hydrides.

Table 46: Selected bond lengths (Å) and angles (°) for **36**.

Atoms	Bond lengths	Atoms	Bond angles
Ni1-N4	1.879(3)	N4-Ni1-N1	177.22(15)
Ni1-N1	1.910(3)	N4-Ni1-N3	95.71(14)
Ni1-N3	1.915(3)	N1-Ni1-N3	85.02(13)
Ni1-K1A	3.074(4)	N4-Ni1-K1A	112.35(13)
Ni2-N6	1.877(4)	N1-Ni1-K1A	64.88(13)
Ni2-C41	1.902(4)	N3-Ni1-K1A	101.8(4)
Ni2-N2	1.933(3)	N6-Ni2-C41	89.12(17)
Ni2-N5	1.936(4)	N6-Ni2-N2	167.15(14)
Ni2-K1A	3.835(2)	C41-Ni2-N2	98.58(16)
Ni1-H1	1.291(3)	N6-Ni2-N5	92.88(15)
Ni1...Ni2	4.266(8)	C41-Ni2-N5	158.55(17)
		N2-Ni2-N5	83.72(14)
		N6-Ni2-K1A	117.7(2)
		C41-Ni2-K1A	91.30(15)

N2-Ni2-K1A	52.3(2)
N5-Ni2-K1A	106.53(16)



Scheme 56: Preparation of dinuclear nickel(II) dihydride complex from **36**.

Treatment of **36** in THF- d_8 with 1 atm H_2 , 1H NMR spectrum did not show a new species generation. However, a dinuclear nickel(II) dihydride complex $KL^3Ni_2(H_2)$ can be obtained in a *J*-Young tube containing the monohydride bridge compound **36** with high pressure H_2 (≥ 3 atm) (**Scheme 56**). 1H NMR spectrum (**Figure 178**) of the new dihydride complex $KL^3Ni_2(H_2)$ revealed a lower field shifted from -26.12 ppm to -23.79 ppm, which is similar to complex **2**. [11] And the new $KL^3Ni_2(H_2)$ complex only exists under H_2 atmosphere.

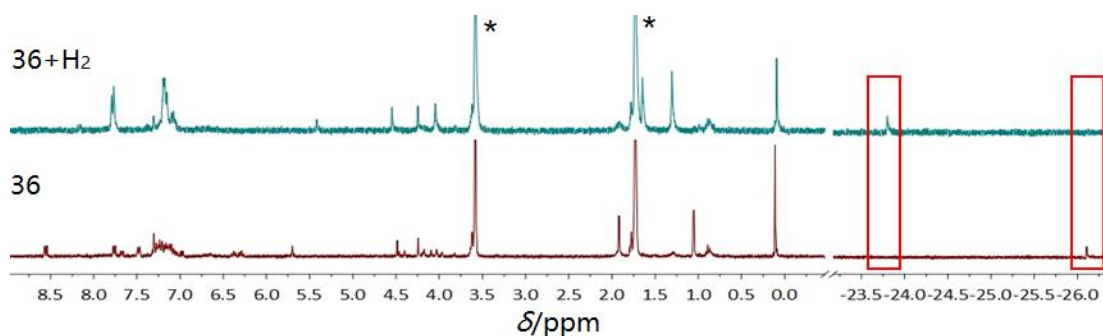
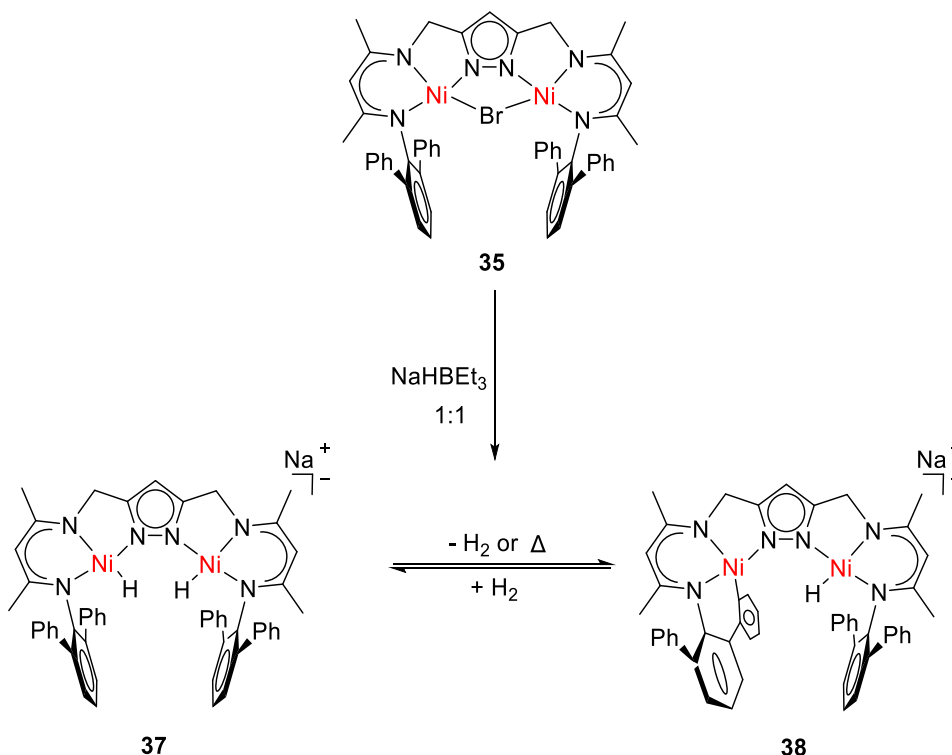


Figure 178: 1H NMR spectrum (300 MHz) of **36** with H_2 (3 atm) in THF- d_8 . Residual solvents are marked with an asterisk (*).

10.4 Synthesis of bimetallic dinickel(II) dihydride complex



Scheme 57: Preparation of **37** and **38** in one pot from **35** with NaHBET₃.

The alkali metals (**Na** and **K**) have led to great interest in investigations on the Ni-H coordination compounds in the H₃L¹ ligand. With this background in mind, we are interested in the fundamental hydride chemistry of the bulky ligand with different alkali metals. Upon addition of 2 equivalents NaHBET₃ to **35** processes two diamagnetic species (**Scheme 57**), **37** and **38**, in different ratios (1:1 or 2:3) depending on the reaction times. Fortunately, the coexistence of **37** and **38** in this case are confirmed by x-ray crystallographic analysis. Single crystals of **37** and **38** suitable for x-ray diffraction were obtained from Et₂O/THF and hexane/THF double solvent recrystallization systems, respectively.

It became obvious that, similar to the **36**, **37** is a monohydride nickel complex with Na cation. And, the x-ray crystallography shows that **38** is a bimetallic dinickel(II) dihydride complex as **3** with Na⁺ cation. **38** is highly soluble in non-polar solvents such as THF, suggesting that in solution it maintains the structure

in which the sodium is surrounded by arenes. The molecular structures of **37** and **38** in ORTEP diagram is shown in **Figure 179** and selected bond lengths (Å) and angles (°) are listed in **Table 47**. **38** crystallizes in the triclinic space group *P*-1. The two nickel central were coordinated in square-planar fashion, with the sum of 360.58° and 359.86°, respectively. The distance of the two nickel atoms of 4.057(6) Å is shorter than **2** and **3**. The sodium is coordinated by the two hydride ligands and two THF molecules.

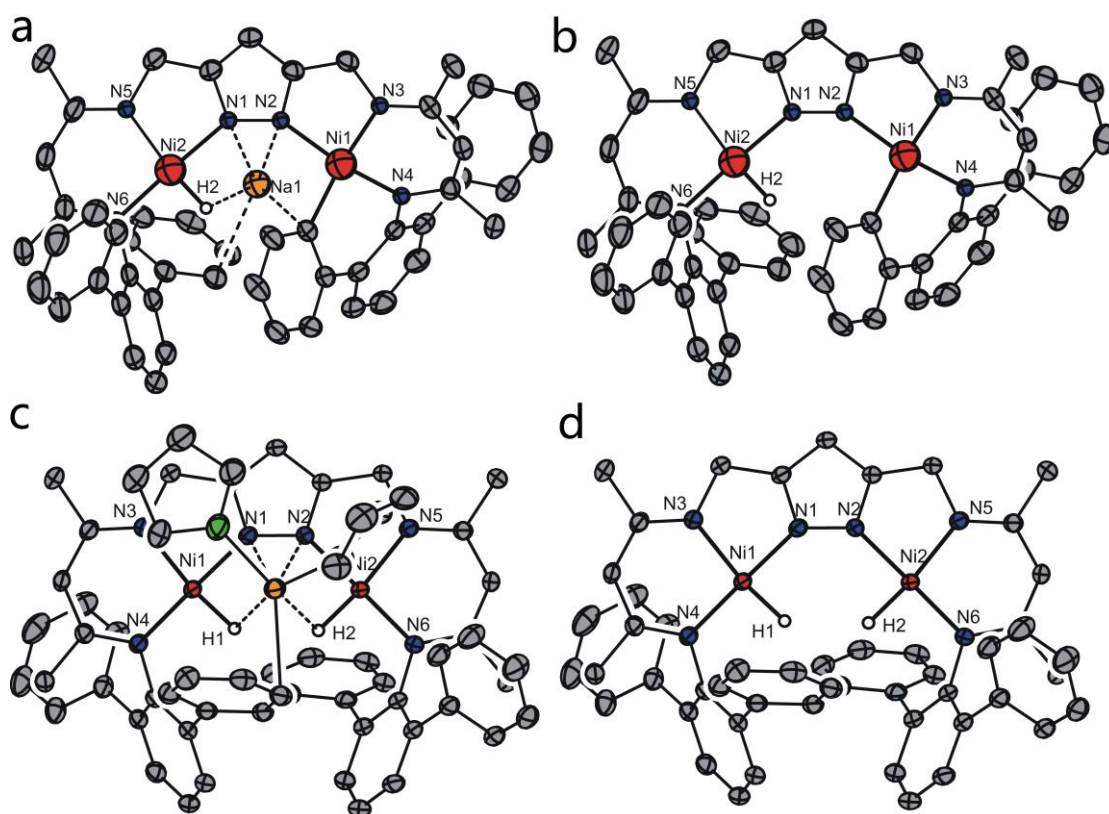


Figure 179: Molecular structure (50% probability thermal ellipsoids) **37** (a), **38** (c) and of the anion of **37** (b), **38** (d). Most hydrogen atoms omitted for clarity, except for the nickel-bound hydrides.

Table 47: Selected bond lengths (Å) and angle (°) for **38**.

Atoms	Bond lengths	Atoms	Bond angles
Ni1-N4	1.859(3)	N4-Ni1-N1	178.19(11)
Ni1-N1	1.863(3)	N4-Ni1-N3	96.62(10)
Ni1-N3	1.914(2)	N1-Ni1-N3	84.57(10)
Ni1-Na1	2.958(1)	N4-Ni1-Na1	117.82(8)
Ni2-N6	1.873(2)	N1-Ni1-Na1	60.38(8)
Ni2-N2	1.873(2)	N3-Ni1-Na1	115.13(8)
Ni2-N5	1.903(3)	N4-Ni1-H1	91.5(15)
Ni2-Na1	3.006(1)	N1-Ni1-H1	87.2(15)
Ni1...Ni2	4.057(6)	N3-Ni1-H1	170.0(14)
H1...H2	2.040(5)	Na1-Ni1-H1	55.5(14)
Ni1-H1	1.40(3)	N6-Ni2-N2	175.91(11)
Ni2-H2	1.46(3)	N6-Ni2-N5	96.25(11)
		N2-Ni2-N5	84.06(10)
		N6-Ni2-Na1	123.42(9)
		N2-Ni2-Na1	59.51(8)
		N5-Ni2-Na1	118.86(8)
		N6-Ni2-H2	91.6(11)
		N2-Ni2-H2	88.6(11)
		N5-Ni2-H2	168.9(11)
		Na1-Ni2-H2	50.0(11)
		H1-Na1-H2	50.24(1)
		N1-Na1-H1	53.52(9)
		N2-Na1-H2	56.09(7).

^1H NMR spectrum (under H_2 atmosphere) shows the pyrazolate ligand resonances and dihydride ligands, indicating C_{2v} symmetry in solution. And the dihydride ligands resonances are at -23.61ppm (**Figure 180**), slightly low shifted compared with complex $\text{KL}^3\text{Ni}_2(\text{H}_2)$ (-23.79ppm).

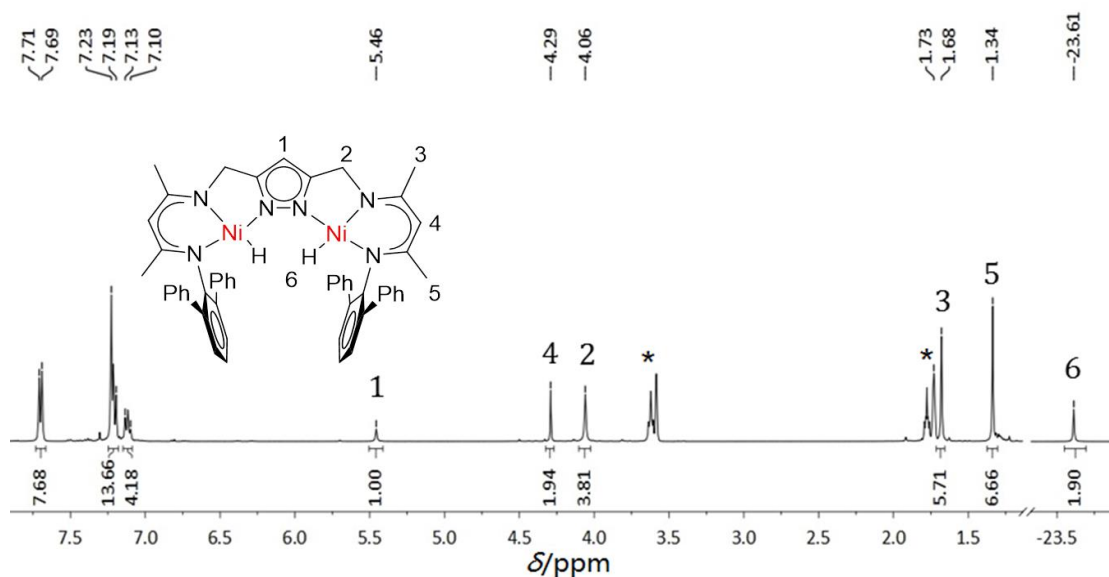
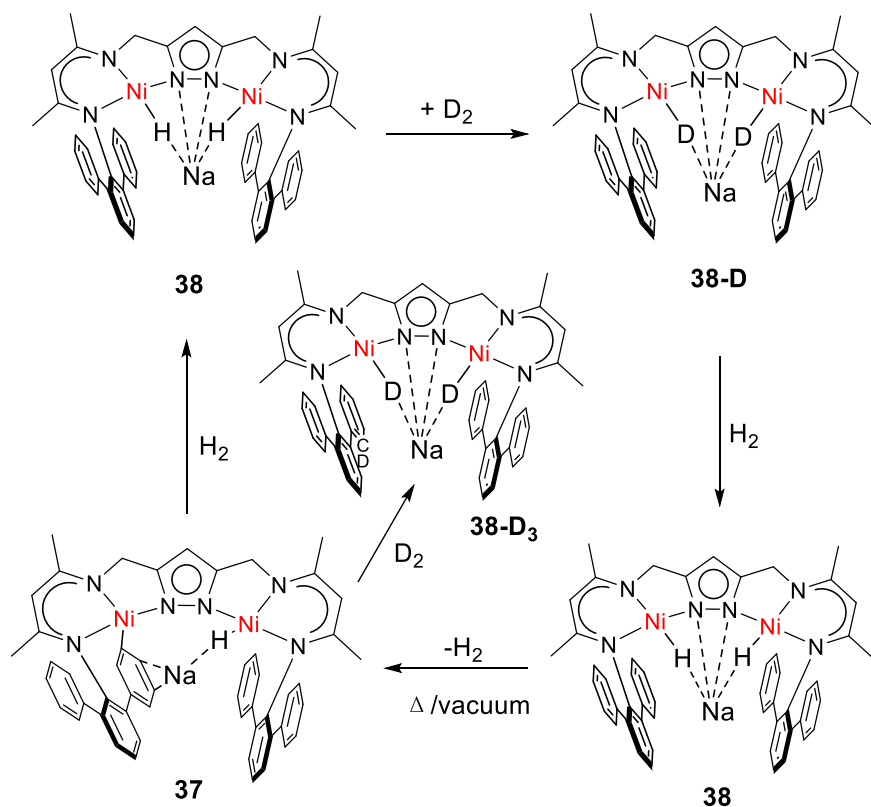


Figure 180: ^1H NMR spectrum (400 MHz) of **38** in THF-d_8 under H_2 . Residual solvents are marked with an asterisk (*).

Exposure of a solution of **38** in THF or THF-D_8 to a D_2 atmosphere led the color change from deep red to orange (**Figure 181a**). Meanwhile, H-D exchange mediated formation of the corresponding **38**. As shown in the ^1H NMR spectrum (**Figure 181a**), the hydride resonance of the new sodium complex is at -23.61 ppm. After exchange with D_2 , however, the ^2H NMR indicates that the hydride peak of -23.57 ppm is slightly different (-0.04 ppm) from the undeuteride **38** (**Figure 181b**). In addition, reaction of mixture with D_2 under the conditions yield $(\text{Ni-D})_2$ complex with incorporation of deuterium atom into the benzylic “arm”. It might be suggested that **37** is present in solution in equilibrium with **38** and is responsible for the unusual reactivity with H_2 .

And this reaction is reversed upon addition of H_2 to solutions of the deuterated complexes in THF. to **38**⁻ is most conveniently followed via ^2H NMR spectroscopy, which shows the disappearance of the signals for Ni-D around -24 ppm (concomitant for the appearance of Ni-H in the ^1H NMR spectrum) and the rise of a signal at 4.57 ppm originating from D_2 (**Figure 181**). Surprisingly, no HD formation is observed during the initial stages of the reaction.



Scheme 58: Possibility process route for the H₂-D₂ exchange of **38**.

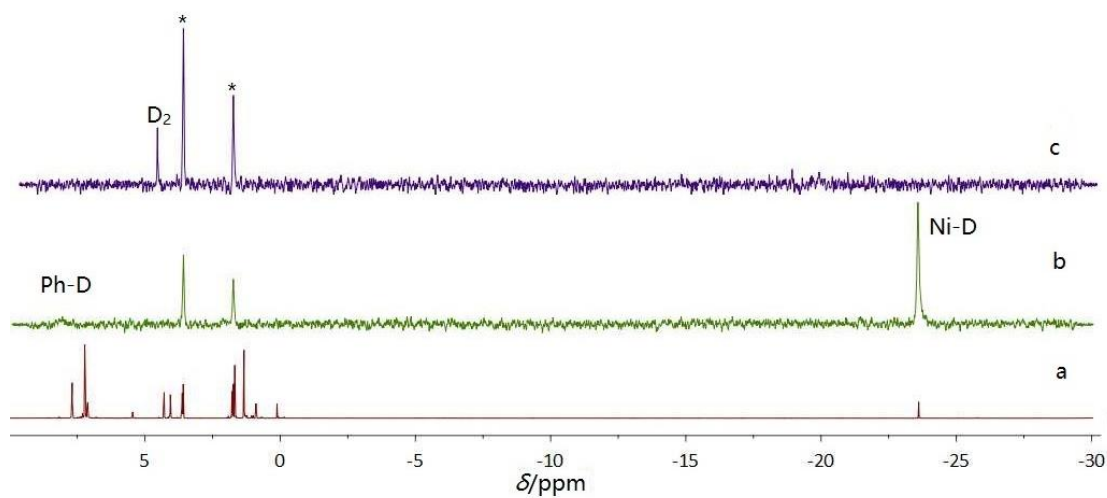
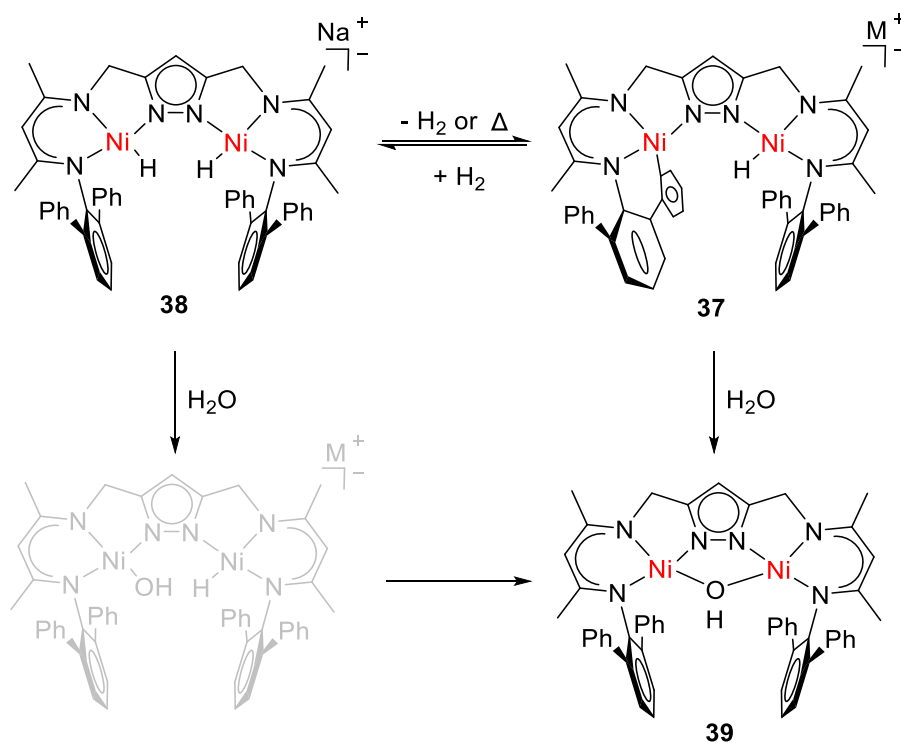


Figure 181: (a) ¹H NMR spectrum of **38** under H₂ atmosphere. (b) ²H NMR spectrum of **38**-D₂. (c) after the degassing sample was loaded with H₂, the deuterio-hydrido signal at -23.57 ppm disappeared and a new signal occurred at 4.57 ppm (D₂).

10.5 Reactivity towards water



Scheme 59: Reactivity towards H₂O of **37** and **38**.

In order to understand the relationship between nickel hydride complexes (**36**, **37** and **38**) and **39**, a ¹H NMR experiment with **38** and one equivalent of water in THF-d₈ was performed to reveal the formation of the intermediate. After the addition of water, **38** is consumed, as can be observed by the decrease of the characteristic hydride and pyrazolate resonance. At the same time, the characteristic at 6.06 ppm emerged alongside other resonance in the low field at -0.86 ppm. In addition, a characteristic for pyrazolate resonance at 5.63 ppm was observed (**Figure 183**).

A similar result was reported by *Manz*^[11a] for the reaction of **2** with water. The chemical shifts for the hydride ligand ($\delta\{^1\text{H}\} = 26.00$ ppm) and the hydroxo ligand ($\delta\{^1\text{H}\} = -2.07$ ppm) are comparable to the shifts observed for Na[L³Ni₂(OH)(H)] despite the fact that the two compounds are quite similar.

However, addition of one equivalent of water into a solution of **37** in THF- d_8 at room temperature led to color change from red to green immediately, and intensity gas was observed. ^1H NMR spectrum indicates that the new species is **39** without any intermediate formation. Suitable crystals for x-ray diffraction were obtained by layering hexane on a solution of **39** in THF in two days. The molecular structure of **39** is shown in **Figure 182** and selected bond lengths (\AA) and angles ($^\circ$) are listed in **Table 47**. **39** crystallizes in the monoclinic crystal space group $P2_1/c$ with six molecules in the unit cell. Hydroxyl complex is a diamagnetic and gives to sharp signals in the ^1H and ^{13}C NMR spectra in the common chemical shift range for the pyrazolate ligands. The bridging hydroxide protons resonate at $\delta = -6.06$ ppm in the ^1H NMR spectrum (**Figure 184**), and the $\nu(\text{O-H})$ stretching modes appears in the IR spectra at 3605 cm^{-1} (**Figure 185a**). After the addition of an excess (5 equivalents) of D_2O to the water free decayed **39** in THF- d_8 , the bridge hydroxide signal has vanished immediately and the $\nu(\text{O-D})$ stretching is at 2681 cm^{-1} ($\nu(\text{O-H})/\nu(\text{O-D}) = 1.35$).

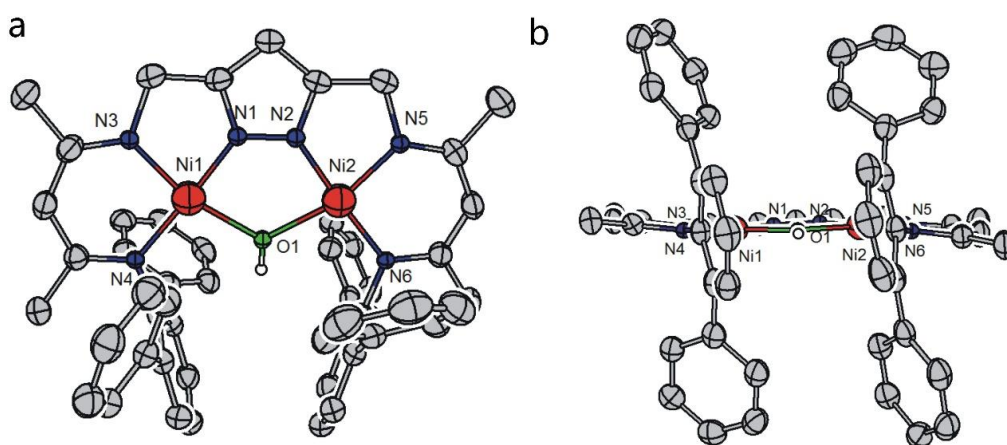
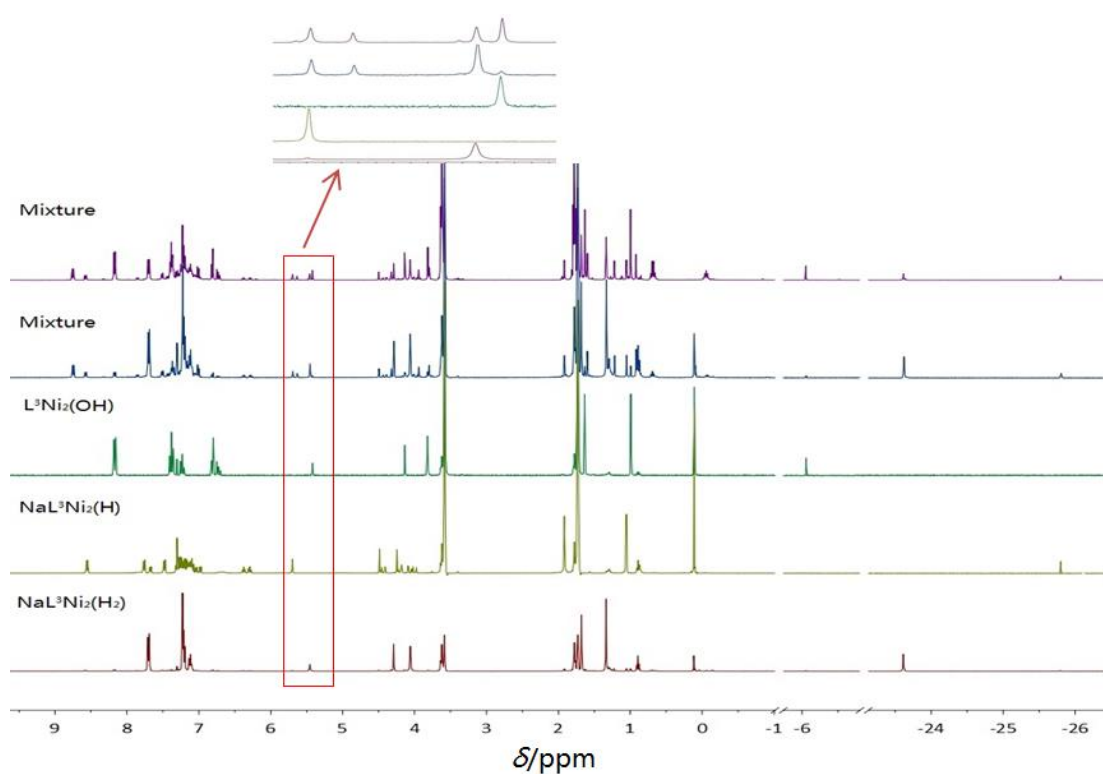


Figure 182: Molecular structure (50% probability thermal ellipsoids) of **39**. Most hydrogen atoms omitted for clarity, except for OH unit.

Table 48: Selected bond lengths (Å) and angles (°) of **39**.

Atoms	Bond lengths	Atoms	Bond angles
Ni1-N1	1.802(3)	N1-Ni1-N4	175.13(12)
Ni1-N4	1.884(2)	N1-Ni1-N3	81.41(12)
Ni1-N3	1.891(3)	N4-Ni1-N3	95.11(11)
Ni1-O1	1.973(2)	N1-Ni1-O1	82.67(10)
Ni2-N2	1.797(3)	N4-Ni1-O1	100.73(10)
Ni2-N6	1.883(2)	N3-Ni1-O1	164.06(11)
Ni2-N5	1.894(3)	N2-Ni2-N6	176.55(12)
Ni2-O1	1.977(2)	N2-Ni2-N5	81.28(11)
Ni1...Ni2	4.105(5)	N6-Ni2-N5	95.48(11)
		N2-Ni2-O1	82.66(10)
		N6-Ni2-O1	100.52(10)
		N5-Ni2-O1	163.74(10)
		Ni1-O1-Ni2	122.13(11)

**Figure 183:** Reactivity toward H₂O and monitoring this reaction by ¹H NMR.

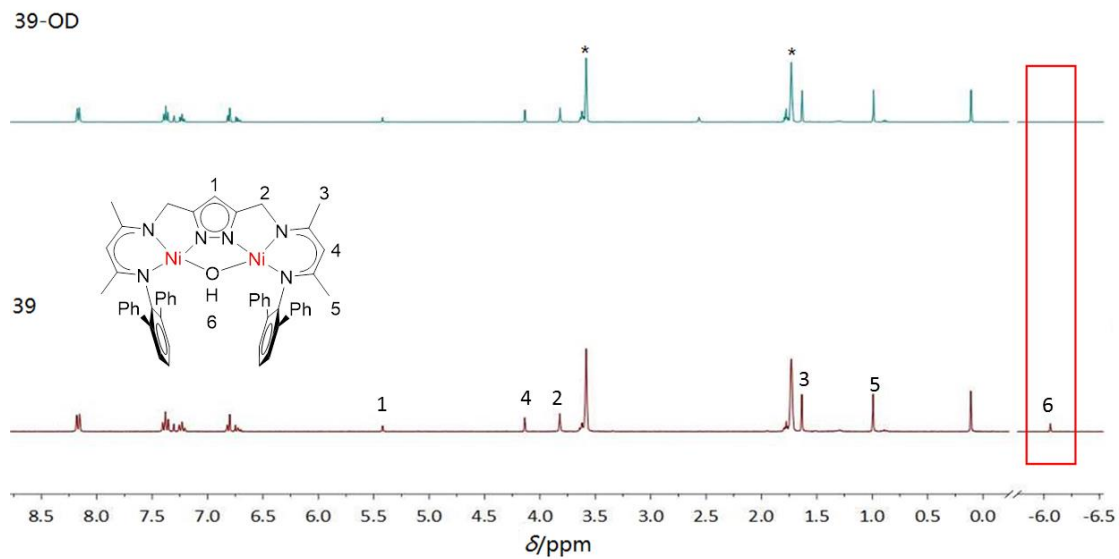


Figure 184: ^1H NMR spectrum (400 MHz) of **39** and **39-OD** in THF-d_8 . Residual solvents are marked with an asterisk (*).

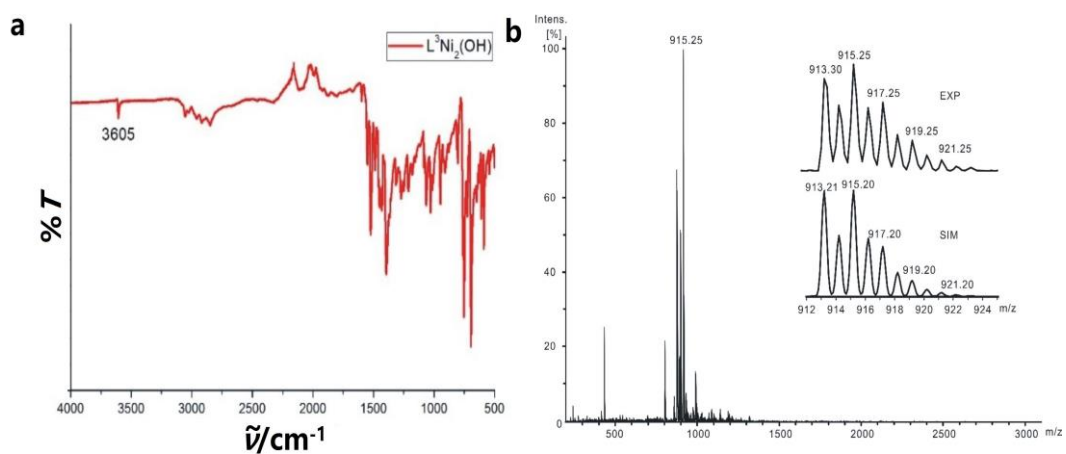
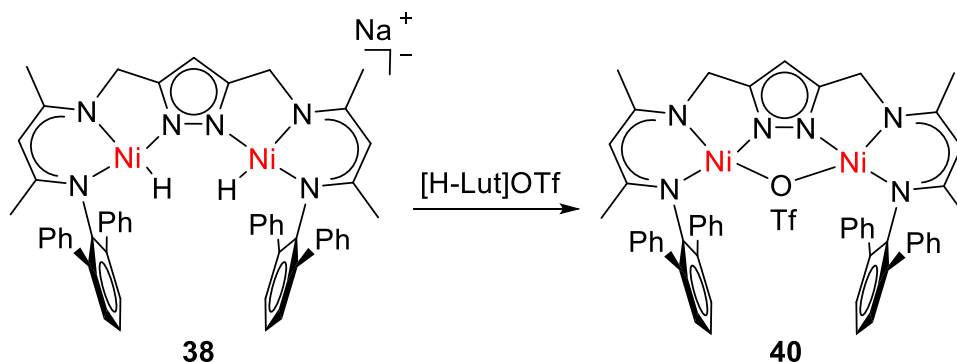


Figure 185: (a) IR spectrum in crystalline material and (b) ESI-MS (+) (in THF) of **39**.

10.6 Reactivity towards lutidinium triflate

Scheme 60: Synthetic route for **40**.

To better understand the influence of the substitute and the chemical properties of the dihydride and monohydride complex its reactivity toward the weak acid [H-Lut]OTf has been investigated also. Similar to the $\mathbf{H}_3\mathbf{L}^1$ ligand, we thought the **38** with [H-Lut]OTf in the presence of N_2 can generate dinitrogen bridge complex. However, upon addition of one equivalent of [H-Lut]OTf with dinickel monohydride and dihydride mixture in THF without any color change and no gas was observed during the reaction process (**Scheme 60**). In this reaction it is very easy to get hydroxide bridge complex. A similar reaction was happened in the *Limberg* and co-works which was using the diiron dihydride complex with [H-Lut]OTf. [20d]

Suitable crystals for X-ray diffraction were obtained from THF slow evaporation under hexane atmosphere. The triflate bridging compound was characterized by x-ray diffraction, ^1H and ^{13}C NMR, FT-IR, ESI-MS spectroscopy and elemental analysis (C, H and N). The molecular structure of **40** is shown in **Figure 186** and selected bond lengths (\AA) and angles ($^\circ$) are listed in **Table 49**. As shown in **Figure 186**, the two nickel centers were coordinated in square-planar fashion, with the sum of 359.95° and 361.25° , respectively. In this structure of **40**, each nickel center is held within an N,N-chelate of a β -diketiminato arm and oxygen from

triflate ligand. And the distance of the two nickel of 4.401 Å is longer than **35**.

To further confirm the identity, an NMR spectroscopic analysis has been performed. From ^1H and $^{13}\text{C}\{^1\text{H}\}$ NMR spectroscopy, the complex is diamagnetic and highly symmetric structure in the solution. In the ^1H NMR spectrum (**Figure 187**), a signal set for the protons of the ligand in the normal ranging field were observed that was characteristic for C_{2h} symmetrical diamagnetic nickel(II) complex. ^{19}F NMR spectrum (**Figure 188**) showed a signal at -77.81 ppm that is for the triflate ion. It indicates that the triflate is not coordinated to the nickel central in the solution state.

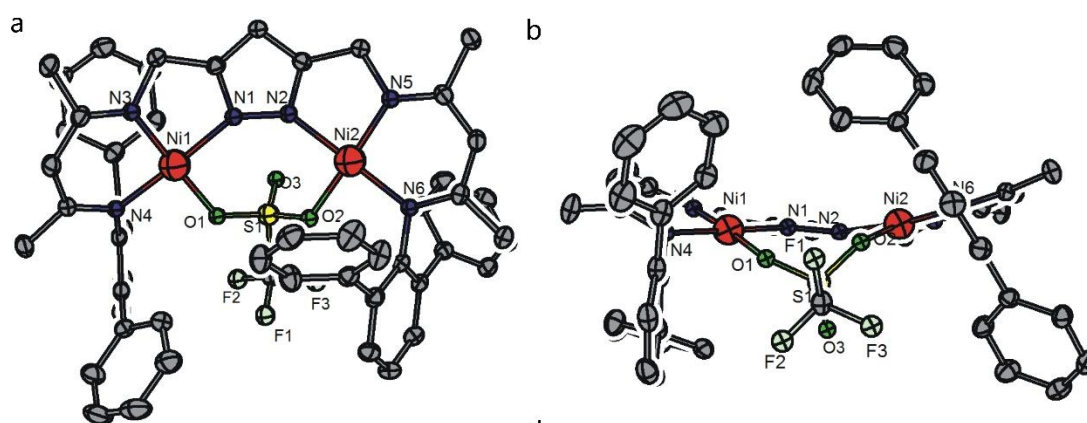


Figure 186: Molecular structure (50% probability thermal ellipsoids) of **40**. All hydrogen atoms omitted for clarity.

Table 49: Selected bond lengths (Å) and angles (°) for **40**.

Atoms	Bond lengths	Atoms	Bond angles
Ni1-N3	1.850(1)	N3-Ni1-N4	92.54(6)
Ni1-N4	1.893(1)	N3-Ni1-O1	176.19(6)
Ni1-O1	1.928(1)	N4-Ni1-O1	87.24(6)
Ni1-N1	1.938(1)	N3-Ni1-N1	84.97(6)
Ni2-N5	1.856(1)	N4-Ni1-N1	177.43(6)
Ni2-N6	1.891(1)	O1-Ni1-N1	95.21(5)
Ni2-O2	1.925(1)	N5-Ni2-N6	94.21(6)
Ni2-N2	1.931(1)	N5-Ni2-O2	169.15(6)
		N6-Ni2-O2	88.65(6)
		N5-Ni2-N2	85.49(6)
		N6-Ni2-N2	173.18(6)

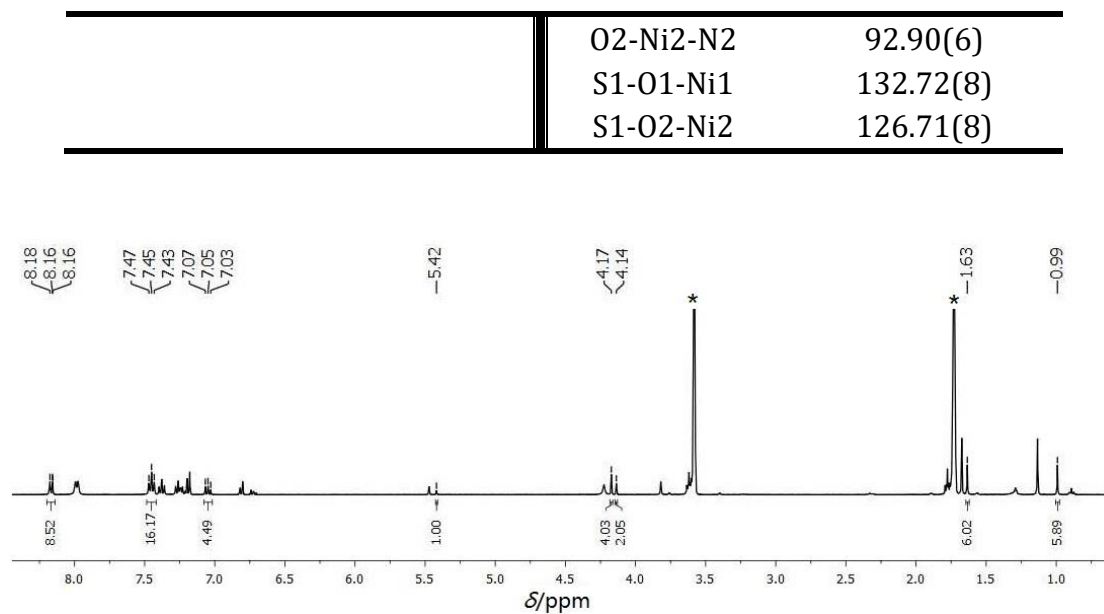


Figure 187: ^1H NMR (400 MHz) spectrum of **40** (Some byproduct **39** was observed). Residual solvents are marked with an asterisk (*).

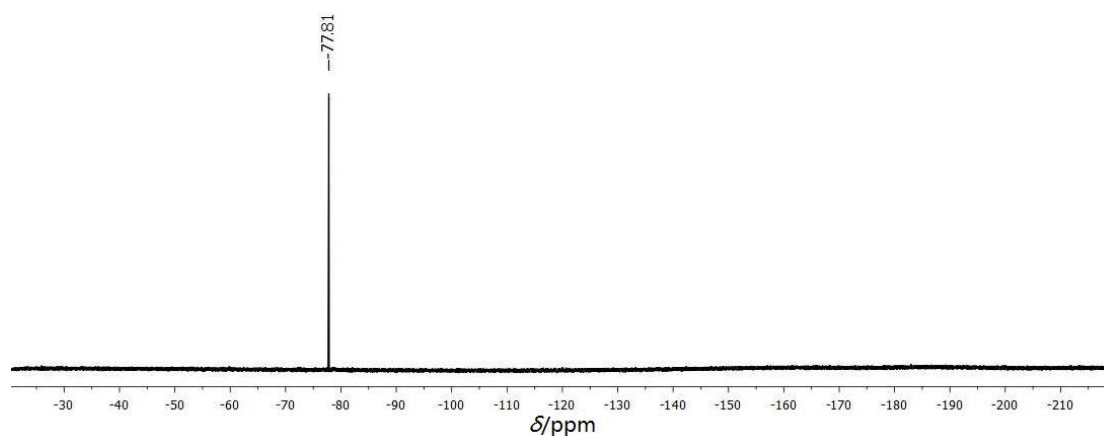


Figure 188: ^{19}F NMR spectrum of **40**.

The IR spectrum of **40** shows three additional strong bands at 1229 cm^{-1} and 696 cm^{-1} , which can be assigned to the triflate vibrations. [135]

10.7 Summary

To conclude, a bunch of bimetallic dinickel(II) complexes based on an expand bis(β -diketiminato) ligand system was prepared and their structures and behavior. Bimeatllic dinickel(II) monohydride complex was isolated after reacting the precursor complex $L^2Ni_2(\mu-Br)$ with $KHBET_3$ in THF. However, bimetallic dinickel(II) monohydride and dihydride complexes were obtained from the precursor complex with $NaHBET_3$. VT 1H NMR experiments suggest that **38** is present in solution in equilibrium with **37** and is responsible for the unusual reactivity with H_2 . Furthermore, **36**, **37** and **38** exhibit reactivity toward to H_2O and Lewis acid.

Chapter 11 Experimental Section

11.1 Material and Methods

All manipulations were performed under an anaerobic and anhydrous atmosphere of dry argon by using standard Schlenk techniques or in a glove box ($O_2 < 0.5$ ppm, $H_2O < 0.5$ ppm). Chemicals used were either present in the working group or were purchased from commercial sources or their synthesis is described below. Glassware was dried at $120^\circ C$. THF, Diethyl ether, Pentane and Hexane were dried over sodium in the presence of benzophenone; DCM and $CHCl_3$ were dried over P_4O_{10} ; MeCN (CH_3CN), EtCN (CH_3CH_2CN) and Et_3N (trimethylamine) were dried over CaH_2 ; MeOH and EtOH were dried over Mg. Toluene is used after drying over molecular sieve using a Mbraun PLC; all solvents were distilled prior to use. THF- d_8 is also dried over sodium in the presence of benzophenone to use and keep in 3 Å molecular sieve condition. Na and K were purchased as dispersions in mineral oil, they were washed repetitively with hexane and fried in vacuum prior to use. 1H NMR, 2H NMR, ^{13}C NMR, ^{19}F and ^{11}B NMR spectra were recorded on Bruker Avance 300 or 400 spectrometers at room temperature or low temperature. Chemical shifts are reported in parts per million relative to residual proton and carbon signals of the solvent ($CDCl_3$, $\delta_H = 7.26$, $\delta_C = 77.16$ ppm; CD_2Cl_2 , $\delta_H = 5.32$, $\delta_C = 53.84$ ppm; DMSO- d_6 , $\delta_H = 2.50$, $\delta_C = 39.52$ ppm; THF, $\delta_H = 1.73$ and 3.59 ppm; $\delta_C = 25.31$ and 67.21 ppm, CD_3CN , $\delta_H = 1.94$, $\delta_C = 1.32$ and 118.26 ppm).

All gas ($^{15}N_2$, $^{16}O_2$, $^{18}O_2$, ^{12}CO , ^{13}CO and $^{12}CO_2$) was dried over sulfuric acid (95%) for overnight. H_3L^1 was prepared according the literature. $[^{11}] S=PMe_3$ was synthesized using a modified published $[^{136}]$ synthesis in which PMe_3 was stirred with 1/8 molar equivalents of S_8 in toluene for 12 hours. $[H-Lut]OTf$ was synthesized using a modified published $[^{137}]$ and dried at $90-100^\circ C$ for overnight. An-

hydrous 1-hydroxy-2,2,6,6-tetramethyl-piperidine (TEMPO-H) [138], [NiBr₂(dme)] (dme=1,2-dimethoxyethane) [139], 2,4,6-tri-tert-butylphenol radical were synthesized from literature directly. [140] BCF (Tris(pentafluorophenyl)borane) was bought from abcr and dried at 110 °C for overnight and used subsequently.

UV-vis spectra were recorded on a Cary 50 Bio (Varian) or Cary 5000 (Varian) using quartz cuvettes (d = 1 cm or 0.1 cm). Low temperature UV-vis spectra were measured with a Varian Cary 50 Bio instrument coupled to a quartz immersion probe (5 mm, Hellma Analytics). Temperature stability was qualitatively assessed using the quartz immersion probe. Spectra were analyzed by Cary win UV software. Solid state spectra were recorded using the Cary 5000 Bio spectrophotometer but with a Praying Mantis™ diffuse reflection attachment equipped with a sample chamber with quartz window (Harrick Scientific Products).

Electron ionization (EI) mass spectra were recorded with a Finnigan MAT 8200. ESI-MS were recorded on Bruker HCT ultra spectrometer.

IR spectra of solid samples were measured with a Cary 630 FTIR spectrometer equipped with a DialPath and Diamond ATR accessory (Agilent) placed in a glovebox (MBRAUN UNIlab, argon atmosphere). IR bands were labeled according to their relative intensities with vs (very strong), s (strong), m (medium), w (weak), and very weak (vw).

Cyclic voltammetry (CV) experiments were performed using a Perkin-Elmer model 263A and a three electrodes setup consisting of a glassy carbon-working electrode, a platinum wire counter electrode and an Ag/AgCl reference electrode. Ferrocene was used as an internal standard with $E^0(\text{Fc}^+/\text{Fc}) = 0$ V. All studies were performed in deoxygenated THF containing NBu₄PF₆ (0.1 M) as supporting electrolyte.

X-band EPR spectra were measured with a Bruker E500 ELEXSYS spectrometer equipped with a standard cavity (ER4102ST, 9.45 GHz). Continuous-wave (cw) Q band EPR measurements were performed on a Bruker E500 Eleksys Q-band spectrometer equipped with an Oxford ESR910 flow cryostat and an ER4102ST rectangular cavity. Pulsed EPR spectra were recorded on a Bruker SuperQ FT EPR spectrometer and a Bruker E580 spectrometer. The sample temperature was maintained constant with an Oxford Instruments Helium flow cryostat (ESP910) and an Oxford temperature controller (ITC-4). The microwave frequency was measured with the built-in frequency counter and the magnetic field was calibrated using an NMR field probe (Bruker ER035M). EPR spectra were simulated using Easy Spin ^[141] or XSophe. ^[142]

Samples for XES experiments were prepared in an inert atmosphere nitrogen glovebox as finely ground dilutions in boron nitride pressed into 1 mm Al spacers and shipped to the experimental site in triple glass jars with fluoropolymer seals on the lids and sealed with Teflon and electrical tape. XES spectra were recorded with a crystal array spectrometer, which employs three spherically bent Ge(620) crystals (100 mm diameter, 1 m radius of curvature) aligned on intersecting Rowland circles. A silicon drift detector was used to detect the resultant fluorescence. Samples were positioned at 45 degrees with respect to the incident beam, and were maintained at a temperature of less than 100 K with an ARS helium duplex cryostat (CHESS) or Oxford CF1208 cryostat (SSRL). A helium-filled flight path was utilized between the cryostat and the spectrometer to minimize signal attenuation of the fluorescence. Spectra were normalized to the incident flux I_0 measured in a He-filled ion chamber (SSRL) or N₂-filled (CHESS). The spectrometer energy resolution is estimated at ~2.5 eV.

Temperature-dependent magnetic susceptibility measurements for peroxo and superoxo dinickel complexes were carried out with a *Quantum-Design* MPMS-XL-5 SQUID magnetometer equipped with a 5 Tesla magnet in the range

from 295 to 2.0 K at a magnetic field of 0.5 T. The powdered sample was contained in a Teflon bucket and fixed in a non-magnetic sample holder. Each raw data file for the measured magnetic moment was corrected for the diamagnetic contribution of the Teflon bucket according to $M^{\text{dia}}(\text{bucket}) = \chi_g \cdot m \cdot H$, with an experimentally obtained gram susceptibility of the Teflon bucket. The molar susceptibility data were corrected for the diamagnetic contribution using the Pascal constants and the increment method according to Haberditzl. ^[143] Magnetic measurement for **4** was collected on freshly crystallized material that was sealed with a small amount of mother liquor in an NMR-tube to prevent the loss of solvents and/or molecular hydrogen. Additionally, complex **4** was isolated and dried in glove-box atmosphere for 1 h (**4***) or dried in vacuum for 15 h (**4****). For **2**, the powdered sample was contained in a Teflon bucket and fixed in a non-magnetic sample holder. Each raw data file for the measured magnetic moment was corrected for the diamagnetic contribution of the sample holder and the sample.

Experimental data were modelled with the *julX* program ^[144] using a fitting procedure to the spin Hamiltonians:

$$\hat{H} = -2J\hat{S}_1\hat{S}_2 + g\mu_B\hat{B}(\hat{S}_1 + \hat{S}_2) \quad (\text{Eq. S1}) \quad \text{for } \mathbf{4}$$

or

$$\hat{H} = g\mu_B\hat{B} \cdot \hat{S} \quad (\text{Eq. S2}) \quad \text{for complexes } \mathbf{2}, \mathbf{6}, \mathbf{9}, \mathbf{16} \text{ and } \mathbf{24}$$

Temperature-independent paramagnetism (*TIP*) and paramagnetic impurities (*PI*) were included according to $c_{\text{calc}} = (1 - PI) \cdot c + PI \cdot c_{\text{mono}} + TIP$. Intermolecular interactions were considered in a mean field approach by using a Weiss temperature θ . ^[145] The Weiss temperature θ (defined as $\theta = zJ_{\text{inter}}S(S + 1)/3k$) relates to intermolecular interactions zJ_{inter} , where J_{inter} is the interaction parameter between two nearest neighbor magnetic centers, k is the Boltzmann constant

($0.695 \text{ cm}^{-1}\cdot\text{K}^{-1}$) and z is the number of nearest neighbors.

Raman spectra of compounds have been recorded using a HORIBA Scientific LabRAM HR 800 (400-1100 nm) spectrometer with open-electrode CCD detector and a confocal pinhole with user controlled variable aperture in combination with a free space optical microscope, and a He:Ne-laser (633 nm) or diode laser (457 nm). All spectra were recorded at room temperature. Raman measurements were performed under air at room temperature with the sample mounted on a glass slide. All samples are measured in the crystalline material.

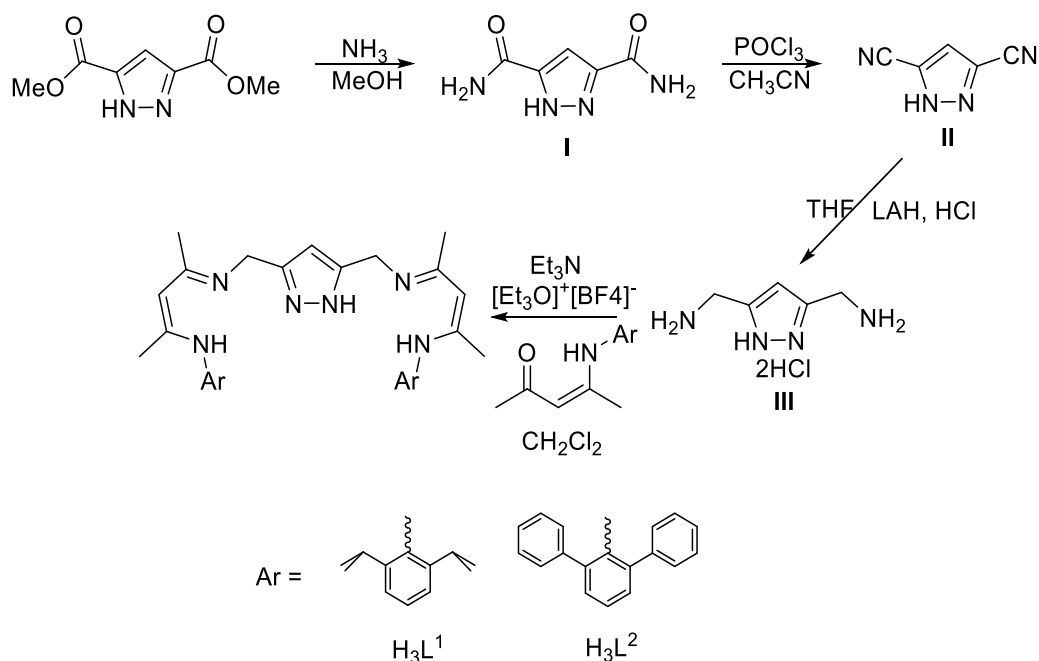
Calibration plot of GC quantification of H_2 : A 10 mL flask was charged with THF (2 mL) and a magnetic stir bar. In addition, 0.8 mL of CH_4 was injected into the closed system as an internal standard. A sample of H_2 was injected to the flask (0.1, 0.2, 0.4, 0.8 and 1.2 mL, at 1 atm). An aliquot of the headspace was then injected into GC-2014 gas chromatography with ShimAdzu, Shincarbon column (4.0 m \times 2.00 mm, oven temperature 100°C, carrier gas Ar, 180 KPa). A calibration plot was obtained by plotting the ratio of the GC peak integrations H_2/CH_4 versus the amount of hydrogen added to the flask.

Elemental analyses were performed by the analytical laboratory of the Institute of Inorganic Chemistry at Georg-August-University using an Elementar Vario EL III instrument.

Column chromatographic purifications (63–200 μm particle size) were performed on silica. TLC was performed on silica gel (Macherey-Nagel, Polygram SIL G/UV254).

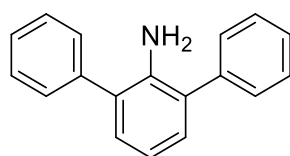
11.2 Experiment

11.2.1 Synthesis of Ligand Precursors and Ligands



Scheme 61: Syntheses route for the Ligands.

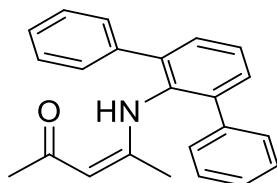
Ligand precursors **I**, **II**, **III**, H_3L^1 was prepared according the literature. ^[11]



Under anaerobic conditions a solution of $\text{PhB}(\text{OH})_2$ (2.19 g, 18.0 mmol) in ethanol (12 mL) was added to a solution of 2,6-dibromoaniline (1.51 g, 6.00 mmol) in toluene (60 mL). Aqueous Na_2CO_3 solution (2 M, 25 mL) and $\text{Pd}(\text{PPh}_3)_4$ (0.83 g, 0.72 mmol) were added, and the mixture was refluxed for 20 h at 85°C . The organic layer was separated, and the aqueous phase extracted with ether (3×50 mL). The combined organic phases were dried over MgSO_4 in air, and solvent was removed. The black residue was purified on a silica column eluted with ethyl acetate: hexane = 1:9 (v:v). Solvent was removed from the eluate, and the residue was crystallized from hot hexanes to afford pure 2,6-diphenylaniline as a white

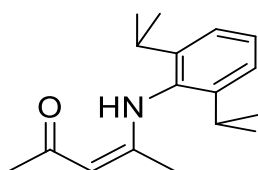
solid. [146]

$^1\text{H NMR}$ (CDCl_3 , 300 MHz) = 3.74 (br, 2H, NH_2), 6.90 (t, 1H, Ar), 7.14 (t, 2H, Ar), 7.37 (m, 2H, Ar), 7.52(m, 8H, Ar).



L2. A mount of 2,6-diphenylaniline (0.106 mol, 18.76 g) was added to a solution of 2,4-pentanedione (16.4 mL, 0.159 mol) and *p*-toluenesulfonic acid in toluene (100 mL) in a round-bottom flask. The resulting mixture was heated to reflux for 8 hours, and water was removed as a toluene azeotrope using a Dean and Stark apparatus. The diethyl ether solution was washed one or two times by a little dilute hydrochloric acid to eliminate raw materials and the by-product diketiminate. The reaction mixture was then evaporated to dryness. The resulting solid was recrystallized from hot hexane to afford the product.

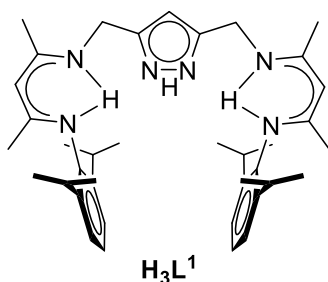
$^1\text{H NMR}$ (CDCl_3 , 300 MHz) = 1.15 (s, 3H, CH_3), 1.78 (s, 3H, CH_3), 4.63 (s, 1H, CH), 7.11-7.30 (m, 13H, Ar), 12.08(br, 1H, NH).



L1. A mixture of 2,6-diisopropylaniline (0.106 mol, 18.79 g, 20 mL, 1 equiv), 2,4-pentanedione (0.116 mol, 11.66 g, 11.96 mL, 1.1 equiv) and *p*-toluenesulfonic acid (0.5 g) in toluene (100 mL) was refluxed for 6 h, with azeotropic removal of water using a Dean-stark trap. After removing the solvent, the crude product was washed by 30 mL water and extracted by 120 mL Et_2O divided three times. The diethyl ether solution was washed one or two times by a little dilute hydrochloric acid to eliminate raw materials and the by-product diketiminate. The resulting

brown solid was recrystallized from hexane at $-30\text{ }^{\circ}\text{C}$ to afford the product.

$^1\text{H NMR}$ (CDCl_3 , 300 MHz) = 1.15 (d, 6H, CH_3), 1.22 (d, 6H, CH_3), 1.63 (s, 3H, CH_3), 2.12 (d, 3H, CH_3), 3.02 (d, 1H, CH), 5.21 (s, 1H, CH), 7.27 (m, 3H, Ph), 12.05 (s, 1H, NH).



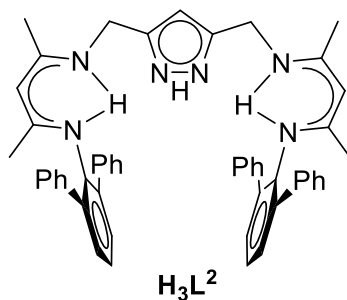
H_3L^1 ^[11]: **Molecular Weight:** 608.90 g/mol ($\text{C}_{39}\text{H}_{56}\text{N}_6$)

$^1\text{H NMR}$ (CDCl_3 , 300 MHz) = 1.06 (d, 12H, $(\text{CH}_3)\text{CHPh}$), 1.15 (d, 12H, $(\text{CH}_3)\text{CHPh}$), 1.64 (s, 6H, CH_3CCH), 1.95 (s, 6H, CH_3CCH), 2.84 (m, 4H, CHPh), 4.39 (s, 4H, CH_2Pz), 4.72 (s, 2H, CHCCH_3), 6.01 (s, 1H, 4-Pz), 6.99-7.16 (m, 6H, Ar).

$^{13}\text{C NMR}$ (CDCl_3 , 300 MHz) = 19.17(CH_3CCH), 21.62 ($\text{CH}(\text{CH}_3)_2$), 22.77 ($\text{CH}(\text{CH}_3)_2$), 23.76 ($\text{CH}(\text{CH}_3)_2$), 32.08, 40.06 (CH_2Pz), 94.52, 101.20 (4C-Pz), 122.80 (Ph), 123.57(Ph), 138.10 (Ph), 146.28 (3,5C-Pz), 155.58 (CH_3CCH), 166.22 (CH_3CCH).

ATR-IR (ν/cm^{-1}) = 3190 (br)(NH), 3130 (NH), 3104 (NH), 3060 (w), 3020 (w), 2960 (m), 2923 (w), 2867 (w), 1621 (vs), 1551 (vs), 1501 (w), 1454 (m), 1432 (m), 1377 (m), 1361 (m), 1292 (m), 1284 (m), 1268 (m), 1226 (m), 1179 (m), 1159 (m), 1090 (m), 1049 (m), 1020 (m), 1005 (w), 934 (w), 919 (w), 879 (w), 819 (w), 804 (w), 784 (s), 758 (s), 728 (s), 695 (m), 664 (w), 626 (w), 607 (w), 582 (w), 519 (w), 497 (w).

Elemental analysis (%) calc. for $\text{C}_{39}\text{H}_{56}\text{N}_6$ ($\text{C}_4\text{H}_8\text{O}$): C 72.84 H 9.47 N 12.34;
Found C 72.92 H 9.20 N 12.48.



H₃L²: Under an argon atmosphere, a solution of [Et₃O]⁺[BF₄]⁻ (2.09 g, 11 mmol, 2.2 equiv) in CH₂Cl₂ (40 mL) was slowly added to a solution of 4-(2,6-diphenylphenyl)amino-3-penten-2-one (3.6 g, 11 mmol, 2.2 equiv) in CH₂Cl₂ (40 mL) at 0°C, then the reaction solution was stirred overnight at ambient temperature. Et₃N (1.11 g, 11 mmol, 1.54 mL, 2.2 equiv) was added at 0°C and the mixture was stirred for another 0.5 h at room temperature. A solution of ethylene diamine (1 g, 5 mmol, 1 equiv) in Et₃N (1.01 g, 10 mmol, 1.4 mL, 2 equiv) was added to the reaction solution and the stirring was continued overnight. The volatiles were removed in vacuo and the obtained residue was treated with 50 mL of toluene for 30 mins. [Et₃NH]⁺[BF₄]⁻ precipitated as an oily solid. After filtration, toluene was removed under reduced pressure to afford a yellow solid. After recrystallization from ethanol/pentane = 1:3 at room temperature, white powder were obtained.

Molecular Weight: 744.96 g/mol (C₅₁H₄₈N₆)

¹H NMR (CDCl₃, 300 MHz) = 1.30 (s, 6H, CH₃CCH), 1.73 (s, 6H, CH₃CCH), 4.19 (s, 4H, CH₂Pz), 4.28 (s, 2H, CHCCH₃), 5.55 (s, 1H, 4-Pz), 7.09-7.34 (m, 26H, Ph), 10.61 (br, 1H, NH).

¹³C NMR (CDCl₃, 75 MHz) = 18.07, 21.36, 38.84, 93.70, 99.96, 121.82, 125.21, 126.67, 127.27, 128.22, 132.66, 140.20, 145.46, 154.43, 165.21.

MS (ESI): *m/z* (%) = 745.93 (M+H)⁺ (100).

Elemental analysis (%) calc. for C₅₁H₄₈N₆ (744.39 g/mol): = C 82.25 H 6.57 N 11.17; Found C 82.21 H 6.50 N 11.28.

11.2.2 Complexes Syntheses

$L^1Ni_2(\mu-Br)$ (**1**).

This complex was prepared according to the literature. ^[11]

Molecular Weight: 803.17 g/mol ($C_{39}H_{53}N_6Ni_2Br$)

1H NMR ($CDCl_3$, 300 MHz) = 6.91-6.80 (m, 2H, Ar), 6.73-6.75 (d, $J_{H-H} = 6$ Hz, 4H, Ar), 5.46 (s, 1H, Pz), 4.68 (s, 2H, $CHCCH_3$), 4.07 (s, 4H, CH_2Pz), 3.30-3.20 (m, 4H, $CH(CH_3)_2$), 1.95 (s, 6H, CH_3CCH), 1.39 (d, $J_{H-H} = 6$ Hz, 12H, $(CH_3)_2CH$), 1.26 (s, 6H, CH_3CCH), 0.95 (d, $J_{H-H} = 6$ Hz, 12H, $(CH_3)_2CH$).

1H NMR (THF- d_8 , 300 MHz): = 6.79-6.95 (m, 6H, Ar), 5.53 (s, 1H, Pz), 4.77 (s, 2H, $CHCCH_3$), 4.15 (s, 4H, CH_2Pz), 3.33-3.40 (m, 4H, $CH(CH_3)_2$), 2.01 (s, 6H, CH_3CCH), 1.47 (d, $J_{H-H} = 6$ Hz, 12H, $(CH_3)_2CH$), 1.30 (s, 6H, CH_3CCH), 1.02 (d, $J_{H-H} = 6$ Hz, 12H, $(CH_3)_2CH$).

^{13}C NMR ($CDCl_3$, 75 MHz) = 159.74 ($CHCCH_3$), 153.24 (3(5)-Pz), 147.66 (Ar), 141.50 (Ar), 125.43 (Ar), 123.30 (Ar), 97.24 (CH_2Pz), 91.51 (4C-Pz), 54.44 ($CHCCH_3$), 28.13 ($(CH_3)_2CH$), 24.84 ($(CH_3)_2CH$), 23.37 (CH_3), 21.53 (CH_3).

ATR-IR (ν/cm^{-1}) = 3058 (w), 2959 (m), 2923 (m), 2862 (m), 1555 (m), 1532 (vs), 1462 (vs), 1435 (s), 1399 (s), 1381 (s), 1369 (vs), 1313 (s), 1279 (s), 1252 (s), 1236 (m), 1186 (m), 1175 (s), 1093 (s), 1052 (s), 1032 (m), 1012 (m), 957 (m), 935 (m), 795 (vs), 759 (vs), 745 (vs), 542 (m).

Elemental analysis (%) calc. for $C_{39}H_{53}N_6Ni_2Br \cdot (CH_2Cl_2)_{1.5}$ (926.15 g/mol) = C 52.48 H 6.10 N 9.07; Found C 52.77 H 6.45 N 9.33.

$NaL^1Ni_2(\mu-H)_2$ (**3**)

A solution of $NaHBEt_3$ in THF (1.0 M) (0.75 mL, 0.75 mmol, 3 equiv) was added dropwise to a stirred brown solution of **1** (200 mg, 0.25 mmol, 1 equiv) in THF (2 mL) at room temperature. After stirring the resulting red-brown solution for 2 hours, all volatiles were removed in *vacuo*. The red-brown residue was washed

twice with hexane (40 mL). After concentration in *vacuo* and get red powder (130 mg, 0.17 mmol, 68 %). The crude powder was recrystallization from Pentane diffusion to a solution of **3** in THF at room temperature yield orange block crystals

3-D: In a Young tube, a solution of **3** in THF (0.5 mL) was freeze-thaw degassed under vacuum three times. Then dry D₂ (*ca.* 1 atm) was then introduced to the headspace of the flask at room temperature.

Molecular Weight: 892.47 g/mol (C₃₉H₅₅N₆Ni₂Na·2THF)

¹H NMR (THF-d₈, 300 MHz) = 6.75 - 6.86 (m, 6H, Ar), 5.61 (s, 1H, 4-Pz), 4.58 (s, 2H, CHCCH₃), 4.27 (s, 4H, CH₂Pz), 3.41-3.49 (m, 4H, (CH₃)₂CHPh), 1.86 (s, 6H, CH₃CCH), 1.23 (s, 6H, CH₃CCH), 1.04 (dd, 24H, *J*_{H-H} = 6 Hz, (CH₃)₂CHPh), - 23.54 (s, 2H, Ni-H).

²H NMR (THF, 77 MHz) = -23.54 (s, 2H, Ni-D).

¹³C {¹H} NMR (THF-d₈, 100 MHz) = 157.91 (CHCCH₃), 156.99 (CHCCH₃), 155.16 (Ar), 139.26 (Ar), 123.15 (Ar), 122.21 (Ar), 95.95 (CH₂Pz), 91.91 (4-Pz), 51.35 (CHCCH₃), 27.25 (CH₃), 25.39 (CH₃), 21.53 (CH₃), 19.61 (CH₃).

ATR-IR (ν/cm⁻¹) = 3052 (w), 2953 (m), 2962 (m), 1846 (Ni-H) (m), 1554 (m), 1521 (s), 1511 (s), 1459 (vs), 1373 (vs), 1396 (s), 1313 (m), 1271 (m), 1251 (m), 1231 (m), 1189 (m), 1100 (m), 1049 (m), 933 (m), 891 (m), 796 (m), 756 (m), 725 (m), 716 (m), 644 (m), 575 (m), 544 (w).

Anal. Calcd. (%) for [NaNi₂(C₃₉H₅₃N₆)O₂](C₄H₈O)₂: C 59.07, H 6.74, N 10.60; found: C 59.32, H 6.82, N 10.37.

ATR-IR (ν/cm⁻¹) = 1337 (Ni-D) (w).

[L¹Ni₂(μ-H₂)]-[K(Dibenzo(18-crown-6))] (4)

DB18C6 (7.2 mg, 0.02 mmol) was added into a solution of **2** (15.2 mg, 0.02 mmol) in THF (2 mL) at room temperature. After stirring the resulting red solution for 2 hours, all volatiles were removed in *vacuo*. The red residue was washed twice

with hexane (10 mL). Suitable crystals for x-ray diffraction were obtained by layering hexane on a solution of **4** in THF at -30°C . (Yield: 90%)

4-D₂: In a Young tube, a solution of **4** in THF (0.5 mL) was freeze-thaw degassed under vacuum three times. Then dry D₂ (*ca.* 1 atm) was then introduced to the headspace of the flask at room temperature.

Molecular Weight: 1343.70 (C₅₉H₇₉N₆O₆Ni₂K)

¹H NMR (THF-d₈, 400 MHz) = -23.99 (s, Ni-H).

ATR-IR (ν/cm^{-1}) = 3052 (w), 2982 (m), 2955 (m), 2924 (m), 2863 (m), 1907 (Ni-H) (m), 1595 (m), 1503 (vs), 1452 (s), 1436 (s), 1426 (s), 1396 (s), 1366 (s), 1356 (m), 1320 (s), 1298 (w), 1270 (w), 1246 (vs), 1211 (vs), 1191 (w), 1118 (vs), 1094 (m), 1055 (s), 1020 (w), 943 (s), 902 (m), 848 (w), 796 (m), 778 (m), 756 (s), 741 (vs), 726 (vs), 715 (vs), 646 (w), 629 (w), 600 (m), 560 (w), 522 (w).

ATR-IR (ν/cm^{-1}) = 1318 (Ni-D) (s).

[L¹Ni₂]-[K(Dibenzo(18-crown-6))] + (**5**)

Keep the complex **4** under the *vacuo* for three days to remove the dihydrogen molecule from Ni-bound hydrides. The residue was washed with hexane (5 mL). Suitable crystals for x-ray diffraction were obtained by layering pentane/Et₂O on a solution of **5** in THF at -30°C .

Magnetic susceptibility: $\mu_{\text{eff}}=1.6 \mu_{\text{B}}$ (dried 1 hour); $\mu_{\text{eff}}=2.0 \mu_{\text{B}}$ (dried 15 hour)

ATR-IR (ν/cm^{-1}) = 3062 (w), 2950 (m), 2931 (m), 2864 (m), 1595 (m), 1519 (s), 1503 (s), 1452 (w), 1436 (w), 1427 (s), 1401 (s), 1357 (m), 1309 (s), 1239 (vs), 1209 (vs), 1193 (w), 1124 (vs), 1089 (m), 1058 (s), 1022 (w), 982 (s), 953 (m), 941 (w), 900 (w), 848 (w), 797 (m), 782 (m), 757 (s), 739 (vs), 718 (vs), 645 (w), 633 (w), 600 (m), 522 (w).

KL¹Ni₂(μ-η¹, η¹-O₂) (6)

(a) Dioxygen (prior dried over concentrated H₂SO₄) (1.28 mg, 890 μL, 0.04 mmol, 1 equiv) was added into a solution of **2** (30.5 mg, 0.04 mmol, 1 equiv) in THF (1 mL) at room temperature. The color changes from orange to red immediately. Suitable crystals for x-ray diffraction were obtained from THF at -30 °C as red block crystal. (Yield: > 95%, from ¹H NMR)

(b) **9** (33 mg, 0.04 mmol, 1 equiv) and potassium (0.8 mg, 0.02 mmol, 2 equiv) were suspended in THF (2 mL) at room temperature, and a color changes from brown to red occurred immediately. The mixture was stirred for 2 hours, and then the solid components were filtered off. Suitable crystals for x-ray diffraction were obtained by layering hexane on a solution of **6** in THF at -30°C. (Yield: 60%)

6-¹⁸O₂: The synthesis of **6-¹⁸O₂** was achieved by the same procedure as reported above for **6** but employing ¹⁸O₂.

Molecular Weight: 792.3 g/mol⁻¹ (C₃₉H₅₃N₆Ni₂KO₂)

¹H NMR (THF-d₈, 400 MHz) = 6.91 (m, 6H, Ar), 5.99 (s, 1H, 4-Pz), 4.53 (s, 2H, CHCCH₃), 3.82 (s, 4H, CH₂Pz), 3.69-3.79 (m, 4H, CH(CH₃)₂), 1.78 (s, 6H, CH₃), 1.49 (d, 12H, ²J_{H-H} = 8 Hz, CH(CH₃)₂), 1.08 (d, 12H, ²J_{H-H} = 8 Hz, CH(CH₃)₂), 1.02 (s, 6H, CH₃).

¹³C NMR (THF-d₈, 100 MHz) = 160.01 (CHCCH₃), 157.13 (CHCCH₃), 151.77 (3,5-Pz), 150.72 (Ar), 144.74 (Ar), 123.46 (Ar), 122.18 (Ar), 96.53 (CHCCH₃), 90.43 (4-Pz), 50.15 (CH₂Pz), 27.77 (CH₃), 22.09 (CH₃), 20.93 (CH₃).

ATR-IR (ν/cm⁻¹) = 3055 (w), 2958 (m), 2924 (m), 2864 (m), 1555 (m), 1527(vs), 1460(s), 1433 (vs), 1397 (vs), 1369 (m), 1315 (s), 1257 (vs), 1196 (w), 1055 (s), 1031 (vs), 1014 (vs), 859 (m), 799 (s), 774(m), 757 (s) (¹⁶O-¹⁶O), 732 (s), 683 (w), 623 (w), 589 (w), 548 (w).

ATR-IR (ν/cm⁻¹) = 714 (m)(¹⁸O-¹⁸O).

Raman (ν/cm⁻¹) = 720 (¹⁶O-¹⁶O), 680 (¹⁸O-¹⁸O).

ESI-MS (THF): m/z (%) = 793.3 (100) (M+H)⁺ (**6**-¹⁶O₂), 819.2 (100) (**6**+Na)⁺ (**6**-¹⁸O₂).

UV-vis (THF): λ_{\max} = 272, 370, 384, 510 nm.

Anal. Calcd. (%) for [(C₃₉H₅₃N₆)KNi₂O₂]: C 59.07, H 6.74, N 10.60; found: C 59.32, H 6.82, N 10.37.

NaL¹Ni₂(μ - η^1 , η^1 -O₂) (7**)**

NaBAR^F₄ (18 mg, 0.02 mmol, 1 equiv) was added into a solution of **6** (16 mg, 0.02 mmol, 1 equiv) at room temperature. The mixture was stirred for 2 hours, and then the solid components were filtered off. Suitable crystals for x-ray diffraction were obtained by layering hexane on a solution of **7** in THF at -30°C.

Molecular Weight: 778.25 g/mol (C₃₉H₅₃N₆Ni₂NaO₂)

¹H NMR (THF-d₈, 400 MHz) = 6.95 (br, 6H, Ar), 5.59 (s, 1H, 4H-Pz), 4.55 (s, 2H, CHCCH₃), 3.82 (s, 4H, CH₂Pz), 1.80 (s, 6H, CH₃), 1.50 (d, 12H, ³J_{H-H} = 4 Hz, (CH₃)₂CH), 1.08 (d+s, 18H, CH₃+(CH₃)₂CH).

[L¹Ni₂(μ - η^1 , η^1 -O₂)] [K(Dibenzo(18-crown-6))]⁺ (8**)**

DB18C6 (7.2 mg, 0.02 mmol, 1 equiv) was added into a solution of **6** (16 mg, 0.02 mmol, 1 equiv) in THF (2 mL) at room temperature resulting the color from wine-red to cherry red. After stirring the resulting red solution for 2 hours, all volatiles were removed in *vacuo*. The red residue was washed twice with hexane (10 mL). Suitable crystals for x-ray diffraction were obtained by layering hexane/Et₂O on a solution of **8** in THF at -30°C (yield: 80%).

⁸-¹⁸O₂: The synthesis of **8**-¹⁸O₂ was achieved by the same procedure as reported above for **8** but employing ¹⁸O₂.

Molecular Weight: 1154.76 g/mol (C₅₉H₇₇N₆O₈Ni₂K)

¹H NMR (THF-d₈, 400 MHz) = 6.83 – 6.94 (m, Ar + Dibenzo(18-crown-6)), 5.57 (s, 1H, 4H-Pz), 4.49 (br, 2H, CHCCCH₃), 4.14 (Dibenzo(18-crown-6)), 4.08

(Dibenzo(18-crown-6)), 3.79 (br, 4H, CH₂Pz), 1.40 (s, 12H, CH₃), 1.05 (s, 12H, CH₃).

¹³C {¹H} NMR (THF-d₈, 100 MHz) = 149.39, 144.47, 135.22, 126.21, 123.94, 121.94, 121.78, 113.45, 113.39, 113.15, 106.12, 97.71, 96.07, 92.59, 70.32, 69.17, 56.45, 56.07, 32.59, 28.99, 27.35, 26.43, 25.90, 23.98, 22.96, 21.18, 20.79, 14.48.

ATR-IR (ν/cm⁻¹) = 3058 (w), 2952 (m), 2925 (m), 2860 (m), 1663 (w), 1594 (m), 1547 (m), 1522 (s), 1502 (s), 1438 (s), 1402 (vs), 1320 (m), 1308 (m), 1281 (w), 1247 (vs), 1209 (s), 1123 (vs), 1099 (w), 1083 (w), 1055 (vs), 987 (w), 953 (w), 940 (s), 912 (w), 900 (w), 807 (w), 796 (m), 778 (m) (¹⁶O-¹⁶O), 739 (s), 715 (s), 600 (m), 582 (w).

ATR-IR (ν/cm⁻¹) = 728 (m) (¹⁸O-¹⁸O).

Raman (ν/cm⁻¹) = 755 (¹⁶O-¹⁶O), 715 (¹⁸O-¹⁸O).

UV-vis (THF): λ_{max} = 274, 380, 410, 520 nm.

ESI-MS (CH₃CN): m/z (%) = 755.44 (15) (L¹Ni₂(O₂)+2H)⁺ (**8**-¹⁶O₂), 759.44 (20) (L¹Ni₂(¹⁸O₂)+2H)⁺ (**8**-¹⁸O₂).

Anal. Calcd. (%) for [K(C₂₀H₂₄O₆)(C₄H₈O)₂]⁺[Ni₂(C₃₉H₅₃N₆)O₂]⁻: C 61.95, H 7.22, N 6.47; found: C 62.12, H 7.33, N 6.18.

L¹Ni₂(μ-η¹,η¹-O₂) (**9**)

(a) A solution of **2** in THF (10 mL) was cooled to -78°C. The nitrogen atmosphere in the young flask was replaced with dry dioxygen. After stirring for 2 hours, the reaction mixture was allowed to warm to room temperature and was further stirred overnight. The color of the solution changed from orange to brown-red. Volatiles were concentrated to 2 mL. Suitable crystals for x-ray diffraction were obtained by layering hexane on a solution of **9** in THF at -30°C. (yield: 60%)

(b) Dioxygen (prior dried over concentrated H₂SO₄) (1.28 mg, 890 μL, 0.04 mmol, 1 equiv) was added into a solution of **6** (31.7 mg, 0.04 mmol, 1 equiv) in THF (1 mL) at room temperature. The color changed from red to brown in 20 minutes.

Suitable crystals for x-ray diffraction were obtained by layering hexane on a solution of **9** in THF at -30°C . (yield: 70%)

9- $^{18}\text{O}_2$: The synthesis of **9- $^{18}\text{O}_2$** was achieved by the same procedure as reported above for **9** but employing $^{18}\text{O}_2$. The setup was prepared using a method similar to that described for $^{15}\text{N}_2$ starting from $^{18}\text{O}_2$.

Molecular Weight: 753.3 g/mol ($\text{C}_{39}\text{H}_{53}\text{N}_6\text{Ni}_2\text{O}_2$)

ATR-IR (ν/cm^{-1}) = 3058 (w), 2956 (m), 2924 (m), 2865 (m), 1553 (m), 1532 (s), 1461 (s), 1437 (s), 1394 (s), 1369 (s), 1313 (s), 1252 (s), 1234 (s), 1187 (s), 1176 (s), 1092 (m), 1032 (s), 982 (^{16}O - ^{16}O) (s), 936 (m), 916 (m), 870 (w), 797 (s), 759 (s), 743 (s), 714 (m), 588 (m), 565(m).

ATR-IR (ν/cm^{-1}) = 936 (m)(^{18}O - ^{18}O).

Raman (ν/cm^{-1}) = 1007 (^{16}O - ^{16}O), 951 (^{18}O - ^{18}O).

ESI-MS (THF: CH_3CN = 10:1): m/z (%) = 792.4 (100) ($\text{M}+\text{K}$)⁺ (**9- $^{16}\text{O}_2$**), 776.4 (20) (**9**+Na)⁺ (**9- $^{16}\text{O}_2$**), 754.3 (5) (**9**+H)⁺ (**9- $^{16}\text{O}_2$**); 796.4 (100)(**9**+K)⁺ (**9- $^{18}\text{O}_2$**).

UV-vis (THF): λ_{max} = 312, 364, 461, 560, 720 nm.

Anal. Calcd. (%) for $[\text{Ni}_2(\text{C}_{39}\text{H}_{53}\text{N}_6)\text{O}_2]$: C 62.13, H 7.09, N 11.15; found: C 62.50, H 7.39, N 10.19.

L¹Ni₂(μ -OH) (11)

(a) Treatment of **6**(31.77 mg, 0.04 mmol, 1 equiv) in THF (2 mL) with [H-Lut]OTf (10.28 mg, 0.04 mmol, 1 equiv) resulted in a color change from red to orange immediately. The mixture was stirred for 1 hour. After filtration, suitable crystals for x-ray diffraction were obtained by layering hexane on a solution of **11** in THF at -30°C . (yield: 80%)

(b) Treatment of **9** (15.10 mg, 0.02 mmol, 1 equiv) in THF (1 mL) with TEMPO-H (3.14 mg, 0.02 mmol, 1 equiv) resulted color change from brown to brown red in 20 mins. The reaction mixture was allowed to react for 12 hours at -30°C . Suitable crystals for x-ray diffraction were obtained by layering hexane on a solution

of **11** in THF at -30°C . (yield: 80%)

(c) Treatment of **2** (30.56 mg, 0.04 mmol, 1 equiv) in THF (2 mL) with H_2O resulted in a color change from red to orange immediately and intensity gas was observed. The mixture was stirred for 1 hour. After filtration, suitable crystals for x-ray diffraction were obtained by layering hexane on a solution of **11** in THF at -30°C . (Yield: 80%)

Molecular Weight: 740.27 g/mol ($\text{C}_{39}\text{H}_{54}\text{N}_6\text{Ni}_2\text{O}$)

$^1\text{H NMR}$ (THF- d_8 , 400 MHz) = 6.94 – 6.98 (t, 4H, Ar), 6.80 - 6.82 (d, 2H, Ar), 5.48 (s, 1H, Pz), 4.60 (s, 2H, CHCCH_3), 4.01 (s, 4H, CH_2Pz), 3.32 - 3.37 (m, 4H, $\text{CH}(\text{CH}_3)_2$), 1.86 (s, 6H, CH_3CCH), 1.61(d, 12H, $^2J_{\text{H-H}} = 4 \text{ Hz}$, $(\text{CH}_3)_2\text{CH}$), 1.08 (s+d, 18H, $\text{CH}_3\text{CCH}+(\text{CH}_3)_2\text{CH}$).

$^{13}\text{C NMR}$ (THF- d_8 , 100 MHz) = 21.36 (CH_3), 23.73 (CH_3), 25.89 (CH_3), 29.20 (CH_3), 55.14 (CH_2Pz), 91.62 (4-Pz), 98.25 (CHCCH_3), 125.33 (Ar), 126.14 (Ar), 142.56 (Ar), 145.40 (Ar), 159.36 (CHCCH_3), 161.25 (CHCCH_3).

ATR-IR (ν/cm^{-1}) = 3608 (m, OH), 3058 (w), 2955 (m), 2864 (m), 1553 (m), 1529 (vs), 1462 (s), 1436 (s), 1394 (vs), 1381 (vs), 1323 (m), 1314 (m), 1271 (m), 1251 (m), 1234 (m), 1196 (w), 1159 (w), 1104 (w), 1082 (w), 1060 (m), 1018 (m), 946 (m), 874 (m), 799 (s), 756 (vs), 732 (vs), 709 (w), 649 (m).

Anal. Calcd. (%) for $[\text{Ni}_2(\text{C}_{39}\text{H}_{53}\text{N}_6)\text{OH}]$: C 63.28, H 7.35, N 11.35; found: C 63.18, H 7.23, N 11.49.

$\text{KL}^1\text{Ni}_2(\mu\text{-}\eta^1, \eta^1\text{-S}_2)$ (12**)**

Elemental sulfur (2.56 mg, 0.04 mmol, 1 equiv) was added into a solution of **2** (30.5 mg, 0.04 mmol, 1 equiv) in THF (1 mL) at room temperature. The color changes from orange to blood red immediately and intensity gas was observed. Suitable crystals for x-ray diffraction were obtained by layering hexane on a solution of **12** in THF at -30°C (Yield: > 95%, from $^1\text{H NMR}$)

Molecular Weight: 826.50 g/mol ($C_{39}H_{53}N_6Ni_2S_2K$)

1H NMR (THF- d_8 , 400 MHz) = 6.91 (m, 6H, Ar), 5.99 (s, 1H, 4-Pz), 4.53 (s, 2H, CHCCH₃), 3.82 (s, 4H, CH₂Pz), 3.69-3.79 (m, 4H, CH(CH₃)₂), 1.78 (s, 6H, CH₃), 1.49 (d, 12H, J_{H-H} = 8 Hz, CH(CH₃)₂), 1.08 (d, 12H, $^3J_{H-H}$ = 8 Hz, CH(CH₃)₂), 1.02 (s, 6H, CH₃).

^{13}C NMR (THF- d_8 , 100 MHz) = 159.79 (C^q -Me), 158.25 (C^q -Me), 156.42 (3(5) C -Pz), 144.16 (Ar) 124.61 (Ar), 122.48 (Ar), 97.23 (CHCCH₃), 91.97 (4C-Pz), 50.83(CH₂Pz) 28.62 ((CH₃)₂CH), 26.43 (CH₃^{iPr}), 24.30 (CH₃^{iPr}), 21.90 (CH₃).

ATR-IR (ν/cm^{-1}) = 3052 (w), 2954 (m), 2924 (m), 2862 (m), 1555 (m), 1528 (vs), 1462 (m), 1433 (vs), 1398 (vs), 1315 (m), 1276 (m), 1249 (m), 1232 (w), 1209 (w), 1188 (w), 1124 (w), 1097 (w), 1054 (m), 1030 (m), 954 (w), 934 (w), 900 (w), 856 (w), 795 (m), 744 (s), 729 (m), 713 (m), 646 (w), 625 (w), 547 (w), 521 (w), 425 (m) (S-S).

UV-vis (THF): λ_{max} = 270, 375, 405, 465, 520 nm.

Anal. Calcd. (%) for $[KNi_2(C_{39}H_{53}N_6)S_2][C_4H_8O]$: C 61.89, H 7.37, N 10.07; found: C 61.53, H 7.11, N 11.17.

$L^1Ni_2(\mu-SH)$ (13)

(a) Elemental sulfur (2.56 mg, 0.04 mmol, 1 equiv) was added into a solution of **1** (30.5 mg, 0.04 mmol, 1 equiv) in THF (2 mL) in the presence of KC_8 at room temperature. Then the brown suspension solvent was stirred for two days at room temperature. Suitable crystals for x-ray diffraction were obtained by layering hexane on a solution of **13** in THF at $-30^\circ C$. (Yield: 80%)

(b) Treatment of **14** (33 mg, 0.04 mmol, 1 equiv) in THF (2 mL) with [H-Lut]OTf (10.28 mg, 0.04 mmol, 1 equiv) resulted in a color change from red to brown immediately. The mixture was stirred for 1 hour. After filtration, Suitable crystals for x-ray diffraction were obtained by layering hexane on a solution of **13** in THF at $-30^\circ C$. (yield: 80%)

(c) Treatment of **12** in THF (2 mL) under air resulted in a color change from red to brown in 2 hours. Suitable crystals for x-ray diffraction were obtained by layering hexane on a solution of **13** in THF at -30°C . (Yield: 80%)

Molecular Weight: 756.34 g/mol ($\text{C}_{39}\text{H}_{54}\text{N}_6\text{Ni}_2\text{S}$)

$^1\text{H NMR}$ (CDCl_3 , 400 MHz) = 6.96 (d, 2H, Ar), 6.84 (d, 4H, Ar), 5.55 (s, 1H, 4-Pz), 4.74 (s, 2H, CHCCH_3), 4.23 (s, 4H, CH_2Pz), 3.21-3.29 (m, 4H, $\text{CH}(\text{CH}_3)_2$), 2.02 (s, 6H, CH_3), 1.47 (d, 12H, $J_{\text{H-H}} = 8$ Hz, $\text{CH}(\text{CH}_3)_2$), 1.33 (s, 6H, $\text{CH}(\text{CH}_3)_2$), 1.02 (d, $J_{\text{H-H}} = 8$ Hz, 12H, CH_3).

$^1\text{H NMR}$ (THF-d_8 , 400 MHz) = 6.95 (d, 2H, $J_{\text{H-H}} = 12$ Hz, Ar), 6.85 (d, 4H, $J_{\text{H-H}} = 8$ Hz, Ar), 5.56 (s, 1H, 4-Pz), 4.75 (s, 2H, CHCCH_3), 4.23 (s, 4H, CH_2Pz), 3.29 (m, 4H, $\text{CH}(\text{CH}_3)_2$), 1.99 (s, 6H, CH_3CCH), 1.48 (d, 12H, $J_{\text{H-H}} = 4$ Hz, $\text{CH}(\text{CH}_3)_2$), 1.30 (s, 6H, CH_3CCH), 1.01 (d, 12H, $J_{\text{H-H}} = 8$ Hz, $\text{CH}(\text{CH}_3)_2$), -3.61 (s, 1H, SH).

$^{13}\text{C NMR}$ (THF-d_8 , 100 MHz) = 160.02, 158.71, 152.91, 148.40, 140.62, 125.30, 123.57, 96.70 (CH_2Pz), 91.10 (4-Pz), 54.43 (3(5)C-Pz), 27.80 (CH_3), 23.42 (CH_3), 22.75 (CH_3), 20.53 (CH_3).

ATR-IR (ν/cm^{-1}) = 3056 (m), 2951 (m), 2924 (m), 2864 (w), 2557 (s) (SH), 1556 (m), 1530 (vs), 1464 (vs), 1434 (vs), 1398 (vs), 1359 (m), 1313 (s), 1282 (w), 1250 (m), 1233 (w), 1191 (w), 1126 (w), 1108 (w), 1087 (w), 1075 (w), 1056 (w), 1032 (m), 1009 (w), 983 (w), 934 (w), 916 (w), 860 (w), 795 (s), 760 (vs), 741 (vs), 714 (w), 641 (w), 543 (w), 529 (w).

ATR-IR (ν/cm^{-1}) = 1817 (SD)

UV-vis (THF): $\lambda_{\text{max}} = 299, 380$ nm.

Anal. Calcd. (%) for $[\text{Ni}_2(\text{C}_{39}\text{H}_{53}\text{N}_6)\text{SH}]$: C 61.93, H 7.20, N 11.11; found: C 62.18, H 7.43, N 10.61.

KL¹Ni₂(μ -S) (14)

(a) PPh_3 (2.26 mg, 0.01 mmol, 1 equiv) was added into a solution of **12** in THF-d_8 at room temperature. Completely conversion happened in around 40 hours. ^1H

and ^{31}P NMR spectra were shown in the 5.2.

(b) S=PMe_3 (4.3 mg, 0.04 mmol, 1 equiv) was added into a solution of **2** (30.5 mg, 0.04 mmol, 1 equiv) in THF (1 mL) at room temperature. No obvious color changing was observed. Suitable crystals for x-ray diffraction were obtained from hexane layering into THF at -30°C as red block crystals in two weeks. (Yield: 95%, from ^1H NMR)

(c) **13** (16.5 mg, 0.02 mmol, 1 equiv) and excess potassium hydride were suspended in 2 mL of THF at room temperature. Intense gas (H_2) development was observed, and a color changes from brown to red occurred in 2 hours. The mixture was stirred for 4 hours continue, solid components were filtered off. Recrystallization of the crude product by layering hexane on a solution of **14** in THF at -30°C yields red block crystal. (Yield: 60%)

(d) **16** (33 mg, 0.04 mmol, 1 equiv) and excess potassium were suspended in 2 mL of THF at room temperature, and a color changes from brown to red occurred immediately. The mixture was stirred for 2 hours continue, solid components were filtered off. The final product was identified by ^1H NMR.

Molecular Weight: 794.43 g/mol ($\text{C}_{39}\text{H}_{53}\text{N}_6\text{Ni}_2\text{S}_2\text{K}$)

^1H NMR (THF- d_8 , 400 MHz) = 6.77 (m, 2H, $^3\text{J}_{\text{H-H}}=4$ Hz, Ar), 6.67 (d, 4H, $^2\text{J}_{\text{H-H}}=8$ Hz, Ar) 5.46 (s, 1H, 4-Pz), 4.47 (s, 2H, CHCCH_3), 4.12 (s, 4H, CH_2Pz), 3.42 (m, 4H, $\text{CH}(\text{CH}_3)_2$), 1.82 (s, 6H, CH_3), 1.33 (d, 12H, $^2\text{J}_{\text{H-H}}=8$ Hz, $(\text{CH}_3)_2\text{CH}$), 1.16 (s, 6H, CH_3), 0.95 (d, 12H, $^2\text{J}_{\text{H-H}}=8$ Hz, $(\text{CH}_3)_2\text{CH}$)

^{13}C NMR (THF- d_8 , 100 MHz) = 159.18, 158.75, 153.91, 149.77, 141.46, 124.27, 123.28, 96.07 (CH_2Pz), 91.29 (4-Pz), 53.88 (3(5)C-Pz), 28.66 (CH_3), 26.41 (CH_3), 25.37 (CH_3), 21.62(CH_3).

ATR-IR (ν/cm^{-1}) = 3056 (w), 2954 (s), 2928 (s), 2861 (s), 1549 (s), 1520 (vs), 1458 (s), 1431 (s), 1400 (vs), 1377 (w), 1366 (w), 1321 (w), 1308 (vs), 1288 (w), 1252 (m), 1231 (m), 1190 (m), 1079 (m), 1055 (vs), 1027 (m), 1005 (w), 950 (w), 938 (w), 894 (m), 855 (w), 806 (w), 793 (s), 754 (vs), 726 (vs), 711 (vs),

659 (w), 640 (w), 542 (w), 523 (m).

ESI-MS (THF:CH₃CN = 10:1): m/z (%) = 754.49 (100) (**14**-K+H)⁺, 755.47 (100) (**16**+H), 792.38 (50) (**14**-K +H)⁺, 793.25 (17+H)⁺, 753.32 (**14**-K)⁻

UV-vis (THF): λ_{max} = 275, 351, 376, 460 nm.

Anal. Calcd. (%) for [KNi₂(C₃₉H₅₃N₆)S·(THF)₂]: C 60.14, H 7.41, N 8.95; found: C 60.28, H 7.55, N 8.64

L¹Ni₂(μ-SCH₃) (15)

A solution of **14** (16 mg, 0.02 mmol, 1 equiv) in THF (2 mL) was treated with excess CH₃I (2 M in Butyl Methyl) with stirring. The solution color changed from orange to green immediately. The reaction was stirred at room temperature for 30 mins. Suitable crystals in black block for x-ray diffraction were obtained by layering hexane on a solution of **15** in THF at -30°C.

Molecular Weight: 770.37 g/mol (C₃₉H₅₃N₆Ni₂SCH₃)

ATR-IR (ν/cm⁻¹) = 3052 (w), 2953 (m), 2922 (m), 2864 (m), 1550 (m), 1528 (vs), 1460 (w), 1435 (s), 1394 (vs), 1380 (vs), 1312 (vs), 1266 (w), 1251 (w), 1178 (m), 1084 (m), 1055 (m), 1033 (m), 940 (w), 799 (s), 763 (vs), 739 (vs), 595 (w), 546 (w), 527 (w), 463 (w), 437 (m), 404 (m).

ESI-MS (THF:CH₃CN = 10:1): m/z (%) = 791.30 (**15**+H)⁺.

L¹Ni₂(μ-S) (16)

(a) S=PMe₃ (4.3 mg, 0.04 mmol, 1 equiv) was added into a solution of **24** (30 mg, 0.04 mmol, 1 equiv) in THF (1 mL) at room temperature. The color changes from brown-red to deep-brown in 10 mins. There is some orange piece formed in 20 mins also. Suitable crystals for x-ray diffraction were obtained by layering hexane on a solution of **16** in THF at -30°C as red block crystals in two days.

(b) To a precooled and blood red solution of **12** (16.5 mg, 0.02 mmol, 1.00 equiv) in THF (2 mL) was added [Cp₂Fe][BF₄] (8.1 mg, 0.030 mmol, 1.5 equiv). The reaction mixture was allowed to react for overnight at -35°C. To the resulting red

solution hexane (20 mL) was added, causing precipitation of a black powder. The solution was removed via a syringe and the solid was washed with hexane (20 mL) and then dried under reduced pressure to give the crude product. Black block crystals suitable for x-ray diffraction were obtained by layering hexane on a solution of **16** in THF at -30°C .

(c) To a pre-cooled and brown solution of **13** (15.6 mg, 0.02 mmol, 1 equiv) in THF (1 mL) was added TBP (3.2 mg, 0.04 mmol, 2 equiv). The reaction mixture was allowed to react for 12 hours at -30°C . Green single crystals suitable for x-ray diffraction were obtained by layering hexane on a solution of **16** in THF at -30°C in two days

Molecular Weight: 755.34 g/mol ($\text{C}_{39}\text{H}_{53}\text{N}_6\text{Ni}_2\text{S}$)

ATR-IR (ν/cm^{-1}) = 3231 (br, w), 3051 (w), 2956 (m), 2866 (m), 1550 (m), 1530 (m), 1462 (w), 1434 (m), 1390 (m), 1310 (w), 1276 (m), 1245 (s), 1150 (m), 1028 (vs), 982 (w), 954 (w), 916 (w), 865 (w), 800(w), 760 (m), 730 (m), 637 (vs), 572 (m), 517 (s).

UV-vis (THF): λ_{max} = 270, 319, 373, 457 nm.

$\text{L}^1\text{Ni}_2(\mu\text{-}\eta^1, \eta^1\text{-NNH}_2\text{Ph})$ (17**)**

Phenylhydrazine (5 μL , 0.05 mmol, 1 equiv) was added to a solution of **1** (40 mg, 0.05 mmol, 1 equiv) and KC_8 (7 mg, 0.05 mmol, 1 equiv) in 2 mL THF at room temperature. During the reaction, a color changes from brown to dark red occurred immediately and intense gas (H_2) is generated. The mixture was stirred for 16 h and filtered. After filtration, THF was removed in *vacuo* to yield dark red powder. Recrystallization of the crude product from Pentane diffusion into THF at room temperature yield red needle crystals of **17**. (18.35 mg, 0.019 mmol, 37%)

Molecular Weight: 830.36 $\text{g}\cdot\text{mol}^{-1}$. ($\text{C}_{45}\text{H}_{60}\text{N}_8\text{Ni}_2$)

^1H NMR (THF- d_8 , 400 MHz) = 9.36 (d, 2H, $^3J_{\text{H-H}} = 8$ Hz, **Ph o-H**), 7.30 (d, 2H, $^3J_{\text{H-H}}$)

= 4 Hz, **Ar**), 7.04 (t, 2H, $^3J_{\text{H-H}} = 12$ Hz, **Ph m-H**), 6.93 (t, 2H, $^3J_{\text{H-H}} = 8$ Hz, **Ar**), 6.80 (d, 1H, $^3J_{\text{H-H}} = 16$ Hz, **Ar**), 6.65 (d, 1H, $^3J_{\text{H-H}} = 12$ Hz, **Ar**), 6.37 (t, 1H, $^3J_{\text{H-H}} = 8$ Hz, **Ph p-H**), 5.43 (s, 1H, **4-Pz**), 4.81 (s, 1H, **CH₃CCH**), 4.63(s, 1H, **CH₃CCH**), 3.99 (q, 4H, $^3J_{\text{H-H}} = 12$ Hz, **CH₂Pz**), 3.81 (t, 2H, $^3J_{\text{H-H}} = 20$ Hz, **CH(CH₃)₂**), 3.08 (t, 1H, $^3J_{\text{H-H}} = 8$ Hz, **CH(CH₃)₂**), 2.77 (t, 1H, $^3J_{\text{H-H}} = 8$ Hz, **CH(CH₃)₂**), 2.16 (s, 1H, **NH**), 2.10 (d, 3H, $J_{\text{H-H}} = 8$ Hz, **(CH₃)₂CH**), 1.99 (d, 3H, $^3J_{\text{H-H}} = 8$ Hz, **(CH₃)₂CH**), 1.93 (d, 6H, $^3J_{\text{H-H}} = 12$ Hz, **CH₃CCH**), 1.61 (s, 1H, **NH**), 1.47 (d, 6H, $^3J_{\text{H-H}} = 12$ Hz, **CH₃CCH**), 1.10 (m, 9H, **(CH₃)₂CH**), 0.85 (d, 3H, $^3J_{\text{H-H}} = 8$ Hz, **(CH₃)₂CH**), 0.71 (d, 3H, $^3J_{\text{H-H}} = 12$ Hz, **(CH₃)₂CH**), 0.31 (d, 3H, $^3J_{\text{H-H}} = 8$ Hz, **(CH₃)₂CH**).

¹³C {¹H} NMR (THF-d₈, 100 MHz) = 20.19 (**CH₃**), 20.37 (**CH₃**), 22.36 (**CH₃**), 22.63 (**CH₃**), 22.82 (**CH₃**), 23.53 (**CH₃**), 23.61 (**CH₃**), 25.07 (**CH₃**), 25.31 (**CH₃**), 25.39 (**CH₃**), 26.14 (**CH₃**), 26.98 (**CH₃**), 27.00 (**CH(CH₃)₂**), 27.23 (**CH(CH₃)₂**), 28.13 (**CH(CH₃)₂**), 28.24 (**CH(CH₃)₂**), 51.05 (**CH₂Pz**), 51.34 (**CH₂Pz**), 90.85 (**4C-Pz**), 96.40 (**CHCCH₃**), 97.93 (**CHCCH₃**), 112.85 (**Ar**), 122.26 (**Ar**), 122.63 (**Ar**), 124.42 (**Ar**), 124.60 (**Ar**), 124.97 (**Ar**), 126.05 (**Ar**), 127.25 (**Ar**), 141.30 (**Ar**), 142.14 (**Ar**), 142.91 (**Ar**), 143.30 (**Ar**), 144.03 (**Ar**), 146.55 (**Ar**), 153.29 (**CHCCH₃**), 153.32 (**CHCCH₃**), 158.94 (**CHCCH₃**), 158.98 (**CHCCH₃**), 159.30 (**Ar**), 159.55 (**Ar**), 160.48 (**Ar**).

MS (ESI) *m/z* (%): = 829.5 (100)(**17+H**)⁺, 721.4 (5)(**17-NH₂NPh**)⁺.

AIR-IR (ν/cm^{-1}) = 3296.09 (w, **NH**), 3218.79 (w, **NH**), 3048.20 (w), 3013.55 (w), 2945.58 (m), 2920.28 (m), 2860.28 (m), 1596.85 (w), 1556.52 (m), 1526.58 (s), 1445.43 (s), 1424.14 (s), 1390.22 (vs), 1309.06 (s), 1271.14 (s), 1249.86 (s), 1181.34 (s), 1087.54 (m), 1023.68 (m), 981.11 (m), 929.88 (w), 848.73 (w), 797.51 (w), 763.58 (s), 746.95 (vs), 733.65 (vs), 729.66 (vs), 687.08 (vs), 644.51(w), 593.29 (m), 546.06 (w), 524.77 (w), 508.14 (w), 422.99 (s), 405.70 (s).

Elemental analysis (%) calc. for C₃₉H₅₃N₆Ni₂ (C₆H₅N₂H₂) (828.36 g/mol): C 52.48 H 6.10 N 9.07; Found C 52.77 H 6.45 N 9.33.

KL¹Ni₂(μ - η^1 , η^1 -NNHPh) (18)

17 (16.5 mg, 0.02 mmol, 1 equiv) and potassium hydride (0.8 mg, 0.02 mmol, 1 equiv) were suspended in 2 mL of THF at room temperature. Intense gas (H₂) development was observed, and a color changes from dark-red to dark green occurred in 2 hours. The mixture was stirred for 4 hours continue, solid components were filtered off. Black rhombus block crystals suitable for x-ray diffraction were obtained by layering hexane on a solution of **18** in THF at -30°C with 60% yield.

Molecular Weight: 866.32 g·mol⁻¹.

¹H NMR (THF-d₈, 400 MHz) = 10.51 (br, 1H, **Ph o-H**), 9.11 ((br, 1H, **Ph o-H**), 6.99 (m, 3H, **Ph m-H** and **p-H**), 6.79 (t, 2H, ³J_{H-H} = 8 Hz, **Ar**), 6.69 (d, 1H, ³J_{H-H} = 4 Hz, **Ar**), 6.64 (d, 2H, ³J_{H-H} = 12 Hz **Ar**), 6.60 (d, 1H, ³J_{H-H} = 12 Hz, **Ar**), 5.47 (s, 1H, 4-Pz), 4.51 (s, 1H, **CHCCH₃**), 4.45 (s, 1H, **CHCCH₃**), 4.15 (m, 1H, **CH(CH₃)₂**), 3.93 (m, 2H, **CH₂Pz**), 3.80 (m, 2H, **CH₂Pz**), 3.30 (m, 1H, **CH(CH₃)₂**), 3.06 (m, 1H, **CH(CH₃)₂**), 2.89 (m, 1H, **CH(CH₃)₂**), 2.02 (d, 3H, ³J_{H-H} = 8 Hz, **(CH₃)₂CH**), 1.80 (m, 6H, **(CH₃)₂CH** + **CH₃)₂CH**), 1.69 (s, 3H, **CH₃CCH**), 1.31 (s, 7H, **CH₃CCH** and **NH**), 1.07 (t, 6H, ³J_{H-H} = 8 Hz, **(CH₃)₂CH**), 0.88 (m, 3H, **CH₃CCH**), 0.84 (d, 3H, ³J_{H-H} = 4 Hz, **(CH₃)₂CH**).

¹³C {¹H} NMR (THF-d₈, 100 MHz) = 20.20 (**CH₃**), 20.38 (**CH₃**), 22.21 (**CH₃**), 22.63 (**CH₃**), 23.28 (**CH₃**), 23.53 (**CH₃**), 25.39 (**CH₃**), 26.92 (**CH(CH₃)₂**), 27.12 (**CH(CH₃)₂**), 27.61 (**CH(CH₃)₂**), 28.20 (**CH(CH₃)₂**), 51.06 (**CH₂Pz**), 51.39 (**CH₂Pz**), 91.05 (4C-Pz), 95.44(**CHCCH₃**), 95.84(**CHCCH₃**), 112.84, 122.40, 122.76, 123.14, 124.41, 124.60, 124.97, 126.05, 127.25, 127.91, 128.03, 141.11, 141.31, 142.14, 143.30, 146.56, 152.19, 153.29 (**CHCCH₃**), 153.32 (**CHCCH₃**), 158.94 (**CHCCH₃**), 158.98 (**CHCCH₃**), 159.31, 159.55, 160.48 (**Ar**).

AIR-IR (ν /cm⁻¹) = 3244 (vw, **NH**), 3054 (w), 2952 (m), 2861 (m), 1584 (m), 1549 (s), 1523 (s), 1461 (s), 1433 (vs), 1400 (vs), 1316 (m), 1306 (m), 1282 (m), 1271 (m), 1250 (m), 1228 (m), 1184 (m), 1159 (m), 1109 (w), 1086 (w),

1053 (m), 1025 (m), 1017 (m), 973 (m), 894 (w), 844 (w), 793 (m), 756 (m), 744 (m), 730 (m), 697 (m).

UV-Vis (THF) = 243 (1016), 264 (998), 377 (391), 587 (505);

Elemental analysis (%) calc. for $C_{45}H_{59}N_8Ni_2K$: C 62.33 H 6.86 N 12.93; Found C 62.77 H 6.75 N 12.33.

[K(dibenzo(18-crown-6))]⁺[L¹Ni₂(μ - η^1 , η^1 -NHNPh)]⁻ (19)

A THF solution of **18** and DB18C6 were stirred for 2 hours, then solid components were filtered off. Suitable crystals for x-ray diffraction were obtained by layering hexane/Et₂O on a solution of **19** in THF at -30°C in 70% yield.

Molecular Weight: 1226.48 g·mol⁻¹.

¹H NMR (THF-d₈, 400 MHz) = 9.36 (d, 2H, ³J_{H-H} = 8 Hz, **Ph o-H**), 7.31 (s, 1H, **Ar**), 7.29 (d, 2H, ³J_{H-H} = 4 Hz, **Ar**), 7.04 (t, 2H, ³J_{H-H} = 8 Hz, **Ar**), 6.93 (m, 9H, dibenzo(18-crown-ether)+**Ar**), 6.87 (m, 6H, dibenzo(18-crown-ether)), 6.87 (dd, 1H, ³J_{H-H} = 8 Hz, **Ar**), 6.65 (dd, 1H, ³J_{H-H} = 8 Hz, **Ar**), 6.38 (tt, 1H, ³J_{H-H} = 8 Hz, **Ar**), 5.43 (s, 1H, **Pz**), 4.81 (s, 1H, **CHCCH₃**), 4.69 (s, 1H, **CHCCH₃**), 4.07 (m, 12H, dibenzo(18-crown-ether) + **CH₂Pz**), 3.98 (m, 16H, dibenzo(18-crown-ether)), 3.84 (d, 1H, **CH₂Pz**), 3.79 (d, 1H, **CH₂Pz**), 3.39 (t, 4H, ³J_{H-H} = 8 Hz, dibenzo(18-crown-ether)), 3.08 (m, 1H, **CH(CH₃)₂**), 2.77 (m, 1H, **CH(CH₃)₂**), 2.10 (d, 3H, ³J_{H-H} = 8 Hz, **(CH₃)₂CH**), 1.98 (d, 3H, ³J_{H-H} = 8 Hz, **(CH₃)₂CH**), 1.93 (d, 6H, ³J_{H-H} = 12 Hz, **CH₃CCH**), 1.53 (s, 1H, **NH**), 1.57 (d, 6H, ³J_{H-H} = 12 Hz, **CH₃CCH**), 1.11 (m, 18H, m, 9H, **(CH₃)₂CH** + pentane), 0.85 (d, 3H, ³J_{H-H} = 8 Hz, **(CH₃)₂CH**), 0.71 (d, 3H, ³J_{H-H} = 12 Hz, **(CH₃)₂CH**), 0.31 (d, 3H, ³J_{H-H} = 8 Hz, **(CH₃)₂CH**).

¹³C {¹H} NMR (THF-d₈, 75.5 MHz) = 14.69, 22.37 (**CH₃**), 22.63 (**CH₃**), 23.54 (**CH₃**), 23.61 (**CH₃**), 24.86 (**CH₃**), 25.39 (**CH₃**), 26.15 (**CH₃**), 26.99 (**CH₃**), 27.00 (**CH(CH₃)₂**), 27.24 (**CH(CH₃)₂**), 28.13 (**CH(CH₃)₂**), 28.24 (**CH(CH₃)₂**), 51.06 (**CH₂Pz**), 51.34 (**CH₂Pz**), 65.33 (18-crown-6), 66.62 (18-crown-6), 67.22 (18-crown-6), 67.84 (18-crown-6), 69.17 (18-crown-6), 90.87(4C-Pz), 96.41 (**CHCCH₃**), 97.94 (**CHCCH₃**), 111.90 (18-crown-6), 112.85 (**Ar**), 120.81, 122.27

(Ar), 122.64 (Ar), 124.42 (Ar), 124.60 (Ar), 124.97 (Ar), 126.06 (Ar), 127.26 (Ar), 141.30 (Ar), 142.13 (Ar), 142.90 (Ar), 143.29 (Ar), 144.03 (Ar), 146.55 (Ar), 147.96 (18-crwon-6), 153.29 (CHCCH₃), 153.32 (CHCCH₃), 158.98 (CHCCH₃), 159.30 (Ar), 159.65 (Ar), 160.48 (Ar).

AIR-IR (ν/cm^{-1}) = 3244 (br, w, NH), 2953 (m), 2926 (m), 2860 (m), 1595 (w), 1572 (m), 1544 (m), 1530 (m), 1517 (s), 1504 (vs), 1471 (m), 1432 (s), 1402 (vs), 1380 (m), 1316 (w), 1303 (m), 1268 (w), 1246 (vs), 1209 (vs), 1184 (m), 1157 (m), 1123 (vs), 1056 (s), 1021 (m), 976 (m), 943 (vs), 902 (m), 855 (m), 845 (m), 793 (m), 779 (m), 733 (vs), 689 (s), 599 (m), 565 (s), 539 (s), 516 (s).

Elemental analysis (%) calc. for C₆₅H₈₃N₈O₆Ni₂: C 63.60 H 6.82 N 9.13; Found C 63.82 H 6.95 N 8.21.

L¹Ni₂(μ - η^1 , η^1 -N=NPh) (20)

17 (16.5 mg, 0.02 mmol, 1 equiv) and excess Pd(OAc)₄ were suspended in 2 mL of THF at room temperature. The mixture was stirred for a day in the dark environment. There is no obviously color changing after reaction. The solution was then filtered through celite. The red powder was analyzed by ESI-MS and IR spectroscopy.

Molecular Weight: 828.36 g·mol⁻¹.

MS (ESI) m/z (%): = 827.5 (100) (**20**+H)⁺.

AIR-IR (ν/cm^{-1}) = 2953 (m), 2926 (m), 2860 (m), 1595 (w), 1572 (m), 1544 (m), 1530 (m), 1517 (s), 1504 (vs), 1471 (m), 1432 (s), 1402 (vs), 1380 (m), 1316 (w), 1303 (m), 1268 (w), 1246 (vs), 1209 (vs), 1184 (m), 1157 (m), 1123 (vs), 1056 (s), 1021 (m), 976 (m), 943 (vs), 902 (m), 855 (m), 845 (m), 793 (m), 779 (m), 733 (vs), 689 (s), 599 (m), 565 (s), 539 (s), 516 (s).

L¹Ni₂(μ - η^1 , η^1 -NNH₂Ph)(BF₄) (21)

[H-Lut]BF₄ (5 mg, 0.02 mmol, 1 equiv) was added into the solution THF of **17** (16.6 mg, 0.02 mmol, 1 equiv) resulted the colore change from red to green immediately. The mixture was stiiired for 4 hours and green precipitate was obtained. The green powder was analyzed by NMR and IR spectroscopy.

Molecular Weight: 918.21 g·mol⁻¹. (C₄₅H₆₁N₈Ni₂BF₄)

¹⁹F NMR (CD₃CN, 376 MHz) = -151.23 ppm.

¹¹B NMR (CD₃CN) = -1.14 ppm.

MS (ESI) *m/z* (%): = 829.5 (100)(**21**-BF₄)⁺.

AIR-IR (*ν*/cm⁻¹) = 3354 (w, br, NH,), 3307(w, br, NH,), 3285 (w, br, NH,), 3054, 2961, 2927, 2868, 1664, 1644, 1588, 1555, 1527, 1483, 1459, 1434, 1398, 1313, 1280, 1252, 1183, 1053, 1026, 934, 864, 797, 758, 746, 693, 625, 594, 554, 519.

[K(Dibenzo(18-crown-6))]⁺[L¹Ni₂(μ-η¹,η¹-PhN-NPh)]⁻ (22**)**

(a) Azobenzene (7.29 mg, 0.04 mmol, 1 equiv) was added into a solution of **4** (42 mg, 0.04 mmol, 1 equiv) in THF (1 mL) at room temperature. The color changes from orange to blood red immediately. Suitable crystals for x-ray were obtained by layering hexane on a solution of **22** in THF at -30 °C.

(b) **23** (36.2 mg, 0.04 mmol, 1 equiv) and potassium (0.8 mg, 0.02 mmol, 2 equiv) were suspended in 2 mL of THF at room temperature, and a color change from black to dark red occurred in 20 mins. The mixture was stirred for 2 hours continue. Suitable crystals for x-ray were obtained by layering hexane on a solution of **22** in THF at -30 °C.

Molecular Weight: 1304.99 g/mol (C₇₁H₈₇N₈O₆Ni₂K)

ATR-IR (*ν*/cm⁻¹) = 3048 (w), 2957 (m), 2924 (m), 2864 (m), 1595 (w), 1572 (m), 1554 (m), 1503 (vs), 1452 (vs), 1431 (vs), 1399 (vs), 1359 (w), 1317 (m), 1307 (m), 1247 (vs), 1211 (s), 1125 (vs), 1089 (m), 1054 (s), 1022 (m), 989 (w), 956 (w), 941 (s), 900 (m), 850 (w), 794 (w), 778 (w), 736 (vs), 690 (s), 600 (m), 532 (s), 510 (s).

UV-vis (THF): λ_{\max} = 372, 462, 577, 738 nm.

L¹Ni₂(μ - η^1 , η^1 -PhNNPh) (23)

(a) Azobenzene (2.56 mg, 0.04 mmol, 1 equiv) was added into a solution of **2** (30.5 mg, 0.04 mmol, 1 equiv) in THF (1 mL) at room temperature. The color changes from orange to blood red immediately and intensity gas was observed. Suitable crystals for x-ray diffraction were obtained by layering hexane on a solution of **23** in THF at -30°C in 10% yield.

(b) Azobenzene (2.56 mg, 0.04 mmol, 1 equiv) was added into a solution of **24** (30.5 mg, 0.04 mmol, 1 equiv) in THF (2 mL) at room temperature. The color changes from brown to black immediately. Suitable crystals for x-ray diffraction were obtained by layering hexane on a solution of **23** in THF at -30°C . Yield: 75%.

Molecular Weight: 605.49 g/mol (C₅₁H₆₃N₈Ni₂K)

ATR-IR (ν/cm^{-1}) = 3058 (w), 2954 (m), 2926 (m), 2869 (m), 2843 (m), 1623 (m), 1593 (m), 1553 (m), 1525 (m), 1504 (vs), 1453 (s), 1433 (m), 1399 (m), 1364 (m), 1321 (m), 1282 (s), 1246 (vs), 1228 (s), 1211 (s), 1157 (s), 1124 (vs), 1097 (m), 1088 (m), 1062 (m), 1048 (m), 1030 (vs), 959 (s), 940 (s), 898 (w), 856 (w), 775 (m), 751 (vs), 637 (vs), 600 (m), 573 (m), 516 (m).

UV-vis (THF): λ_{\max} = 372, 462, 577, 738 nm.

Anal. Calcd. (%) for [Ni₂(C₃₉H₅₃N₆)(C₁₂H₁₀N₂)] [C₄H₈O]: C 61.89, H 7.37, N 10.07; found: C 61.53, H 7.11, N 9.67.

L¹Ni₂(μ - η^1 , η^1 -N₂) (24)

(a) **2** (318 mg, 0.4 mmol, 1 equiv) and [H-Lut]OTf (64.5 mg, 0.4 mmol, 1 equiv) were dissolved in THF (2 mL), and the reaction mixture were stirred for 2 h at room temperature in a dinitrogen atmosphere. All volatiles were subsequently removed under vacuum, and the resulting solid was dried under vacuum. Suitable crystals for x-ray were obtained by layering hexane on a solution of **24** in THF

at $-30\text{ }^{\circ}\text{C}$. The mother liquor was pumped down, dissolved in THF, and layered with hexane to afford a second crop.

(b) **2** (318 mg, 0.4 mmol, 1 equiv) and tris(pentafluorophenyl)borane (204.8 mg, 0.4 mmol, 2 equiv) were dissolved in THF (5 mL), and the reaction mixture were stirred for 2 days at room temperature in a dinitrogen atmosphere. Suitable crystals for x-ray diffraction were obtained from THF slow evaporation in a week.

24- $^{15}\text{N}_2$: The solid **2** (318 mg, 0.4 mmol, 1 equiv) and [H-Lut]OTf (64.5 mg, 0.4 mmol, 1 equiv) were loaded into a two-neck round-bottom flask and a T-adapter attached to a Yong-flask of $^{15}\text{N}_2$ which was dried from H_2SO_4 (95%) for 2 days and Vacuum. The hoses used were placed under vacuum for at least 12 hours before use. After 12 hour, 2 mL THF was added into the two-neck round-bottom flask and the solution was stirred for 4 hours. After 4 hours, the solution followed an analogous work-up procedure as a described for unlabeled **24**. IR and Raman spectra are the same as for the unlabeled material expect the stretching of N_2 .

Detection of evolved H_2 from **2 with [H-Lut]OTf**: In the N_2 box, the same flask used for the H_2 calibration was charged with **2** (15.2 mg, 0.02 mmol), [H-Lut]OTf (5.1 mg, 0.02 mmol) and stir bar. The flask was then closed. 2 mL of THF was then injected and the mixture was stirred at room temperature for 3 hours. The whole set-up was then taken out of the glove box, 0.8 mL CH_4 was added and the headspace was subjected to GC-2014 analysis as describe in the general methods. The integration ratio was compared to the calibration plot to quantify the amount of free hydrogen released from the reaction.

Molecular Weight: $751.27\text{g}\cdot\text{mol}^{-1}$ ($\text{C}_{39}\text{H}_{53}\text{N}_8\text{Ni}_2$)

ATR-IR (ν/cm^{-1}) = 3056 (w), 2959 (m), 2920 (m), 2862 (m), 1896 ($^{14}\text{N}\equiv^{14}\text{N}$)(m), 1618 (w), 1551 (s), 1528 (s), 1459 (s), 1433 (s), 1393 (s), 1312 (s), 1250 (vs), 1230 (vs), 1174 (s), 1092 (s), 1030 (vs), 945 (s), 915 (s), 866 (s), 795 (s), 755 (s), 732 (s), 641 (vs), 575 (s), 516 (vs), 480 (s), 435 (m), 399 (m).

ATR-IR (ν/cm^{-1}) = 1830 ($^{15}\text{N}\equiv^{15}\text{N}$) (m).

Raman (ν/cm^{-1}) = 1900 ($^{14}\text{N}=^{14}\text{N}$); 1836 ($^{15}\text{N}=^{15}\text{N}$).

UV-vis (THF): λ_{max} = 276 (12680), 320 (9090), 378 (5750).

Elemental analysis (%) calc. for $\text{C}_{39}\text{H}_{53}\text{N}_8\text{Ni}_2$: C 62.35 H 7.11 N 14.92; Found C 62.73 H 7.47 N 14.37.

$\text{L}^1\text{Ni}_2(\mu\text{-}\eta^1, \eta^1\text{-N=NH})$ (25**)**

(a) To a pre-cooled and red solution of **27** (15.6 mg, 0.02 mmol, 1 equiv) in THF (2 mL) was added TEMPO (3.2 mg, 0.04 mmol, 2 equiv). The reaction mixture was allowed to react for 12 hours at -35°C . Green single crystals suitable for x-ray diffraction were obtained by layering hexane on a solution of **25** in THF at -35°C . *Attention: The compound is unstable at room temperature under this condition.*

(b) To a pre-cooled and red solution of **27** (15.6 mg, 0.02 mmol, 1 equiv) in THF (2 mL) was added galvinoxyl radical (16.82 mg, 0.04 mmol, 2 equiv). The reaction mixture was allowed to react for 12 hours at -30°C . Brown single crystals suitable for x-ray diffraction were obtained by layering hexane on a solution of **25** in THF at -30°C Yield: 10 mg.

(c) To a pre-cooled and brown solution of **24** (15.6 mg, 0.02 mmol, 1 equiv) in THF (1 mL) was added TEMPO-H (3.2 mg, 0.04 mmol, 2 equiv). The reaction mixture was allowed to react for 12 hours at -30°C . Green single crystals suitable for x-ray diffraction were obtained by layering hexane on a solution of **25** in THF at -35°C in two days.

(d) **29** (15.6 mg, 0.02 mmol, 1 equiv) and TlOTf (7.07 mg, 0.02 mmol, 1 equiv) were dissolved in THF (2 mL), and the reaction mixture were stirred for 2 h at room temperature in a dinitrogen atmosphere. All volatiles were subsequently removed under vacuum, and the resulting solid was dried under vacuum. The crude powder was recrystallization by layering hexane on a solution of **25** THF at -30°C .

25-¹⁵N₂: Firstly have to synthesize **24-¹⁵N₂** under Ar atmosphere in case of the ¹⁴N₂ exchange with ¹⁵N₂ ligand. The solution of **24-¹⁵N₂** followed an analogous work-up procedure as a described for unlabeled **24** of method C. rRaman spectra are the same as for the unlabeled material expect the stretching of N₂H.

Molecular Weight: 752.32 g·mol⁻¹ (C₃₉H₅₄N₈Ni₂)

¹H NMR (THF-d₈, 400 MHz) = 9.46 (s, 1H, NH), 7.15 (t, 1H, ³J_{H-H} = 8 Hz, Ar), 6.97 (d, 2H, ³J_{H-H} = 8 Hz, Ar), 6.89 (t, 1H, ³J_{H-H} = 8 Hz, Ar), 7.15 (d, 2H, ³J_{H-H} = 8 Hz, Ar), 5.70 (s, 1H, Pz), 4.99 (d, 2H, ³J_{H-H} = 8 Hz, CHCCH₃), 4.99 (d, 2H, ³J_{H-H} = 8 Hz, CHCCH₃), 4.24 (d, 2H, ³J_{H-H} = 12 Hz, CH₂Pz), 3.40 (m, 2H, CH(CH₃)₂), 3.20 (m, 2H, CH(CH₃)₂), 2.02 (d, 6H, ³J_{H-H} = 8 Hz, CH₃), 1.58 (d, 6H, ³J_{H-H} = 8 Hz, CH₃), 1.12 (d, 6H, ³J_{H-H} = 8 Hz, CH₃), 1.05 (dd, 12H, ³J_{H-H} = 8 Hz, CH₃), 0.88 (d, 6H, ³J_{H-H} = 8 Hz, CH₃).

¹³C {¹H} NMR (THF-d₈, 100 MHz) = 162.61 (CHCCH₃), 161.74 (CHCCH₃), 161.26 (CHCCH₃), 160.68 (CHCCH₃), 160.27 (3(5)-Pz), 159.46 (3(5)-Pz), 147.31 (Ar), 144.89 (Ar), 143.31 (Ar), 143.12 (Ar), 125.35 (Ar), 125.01 (Ar), 124.93 (Ar), 122.60 (Ar), 99.18 (CHCCH₃), 98.89 (CHCCH₃), 92.87 (4-Pz), 54.31 (CH₂Pz), 53.93 (CH₂Pz), 29.22 (CHCH₃), 28.87 (CH₃), 28.53 (CH₃), 25.31 (CH₃), 24.04 (CH₃), 21.38 (CH₃).

ATR-IR (ν/cm⁻¹) = 3054 (w), 3022 (m), 3958 (m), 2923 (m), 2862 (m), 1558 (s), 1524 (w), 1456 (w), 1434 (w), 1396 (w), 1369 (N=N, w), 1308 (w), 1282 (w), 1247 (w), 1232 (w), 1186 (w), 1175 (w), 1104 (w), 1089 (w), 1074 (w), 1055 (w), 1030 (w), 1015 (w), 956 (w), 936 (w), 914 (w), 865 (w), 855 (w), 800 (w), 793 (w), 759 (w), 741 (w), 713 (w), 672 (w), 652 (w), 641 (w), 623 (w), 568 (w), 547 (w), 525 (w), 439 (w), 411 (w), 403 (w).

Raman (ν/cm⁻¹) = 1392 (¹⁴N=¹⁴N), 1323(¹⁵N=¹⁵N).

UV-vis (THF): λ_{max} = 270(1174), 315 (shoulder) (319), 384 (428).

Elemental analysis (%) calc. for C₃₉H₅₄N₈Ni₂: C 60.70 H 7.61 N 13.06; found C 60.33 H 7.47 N 13.39.

L¹Ni₂(μ-η¹,η¹-NH₂) (26)

(1) A solution of **27** (100 mg, 0.169 mmol) in THF (20 mL) was rapidly stirred at 70°C for 13 weeks. After concentration of the solution to 2 mL and cooling to room temperature, brown-red crystals suitable for x-ray diffraction were grown by layering hexane on a solution of **26** in THF.

(2) A solution of **25** (14.6 mg, 0.02 mmol) with KH in THF (20 mL) was rapidly stirred for 1 hour, the color changes from brown to orange in 10 mins. Brown-red crystals suitable for x-ray diffraction were grown by layering hexane on a solution of **26** in THF in 2 days.

(3) **1** (100 mg, 0.125 mmol, 1 equiv) and NH₃ (0.5 M in THF) (10 mL) were suspended in THF at -78°C for 2 hours. Then the solution was allowed to room temperature and stirred for overnight. The color changed from brown to yellow-red. Brown-red crystals suitable for x-ray diffraction were grown by layering hexane on a solution of **26** in THF.

Molecular Weight: 739.29 g·mol⁻¹ (C₃₉H₅₅N₇Ni₂)

¹H NMR (THF-d₈, 400 MHz) = 6.99 (t, 2H, Ar), 6.87 (d, 4H, Ar), 5.54 (s, 1H, 4-Pz), 4.66 (s, 2H, CHCCH₃), 4.16 (s, 4H, CH₂Pz), 3.37 (m, 4H, CH(CH₃)₂), 1.92 (s, 6H, CH₃), 1.53 (d, 12h, (CH₃)₂CH), 1.18 (s, 6H, CH₃), 1.08 (d, 12h, (CH₃)₂CH), -3.87 (s, 2H, NH₂)

¹³C {¹H } NMR (THF-d₈, 100 MHz) = 20.48 (CH₃), 22.79 (CH₃), 23.06 (CH₃), 24.85 (CH₃), 27.89 (CH(CH₃)₂), 54.56 (CH₂Pz), 90.61 (4-Pz), 96.54 (CHCCH₃), 124.37 (Ar), 124.93 (Ar), 140.24 (Ar), 146.93 (Ar), 149.84 (3,5-Pz), 158.49(CH₃CCH), 160.28 (CH₃CCH).

ATR-IR (ν/cm⁻¹) = 3348 (w), 3333 (w), 3311 (vw), 3059 (w), 2960 (vs), 2927 (s), 2867 (s), 2235 (w), 2082 (w), 1680 (m), 1629 (m), 1557 (s), 1531 (vs), 1463 (s), 1439 (vs), 1404 (vs), 1322 (m), 1260 (m), 1195 (w), 1098 (m), 1048 (m), 956 (w), 936 (w), 802 (m), 764 (m), 735 (m).

L¹Ni₂(μ-η¹,η¹-N₂H₃) (27)

(a) Hydrazine in THF (1.0 M) (0.75 mL, 0.75 mmol, 3 equiv) was added to a solution of **1** (200 mg, 0.25 mmol, 1 equiv) in 3 mL of THF at room temperature. During the reaction, a color change from brown to dark red occurred immediately. The mixture was stirred for 20 hours and filter. Suitable crystals for x-ray were obtained from pentane slow diffusion on a solution of **27** in THF at -30 °C. (75 mg, 37%)

(b) Hydrazine in THF (1.0 M) (40 μL, 0.04 mmol, 2 equiv) was added to a solution of **2** (15 mg, 0.02 mmol, 1 equiv) in 1 mL of THF at room temperature. The mixture was stirred for 10 mins and filter. Suitable crystals for x-ray were obtained from pentane slow diffusion on a solution of **27** in THF at -30 °C. The compound was identified from ¹H NMR spectroscopy.

Molecular Weight: 754.31 g·mol⁻¹ (C₃₉H₅₆N₈Ni₂)

¹H NMR (THF-d₈, 400 MHz): = 6.83-7.11 (m, 6H, Ph), 5.69 (s, 1H, 4-Pz), 4.76(s, 1H, CH), 4.58(s, 1H, CH), 4.0 (d, 4H, ³J_{H-H} = 12 Hz, CH₂Pz), 3.42-3.47 (m, 4H, (CH₃)₂CHPh), 2.26 (s, 2H, NH₂), 1.95 (s, 3H, CH₃), 1.85 (s, 3H, CH₃), 1.42 (s, 3H, CH₃), 1.30 (s, 3H, CH₃), 1.20 (t, 12H, ³J_{H-H} = 9 Hz, (CH₃)₂CHPh), 1.04 (t, 12H, ³J_{H-H} = 9 Hz, (CH₃)₂CHPh), -0.90 (s, 1H, NH).

¹³C {¹H} NMR (THF-d₈, 100 MHz): = 20.59 (CH₃), 20.79 (CH₃), 23.09 (CH₃), 23.18 (CH₃), 23.62 (CH₃), 25.39 (CH₃), 27.48 (CH(CH₃)), 27.61 (CH(CH₃)), 50.34 (CH₂Pz), 51.13 (CH₂Pz), 91.28 (4-Pz), 95.84 (CHCCH₃), 96.75 (CHCCH₃), 122.35 (Ar), 123.69 (Ar), 124.13 (Ar), 125.83 (Ar), 142.43 (Ar), 144.32 (Ar), 145.51 (Ar), 153.51 (3,5-Pz), 155.04 (3,5-Pz), 157.86(CHCCH₃), 158.31(CHCCH₃), 159.25 (CHCCH₃), 160.58 (CHCCH₃).

ATR-IR (ν/cm⁻¹) = 3301 (w), 3271 (w), 3254 (w), 3160 (w), 3054 (w), 2961 (m), 2923 (m), 2862 (m), 1558 (s), 1529 (vs), 1460 (vs), 1437 (vs), 1399 (vs), 1367 (s), 1312 (s), 1278 (s), 1261 (s), 1252 (s), 1232 (s), 1190 (s), 1172 (s), 1093 (s), 1072 (s), 1054 (s), 1031 (s), 1017 (s), 956 (w), 933 (s), 912 (m),

867 (m), 798 (s), 760 (vs), 736 (vs), 707 (s), 647 (m), 623 (s), 519 (s), 484 (s), 458 (s), 445 (s), 423 (s), 408 (s).

UV-vis (THF): λ_{\max} = 262 (12680), 360 (5780).

Elemental analysis (%) calc. for $C_{39}H_{56}N_8Ni_2$: C 60.70 H 7.61 N 13.06; found C 60.33 H 7.47 N 13.39.

$L^1Ni_2(\mu-\eta^1, \eta^1-N_2H_4)(BF_4)$ (28**)**

Treatment of **27** (30 mg, 0.04 mmol, 1 equiv) in THF (2 mL) with [H-Lut]BF₄ (8 mg, 0.04 mmol, 1 equiv) results in a color change from red to green immediately. The mixture was stirred for 1 hour. After filtration, green crystals suitable for x-ray diffraction were obtained by layering hexane on a solution of **28** in THF at -30°C.

Molecular Weight: 842.12 g·mol⁻¹($C_{39}H_{57}N_8Ni_2BF_4$)

¹H NMR (THF-d₈, 400 MHz) = 7.35 (t, 2H, ³J_{H-H} = 12 Hz, Ar), 7.18 (d, 4H, ³J_{H-H} = 8 Hz, Ar), 6.00 (s, 1H, 4H-Pz), 4.99 (s, 2H, CHCCH₃), 4.25 (s, 4H, CH₂Pz), 3.72 (s, 4H, NH₂), 2.10 (s, 6H, CH₃CCH), 1.50 (s, 6H, CH₃CCH), 1.17 (d, 12H, ³J_{H-H} = 8 Hz, (CH₃)₂CH), 1.09 (d, 12H, ³J_{H-H} = 4 Hz, (CH₃)₂CH).

¹³C NMR (THF-d₈, 100 MHz) = 20.84 (CH₃), 22.85 (CH₃), 23.19 (CH₃), 24.02 (CH₃), 27.73 (CH(CH₃)₂), 52.39 (CH₂Pz), 93.09(4-Pz), 98.09 (CHCCH₃), 124.88 (Ar), 127.41 (Ar), 143.33 (Ar), 155.94 (3,5-Pz), 158.98 (CHCCH₃), 161.74 (CHCCH₃).

ATR-IR (ν/cm^{-1}) = 3300 (w), 3284 (w), 3265 (w), 3201 (w), 2963 (m), 2940 (m), 2861 (m), 1650 (s), 1626 (w), 1563 (s), 1531 (s), 1463 (s), 1434 (s), 1393 (s), 1320 (s), 1285 (vs), 1241 (vs), 1222 (vs), 1178 (s), 1152 (vs), 1093 (m), 1053 (w), 1027 (vs), 932 (w), 885 (w), 807 (s), 768 (s), 754 (m), 714 (m), 635 (vs), 572 (s), 559 (m), 517 (vs), 559 (m), 517 (s), 448 (m), 416 (m).

UV-vis (THF): λ_{\max} = 264 (10620), 364 (5580).

Elemental analysis (%) calc. for $C_{39}H_{54}N_8Ni_2$: C 60.70 H 7.61 N 13.06; Found C 60.33 H 7.47 N 13.39.

[K(DB18C6)][L¹Ni₂(μ-η¹,η¹-N₂H₂)] (30)

27 (40 mg, 0.05 mmol, 1 equiv) and excess potassium hydride were suspended in 2 mL of THF at room temperature. Intense gas (H₂) development was observed, and a color changes from dark-red to dark green occurred in 2 hours. The mixture was stirred for 4 hours continue, solid components were filtered off. Then DB18C6 was added to the green solution and the mixture stirred for next 30 mins. The color changes from deep green to brown-green in 30 mins. Black rhombus block crystals suitable for x-ray diffraction were obtained by layering hexane on a solution of **30** in THF at -30°C. (Yield: 80%)

Molecular Weight: 1152.3 g·mol⁻¹ (C₅₉H₈₉N₈Ni₂O₆K)

¹H NMR (THF-d₈, 400 MHz) = 7.41 (br, 4H, DB18C6), 6.83 (br, 4H, DB18C6), 6.81 (d, 2H, Ar), 6.75 (d), 4H, Ar), 5.52 (s, 1H, 4-Pz), 4.79 (s, 2H, CHCCH₃), 3.73(s+m, 8H, CH₂Pz+CH(CH₃)₂), 1.79 (s, 6H, CHCCH₃), 1.66 (s, 2H. NH), 1.27(s, 6H, CHCCH₃), 1.10 (d, 12H, ³J_{H-H} = 8 Hz, (CH₃)₂CH), 0.97(d, 12H, ³J_{H-H} = 8 Hz, (CH₃)₂CH).

¹³C NMR (THF-d₈, 100 MHz) = 14.41, 15.73, 21.51, 22.69, 23.25, 25.90, 26.43, 28.27, 28.93, 35.12, 47.80, 55.59, 92.53, 95.82, 97.58, 111.13, 121.89, 123.22, 123.59, 125.41, 125.98, 141.27, 142.59, 148.01, 148.42, 150.88, 152.33, 156.95, 157.69, 159.52, 161.33.

ATR-IR (ν/cm⁻¹) = 3263 (NH, br, w), 3065 (w), 2951 (m), 2924 (m), 2861 (m), 1594 (m), 1545 (m), 1517 (s), 1502 (s), 1452 (s), 1434 (s), 1402 (vs), 1380 (w), 1358 (w), 1319 (m), 1303 (w), 1246 (vs), 1208 (s), 1122 (vs), 1079 (w), 1055 (s), 1025 (w), 941 (m), 900 (w), 844 (w), 796 (w), 761 (m), 737 (vs), 726 (s), 668 (w), 656 (w), 631 (w), 600 (m).

[K(cryptand)][L¹Ni₂(μ-η¹,η¹-N₂H₂)] (31)

29 (40 mg, 0.05 mmol, 1 equiv) and cryptand were mixed in THF at room temperature for 3 hours. The color changes from deep green to brown. Recrystalliza-

tion of the crude product from THF or Toluene slow evaporation yielded black rhombus block crystals. (Yield: 80%)

ATR-IR (ν/cm^{-1}) = 3118 (w), 3051 (w), 3013 (w), 295w (m), 2865 (m), 2804 (m), 1550 (m), 1515 (vs), 1499 (m), 1477 (s), 1460 (s), 1428 (s), 1404 (s), 1353 (s), 1306 (m), 1294 (w), 1229 (w), 1190 (w), 1126 (vs), 1103 (m), 1075 (s), 981 (w), 947 (s), 932 (m), 878 (w), 862 (w), 827 (w), 795 (w), 750 (m), 723 (s), 646 (w), 582 (w), 565 (w), 521 (w).

L¹Ni₂(μ -NH₃) (32)

A suspension of excess NaNH₂ in THF (2 mL) was added dropwise to a stirred solution of **1** (100 mg, 0.025 mmol) in THF (8 mL). After 2 days, the mixture was dried under vacuum. The residue was extracted with THF (8 mL) and filtered through Celite. The resulting dark red yellow solution was cooled to -30 °C overnight to yield a yellow crystalline solid (21 mg). The mother liquor was concentrated to 5 mL and returned to the freezer for additional product crystallization.

Molecular Weight: 739.29 g·mol⁻¹ (C₃₉H₅₅N₇Ni₂)

¹H NMR (THF-d₈, 400 MHz) = 6.97 (s, 3H, Ar), 6.87 (d, 2H, Ar), 6.70 (t, 1H, Ar), 5.67 (s, 1H, 4-Pz), 4.58 (s, 1H, CHCCH₃), 4.19 (s, 2H, CH₂Pz), 4.02 (s, 1H, CHCCH₃), 3.96 (s, 2H, CH₂Pz), 3.84 (m, 2H, CH(CH₃)₂), 3.20(m, 2H, CH(CH₃)₂), 1.83(s, 3H, CH₃), 1.79(s, 3H, CH₃), 1.41(d, 6H, CH₃), 1.31(s, 3H, CH₃), 1.12(d, 6H, CH₃), 1.08(d, 6H, CH₃), 0.97(s, 6H, CH₃), -3.28 (s, 3H, NH₃).

¹³C NMR (THF-d₈, 100 MHz) = 20.82 (CH₃), 23.11 (CH₃), 23.72 (CH₃), 25.39 (CH₃), 26.88 (CH(CH₃)₂), 27.44 (CH(CH₃)₂), 49.59 (CH₂Pz), 50.89 (CH₂Pz), 89.23 (4-Pz), 94.13 (CHCCH₃), 95.92 (CHCCH₃), 121.92 (Ar), 122.55 (Ar), 123.94 (Ar), 139.94 (Ar), 140.24 (Ar), 142.59 (Ar), 147.91 (Ar), 151.83 (3,5-Pz), 157.40 (CH₃CCH), 158.72 (CH₃CCH).

ATR-IR (ν/cm^{-1}) = 3054 (w), 3023 (w) (NH₃), 2956 (m), 2924 (m), 2865 (m), 1552 (m), 1530 (s), 1460 (s), 1426 (s), 1404 (vs), 1358 (s), 1311 (s), 1274 (m),

1252 (m), 1224 (w), 1190 (w), 1178 (w), 1102 (w), 1088 (w), 1044 (m), 1032 (m), 1010 (m), 933(w), 900 (w), 799 (w), 787 (s), 759 (vs), 732 (s), 719 (w), 646 (w), 621 (w), 597 (w), 561 (w), 534 (w).

Elemental analysis (%) calc. for $C_{39}H_{54}N_8Ni_2$: C 60.70 H 7.61 N 13.06; found C 60.33 H 7.47 N 13.39.

$L^1Ni_2(\mu-\eta^1, \eta^1-CO)$ (33)

In a Schlenk-tube (50 mL), a solution of **24** (42 mg, 0.05 mmol, 1 equiv) in THF (2 mL) was freeze-thaw degassed under vacuum three times. High purity and dried CO (*ca.* 1 atm) was then introduced to the flask at $-78\text{ }^\circ\text{C}$. The reaction solution was stirred at room temperature for overnight during which time the color of the solution became red-brown. The volatiles were filtered and orange crystals were obtained by layering hexane or pentane on a solution of **33** in THF at $-30\text{ }^\circ\text{C}$ in 2 days.

33- ^{13}CO : The solution of **33- ^{13}CO** followed an analogous work-up procedure as described for unlabeled **33**. IR and rRaman spectra are the same as for the unlabeled material expect the stretching of CO triple bond.

Molecular Weight: 751.28 $\text{g}\cdot\text{mol}^{-1}$ ($C_{40}H_{53}N_6Ni_2O$)

ATR-IR (ν/cm^{-1}) = 3058 (w), 2957 (m), 2925 (m), 2865 (m), 1735(CO^-) (m), 1556 (m), 1525 (m), 1450 (m), 1436 (m), 1397 (m), 1369 (m), 1314 (m), 1277 (m), 1251 (m), 1234 (m), 1188 (m), 1073 (m), 1055 (w), 1033 (m), 935 (m), 917 (m), 868 (m), 796 (m), 760 (m), 744 (m), 714 (m), 644 (m), 620 (m), 578 (m), 549 (m), 522 (m).

ATR-IR (ν/cm^{-1}) = 3058 (w), 2957 (m), 2925 (m), 2865 (m), 1691($^{13}CO^-$) (m), 1556 (m), 1525 (m), 1450 (m), 1436 (m), 1397 (m), 1369 (m), 1314 (m), 1277 (m), 1251 (m), 1234 (m), 1188 (m), 1073 (m), 1055 (m), 1033 (m), 935 (m), 917 (m), 868 (m), 796 (m), 760 (m), 744 (m), 714 (m), 644 (m), 620 (m), 578 (m), 549 (m), 522 (m).

ESI-MS (THF): m/z (%) = 789.3 ((33+H)+K)⁺(60).

Elemental analysis (%) calc. for C₄₀H₅₃N₆Ni₂O: C 63.95 H 7.11 N 11.19; found C 64.12 H 7.15 N 10.96.

L¹Ni₂(μ-η¹,η¹-CH₃CO) (34)

In a Schlenk-tube (50 mL), a solution of **33** with excess elemental potassium in THF (3 mL) was stirred at -78°C and then warmed up to room temperature for overnight. MeI was added using a micro-syringe at -30°C, resulting in an immediate color change from red to orange. The reaction mixture was stirred for 1 hour at room temperature and volatiles were removed under vacuum. The resulting product **34** was isolated as orange solid after drying under vacuum.

ATR-IR (ν/cm^{-1}) = 3058 (w), 2958 (m), 2925 (m), 2866 (m), 1993 (m), 1842 (m), 1626 (CH₃C=O)(m), 1548 (m), 1532 (s), 1464 (w), 1435 (s), 1399 (m), 1371 (m), 1315 (m), 1280 (m), 1251 (vs), 1175 (w), 1158 (w), 1093 (w), 1030 (vs), 959 (w), 935 (w), 916 (w), 865 (w), 799 (s), 762 (s), 747 (s), 637 (vs), 579 (m), 546 (m), 518 (m).

L²Ni₂(μ-Br) (35). This complex was prepared in a similar way to the method for complex **2** using H₃L² instead of H₃L¹ and at 50°C.

¹H NMR (CD₂Cl₂, 300 MHz): = 7.90 (d, 8H, Ar), 7.34-7.46 (m, 12H, Ar), 7.07 (s, 6H, Ar), 5.45 (s, 1H, 4-Pz), 4.48 (s, 2H, CHCCH₃), 3.92 (s, 4H, CH₂Pz), 1.82 (s, 6H, CH₃CCH), 1.35 (s, 6H, CH₃CCH).

¹³C NMR (CD₂Cl₂, 75 MHz): = 160.83, 159.32, 154.02, 148.60, 141.76, 137.94, 131.04, 130.52, 128.17, 127.17, 126.99, 97.52 (CH₂Pz), 92.43 (4C-Pz), 55.01 (CHCCH₃), 24.22(CH₃), 21.67 (CH₃).

ATR-IR (ν/cm^{-1}) = 3025 (w), 2922 (m), 1597 (w), 1549 (m), 1529 (s), 1496 (w), 1456 (w), 1428 (w), 1392 (s), 1314 (w), 1280 (w), 1261 (w), 1206 (w), 1179 (w), 1085 (w), 1072 (w), 1029 (m), 1016 (m), 957 (w), 946 (w), 912 (w), 872 (w),

802 (m), 752 (s), 732 (m), 695 (vs), 611 (m), 589 (m), 539 (w), 504 (w).

ESI-MS (THF): m/z (%) = 939.3 (100)(M+H)⁺.

Elemental analysis (%) calc. for C₅₁H₃₅N₆Ni₂Br·(CH₂Cl₂)₄: C 51.65 H 4.18 N 6.57;
Found C 51.89 H 4.20 N 6.61.

KL²Ni₂(μ-H) (**36**)

A solution of KHBet₃ in THF (1.0 M) (0.75 mL, 0.75 mmol, 3 equiv) was added to a stirred brown solution of **35** (250 mg, 0.25 mmol, 1 equiv) in THF (4 mL) at room temperature. After stirring the resulting red solution for 40 minutes all volatiles were removed in *vacuo*. The red residue was washed twice with hexane (20 mL). After concentration in *vacuo* and get red powder (134 mg, 0.15 mmol, 60%). The crude powder was recrystallization from pentane diffusion into THF at room temperature yield red block crystals of **36**.

Molecular Weight: 896.20 g/mol (C₅₁H₄₅N₆Ni₂K)

¹H NMR (THF-d₈, 400 MHz) = 8.54 (d, 2H, J_{H-H} = 8 Hz, Ph), 7.75 (d, 2H, J_{H-H} = 8 Hz, Ph), 7.66 (d, 1H, J_{H-H} = 8 Hz, Ph), 7.47 (d, 2H, J_{H-H} = 8 Hz, Ph), 6.85 (m, 16H, Ph), 6.37 (t, 1H, J_{H-H} = 8 Hz, Ph), 6.28 (t, 1H, J_{H-H} = 8 Hz, Ph), 5.69 (s, 1H, 4-Pz), 4.49 (s, 1H, CHCCH₃), 4.43 (d, J_{H-H} = 16 Hz, 1H, CH₂Pz), 4.25 (s, 1H, CHCCH₃), 4.21 (d, 1H, J_{H-H} = 20Hz, CH₂Pz), 4.07 (d, 1H, J_{H-H} = 20Hz, CH₂Pz), 3.97 (d, 1H, J_{H-H} = 20Hz, CH₂Pz), 1.91 (s, 4H, CH₃CCH), 1.04 (s, 4H, CH₃CCH), 0.88 (t, 2H, CH₃CCH), -26.12 (s, 1H, Ni-H).

¹³C {¹H} NMR (THF-d₈, 100 MHz) = 19.04 (CH₃CCH), 19.81 (CH₃CCH), 22.02 (CH₃CCH), 22.31 (CH₃CCH), 51.06 (3(5)C-Pz), 51.48 (3(5)C-Pz), 91.81 (4C-Pz), 96.58 (CH₂Pz), 102.64 (CHCCH₃), 119.72 (Ph), 121.86 (Ph), 122.30 (Ph), 123.16 (Ph), 124.21 (Ph), 124.54 (Ph), 125.12 (Ph), 125.27 (Ph), 125.57 (Ph), 125.68 (Ph), 126.62 (Ph), 127.09 (Ph), 127.72 (Ph), 127.42 (Ph), 127.64 (Ph), 128.72 (Ph), 128.93 (Ph), 129.88 (Ph), 130.02 (Ph), 131.12 (Ph), 131.30 (Ph), 134.71 (Ph), 135.69 (Ph), 136.15 (Ph), 138.92 (Ph), 140.99 (Ph),

141.04 (Ph), 141.81 (Ph), 142.05 (Ph), 142.10 (Ph), 153.52, 155.30, 155.88, 155.99, 157.75, 158.18, 158.42, 159.56.

ATR-IR (ν/cm^{-1}) = 3136 (w), 3023 (w), 2911 (w), 2851 (w), 2815 (w), 1599 (w), 1565 (w), 1531 (w), 1510 (s), 1491 (m), 1457 (s), 1421 (s), 1387 (vs), 1303 (m), 1266 (m), 1248 (m), 1203 (m), 1154 (m), 1067 (m), 1015 (m), 997 (m), 853 (m), 796 (m), 770 (m), 748 (vs), 691 (vs), 630 (m), 604 (m), 539 (m).

NaL²Ni₂(μ -H) (37)

A solution of NaHBEt₃ in THF (1.0 M) (0.75 mL, 0.75 mmol, 3 equiv) was added to a stirred brown solution of **35** (250 mg, 0.25 mmol, 1 equiv) in THF (4 mL) at room temperature. After stirring the resulting red solution for 40 minutes all volatiles were removed in *vacuo*. The red residue was washed twice with hexane (20 mL). After concentration in *vacuo* and get red powder (130 mg, 0.15 mmol, 60%). The crude powder was recrystallization by layering Et₂O on a solution of **37** in THF at room temperature.

Molecular Weight: 882.32 g/mol (C₅₁H₄₅N₆Ni₂Na)

¹H NMR (THF-d₈, 400 MHz) = 8.54 (d, 2H, $J_{\text{H-H}} = 8$ Hz, Ph), 7.75 (d, 2H, $J_{\text{H-H}} = 8$ Hz, Ph), 7.66 (d, 1H, $J_{\text{H-H}} = 8$ Hz, Ph), 7.47 (d, 2H, $J_{\text{H-H}} = 8$ Hz, Ph), 6.85 (m, 16H, Ph), 6.37 (t, 1H, $J_{\text{H-H}} = 8$ Hz, Ph), 6.28 (t, 1H, $J_{\text{H-H}} = 8$ Hz, Ph), 5.69 (s, 1H, 4-Pz), 4.49 (s, 1H, CHCCH₃), 4.43 (d, $J_{\text{H-H}} = 16$ Hz, 1H, CH₂Pz), 4.25 (s, 1H, CHCCH₃), 4.21 (d, 1H, $J_{\text{H-H}} = 20$ Hz, CH₂Pz), 4.07 (d, 1H, $J_{\text{H-H}} = 20$ Hz, CH₂Pz), 3.97 (d, 1H, $J_{\text{H-H}} = 20$ Hz, CH₂Pz), 1.91 (s, 4H, CH₃CCH), 1.04 (s, 4H, CH₃CCH), 0.88 (t, 2H, CH₃CCH). -25.67 (s, 1H, Ni-H).

¹³C {¹H} NMR (THF-d₈, 100 MHz) = 19.04 (CH₃CCH), 19.81 (CH₃CCH), 22.02 (CH₃CCH), 22.31 (CH₃CCH), 51.06 (3(5)C-Pz), 51.48 (3(5)C-Pz), 91.81 (4C-Pz), 96.58 (CH₂Pz), 102.64 (CHCCH₃), 119.72 (Ph), 121.86 (Ph), 122.30 (Ph), 123.16 (Ph), 124.21 (Ph), 124.54 (Ph), 125.12 (Ph), 125.27 (Ph), 125.57 (Ph), 125.68 (Ph), 126.62 (Ph), 127.09 (Ph), 127.72 (Ph), 127.42 (Ph),

127.64 (Ph), 128.72 (Ph), 128.93 (Ph), 129.88 (Ph), 130.02 (Ph), 131.12 (Ph), 131.30 (Ph), 134.71 (Ph), 135.69 (Ph), 136.15 (Ph), 138.92 (Ph), 140.99 (Ph), 141.04 (Ph), 141.81 (Ph), 142.05 (Ph), 142.10 (Ph), 153.52, 155.30, 155.88, 155.99, 157.75, 158.18, 158.42, 159.56.

NaL²Ni₂(μ -H₂) (38)

A solution of NaHBet₃ in THF (1.0 M) (0.50 mL, 0.50 mmol, 2.5 equiv) was added dropwise to a stirred brown solution of **35** (250 mg, 0.25 mmol, 1 equiv) in THF (2 mL) at room temperature. After stirring the resulting red-brown solution for 40 mins, all volatiles were removed in *vacuo*. The red-brown residue was washed twice with hexane (40 mL). After concentration in *vacuo* and get red powder (129 mg, 0.15 mmol, 60 %). The crude powder was recrystallization from pentane diffusion into THF at room temperature yield red block crystals of **38**.

38-D, In a Young tube, a solution of **38** in THF (0.5 mL) was freeze-thaw degassed under vacuum three times. Then dry D₂ (*ca.* 1 atm) was then introduced to the head space of the flask at room temperature.

Molecular Weight 861.35 g/mol (C₅₁H₄₇N₆Ni₂)

¹H NMR (THF-d₈, 400 MHz) = 7.71-7.69 (d, 8H, Ar), 7.23-7.19 (m, 14H, Ar), 7.13-7.10 (m, 4H, Ar), 5.46 (s, 1H, 4-Pz), 4.29 (s, 2H, CHCCH₃), 4.06 (s, 4H, CH₂Pz), 1.68 (s, 6H, CH₃CCH), 1.34 (s, 6H, CH₃CCH), -23.61(s, 2H, Ni-H).

¹³C NMR (THF-d₈, 75 MHz) = 158.13, 156.23, 156.16, 156.06, 142.54, 130.26, 129.88, 127.03, 125.49, 123.21, 96.90, 91.87, 52.34, 25.40, 22.23, 19.51, 13.40.

ATR-IR (ν /cm⁻¹) = 3052 (m), 3024 (m), 2973 (m), 2950 (m), 2920 (m), 2853 (m), 1896 (Ni-H) (m), 1595 (w), 1559 (m), 1519 (m), 1451 (m), 1427 (m), 1377 (vs), 1313 (m), 1269 (s), 1210 (m), 1179 (w), 1068 (m), 1047 (m), 1028 (m), 907 (m), 802 (w), 769 (s), 753 (vs), 741 (vs), 719 (m), 697 (vs), 605 (m), 590 (m), 540 (w).

²H NMR (THF, 400 MHz) = -23.61 (s, 2H, Ni-D).

L²Ni₂(μ-OH) (39)

Water was added into a solution of **38** (30.5 mg, 0.04 mmol, 1 equiv) in THF (1 mL) at room temperature. The color changes from dark red to green immediately and intensity gas was observed. Suitable crystals for x-ray diffraction were obtained from THF at -30 °C as dark green block crystal.

39-OD: In a Young tube, a solution of **39** in THF (0.5 mL) was freeze-thaw degassed under vacuum three times. Then D₂O (10 eq.) was then introduced to the head space of the flask at room temperature.

Molecular Weight 876.34 g/mol (C₅₁H₄₆N₆Ni₂O)

¹H NMR (THF-d₈, 400 MHz) = 8.17 (d, 8H, Ar), 7.38 (dd, 8H, Ar), 7.23 (dd, 4H, Ar), 6.69-6.82 (m, 6H, Ar), 5.42 (s, 1H, Pz), 4.14 (s, 2H, CHCCH₃), 3.83 (s, 4H, CH₂Pz), 1.64 (s, 6H, CH₃), 0.99 (s, 6H, CH₃), -6.06 (s, 1H, OH).

¹³C NMR (THF-d₈, 100 MHz) = 159.76, 156.71, 148.79, 143.91, 140.95, 138.00, 130.21, 127.25, 126.11, 124.99, 97.01 (CHCCH₃), 90.79 (4-Pz), 54.52 (CH₂Pz), 25.29 (CH₃CCH), 22.08 (CH₃CCH), 19.74 (CH₃CCH).

ATR-IR (ν/cm⁻¹) = 3605 (OH) (m), 3056 (w), 3023 (w), 2957 (w), 2918 (w), 2847 (w), 1599 (m), 1550 (m), 1521 (m), 1484 (m), 1451 (vs), 1429 (m), 1395 (m), 1310 (m), 1270 (m), 1244 (m), 1211 (m), 1175 (m), 1063 (m), 1030 (m), 948 (m), 912 (m), 810 (m), 751 (vs), 724 (w), 698 (vs), 606 (m), 589 (m), 540 (w).

ATR-IR (ν/cm⁻¹) = 2681 (OD) (s).

ESI-MS (THF) = 913.30 (M+K)⁺ (100), 875.33 (M+H)⁺ (70), 899.34 (M+Na)⁺ (30).

²H NMR (400 MHz, THF) = -6.06 (s, 1H, OD)

Anal. Calcd for [Ni₂(C₅₁H₄₆N₆O)]: C 68.11, H 5.16, N 9.34; found: C 68.22, H 5.27, N 9.18.

L²Ni₂(μ-CF₃SO₃) (40)

38 (31.8 mg, 0.04 mmol, 1 equiv) and [H-Lut]OTf (6.45 mg, 0.04 mmol, 1 equiv)

were dissolved in THF (2 mL), and the reaction mixture were stirred for 2 h at room temperature in a dinitrogen atmosphere. All volatiles were subsequently removed under vacuum, and the resulting solid was dried under vacuum. The crude powder was recrystallization by layering hexane on a solution of **40** in THF at -30°C yield block crystals of **40**. The mother liquor was pumped down, dissolved in THF, and layered with hexane to afford a second crop.

Molecular Weight 1008.40 g/mol ($\text{C}_{52}\text{H}_{45}\text{N}_6\text{Ni}_2\text{F}_3\text{SO}_3$)

^1H NMR (THF- d_8 , 400 MHz) = 8.17 (d, 8H, Ar), 7.45 (t, 16H, Ar), 7.05 (t, 2H, Ar), 5.42 (4-Pz), 4.17 (s, 4H, CH_2Pz), 4.14 (s, 2H, CHCCH_3), 1.63 (s, 6H, CH_3), 0.99 (s, 6H, CH_3).

^{13}C NMR (THF- d_8 , 100 MHz) = 19.73 (CH_3), 22.07 (CH_3), 25.39 (CH_3), 51.25 (CH_2Pz), 93.16 (4-Pz), 99.76 (CHCCH_3), 125.16, 126.33, 127.58, 128.94, 130.19, 139.55, 141.52, 145.38, 155.86 (Ar), 156.56 (CF_3SO_3), 158.25 (Ar).

^{19}F NMR (THF- d_8 , 376 MHz) = -77.81 .

ATR-IR (ν/cm^{-1}) = 3052, 2923, 1598, 1555, 1525, 1229, 1210, 1200, 1170, 1111, 1053, 1031, 908, 868, 838, 809, 755, 696, 641, 586, 508.

Chapter 12 DFT Calculations

Geometry optimization calculations were performed with the coordinates obtained from the X-ray crystallographic structure determination. Unrestricted DFT calculations using the ORCA program (Ver. 3.0.1 or 3.0.2) were performed with BP86 respectively B3LYP functional, RI resp. RIJCOSX approximation, def2-tzvp and def2-tzvp/j basis sets ^[247] Solvent effects were considered by invoking the conductor like screening model (COSMO) with THF as the solvent. 80 excited states were calculated; the maximum dimension of the expansion space in the Davidson procedure (MaxDim) was 800.

DFT Table 1. Coordinates of the energy-optimized structure of Structure 2-

Ni	-0.68869262397851	17.17489938464608	18.87906371064496
Ni	-1.41515153487665	15.58251351289467	15.31148013058432
C	-3.07622169902548	18.14173532358329	17.94770281610725
C	-3.94304271614359	18.25647489085641	16.84067727920180
H	-4.86772190584580	18.83984022776006	16.76488931990406
C	-3.35080720902569	17.43754397715647	15.85677275187850
C	-3.67739512974857	17.07152076947943	14.44054435125935
H	-4.71098359717760	16.65059152296007	14.37432585128001
H	-3.68909842325979	17.98809961167770	13.79939189908899
C	-2.73849132582984	15.62383777402922	12.73760923711351
C	-3.81587059031133	16.10971230838273	11.78769351314391
H	-4.83149795862547	15.87906405407793	12.17836285254848
H	-3.71799463139211	15.63885468980650	10.79167152333322
H	-3.77665465561897	17.21318514889711	11.65633798674392
C	-1.82150644204174	14.64813628168210	12.26685141308028
H	-1.92851377453640	14.33567951866911	11.21816805568514
C	-0.81730896767705	14.00070900244267	13.01936812009976
C	0.00822151880901	12.92870589501205	12.33246652889802
H	1.09420753101744	13.14419379634333	12.41693541532362
H	-0.25979077652061	12.84895124424981	11.26197160775940
H	-0.14014907575848	11.93618230893268	12.80845064994584
C	0.36855032043898	13.45418846729255	15.02170029505425
C	-0.08327804453132	12.23366214610976	15.59840982739276
C	0.83546859373594	11.44542847881057	16.31595392826467
H	0.49563208864464	10.50558405096132	16.77679996900063
C	2.16996370525917	11.84986083039746	16.47107549887792
H	2.87354807175732	11.22768498826797	17.04669363866645
C	2.60142850358454	13.05413426431131	15.89693787500757
H	3.64385672132672	13.37791195452812	16.03340292902591
C	1.72334277152454	13.86260418664092	15.15177537591071

C	2.18101405920993	15.18289785463135	14.54662107810832
H	1.49119310605907	15.40114285501371	13.70382371159733
C	3.61194994407609	15.13011995153585	13.98963452421504
H	3.85812086318007	16.08031541079022	13.47006958635354
H	3.74747822571077	14.29534402153878	13.26933655840273
H	4.36149647860772	15.00260662847689	14.79968642434145
C	2.01986842100963	16.31659156897761	15.57514308517488
H	2.68928559504155	16.16008127700690	16.44384748724223
H	0.97782238294086	16.34398315778268	15.95676483765672
H	2.25990007601768	17.30168807221096	15.12095122278643
C	-1.55982710239245	11.86219677092824	15.51222255384843
H	-1.94722076618540	12.28679248425679	14.56295887640418
C	-2.33405034800809	12.55533014255028	16.65004518497818
H	-3.43088211899136	12.43189569608174	16.52180072844345
H	-2.09793660862373	13.64341052784149	16.66188459865092
H	-2.04453956138690	12.13208178261658	17.63419573577094
C	-1.82055441750071	10.35019652831423	15.48875023250856
H	-1.24589369272462	9.84424630654391	14.68467821256029
H	-2.89907950080263	10.14788162143063	15.32030640878386
H	-1.54814965012280	9.86766165946034	16.45170247963250
C	-3.05779490040488	18.68457717169119	19.34415738548359
H	-3.08456069791490	19.80222544399173	19.33315594002270
H	-3.98359129949226	18.37072390863426	19.88841792455357
C	-1.61198851368140	18.50398229769750	21.28102950058035
C	-2.61237681069007	19.34067584316209	22.05500701036519
H	-2.76633684528070	20.33190255920444	21.57548679959450
H	-2.27572121512278	19.51175925927960	23.09448082657306
H	-3.61100724252307	18.85287562488563	22.08646085524496
C	-0.43219968273219	18.08521044496898	21.94858073784644
H	-0.33644772681809	18.36597979857020	23.00696369135609
C	0.65809902086352	17.39102851405338	21.38068189466873

C	1.86473309173948	17.12421382227925	22.26145030275086
H	2.12914620751691	16.04663235112809	22.26668685377978
H	1.67488708403730	17.45168881460743	23.30114207047797
H	2.76367275286344	17.65333982850802	21.88211884775500
C	1.91555742790925	16.43977608991858	19.58746613912139
C	2.13914472651998	15.03571795113204	19.58865610717690
C	3.34559971625953	14.54814533797006	19.05246393868434
H	3.52338960963985	13.46269843850025	19.02811450467004
C	4.32461745641116	15.41893315743998	18.55269444688996
H	5.26330701791618	15.01625934908133	18.13991827559109
C	4.10068857227412	16.80340683077640	18.57628426384541
H	4.86799653091512	17.48425765922187	18.17687592734893
C	2.90284115485701	17.33532182109320	19.08865562804104
C	2.60970286869486	18.83115462256799	19.04312236894757
H	1.91184416608512	19.04868415360110	19.87867697625854
C	1.85700876787603	19.17616731845802	17.74291729851628
H	2.50281138744959	18.99832821245965	16.85752040995287
H	1.53231381573758	20.23807107747166	17.73817443626115
H	0.95589630037899	18.53066898614876	17.64729798553029
C	3.85244417745640	19.71151239612673	19.22897571089185
H	4.41723031568851	19.44089358025080	20.14683318881455
H	3.56009491980109	20.77972830531325	19.30768971255267
H	4.55061461403715	19.63080309748039	18.36801089704590
C	1.06534188849978	14.09701452916372	20.12367146869819
H	0.54503396992328	14.64644997118462	20.93724663545024
C	0.01935305593232	13.80316903312258	19.03294085437712
H	-0.36799640784771	14.75242362139995	18.60635069716799
H	-0.83228189735578	13.22355275152239	19.44645138746302
H	0.46893057224875	13.22075242416148	18.20515255271184
C	1.62792455158097	12.79396007103616	20.71020800967596
H	0.81350578384249	12.20703232205730	21.18459699468287

H	2.41308723933729	12.98299604528860	21.47272958248286
H	2.06664211091545	12.15317500527309	19.91620211559389
N	-2.04221831661604	17.31371845698623	17.62897714869674
N	-2.21436676818090	16.87748032843916	16.35837907639020
N	-2.67984591772314	16.10426031368385	13.98017498262885
N	-0.56185185176709	14.27607613947191	14.31613251370108
N	-1.84941718744102	18.19030573781354	20.00683569961318
N	0.69181640563225	16.97238342415276	20.09685576026003
H	0.11415847387532	16.51691574696168	17.85589916079963
H	-0.58518660241204	15.24272508175843	16.45931862412747

DFT Table 2. Coordinates of the energy-optimized structure of Structure 2.

Ni	-0.84779151694222	16.88452507003262	19.12127948015371
Ni	-1.21672547290550	15.76014818204264	15.18069752158587
C	-3.07891539203923	18.00099686454774	18.01067761249681
C	-3.78779419357733	18.32104159908885	16.84041773426616
H	-4.67159353034677	18.95973413229359	16.73921170264163
C	-3.10186708398172	17.62574868410968	15.83087747880241
C	-3.29215081224702	17.50563420264949	14.35658602658692
H	-4.36083616131333	17.28708360420774	14.12555287500612
H	-3.06893411718607	18.48072088939323	13.85733252555605
C	-2.50069809044707	16.06901045164647	12.59276023085709
C	-3.46735979680113	16.76815996434964	11.65993713057898
H	-4.51600701330930	16.66881096259622	12.01372350938207
H	-3.40927908943668	16.35114973013410	10.63799935942154
H	-3.25619213684530	17.85736088231600	11.60339738546906
C	-1.74055955009941	14.99114803191362	12.07286299369202
H	-1.92844169853088	14.71066082441520	11.02854728743760
C	-0.82389885398668	14.20245396374938	12.78602788513798
C	-0.24488316999615	12.98658446331456	12.08691541878480

H	0.86183722538781	13.02054715201397	12.01782724001644
H	-0.65321611318891	12.89383301365211	11.06434085180387
H	-0.48793337383671	12.05905939070663	12.64588907909697
C	0.47915476074298	13.57508851804364	14.66459251412315
C	0.03094547274253	12.50876730385107	15.49738895353747
C	0.99309205791804	11.68346098849569	16.11489660484358
H	0.65888300612790	10.86658175814411	16.77419615252186
C	2.36753183291327	11.87501294562170	15.89155299767132
H	3.10437293808316	11.21149832555998	16.36960600148887
C	2.79715473507561	12.91086460122761	15.04158634857331
H	3.87413853212729	13.04539427682979	14.85848659792718
C	1.87122667740614	13.77277392473171	14.41787443217573
C	2.32335416277047	14.95420948201568	13.56265103384341
H	1.56404012971832	15.08905495239062	12.76600371866320
C	3.68606550171359	14.75003316335105	12.89096625622861
H	3.90690628800515	15.59116437266632	12.20261948882439
H	3.71853249436255	13.80982552752694	12.30321594911329
H	4.51381375170486	14.71256612553858	13.63210346250276
C	2.29735796454139	16.24787669233148	14.40105719688286
H	3.10003026369555	16.23428713746703	15.17350612592954
H	1.30242719646933	16.37383035640391	14.88531311106078
H	2.47115131638015	17.14225283121245	13.76958306638632
C	-1.45734293966542	12.30678766784791	15.74853445921853
H	-1.98905773865066	12.95956004477297	15.02735510147604
C	-1.84369619390009	12.78763568405115	17.16028453322808
H	-2.93712447478929	12.68810851393115	17.32094546715715
H	-1.57767496160902	13.85654103423113	17.28988155985119
H	-1.32701721383538	12.19218292233929	17.94078755612300
C	-1.89716577963432	10.85423590280622	15.50079346861581
H	-1.61489482645781	10.51034413900231	14.48471224732029
H	-2.99857744266892	10.76172650227601	15.59977936213419

H	-1.44164472775547	10.15297291715846	16.23138963774722
C	-3.23301518607002	18.38284636974739	19.44400867104889
H	-3.37890337585171	19.48450974724700	19.53480905935164
H	-4.15613802847455	17.92011479106678	19.87106202424109
C	-1.90729181937550	18.25126360024646	21.45243665549721
C	-3.01190782710121	19.00128064388854	22.16653021638568
H	-3.19920194142292	19.99028812493301	21.69612204309191
H	-2.76002301474874	19.17013105327687	23.22912378025291
H	-3.97168953864497	18.44406385075659	22.11868535404972
C	-0.73497681629463	17.93581676585024	22.18437743439449
H	-0.69763896482533	18.27185686600733	23.22850575343916
C	0.41424121999825	17.30867653629407	21.67744356354764
C	1.64099251683975	17.25906828639543	22.56824977497130
H	1.99902441679310	16.22255667659242	22.73375018399456
H	1.42627586098573	17.71402809779797	23.55214690864146
H	2.48809691331676	17.80893679539399	22.10770918214494
C	1.75132594325080	16.29779735065488	20.00243403035860
C	2.15466049375607	14.96905039646693	20.33373255112102
C	3.42105382101833	14.51824274248306	19.90861995566377
H	3.74652691366450	13.49884960962191	20.16303036340771
C	4.27890331699237	15.35144797268881	19.16864883501928
H	5.26914847603725	14.98729126531298	18.85585330157853
C	3.86623968147195	16.65285333460262	18.83687624428707
H	4.53726673009798	17.30311337398177	18.25393581034762
C	2.61152735814253	17.14844755415814	19.24860445746827
C	2.14040295775530	18.53338100637538	18.82447453332584
H	1.26256267993355	18.77950274082392	19.45562696704752
C	1.64004679615143	18.49201261703925	17.36620200616652
H	2.45688437376022	18.20944246423109	16.66792976379102
H	1.25467325230355	19.48303098586650	17.05135637203414
H	0.80330307268780	17.76781085599053	17.26546803422907

C	3.20821425174608	19.61750791124397	19.03174773992266
H	3.57040218549792	19.63807614349460	20.07970420671451
H	2.79160251403578	20.61789533901396	18.79483465159931
H	4.08914448645855	19.46859809579487	18.37193431781351
C	1.17195468892324	14.04275535877115	21.03970886308478
H	0.55998657648375	14.67442824404949	21.71460142865639
C	0.20391309065252	13.46307582868736	19.99141097605111
H	-0.26153530597038	14.28952470803815	19.41150274085595
H	-0.61307571763185	12.88205714104884	20.46549406794549
H	0.73893194431551	12.77797293786197	19.29568913975021
C	1.83401005452325	12.94519952787514	21.87935188374842
H	1.06561473365922	12.38666434481062	22.45147180646300
H	2.56347327800165	13.36130204335577	22.60502995341959
H	2.36920996792199	12.20326064270353	21.24983350492443
N	-2.04136768809992	17.16867490151144	17.71305706795525
N	-2.05524147082469	16.93561941787581	16.36764779605251
N	-2.40845431371692	16.44782709409451	13.86721542760080
N	-0.46978010544762	14.45163465278720	14.07054705819608
N	-2.04018737956355	17.93692932143648	20.16460620336278
N	0.48713830451615	16.78663616918247	20.42784185860717
K	1.71626894280193	14.86644056918994	17.27441293070832
H	-0.13167055209665	15.98737890482600	18.21852499015344
H	-0.40760561023590	15.30867755555502	16.30709282157190

DFT Table 3. Coordinates of the energy-optimized structure of Structure A.

N	-2.20616598256472	16.87252637926337	16.38924594688450
C	-3.36754862246396	17.39411479165334	15.90429975956918
C	-3.98871940814366	18.16667855876951	16.90830439818616
C	-3.11268769091747	18.06640745278095	18.00995924886945
N	-2.04770324911161	17.28796522955709	17.66746765709536

C	-3.10900360266203	18.57263270170368	19.42096346278932
N	-1.86279104997566	18.13784363515259	20.05605289844398
C	-1.62434544651852	18.42944596702821	21.33522445009842
C	-0.42563137744599	18.03488440353915	21.98299789868408
C	0.67260733425413	17.36589441150970	21.39946507877728
N	0.70020656160674	16.95374541142541	20.11427981257315
C	1.92085797661534	16.43247206309376	19.58607051921230
C	2.15692850168319	15.03053012633264	19.58363596848723
C	3.35342699377497	14.55352462666329	19.01649488635621
C	4.31163317332621	15.43240711070061	18.49127116688688
C	4.07713299897746	16.81484290821768	18.52148964831666
C	2.88790288971018	17.33652419566938	19.06375601590099
C	-3.68258129287653	17.03969755499964	14.48232597744347
N	-2.64686941056432	16.12153774348108	14.00351932440285
C	-2.68805342627698	15.66268858043076	12.75221039837991
C	-1.74072050770064	14.72384301474019	12.26640837318147
C	-0.72661815937154	14.08569826261829	13.01387884605334
N	-0.46451355852652	14.36628041909658	14.30828934517668
C	0.42719557038281	13.51186642244843	15.02559287487140
C	-0.08587876346356	12.31875371484836	15.60771767205731
C	0.79073430913654	11.48913666689912	16.33114629608140
C	2.14375294611891	11.82564766809048	16.48288393321270
C	2.63664066275216	13.00315769302630	15.90145346369550
C	1.80137184784643	13.85327005622143	15.15313794841389
C	-1.57857938232309	12.01947146685699	15.52055897410025
C	-1.90353576045166	10.52446101793153	15.39420535932461
C	2.32530872023685	15.14081677100014	14.52822480442466
C	2.06614571706722	16.33407002696355	15.46657098096738
C	1.10698803645676	14.08129270273163	20.14698147936487
C	1.69991029106309	12.77902567874974	20.70567729608469
C	2.57851104031460	18.82913802935454	19.02085969824076

C	3.81512645163253	19.72242506797948	19.18419268757334
Ni	-0.69090092208379	17.14752549671622	18.90937833083151
Ni	-1.35053524212880	15.63651015354812	15.31890877190407
C	-3.78191129064376	16.12707042269243	11.81050437284520
C	0.08500004217703	13.00082676657385	12.33049050626419
C	3.80309951145227	15.06427688196268	14.12019753353600
C	-2.31082624557083	12.66339849583284	16.71439790804503
C	-2.64768933206951	19.20925274848261	22.13743260293927
C	1.89482766862106	17.11956109446681	22.26449809647461
C	1.80059551315335	19.16231154260510	17.73244477270542
C	0.02818024959012	13.78226657741703	19.09080915936184
H	-4.93747802227685	18.71179624451463	16.84868828788622
H	-4.69812489216329	16.57778420586784	14.41079230927097
H	-3.73295043663874	17.96528265591049	13.85648133936440
H	-4.78872160691365	15.85648679014646	12.19810623514599
H	-3.66928656551208	15.67568600970718	10.80709940894494
H	-3.77997605079569	17.23322305550869	11.69669952656062
H	-1.84151200513610	14.41991845848579	11.21457986995029
H	1.17505310881421	13.18053523766507	12.43919830483027
H	-0.16431018884613	12.94052358968167	11.25407759651067
H	-0.10600123015044	12.00816415653670	12.79113645613623
H	0.40279626866077	10.57087476572020	16.79806311533789
H	2.81547246452249	11.17122156979848	17.06089161112252
H	3.69592986547504	13.26802599104865	16.03178298826080
H	1.72306035436761	15.31396971151307	13.60952955051672
H	4.09625300481512	15.97991640043393	13.56441963657266
H	4.01220604838526	14.18463985096831	13.47480474854109
H	4.46730537708681	15.00063532582199	15.00789160878029
H	2.62483370451256	16.22207877109360	16.41564950546340
H	0.98706795481056	16.38697422317589	15.72088673080529
H	2.37405296261676	17.28803092486491	14.98763262028882

H	-1.95547006333382	12.52520883077711	14.60795446702353
H	-3.41278427249392	12.59118605571171	16.59375065773088
H	-2.03641115573696	13.73846725413685	16.79700161894669
H	-2.02791194987658	12.16298383333782	17.66353132793092
H	-1.35862609118595	10.05497266040759	14.54837837670513
H	-2.99138804474095	10.38029477252660	15.22459220164201
H	-1.64320825063447	9.96085349991266	16.31563750677750
H	-3.20936686192791	19.68523010253641	19.44159505223742
H	-4.00080013369678	18.17950104084189	19.96970894233538
H	-2.85239854615127	20.20003985124019	21.67672036206293
H	-2.30370173573841	19.37747464684165	23.17495207166433
H	-3.62237728031862	18.67602483210061	22.17441390177079
H	-0.32453444645232	18.30819351325955	23.04275650028594
H	2.17688474006487	16.04651365938949	22.26618885606013
H	1.71401107615894	17.44401428110204	23.30668009742790
H	2.77956508934910	17.66340739657150	21.87261051567242
H	3.53990683077124	13.46981414473102	18.98757364363383
H	5.24250917808246	15.03762947221741	18.05410071289118
H	4.82769811480669	17.50215666051033	18.10191935722246
H	1.89290349975036	19.04145384980448	19.86778573342976
H	2.43426933400540	18.99214516814655	16.83687981311236
H	1.46154824473168	20.21968750684590	17.73101615211704
H	0.90682806329062	18.50392256578461	17.65262774881607
H	4.39666411808919	19.45963279989116	20.09374816423015
H	3.51386076082005	20.78803445515546	19.26458151926592
H	4.50030508612848	19.64617557332824	18.31254628684773
H	0.60851401092822	14.61981303200323	20.98138557873861
H	-0.41613930746813	14.72688734468612	18.71465670106454
H	-0.78215368339607	13.15703706223244	19.51992614735813
H	0.46485435882307	13.24875750012157	18.22513953313733
H	0.91007301635135	12.18886262919326	21.21598726640143

H	2.51874264194700	12.96978437620702	21.43134000493975
H	2.10409478033388	12.14071718279155	19.89145174023038
H	0.10123058712029	16.48024606529773	17.88383603469795
H	-0.48935443433855	15.33239226660577	16.45890861986126
H	-2.65299442134881	15.57424675895429	19.84570765137464
H	-3.16981748269442	15.10428313421941	20.18396179591873

DFT Table 4: Coordinates of the energy-optimized structure of Structure C.

N	-2.12459676246702	16.93918724508929	16.36449879996588
C	-3.22194148909542	17.56112661224279	15.84629690390961
C	-3.92926565447942	18.20994914206058	16.87679300071058
C	-3.17709014748868	17.92897153457674	18.03412524386101
N	-2.09857790715165	17.16286102129708	17.70417198343217
C	-3.30509989831568	18.29093618835764	19.48014091657908
N	-2.08543984816977	17.86238868185710	20.16272366905418
C	-1.90753927065312	18.16170582258124	21.45003093264348
C	-0.70432712194684	17.85075391704454	22.13111244134742
C	0.44248495447896	17.24537925661630	21.57359400659974
N	0.48681530541422	16.74091870073556	20.32187303650745
C	1.74548104707088	16.28515032917013	19.82391913703691
C	2.19323250456286	14.96730420807296	20.11291375733565
C	3.44039438929225	14.55363937167163	19.60930573799912
C	4.22634766471091	15.41155898941771	18.82511242200857
C	3.76048607165040	16.70001048341669	18.52701904269486
C	2.52706909281924	17.16110153507212	19.02404677776858
C	-3.42275119314518	17.41210065093821	14.37149641408524
N	-2.44641409065033	16.44298575201165	13.87809479881380
C	-2.48861577236894	16.05483733483097	12.60292424886410
C	-1.64171448177629	15.03447305232890	12.10279891285781
C	-0.70484969823577	14.28396978783957	12.84533801434833

N	-0.37556388117931	14.55681260826547	14.12652573228096
C	0.48726772056041	13.64033978784117	14.80179659702701
C	-0.08694898259580	12.62872399325482	15.61692124033649
C	0.76975717287984	11.73906731898638	16.29134912046724
C	2.16171772030369	11.82473356920719	16.14736459091485
C	2.71536745142949	12.82617467494519	15.33545559897849
C	1.89751698614596	13.74924384009512	14.65864586358883
C	-1.59865058255953	12.55087682156327	15.79499102670820
C	-2.14770214651144	11.14321393919875	15.50752697963826
C	2.48345510771162	14.91900654735719	13.87724883500299
C	2.46861670268953	16.17466106001910	14.76872312388094
C	1.26185971027327	14.00906939496211	20.84443832240555
C	1.98117810346020	12.88586547141504	21.60083917278995
C	1.99863985556387	18.54343346370630	18.66055888590131
C	3.00887619815842	19.65935489135129	18.97365167465778
Ni	-0.88268391166084	16.85138565072031	19.06896241495298
Ni	-1.17787503818045	15.85916069751579	15.18863273344917
C	-3.49146128705322	16.67831733965194	11.65170702296557
C	-0.08791756409621	13.07151700635114	12.16938502586439
C	3.88018333643005	14.64912773359862	13.30277042272761
C	-2.01915181723753	13.05443479411172	17.18822116781082
C	-2.99625747210415	18.88588203725956	22.21790933101334
C	1.69967151751830	17.20895971711629	22.42460714181764
C	1.53625389833365	18.58207376757695	17.19233020930106
C	0.23369914597925	13.45622811127236	19.84080428389042
H	-4.85418342318262	18.79220179403185	16.79740625101010
H	-4.47092975394353	17.08788349591314	14.15836553351245
H	-3.30968175703726	18.40148849485460	13.86031241311992
H	-4.53664565510233	16.50054425698507	11.98811059078767
H	-3.38589053019839	16.26663545312906	10.63027484480168
H	-3.36548037005458	17.78177905264220	11.59711282805121

H	-1.78049374802118	14.74787614827327	11.05096624496052
H	1.02086061059648	13.09718939420184	12.18393778793529
H	-0.42867339720091	12.99345108850714	11.11980295957352
H	-0.37570583823427	12.14024675509072	12.70178272447326
H	0.33575330759719	10.96320325521826	16.94259749251796
H	2.81813157401781	11.12015441873816	16.68210568913020
H	3.80972819555803	12.90490555245846	15.24673402557966
H	1.79975906895655	15.12089344085265	13.02565652438171
H	4.20143933390339	15.49340223112280	12.65695782137911
H	3.90603666263150	13.72015991093924	12.69464735235714
H	4.64223025475001	14.54810409501628	14.10531598147178
H	3.13745827204266	16.04217397616279	15.64341044559118
H	1.44447697108652	16.34873578225722	15.15712667191142
H	2.79204530108253	17.07401176330215	14.20199190678678
H	-2.04218039366103	13.24744911669023	15.05494278016318
H	-3.12587572241003	13.08454416896440	17.27562453830541
H	-1.63683248338237	14.07952973332853	17.36452294626758
H	-1.62510401087543	12.39417571692005	17.98809841345656
H	-1.85000272499139	10.79075812038672	14.49774369105343
H	-3.25751135921120	11.13813460523059	15.55993868911244
H	-1.77941696385992	10.39628349830326	16.24369643918671
H	-3.47506099222291	19.38999393251586	19.58636337939732
H	-4.21030349839563	17.80487034600187	19.92395677893091
H	-3.22242044448287	19.87613952935871	21.76557002313140
H	-2.70366210344959	19.04980326422703	23.27190484904942
H	-3.94890670589573	18.31299005105251	22.20457342673690
H	-0.63251761312115	18.17062328253677	23.17983408918582
H	2.08337530801202	16.17657282173286	22.55544743105442
H	1.51016273249972	17.64575034175963	23.42316497915068
H	2.51965284425765	17.77845697707432	21.93946771518699
H	3.79554020045419	13.53287298628494	19.81481534893389

H	5.19491965613781	15.06756666824609	18.43050277274967
H	4.36788241878735	17.36533973138950	17.89170134991520
H	1.09738344274474	18.71134196358068	19.28440785300841
H	2.39276088975539	18.44971876560061	16.49954962306266
H	1.05440377095320	19.55601340152428	16.95995413411846
H	0.79801460568407	17.77823574765032	16.99369442325030
H	3.31156281820389	19.64529753824551	20.04107872877347
H	2.56998580664805	20.65626693235563	18.75471183704415
H	3.93201432374761	19.56748153166295	18.36214806314002
H	0.69243996211981	14.60878553428822	21.58546289338714
H	-0.25485926208742	14.29633727525848	19.30405499345349
H	-0.54895982989120	12.85703239270347	20.35347152016404
H	0.72942191071007	12.82443724074833	19.07560954533528
H	1.25184593001850	12.29210030623845	22.19105033882576
H	2.75121287020618	13.27798517425650	22.29906508136401
H	2.48526067447751	12.17973742592121	20.90708136480124
H	-0.12241543650828	16.01778844678617	18.14134995082590
H	-0.23354049537882	15.58185975721553	16.27408182584009
H	1.87910143284846	14.45133475938212	17.41694130407611
H	1.23811372399650	14.84058570030820	17.22144607243340

DFT Table 5: Coordinates of the energy-optimized structure of **5**.

Ni	-2.03596	1.016084	-0.26903
Ni	2.0355	1.016875	0.268723
N	3.182989	2.507175	0.623602
N	3.302997	-0.33313	0.432953
N	-0.66777	2.315355	-0.11969
N	-3.18407	2.505945	-0.62363
N	-3.30296	-0.33442	-0.43304
N	0.666834	2.315614	0.119146
C	-1.09035	3.602394	-0.20579
C	-2.54403	3.814334	-0.50478

C	-4.45342	2.39468	-0.99008
C	-4.57051	-0.13247	-0.82888
C	-2.8988	-1.59841	0.06274
C	1.088859	3.602807	0.205594
C	-0.00094	4.463756	5.31E-05
C	-5.09878	1.139239	-1.11262
C	-5.2641	3.636912	-1.29386
C	-5.48226	-1.33109	-0.98461
C	-3.27562	-1.98775	1.376875
C	-2.08322	-2.44144	-0.73207
C	2.542461	3.815311	0.504591
C	-2.84525	-3.22788	1.857893
C	-4.05411	-1.02043	2.256121
C	-1.67523	-3.67112	-0.20645
C	-1.63072	-1.97689	-2.10433
C	4.452356	2.396402	0.990126
C	4.570433	-0.1307	0.828868
C	2.899337	-1.59733	-0.06272
C	-2.05512	-4.07215	1.074874
C	-3.09065	-0.03153	2.932779
C	-4.94869	-1.71337	3.289368
C	-0.33059	-1.16512	-1.98478
C	-1.45788	-3.1213	-3.10963
C	5.098202	1.141211	1.112649
C	5.262538	3.638943	1.293974
C	5.482659	-1.32897	0.984538
C	3.276279	-1.98656	-1.37684
C	2.084231	-2.44071	0.732198
C	2.846521	-3.22694	-1.85777
C	4.054093	-1.01881	-2.2562
C	1.676827	-3.67062	0.206666
C	1.631526	-1.9763	2.104434
C	2.056889	-4.07156	-1.07464
C	3.089893	-0.03062	-2.93285
C	4.949135	-1.71123	-3.28938
C	0.331158	-1.16492	1.984732

C	1.4589	-3.12077	3.109707
H	-3.0207	4.414324	0.296884
H	-2.65692	4.403615	-1.43632
H	-0.00118	5.550569	0.000225
H	-6.13053	1.161599	-1.4618
H	-6.28785	3.37545	-1.58846
H	-4.80756	4.223409	-2.1085
H	-5.31586	4.301671	-0.41572
H	-6.435	-1.03492	-1.44063
H	-5.69782	-1.80561	-0.01412
H	-5.01279	-2.10542	-1.61046
H	3.018933	4.415339	-0.29717
H	2.655119	4.404784	1.436026
H	-3.11983	-3.53912	2.866889
H	-4.70578	-0.4251	1.599433
H	-1.0428	-4.32304	-0.80844
H	-2.40978	-1.29514	-2.48107
H	-1.72825	-5.0365	1.467701
H	-3.6454	0.712861	3.525296
H	-2.49597	0.509297	2.175337
H	-2.39786	-0.56634	3.600859
H	-5.5711	-0.96925	3.809313
H	-4.36036	-2.23763	4.058316
H	-5.61661	-2.4493	2.816009
H	-0.00479	-0.79969	-2.96897
H	0.474233	-1.77435	-1.55417
H	-0.47575	-0.27784	-1.3396
H	-1.26015	-2.71217	-4.11175
H	-2.35817	-3.75279	-3.16677
H	-0.60346	-3.76327	-2.84731
H	6.129942	1.163953	1.461848
H	6.286366	3.377866	1.58862
H	4.805735	4.225246	2.108605
H	5.314087	4.303735	0.41585
H	6.435211	-1.03248	1.440741
H	5.698561	-1.80323	0.013986

H	5.013424	-2.10361	1.610185
H	3.121189	-3.53807	-2.86677
H	4.705337	-0.42296	-1.59956
H	1.044771	-4.32283	0.808731
H	2.410345	-1.29432	2.481244
H	1.73048	-5.0361	-1.46737
H	3.644031	0.713999	-3.52565
H	2.495097	0.509966	-2.1753
H	2.397172	-0.56591	-3.60061
H	5.570914	-0.96673	-3.80951
H	4.361202	-2.23616	-4.05816
H	5.617671	-2.44652	-2.81588
H	0.005027	-0.79973	2.968895
H	-0.47335	-1.7744	1.553871
H	0.476135	-0.27752	1.339696
H	1.261029	-2.7117	4.111825
H	2.359327	-3.75206	3.166879
H	0.60463	-3.76291	2.847318
Ni	-2.03596	1.016084	-0.26903
Ni	2.0355	1.016875	0.268723

DFT Table 6: Coordinates of the energy-optimized structure of **6**

Ni	1.93772	-1.06382	0.158769
Ni	-1.88799	-1.16272	-0.10303
O	0.583732	0.153264	-0.3799
O	-0.59575	0.14627	0.364486
N	0.71915	-2.49727	0.172922
N	3.210943	-2.49508	0.551531
N	3.255106	0.340947	0.144527
N	-0.60255	-2.53482	-0.03461
N	-3.09102	-2.67365	-0.41153
N	-3.27102	0.17668	-0.17044
C	1.182481	-3.76185	0.28008
C	2.652627	-3.8601	0.532702
C	4.500691	-2.32694	0.825917

C	4.547161	0.174206	0.462458
C	2.852441	1.628846	-0.33035
C	-1.0046	-3.82419	-0.07004
C	0.109713	-4.65854	0.12944
C	5.122984	-1.06135	0.814703
C	5.367816	-3.52555	1.157871
C	5.486604	1.365642	0.400935
C	2.147819	2.499883	0.529849
C	3.134594	1.993479	-1.66729
C	-2.46771	-4.00745	-0.31642
C	-4.3865	-2.58285	-0.69599
C	-4.55242	-0.06935	-0.4789
C	-2.92931	1.512912	0.209632
C	1.812643	3.774039	0.057331
C	1.778318	2.052609	1.934963
C	2.794602	3.283949	-2.09271
C	3.701239	0.96389	-2.63478
C	-5.06826	-1.34958	-0.75691
C	-5.19387	-3.83789	-0.96319
C	-5.54614	1.078463	-0.49363
C	-3.2313	1.962072	1.516028
C	-2.26799	2.350897	-0.71494
C	2.153574	4.176692	-1.23417
C	0.389743	2.532646	2.364299
C	2.863541	2.463219	2.946399
C	2.54142	0.197428	-3.30035
C	4.647173	1.556799	-3.68713
C	-2.95209	3.295188	1.843995
C	-3.75963	0.983523	2.555814
C	-1.99409	3.671481	-0.33945
C	-1.87914	1.820134	-2.08479
C	-2.35337	4.151584	0.920048
C	-2.57408	0.282132	3.246513
C	-4.70043	1.620439	3.586615
C	-0.50811	2.320269	-2.54593
C	-2.97325	2.121192	-3.12505

H	0.13541	-5.74412	0.160532
H	2.838351	-4.38117	1.491988
H	3.141122	-4.46951	-0.25255
H	6.179662	-1.04045	1.077986
H	4.984693	-4.06549	2.039213
H	6.399004	-3.2156	1.366188
H	5.387367	-4.24816	0.325692
H	5.750021	1.596863	-0.64277
H	6.413392	1.154273	0.949616
H	5.022931	2.271821	0.812193
H	1.258037	4.453977	0.705628
H	1.881144	5.173545	-1.58669
H	3.005032	3.586712	-3.11967
H	1.742182	0.952383	1.908187
H	0.322637	3.629161	2.442819
H	0.143636	2.115898	3.352632
H	-0.3673	2.183848	1.651267
H	2.994011	3.557587	2.959205
H	3.832146	2.004123	2.701237
H	2.586893	2.13822	3.962309
H	4.270489	0.229203	-2.04701
H	1.881785	-0.24805	-2.5403
H	2.92489	-0.605	-3.95102
H	1.934097	0.88295	-3.91145
H	4.112107	2.204626	-4.39909
H	5.116674	0.750373	-4.27074
H	5.446211	2.156248	-3.22412
H	-2.92876	-4.59552	0.501273
H	-2.62626	-4.58754	-1.24574
H	-6.12318	-1.39328	-1.02393
H	-4.77671	-4.40997	-1.80818
H	-6.23604	-3.5897	-1.19838
H	-5.18931	-4.51102	-0.09036
H	-5.8158	1.371387	0.532867
H	-6.46487	0.786833	-1.0188
H	-5.12675	1.974093	-0.97043

H	-3.17817	3.662254	2.846093
H	-2.12897	5.183702	1.197195
H	-1.47452	4.327873	-1.03907
H	-4.32392	0.202278	2.025149
H	-1.92459	-0.20723	2.504658
H	-2.92977	-0.47792	3.960879
H	-1.96296	1.017015	3.792999
H	-4.16568	2.314789	4.253294
H	-5.14826	0.840785	4.221601
H	-5.51584	2.18037	3.103238
H	-1.80446	0.726301	-1.98152
H	-0.48938	3.407656	-2.72037
H	-0.23487	1.830821	-3.49243
H	0.257673	2.067628	-1.80198
H	-3.92843	1.649391	-2.8529
H	-2.67995	1.735917	-4.1147
H	-3.13948	3.206916	-3.21578

DFT Table 7: Coordinates of the energy-optimized structure of **9**.

Ni	1.930916	-1.07123	0.239879
Ni	-1.88281	-1.17543	-0.17473
O	0.665497	0.219444	-0.06823
O	-0.68306	0.188539	0.076895
N	0.714525	-2.46255	0.205565
N	3.176065	-2.44818	0.622712
N	3.238467	0.317266	0.195643
N	-0.60155	-2.50181	-0.05511
N	-3.0587	-2.63015	-0.48201
N	-3.2523	0.14995	-0.22492
C	1.171358	-3.72703	0.321982
C	2.626536	-3.81906	0.606687
C	4.462798	-2.28907	0.941882
C	4.525971	0.177141	0.52544
C	2.83412	1.590297	-0.32965
C	-0.99611	-3.79143	-0.10233

C	0.108683	-4.62221	0.133427
C	5.097783	-1.04172	0.926697
C	5.295434	-3.49301	1.324723
C	5.457449	1.365831	0.411893
C	2.222445	2.532502	0.523894
C	3.05756	1.8652	-1.69818
C	-2.4439	-3.97017	-0.38418
C	-4.34965	-2.55144	-0.81451
C	-4.52963	-0.06959	-0.55137
C	-2.90984	1.475348	0.206831
C	1.899211	3.788766	-0.0029
C	1.919568	2.19594	1.97521
C	2.724093	3.136789	-2.17735
C	3.587626	0.784567	-2.6298
C	-5.04232	-1.33633	-0.877
C	-5.1227	-3.81379	-1.12687
C	-5.51228	1.081603	-0.52168
C	-3.14903	1.837726	1.552702
C	-2.34867	2.383832	-0.7147
C	2.162238	4.097332	-1.3359
C	0.464796	2.518735	2.340866
C	2.90477	2.890663	2.930648
C	2.409104	0.01251	-3.25557
C	4.531912	1.319488	-3.71486
C	-2.88189	3.15639	1.936893
C	-3.62871	0.802785	2.56049
C	-2.09211	3.690844	-0.28216
C	-2.02641	1.961074	-2.13893
C	-2.37117	4.081501	1.025806
C	-2.41695	0.126117	3.231257
C	-4.59029	1.370065	3.613332
C	-0.58239	2.313964	-2.51962
C	-3.0306	2.554969	-3.14197
H	0.13495	-5.70633	0.163125
H	2.794994	-4.3248	1.574402
H	3.135124	-4.42786	-0.16271

H	6.14791	-1.021	1.20823
H	4.881176	-4.00011	2.209913
H	6.324029	-3.19301	1.551932
H	5.326182	-4.23508	0.51181
H	5.68189	1.568267	-0.64638
H	6.401559	1.167399	0.932228
H	5.005105	2.279722	0.81572
H	1.424931	4.531436	0.640316
H	1.904799	5.081858	-1.7301
H	2.888782	3.37711	-3.22805
H	2.052582	1.109315	2.084261
H	0.270122	3.601207	2.340085
H	0.239331	2.145566	3.351028
H	-0.23245	2.052333	1.63493
H	2.846517	3.985793	2.827058
H	3.942784	2.586002	2.732758
H	2.672538	2.635718	3.976391
H	4.153075	0.064926	-2.01928
H	1.764042	-0.41854	-2.47597
H	2.774832	-0.80337	-3.8976
H	1.791463	0.686496	-3.86755
H	4.000707	1.94552	-4.4475
H	4.982548	0.482918	-4.2681
H	5.344314	1.923347	-3.28385
H	-2.92717	-4.55776	0.417615
H	-2.58308	-4.53663	-1.32189
H	-6.08959	-1.38045	-1.16598
H	-4.67574	-4.3579	-1.97348
H	-6.16088	-3.57655	-1.38318
H	-5.13035	-4.50238	-0.2677
H	-5.73021	1.36392	0.51916
H	-6.45366	0.799901	-1.00755
H	-5.10584	1.977033	-1.00826
H	-3.0592	3.46372	2.967642
H	-2.16599	5.104185	1.346785
H	-1.65791	4.407898	-0.98023

H	-4.16557	0.01955	2.004127
H	-1.75066	-0.32399	2.480704
H	-2.74567	-0.66192	3.925914
H	-1.83163	0.865547	3.798123
H	-4.07968	2.059073	4.302644
H	-5.00793	0.553776	4.220272
H	-5.42574	1.915666	3.150357
H	-2.12006	0.865401	-2.1785
H	-0.42655	3.401381	-2.57302
H	-0.34114	1.897905	-3.50908
H	0.129369	1.909631	-1.79013
H	-4.05803	2.228028	-2.92597
H	-2.7853	2.237417	-4.16718
H	-3.01088	3.655609	-3.11284

DFT Table 8: Coordinates of the energy-optimized structure of **16**.

Ni	-1.75686	1.25239	0.152293
Ni	1.813274	1.105961	-0.28475
S	-0.02822	-0.07466	-0.05837
N	-0.57921	2.623605	-0.03837
N	0.731376	2.56592	-0.27974
N	-2.98943	2.706877	0.412159
N	-3.07615	-0.10641	0.240474
N	3.163598	2.443413	-0.58562
N	3.040209	-0.33611	-0.15452
C	-0.96686	3.913691	0.007777
C	-2.41875	4.06557	0.290037
C	-4.28285	2.599713	0.70962
C	-4.37272	0.102265	0.504814
C	-2.7077	-1.44619	-0.11671
C	1.218321	3.817825	-0.39425
C	0.159064	4.727044	-0.21805
C	-4.93108	1.360741	0.7774
C	-5.10846	3.838211	0.966102
C	-5.32951	-1.06875	0.478576

C	-2.37357	-2.37528	0.890523
C	-2.72588	-1.80998	-1.48086
C	2.684094	3.840817	-0.64201
C	4.465482	2.225879	-0.76399
C	4.365949	-0.23736	-0.31217
C	2.53782	-1.6065	0.271423
C	-2.02656	-3.67477	0.502175
C	-2.41146	-1.99973	2.362445
C	-2.40122	-3.12874	-1.81658
C	-3.09297	-0.80413	-2.56052
C	5.031553	0.950786	-0.6539
C	5.391374	3.379169	-1.07191
C	5.243742	-1.44784	-0.06758
C	2.598851	-1.94132	1.641722
C	2.009976	-2.49056	-0.69515
C	-2.04644	-4.05514	-0.83688
C	-0.99574	-1.93192	2.946401
C	-3.28695	-2.9616	3.182643
C	-1.85966	-0.39535	-3.38184
C	-4.21757	-1.31626	-3.47281
C	2.126917	-3.20019	2.028362
C	3.166744	-0.95847	2.657285
C	1.543643	-3.73478	-0.25413
C	1.965857	-2.09563	-2.16474
C	1.605015	-4.09076	1.091464
C	2.083461	-0.01341	3.202132
C	3.916727	-1.64728	3.803431
C	0.886173	-2.8434	-2.94697
C	3.326556	-2.26535	-2.86577
H	-2.92425	4.624621	-0.5182
H	-2.57811	4.640902	1.219279
H	0.200988	5.810675	-0.2476
H	-5.99108	1.378404	1.019102
H	-6.13929	3.567018	1.217603
H	-5.1302	4.495229	0.082903
H	-4.6934	4.429765	1.796947

H	-6.34275	-0.7423	0.737402
H	-5.0195	-1.85707	1.176211
H	-5.34967	-1.52948	-0.5192
H	3.200523	4.457308	0.115195
H	2.911894	4.291202	-1.62513
H	-1.74436	-4.40084	1.26591
H	-2.84861	-0.99339	2.431556
H	-2.41979	-3.4341	-2.86423
H	-3.4597	0.100101	-2.05527
H	6.107698	0.879274	-0.79784
H	6.418683	3.021906	-1.20013
H	5.384481	4.125375	-0.26226
H	5.08955	3.901018	-1.9933
H	6.221047	-1.30935	-0.544
H	4.788495	-2.37295	-0.43693
H	5.40853	-1.58207	1.012769
H	-1.78119	-5.07445	-1.12071
H	-1.02592	-1.61692	4.000583
H	-0.37894	-1.22503	2.379462
H	-0.50333	-2.91296	2.892913
H	-3.37203	-2.60669	4.220176
H	-2.84966	-3.97036	3.21119
H	-4.3018	-3.05159	2.769803
H	-2.12582	0.388925	-4.10622
H	-1.45889	-1.25361	-3.94001
H	-1.06289	-0.01315	-2.729
H	-4.5167	-0.53249	-4.18391
H	-5.10609	-1.60976	-2.89472
H	-3.89773	-2.18994	-4.06097
H	2.166217	-3.48937	3.078988
H	3.88992	-0.32514	2.124327
H	1.11605	-4.43108	-0.97388
H	1.714797	-1.02236	-2.18944
H	1.236091	-5.06544	1.413886
H	2.537116	0.759906	3.840804
H	1.346998	-0.56568	3.801798

H	1.546347	0.484309	2.383187
H	4.427216	-0.89663	4.424286
H	4.671566	-2.35466	3.428466
H	3.233658	-2.20414	4.462109
H	0.772975	-2.40092	-3.94677
H	-0.08011	-2.78772	-2.43416
H	1.143517	-3.90522	-3.08669
H	3.22169	-2.04165	-3.93813
H	3.688168	-3.30126	-2.77174
H	4.090391	-1.59079	-2.46225

DFT Table 9: Coordinates of the energy-optimized structure of **23**.

Ni	1.922597	-1.1546	-0.1624
Ni	-2.05485	-1.0384	-0.13024
N	0.547142	-2.26638	-0.85391
N	-0.79862	-2.28448	-0.72457
N	3.036831	-2.60423	-0.72543
N	3.419759	-0.07436	0.359779
N	-3.25249	-2.49422	-0.31459
N	-3.44257	0.197284	0.336386
N	0.491884	-0.21015	0.768519
N	-0.5774	0.160361	0.050452
C	0.925052	-3.41436	-1.46125
C	2.392489	-3.58267	-1.60897
C	4.244748	-2.86472	-0.23983
C	4.648114	-0.55817	0.591737
C	3.352978	1.343029	0.143478
C	0.229586	-0.8591	1.989692
C	-0.27573	1.029604	-1.0283
C	2.938769	0.361478	-3.01697
C	1.305883	-1.48116	2.658918
C	-1.27383	-3.43567	-1.24939
C	-0.20373	-4.1941	-1.74345
C	4.985354	-1.91364	0.477871
C	4.90356	-4.20325	-0.49134

C	5.79433	0.383796	0.892943
C	3.010481	2.236692	1.187546
C	3.758037	1.814515	-1.13005
C	-1.04554	-0.89132	2.589991
C	0.253256	2.302089	-0.77515
C	-0.55198	0.643952	-2.3479
C	4.16488	0.840568	-2.22701
C	1.103114	-2.12945	3.873155
C	-2.7464	-3.60895	-1.12516
C	3.076363	3.609921	0.909415
C	2.568696	1.754327	2.567433
C	3.787114	3.19324	-1.35644
C	-4.4117	-2.60616	0.321263
C	-4.61137	-0.18285	0.866159
C	-3.26246	1.56421	-0.05609
C	-1.2362	-1.54451	3.805005
C	0.480848	3.184072	-1.82696
C	-0.29133	1.522301	-3.39746
C	5.232163	1.401195	-3.17446
C	-0.16951	-2.17242	4.454716
C	3.455213	4.087826	-0.34354
C	2.012432	2.876006	3.450959
C	3.648987	1.008913	3.37318
C	-5.01135	-1.5221	0.981373
C	-5.15781	-3.92121	0.316787
C	-5.60263	0.857136	1.342097
C	-2.87272	2.551353	0.872846
C	-3.47551	1.892495	-1.42159
C	0.212434	2.79998	-3.14314
C	-2.64898	3.855454	0.410226
C	-2.71345	2.262197	2.356373
C	-3.24386	3.208373	-1.83174
C	-3.97058	0.840432	-2.40472
C	-2.82179	4.183754	-0.92904
C	-1.25666	2.415546	2.803292
C	-3.61321	3.170719	3.212399

C	-3.72561	1.195735	-3.87399
C	-5.47034	0.541158	-2.21541
H	-0.23746	-5.17281	-2.20888
H	2.681828	-4.61515	-1.36198
H	2.706954	-3.4038	-2.65602
H	5.977297	-2.20688	0.812924
H	5.887914	-4.2321	-0.01337
H	5.037721	-4.39199	-1.56711
H	4.29944	-5.02878	-0.0848
H	6.577313	-0.14825	1.448033
H	5.483087	1.268962	1.454523
H	6.23635	0.738237	-0.05144
H	2.830098	4.325873	1.691744
H	3.494545	5.163287	-0.52707
H	4.085318	3.572585	-2.33324
H	1.753217	1.038912	2.387609
H	1.570938	2.442424	4.358555
H	1.23335	3.458873	2.944688
H	2.80725	3.568832	3.768521
H	3.229349	0.708289	4.343624
H	4.513691	1.661367	3.567072
H	3.998914	0.101829	2.871313
H	4.598489	-0.04534	-1.74158
H	3.222414	-0.41977	-3.7383
H	2.482063	1.196264	-3.56605
H	2.170299	-0.0544	-2.34748
H	2.30074	-1.44653	2.214629
H	5.582506	0.606615	-3.84871
H	6.101918	1.791197	-2.6255
H	4.83998	2.212126	-3.8063
H	-3.23312	-3.60461	-2.11924
H	-2.97447	-4.58475	-0.66622
H	-5.95678	-1.71122	1.484225
H	-6.08109	-3.83702	0.899473
H	-4.54824	-4.72859	0.751242
H	-5.42498	-4.22678	-0.70594

H	-6.62034	0.450292	1.328505
H	-5.56891	1.762986	0.72565
H	-5.37202	1.156447	2.374617
H	-2.33046	4.623308	1.117345
H	-2.62777	5.199679	-1.27572
H	-3.37969	3.476542	-2.87867
H	-3.01975	1.221182	2.529007
H	-1.13373	2.118667	3.854753
H	-0.94237	3.46538	2.710724
H	-0.58073	1.80323	2.196064
H	-3.56689	2.867858	4.269174
H	-4.66155	3.135768	2.887269
H	-3.28341	4.218437	3.152875
H	-3.41593	-0.08712	-2.17339
H	-3.94142	0.323085	-4.50705
H	-2.68993	1.503266	-4.05391
H	-4.38836	2.009695	-4.20639
H	-5.80144	-0.2016	-2.95668
H	-6.06332	1.456512	-2.36411
H	-5.69993	0.13995	-1.22254
H	1.950239	-2.60457	4.369483
H	-0.32405	-2.67993	5.407207
H	-2.23384	-1.55776	4.247321
H	-1.87755	-0.38752	2.104631
H	-0.95123	-0.35216	-2.53356
H	0.450485	2.600994	0.250304
H	0.869854	4.178216	-1.6114
H	0.397592	3.491092	-3.96646
H	-0.47482	1.20154	-4.42406

DFT Table 10: Coordinates of the energy-optimized structure of **24**

Ni	-1.99681	1.042045	0.222707
Ni	1.946864	1.152917	-0.16484
N	-0.56431	-0.12766	0.082405
N	0.581821	-0.09477	-0.01574

N	-0.73312	2.429969	0.151236
N	0.611769	2.46874	-0.04033
N	-3.22989	2.46252	0.490402
N	-3.30637	-0.33344	0.194357
N	3.101644	2.645222	-0.38995
N	3.32514	-0.15347	-0.21781
C	-1.19046	3.69848	0.23197
C	-2.65739	3.81806	0.44923
C	-4.53058	2.32451	0.74399
C	-4.60745	-0.16354	0.445178
C	-2.86083	-1.62129	-0.24377
C	1.000427	3.761779	-0.0837
C	-0.11806	4.590642	0.086747
C	-5.17936	1.08154	0.748519
C	-5.36794	3.549169	1.032229
C	-5.54102	-1.35158	0.367266
C	-2.21105	-2.48014	0.66753
C	-3.02863	-1.97685	-1.60165
C	2.458104	3.966597	-0.29913
C	-1.76538	-3.72456	0.203873
C	-2.01008	-2.07403	2.117451
C	-2.58714	-3.23936	-2.01325
C	-3.61509	-0.98209	-2.59231
C	4.406794	2.586138	-0.65261
C	4.613024	0.093865	-0.47097
C	2.946025	-1.48892	0.130855
C	-1.96372	-4.11009	-1.11946
C	-0.603	-2.40429	2.627846
C	-3.08202	-2.69935	3.025838
C	-2.5151	-0.04121	-3.11531
C	-4.36382	-1.64346	-3.75418
C	5.119163	1.380021	-0.71359
C	5.176974	3.864072	-0.89303
C	5.604341	-1.04832	-0.46306
C	3.141928	-1.93341	1.457369
C	2.328706	-2.30851	-0.8377

C	2.758713	-3.24045	1.779443
C	3.690628	-0.98805	2.516154
C	1.944372	-3.60258	-0.46383
C	2.096207	-1.80289	-2.25097
C	2.168586	-4.07224	0.828026
C	2.546717	-0.16227	3.129568
C	4.503231	-1.69654	3.605522
C	0.705653	-2.16672	-2.78107
C	3.194955	-2.29737	-3.20711
H	-0.14684	5.675206	0.102599
H	-2.86106	4.361621	1.38991
H	-3.122	4.409893	-0.36112
H	-6.24267	1.08647	0.976965
H	-4.98718	4.095572	1.909157
H	-6.4075	3.265451	1.227647
H	-5.35441	4.252033	0.184827
H	-5.74944	-1.61007	-0.68191
H	-6.49415	-1.11972	0.856329
H	-5.1032	-2.24434	0.829967
H	-1.25149	-4.39865	0.889706
H	-1.61644	-5.08566	-1.46215
H	-2.71491	-3.54158	-3.05278
H	-2.13644	-0.98142	2.164658
H	-0.44815	-3.48841	2.727755
H	-0.44672	-1.95829	3.621029
H	0.171398	-2.02097	1.953654
H	-3.04057	-3.79864	2.978598
H	-4.09291	-2.38401	2.733788
H	-2.92508	-2.39615	4.072328
H	-4.33348	-0.35392	-2.04609
H	-2.01928	0.483779	-2.28429
H	-2.94092	0.717659	-3.78913
H	-1.75002	-0.60635	-3.66672
H	-3.67941	-2.17932	-4.42869
H	-4.87799	-0.87842	-4.35359
H	-5.11575	-2.3629	-3.39779

H	2.629881	4.551671	-1.22056
H	2.894173	4.553273	0.530795
H	6.179659	1.44969	-0.94477
H	4.764105	4.423302	-1.74708
H	6.229508	3.645059	-1.1022
H	5.129463	4.531426	-0.01867
H	5.83391	-1.35033	0.569878
H	6.540853	-0.74501	-0.94519
H	5.205425	-1.93622	-0.96857
H	2.905296	-3.60722	2.795305
H	1.866848	-5.08419	1.101456
H	1.45618	-4.24835	-1.1943
H	4.360209	-0.27626	2.011549
H	2.025113	0.422155	2.355945
H	2.932017	0.540744	3.883489
H	1.809879	-0.82099	3.61111
H	3.870079	-2.32664	4.247739
H	4.987829	-0.95387	4.255639
H	5.287209	-2.33636	3.173945
H	2.163522	-0.70471	-2.21122
H	0.595613	-3.25004	-2.93478
H	0.53111	-1.67872	-3.75107
H	-0.08541	-1.84985	-2.09128
H	4.190408	-1.96055	-2.88743
H	3.021744	-1.9145	-4.22422
H	3.206189	-3.39712	-3.25316

DFT Table 11: Coordinates of the energy-optimized structure of **33**.

Ni	2.072221	-1.01477	0.330816
Ni	-1.93204	-1.1715	-0.0289
O	0.473968	0.272267	0.495744
C	-0.68225	0.048727	0.373351
N	0.80256	-2.4024	0.230235
N	-0.54712	-2.45685	0.041999
N	3.321998	-2.41145	0.442811

N	3.326317	0.381178	0.273639
N	-3.04575	-2.70326	-0.37514
N	-3.36529	0.095623	-0.18279
C	1.28507	-3.66295	0.206827
C	2.759778	-3.77159	0.382932
C	4.631666	-2.25823	0.632858
C	4.649497	0.234852	0.392423
C	2.798843	1.637469	-0.1603
C	-0.90608	-3.75571	-0.09873
C	0.232206	-4.56627	-8.4E-05
C	5.262318	-1.0043	0.630789
C	5.498283	-3.47797	0.842311
C	5.550081	1.435527	0.209803
C	2.210581	2.510378	0.781291
C	2.812497	1.941471	-1.54143
C	-2.35522	-4.00093	-0.33129
C	-4.34685	-2.68243	-0.66147
C	-4.63346	-0.19379	-0.48577
C	-3.01717	1.456309	0.10476
C	1.663308	3.71176	0.317869
C	2.161303	2.143653	2.254806
C	2.253248	3.155202	-1.95656
C	3.374988	0.947001	-2.54575
C	-5.09567	-1.49662	-0.72361
C	-5.07447	-3.97861	-0.93429
C	-5.63765	0.933004	-0.56648
C	-3.08082	1.915339	1.437485
C	-2.52501	2.278301	-0.93119
C	1.686225	4.037202	-1.03673
C	0.848188	2.566922	2.92339
C	3.369288	2.71142	3.019295
C	2.284064	-0.0368	-3.00332
C	4.045994	1.616228	-3.75086
C	-2.60128	3.199711	1.721018
C	-3.61837	1.03051	2.54978
C	-2.05153	3.553089	-0.59956

C	-2.47681	1.783894	-2.36689
C	-2.08064	4.011706	0.715602
C	-2.47675	0.505412	3.433974
C	-4.68401	1.747183	3.391746
C	-1.06038	1.317467	-2.73752
C	-2.98597	2.835347	-3.36338
H	0.285431	-5.64744	-0.07515
H	2.995278	-4.33529	1.304545
H	3.207671	-4.33662	-0.4551
H	6.340142	-0.99769	0.779582
H	5.17237	-4.05518	1.721955
H	6.54235	-3.18285	0.992781
H	5.452385	-4.15808	-0.02242
H	5.688498	1.64738	-0.86191
H	6.537108	1.242004	0.64592
H	5.12536	2.34091	0.658636
H	1.196126	4.395279	1.026666
H	1.252343	4.977531	-1.37971
H	2.255755	3.413119	-3.01635
H	2.228955	1.045286	2.309072
H	0.776798	3.659902	3.028641
H	0.783889	2.13577	3.93283
H	-0.02189	2.229344	2.347083
H	3.396623	3.809848	2.947212
H	4.314652	2.31981	2.623018
H	3.312441	2.439675	4.084256
H	4.139912	0.351746	-2.02706
H	1.822143	-0.54076	-2.13901
H	2.710455	-0.81222	-3.65748
H	1.493283	0.488171	-3.55836
H	3.314447	2.129417	-4.39299
H	4.548471	0.859236	-4.37033
H	4.795203	2.357688	-3.43694
H	-2.49848	-4.5582	-1.27451
H	-2.77296	-4.63636	0.472347
H	-6.14951	-1.59834	-0.97296

H	-4.63655	-4.50748	-1.79505
H	-6.13211	-3.79153	-1.14873
H	-5.01099	-4.66076	-0.07237
H	-5.73581	1.435537	0.406691
H	-6.62064	0.5546	-0.86865
H	-5.31343	1.700844	-1.2831
H	-2.62265	3.563895	2.749863
H	-1.69821	5.00388	0.958048
H	-1.64577	4.19426	-1.38289
H	-4.09204	0.158129	2.07794
H	-1.75754	-0.07519	2.839601
H	-2.8682	-0.14559	4.230154
H	-1.93206	1.3371	3.904125
H	-4.25624	2.59172	3.952146
H	-5.12565	1.055305	4.124303
H	-5.49405	2.142494	2.761885
H	-3.13805	0.907324	-2.43403
H	-0.31916	2.106163	-2.54249
H	-1.00925	1.041761	-3.80149
H	-0.76814	0.437815	-2.14812
H	-3.98029	3.209289	-3.08096
H	-3.0558	2.398739	-4.37022
H	-2.30716	3.698115	-3.42741

Chapter 13 Crystallography

Crystal data and details of the data collections are given in **Table 50–Table 59**. x-ray data were collected on a STOE IPDS II diffractometer (graphite monochromated Mo-K α radiation, $\lambda = 0.71073 \text{ \AA}$) by use of scans at -140°C . The structures were solved by SHELXT^[147] and refined on F^2 using all reflections with SHELXL-2013/14/16.^[148] Non-hydrogen atoms were refined anisotropically. Most hydrogen atoms were placed in calculated positions and assigned to an isotropic displacement parameter of 1.2/1.5 $U_{\text{eq}}(\text{C})$. Face-indexed absorption corrections were performed numerically with the program X-RED.^[149]

The nickel bound hydrogen atoms in **3** were refined freely. In case of **4** a fixed isotropic displacement parameter of 0.08 \AA^2 was applied. In case of the coordinating solvents, THF and Et₂O occupy the same coordination site of the potassium atom.

Table 50: Crystal data and refinement details of **1**, **3** and **4**.

Compound	1 pd 40	3 pd 127b	4 pd 184
Empirical formula	C ₃₁ H ₃₇ BrN ₆ Ni ₂	C ₄₇ H ₇₁ N ₆ NaNi ₂ O ₂	C ₇₁ H _{105.58} KN ₆ Ni ₂ O ₉
Formula weight	690.99	892.50	1343.70
<i>T</i> [K]	133(2)	133(2)	133(2)
Crystal size	0.39×0.29×0.12	0.50×0.45×0.32	0.49×0.36×0.21
Crystal system	Monoclinic	Triclinic	Monoclinic
Space group	<i>P</i> 2 ₁ / <i>c</i>	<i>P</i> -1	<i>C</i> 2/ <i>c</i>
<i>a</i> [Å]	14.0090(4)	11.1496(5)	26.6234(4)
<i>b</i> [Å]	10.6603(4)	13.0401(7)	23.4343(3)
<i>c</i> [Å]	20.2858(6)	17.3856(8)	23.2487(3)
α [°]	90	110.631(4)	90
β [°]	97.172(2)	94.584(4)	94.7290(10)
γ [°]	90	98.545(4)	90
<i>V</i> [Å ³]	3005.78(17)	2315.3(2)	14455.5(3)
<i>Z</i>	4	2	8
ρ [g/cm ³]	1.527	1.280	1.235
<i>F</i> (000)	1424	956	5765
μ [mm ⁻¹]	2.613	0.866	0.635
<i>T</i> _{min} / <i>T</i> _{max}	0.4904 / 0.7882	0.6473 / 0.7971	0.8795 / 0.9837
θ range [°]	1.465 - 26.774	1.699 - 26.830	1.159 - 25.688
<i>hkl</i> -range	±17 ±13 ±25	-12 - 14 ±16 ±21	±32 ±28 ±28
Measured refl.	38800	30911	82295
Unique refl. [<i>R</i> _{int}]	6375 [0.0695]	9822 [0.0350]	13658 [0.0331]
Observed refl. (<i>I</i> > 2(<i>I</i>))	5206	7866	11503
Data / Res. / Param.	6375 / 0 / 369	9822 / 0 / 543	13658 / 283 / 938
Goodness-of-fit (<i>F</i> ²)	1.060	0.991	1.088
<i>R</i> ₁ , <i>wR</i> ₂ (<i>I</i> > 2(<i>I</i>))	0.0405, 0.0842	0.0355, 0.0854	0.0402, 0.0950
<i>R</i> ₁ , <i>wR</i> ₂ (all data)	0.0562, 0.0887	0.0491, 0.0896	0.0521, 0.1020
Resid. el. dens. [e/Å ³]	-0.476 / 0.706	-0.277 / 0.582	-0.399 / 0.638

Table 51: Crystal data and refinement details of **6**, **8** and **9**.

Compound	6 pd 170	8 pd 212c	9 pd 135b
Empirical formula	C ₇₈ H ₁₀₇ KN ₁₂ Ni ₄ O ₃	C ₇₉ H ₁₁₇ KN ₆ Ni ₂ O ₁₃	C ₄₁ H ₅₇ N ₆ Ni ₂ O _{2.5}
Formula weight	1534.69	1515.30	791.34
<i>T</i> [K]	133(2)	133(2)	133 (2)
Crystal size	0.42×0.18×0.06	0.50×0.22×0.20	0.48×0.22×0.21
Crystal system	Triclinic	Orthorhombic	Monoclinic
Space group	<i>P</i> -1	<i>Pbcm</i>	<i>P</i> 2 ₁ / <i>c</i>
<i>a</i> [Å]	11.1186(5)	11.2912(2)	17.3032(5)
<i>b</i> [Å]	15.8136(8)	25.8683(4)	14.2469(4)
<i>c</i> [Å]	23.5352(12)	27.1074(4)	17.1692(5)
α [°]	73.085(4)	90	90
β [°]	86.315(4)	90	113.291(2)
γ [°]	69.691(4)	90	90
<i>V</i> [Å ³]	3709.8(3)	7917.6(2)	3887.6(2)
<i>Z</i>	2	4	4
ρ [g/cm ³]	1.374	1.271	1.352
<i>F</i> (000)	1628	3248	1684
μ [mm ⁻¹]	1.112	0.592	1.013
<i>T</i> _{min} / <i>T</i> _{max}	0.5509 / 0.7771	0.6134 / 0.8007	0.5050/0.8761
θ range [°]	1.433 - 26.737	1.502 - 25.722	1.920 - 26.802
<i>hkl</i> -range	-14 - 13 -19 - 20 ± 29	± 13 ± 31 -32 - 30	±21 ±18 ±21
Measured refl.	38831	65467	53345
Unique refl. [<i>R</i> _{int}]	15680 [0.0948]	7668 [0.0468]	8239 [0.0475]
Observed refl. (<i>I</i> > 2(<i>I</i>))	8841	6102	6848
Data / Res. / Param.	15680 / 29 / 940	7668 / 145 / 577	8239 / 7 / 508
Goodness-of-fit (<i>F</i> ²)	0.863	1.114	1.027
<i>R</i> ₁ , <i>wR</i> ₂ (<i>I</i> > 2 (<i>I</i>))	0.0513, 0.0978	0.0418, 0.0994	0.0347, 0.0776
<i>R</i> ₁ , <i>wR</i> ₂ (all data)	0.1098, 0.1141	0.0600, 0.1144	0.0477, 0.0817
Resid. el. dens.	-0.683/0.467	-0.279/0.457	-0.521/0.894

Table 52: Crystal data and refinement details of **11**, **12** and **13**

Compound	11 pd 175	12 pd 153d	13 pd 153b
Empirical formula	C ₄₁ H ₅₈ N ₆ Ni ₂ O _{1.5}	C ₅₁ H ₇₇ KN ₆ Ni ₂ O ₃ S ₂	C ₄₁ H ₅₈ N ₆ Ni ₂ O _{0.5} S
Formula weight	776.35	1042.82	792.41
<i>T</i> [K]	133(2)	133(2)	133(2)
Crystal size [mm ³]	0.50×0.42×0.32	0.45×0.23×0.14	0.50×0.35×0.24
Crystal system	Monoclinic	Monoclinic	Monoclinic
Space group	<i>P2</i> ₁ / <i>c</i>	<i>P2</i> ₁ / <i>n</i>	<i>P2</i> ₁ / <i>c</i>
<i>a</i> [Å]	18.3096(6)	17.3254(11)	17.2715(5)
<i>b</i> [Å]	13.9053(5)	15.5369(6)	13.9903(4)
<i>c</i> [Å]	16.6162(6)	20.4719(12)	17.3028(6)
α [°]	90	90	90
β [°]	113.902(2)	109.707(4)	112.467(2)
γ [°]	90	90	90
<i>V</i> [Å ³]	3867.7(2)	5187.9(5)	3863.6(2)
<i>Z</i>	4	4	4
ρ [g/cm ³]	1.333	1.335	1.362
<i>F</i> (000)	1656	2224	1688
μ [mm ⁻¹]	1.015	0.933	1.068
<i>T</i> _{min} / <i>T</i> _{max}	0.4508/0.6844	0.5016 / 0.8051	0.6070 / 0.8085
θ range [°]	1.904 - 26.819	1.336 - 25.839	1.934 - 26.764
<i>hkl</i> -range	-20 - 23 ± 17 -21 - 20	±21 ±18 ±24	-19 - 21 ±17 ±21
Measured refl.	40322	37636	33399
Unique refl. [<i>R</i> _{int}]	8214 [0.0526]	9830 [0.1421]	8176 [0.0405]
Observed refl. (<i>I</i> > 2(<i>I</i>))	6476	5586	6789
Data / Res. / Param.	8214 / 73 / 554	9830 / 185 / 684	8176/10/503
Goodness-of-fit (<i>F</i> ²)	0.986	1.074	1.010
<i>R</i> ₁ , <i>wR</i> ₂ (<i>I</i> > 2 (<i>I</i>))	0.0425, 0.0995	0.0703, 0.1455	0.0300, 0.0664
<i>R</i> ₁ , <i>wR</i> ₂ (all data)	0.0595, 0.1057	0.1475, 0.1857	0.0423, 0.0698
Resid. el. dens. [e/Å ³]	-0.376/0.658	-0.539/1.194	-0.256/0.371

Table 53: Crystal data and refinement details of **14**, **15** and **16**.

Compound	14 pd 170b	15 pd 243	16 pd 222
Empirical formula	C ₅₁ H ₇₇ KN ₆ Ni ₂ O ₃ S	C _{44.8} H _{66.4} N ₆ Ni ₂ O _{0.6} S	C ₄₁ H ₅₇ N ₆ Ni ₂ O _{0.5} S
Formula weight	1010.76	848.12	791.40
<i>T</i> [K]	133(2)	133(2)	133(2)
Crystal size [mm ³]	0.50×0.49×0.46	0.37×0.14×0.13	0.30×0.10×0.070
Crystal system	Triclinic	Triclinic	Monoclinic
Space group	<i>P</i> -1	<i>P</i> -1	<i>P</i> 2 ₁ / <i>c</i>
<i>a</i> [Å]	12.9841(6)	12.1569(5)	17.2564(4)
<i>b</i> [Å]	13.4180(6)	13.2965(5)	14.0118(2)
<i>c</i> [Å]	18.0609(8)	14.2127(6)	17.2717(4)
α [°]	75.444(4)	86.865(3)	90
β [°]	74.712(4)	70.848(3)	112.378(2)
γ [°]	62.255(3)	85.265(3)	90
<i>V</i> [Å ³]	2655.6(2)	2161.91(16)	3861.68(15)
<i>Z</i>	2	2	4
ρ [g/cm ³]	1.264	1.303	1.361
<i>F</i> (000)	1080	908	1684
μ [mm ⁻¹]	0.871	0.959	1.068
<i>T</i> _{min} / <i>T</i> _{max}	0.6731 / 0.7859	0.4983 / 0.7187	0.5630 / 0.8699
θ range [°]	1.182 - 25.829	1.517 - 26.945	1.933 - 26.787
<i>hkl</i> -range	-13 - 15 ±16 ±21	±15 ±16 -18 - 17	±21 ±17 ±21
Measured refl.	31554	30771	46739
Unique refl. [<i>R</i> _{int}]	10012 [0.0258]	9177 [0.0313]	8190 [0.0410]
Observed refl. (<i>I</i> > 2(<i>I</i>))	8477	7142	6505
Data / Res. / Param.	10012/336/715	9177 / 90 / 586	8190 / 5 / 499
Goodness-of-fit (<i>F</i> ²)	1.060	1.019	1.122
<i>R</i> ₁ , <i>wR</i> ₂ (<i>I</i> > 2(<i>I</i>))	0.0386, 0.1115	0.0400, 0.1005	0.0380, 0.0861
<i>R</i> ₁ , <i>wR</i> ₂ (all data)	0.0484, 0.1201	0.0587, 0.1117	0.0589, 0.0983
Resid. el. dens. [e/Å ³]	-0.479 / 0.874	-0.800 / 1.066	-0.381 / 1.211

Table 54: Crystal data and refinement details of **17**, **18** and **19**.

Compound	17 pd 43	18 pd 68	19 pd 194b
Empirical formula	C ₅₁ H ₇₂ N ₈ Ni ₂ O _{1.50}	C ₆₃ H ₉₅ KN ₈ Ni ₂ O _{4.50}	C ₈₁ H ₁₁₉ KN ₈ Ni ₂ O ₁₀
Formula weight	938.58	1192.98	1521.35
<i>T</i> [K]	133(2)	133(2)	133(2)
Crystal size [mm ³]	0.48×0.15×0.12	0.50×0.48×0.38	0.30×0.15×0.14
Crystal system	Triclinic	Triclinic	Orthorhombic
Space group	<i>P</i> -1	<i>P</i> -1	<i>Pbca</i>
<i>a</i> [Å]	11.7268(5)	14.7187(6)	22.9237(4)
<i>b</i> [Å]	14.1109(6)	14.8852(6)	25.1977(6)
<i>c</i> [Å]	16.1664(7)	17.8081(9)	27.7992(5)
α [°]	105.000(3)	96.053(4)	90
β [°]	93.729(4)	103.644(4)	90
γ [°]	111.015(3)	118.674(3)	90
<i>V</i> [Å ³]	2374.87(18)	3215.3(3)	16057.5(6)
<i>Z</i>	2	2	8
ρ [g/cm ³]	1.313	1.232	1.259
<i>F</i> (000)	1004	1280	6528
μ [mm ⁻¹]	0.840	0.701	0.582
<i>T</i> _{min} / <i>T</i> _{max}	0.7430 / 0.9274	0.5473 / 0.8059	0.7437 / 0.8746
θ range [°]	1.324 - 26.759	1.217 - 25.687	1.407 - 25.804
<i>hkl</i> -range	-13 - 14 ±17 ±20	±17 ±18 ±21	-26 - 28 -30 - 28 ±33
Measured refl.	34424	40089	97945
Unique refl. [<i>R</i> _{int}]	10071 [0.0526]	12134 [0.0783]	15177 [0.0950]
Observed refl. (<i>I</i> > 2(<i>I</i>))	7112	8452	10105
Data / Res. / Param.	10071 / 129 / 669	12134 / 661 / 981	15177 / 63 / 981
Goodness-of-fit (<i>F</i> ²)	0.964	0.969	1.090
<i>R</i> ₁ , <i>wR</i> ₂ (<i>I</i> > 2(<i>I</i>))	0.0493, 0.1108	0.0518, 0.1290	0.0552, 0.1049
<i>R</i> ₁ , <i>wR</i> ₂ (all data)	0.0810, 0.1213	0.0795, 0.1389	0.1040, 0.1271
Resid. el. dens. [e/Å ³]	-0.506 / 0.667	-0.385 / 0.712	-0.296 / 0.472

Table 55: Crystal data and refinement details of **22**, **23** and **24**.

Compound	22 pd 210	23 pd 198	24 pd 211
Empirical formula		C ₅₇ H ₇₇ N ₈ Ni ₂	C ₄₁ H ₅₈ N ₈ Ni ₂ O _{0.5}
Formula weight		991.68	788.37
<i>T</i> [K]	133.(2)	133(2)	133(2)
Crystal size [mm ³]		0.24×0.20×0.14	0.27×0.22×0.20
Crystal system	Monoclinic	Triclinic	Monoclinic
Space group	<i>P</i> 2 ₁ / <i>c</i>	<i>P</i> -1	<i>P</i> 2 ₁ / <i>c</i>
<i>a</i> [Å]	14.990(3)	11.0702(5)	17.3031(7)
<i>b</i> [Å]	23.095(5)	14.2193(7)	14.1567(7)
<i>c</i> [Å]	25.016(5)	17.8105(8)	17.4780(8)
α [°]	90	75.272(4)	90
β [°]	92.60(3)	74.083(4)	112.838(3)
γ [°]	90	74.102(4)	90
<i>V</i> [Å ³]		2543.9(2)	3945.7(3)
<i>Z</i>		2	4
ρ [g/cm ³]		1.295	1.327
<i>F</i> (000)		1062	1680
μ [mm ⁻¹]		0.786	0.996
<i>T</i> _{min} / <i>T</i> _{max}		0.8589 / 0.9370	0.7621 / 0.8822
θ range [°]		1.518 - 26.866	1.915 - 26.874
<i>hkl</i> -range		-13 - 14 ±18 ±22	-21 - 20 ±17 ±22
Measured refl.		30736	35871
Unique refl. [<i>R</i> _{int}]		10757 [0.0329]	8405 [0.0743]
Observed refl. (<i>I</i> > 2(<i>I</i>))		8351	5608
Data / Res. / Param.		10757 / 0 / 618	8405 / 162 / 542
Goodness-of-fit (<i>F</i> ²)		1.114	1.049
<i>R</i> ₁ , <i>wR</i> ₂ (<i>I</i> > 2 (<i>I</i>))		0.0467, 0.1003	0.0623, 0.1098
<i>R</i> ₁ , <i>wR</i> ₂ (all data)		0.0721, 0.1170	0.1080, 0.1230
Resid. el. dens. [e/Å ³]		-0.311 / 0.627	-0.377 / 0.474

Table 56: Crystal data and refinement details of **25**, **26** and **27**.

Compound	25 pd 114	26 dm 266	27 pd 79b
Empirical formula	C ₄₁ H ₅₈ N ₈ Ni ₂ O _{0.50}	C ₃₉ H ₅₅ N ₇ Ni ₂	C ₄₁ H ₆₀ N ₈ Ni ₂ O _{0.50}
Formula weight	788.37	739.32	790.39
<i>T</i> [K]	133(2)	133(2)	133(2)
Crystal size [mm ³]	0.27×0.22×0.20	0.25×0.14×0.12	0.50×0.50×0.32
Crystal system	Monoclinic	Monoclinic	Monoclinic
Space group	<i>P</i> 2 ₁ / <i>c</i>	<i>C</i> 2/ <i>c</i>	<i>P</i> 2 ₁ / <i>c</i>
<i>a</i> [Å]	17.3031(7)	18.4847(13)	17.2013(9)
<i>b</i> [Å]	14.1567(7)	16.4274(9)	14.2468(7)
<i>c</i> [Å]	17.4780(8)	13.6837(9)	17.4667(10)
α [°]	90	90	90
β [°]	112.838(3)	117.818(5)	112.975(4)
γ [°]	90	90	90
<i>V</i> [Å ³]	3945.7(3)	3674.9(4)	3940.9(4)
<i>Z</i>	4	4	4
ρ [g/cm ³]	1.327	1.336	1.332
<i>F</i> (000)	1680	1576	1688
μ [mm ⁻¹]	0.996	1.062	0.997
<i>T</i> _{min} / <i>T</i> _{max}	0.7621 / 0.8822	0.7541 / 0.8962	0.5259 / 0.7449
θ range [°]	1.915 - 26.874	1.757 - 26.859	1.910 - 26.810
<i>hkl</i> -range	-21 - 20, ±17 ±22	±23 ±20 -17 - 14	±21 ±18 ±22
Measured refl.	35871	23469	54479
Unique refl. [<i>R</i> _{int}]	8405 [0.0743]	3908 [0.0660]	8355 [0.0799]
Obs. Refl. (<i>I</i> > 2 σ (<i>I</i>))	5608	3142	6583
Data / Res. / Param.	8405 / 162 / 542	3908 / 1 / 228	8355 / 77 / 511
Goodness-of-Fit (<i>F</i> ²)	1.049	1.134	0.958
<i>R</i> ₁ , <i>wR</i> ₂ (<i>I</i> > 2 σ (<i>I</i>))	0.0623, 0.1098	0.0516, 0.0971	0.0397, 0.0929
<i>R</i> ₁ , <i>wR</i> ₂ (all data)	0.1080, 0.1230	0.0727, 0.1035	0.0564, 0.0982
Resid. el. dens. [e/Å ³]	-0.377 / 0.474	-0.401 / 0.483	-0.442 / 0.715

Table 57: Crystal data and refinement details of **28**, **31** and **33**.

Compound	28 pd 144d	31 pd 246	33 pd 193
Empirical formula	C ₄₇ H ₇₃ BF ₄ N ₈ Ni ₂ O ₂	C ₅₇ H ₉₁ KN ₁₀ Ni ₂ O ₆	C ₄₂ H ₅₇ N ₆ Ni ₂ O _{1.50}
Formula weight	986.36	1168.91	787.35
<i>T</i> [K]	133(2)	133(2)	133(2)
Crystal size [mm ³]	0.28×0.20×0.19	0.50×0.49×0.19	0.37×0.29×0.20
Crystal system	Monoclinic	Orthorhombic	Monoclinic
Space group	<i>P2</i> ₁	<i>Pbca</i>	<i>P2</i> ₁ / <i>c</i>
<i>a</i> [Å]	15.0277(3)	20.3044(3)	17.1690(8)
<i>b</i> [Å]	16.6068(7)	20.9868(3)	14.2075(5)
<i>c</i> [Å]	19.4215(4)	27.9574(6)	17.4227(9)
α [°]	90	90	90
β [°]	95.325(2)	90	112.598(4)
γ [°]	90	90	90
<i>V</i> [Å ³]	4826.0(2)	11913.3(4)	3923.6(3)
<i>Z</i>	4	8	4
ρ [g/cm ³]	1.358	1.303	1.333
<i>F</i> (000)	2096	5008	1676
μ [mm ⁻¹]	0.842	0.758	1.002
<i>T</i> _{min} / <i>T</i> _{max}	0.7243 / 0.8651	0.7237 / 0.9366	0.6735 / 0.8294
θ range [°]	1.616 - 26.787	1.457 - 25.738	1.912 - 26.829
<i>hkl</i> -range	±18 ±20 -23 - 24	-23 - 24 ±25 ±34	-21 - 19 ±17 -22 - 21
Measured refl.	51621	110797	34317
Unique refl. [<i>R</i> _{int}]	20447 [0.0917]	11288 [0.0646]	8297 [0.0454]
Obs. Refl. (<i>I</i> > 2 σ (<i>I</i>))	15245	9156	6381
Data / Res. / Param.	20447 / 223 / 1270	11288 / 2 / 703	8297 / 59 / 508
Goodness-of-Fit (<i>F</i> ²)	0.976	1.088	1.027
<i>R</i> ₁ , <i>wR</i> ₂ (<i>I</i> > 2 σ (<i>I</i>))	0.0589, 0.1232	0.0441, 0.1057	0.0473, 0.1022
<i>R</i> ₁ , <i>wR</i> ₂ (all data)	0.0831, 0.1328	0.0610, 0.1175	0.0705, 0.1099
Resid. el. dens. [e/Å ³]	-0.752 / 0.602	-0.538 / 0.777	-0.324 / 0.990

Table 58: Crystal data and refinement details of **35**, **36** and **37**

Compound	35 pd 72	36 pd 82-2	37 pd 126b
Empirical formula	C ₅₅ H ₅₃ BrCl ₈ N ₆ Ni ₂	C ₅₁ H ₄₅ KN ₆ Ni ₂	C ₅₉ H _{61.25} N ₆ NaNi ₂ O ₂
Formula weight	1278.96	898.45	1026.80
<i>T</i> [K]	133(2)	133(2)	133(2)
Crystal size [mm ³]	0.50×0.50×0.26	0.23×0.21×0.09	0.5×0.49×0.22
Crystal system	Monoclinic	Monoclinic	Triclinic
Space group	<i>P</i> 2 ₁ / <i>c</i>	<i>P</i> 2 ₁ / <i>n</i>	<i>P</i> -1
<i>a</i> [Å]	13.2136(6)	16.8007(11)	14.2900(3)
<i>b</i> [Å]	17.6293(5)	15.0508(7)	18.5010(4)
<i>c</i> [Å]	24.0942(11)	17.0678(10)	19.5019(5)
α [°]	90	90	80.688(2)
β [°]	102.685(4)	106.969(5)	82.043(2)
γ [°]	90	90	81.867(2)
<i>V</i> [Å ³]	5475.7(4)	4127.9(4)	5001.4(2)
<i>Z</i>	4	4	4
ρ [g/cm ³]	1.551	1.446	1.364
<i>F</i> (000)	2608	1872	2161
μ [mm ⁻¹]	1.852	1.058	0.812
<i>T</i> _{min} / <i>T</i> _{max}	0.3418 / 0.7380	0.6056 / 0.8593	0.5170 / 0.7360
θ range [°]	1.444 - 25.718	1.496 - 26.819	1.432 - 26.959
<i>hkl</i> -range	±16 -21 - 18 -28 - 29	-20 - 21 -18 - 19 ±21	±18 ±23 ±24
Measured refl.	38697	53223	70438
Unique refl. [<i>R</i> _{int}]	10327 [0.0567]	8792 [0.1400]	21215 [0.0203]
Observed refl. (<i>I</i> > 2(<i>I</i>))	8494	5294	17846
Data / Res. / Param.	10327 / 0 / 681	8792 / 0 / 559	21215 / 57 / 1314
Goodness-of-fit (<i>F</i> ²)	1.050	1.009	1.036
<i>R</i> ₁ , <i>wR</i> ₂ (<i>I</i> > 2 (<i>I</i>))	0.0393, 0.0863	0.0643, 0.1002	0.0327, 0.0809
<i>R</i> ₁ , <i>wR</i> ₂ (all data)	0.0539, 0.0913	0.1253, 0.1155	0.0432, 0.0873
Resid. el. dens. [e/Å ³]	-0.492 / 0.668	-0.378 / 0.482	-0.512 / 0.620

Table 59: Crystal data and refinement details of **38**, **39** and **40**.

Compound	38 pd 126	39 pd 82	40 pd 130c
Empirical formula	C _{67.25} H ₈₀ N ₆ NaNi ₂ O _{3.75}	C ₅₅ H ₅₄ N ₆ Ni ₂ O ₂	C ₅₆ H ₅₃ F ₃ N ₆ Ni ₂ O ₄ S
Formula weight	1172.78	948.46	1080.52
<i>T</i> [K]	133(2)	133(2)	133(2)
Crystal size [mm ³]	0.44×0.21×0.19	0.50×0.41×0.32	0.50×0.45×0.34
Crystal system	Triclinic	Monoclinic	Triclinic
Space group	<i>P</i> -1	<i>P</i> 2 ₁ / <i>c</i>	<i>P</i> -1
<i>a</i> [Å]	12.7288(7)	14.8186(6)	13.3477(5)
<i>b</i> [Å]	15.5000(7)	20.5006(5)	13.6456(5)
<i>c</i> [Å]	17.7274(9)	15.9398(6)	16.3846(6)
α [°]	112.663(4)	90	95.582(3)
β [°]	92.988(4)	110.434(3)	105.945(3)
γ [°]	99.314(4)	90	115.768(3)
<i>V</i> [Å ³]	3159.7(3)	4537.6(3)	2501.87(17)
<i>Z</i>	2	4	2
ρ [g/cm ³]	1.233	1.388	1.434
<i>F</i> (000)	1245	1992	1124
μ [mm ⁻¹]	0.653	0.881	0.859
<i>T</i> _{min} / <i>T</i> _{max}	0.7802 / 0.9144	0.6259 / 0.8043	0.6051 / 0.7239
θ range [°]	1.452 - 26.874	1.466 - 26.846	1.335 - 26.923
<i>hkl</i> -range	±16 ±19 ±22	±18 -23 - 25 ±20	±16 -17 - 16, ±20
Measured refl.	41104	58690	34813
Unique refl. [<i>R</i> _{int}]	13405 [0.0595]	9634 [0.0677]	10594 [0.0242]
Observed refl. (<i>I</i> > 2(<i>I</i>))	8722	7728	9326
Data / Res. / Param.	13405 / 219 / 863	9634 / 75 / 640	10594 / 0 / 653
Goodness-of-fit (<i>F</i> ²)	0.957	1.133	1.038
<i>R</i> ₁ , <i>wR</i> ₂ (<i>I</i> > 2 (<i>I</i>))	0.0490, 0.1066	0.0555, 0.1255	0.0291, 0.0710
<i>R</i> ₁ , <i>wR</i> ₂ (all data)	0.0903, 0.1192	0.0738, 0.1328	0.0361, 0.0763
Resid. el. dens. [e/Å ³]	-0.401 / 0.557	-0.754 / 0.548	-0.478 / 0.880

Chapter 14 Appendix

ESI-MS, NMR, IR, UV-Vis Spectra, SQUID and X-ray structures

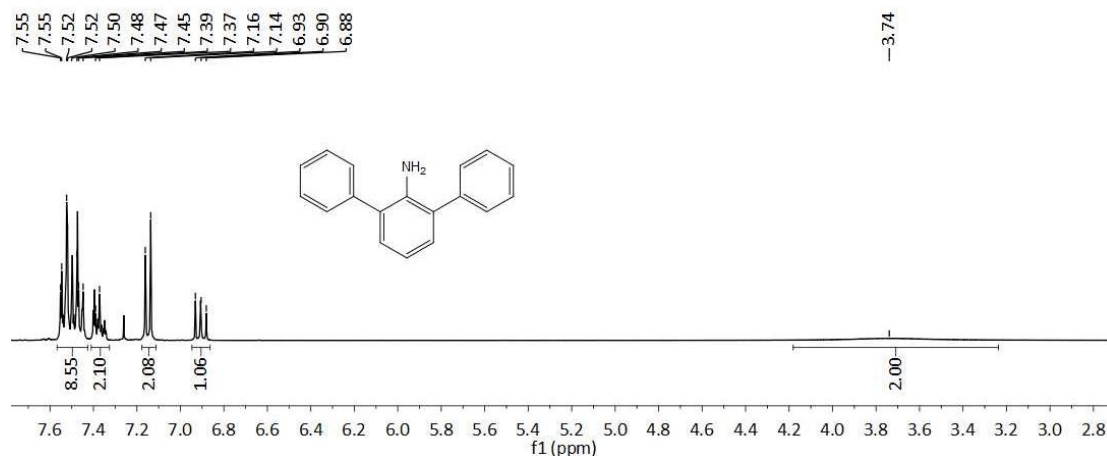


Figure A1: $^1\text{H NMR}$ (300 MHz) spectrum of **IV** in CDCl_3 .

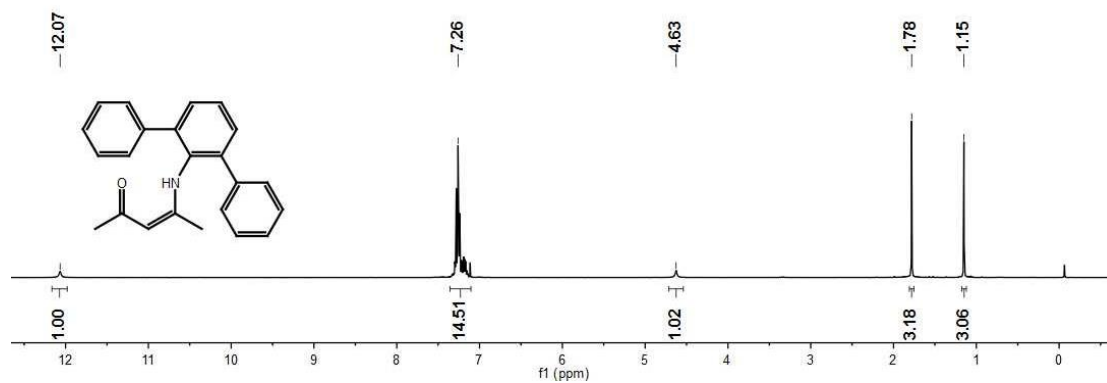


Figure A2: $^1\text{H NMR}$ (300 MHz) spectrum of **VIII** in CDCl_3 .

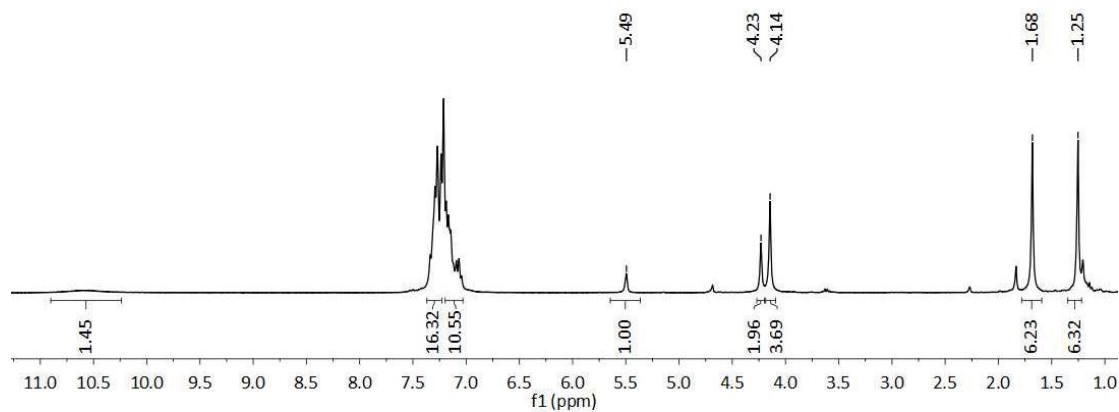


Figure A3: $^1\text{H NMR}$ (300 MHz) spectrum of **H₃L³** in CDCl_3 .

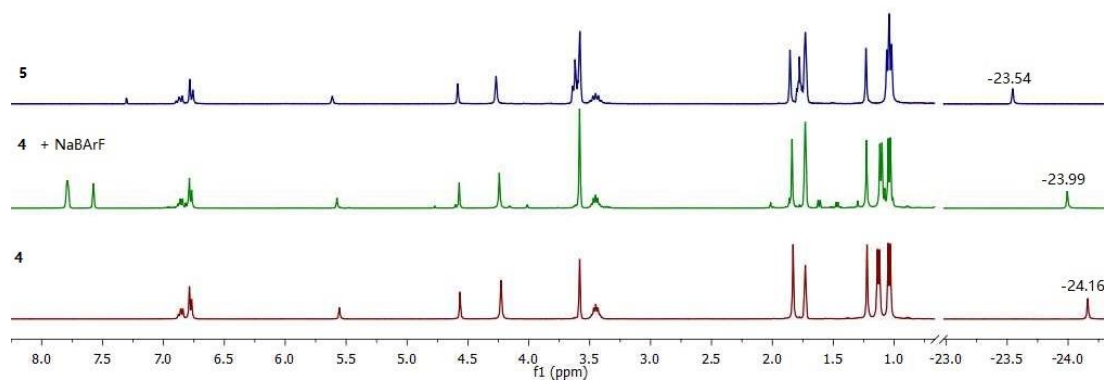


Figure A4: ^1H NMR spectra of **2** (bottom), **2**+NaBArF (middle), **3** (top) in THF- d_8 . The Ni-H resonance in the Na/K mixture appears as a rapid average of that in **2** and **3**.

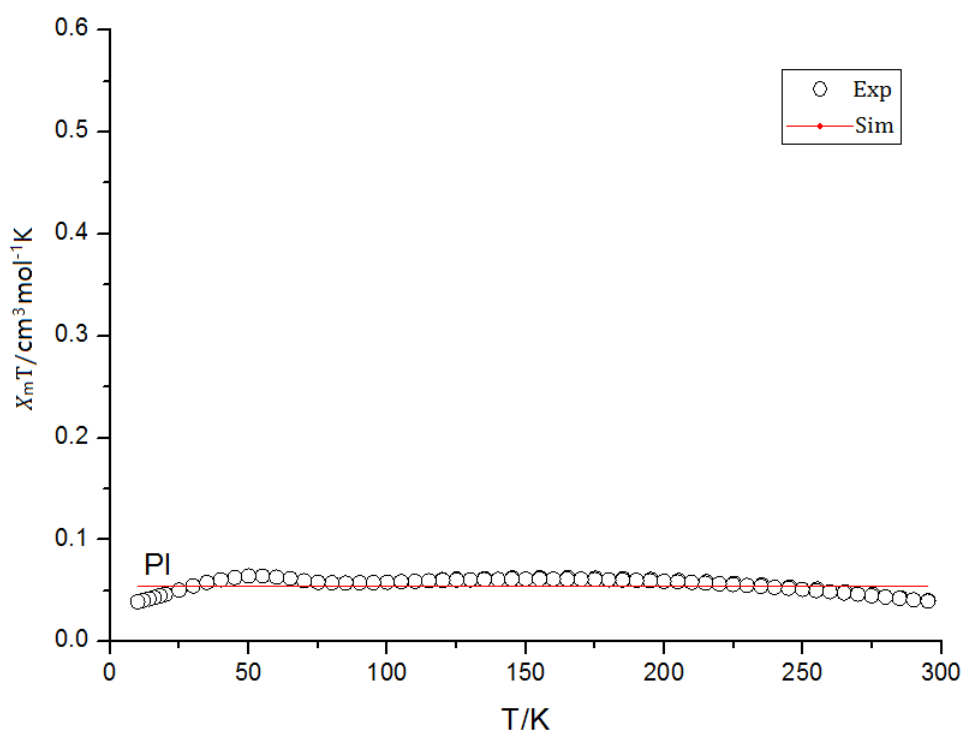


Figure A5: $\chi_m T$ vs. T measurement in the temperature range of 2 – 295 K at 0.5 T for solid samples of **2**. The solid red lines represent the best fit with $PI = 5.4\%$ ($S = 1$) and $TIP = 60 \cdot 10^{-6} \text{ cm}^3 \cdot \text{mol}^{-1}$.

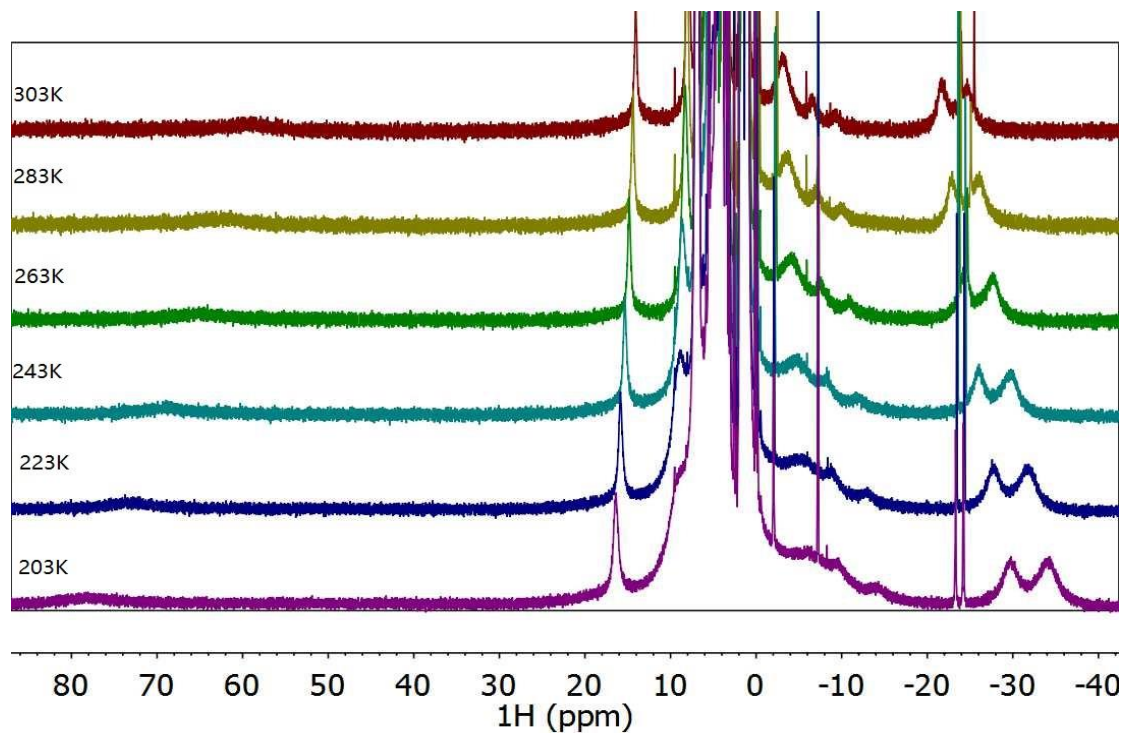


Figure A6: Variable temperature ^1H NMR spectrum (400 MHz) of **4** in THF-d_8 . The broad peaks show a $1/T$ (Curie) behavior indicating a paramagnetic species.

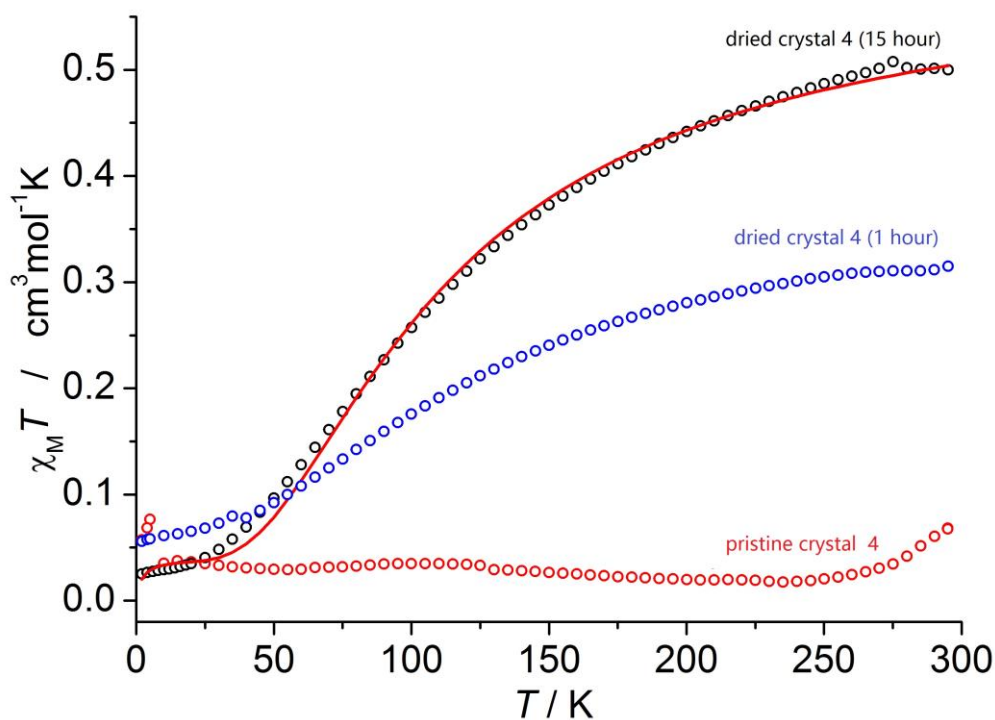


Figure A7: $\chi_M T$ vs. T measurement in the temperature range of 2–295 K at 0.5 T for solid samples of **4** for different sample preparation.

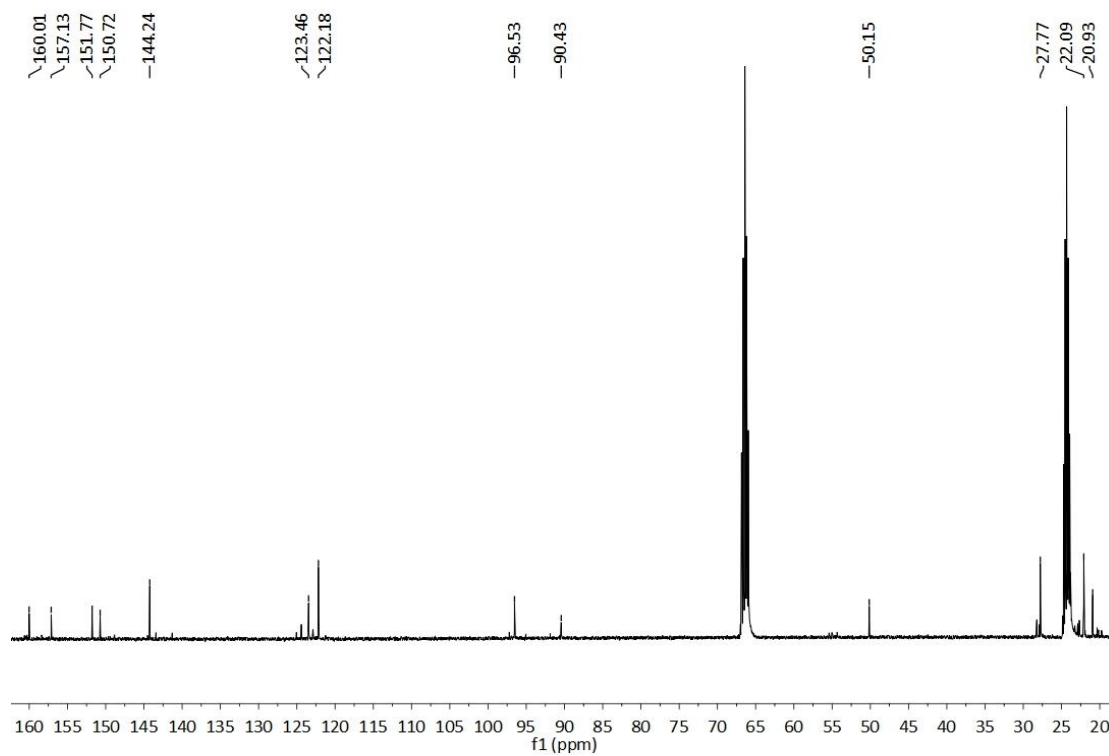


Figure A8: ^{13}C NMR (100 MHz) spectra of **6** in THF- d_8 .

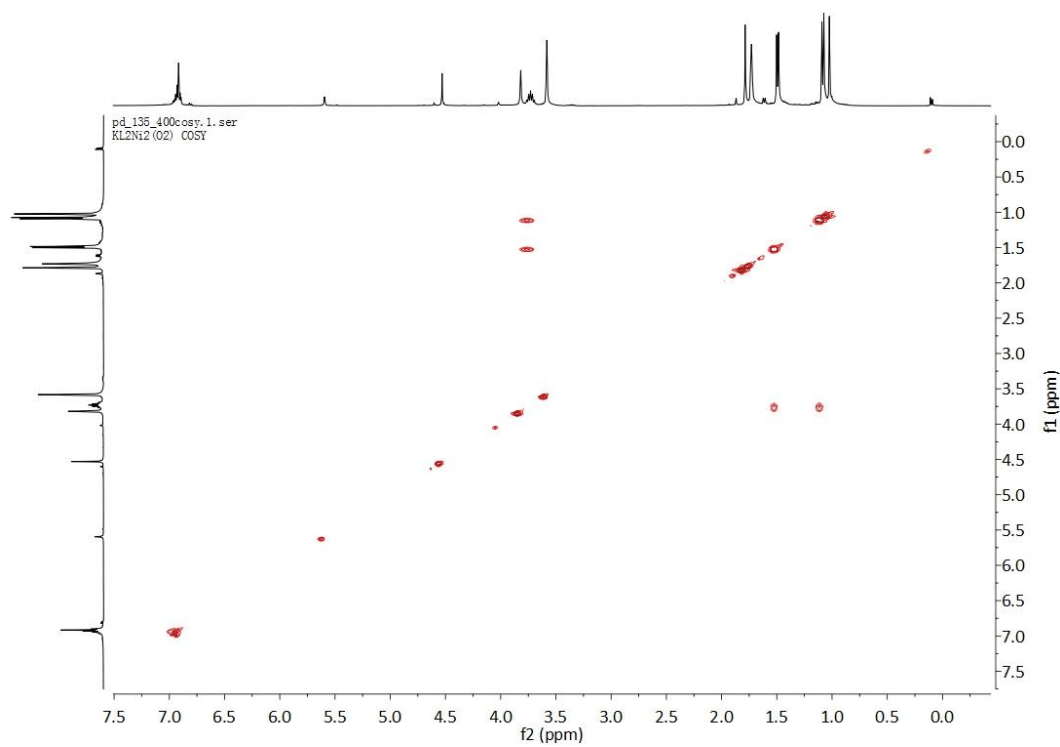


Figure A9: ^1H - ^1H COSY (400 MHz) spectra of **6** in THF- d_8 .

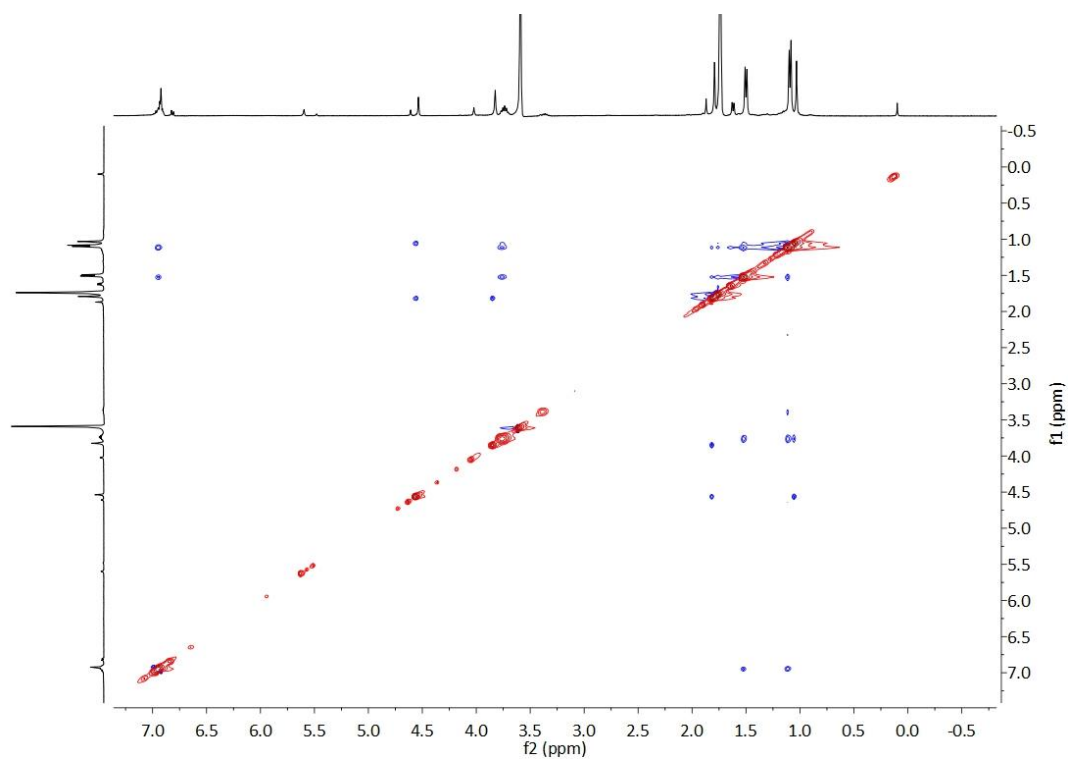


Figure A10: ^1H - ^1H NOSTY (400 MHz) spectra of **6** in THF- d_8 .

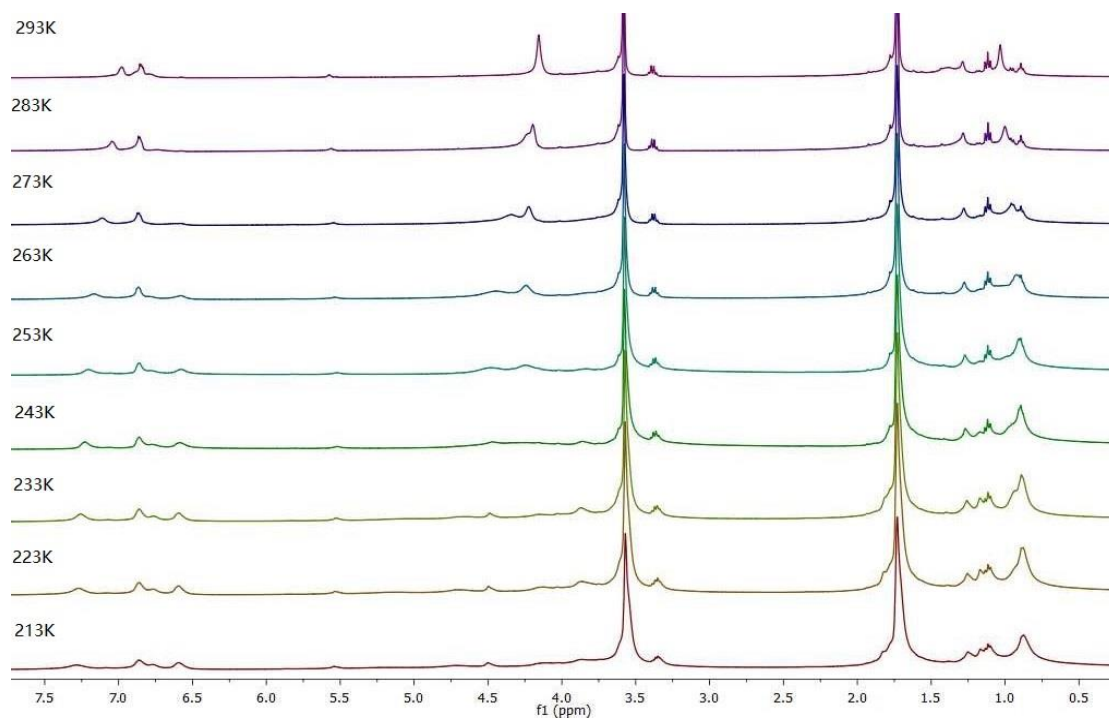


Figure A11: Variable temperatures ^1H NMR (400 MHz) spectrum of **8** in THF- d_8 .

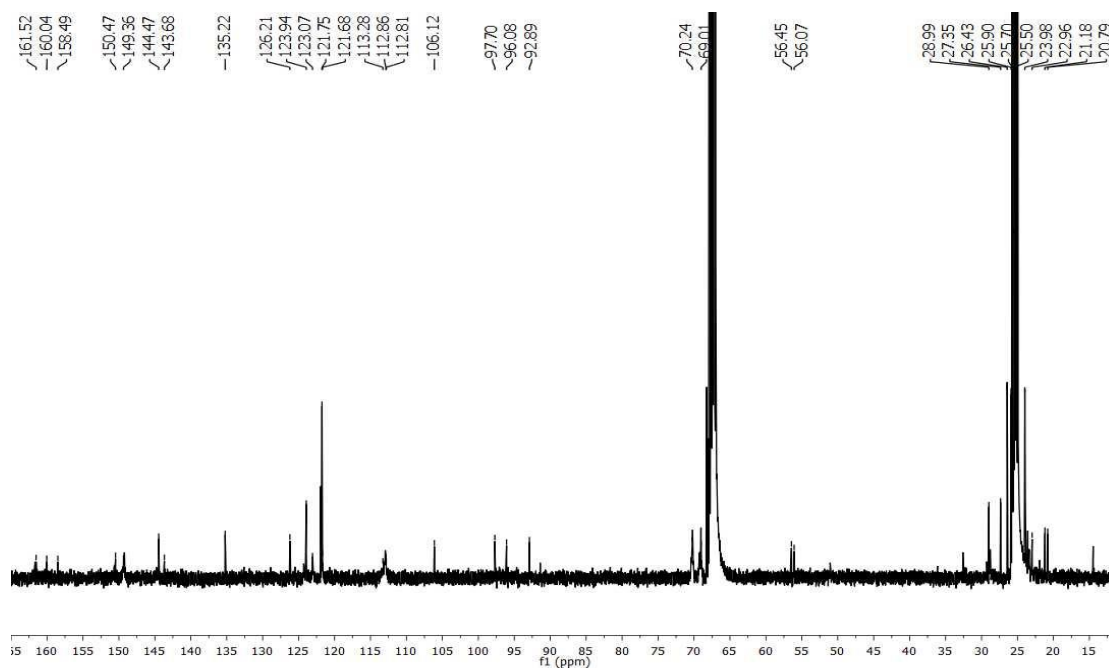


Figure A12: ^{13}C $\{^1\text{H}\}$ NMR (100 MHz) spectrum of **8** in THF- d_8

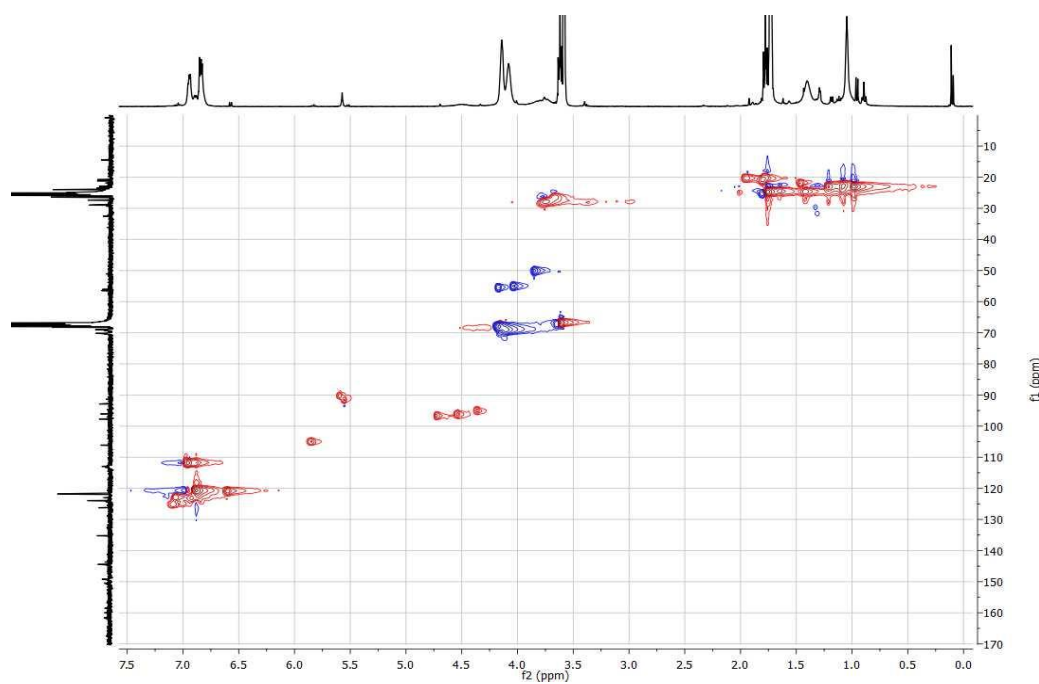


Figure A13: ^1H - ^{13}C HSQC spectrum of **8** in THF- d_8 .

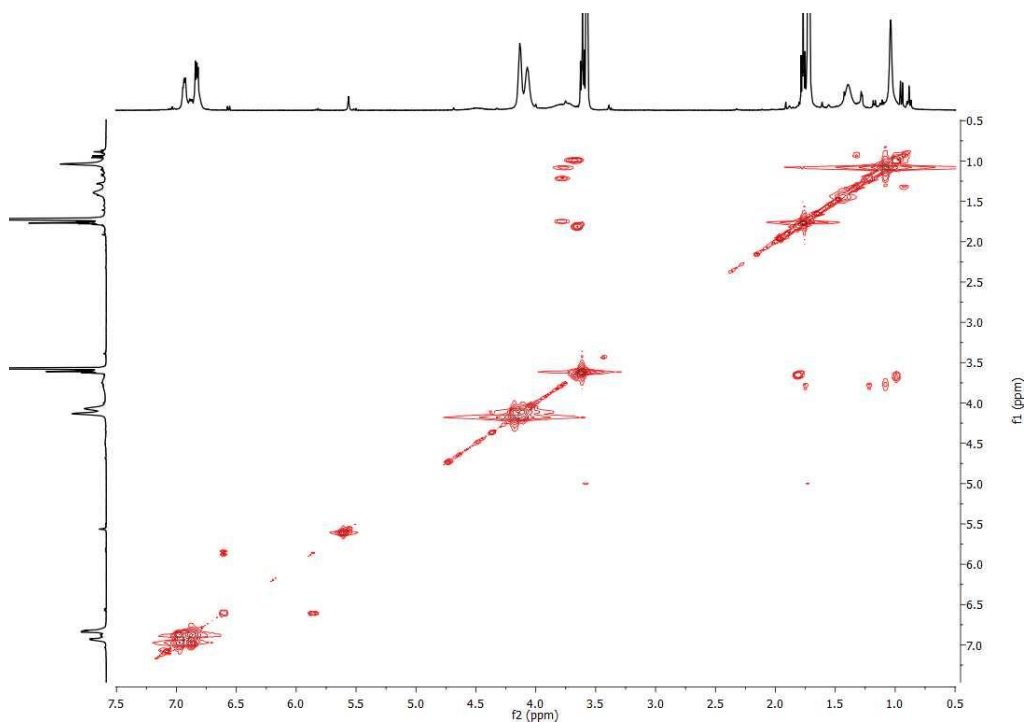


Figure A14: ^1H - ^1H COSY (400 MHz) spectrum of **8** in THF-d_8 .

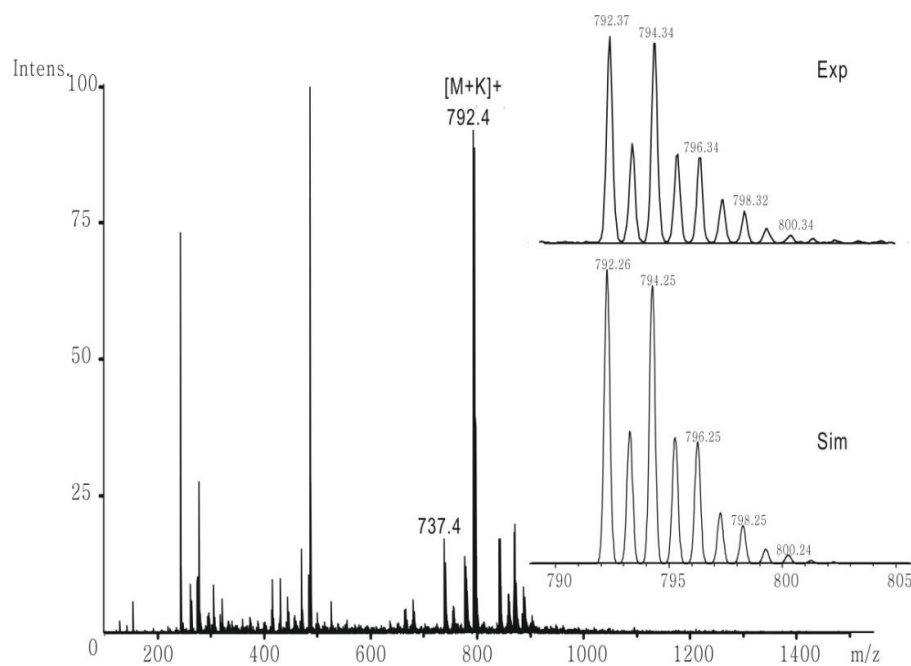


Figure A15: ESI mass spectrum of **9** in THF: 792.6 (100) $[\text{M}+\text{K}]^+$, 776.4 (20) $[\text{M}+\text{Na}]^+$, 754.3(7) $[\text{M}+\text{H}]^+$. The inset shows the experimental (top) and simulated (bottom). Isotopic distribution pattern for $[\text{M}+\text{K}]^+$.

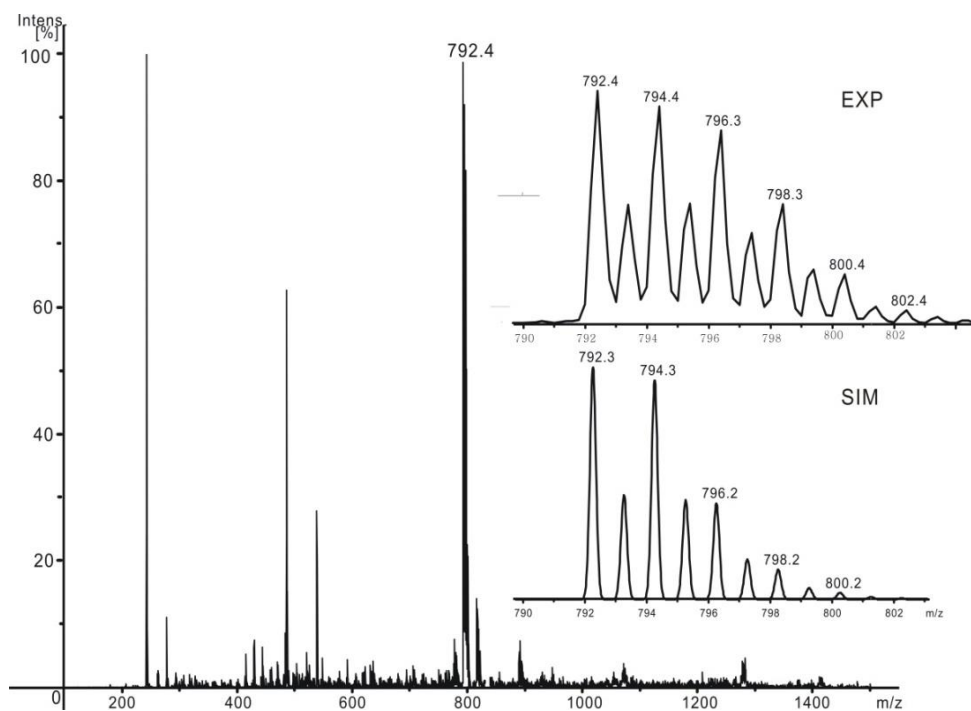


Figure A16: ESI mass spectrum of **9**- $^{18}\text{O}_2$ in THF: 792.6 (100) $[\text{M}+\text{K}]^+\{^{16}\text{O}_2\}$, 796.6 (100) $[\text{M}+\text{K}]^+\{^{18}\text{O}_2\}$. The inset shows the experimental (top) and simulated (bottom) isotopic distribution pattern for $[\text{M}+\text{K}]^+$.

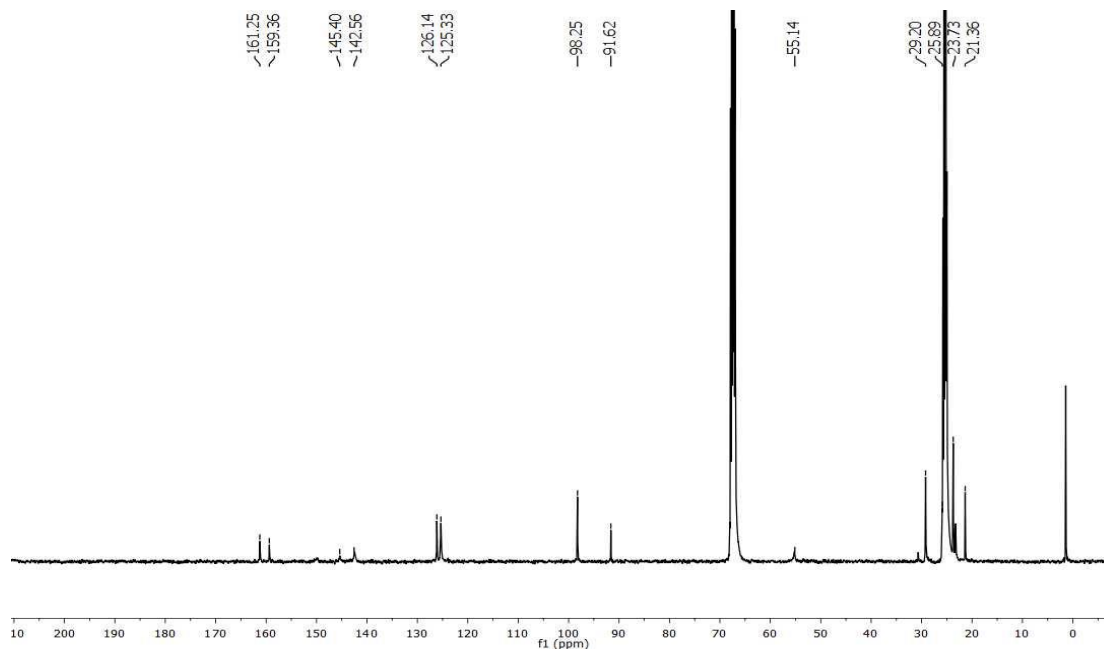


Figure A17. ^{13}C NMR (100 MHz) spectrum of **11** in THF- d_8 .

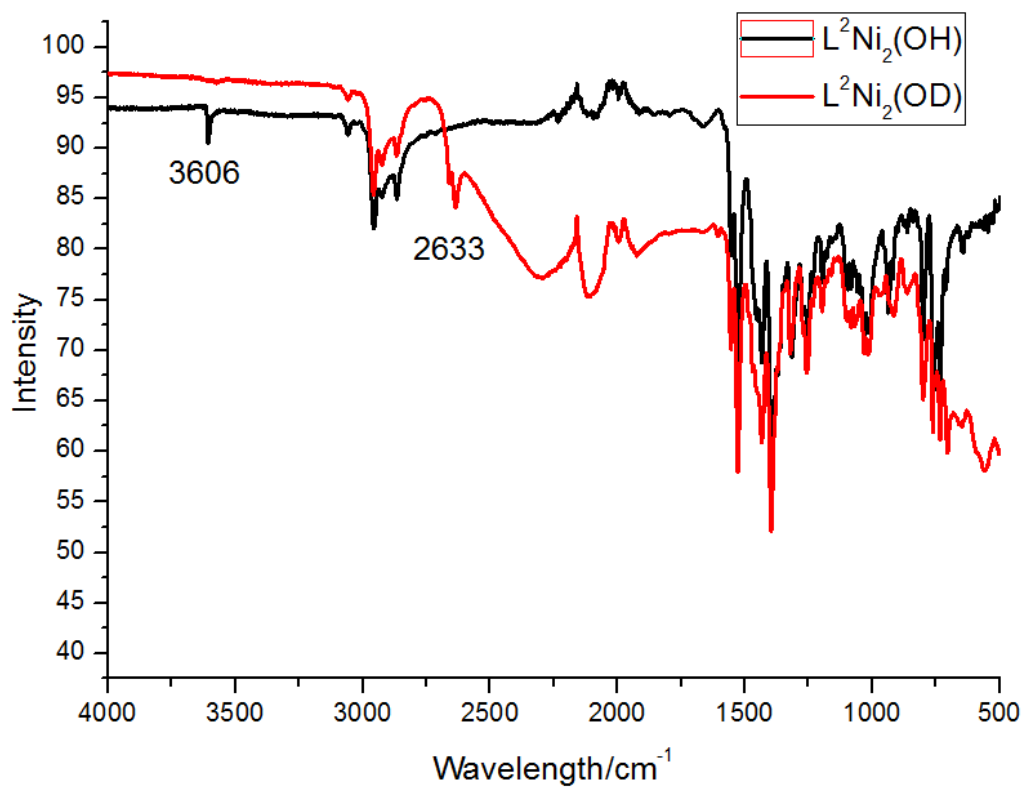


Figure A18: Comparison of the IR spectra of **11** and **11-OD** in solid state.

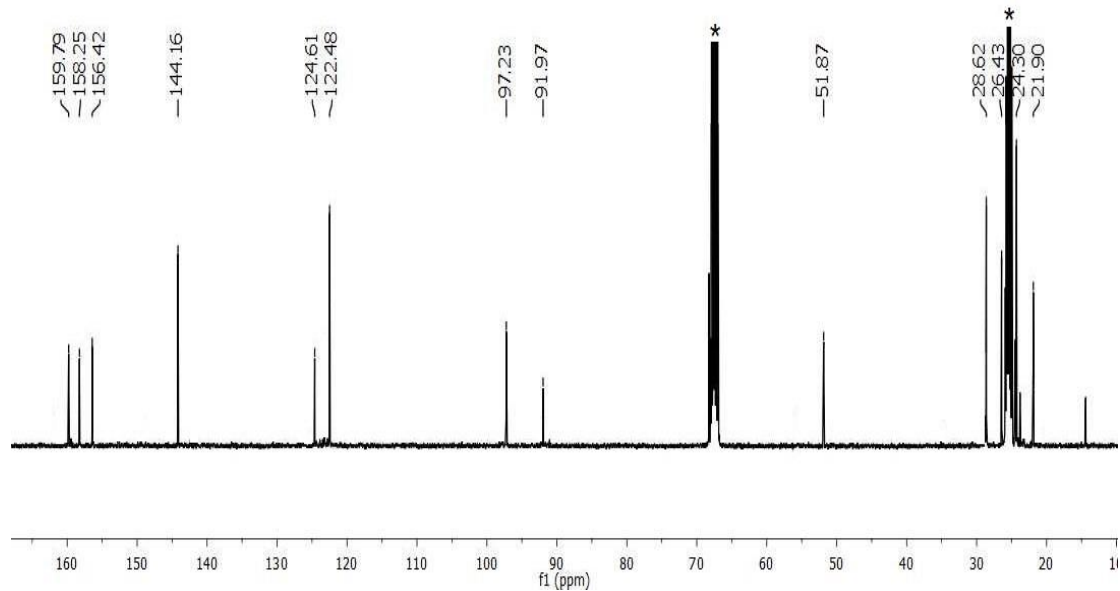


Figure A19: ¹³C NMR (100 MHz) spectrum of **12** in THF-d₈.

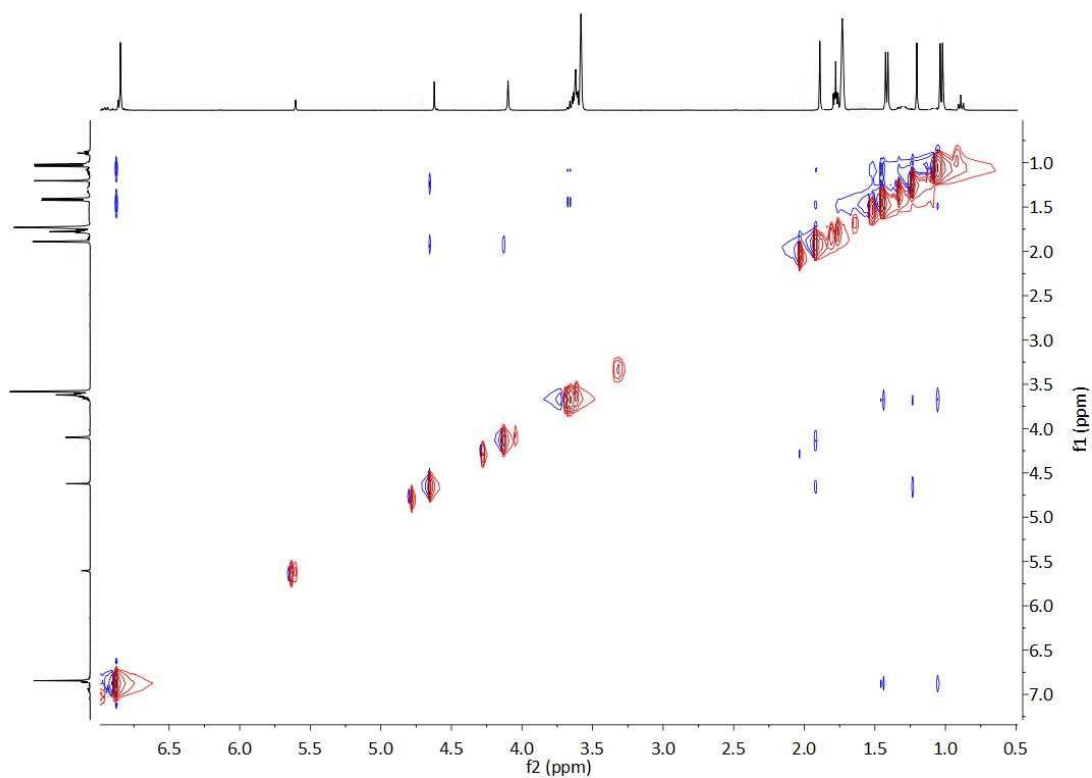


Figure A20: ^1H - ^1H NOSTY (400 MHz) spectrum of **12** in THF-d_8 .

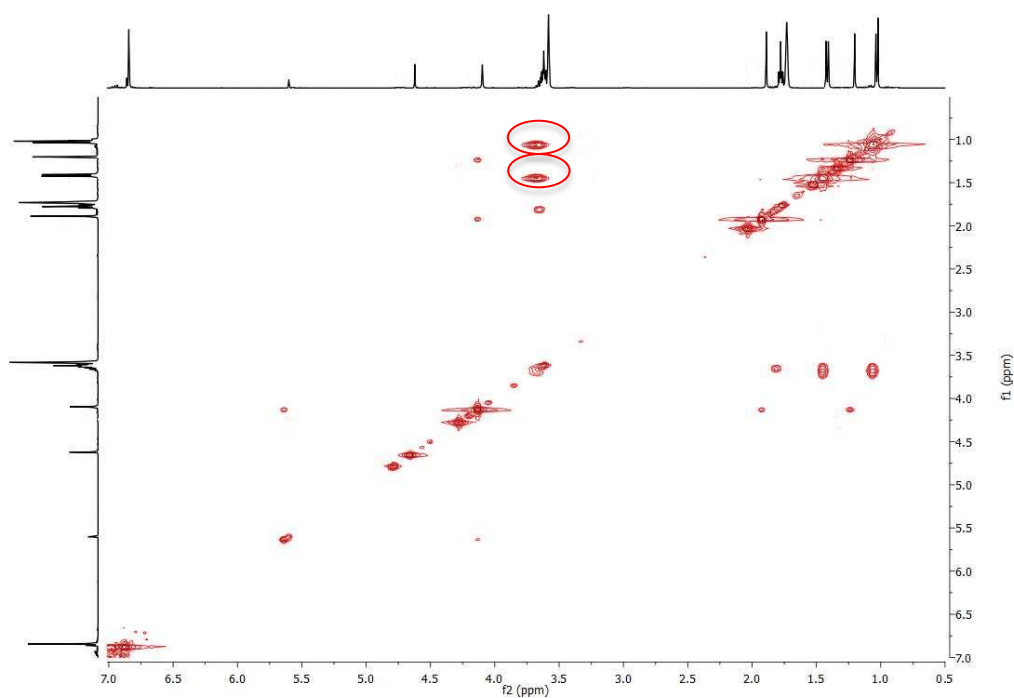


Figure A21: ^1H - ^1H COSY (400 MHz) spectrum of **12** in THF-d_8 . The correlation resonances between the isopropyl CH and CH_3 group are marked.

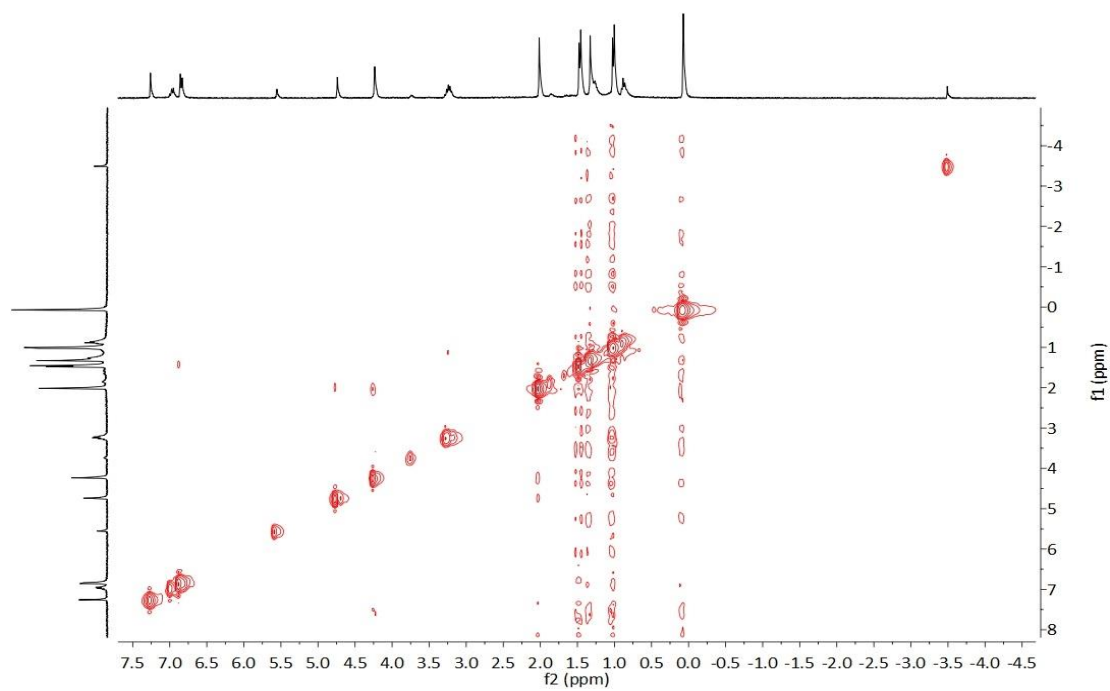


Figure A22: ^1H - ^1H NOESY (300 MHz) spectrum of **13** in CDCl_3

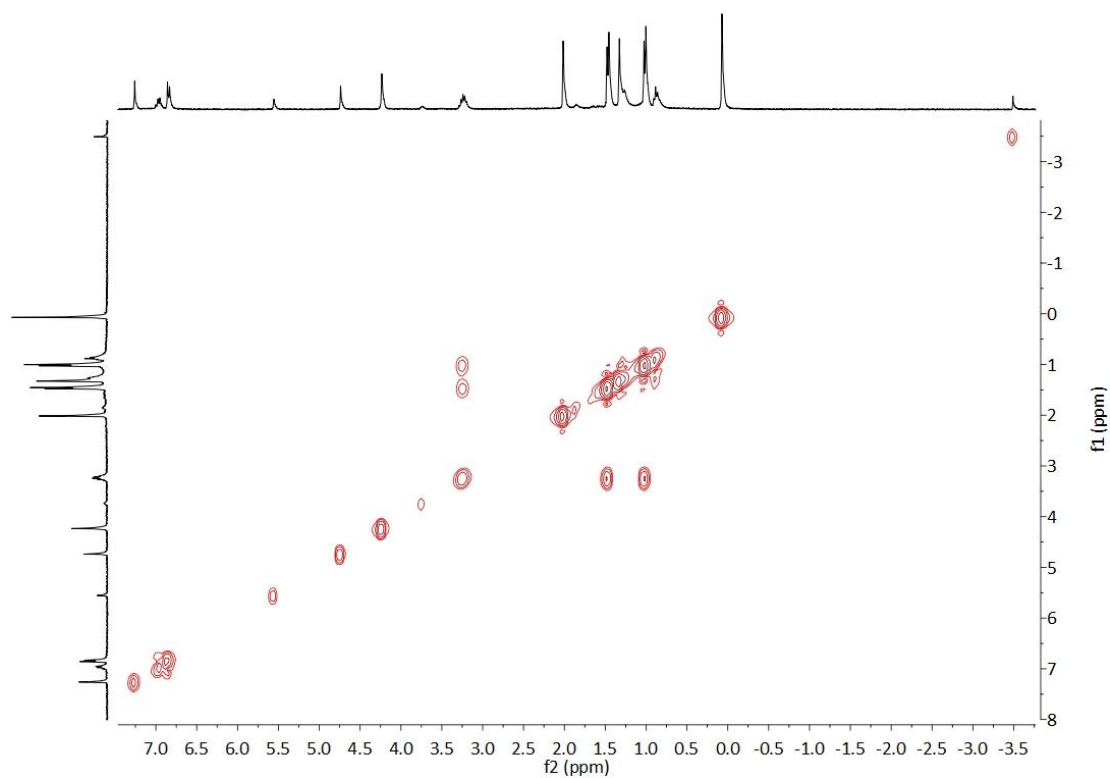


Figure A23: ^1H - ^1H COSY (300 MHz) spectrum of **13** in CDCl_3

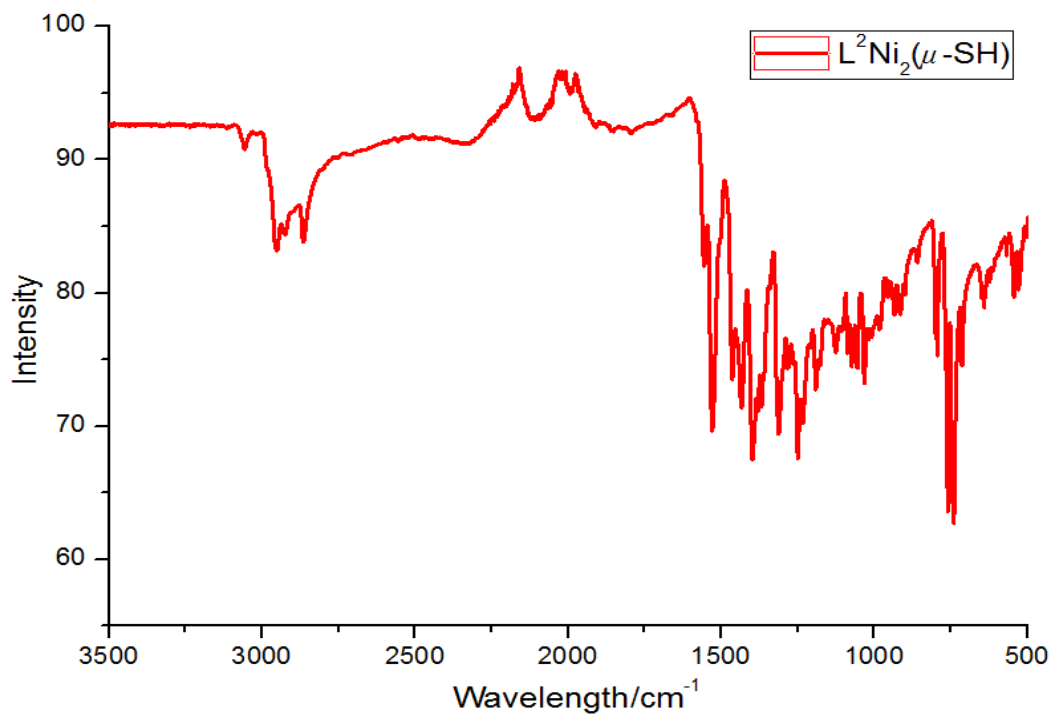


Figure A24: ATR-IR spectrum of **13** in crystalline material.

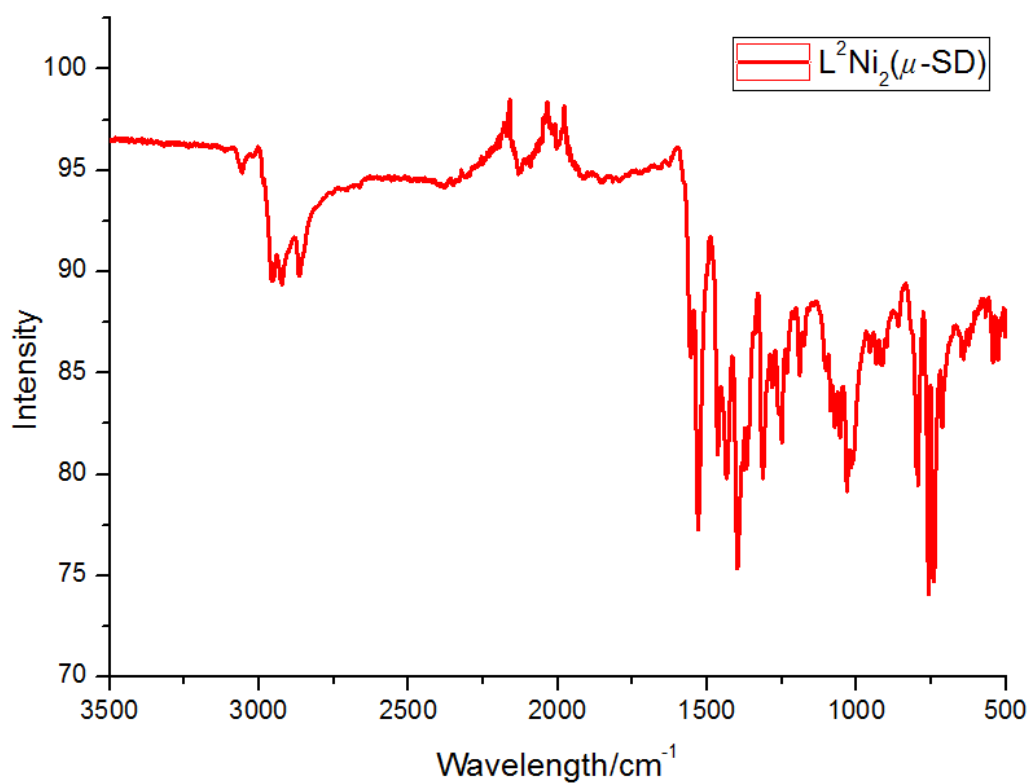


Figure A25: ATR-IR spectrum of **13-SD** in solid state.

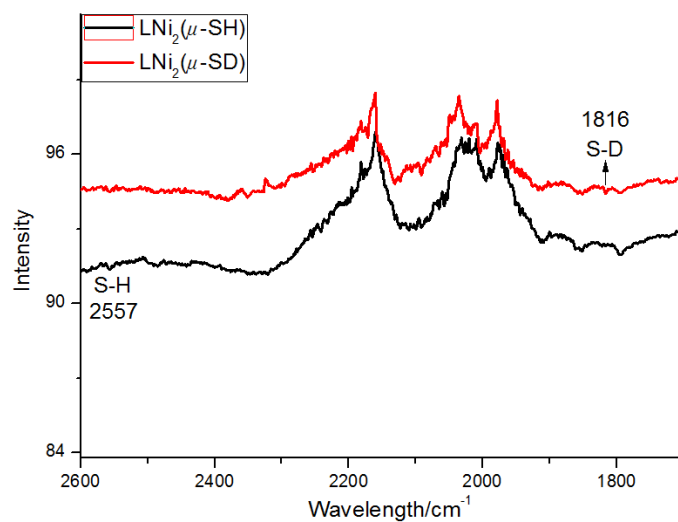


Figure A26: Comparison of the FT-IR spectra of the complex **13** and **13-SD** in the range 2600–1700 cm⁻¹.

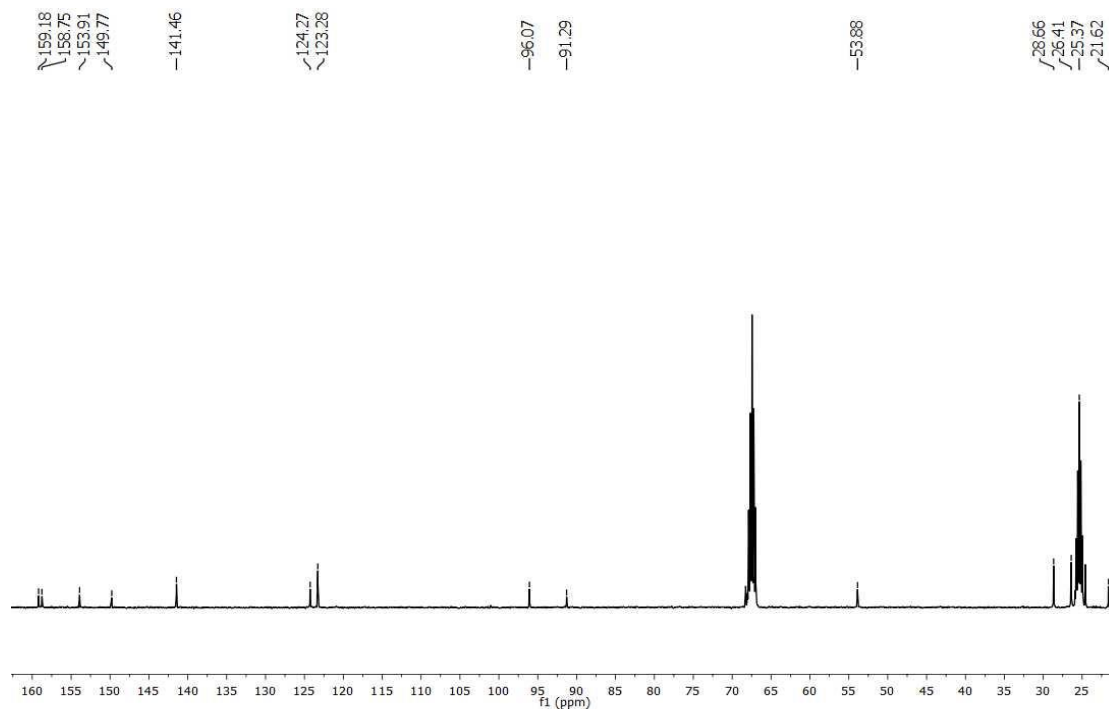


Figure A27: ¹³C NMR (100 MHz) spectrum of **14** in THF-d₈ (400 MHz).

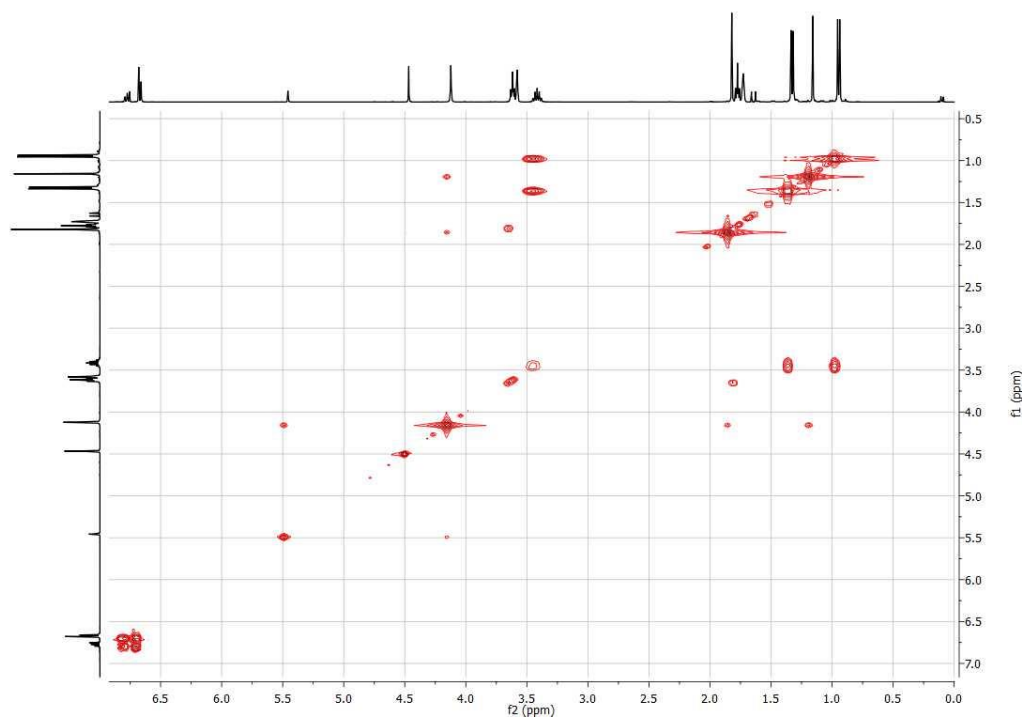


Figure A28: ^1H - ^1H COSY (400 MHz) spectrum of **14** in THF-d_8 .

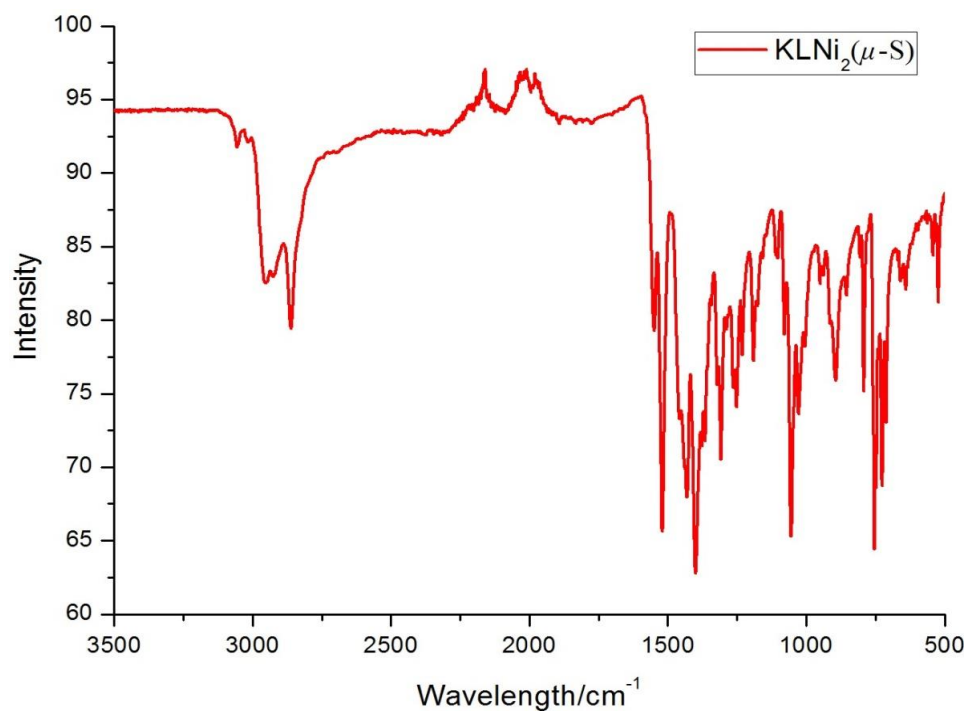


Figure A29: ATR-IR spectrum of **14** in crystalline material.

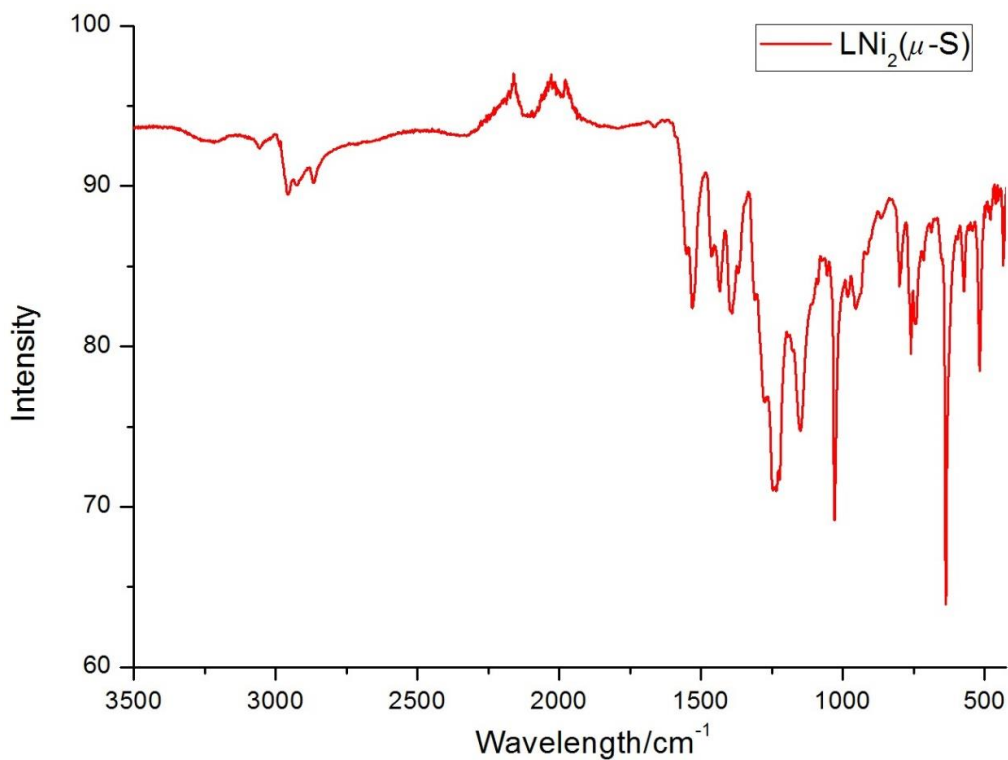


Figure A30: ATR-IR spectrum of **16** in crystalline material.

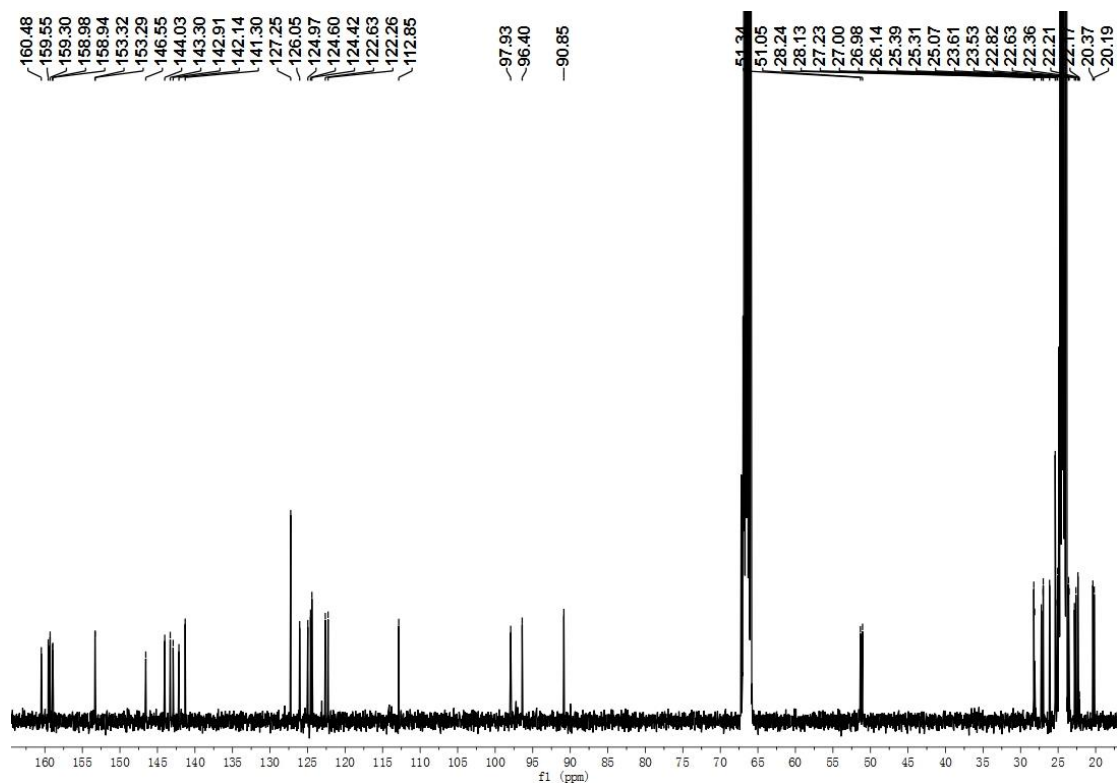


Figure A31: ^{13}C NMR (100 MHz) spectra of **17** in THF-d_8 .

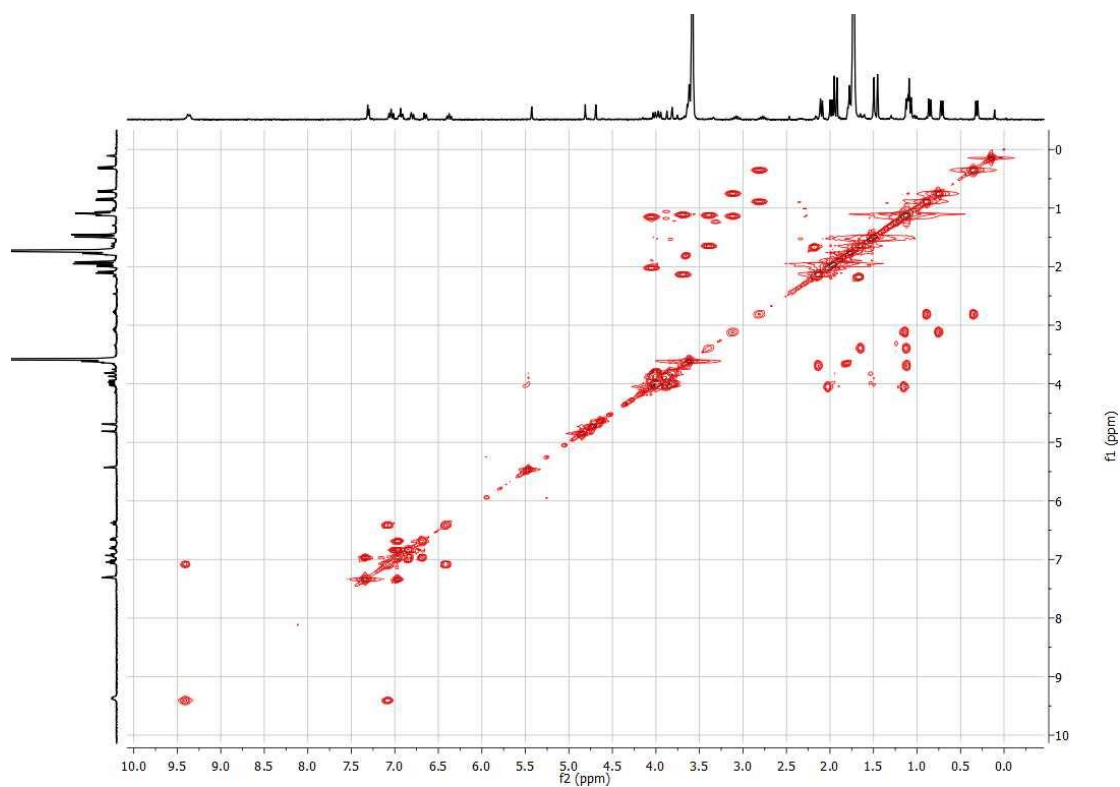


Figure A32: ^1H - ^1H COSY spectrum of spectra of **17** in THF-d_8 .

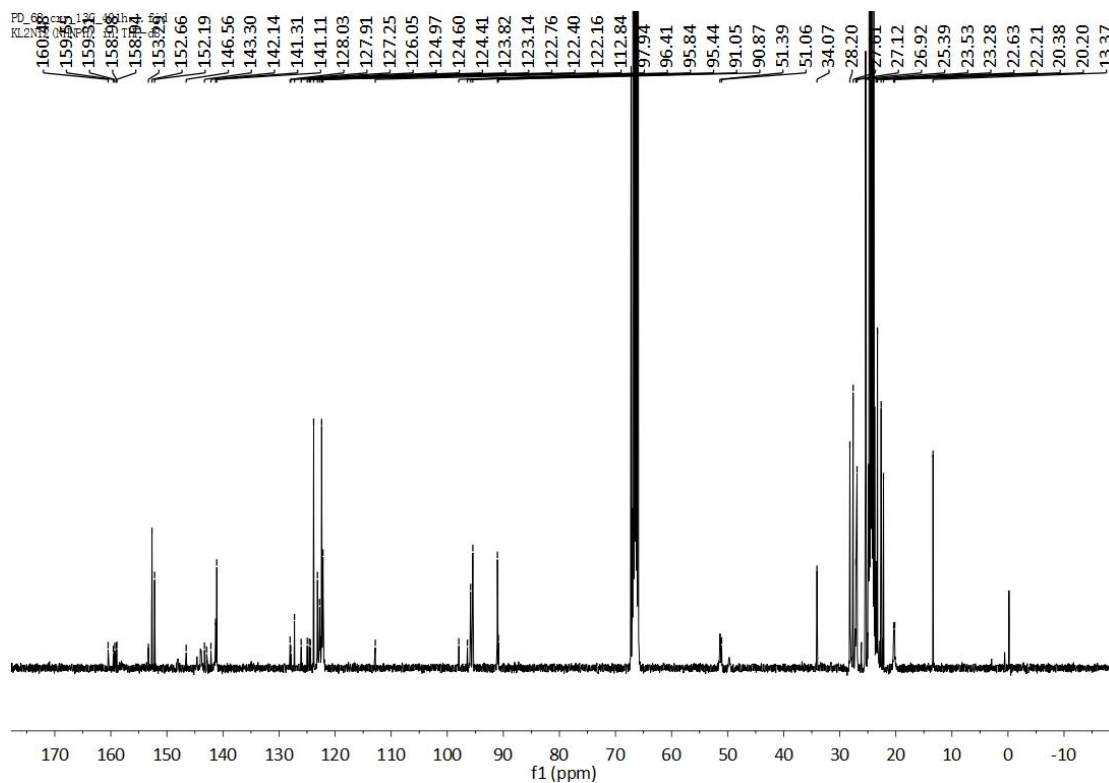


Figure A33: ^{13}C NMR (100 MHz) spectra of **18** in THF-d_8 .

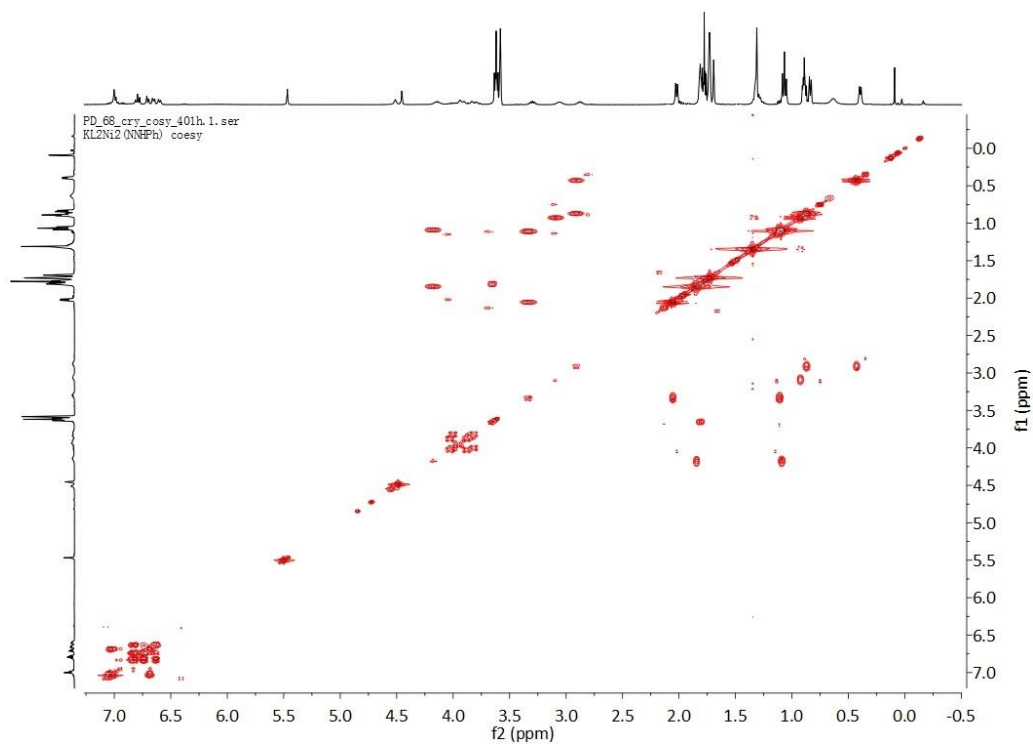


Figure A34: ^1H - ^1H COESY (400 MHz) spectra of **18** in THF- d_8 .

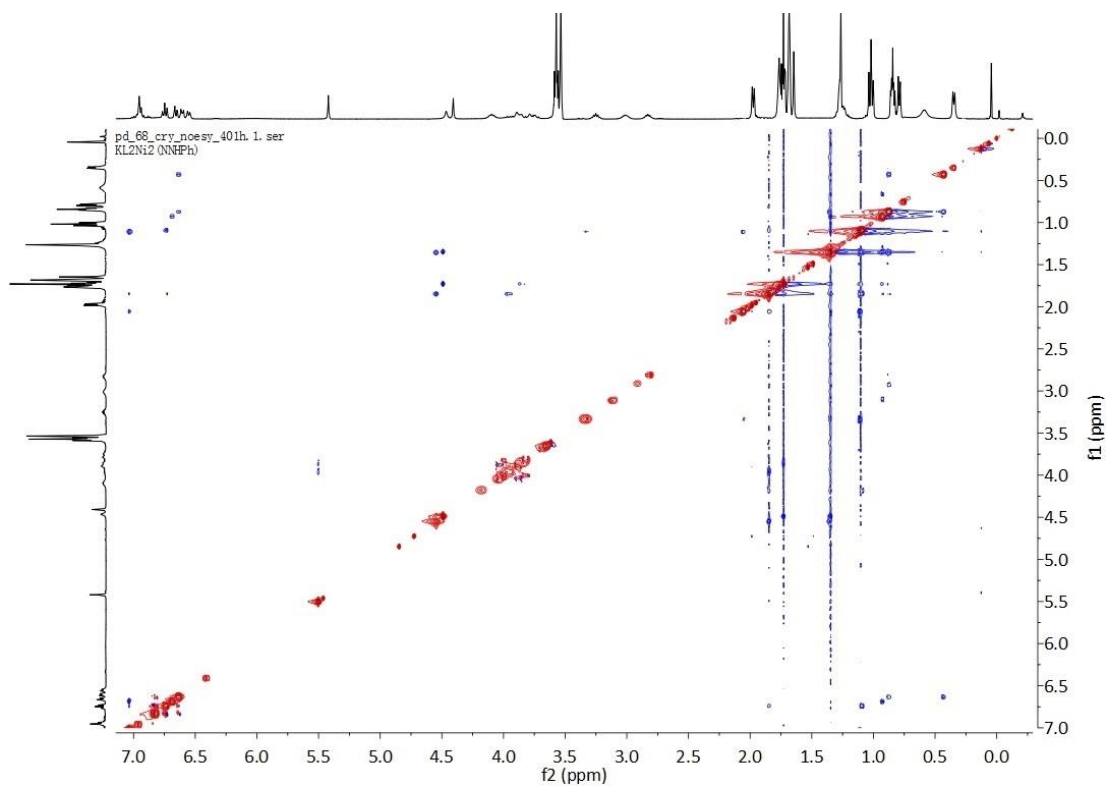


Figure A35: ^1H - ^1H NOESY (400 MHz) spectra of **18** in THF- d_8 .

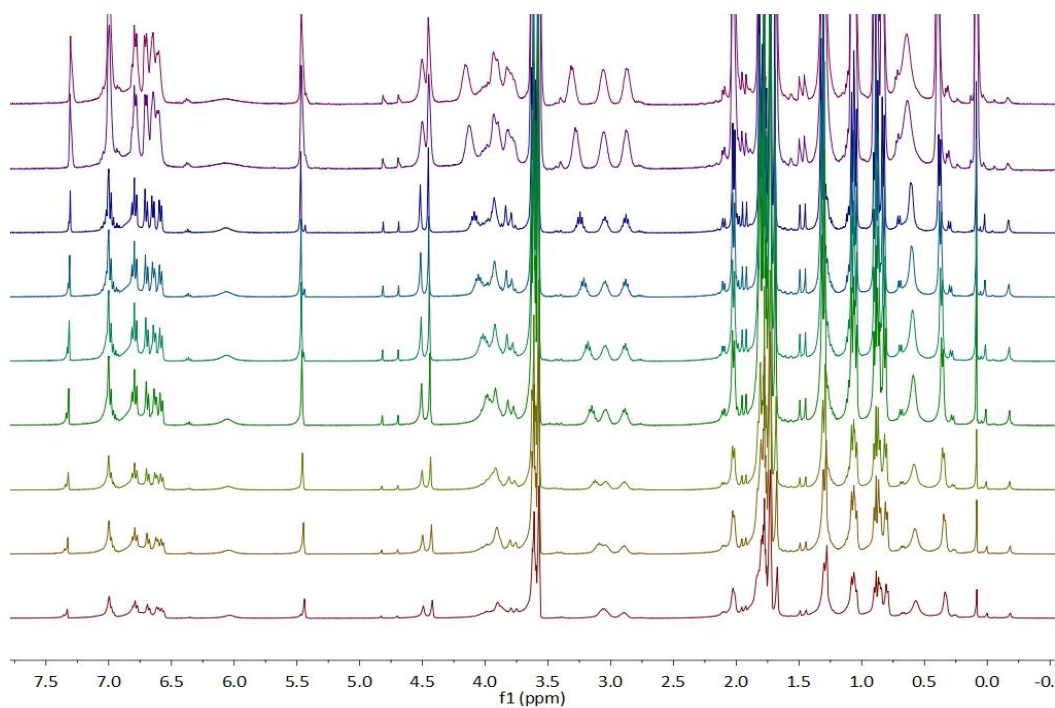


Figure A36: VT ^1H NMR (400 MHz) spectra of **18** in the range of 0-7.5 ppm in THF-d_8 .

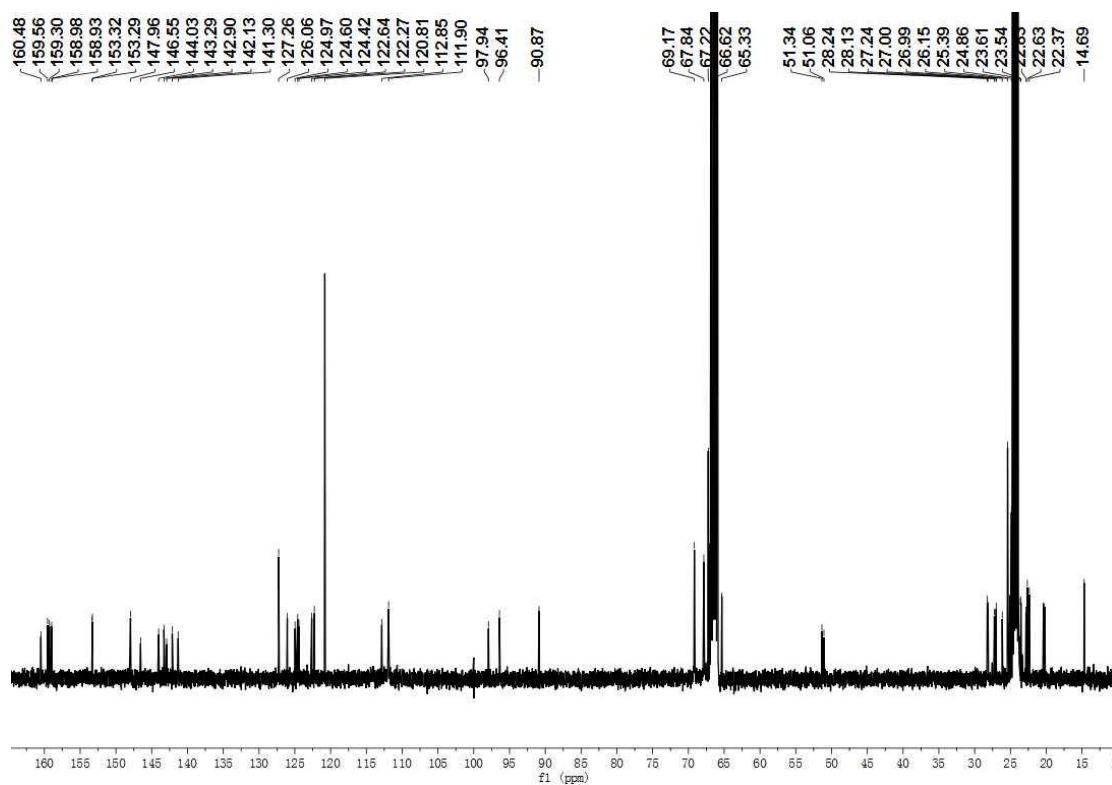


Figure A37: ^{13}C NMR (100 MHz) spectrum of **19** in THF-d_8 .

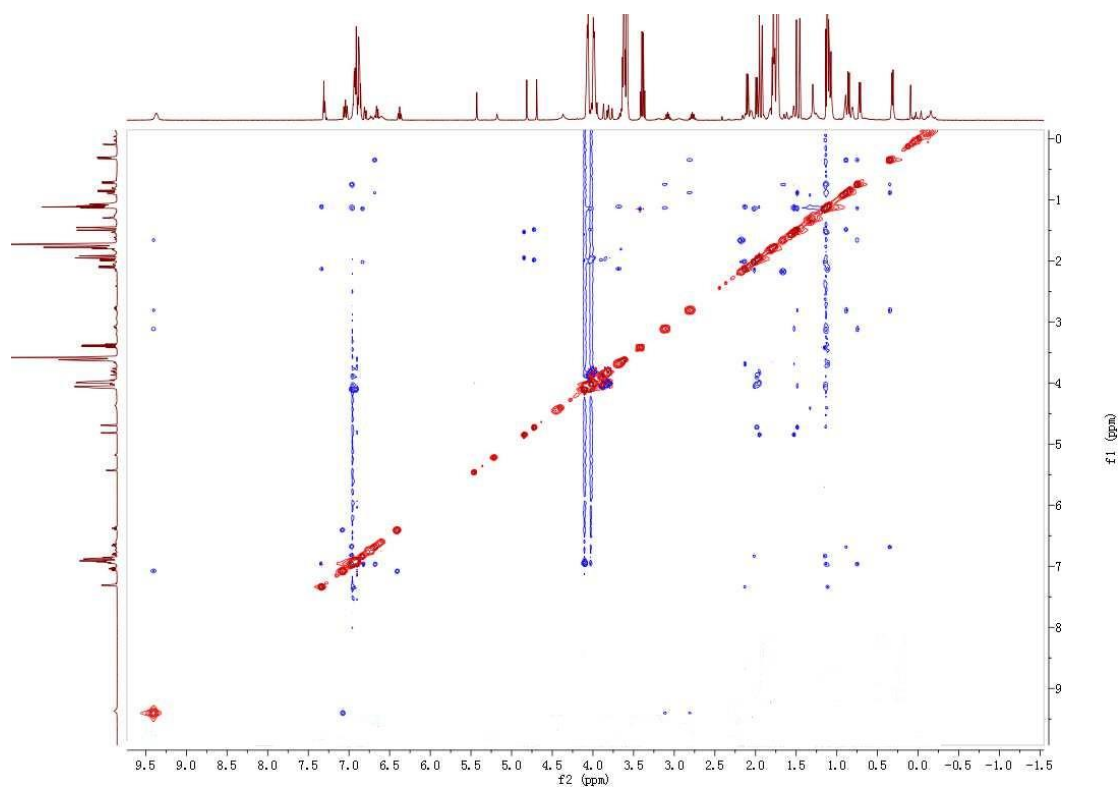


Figure A38: ^1H - ^1H NOESY (400 MHz) spectrum of **19** in THF- d_8 .

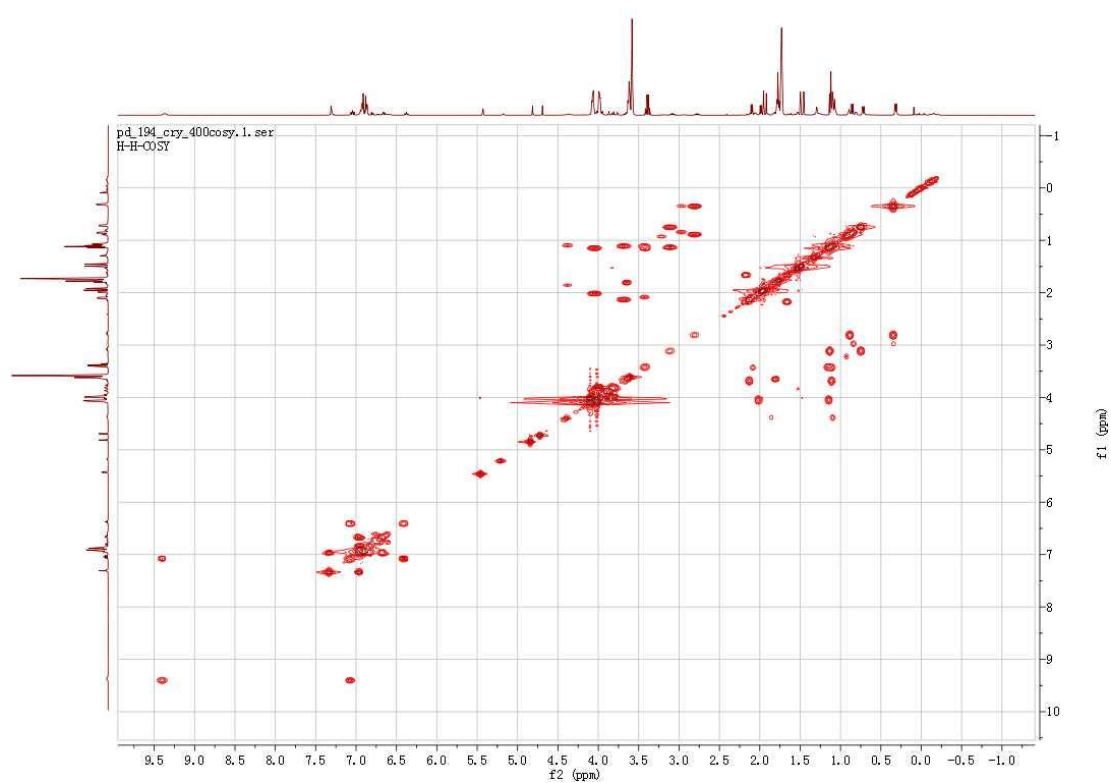


Figure A39: ^1H - ^1H COSY (400 MHz) spectrum of **19** in THF- d_8 .

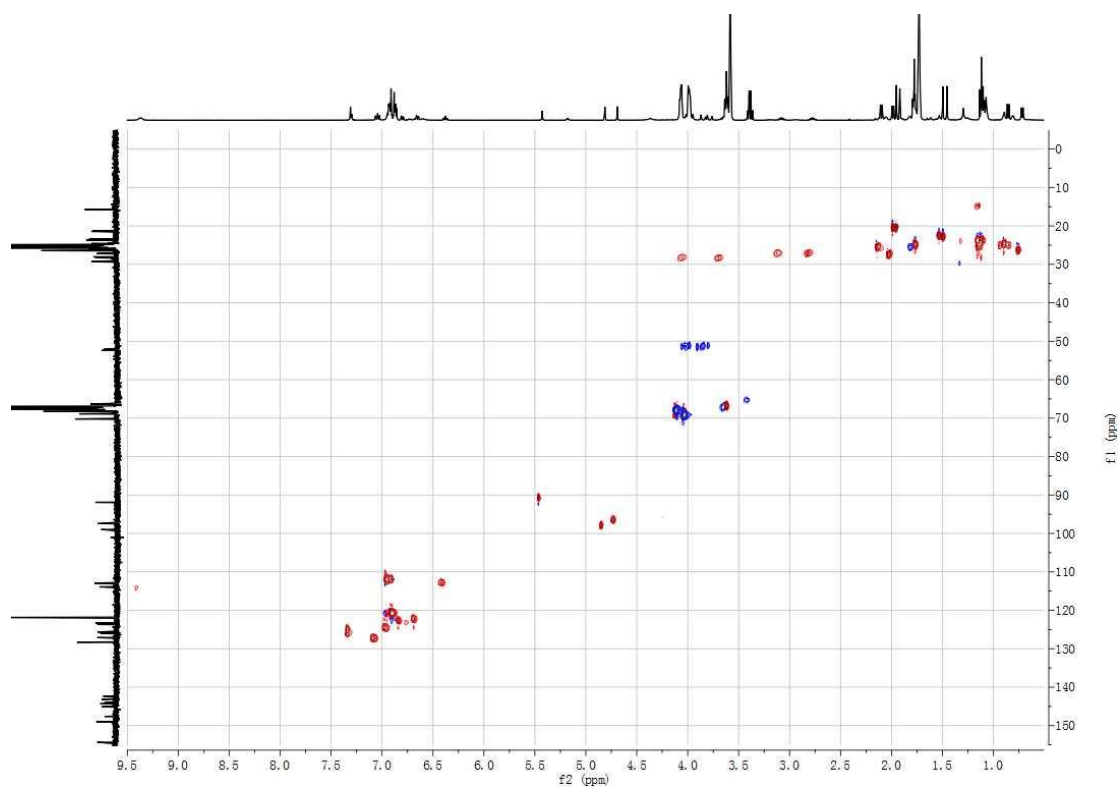


Figure A40: ^1H - ^{13}C HSQC spectrum of **19** in THF-d_8 .

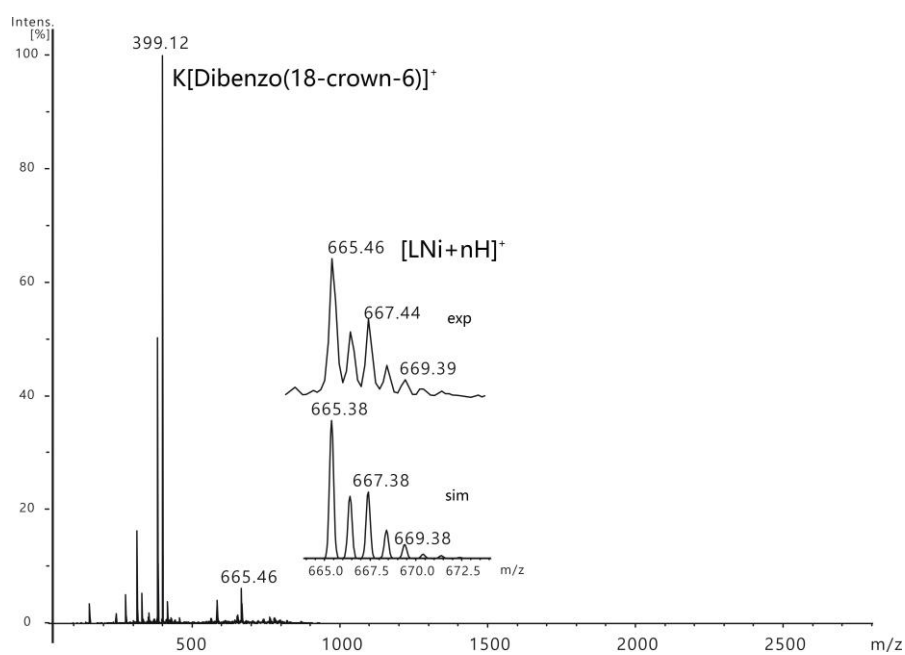


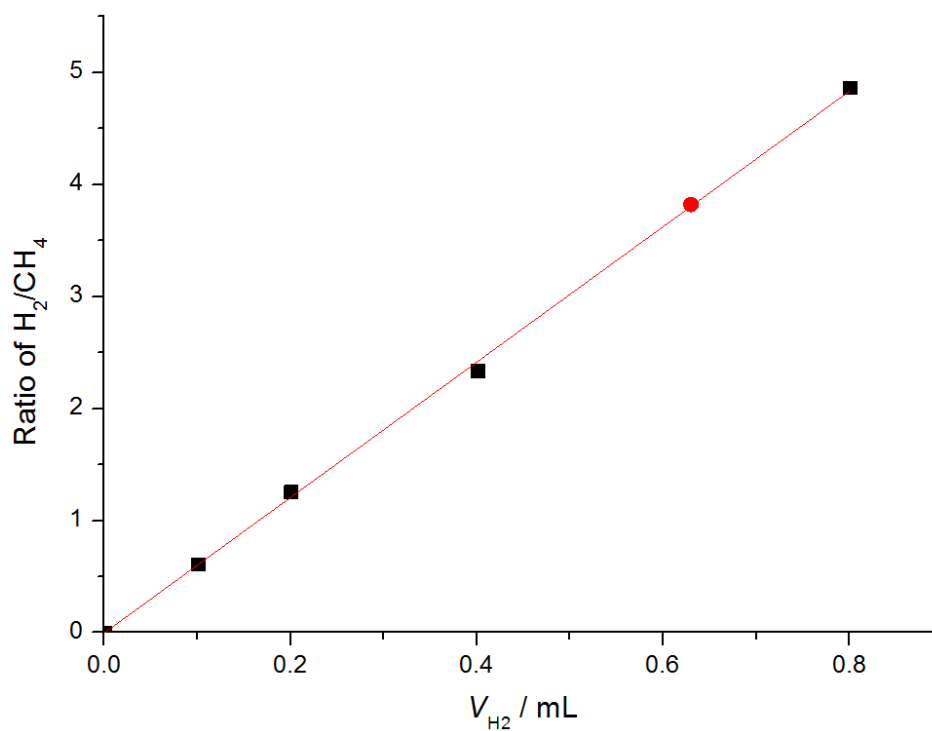
Figure A41: ESI-MS (+) of **19**: (inset) experiment (upper) and simulated (lower) isotopic distribution pattern for the peak pattern around $m/z = 665.46$ characteristic for the $[\text{L}^1\text{Ni}+2\text{H}]^+$.

Table A1: GC-calibration plot data.

V_{H_2} / mL	Intergration of H_2 peak	Intergration of CH_4 peak	Integration ratio of $\text{H}_2:\text{CH}_4$
0.1	6588	10811	0.609
0.2	16539	13161	1.257
0.4	28232	12081	2.337
0.8	46748	9613	4.863

Table A2: Hydrogen detection data.

2 / mmol	H_2 Detected (mL)	Yield
0.02	~ 0.63 (0.674)	140.3 %

**Figure A42:** Hydrogen detection data for synthesis of **24**.

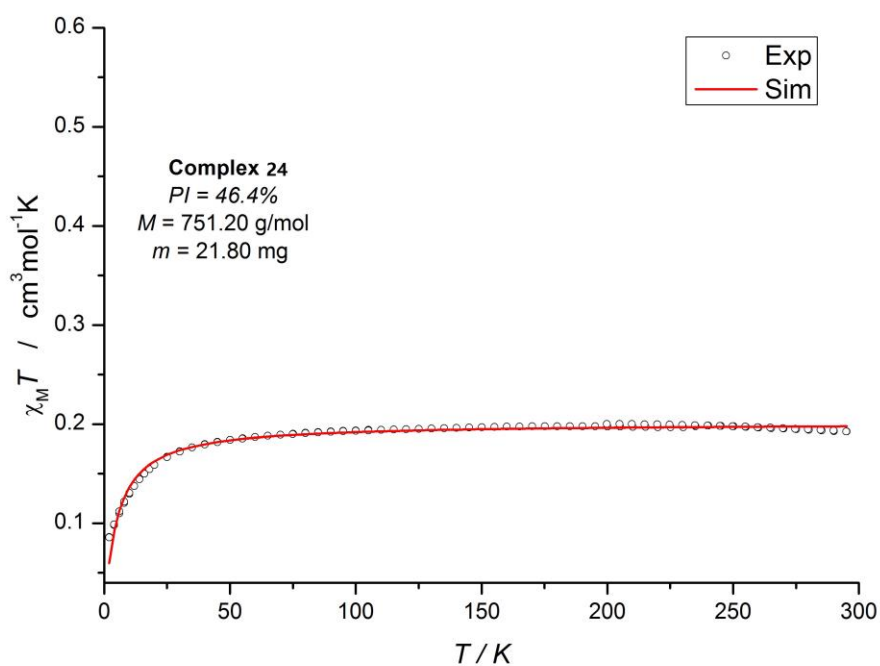


Figure A43: $\chi_m T$ vs. T measurement in the temperature range of 2–295 K at 0.5 T for solid samples of **24**.

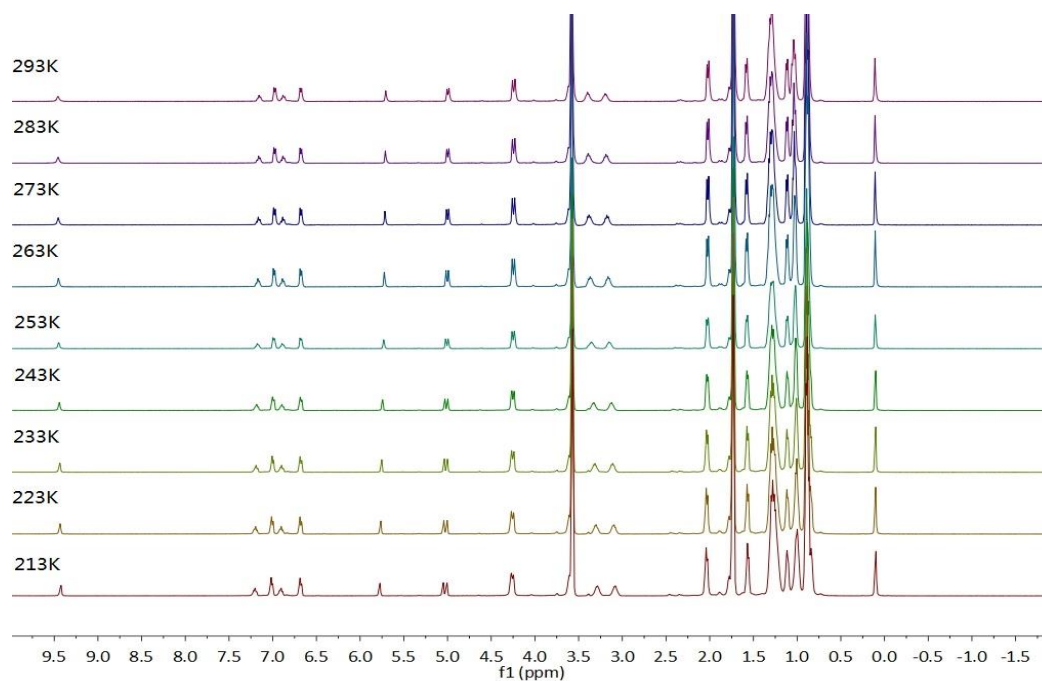


Figure A44: VT ^1H NMR (400 MHz) spectrum of **25** in THF- d_8 .

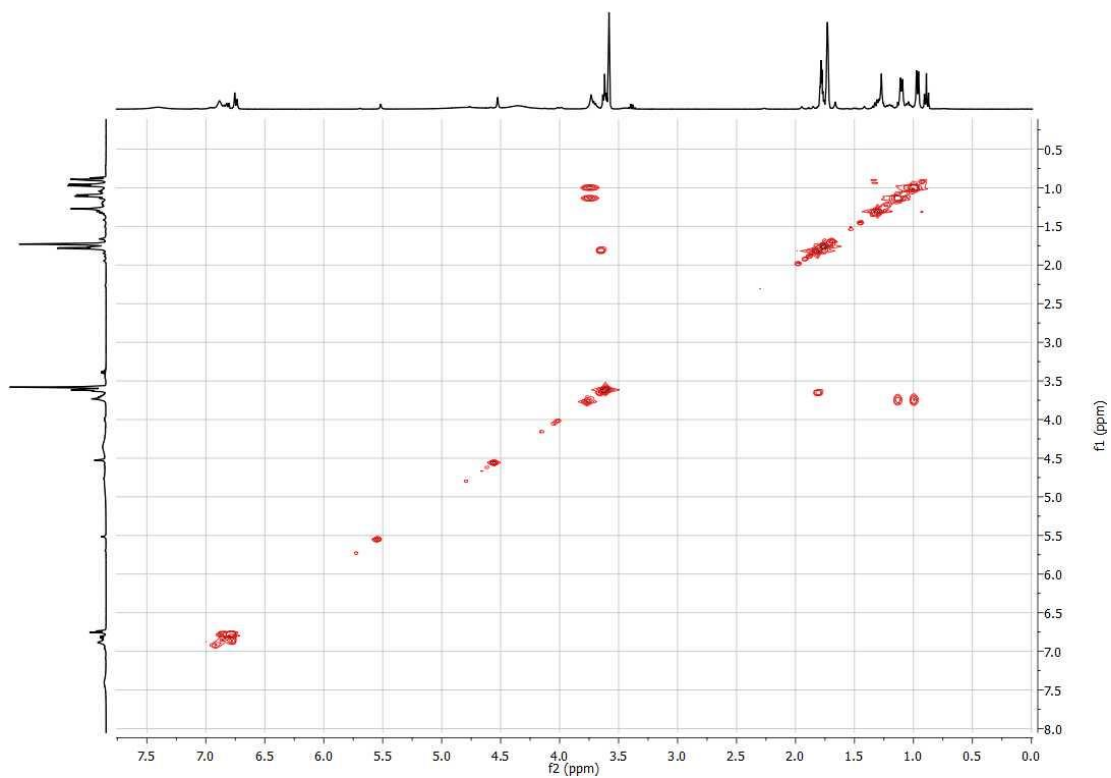


Figure A45: ¹H-¹H COSY (400 MHz) spectra of **30** in THF-d₈.

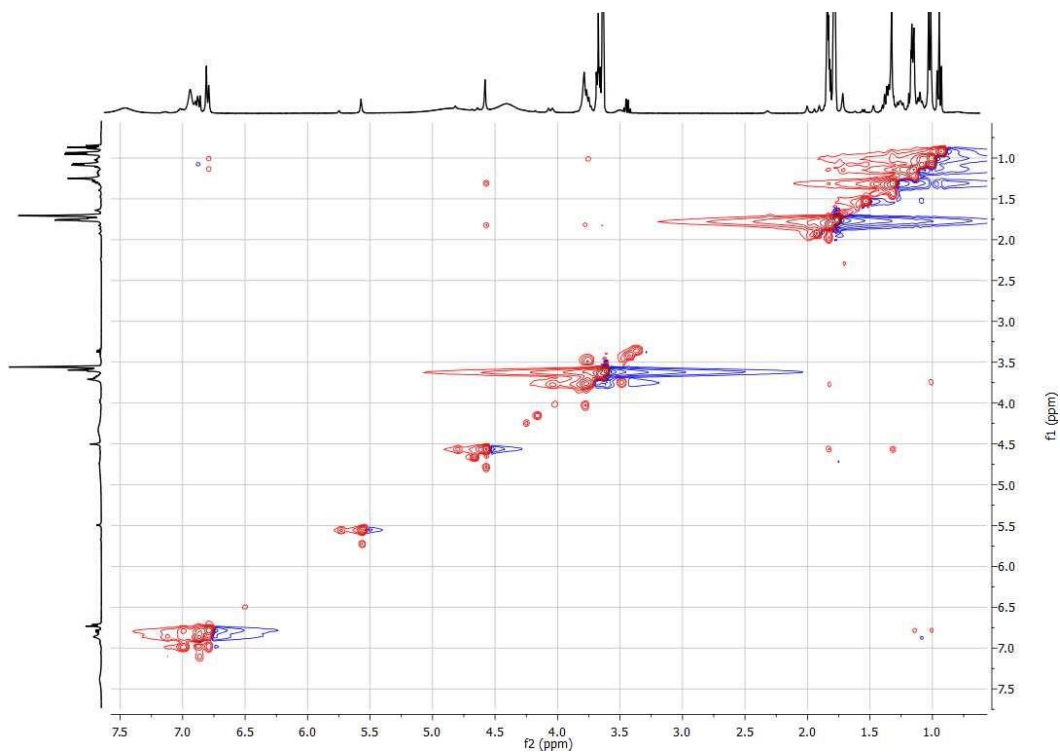


Figure A46: ¹H-¹H NOESY (400 MHz) spectrum of **30** in THF-d₈.

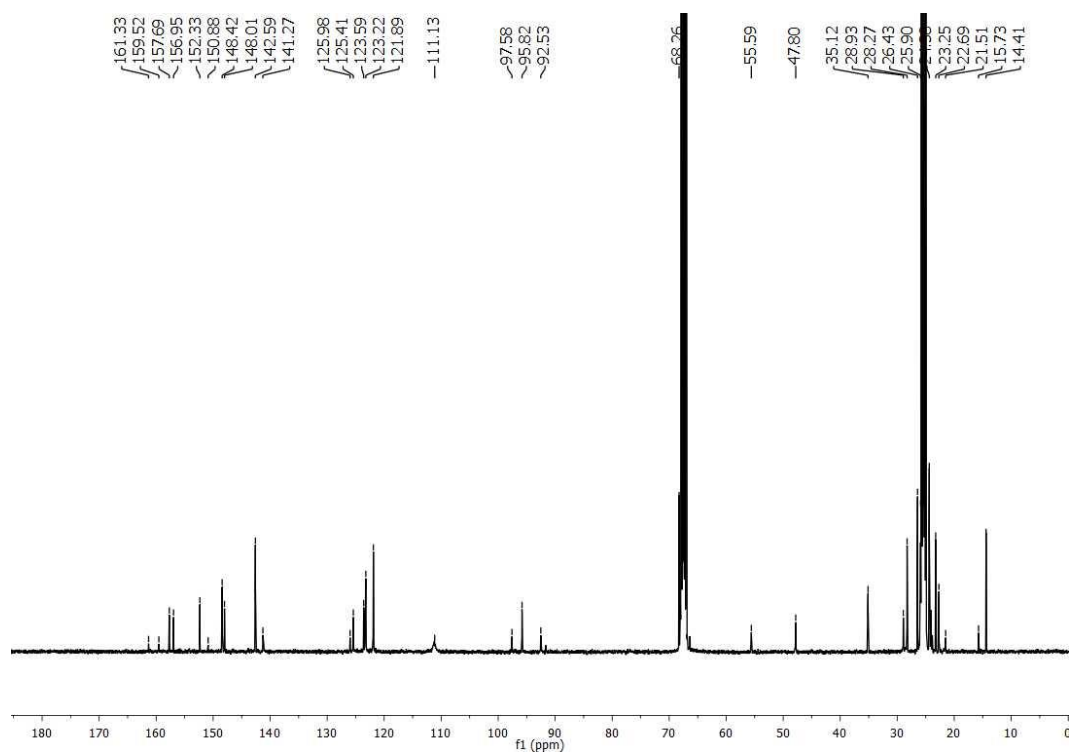


Figure A47: ^{13}C $\{^1\text{H}\}$ NMR (100 MHz) spectrum of **30** in THF- d_8 .

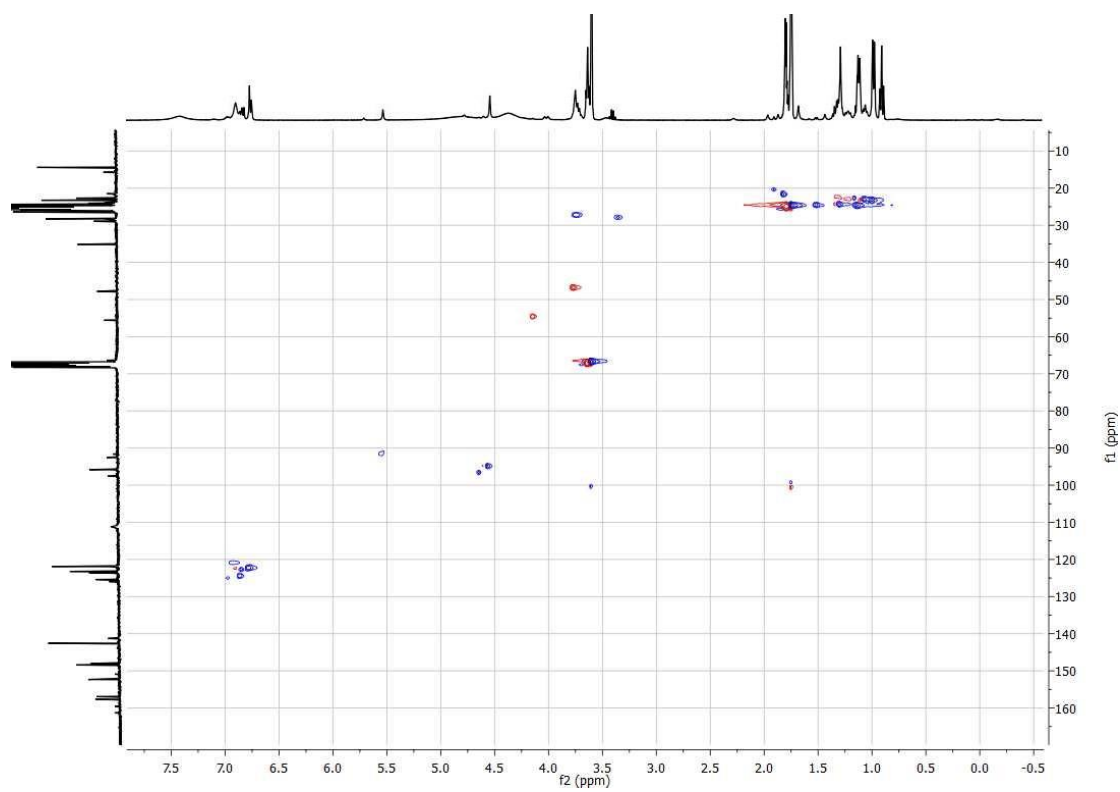


Figure A48: ^1H - ^{13}C HSQC spectrum of **30** in THF- d_8 .

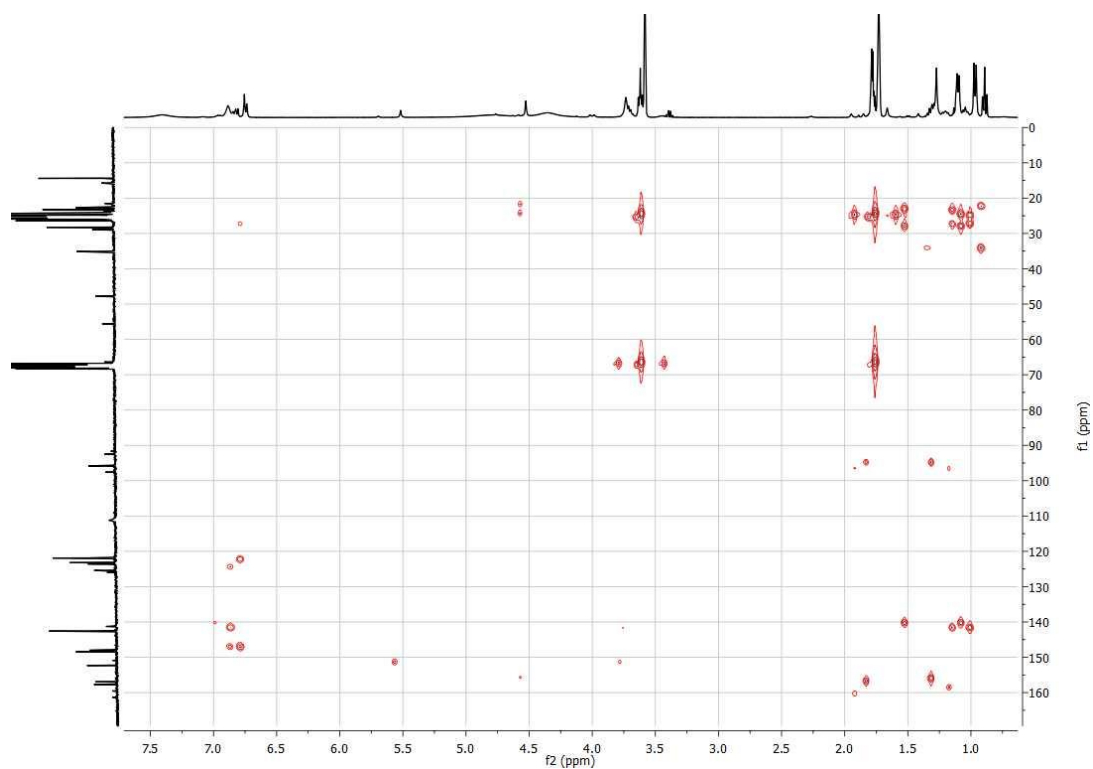


Figure A49: ^1H - ^{13}C HMBC spectrum of **30** in THF-d_8 .

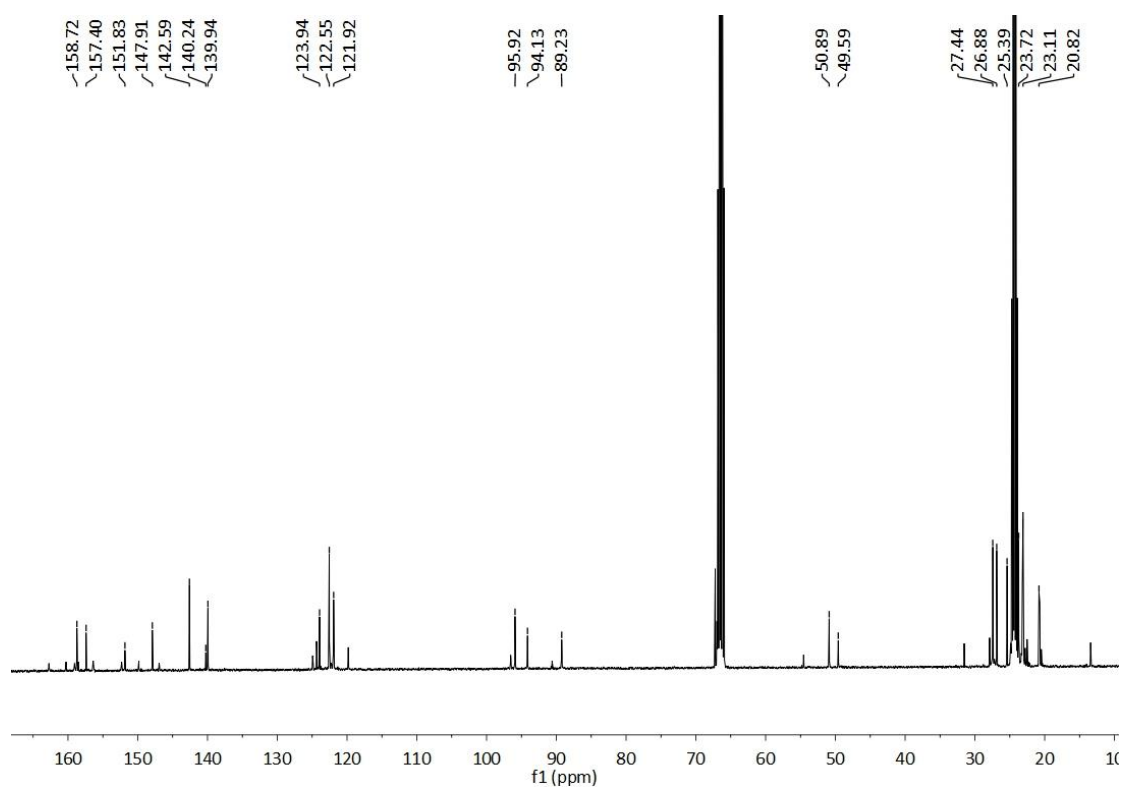


Figure A50: ^{13}C $\{^1\text{H}\}$ NMR (100 MHz) spectra of **32** in THF-d_8 .

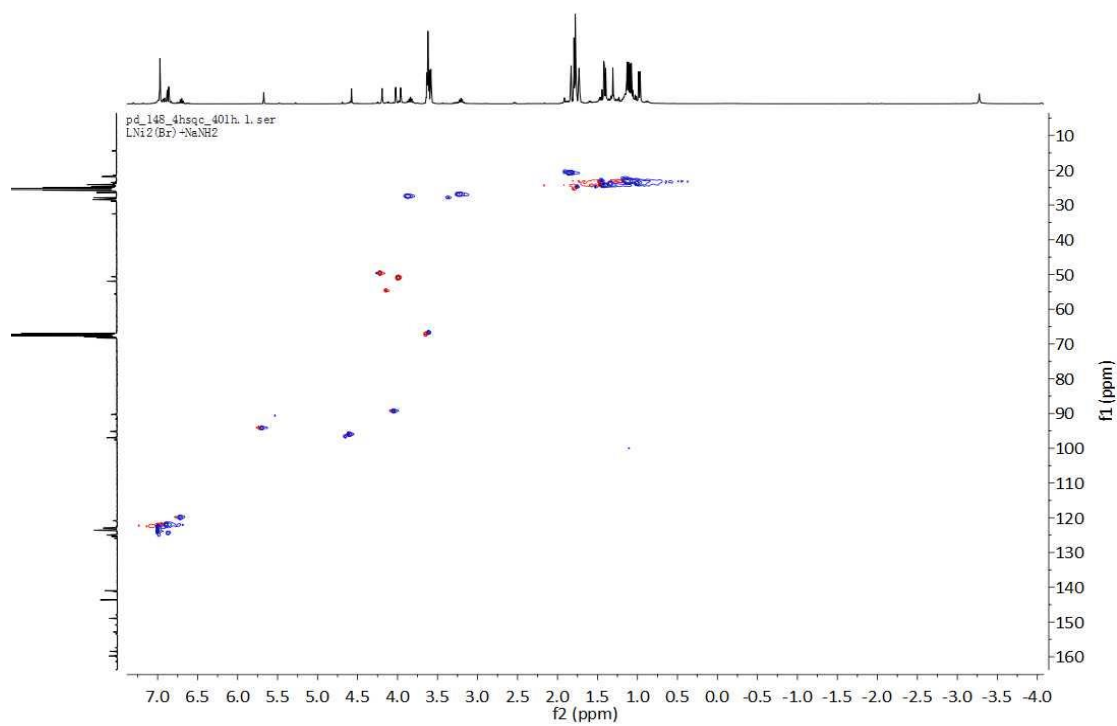


Figure A51: ^{13}C $\{^1\text{H}\}$ HSQC spectra of **32** in THF- d_8 .

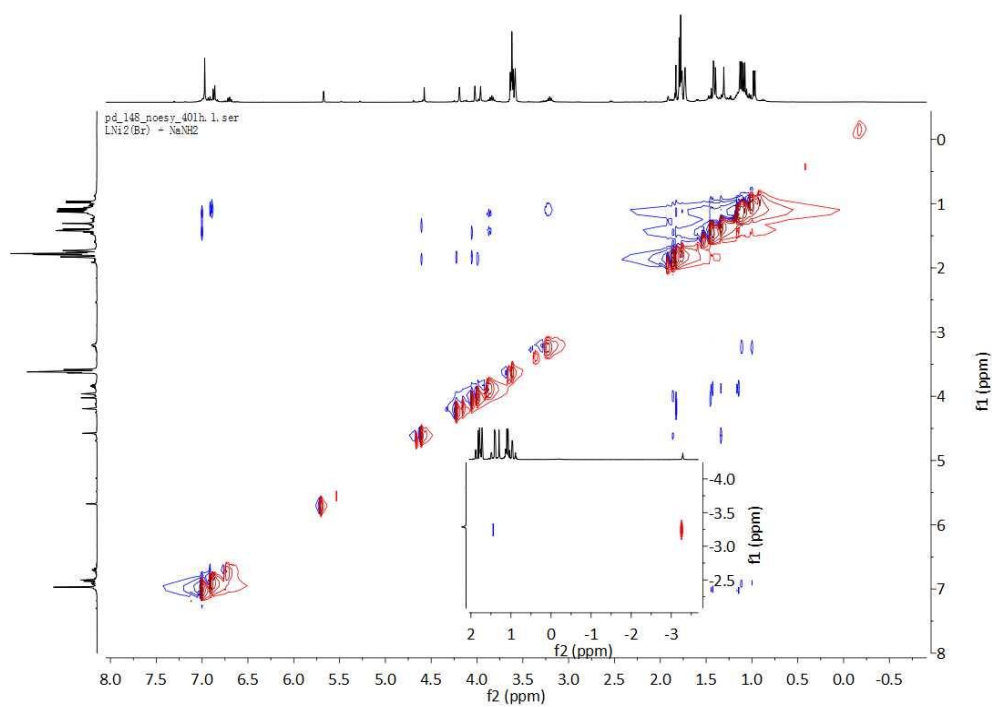


Figure A52: ^1H - ^1H NOESY (400 MHz) spectrum of **32** in THF- d_8 .

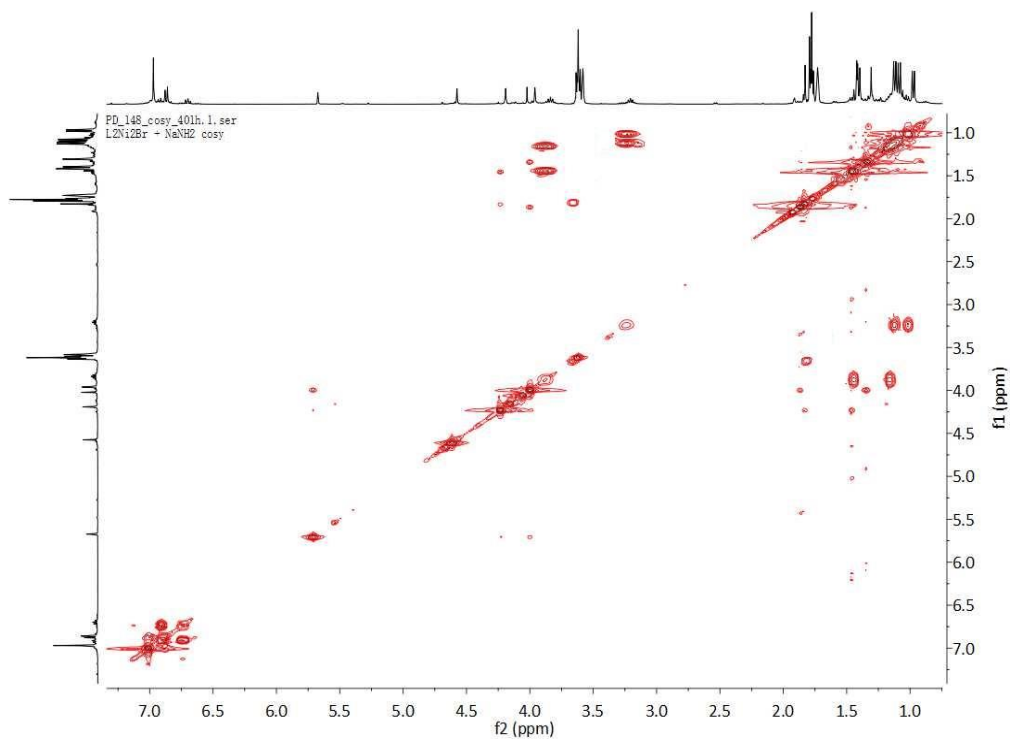


Figure A53: ^1H - ^1H COSY (400 MHz) spectrum of **32** in THF-d_8 .

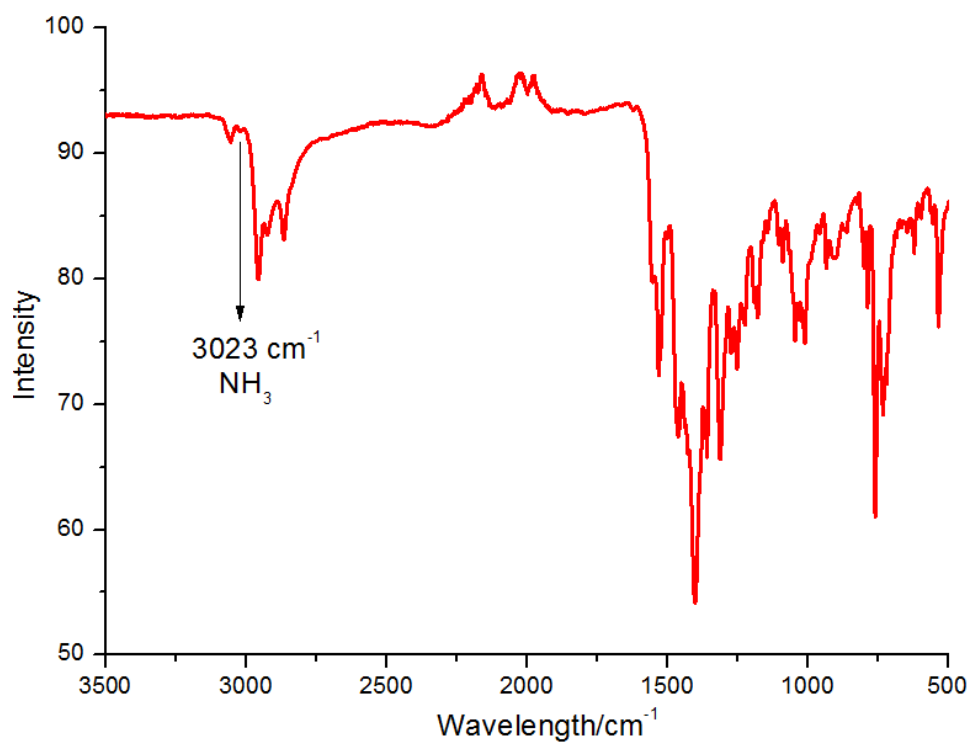


Figure A54: ATR-IR spectra of complex **32**.

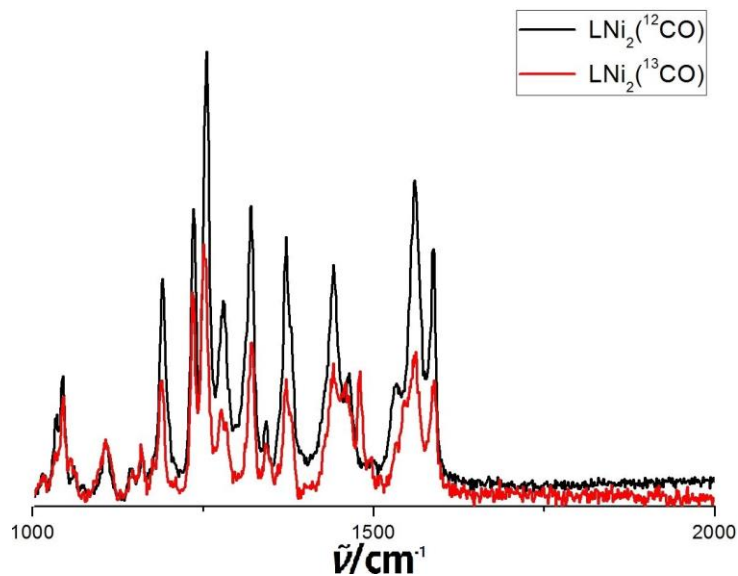


Figure A55: rRaman spectrum of **33** and **33**- ^{13}C O complex in crystalline material.

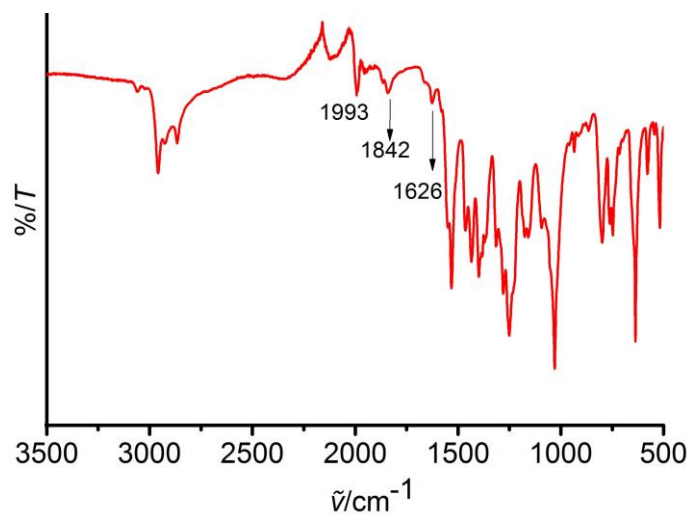


Figure A56: IR spectrum of **34** in crude product.

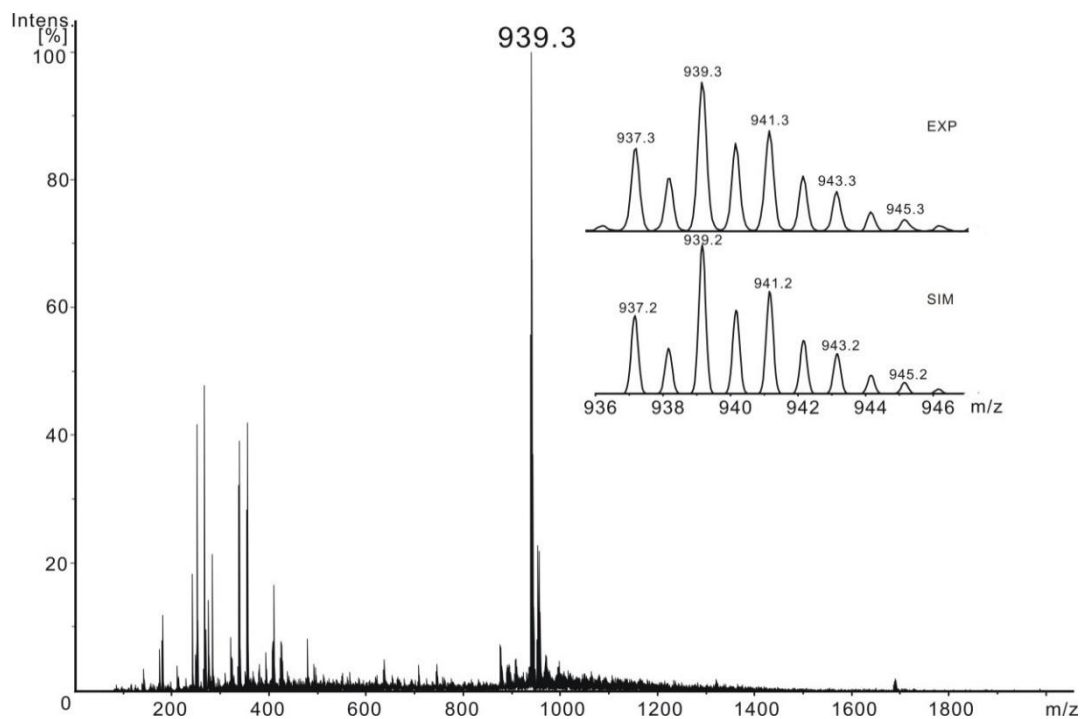


Figure A57: ESI-MS (+) of 35 in THF.

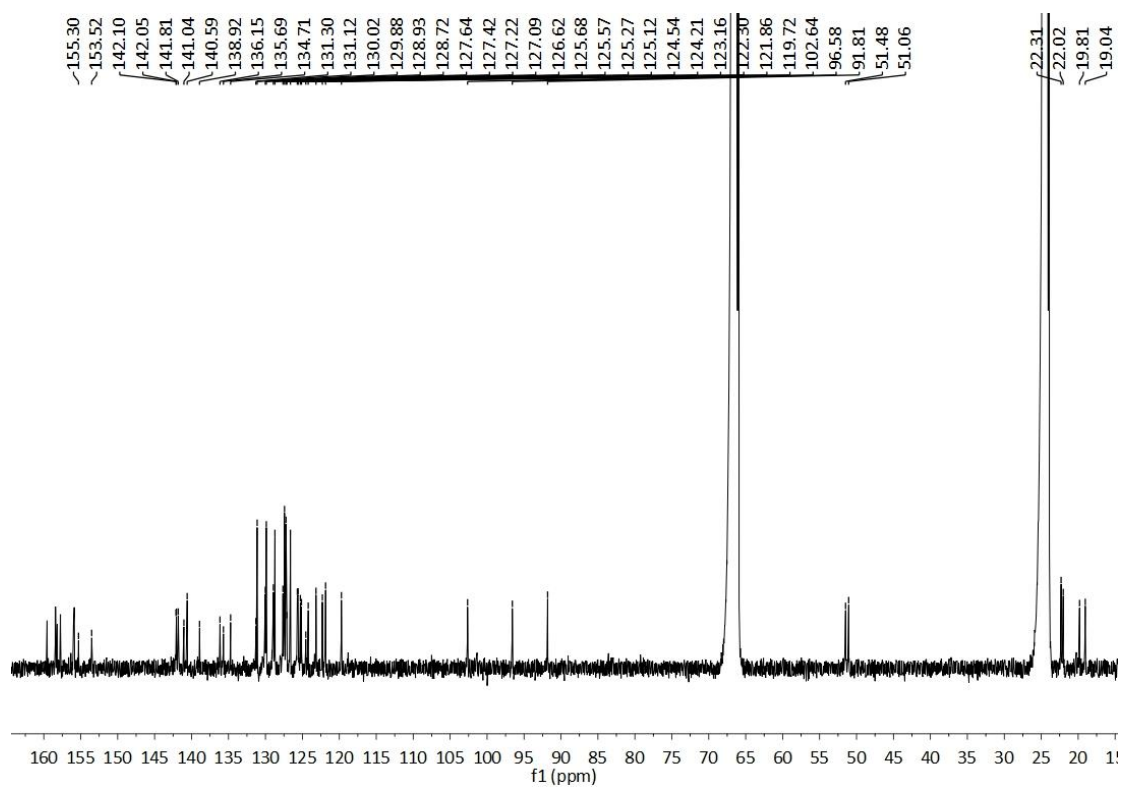


Figure A58: ^{13}C NMR (100 MHz) spectrum of 36 in THF- d_8 .

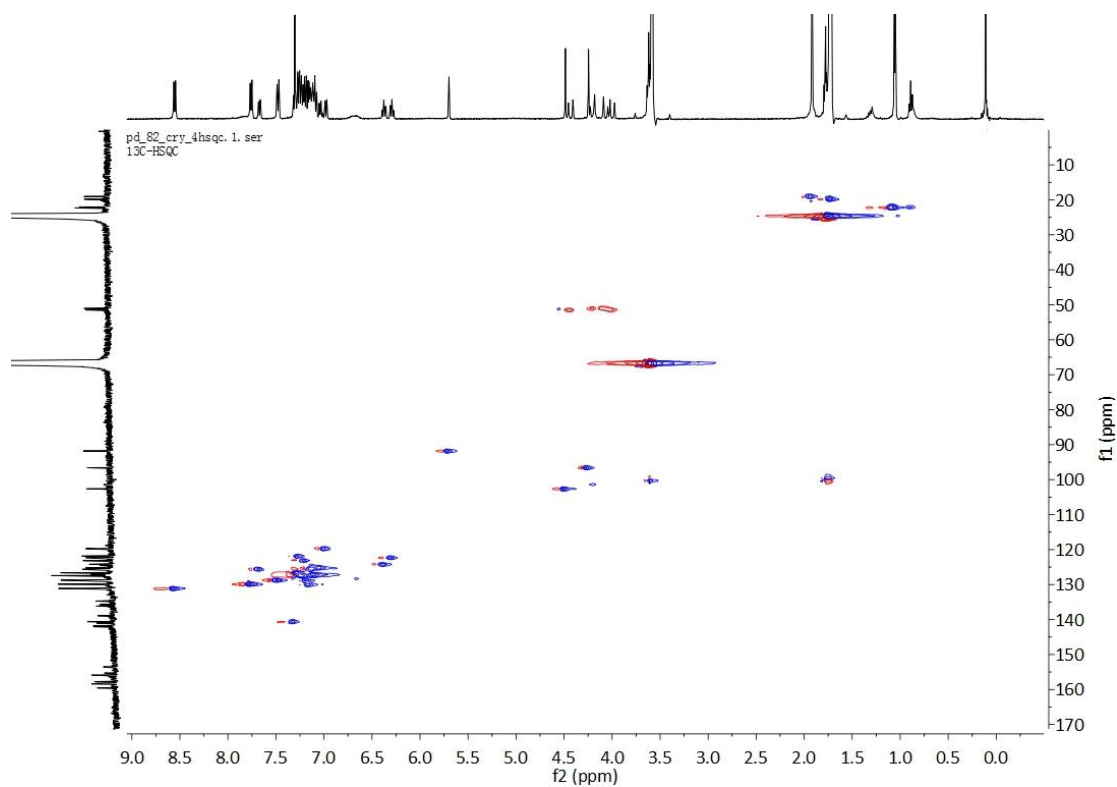


Figure A59: ^1H - ^{13}C HSQC spectrum of **36** in THF- d_8 .

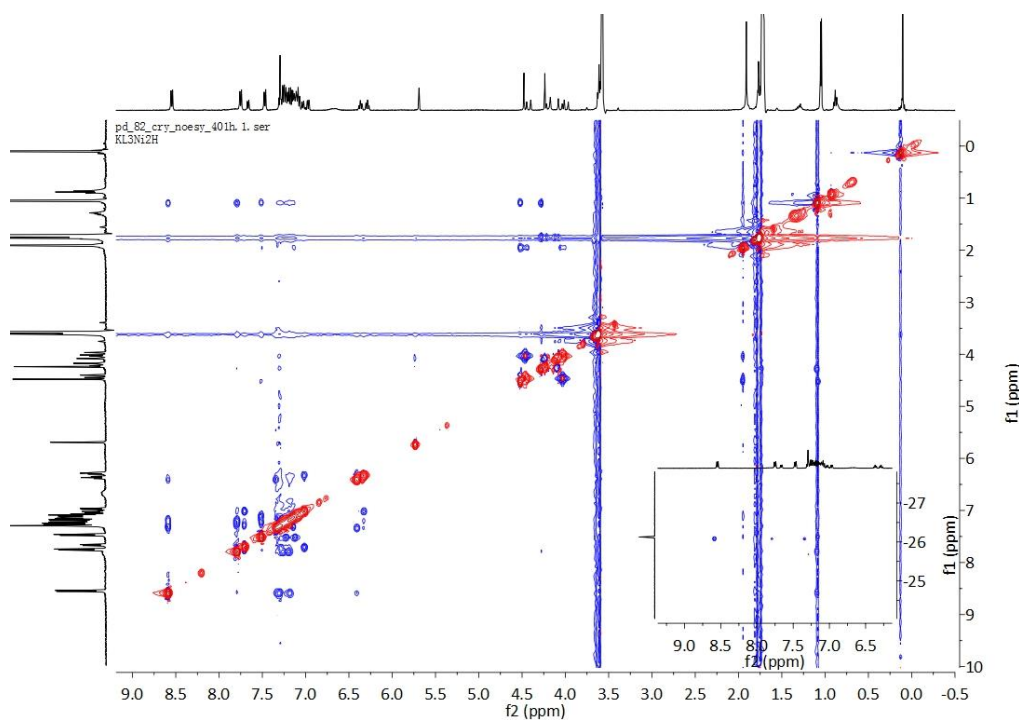


Figure A60: ^1H - ^1H NOESY (400 MHz) spectrum of **36** in THF- d_8 .

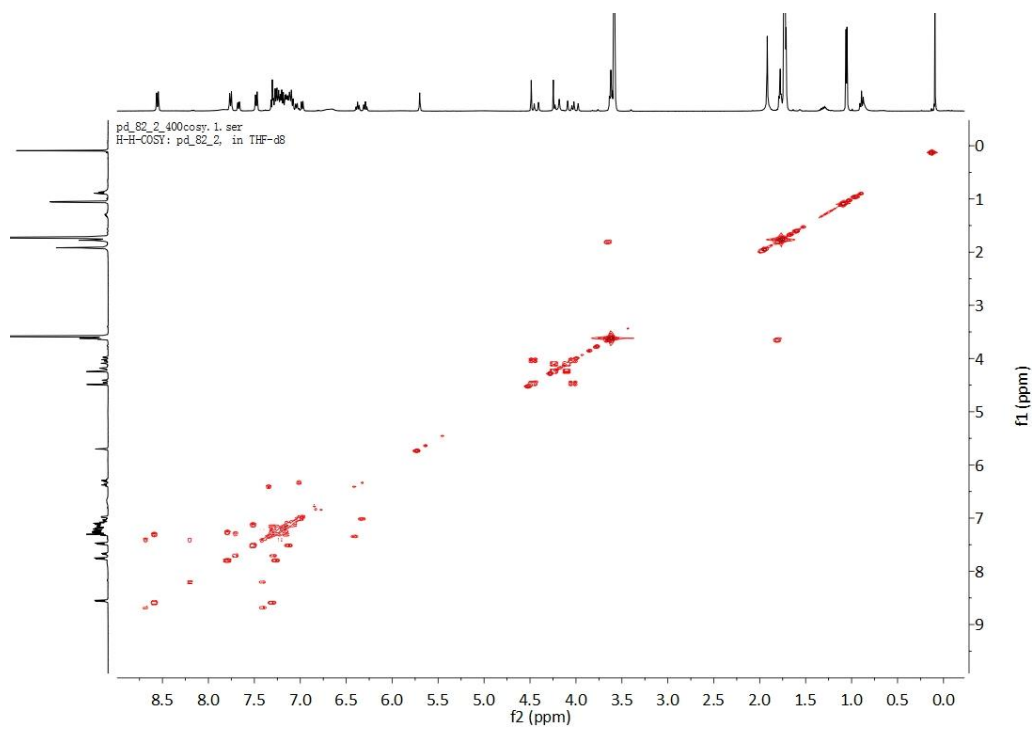


Figure A61: ^1H - ^1H COSY (400 MHz) spectrum of **36** in THF- d_8 .

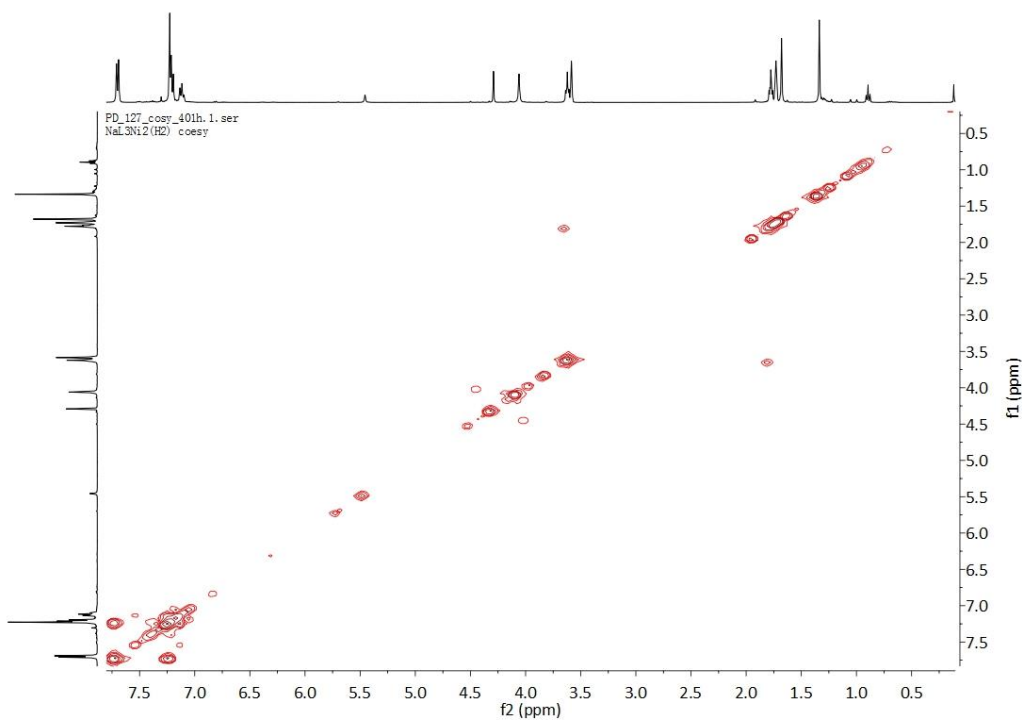


Figure A62: ^1H - ^1H COSY (400 MHz) spectrum of **38** in THF- d_8 .

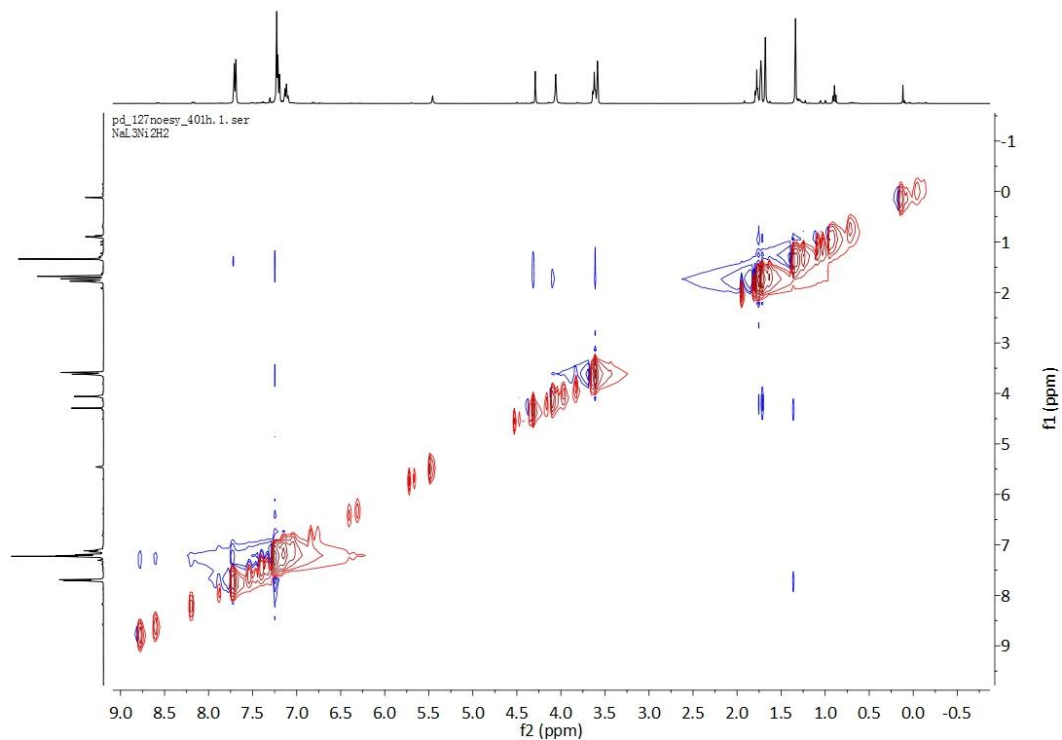


Figure A63: ^1H - ^1H NOESY (400 MHz) spectrum of **38** in THF- d_8 .

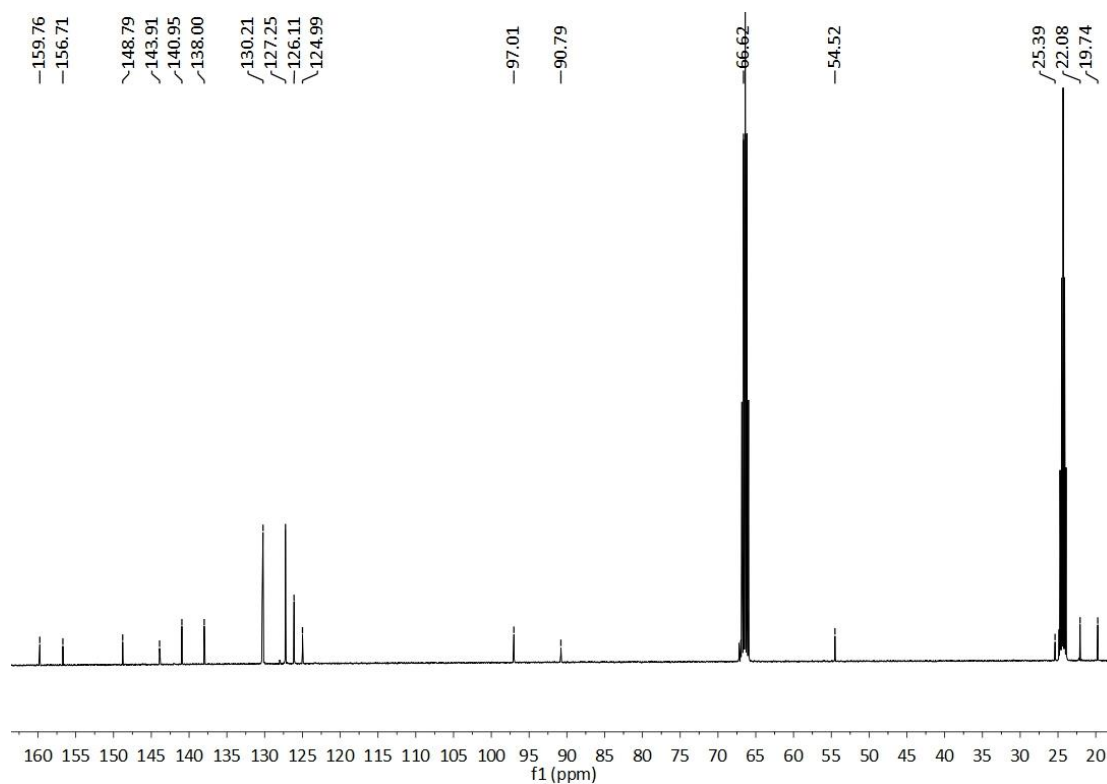


Figure A64: ^{13}C NMR (100 MHz) spectrum of **38** in THF- d_8 .

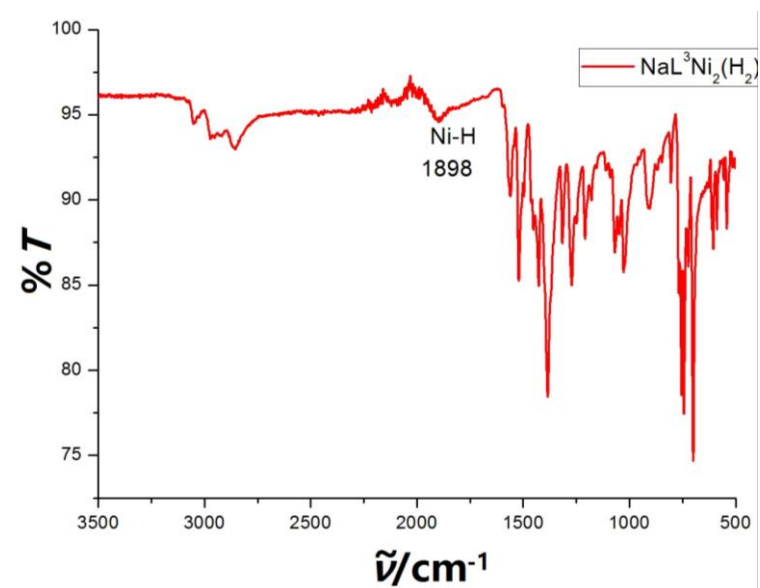


Figure A65: IR spectrum of complex **38** in crystalline material.

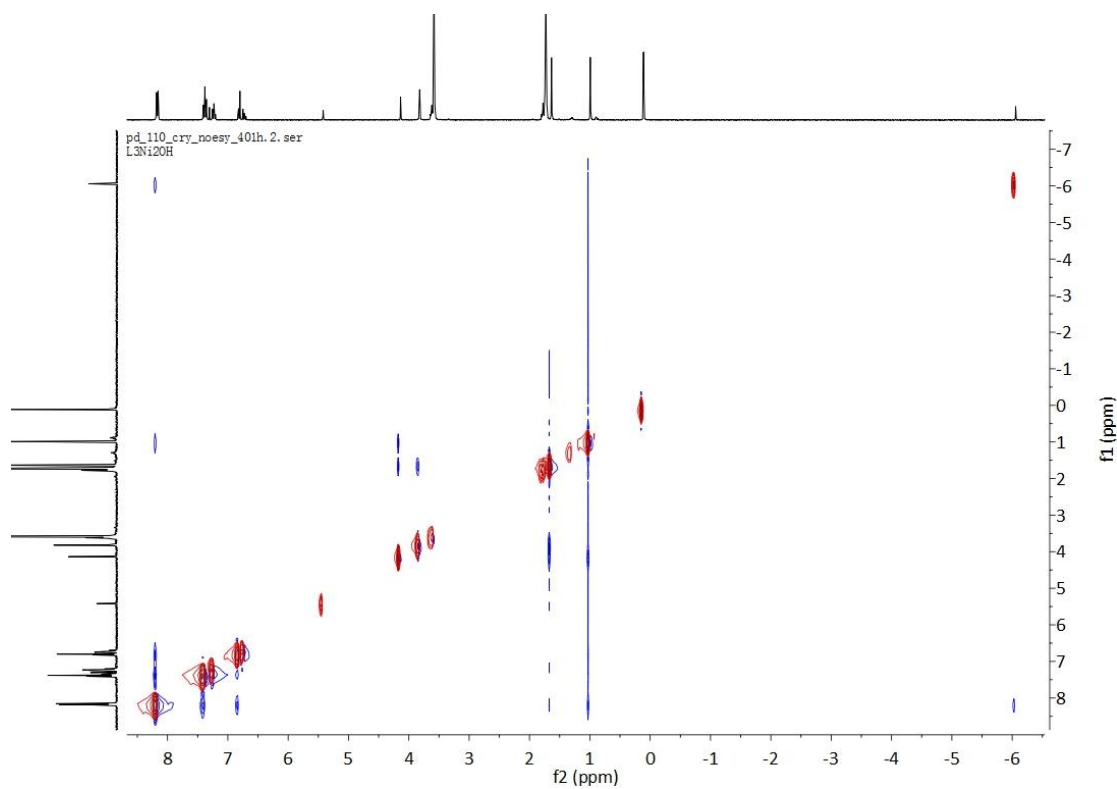


Figure A66: ^1H - ^1H NOESY (400 MHz) spectrum of **39** in THF-d_8 .

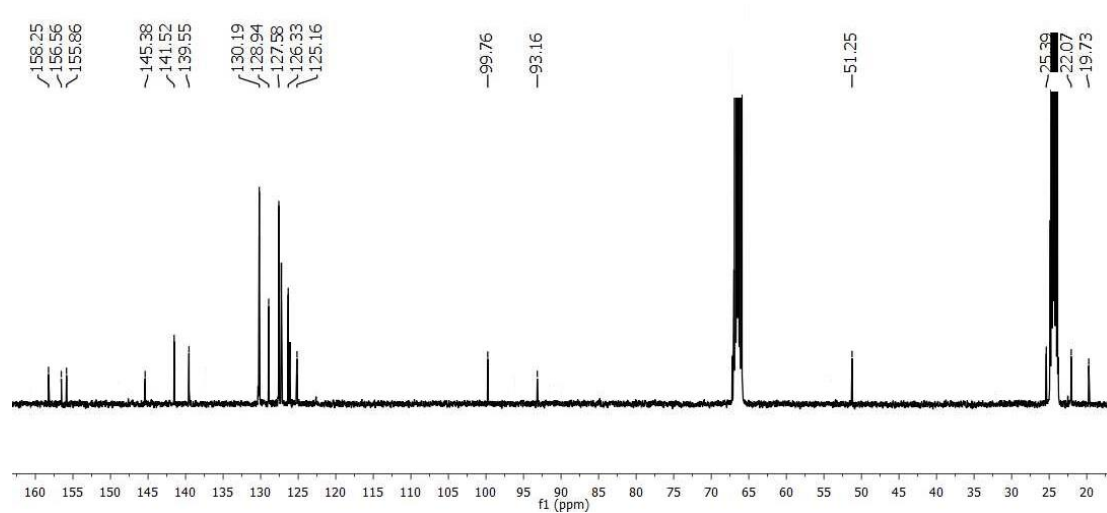


Figure A67: ^{13}C NMR (100 MHz) spectrum of **39** in THF- d_8 .

Reference

- [1] S. W. Ragsdale, *J. Inorg. Biochem.* **2007**, *101*, 1657–1666.
- [2] (a) S. G. McGeachin, *Can. J. Chem.* **1968**, *46*, 1903 – 1912; (b) R. Bonnett, D. C. Bradley, K. J. Fisher, *Chem. Commun.* **1968**, 886 – 887; (c) J. E. Parks, R. H. Holm, *Inorg. Chem.* **1968**, *7*, 1408 – 1416.
- [3] C. Chen, S. M. Bellows, and P. L. Holland, *Dalton Trans.* **2015**, *44*, 16654 – 16670
- [4] (a) L. Bourget-Merle, M. F. Lappert, J. R. Severn, *Chem. Rev.* **2002**, *102*, 3031 – 3066; (b) Y. Tsai, *Coord. Chem. Rev.*, **2012**, *256*, 722 – 758.
- [5].(a) P. L. Holland, W. B. Tolman, *J. Am. Chem. Soc.* **1999**, *121*, 7270 – 7271; (b) D. W. Randall, S. D. George, P. L. Holland, B. Hedman, K. O. Hodgson, W. B. Tolman, E. I. Solomon, *J. Am. Chem. Soc.* **2000**, *122*, 11632 – 11648; (c) J. M. Smith, R. J. Lachicotte, K. A. Pittard, T. R. Cundari, G. Lukat-Rodgers, K. R. Rodgers, P. L. Holland, *J. Am. Chem. Soc.* **2001**, *123*, 9222 – 9223; (d) D. J. E. Spencer, N. W. Aboeella, A. M. Reynolds, P. L. Holland, W. B. Tolman, *J. Am. Chem. Soc.* **2002**, *124*, 2108 – 2109; (e) N. W. Aboeella, E. A. Lewis, A. M. Reynolds, W. W. Brennessel, C. J. Cramer, W. B. Tolman, *J. Am. Chem. Soc.* **2002**, *124*, 10660 – 10661; (f) J. Vela, S. Stoian, C. J. Flaschenriem, E. Münck, P. L. Holland, *J. Am. Chem. Soc.* **2004**, *126*, 4522 – 4523; (g) E. C. Brown, J. T. York, W. E. Antholine, E. Ruiz, S. Alvarez, W. B. Tolman, *J. Am. Chem. Soc.* **2005**, *127*, 13752 – 13753; (h) N. W. Aboeella, B. F. Gherman, L. M. R. Hill, J. T. York, N. Holm, V. G. Young, C. J. Cramer, W. B. Tolman, *J. Am. Chem. Soc.* **2006**, *128*, 3445 – 3458; (i) Z. J. Tonzetich, L. H. Do, S. J. Lippard, *J. Am. Chem. Soc.* **2009**, *131*, 7964 – 7965.
- [6] (a) D. V. Vitanova, F. Hampel, K. C. Hultzsich, *Dalton Trans.* **2005**, 1565–1566; (b) D. F. J. Piesik, S. Range, S. Harder, *Organometallics.* **2008**, *27*, 6178 – 6187; (c) S. Harder, J. Spielmannb, J. Intemanna, *Dalton Trans.* **2014**, *43*, 14284–14290.

- [7] (a) A. P. Sadimenko, S. S. Basson, *Coord. Chem. Rev.* **1996**, *147*, 247 – 297; (b) J. Klingele, S. Dechert, F. Meyer, *Coord. Chem. Rev.* **2009**, *253*, 2698 – 2741; (c) J. P. Zhang, Y. B. Zhang, J. B. Lin, X. M. Chen, *Chem. Rev.* **2012**, *112*, 1001 – 1033.
- [8] K. E. Dalle, F. Meyer, *Eur. J. Inorg. Chem.* **2015**, 3391 – 3405.
- [9] (a) F. Meyer, P. Rutsch, *Chem. Commun.* **1998**, 1037 – 1038; (b) F. Meyer, E. Kaifer, P. Kircher, K. Heinze, H. Pritzkow, *Chem. Eur. J.* **1999**, *5*, 1617–1630; (c) K. E. Dalle, T. Gruene, S. Dechert, S. Demeshko, F. Meyer, *J. Am. Chem. Soc.* **2014**, *136*, 7428 – 7434; (d) N. Kindermann, E. Bill, S. Dechert, S. Demeshko, E. J. Reijerse, F. Meyer, *Angew. Chem. Int. Ed.* **2015**, *54*, 1738 – 1743; (e) N. Kindermann, S. Dechert, S. Demeshko, F. Meyer, *J. Am. Chem. Soc.* **2015**, *137*, 8002 – 8005.
- [10] J. Vela, S. Vaddadi, S. Kingsley, C. J. Flaschenriem, R. J. Lachicotte, T. R. Cundari, P. L. Holland, *Angew. Chem. Int. Ed.* **2006**, *45*, 1607 – 1611.
- [11] (a) D. H. Manz. Doctoral Thesis, Preorganized Bimetallic Nickel Complexes of Pyrazolate-Bridged Ligands for Cooperative Substrate Transformation, University of Göttingen, 2016; (b) D. H. Manz, P. C. Duan, S. Dechert, S. Demeshko, M. John, R. Oswald, R. Mata, F. Meyer, *J. Am. Chem. Soc.* **2017**, DOI: 10.1021/jacs.7b08629.
- [12] F. Meyer, W. B. Tolman, *Inorg. Chem.* **2015**, *54*, 5039.
- [13] (a) H. D. Kaesz, R. B. Saillant, *Chem. Rev.* **1972**, *72*, 231 – 281; (b) G. J. Leigh, N. Winterton, *Modern Coordination Chemistry: The Legacy of Joseph Chatt*, Royal Society of Chemistry, London, **2002**.
- [14] (a) J. C. Fontecilla-Camps, A. Volbeda, C. Cavazza, Y. Nicolet, *Chem. Rev.* **2007**, *107*, 4273 – 4303; (b) J. A. Wright, P. J. Turrell, C. J. Pickett, *Organometallics.* **2010**, *29*, 6146 – 6156.
- [15] (a) R. N. F. Thorneley, R. R. Eady, D. J. Lowe, *Nature.* **1978**, *272*, 557 – 558; (b) G. J. Leigh, C. N. McMahon, *J. Organomet. Chem.* **1995**, *500*, 219 – 231.
- [16] J. Ballmann, R. F. Munhá, M. D. Fryzuk, *Chem. Commun.* **2010**, 46, 1013 – 1025.
- [17] S. Pfirrmann, C. Limberg, B. Ziemer, *Dalton Trans.* **2008**, 6689–6691.
- [18] S. Pfirrmann, S. Yao, B. Ziemer, R. Stösser, M. Driess, C. Limberg,

- Organometallics*. **2009**, *28*, 6855 – 6860.
- [19] Y. Yu, A. R. Sadique, J. M. Smith, T. R. Dugan, R. E. Cowley, W. W. Brennessel, C. J. Flaschenriem, E. Bill, T. R. Cundari, P. L. Holland, *J. Am. Chem. Soc.* **2008**, *130*, 6624–6638.
- [20] (a) L. P. Bheeter, M. Henrion, L. Brelot, C. Darcel, M. J. Chetcuti, J. B. Sortais, V. Ritleng, *Adv. Synth. Catal.* **2012**, *354*, 2619 – 2624; (b) H. Gehring, R. Metzinger, C. Herwig, J. Intemann, S. Harder, C. Limberg, *Chem. Eur. J.* **2013**, *19*, 1629 – 1636; (c) S. Pelties, D. Herrmann, B. de Bruin, F. Hartl, R. Wolf, *Chem. Commun.* **2014**, *50*, 7014 – 7016; (d) H. Gehring, R. Metzinger, B. Braun, C. Herwig, S. Harder, K. Ray, C. Limberg, *Dalton Trans.* **2016**, *45*, 2989 – 2996.
- [21] (a) Y. Lee, K. J. Anderton, F. T. Sloane, K. A. Abboud, R. Garcia-Serres, L. J. Murray, *J. Am. Chem. Soc.* **2015**, *137*, 10610–10617. (b) D. M. Ermert, L. J. Murray, *Dalton Trans.* **2016**, *45*, 14499–14507.
- [22] K. J. Anderton, B. J. Knight, A. L. Rheingold, K. A. Abboud, R. Garcia-Serres, L. J. Murray, *Chem. Sci.* **2017**, *8*, 4123–4129.
- [23] (a) M. Aresta, P. Giannoccaro, M. Rossi, A. Sacco, *Inorg. Chim. Acta.* **1971**, *5*, 115 – 118; (b) M. Gargano, P. Giannoccaro, M. Rossi, G. Vasapollo, A. Sacco, *J. Chem. Soc. Dalton Trans.* **1975**, *9* – 12.
- [24] (a) A. Misono, Y. Uchida, T. Saito, K. M. Song, *Chem. Commun.* **1967**, 419 – 420; (b) A. Yamamoto, L. S. Pu, S. Kitazume, S. Ikeda, *J. Am. Chem. Soc.* **1967**, *89*, 3071 – 3073; (c) A. Misono, Y. Uchida and T. Saito, *Bull. Chem. Soc. Jpn.* **1967**, *40*, 700; (d) S. C. Srivastava, M. Bigorgne, *J. Organomet. Chem.* **1969**, *19*, 241.
- [25] (a) I. Bach, R. Goddard, C. Kopsike, K. Seevogel, K.R. Pörschke, *Organometallics*. **1999**, *18*, 10 – 20; (b) C. D. Abernethy, R. J. Baker, M. L. Cole, A. J. Davies, C. Jones, *Trans. Met. Chem.* **2003**, *28*, 296 – 299; (c) W. Chen, S. Shimada, M. Tanaka, Y. Kobayashi, K. Saigo, *J. Am. Chem. Soc.* **2004**, *126*, 8072 – 8073; (d) R. Beck, M. Shoshani, S. A. Johnson, *Angew. Chem., Int. Ed.* **2012**, *51*, 11753 – 11756; (e) D. Schmidt, T. Zell, T. Schaub, U. Radius, *Dalton Trans.* **2014**, *43*, 10816 – 10827; (f) N. A. Eberhardt, H. R. Guan, *Chem. Rev.* **2016**, *116*, 8373 – 8426.
- [26] C. Rettenmeier, H. Wadepohl, L. H. Gade, *Chem-Eur. J.* **2014**, *20*, 9657 – 9665.

- [27] M. J. Ingleson, B. C. Fullmer, D. T. Buschhorn, H. Fan, M. Pink, J. C. Huffman, K. G. Caulton, *Inorg. Chem.* **2008**, *47*, 407 – 409.
- [28] C. Yoo, Y. Lee, *Angew. Chem. Int. Ed.* **2017**, *56*, 9502 – 9506.
- [29] A. F. Holleman, E. Wiberg, N. Wiberg, *Lehrbuch der Anorganischen Chemie*, de Gruyter, Berlin, **1995**.
- [30] (a) H. Imoto, H. Moriyama, T. Saito, Y. Sasaki, *J. Organomet. Chem.* **1976**, *120*, 453 – 460; (b) M. J. Tenorio, M. C. Puerta, P. Valerga, *J. Chem. Soc., Dalton Trans.* **1996**, 1305 – 1308; (c) I. Bach, R. Goddard, C. Kopiske, K. Seevogel, K. R. Pörschke, *Organometallics.* **1999**, *18*, 10 – 20; (d) W. H. Harman, T. P. Lin, J. C. Peters, *Angew. Chem. Int. Ed.* **2014**, *53*, 1081 – 1086; (e) B. A. Connor, J. Rittle, D. VanderVelde, J. C. Peters, *Organometallics.* **2016**, *35*, 686 – 690; (b) S. Ramakrishnan, S. Chakraborty, W. W. Brennessel, C. E. D. Chidsey, W. D. Jones, *Chem. Sci.* **2016**, *7*, 117–127.
- [31] S. Yao, M. Driess, *Acc. Chem. Res.* **2012**, *45*, 276 – 287.
- [32] (a) R. B. Lansing, K. I. Goldberg, R. A. Kemp, *Dalton Trans.* **2011**, *40*, 8950 – 8958; (b) T. Punniyamurthy, S. Velusamy, J. Iqbal, *Chem. Rev.* **2005**, *105*, 2329 – 2363; (c) C. C. Cheng, S. E. Rokita, C. J. Burrows, *Angew. Chem. Int. Ed. Engl.* **1993**, *32*, 277 – 278; *Angew. Chem.* **1993**, *105*, 290 – 292; (d) D. Chen, R. J. Motekaitis, A. E. Martell, *Inorg. Chem.* **1991**, *30*, 1396 – 1402; (e) A. Berkessel, J. W. Bats, C. Schwarz, *Angew. Chem. Int. Ed. Engl.* **1990**, *29*, 106 – 108; *Angew. Chem.* **1990**, *102*, 81 – 84. (f) E. Kimura, R. Machida, M. Kodama, *J. Am. Chem. Soc.* **1984**, *106*, 5497 – 5505.
- [33] J. H. Jeoung, D. Nianios, S. Fetzner, H. Dobbek, *Angew. Chem. Int. Ed.* **2016**, *55*, 3281 – 3284; *Angew. Chem.* **2016**, *128*, 3339 – 3343.
- [34] P. Holze, T. Corona, N. Frank, B. Braun-Cula, C. Herwig, A. Company, C. Limberg, *Angew. Chem. Int. Ed.* **2017**, *56*, 2307 – 2311; *Angew. Chem.* **2017**, *129*, 2347 – 2351.
- [35] (a) K. Fujita, R. Schenker, W. Gu, T. C. Brunold, S. P. Cramer, C. G. Riordan, *Inorg. Chem.* **2004**, *43*, 3324 – 3326. (b) M. T. Kieber-Emmons, J. Annaraj, M. S. Seo,

- K. M. W. V. Heuvelen, T. Tosha, T. Kitagawa, T. C. Brunold, W. Nam, C. G. Riordan, *J. Am. Chem. Soc.* **2006**, *128*, 14230 – 14231.
- [36] S. Yao, E. Bill, C. Milsmann, K. Wieghardt, M. Driess, *Angew. Chem. Int. Ed.* **2008**, *47*, 7110 – 7113.
- [37] C. A. Rettenmeier, H. Wadepohl, L. H. Gade; *Angew. Chem. Int. Ed.* **2015**, *54*, 4880 – 4884.
- [38] (a) K. Shiren, S. Ogo, S. Fujinami, H. Hayashi, M. Suzuki, A. Uehara, Y. Watanabe, Y. Morooka, *J. Am. Chem. Soc.* **2000**, *122*, 254 – 262; (b) J. Cho, H. Y. Kang, L. V. Liu, R. Sarangi, E. I. Edward, W. Nam, *Chem. Sci.* **2013**, *4*, 1502 – 1508.
- [39] S. Yao, Y. Xiong, M. Vogt, H. Grützmacher, C. Herwig, C. Limberg, M. Driess, *Angew. Chem. Int. Ed.* **2009**, *48*, 8107 – 8110.
- [40] (a) M. H. Gubelmann, A. F. Williams, *Struct. Bonding* (Berlin), **1983**, *55*, 1; (b) M. Suzuki, T. Ishiguro, M. Kozuka, K. Nakamoto, *Inorg. Chem.* **1981**, *20*, 1993 – 1996.
- [41] M. T. Kieber-Emmons, R. Schenker, G. P. A. Yap, T. C. Brunold, C. G. Riordan, *Angew. Chem.* **2004**, *116*, 6884 – 6886.
- [42] J. Cho, R. Sarang, J. Annaraj, S. Y. Kim, M. Kubo, T. Ogura, E. I. Solomon, W. Nam, *Nat. Chem.* **2009**, *1*, 568 – 572.
- [43] (a) L. Que, Y. Dong, *Acc. Chem. Res.* **1996**, *29*, 190 – 196; (b) E. I. Solomon, T. C. Brunold, M. I. Davis, J. N. Kemsley, S. K. Lee, N. Lehnert, F. Neese, A. J. Skulan, Y. S. Yang, J. Zhou, *Chem. Rev.* **2000**, *100*, 235 – 350.
- [44] (a) K. Chen, L. Que, *J. Am. Chem. Soc.* **2001**, *123*, 6327 – 6337; (b) M. Costas, M. P. Mehn, M. P. Jensen, L. Que, *Chem. Rev.* **2004**, *104*, 939 – 986; (c) R. Mas-Ballester, L. Que, *J. Am. Chem. Soc.* **2007**, *129*, 15964 – 15972; (d) J. L. Fillol, Z. Codol, I. Garcia-Bosch, L. Gómez, J. J. Pla, M. Costas, *Nat. Chem.* **2011**, *3*, 807 – 813; (e) W. N. Oloo, A. J. Fielding, L. Que, *J. Am. Chem. Soc.* **2013**, *135*, 6438 – 6441; (f) K. Ray, F. F. Pfaff, B. Wang, W. Nam, *J. Am. Chem. Soc.* **2014**, *136*, 13942 – 13958.
- [45] (a) D. Carmona, M. P. Lamata, J. Ferrer, J. Modrego, M. Perales, F. J. Lahoz, R. Atencio, L. A. Oro, *J. Chem. Soc. Chem. Commun.* **1994**, 575 – 576; (b) A. Wada, M. Harata, K. Hasegawa, K. Jitsukawa, H. Masuda, M. Mukai, T. Kitagawa, H. Einaga,

Angew. Chem. Int. Ed. **1998**, *37*, 798 – 799; (c) Y. Takahashi, M. Hashimoto, S. Hikichi, M. Akita, Y. Morooka, *Angew. Chem. Int. Ed.* **1999**, *38*, 3074 – 3077; (d) D. D. Wick, K. I. Goldberg, *J. Am. Chem. Soc.* **1999**, *121*, 11900 – 11901; (e) I. A. Guzei, A. Bakac, *Inorg. Chem.* **2001**, *40*, 2390 – 2393; (f) M. Ahijado, T. Braun, D. Noveski, N. Kocher, B. Neumann, D. Stalke, H.-G. Stammer, *Angew. Chem. Int. Ed.* **2005**, *44*, 6947 – 6951; (g) M. C. Denney, N. A. Smythe, K. L. Cetto, R. A. Kemp, K. I. Goldberg, *J. Am. Chem. Soc.* **2006**, *128*, 2508 – 2509; (h) G. Katona, P. Carpentier, V. Nivière, P. Amara, V. Adam, J. Ohana, N. Tsanov, D. Bourgeois, *Science*. **2007**, *316*, 449 – 453; (i) D. Barats, G. Leitius, R. Popovitz-Biro, L. J. W. Shimon, R. Neumann, *Angew. Chem. Int. Ed.* **2008**, *47*, 9908 – 9912; (j) R. Dragos, Adrian, A. W. Joseph, L. H. David, B. Manfred, *Nat. Commun.* **2013**, *4*, 2167.

[46] (a) A. Abou Hamdan, B. Burlat, O. Gutierrez-Sanz, P. P. Liebgott, C. Baffert, A. L. De Lacey, M. Rousset, B. Guigliarelli, C. Lfger, S. Dementin, *Nat. Chem. Biol.* **2013**, *9*, 15 – 17; (b) W. Lubitz, H. Ogata, O. Rüdiger, E. Reijerse, *Chem. Rev.* **2014**, *114*, 4081 – 4148.

[47] C. A. Rettenmeier, H. Wadepohl, L. H. Gade. *Angew. Chem. Int. Ed.* **2015**, *54*, 4880 – 4884.

[48] (a) S. Otsuka, A. Nakamura, Y. Tatsuno, *J. Am. Chem. Soc.* **1969**, *91*, 6994 – 6999; (b) A. Nakamura, Y. Tatsuno, M. Yamamoto, S. Otsuka, *J. Am. Chem. Soc.* **1971**, *93*, 6052 – 6058; (c) M. Matsumoto, K. Nakatsu, *Acta Crystallogr. B.* **1975**, *31*, 2711 – 2713.

[49] K. T. Neumann, S. Klimczyk, M. N. Burhardt, B. Bang-Andersen, T. Skrydstrup, A. T. Lindhardt, *ACS Catal.* **2016**, *6*, 4710–4714.

[50] T. Lu, C.-F. Yang, L.-Y. Zhang, F. Fei, X.-T. Chen, Z.-L. Xue, *Inorg. Chem.* **2017**, *56*, 11917–11928

[51] R. M. Kadam, M. D. Sastry, *Phase Transition.* **1997**, *60*, 79 – 87.

[52] N. Kindermann, C. J. Günes, S. Dechert, F. Meyer, *J. Am. Chem. Soc.* **2017**, *139*, 9831 – 9834

[53] (a) D. A. Vicic, W. D. Jones, *J. Am. Chem. Soc.* **1999**, *121*, 4070 – 4071; (b) W. Zhu, A. C. Marr, Q. Wang, F. Neese, D. J. E. Spencer, A. J. Blake, P. A. Cooke, C. Wilson,

M. Schröder, *Proc. Natl. Acad. Sci. U.S.A.* **2005**, *102*, 18280 – 18285; (c) A. G. Tennyson, S. Dhar, S. J. Lippard, *J. Am. Chem. Soc.* **2008**, *130*, 15087 – 15098; (d) S. Yao, C. Milsmann, E. Bill, K. Wieghardt, M. Driess, *J. Am. Chem. Soc.* **2008**, *130*, 13536 – 13537; (e) M. T. Kieber-Emmons, K. M. Van Heuvelen, T. C. Brunold, G. R. Charles, *J. Am. Chem. Soc.* **2009**, *131*, 440 – 441; (f) S. Yao, P. Hrobárik, F. Meier, R. Rudolph, E. Bill, E. Irran, M. Kaupp, M. Driess, *Chem. Eur. J.* **2013**, *19*, 1246 – 1253; (g) F. Olechnowicz, G. L. Hillhouse, R. F. Jordan, *Inorg. Chem.* **2015**, *54*, 2705 – 2712.

[54] (a) J. C. Fontecilla-Camps, *Struct. Bonding.* **1998**, *1*, 91,. (b) S. P. Albracht, *J. Biochim. Biophys. Acta* **1994**, *167*, 1188.

[55] M. T. Kieber-Emmons, K. M. Van Heuvelen, T. C. Brunold, C. G. Riordan, *J. Am. Chem. Soc.* **2009**, *131*, 440 – 441.

[56] F. Pelties, D. Herrmann, B. Bruin, F. Hartl, R. Wolf, *Chem. Commun.* **2014**, *50*, 7014 – 7016.

[57] (a) R. C. Elder, M. Trkula, *Inorg. Chem.* **1977**, *16*, 1048 – 1051. (b) M. M. Taqui Khan, M. R. H. Siddiqui, *Inorg. Chem.* **1991**, *30*, 1157 – 1159.

[58] Linear $[M(m-S)M]^{n+}$ arrangements have been observed for only a few Fe, V, Mo, Co, Ni, Cu, U, and Pb compounds: (a) O. P. Lam, F. W. Heinemann, K. Meyer, *Chem. Sci.* **2011**, *2*, 1538 – 1547; (b) J. E. McDonough, A. Mendiratta, J. J. Curley, G. C. Fortman, S. Fantasia, C. C. Cummins, E. V. Rybak-Akimova, S. P. Nolan, C. D. Hoff, *Inorg. Chem.* **2008**, *47*, 2133 – 2141; (c) J. Cho, K. M. Van Heuvelen, G. P. A. Yap, T. C. Brunold, C. G. Riordan, *Inorg. Chem.* **2008**, *47*, 3931 – 3933; (d) S. Delgado, P. J. S. Miguel, J. L. Priego, R. Jiménez-Aparicio, C. J. Gémez-Garcéa, F. Zamora, *Inorg. Chem.* **2008**, *47*, 9128 – 9130; (e) S. C. Davies, D. L. Hughes, R. L. Richards, J. R. Sanders, *J. Chem. Soc. Dalton Trans.* **2000**, 719 – 725.

[59] M. M. Rodriguez, B. D. Stubbert, C. C. Scarborough, W. W. Brennessel, E. Bill, P. L. Holland, *Angew. Chem. Int. Ed.* **2012**, *51*, 8247 – 8250.

[60] P. Holze, B. Horn, C. Limberg, C. Matlachowski, S. Mebs, *Angew. Chem. Int. Ed.* **2014**, *53*, 2750 – 2753.

[61] D. A. Vicic and, W. D. Jones, *J. Am. Chem. Soc.* **1999**, *121*, 4070 – 4071.

- [62] N. J. Hartmann, G. Wu, T. W. Hayton, *Angew. Chem. Int. Ed.* **2015**, *54*, 14956 – 14959.
- [63] N. J. Hartmann, G. Wu, T. W. Hayton, *Dalton Trans.* **2016**, *45*, 14508 – 14510.
- [64] N. J. Hartmann, G. Wu, T. W. Hayton *J. Am. Chem. Soc.* **2016**, *138*, 12352–12355.
- [65] P. Chen, K. Fujisawa, M. E. Helton, K. D. Karlin, E. I. Solomon, *J. Am. Chem. Soc.* **2003**, *125*, 6394.
- [66] (a) N. Baidya; M. Olmstead, P. K. Mascharak, *Inorg. Chem.* **1991**, *30*, 929 – 937; (b) Y. Journaux, T. Glaser, G. Steinfeld, V. Lozan, B. Kersting, *Dalton Trans.*, **2006**, 1738–1748; (c) V. Lozan, B. Kersting, *Inorg. Chem.* **2008**, *47*, 5386 – 5393
- [67] R. J. Pleus, H. Waden, W. Saak, D. Haase, S. Pohl, *J. Chem. Soc., Dalton Trans.* **1999**, 2601 – 2610.
- [68] (a) V. M. Iluc, A. J. M. Miller, J. S. Anderson, M. J. Monreal, M. P. Mehn, G. L. Hillhouse, *J. Am. Chem. Soc.* **2011**, *133*, 13055 – 13063; (b) V. M. Iluc, G. L. Hillhouse, *J. Am. Chem. Soc.* **2014**, *136*, 6479 – 6488; (c) P. Pyykkö, *J. Phys. Chem. A*, **2015**, *119*, 2326 – 2337.
- [69] (a) Dilworth, J. R. *Coord. Chem. Rev.* **2017**, *330*, 53–94. (b) MacKay, B.; Fryzuk, M. *Chem. Rev.* **2004**, *104*, 385–401.
- [70] J. R. Dilworth, *Coord. Chem. Rev.* **2017**, *330*, 53 – 94.
- [71] (a) A. Nakamura, T. Yoshida, M. Cowie, S. Otsuka, J. Ibers, *J. Am. Chem. Soc.* **1977**, *99*, 2108–2117. (b) D. Mindiola, G. Hillhouse, *J. Am. Chem. Soc.* **2002**, *124*, 9976 – 9977.
- [72] C. Köthe, R. Metzinger, C. Herwig, C. Limberg; *Inorg. Chem.* **2012**, *51*, 9740 – 9747.
- [73] (a) J. Vela, S. Stoian, C. J. Flaschenriem, E. Münck, P. L. Holland, *J. Am. Chem. Soc.* **2004**, *126*, 4522 – 4523. (b) N. S. Lees, R. L. McNaughton, W. Vargas Gregory, P. L. Holland, B. M. Hoffman. *J. Am. Chem. Soc.* **2008**, *130*, 546 – 555.
- [74] B. T. Heaton, C. Jacob, P. Page, *Coord. Chem. Rev.* **1996**, *154*, 193 – 218.
- [75] L. D. Field, H. L. Lim, S. J. Dalgarno, R. D. McIntosh, *Inorg. Chem.* **2012**, *51*, 3733 – 3742.

- [76] Y. Lee, N. P. Mankad, J. C. Peters, *Nat. Chem.* **2010**, *2*, 558 – 565.
- [77] Selected examples: (a) P. L. Diaconescu, P. L. Arnold, T. A. Baker, D. J. Mindiola, C. C. Cummins, *J. Am. Chem. Soc.* **2000**, *122*, 6108 – 6109; (b) E. D. Brady, D. L. Clark, W. Keogh, B. L. Scott, J. G. Watkin, *J. Am. Chem. Soc.* **2002**, *124*, 7007 – 7015; (c) W. J. Evans, S. A. Kozimor, J. W. Ziller, *Chem. Commun.* **2005**, 4681 – 4683; (d) U. J. Kilgore, X. Yang, J. Tomaszewski, J. C. Huffman, D. J. Mindiola, *Inorg. Chem.* **2006**, *45*, 10712 – 10721; (e) W. H. Monillas, G. P. A. Yap, L. A. MacAdams, K. H. Theopold, *J. Am. Chem. Soc.* **2007**, *129*, 8090 – 8091; (f) Y. C. Tsai, P. Y. Wang, S. A. Chen, J. M. Chen, *J. Am. Chem. Soc.* **2007**, *129*, 8066 – 8067; (g) Y. C. Tsai, P. Y. Wang, K. M. Lin, S. A. Chen, J. M. Chen, *Chem. Commun.* **2008**, 205 – 207; (h) K. Kaleta, P. Arndt, T. Beweries, A. Spannenberg, O. Theilmann, *Organometallics*. **2010**, *29*, 2604 – 2609; (i) C. Milsmann, Z. R. Turner, S. P. Semproni, P. J. Chirik, *Angew. Chem. Int. Ed.* **2012**, *51*, 5386 – 5390.
- [78] (a) A. K. Verma, S. C. Lee, *J. Am. Chem. Soc.* **1999**, *121*, 10838 – 10839; (b) J. S. Duncan, M. J. Zdilla, S. C. Lee, *Inorg. Chem.* **2007**, *46*, 1071 – 1080; (c) M. J. Zdilla, A. K. Verma, S. C. Lee, *Inorg. Chem.* **2011**, *50*, 1551 – 1562.
- [79] For selected papers on reduction of azobenzene by early transition-metal complexes: (a) F. A. Cotton, S. A. Duraj, W. J. Roth, *J. Am. Chem. Soc.* **1984**, *106*, 4749 – 4751; (b) P. L. Diaconescu, P. L. Arnold, T. A. Baker, D. J. Mindiola, C. C. Cummins, *J. Am. Chem. Soc.* **2000**, *122*, 6108 – 6109; (c) W. H. Monillas, G. P. A. Yap, L. A. MacAdams, K. H. Theopold, *J. Am. Chem. Soc.* **2007**, *129*, 8090 – 8091; (d) W. J. Evans, K. A. Miller, J. W. Ziller, *Angew. Chem. Int. Ed.* **2008**, *47*, 589 – 592; (e) Y. C. Tsai, P. Y. Wang, K. M. Lin, S. A. Chen, J. M. Chen, *Chem. Commun.* **2008**, 205 – 207; (f) W. J. Evans, C. A. Traina, J. W. Ziller, *J. Am. Chem. Soc.* **2009**, *131*, 17473 – 17481; (g) K. Kaleta, P. Arndt, T. Beweries, A. Spannenberg, O. Theilmann, U. Rosenthal, *Organometallics*. **2010**, *29*, 2604 – 2609.
- [80] For selected papers on reduction of azobenzene by lanthanide complexes: (a) W. J. Evans, D. K. Drummond, L. R. Chamberlain, R. J. Doedens, S. G. Bott, H. Zhang, J. L. Atwood, *J. Am. Chem. Soc.* **1988**, *110*, 4983 – 4994; (b) A. A. Trifonov, M. N. Bochkarev, H. Schumann, J. Loebel, *Angew. Chem. Int. Ed. Engl.* **1991**, *30*, 1149 – 1151; (c) Z. Hou, T. Koizumi, M. Nishiura, Y. Wakatsuki, *Organometallics*. **2001**, *20*,

3323 – 3328; (d) A. Kornienko, D. Freedman, T. J. Emge, J. G. Brennan, *Inorg. Chem.* **2001**, *40*, 140 – 145; (e) D. Turcitu, F. Nief, L. Ricard, *Chem. - Eur. J.* **2003**, *9*, 4916 – 4923; (g) W. J. Evans, T. M. Champagne, J. W. Ziller, *Organometallics.* **2007**, *26*, 1204 – 1211; (h) M. MacDonald, J. W. Ziller, W. J. Evans, *Inorg. Chem.* **2011**, *50*, 4092 – 4106; (i) C. A. P. Goodwin, N. F. Chilton, G. F. Vettese, E. M. Pineda, I. F. Crowe, J. W. Ziller, R. E. P. Winpenny, W. J. Evans, D. P. Mills, *Inorg. Chem.* **2016**, *55*, 10057 – 10067.

[81] For selected papers on reduction of azobenzene by main-group metal: (a) C. Cui, M. M. Olmstead, J. C. Fettinger, G. H. Spikes, P. P. Power, *J. Am. Chem. Soc.* **2005**, *127*, 17530 – 17541; (b) R. J. Wright, M. Brynda, J. C. Fettinger, A. R. Betzer, P. P. Power, *J. Am. Chem. Soc.* **2006**, *128*, 12498 – 12509; (c) S. J. Bonyhady, S. P. Green, C. Jones, S. Nembenna, A. A. Stasch, *Angew. Chem. Int. Ed.* **2009**, *48*, 2973 – 2977; (d) S. S. Sen, D. Kratzert, D. Stern, H. W. Roesky, D. Stalke, *Inorg. Chem.* **2010**, *49*, 5786 – 5788; (e) K. Takeuchi, M. Ichinohe, A. Sekiguchi, *J. Am. Chem. Soc.* **2011**, *133*, 12478 – 12481; (f) W. S. Ren, D. F. Gu, *Inorg. Chem.* **2016**, *55*, 11962 – 11970.

[82] S. M. Bellows, N. A. Arnet, P. M. Gurubasavaraj, W. W. Brennessel, E. Bill, T. R. Cundari, P. L. Holland, *J. Am. Chem. Soc.* **2016**, *138*, 12112 – 12123.

[83] A. R. Sadique, E. A. Gregory, W. W. Brennessel, P. L. Holland, *J. Am. Chem. Soc.* **2007**, *129*, 8112 – 8121.

[84] (a) R. Allmann, *The Chemistry of the Hydrazo, Azo and Azoxy Groups*; Wiley: New York, **1975**; Chapter 2; (b) C. J. Brown, *Acta Crystallogr.* **1966**, *21*, 146 – 152.

[85] E. D. Brady, D. L. Clark, D. W. Keogh, B. L. Scott, J. G. Watkin, *J. Am. Chem. Soc.* **2002**, *124*, 7007 – 7015.

[86] V. Kalyanaraman, S. S. Dua, C. N. R. Rao, M. V. George. *Tetrahedron Lett.* **1968**, *9*, 235 – 238.

[87] P. J. Chirik, *Nat. Chem.* **2009**, *1*, 520 – 522.

[88] M. Appl. "Ammonia" in *Ullmann's Encyclopedia of Industrial Chemistry* **2006** Wiley-VCH, Weinheim.

[89] (a) P. L. Holland, *Dalton Trans.* **2010**, *39*, 5415 – 5425; (b) I. Klopsch, E.Y. Yuzik-Klimova, S. Schneider, *Top. Organomet. Chem.* **2017**, *1* – 42.

- [90] W. J. Evans, M. Fang, G. L. Zucchi, F. Furche, J. W. Ziller, R. M. Hoekstra, J. I. Zink. *J. Am. Chem. Soc.* **2009**, *131*, 11195 – 11202.
- [91] M. Chiesa, E. Giamello, D. M. Murphy, G. Pacchioni, M. C. Paganini, R. Soave, Z. Sojka. *J Phys Chem B*. 2001, *105*, 497 – 505.
- [92] (a) R. Waterman, G. L. Hillhouse, *Can. J. Chem.* **2005**, *83*, 328 – 331; (b) S. Pfirrmann, C. Limberg, C. Herwig, R. Stößer, B. Ziemer, *Angew. Chem. Int. Ed.* **2009**, *48*, 3357 – 3361; (c) B. Horn, S. Pfirrmann, C. Limberg, C. Herwig, B. Braun, S. Mebs, R. Metzinger, *Z. Anorg. Allg. Chem.* **2011**, *637*, 1169 – 1174; (d) D. Zhu, I. Thapa, I. Korobkov, S. Gambarotta,; P. H. M. Budzelaar, *Inorg. Chem.* **2011**, *50*, 9879 – 9887; (e) C. Tsay, J. C. Peters, *Chem. Sci.* **2012**, *3*, 1313 – 1318; (f) S. J. Connelly, A. C. Zimmerman, W. Kaminsky, D. M. Heinekey, *Chem. Eur. J.* **2012**, *18*, 15932 – 15934; (g) R. Beck, M. Shoshani, J. Krasinkiewicz, J. A. Hatnean, S. A. Johnson, *Dalton Trans.* **2013**, *42*, 1461 – 1475; (h) W. H. Harman, T. P. Lin, J. C. Peters, *Angew. Chem. Int. Ed.* **2014**, *53*, 1081 – 1086; (i) Y. E. Kim, J. Kim, Y. Lee, *Chem. Commun.*, **2014**, *50*, 11458 – 11461; (j) Y. E. Kim, S. Oh, S. Kim, O. Kim, J. Kim,; S. W. Han,; Y. Lee, *J. Am. Chem. Soc.* **2015**, *137*, 4280 – 4283; (k) D. J. Charboneau, D. Balcells, N. Hazari, H. M. C. Lant, J. M. Mayer, P. R. Melvin, B. Q. Mercado, W. D. Morris, M. Repisky, H. W. Suh, *Organometallics*. **2016**, *35*, 3154 – 3162.
- [93] D. J. Mindiola, *Angew. Chem. Int. Ed.* **2009**, *48*, 6198 – 6200.
- [94] B. P. Stoicheff, *Can. J. Phys.* **1954**, *32*, 630 – 634.
- [95] (a) R. R. Schrock, *Acc. Chem. Res.* **2005**, *38*, 955 – 962; (b) Y. Nishibayashi, *Inorg. Chem.* **2015**, *54*, 9234 – 9247.
- [96] (a) J. S. Anderson, G. E. Cutsail, J. Rittle, B. A. Connor, W. A. Gunderson, L. Zhang, B. M. Hoffman, J. C. Peters, *J. Am. Chem. Soc.* **2015**, *137*, 7803 – 7809. (b) B. M. Hoffman, D. Lukoyanov, D. R. Dean, L. C. Seefeldt, *Acc. Chem. Res.* **2013**, *46*, 587 – 595.
- [97] M. J. Bezdek, I. Pappas, P. J. Chirik, *Top. Organomet. Chem.* **2016**, *60*, 1 – 21.
- [98] (a) T. Munisamy, R. R Schrock, *Dalton Trans.* **2012**, *41*, 130 – 137; (b) Y. Nishibayashi, *Inorg. Chem.* 2015, *54*, 9234 – 9247.
- [99] R. N. F. Thorneley, D. J. Lowe, *Metal Ions in Biology.* **1985**, *7*, 221–284.

- [100] (a) B. M. Hoffman, D. Lukoyanov, Z. Y. Yang, D. R. Dean, L. C. Seefeldt, *Chem. Rev.* **2014**, *114*, 4041–4062. (b) D. Lukoyanov, N. Khadka, Z. Y. Yang, D. R. Dean, L. C. Seefeldt, B. M. Hoffman, *J. Am. Chem. Soc.* **2016**, *138*, 10674–10683.
- [101] D. Lukoyanov, N. Khadka, D. R. Dean, S. Raugei, L. C. Seefeldt, B. M. Hoffman, *Inorg. Chem.* **2017**, *56*, 2233–2240.
- [102] Selected examples: (a) D. V. Yandulov, R. R. Schrock, *Inorg. Chem.* **2005**, *44*, 1103 – 1117 ; (b) J. D. Gilbertson, N. K. Szymczak, D. R. Tyler, *J. Am. Chem. Soc.* **2005**, *127*, 10184 – 10185; (c) P. Avenier, M. Taoufik, A. Lesage, X. Solans-Monfort,; A. Baudouin, A. de Mallmann, L. Veyre, J. M. Basset, O. Eisenstein, L. Emsley, E. A. Quadrelli, *Science*. **2007**, *317*, 1056 – 1060.
- [103] (a) F. Akagi, T. Matsuo, H. Kawaguchi, *Angew. Chem. Int. Ed.* **2007**, *46*, 8778 – 8781; (b) K. Ding, W. W. Brennessel, P. L. Holland, *J. Am. Chem. Soc.* **2009**, *131*, 10184 – 10185.
- [104] W. E. Piers, A. J. V. Marwitz, L. G. Mercier, *Inorg. Chem.* **2011**, *50*, 12252 – 12262.
- [105] L. J. Murray, W. W. Weare, J. Shearer, A. D. Mitchell, K. A. Abboud, *J. Am. Chem. Soc.* **2014**, *136*, 13502 – 13505.
- [106] A. J. L. Pombeiro *Rev. Port. Quim.* **1984**, *26*, 30 – 60.
- [107] K. Ding, A. W. Pierpont, W. W. Brennessel, G. Lukat-Rodgers, K. R. Rodgers, T. R. Cundari, E. Bill, P. L. Holland, *J. Am. Chem. Soc.* **2009**, *131*, 9471 – 9472.
- [108] T. R. Dugan, K. C. MacLeod, W. W. Brennessel, P. L. Holland, *Eur. J. Inorg. Chem.* **2013**, 3891 – 3897.
- [109] P. A. Rudd, N. Planas, E. Bill, L. Gagliardi, C. C. Lu, *Eur. J. Inorg. Chem.* **2013**, 3898 – 3906.
- [110] T. Takahashi, Y. Mizobe, M. Sato, Y. Uchida, M. Hidai, *J. Am. Chem. Soc.* **1980**, *102*, 7461 – 7467.
- [111] M. B. O'Donoghue, W. M Davis, R, R, Schrock, *Inorg Chem.* **1998**, *37*, 5149 – 5158.
- [112] K. C. Chew, W. Clegg, M. P. Coles, M. R. J. Elsegood, V. C. Gibson, A. J. P. White, D. J. Williams, *J. Chem. Soc. Dalton Trans.* **1999**, 2633 – 2640.

- [113] G. E. Bossard, D.C. Busby, M. Chang, T. A. George, S. D.A. Jr. Iske, *J Am Chem Soc.* **1980**, *102*, 1001 – 1008.
- [114] N. Lehnert, F. Tuczek, *Inorg. Chem.* **1999**, *38*, 1671 – 1682.
- [115] J. J. Warren, T. A. Tronic, J. M. Mayer, *Chem. Rev.* **2010**, *110*, 6961–7001.
- [116] P. Schollhammer, B. Didier, N. Le Grand, F. Y. Pétillon, J. Talarmin, K. W. Muir, S. J. Teat, *Eur. J. Inorg. Chem.* **2002**, 658 – 663.
- [117] J. Demasion, F. Hegelund, H. Bürger, *J. Mol. Struct.* **1997**, 413-414, 447 – 456.
- [118] (a) N. Lehnert, B. E. Wiesler, F. Tuczek, A H ennige, D. Sellmann, *J. Am. Chem. Soc.* **1997**, *119*, 8869 – 8878. (b) K. Fujisawa, N. Lehnert, Y. Ishikawa, K. Okamoto, *Angew. Chem.* **2004**, *116*, 5052 – 5055.
- [119] Y. Li, Y. Li, B. M. Wang, Y. Luo, D. W. Yang, P. Tong, J. F. Zhao, L. Luo, Y. H. Zhou, S. Chen, F. Cheng, J. P. Qu, *Nat. Chem.* **2013**, *5*, 320 – 326.
- [120] G. C. Bai, P. R. Wei, Douglas W. Stephan, *Organometallics.* **2005**, *24*, 5901 – 5908.
- [121] E. Kogut, H. L. Wiencko, L. Zhang, D. E. Cordeau, T. H. Warren, *J. Am. Chem. Soc.* **2005**, *127*, 11248 – 11249.
- [122] (a) D. Sellmann, A. Hille, A. Rösler, F. W. Heinemann, M. Moll, G. Brehm, S. Schneider, M. Reiher, B. A. Hess, W. Bauer, *Chem. Eur. J.* **2004**, *10*, 819 – 830; (b) C. T. Saouma, C. E. Moore, A. L. Rheingold, J. C. Peters, *Inorg. Chem.* **2011**, *50*, 11285 – 11287; (c) J. L. Crossland, C. G. Balesdent, D. R. Tyler, *Inorg. Chem.* **2012**, *51*, 439 – 445; (d) C. T. Saouma, C. C. Lu, J. C. Peters, *Inorg. Chem.* **2012**, *51*, 10043 – 54; (e) J. S. Anderson, M.-E. Moret, J. C. Peters, *J. Am. Chem. Soc.* **2013**, *135*, 534 – 537.
- [123] A. L. Chaney, E. P. Marbach, *Clin. Chem.* **1962**, *8*, 130 – 132.
- [124] C. Köthe, B. Braun, C. Herwig, C. Limberg, *Eur. J. Inorg. Chem.* **2014**, 5296 – 5303.
- [125] M. Fang, D. S. Lee, J. W. Ziller, R. J. Doedens, J. E. Bates, F. Furche, W. J. Evans, *J. Am. Chem. Soc.* **2011**, *133*, 3784 – 3787.
- [126] R. A. Bernheim, H. Batiz-Hernandez, *J. Chem. Phys.* **1964**, *40*, 3446 – 3447.

- [127] (a) N. Lee, T. Petrenko, U. Bergmann, F. Neese, S. DeBeer, *J. Am. Chem. Soc.* **2010**, *132*, 9715 – 9727. (b) K. M. Lancaster, K. D. Finkelstein, S. DeBeer, *Inorg. Chem.* **2011**, *50*, 6767 – 6774. (c) M. A. Beckwith, M. Roemelt, M. Collomb, C. DuBoc, T. Weng, U. Bergmann, P. Glatzel, F. Neese, S. DeBeer, *Inorg. Chem.* **2011**, *50*, 8397 – 8409.
- [128] P. Glatzel, U. Bergmann, *Coord. Chem. Rev.* **2005**, *249*, 65 – 95.
- [129] (a) U. Bergmann, C. R. Horne, T. J. Collins, J. M. Workman, S. P. Cramer, *Chem. Phys. Lett.* **1999**, *302*, 119 – 207. (b) U. Bergmann, J. Bendix, P. Glatzel, H. B. Gray, S. P. Cramer, *J. Chem. Phys.* **2002**, *116*, 2011 – 2015.
- [130] G. Bender, E. Pierce, J. A. Hill, J. E. Darty and S. W. Ragsdale, *Metallomics.* **2011**, *3*, 797 – 815; (b) G. Bender, T. A. Stich, L. Yan, R. D. Britt, S. P. Cramer, S. W. Ragsdale, *Biochemistry.* **2010**, *49*, 7516 – 7523.
- [131] S. Pfirrmann, C. Limberg, C. Herwig, C. Knispel, B. Braun, E. Bill, R. Stösser. *J. Am. Chem. Soc.* **2010**, *132*, 13684 – 13691.
- [132] B. Horn, C. Limberg, C. Herwig, S. Mebs, *Angew. Chem. Int. Ed.* **2011**, *50*, 12621 – 12625.
- [133] C. Yoo, S. Oh, J. Kim, Y. Lee, *Chem. Sci.* **2014**, *5*, 3853 – 3858.
- [134] National Institute of Standards and Technology.
<http://webbook.nist.gov/chemistry/>.
- [135] G. A. Lawrance, *Chem. Rev.* **1986**, *86*, 17 – 33.
- [136] W. D. Jones; A. D. Selmecky, *Organometallics.* **1992**, *11*, 889 – 893.
- [137] A. M. Thomas, B. L. Lin, E. C. Wasinger, T. D. P. Stack. *J. Am. Chem. Soc.* **2013**, *135*, 18912 – 18919.
- [138] N. A. Giffin, M. Makramalla, A. D. Hendsbee, K. N. Robertson, C. Sherren, C. C. Pye, J. D. Masuda, J. A. C. Clyburne, *Org. Biomol. Chem.* **2011**, *9*, 3672–3680.
- [139] A. Kermagoret, P. Braunstein. *Organometallics.* **2008**, *27*, 88 – 99.
- [140] V. W. Manner, T. F. Markle, J. H. Freudenthal, J. P. Roth J. M. Mayer, *Chem. Commun.* **2008**, 256–258.
- [141] S. Stoll, A. Schweiger, *J. Magn. Reson.* **2006**, *178*, 42 – 55.
- [142] G. R. Hanson, K. E. Gates, C. J. Noble, M. Griffin, A. Mitchell, S. Benson, *J.*

Inorg. Biochem. **2004**, *98*, 903–916.

[143] (a) W. Haberditzel, *Angew. Chem. Int. Ed. Engl.*, **1966**, *5*, 288; b) G. A. Bain, J. F. Berry, *J. Chem. Educ.* **2008**, *85*, 532.

[144] E. Bill, *julX, Program for Simulation of Molecular Magnetic Data*, Max-Planck Institute for Chemical Energy Conversion, Mülheim/Ruhr, **2008**.

[145] O. Kahn, *Molecular Magnetism*, VCH Publishers Inc., New York, **1993**.

[146] D. G. Huang, O. V. Makhlynets, L.L. Tan, S. C. Lee, E. V. Rybak-Akimova, R. H. Holm, *Inorg. Chem.* **2011**, *50*, 10070-10081.

[147] G. M. Sheldrick, *Acta Cryst.* **2015**, *A71*, 3-8.

[148] G. M. Sheldrick, *Acta Cryst.* **2015**, *C71*, 3-8.

[149] *X-RED*; STOE & CIE GmbH, Darmstadt, Germany, **2002**.

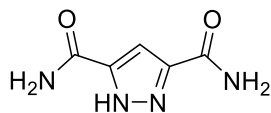
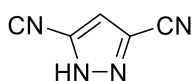
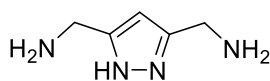
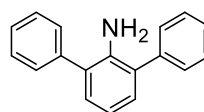
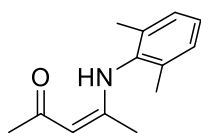
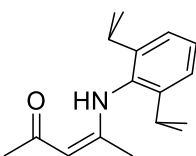
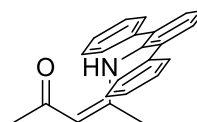
List of Abbreviations

2D	Two dimensions
Å	Angstrom (s) 10^{-10} m
Abs	Absorber (XAS)
Ac	Acetyl
cat	catalyst
COSY	Correlation spectroscopy
d	Doublet (NMR)
DB18C6	Dibenzo(18-crown-6)
DCM	Dichloromethane
DFT	density functional theory
DIAD	1,2-diisopropyl azodicarboxylate
DI	Diamagnetic impurity
DME	1,2-Dimethoxyethane
DMSO	Dimethyl Sulfoxide
EA	Elemental analysis
EI	Electron ionization
EPR	Electron Paramagnetic Resonance
eq.	equivalent(s)
ESI	Electrospray Ionization
Et	Ethyl
g	landé <i>g</i> - factor
galvinoxyl radical	2,6-Di-tert-butyl- α -(3,5-di-tert-butyl-4-oxo-2,5-cyclohexadien-1-ylidene)-p-tolyloxy
HMBC	Heteronuclear Multiple Bond Correlation
HSQC	Heteronuclear Single Quantum Coherence
<i>i</i> pr	<i>iso</i> -propyl
<i>J</i>	coupling constant
LAH	lithium aluminum hydride
[Lut-H] ⁺ OTf	[2,6-Lutidine]trifluoromethanesulfonate
[Lut-H] ⁺ BF ₄	[2,6-Lutidine]tetrafluoroboric
m	medium (IR)
M	Molar, Lmol ⁻¹
m/z	mass per charge (MS)

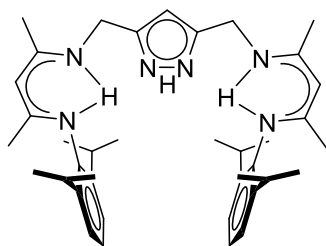
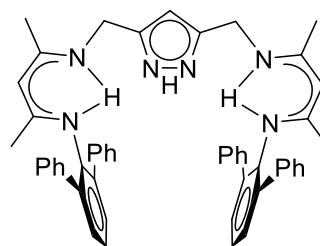
Me	Methyl
MeOTf	Methyl trifluoromethanesulfonate
Min	minutes
MS	Mass Spectrometry
NaBARf	Sodium Tetrakis[3,5-bis(trifluoromethyl)phenyl]borate
NMR	Nuclear Magnetic resonance
NOESY	Nuclear Overhauser Effect Spectroscopy
OAc	Acetate
OTf	Trifluoromethanesulfonate
<i>PI</i>	Paramagnetic impurity
pH	Proton concentration in aqueous solution
Ph	Phenyl group
ppm	parts per million
Pz	pyrazole
RT	Room temperature (25°C)
s	singlet (NMR), Strong (IR)
SWV	square wave voltammetry
t	time
^t Bu	Tert-buthyl
^t BuOK	Potassium tert-butoxide
TEMPO	2,2,6,6-tetramethyl-piperidine-1-oxyl
TEMPO-H	1-hydroxyl-2,2,6,6-tetramethyl-piperidine
TBP	2,4,6-tert-butylphenoxy radical
THF	Tetrahydrofuran
TIP	Temperature independent paramagnetic
UV-vis	Ultraviolet-visible spectroscopy
<i>V</i>	volume
VT	Variable temperature
V2C	Valance to Core
w	weak(IR)

Formula Overview

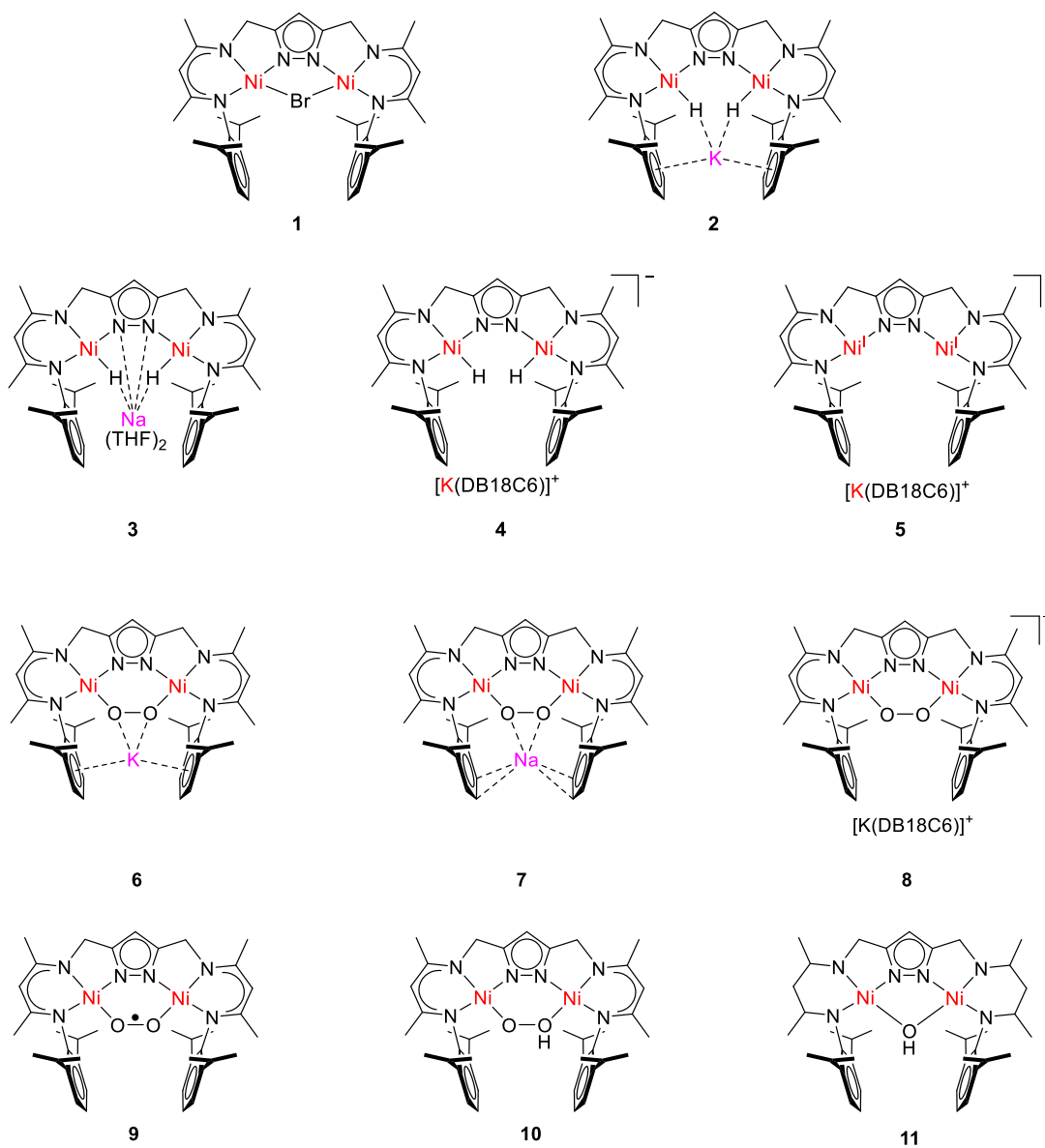
Ligand Precursors

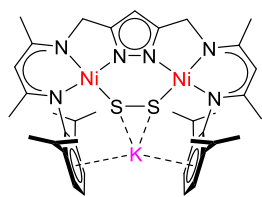
**I****II****III****IV****V****VI****VII**

Ligands

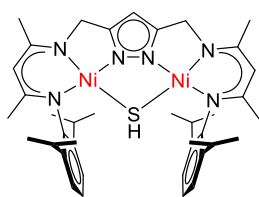
**H₃L¹****H₃L²**

Complexes

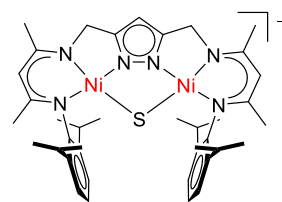




12

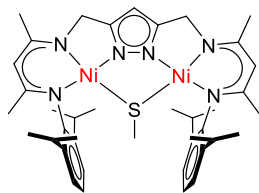


13

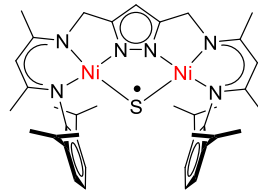


$[K(THF)_3]^+$

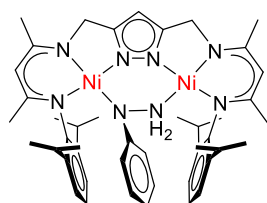
14



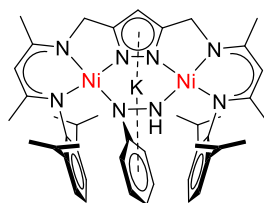
15



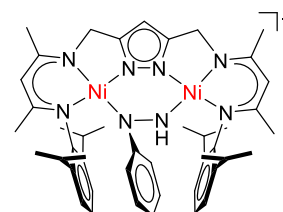
16



17

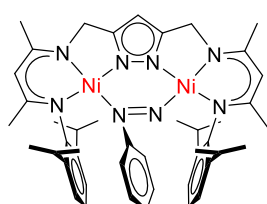


18

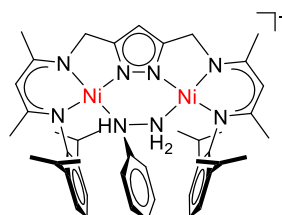


$K(DB18C6)^+$

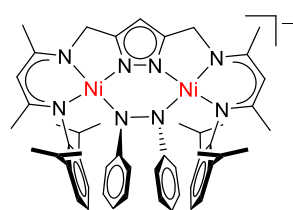
19



20

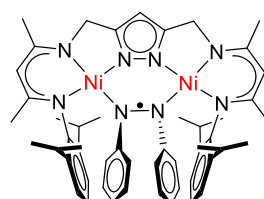


21

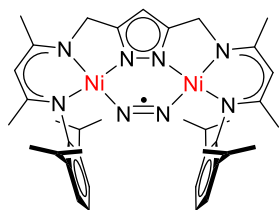


$K(DB18C6)$

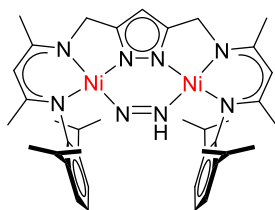
22



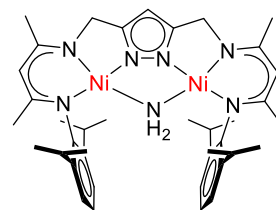
23



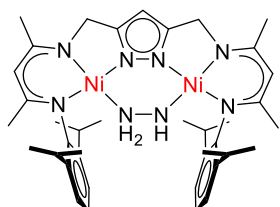
24



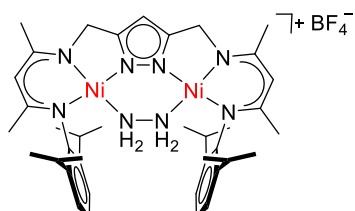
25



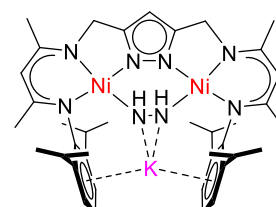
26



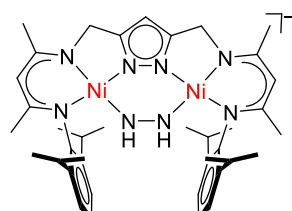
27



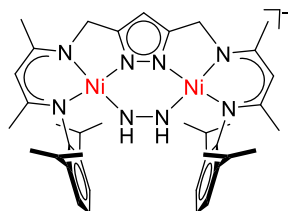
28



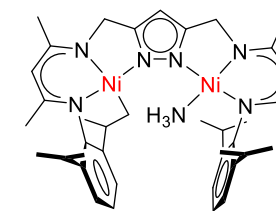
29

[K(DB18C6)]⁺

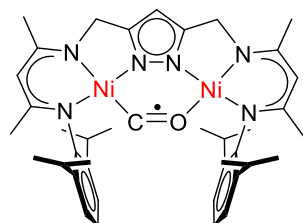
30

[K(Cryptand)]⁺

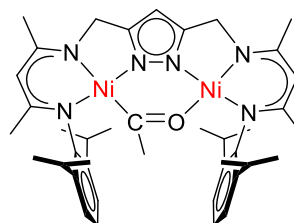
31



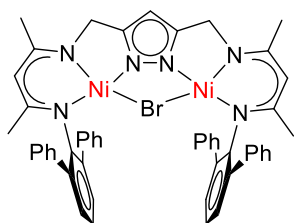
32



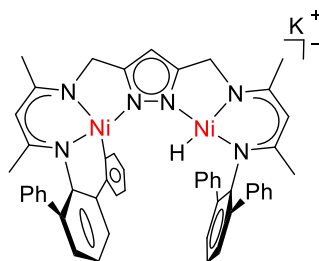
33



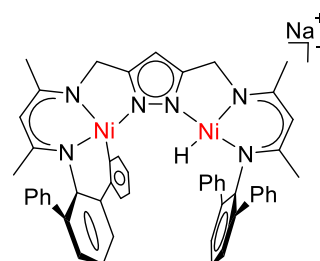
34



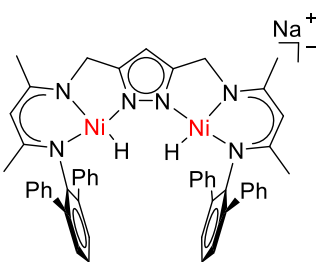
35



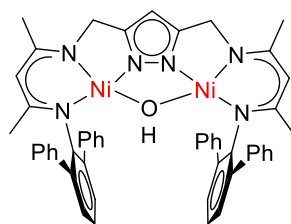
36



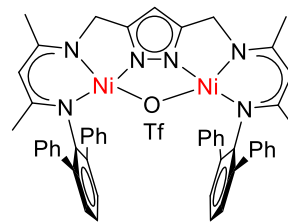
37



38



39



40

Scientific Contribution

Posters

- **Dioxygen Binding to a Dinickel(II) Dihydride Complex and Redox Interconversion of the μ -1,2-Peroxo and Superoxo Dinickel Intermediates** “EICC 4th EuChemS Inorganic chemistry conference” Copenhagen, Denmark, 2 - 5th July 2017; **Peng-Cheng Duan**, *et.al.*, Franc Meyer*
- **Dioxygen Binding to a Dinickel(II) Dihydride Complex and Redox Interconversion of the μ -1,2-Peroxo and Superoxo Dinickel Intermediates** 9th “Göttinger Chemie-Forum 2017” Göttingen, Germany; **Peng-Cheng Duan**, *et.al.*, Franc Meyer*

Publication

Ph.D study period

1. Pairwise H₂/D₂ Exchange and H₂ substitution at a Bimetallic Dinickel(II) complex Featuring Two terminal Hydrides
Dennis H. Manz[‡], **Peng-Cheng Duan**[‡], Sebastian Dechert, Serhiy Demeshko, Rainer Oswald, Michael John, Ricardo Mata* and Franc Meyer*
J. Am. Chem. Soc. **2017**, 139, 16720 – 16731.
2. Reductive O₂ Binding at a Dihydride Complex Leading to Redox Interconvertible μ -1,2-Peroxo and μ -1,2-Superoxo Dinickel(II) Intermediates
Peng-Cheng Duan, Dennis H. Manz, Sebastian Dechert, Serhiy Demeshko, and Franc Meyer*
J. Am. Chem. Soc. **2018**, *Revised*
3. Dichalcogen Binding to the Dinickel Dihydrido and stepwise transformation to the Sulfide-Ligand-Radical.
Peng-Cheng Duan, Sebastian Dechert, Serhiy Demeshko and Franc Meyer*
Manuscript

4 N₂ to NH₃ Conversion in the Dinickel Cofactor

Peng-Cheng Duan, Dennis H. Manz, Van Kuiken Benjamin, Sebastian Dechert, Serhiy Demeshko, Van Gastel Maurice, Eckhard Bill, Serena DeBeer and Franc Meyer*

Manuscript

5 Syntheses, characterization and interconversion of Dinuclear Nickel Phenylhydrazine Complexes.

Peng-Cheng Duan, Sebastian Dechert and Franc Meyer*

Manuscript

6 Interconversion in the Mono- and Dihydride Dinickel Complexes and Reactivity

Peng-Cheng Duan, Sebastian Dechert, and Franc Meyer*

Manuscript

Master study period

1. Group 11 metal pyrazolato trigonal prismatic nanocages showing a preferential encapsulation of sulfur over hydrocarbons

Peng-Cheng Duan, Zhao-Yang Wang, Guang Yang* and Raphael G. Raptis*

Dalton Transactions, **2013**, 42, 14951 – 14954.

2. Relaying Isomerism from Ligands to Metal Complexes: Synthesis and Structures of Four Isomeric Binary Silver(I) 3,5-Dibutyl-1,2,4-triazolates

Guang Yang*, **Peng-Cheng Duan**, Kai-Ge Shi and Raphael G. Raptis

Crystal growth & design, **2011**, 12, 1882 – 1889.

3. Synthesis and crystal structures of copper(II) and silver(I) complexes of a biphenyl-bridged bipyrazolyl ligand

Peng-Cheng Duan, Zhan-Dong Huang, Fang-Fang Zhang and Guang Yang*

Transition Met Chem, **2012**, 37, 595 – 600.

Acknowledgement

It is hard to believe that I have finished four years in Göttingen already. During these times, happiness, excitement, depression and anger passed by. But time moves on, so do I. It is time to thank the many helpful hands that have played an important part, directly or indirectly, in the successful completion of my thesis. It fills me with immense pleasure to be able to express my gratitude. Yet, it is difficult to express my gratitude completely and I make a humble attempt while fighting with many different emotions.

First, I would like to thank my supervisor Prof. Dr. Franc Meyer offering the chance to work in his wonderful working group. I appreciated his motivating guidance and the great scientific freedom. Thank you for creating a good working atmosphere and providing excellent lab equipment. He gave me courage and confidence in my full time of my Ph.D study. I also would like to say thank to my second supervisor Prof. Dr. Sven Schneider.

The other members of my thesis committee and examination board are gratefully acknowledged for spending their precious time with my thesis.

From our group, I am thankful for their help of Dr. Sebastian Dechert, Dr. Anne Schöber and Anna Kölpin, for their assistance in collecting X-ray diffraction data, solving the structures and analyzing the results. Especially Dr. Sebastian Dechert has taken so much time to check my stupid small and bad quality crystals. Furthermore, he spent times for collecting and analyzing the rRaman datas and DFT calculating. I would like to thank Dr. Alexander Gers-Barlag for the maintenance of ESI-MS; to Dr. Alexander Gers-Barlag and Eleonora Ferreti for their assistance of taking care of the glove box; to Marie Bergner, Dr. Claudia Stückl, Dr. Van Gastel Maurice and Dr. Eckhard Bill for their help in EPR-related concerns; to Van Kuiken Benjamin for his help in XES/XAS-related concerns; to Dr. Michel John and Ralf

Schöne for his help in NMR-related concerns; to Dr. Serhiy Demeshko for magnetization measurements and detailed explanations; to Jörg Teichgräber, Jiapei Du and Marcus Thater for cyclic voltammetry measurement and to Andreas Schwarz for assistance in lab-related questions; to Britta Müller, Peter Unger and Dr. Claudia Stückl for handling of administrative issues. I would also like to acknowledge all people from the NMR and MS facilities, the electrical, mechanical glass workshops.

I would like to say thanks to all the past and present members in Prof. Dr. Franc Meyer's working group, especially to my laboratory mates Dr. Tongxun Guo, Dr. Jin Tong, Dr. Dennis. H Manz, Dr. Claudia Kupper, Pierre Goursot, Stefan Resch, Andreas Schwarz and Ming Li for their daily help. For corrections, suggestions and linguistic improvements of this work, I would like to thank Eleonora Ferretic, Joanne Wong, Munmun Ghosh, Jana Lücken, Pierre Goursot, Stefan Resch, Roland Alexander Schulz and Keno Hennecke.

I am particularly grateful for the financial support from the Chinese Scholarship Council. Finally, I am very gratefully for my family and friends for their love. Thanks for their support and encouragement during the preparation of this work.

Curriculum Vitae

Personal Data

Name	Peng-Cheng Duan
Date of Birth	21 st January 1988
Place of Birth	Huangshi, Hubei
Nationality	Chinese

Education

10/2013-Present	PhD candidate , Institute of Inorganic Chemistry, University of Göttingen, Germany Supervisor: Prof. Dr. Franc Meyer Thesis: A Dinuclear Dihydride complex for Bimetallic Reductive Activation and Transformation of a Range of Inert Substrates
09/2010-06/2013	Master in Applied Chemistry, College of Chemistry and Molecular Engineering, Zhengzhou University, China Supervisor: Prof. Dr. Guang Yang Thesis: Syntheses, Structure and Host-Guest Chemistry Property Research of Complexes Based on Coinage-metals and bipyrazolyl ligands (Note:Excellent)
09/2006-06/2010	Bachelor in Science and Engineering of Materials, Henan University of Technology, Zhengzhou, China Supervisor: Prof. Dr. Shi-Kai Liu Thesis: Syntheses Cu ₂ O nanoparticles by hydrothermal method (Note:Excellent)

Work and training experiences

04/2015-05/2015	Teaching assistant for biochemistry practical experiments in Institute of Inorganic Chemistry, University of Göttingen, Germany
08/2015-10/2015	Supervisor for Master student, University of Göttingen, Germany
04-2017	Cooperation with MPI-CEC Max Planck institute for Chemical Energy Conversion in Mülheim (Ruhr)

Instruments Skill

ESI-MS, NMR, IR, UV-vis, Luminescence and Electrochemistry measurement and data analysis. Taking care of and using glove box as well as Schlenk technology. Shelxl and Wingx date analysis

Selected Awards and Honors**10/2013-9/2017**

Financial Support from China Scholarship Council

2013

National Postgraduate Scholarship, Ministry of Education, P. R. China

Outstanding Graduate School of Zhengzhou University

Outstanding Diploma thesis

2012

Scholarship for Outstanding Student of Zhengzhou University

Excellent Student Union Leader Award of Zhengzhou University

Excellent Student Leader Award of Zhengzhou University

Top 100 Research Award of Zhengzhou University

2011

Excellent Student Leader Award of Zhengzhou University